ISSN 0386-5878
Technical Report
of PWRI No.4279

PROCEEDINGS OF THE 29th U.S. – JAPAN BRIDGE ENGINEERING WORKSHOP

Tsukuba, Japan
November 11, 12 and 13, 2013

CENTER FOR ADVANCED ENGINEERING STRUCTURAL ASSESSMENT AND RESEARCH
PUBLIC WORKS RESEARCH INSTITUTE
Incorporated Administrative Agency

1-6, Minamihara, Tsukuba-shi, Ibaraki-ken, 305-8516 Japan

Opinions, findings, conclusions and recommendations expressed in the papers contained in this publication are those of the author(s).

Technical Report
of PWRI No.4279

PROCEEDINGS OF THE 29th U.S. – JAPAN BRIDGE ENGINEERING WORKSHOP

By

Editor: Hideaki Nishida

Synopsis:

The proceeding documents the results of the 29th U.S. – Japan Bridge Engineering Workshop which was held at Tsukuba, Japan, on November 11, 12, and 13, 2013, as a part of the activities of the Panel on Wind and Seismic Effects, UJNR. The Workshop was organized by Task Committee G "Transportation System" (U.S. side chair: Dr. W. Philip Yen, FHWA, Japan side chair: Mr. Hiroshi Matsuura, CAESAR, PWRI) of the Panel.

Key Words: Bridge, Design, Construction, Maintenance, Seismic, UJNR

PREFACE

The 29th US-Japan Bridge Engineering Workshop is a continuation of a series of technical interchanges between the United States and Japan on all topics related to bridge engineering. This series of workshops has been conducted under the auspices of Task Committee "G" of the US-Japan Panel on Wind and Seismic Effects, which is one of the 18 panels making up the United States-Japan Cooperative Program in Natural Resources (UJNR). The previous workshops are indicated below.

1st	February 20-23, 1984	Tsukuba Science City, *Japan*
2nd	August 19-20, 1985	San Francisco, California, *United States*
3rd	May 8-9, 1987	Tsukuba Science City, *Japan*
4th	May 11-12, 1988	San Diego, California, *United States*
5th	May 9-10, 1989	Tsukuba Science City, *Japan*
6th	May 7-8, 1990	Lake Tahoe, Nevada, *United States*
7th	May 8-9, 1991	Tsukuba Science City, *Japan*
8th	May 11-12, 1992	Chicago, Illinois, *United States*
9th	May 10-11, 1993	Tsukuba Science City, *Japan*
10th	May 10-11, 1994	Lake Tahoe, Nevada, *United States*
11th	May 30-31, 1995	Tsukuba Science City, *Japan*
12th	October 29-30, 1996	Buffalo, New York, *United States*
13th	October 2-3, 1997	Tsukuba Science City, *Japan*
14th	November 3-4, 1998	Pittsburgh, Pennsylvania, *United States*
15th	November 9-10, 1999	Tsukuba Science City, *Japan*
16th	October 2-4, 2000	South Lake Tahoe, Nevada, *United States*
17th	November 12-14, 2001	Tsukuba Science City, *Japan*
18th	October 22-24, 2002	St. Louis, Missouri, *United States*
19th	October 27-29, 2003	Tsukuba Science City, *Japan*
20th	October 4-6, 2004	Washington, DC, *United States*
21st	October 3-5, 2005	Tsukuba Science City, *Japan*
22nd	October 23-25, 2006	Seattle, Washington, *United States*
23rd	November 5-7, 2007	Tsukuba Science City, *Japan*
24th	September 22-27, 2008	Minneapolis, Minnesota, *United States*
25th	October 19-21, 2009	Tsukuba Science City, *Japan*
26th	September 20-22, 2010	New Orleans, Louisiana, *United States*
27th	November 7-9, 2011	Tsukuba Science City, *Japan*

28th	October 8-10, 2012	Portland, Oregon, *United States*
29th	November 11-13, 2013	Tsukuba Science City, *Japan*

The steering committee for the 29th US-Japan Bridge Engineering Workshop consisted of Hiroshi Matsuura, Phillip Yen, David Sanders, and Hideaki Nishida.
The workshop was held at the NILIM and the CAESAR, PWRI, in Tsukuba, Japan. The 2-1/2 day workshop focused on: 1) Seismic and Tsunami, 2) Maintenance, 3) Inspection, 4) Retrofit and Repair Work, 5) Design, and 6) Construction. Fourteen participants from the US and twenty-eight participants from Japan attended the workshop who were arranged by both T/C chairs in terms of the focused themes. The papers contained within this proceeding are the papers that were presented at the workshop (19 papers from the Japan side and 15 papers from the US side).

In addition to the workshop, there was a bridge study held after the workshop, November 13-15, 2013, visiting bridge sites:

- Seismic Retrofit Bridges, Chamagawa Bridge (Honshu-Shikoku Bridge Expwy(HSBE)), Higashi-Kobe Ohhashi Bridge (Hanshin Expwy)
- Rehabilitated Bridges, Kameura Viaduct (HSBE), Dojima Ohhashi Bridge(City of Osaka, this bridge has a plan of rehabilitation)
- Bridges which were designed or constructed by some unique concepts, Tonegawa Viaduct (Metropolitan Inter-city Expwy, constructed by Kanto Regional Development Bureau), Ebie JCT and Sambo JCT (Hanshin Expwy)
- Long span Bridges, Ohnaruto Bridge and Akashi Kaikyo Bridge (HSBE)

ACKNOWLEDGEMENTS
There are many people that made the 29th US-Japan Bridge Engineering Workshop a success. I really appreciate cooperation of Honshu-Shikoku Bridge Expressway, Hanshin Expressway, City of Osaka and Kanto Regional Development Bureau.

Editor: Hideaki Nishida, Senior Researcher, Bridges and Structures Research Group, Center for Advanced Engineering Structural Assessment and Research (CAESAR), Public Works Research Institute (PWRI)

TABLE OF CONTENTS
29th US-Japan Bridge Engineering Workshop
Tsukuba, Ibaraki November 11 to 13, 2013

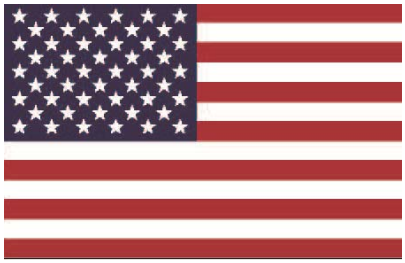

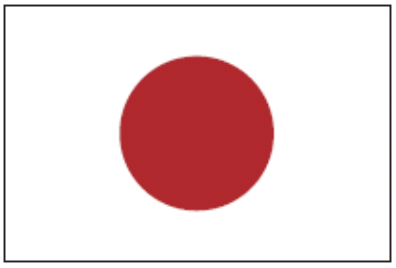

29th US-Japan

Bridge Engineering Workshop

Workshop Program

29th U.S.-JAPAN BRIDGE ENGINEERING WORKSHOP
PROGRAM SCHEDULE

November 11, 12 and 13, 2013
Tsukuba, Japan

November 11th (Monday) … Day 1

9:00- 9:30 **Opening Session (Conference Hall)**
Moderators: Hideaki Nishida & David Sanders
Welcome Remarks: Taketo Uomoto (Chief Executive, PWRI)
Remarks: W. Phillip Yen (Chairman for the U.S.A Side)
Remarks: Hiroshi Matsuura (Chairman for the Japan Side)

9:40-11:30 (110 min.) **Session 1: Seismic and Tsunami1 (Conference Hall)**
Moderators: Shigeki Unjoh & Ian Buckle

1. Kenji Kosa — Tsunami Force on Bridge Comparison of Two Wave Types by Experimental Test
2. Mark Yashinsky — Recent Changes to Seismic Design Practice in California
3. Hisashi Nakao — Numerical Assessment of Tsunami-induced Effect on Bridge Behavior
4. Chris Higgins — Hybrid Testing of a Prestressed Girder Bridge to Resist Wave Forces
5. Hidekazu Hayashi — Study on Tsunami Wave Force Acting on a Bridge Superstructure

11:30-11:50 **Photograph (Entrance of NILIM Main Building)**

11:50-12:50 **Lunch**

12:50-14:20 (90 min.) **Session 2: Maintenance (Conference Hall)**
Moderators: Yoshitomi Kimura & Raimondo Betti

1. Bruce Johnson — A comprehensive Bridge Preservation Program to Extend Service Life
2. Tsuyoshi Kosugi — Investigation and Countermeasures for Fatigue Cracks that Emerged on the Finger Joint of the Cable-Stayed Bridge "Tsurumi-Tsubasa Bridge"
3. Hannah Cheng — Preliminary Seismic Considerations for Pulaski Skyway Rehabilitation Project
4. Yuichi Ishikawa — Development of Fast Accelerated Set Concrete Application for Repairing the Deteriorated Reinforced Concrete Decks

14:20-14:40 **Coffee Break**

14:40-16:30 (110 min.) **Session 3: Inspection (Conference Hall)**
Moderators: Takashi Tamakoshi & Chris Higgins

1. Masahiro Shirato — Bridge Inspection Standards in Japan and US
2. Raimondo Betti — Non-Destructive Monitoring and Active Prevention of Corrosion in Suspension Bridge Main Cables
3. Hidetaka Honma — Soundness Evaluation of Prestressed Concrete Structures by Vibration Measurement
4. Ali Maher — Concrete Bridge Deck Condition Assessment using Robotic System Rabit
5. Masato Matsumoto — Non-Destructive Bridge Deck Assessment using Image Processing and Infrared Thermography

18:30 Reception hosted by Chief Executive of PWRI at The Espoir
http://www.sansuitei.jp/espoir.php

November 12th (Tuesday) … Day 2

9:00-10:30 (90 min.) **Session 4: Retrofit and Repair Work (Conference Hall)**
Moderators: Jun Murakoshi & Mark Yashinsky

1. Bijan Khaleghi — The Skagit River Bridge Collapse and Recovery Plan
2. Tomonobu Tokuchi — Repair Works on a Composite Girder Cable-Stayed Bridge damaged by Ship Collision (Binh Bridge in Vietnam)
3. Mark Reno — Incorporating Buckling Restrained Braces (BRB) as part of the Auburn-Foresthill Bridge Seismic Retrofit
4. Eiki Yamaguchi — Load-carrying Capacity of Corroded End Cross-girder

10:30- 10:50 **Coffee Break**

10:50- 12:20 (90 min.) **Session 5: Design1 (Conference Hall)**
Moderators: Toshiaki Nanazawa & Bijan Khaleghi

1. Yusuke Honjo — Which uncertainty (or error) is the most critical in geotechnical design
2. Tony Allen — 2010 Maule Chile Earthquake wall performance and its application to improvement of the AASHTO LRFD seismic wall design specifications
3. Hideaki Nishida — The Structural Design of Pile Foundations Based on LRFD for Japanese Highways
4. Jun Murakoshi — Effect of Deck Plate Thikness of Orthotropic Steel Deck on Fatigue Durability

12:20-13:20 **Lunch**

13:20- 15:10 **Session 6: Seismic and Tsunami2 (Conference Hall)**
(110 min.) Moderators: Takaaki Kusakabe & Bruce Johnson

1.	Masahiro Shirato	Concepts for Tsunami-Resistant Design Criteria for Coastal Bridges
2.	Ian Buckle	Quantifying the Seismic Resilience of Highway Networks using a Loss-estimation Tool
3.	Masatsugu Shinohara	Seismic Requirements for Laminated Elastomeric Bearings and Test Protocol for Verification
4.	Peter Dusicka	Cyclic Loading Protocol for Bridge Columns subjected to Subduction Mega Earthquakes
5.	Shojiro Kataoka	Preliminary Analysis on Seismic Input Loss at a Pile Foundation

15:10- 15:30 **Coffee Break**

15:30-16:50 **Breakout Session**
(80 min.) **Group A Seismic Engineering (Conference Hall)**
Moderators: Jun-ichi Hoshikuma & David Sanders
Group B Maintenance (ICHARM Auditorium)
Moderators: Hiroshi Matsuura & Phillip Yen

18:30 Reception hosted by the U.S. Delegation at The Rogairo

November 13th (Wednesday) … Day 3

9:00-11:30 (150 min.) **Session 7: Construction and Design2 (Conference Hall)**
Moderators: Masahiro Ishida & Mark Reno

1. Wei-huei "Phil" Yen	Performance of Accelerated Bridge Construction Connection in Bridges subjected to Extreme Events (NCHRP DOMESTIC SCAN 11-02)
2. Ryohei Nakamura	Development and Design of New Steel Pipe Integrated Pier with Shear Link
3. David Sanders	A Precast, Pretensioned, Rocking Bridge Bent for Rapid Construction and High Seismic Performance
4. Kiyoshi Ono	An Experimental Study on Seismic Performance of Hybrid Steel piers with Vertical Ribs Made from SBHS700
5. Jamie Padgett	A New Model for Sustainable Solutions to Bridge Infrastructure subjected to Multiple Threats (SSIMT)
6. Hiroyuki Nagareta	A Design, Construction of the Socket Anchoring System between Steel Pier and the Foundation in MORIGUCHI JCT
7. Bijan Khaleghi	Seismic Performance of Precast Concrete Bents used for Accelerated Bridge Construction

11:30-12:00 (30 min.) **Closing Session (Conference Hall)**
Moderators: Hideaki Nishida& David Sanders

Settlement of Resolution
Remarks: W. Phillip Yen (Chairman for the U.S.A Side)
Closing Remarks: Hiroshi Matsuura (Chairman for the Japan Side)

12:00-13:00 **Lunch**

13:00- **US Delegation:**
Group A Short Course of Bridge Study
Group B NILIM / FHWA / CAESAR / DOT meeting

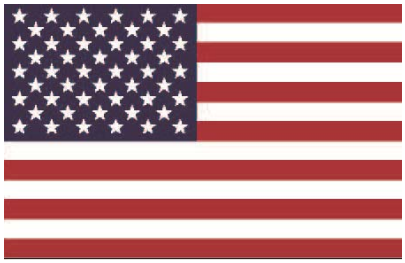

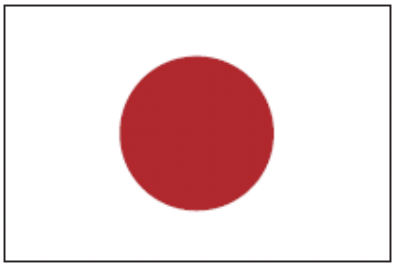

29th US-Japan

Bridge Engineering Workshop

Session 1

Seismic and Tsunami1

TSUNAMI FORCE ON BRIDGE COMPARISON OF TWO WAVE TYPES BY EXPERIMENTAL TEST

Kenji Kosa[1]

Abstract

Many bridges were washed away by tsunami due to Great East Japan Earthquake and it is significant to study how to evaluate wave force on bridge girder. The author firstly summarized that tsunami mainly shows steady flow shape, based on the video and photo recording tsunami along Kesen River. Besides, 1~3m waves are also found at surge front and water surface of steady flow. Afterwards, the experiments simulating bore wave and steady flow are conducted to study the characteristics of wave shape and horizontal wave forces on bridge girder. As a result, it is found that with same wave heights, wave force of broken bore wave is larger than un-broken bore wave and with similar inundation depths, the wave force of broken bore wave (prototype: inundation depth 20m, static water 7.5m, bore wave height 12.5m) is much greater than steady flow (prototype: inundation depth 17.5m).

Introduction

The 2011 Tohoku Earthquake, known as the Great East Japan Earthquake as well, occurred at 2:46 p.m. (JST) on March 11th 2011 with a magnitude 9.0. It was one of the most powerful earthquakes to have hit Japan. Besides that, the earthquake caused an extremely destructive tsunami which induced an extensive loss in Tohoku region. After the tsunami damage, the author carried out a reconnaissance visit to the coast of Rikuzentakata region and observed outflow condition of bridges. As illustrated in **Fig. 1**, in the tsunami affecting area drawn by Geospatial Information Authority of Japan, the 10 of 26 bridges across Kesen, Kawahara and Hamada Rivers were washed away and particularly all the three bridges across the widest Kesen River flowed out. Therefore the author tried to observe and draw the tsunami wave shape running along

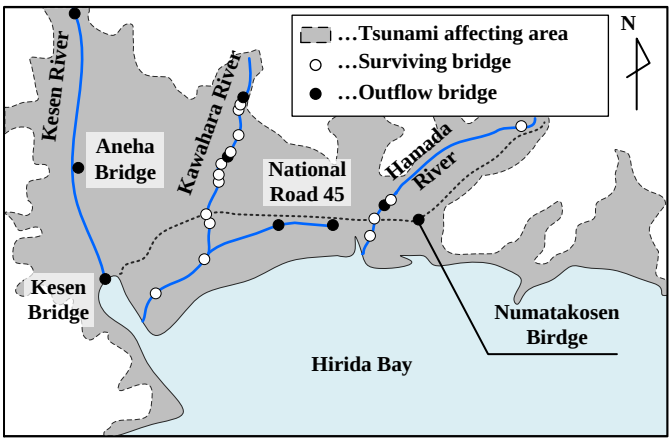

Fig.1 Tsunami Damage in Rikuzentakata Area

[1] Ph.D, Prof, Dept. of Civil Eng, Kyushu Institute of Technology

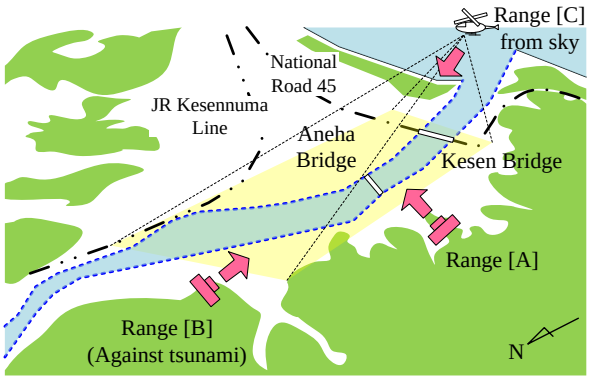

Fig.2 Photo or Video Ranges

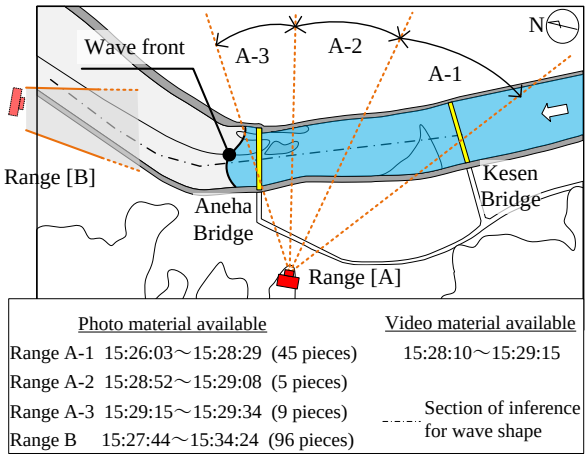

Fig.3 Introduction of Photo and Video Materials

Fig.4 Photo From Range A

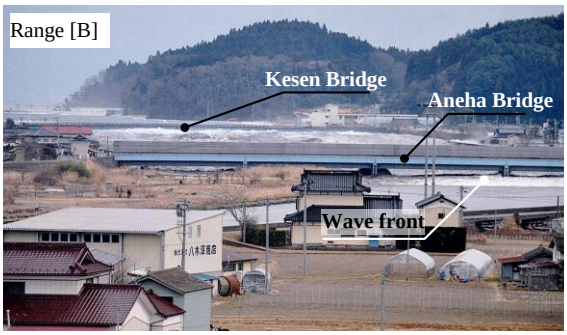

Fig.5 Photo From Range B

Kesen River by using the photos and videos recording tsunami.

During the field survey, the author collected the photos/videos recording tsunami along Kesen River. As shown in Fig. 2, three kinds of photos/video are used to draw wave shape. The photos of Range A were shot from upstream of Aneha Bridge and the photos of Range B were shot from the left bank of Kesen River. The video of Range C was shot by the Police of Iwate Prefecture in helicopter. The detailed camera angles and shooting time spans are given in **Fig. 3**. From Range A, the tsunami wave between Aneha and Kesen Bridge can be observed (**Fig. 4**) and the variation of wave height near Kesen Bridge can be estimated. From Range B, the tsunami surge front is able to be observed (**Fig. 5**), so the shape of surge front and the comparison of wave heights at Aneha and Kesen Bridges can be known. The shooting time of video from Range C is a little later than Range A and B. In the video, the surge front has passed Aneha Bridge (**Fig .6**). With the research of above photos and videos, the tsunami wave shape and flow velocity are evaluated.

Firstly, the flow velocity of surge front is estimated many times and it is computed by the ratio of flow distance and time span between two locations. As shown in **Fig. 7**, flow velocity is estimated at eight intervals ([1]~[2], [2]~[3], ⋯), and the ave. velocity is about 5~6m/s.

Fig.6 Video from Range C

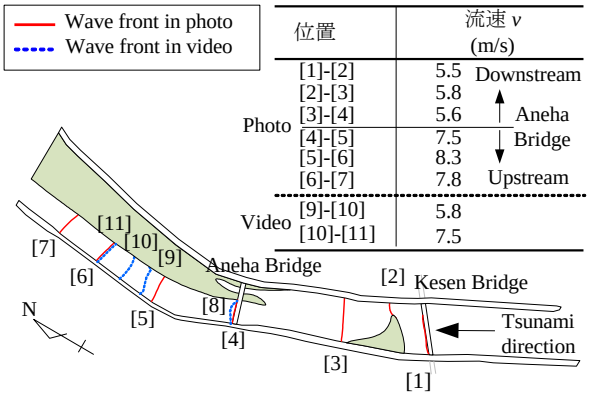

Fig.7 Wave Front and Velocity

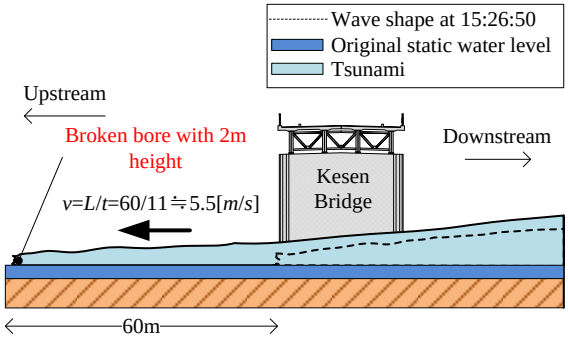

Fig.8 Shape of Wave Front

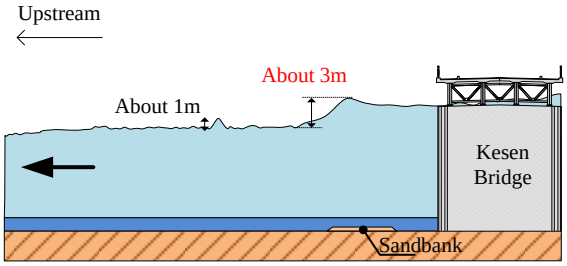

Fig.9 Wave Shape ahead of Kesen Bridge

Besides that, with the use of photos shot at Range A, the surge front of tsunami at location of Kesen Bridge is able to be drawn (**Fig. 8**). It is notable that the surge front kept the broken bore wave shape with 2m height. Besides, the flow velocity is estimated about 5.5m/s. As time went on, as plotted in **Fig .9**, when the water level reached to the bottom of Kesen Bridge, the 1m~3m small waves can be noted in front of Kesen Bridge and these waves were caused by the abrupt change of riverbed level. Further, the wave height at this time is estimated about 8.0m. With the method of wave shape estimation in **Fig. 8** and **Fig. 9**, the general wave shape from surge front to Kesen Bridge is able to be drawn roughly. As plotted in **Fig. 10**, the surge front just passed through Aneha Bridge with 2.0m height. On the other hand, the general wave shape from surge front to Kesen Bridge shows steady flow because the water surface gradient is computed as 1/85, which is a relatively small value. Therefore, according the observation of real tsunami, it is concluded that tsunami wave shows steady flow shape while the 1~3m small waves happens because of level change of riverbed.

Finally, the tsunami images from 15:28:23 to 15:30:52 before and after outflow of Kesen Bridge are illustrated in **Fig. 11**. It is obvious that the tsunami overflowed Kesen Bridge with a small speed, which was steady flow shape. By comparing the lamp positions at 15:29:36 and 15:30:52, it is known that due to the effect of steady flow, Kesen Bridge moved out gradually after submerging. From above survey, it is noted that the tsunami mainly shows steady flow shape, while 1m~3m waves happens on steady flow. Thus, in the following study, the experiments of steady flow and bore

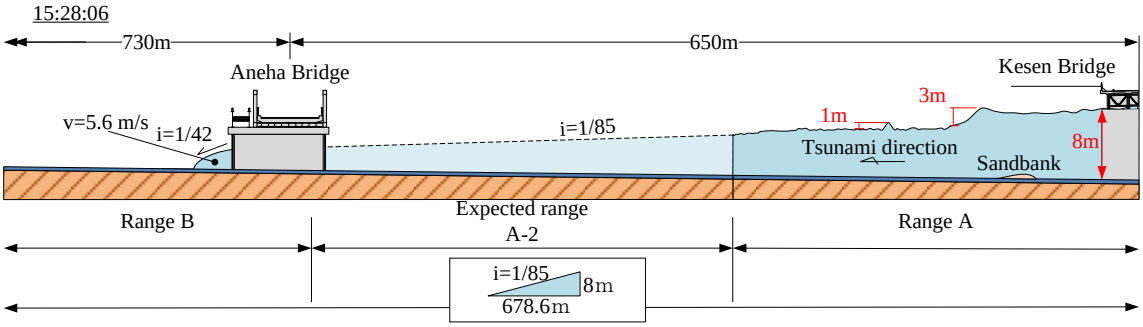

Fig.10 Wave Shape along Kesen River

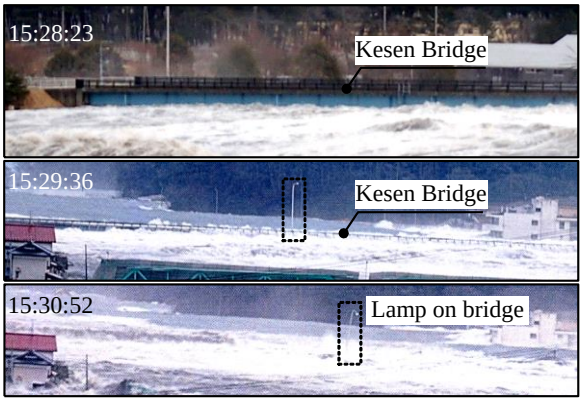

Fig.11 Wave Shape at the Moment that Kesen Birdge Flowed out

wave are conducted to research the characteristics of wave forces on girder.

Measurement of Bore Wave

In this chapter, the facilities for bore wave experiment are introduced. As illustrated in **Fig. 12-(a)**, the 41m-long, 80cm-wide, 125cm-high water channel is used for experiment. At the left side of channel, a vertical wave making plate is controlled by computer to create sine bore wave (input static water depth and wave height into computer). From the command of computer, the wave with target height is able to be created. At the location of bridge girder model, a seabed is set up to simulate seabed terrain. The model is located at the middle of horizontal plane.

The facilities near model are shown in **Fig. 12-(b)** and **Fig 12-(c)**. As the characteristic of experiment, two side walls are installed to be close to the ends of model. Six wave gauges are set up along the water channel. H1 and H2 are used to check the difference between creating wave height and input wave height. H3 and H4 are applied to check the variation of wave height due to effect of seabed. H5 is used to get the variation of wave height after the wave impacts on model. H6, at the outside of side wall, is set at the location of model to measure the wave height acting on model. Since being at the outside of side wall, the measurement of H6 is not influenced by the wave turbulence caused by the impact of wave and model. The force transducer, the range of which is 0~980N, can measure the wave horizontal force (called wave force in the following content), uplift force and acting moment caused by wave force on girder.

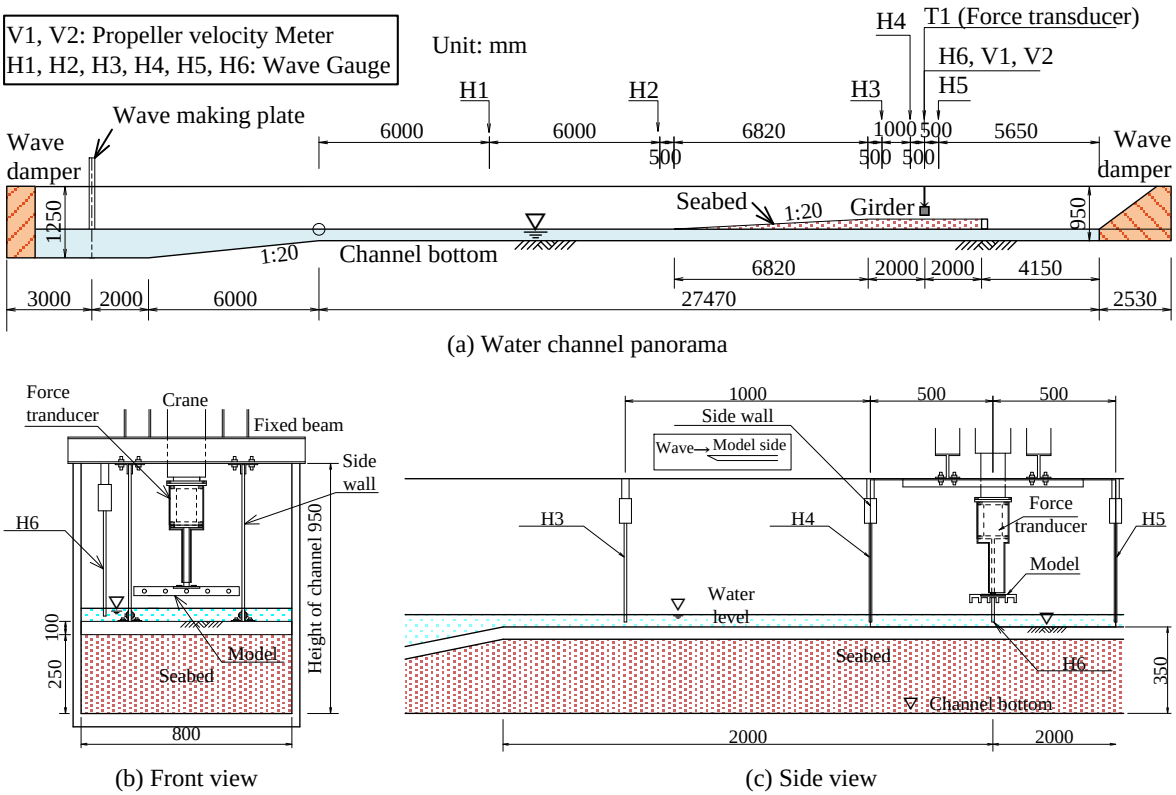

Fig.12 Facility Condition (Bore Wave, Unit: mm)

Before experiment, the natural frequency of force transducer is confirmed as 30Hz while the intervals of output data of all facilities is 1/1000s.

The prototype of bridge girder model is the damaged Lueng Ie Bridge at Sumatra of Indonesia, due to Indian Ocean Tsunami. With the scale of 1/50, the length, width and height of model are made by 40cm, 19cm and 3.4cm respectively (prototype: 19.1m-long, 10.2m-wide and 1.7m-high).

Evaluation for Bore Wave

Fig. 13 plots the parameters of experiment for bore wave. Three kinds of parameters are mainly considered: ① wave height (a); ② model position (Z: height from static water level to model bottom); ③ bore wave shapes (broken wave and un-broken wave). With the model scale 1/50, based on the Froude similarity law, the wave height and girder position in standard case is set as 25cm and 4.8cm (wave height mentioned in the following content refers to the wave height measured by H6). Referring that the ave. wave height of tsunami attacking East Japan was 10~20m, so the 12.5m-high bore wave is simulated in standard case. And considering the girder height of the damaged bridges in East Japan from ground level is about 10m, the model position 2.4m (10m minus static water depth 7.5m) is simulated in standard case. After that, three patterns of experimental cases are set by changing parameters. In Pattern 1, the wave height is 25cm, and the model position Z is changed with 1cm pitch from -4cm to 18cm (Z=4.8cm included). The creating wave becomes broken wave when acting on model. In Pattern 2, the wave height is 11cm, and the model position Z is

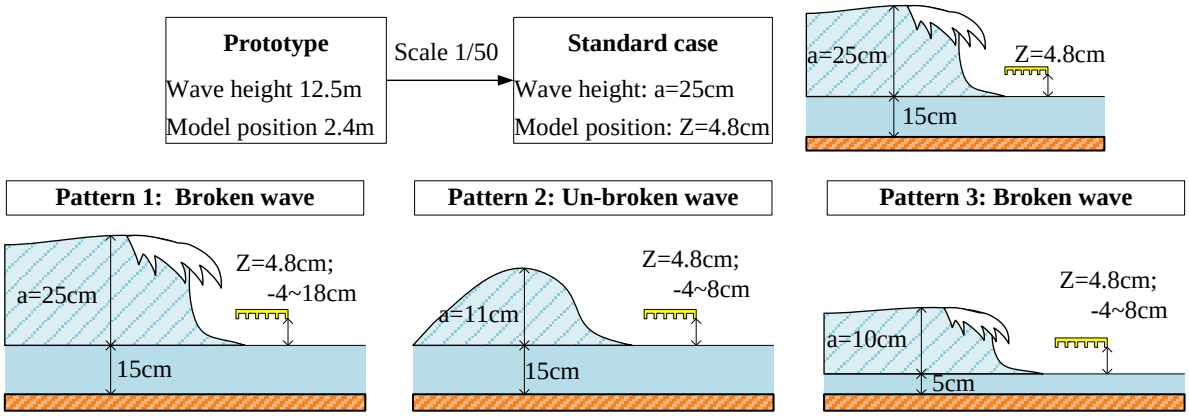

Fig.13 Parameters of Bore Wave Experiment

changed from -4cm to 8cm with 1cm pitch (Z=4.8cm included). The creating wave keeps mountain shape of un-broken wave when acting on model. In Pattern 3, the wave height is 10 cm, which is close to Pattern 2, and the model position Z is changed from -4cm to 8cm with 1cm pitch (Z=4.8cm included). But different from Pattern 2, the creating wave becomes broken wave when acting on model. In summary, the three patterns of cases are presented by: Pattern 1 [h=15cm, a=25cm, broken wave]; Pattern 2 [h=15cm, a=11cm, un-broken wave]; Pattern 3 [h=5cm, a=10cm, broken wave]. From the study of pattern 1 and 3, the relationship between wave force and wave height can be studied. From the comparison of Pattern 2 and 3, the difference of wave forces between broken and un-broken waves can be understood.

In the experiment, the max. wave force on model is concentrated. As plotted in **Fig. 14**, it is introduced as the representative result of wave force. It is known that the vibration period of 1/1000s output is about 0.033s (frequency: 30.3Hz). As mentioned in previous chapter, the natural frequency of force transducer is 30Hz, so it is considered that the resonance occurs in the result of 1/1000s time interval. In order to eliminate the resonance effect, the output by moving average of 1/10s time interval (called 1/10s average in the following content of this chapter) is also plotted. After conducting 1/10s average, the vibration larger than 5Hz is eliminated. And it is known that the max. wave force decreases about 20% (from 23.8N to 19.6N). The result of 1/10s average is used for evaluation of wave force. Besides, in order to ensure the reappearance of experiment, each case is conducted by three times.

Afterwards, as an example of broken wave, the result of standard case (Pattern 1, a=25cm, Z=4.8cm, broken wave) is introduced. **Fig. 15** is outlined based on the video recording experiment. It is notable that when wave is acting on girder, the white spray jumps on model top and then the wave block (blue color) without white spray moves to girder from lower left. In summary, the broken wave is the combination of white spray and blue water block, and the white spray mainly acts on girder.

In **Fig .16**, the relationship between wave height and wave force of standard case is illustrated. The wave height does not display the regular sine shape, which means the original sine wave deforms to broken wave at girder location. The peak

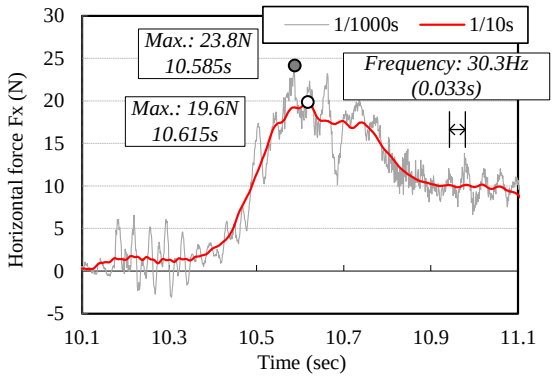

Fig.14 Evaluation Method of Bore Wave (a=10cm, Broken Wave, Z=4.8cm)

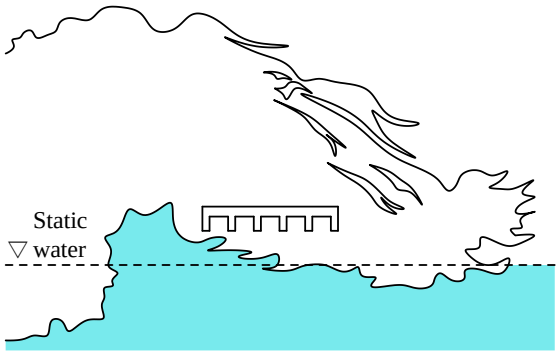

Fig.15 Wave Shape of Broken Wave (Standard Case)

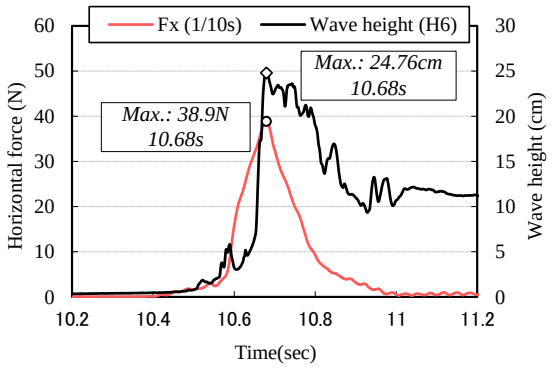

Fig.16 Wave Height and Wave Force (Standard Case)

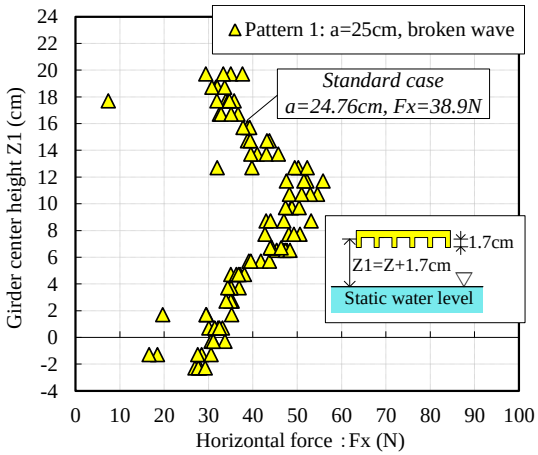

Fig.17 Wave Force Distribution (Pattern 1)

height 24.8cm is recorded at 10.68s. The max. wave force, which is 38.9N happens at the same time while the peak wave height occurs. The wave height and force change with the similar trend. Afterwards, in **Fig. 17**, the max. wave forces of each case of Pattern 1 are extracted. Considering the wave force mainly acting on model front surface, the vertical coordinate is defined by model center height Z1 (=Z+1.7cm) from static water level to model center. When the model position is fixed at the half of wave height (Z=12cm), the max. wave force occurs. When the model position is fixed at the static water surface (Z=0cm) and close to wave crest (Z=18cm), the wave force decreases to half of the max. force. So in the condition of broken wave, the model position is a significant parameter affecting wave force.

Next, to un-broken wave of Pattern 2, the result of a representative case (a=11cm, Z=4.8cm) would be described. The procedure that wave acts on model is plotted in **Fig. 18**. The blue wave water block acts on girder and keeps mountain shape. Compared with broken wave in **Fig. 15**, it is obvious that different from broken wave, there is no large amount of white sprays produced.

In **Fig. 19**, the relationship between wave height and wave force of the case in

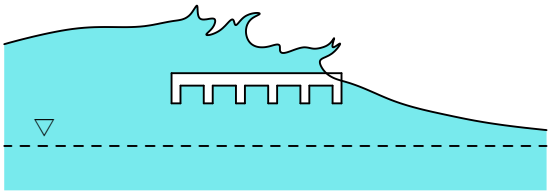

Fig.18 Wave Shape of Un-broken Wave (Pattern 2, Z=4.8cm)

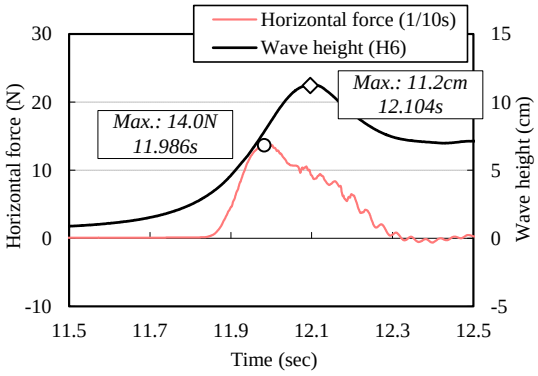

Fig.19 Wave Height and Wave Force (Standard Case)

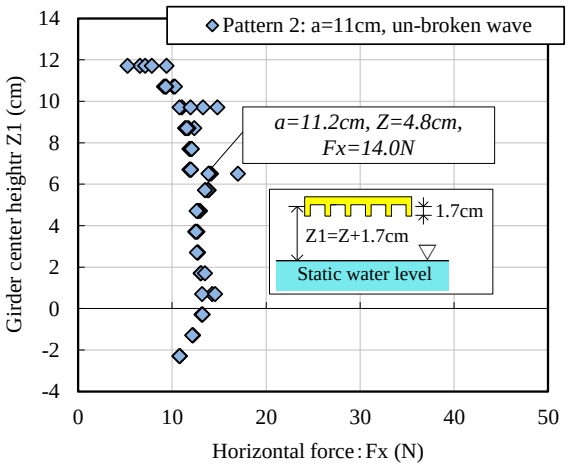

Fig.20 Wave Force Distribution (Pattern 3)

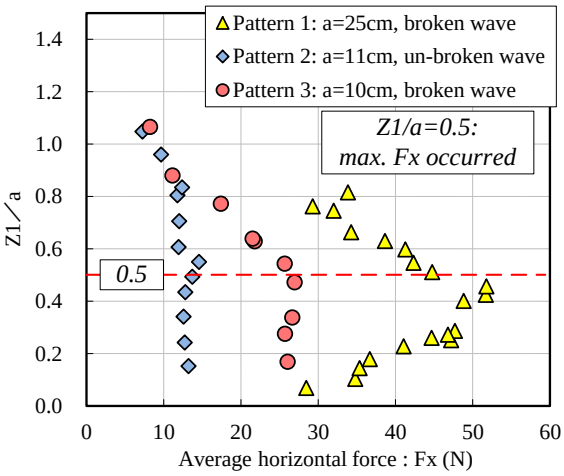

Fig.21 Wave Force Distribution (Ave.)

Fig. 18 is illustrated. The wave height result is a smooth curve, which is like a mountain shape. The peak height happens at about 12.1s. Although the variations of wave height and wave force show same trend, the max. force 14.0N happens a little earlier than peak wave height. Afterwards, in **Fig. 20**, the max. wave forces of all cases of Pattern 2 are extracted, with vertical coordinate as model center height Z1. It is found that the wave forces almost present a constant 13N for the cases with model position of Z=0~10cm and this trend is different from the distribution of wave forces by broken wave in Fig. 17 that whatever Z1/a<0.5 or Z1/a>0.5, the wave forces decrease fast.

On the basis that the representative cases of broken and un-broken waves have been introduced, the wave force of cases of all three patterns are put together for comparison (ave. wave force of three times of repeated measurements are used). As shown in **Fig. 21**, for comparison of three patterns, the vertical coordinate is conducted by dimensionless value Z1/a. Considering that real bridges are set above static water level, the cases that model under static water level (Z1<0) are ignored. Firstly, it is obvious that generally the wave forces of Pattern 3 present greatest level, and it is considered as main reason that the wave height of Pattern 1 is greatest. Secondly,

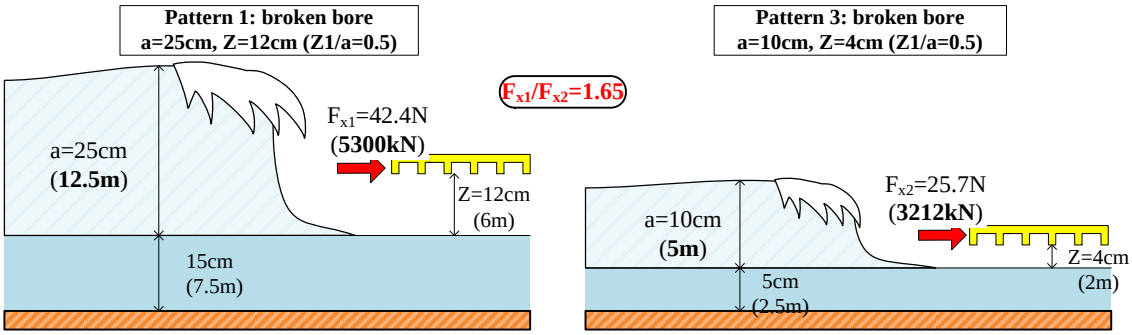

Fig.22 Wave Shape of Un-broken Wave (Pattern 2, Z=4.8cm)

although the wave height of Pattern 2 is slightly larger than Pattern 3, the wave force of Pattern 2 is smaller than Pattern 3. Therefore, it is considered that with same wave height, the wave force of broken wave is stronger than un-broken wave. Furthermore, the common point of three patterns is found that the max. forces always happens when the model central height Z1 is set at half of wave height (Z1/a=0.5).

After that in order to understand the wave force difference between 12.5m-high and 5.0m-high bore wave, the two representative cases with max. forces of Pattern 1 and 3 are selected, and besides, the experimental wave forces are converted to conditions of prototypes based on Froude similarity law. As a result, the max. wave forces of 12.5m-high and 5.0m-high bore waves are 5300kN and 3212kN, namely the max. wave force of 12.5m broken wave is about 1.65 times larger than the max. wave force of 5.0m-high broken wave (F_{x1}/F_{x2}=1.65,). Therefore, the larger wave height would cause greater wave force and the wave height should be considered as a significant parameter for evaluation of max. wave force of bore wave.

Measurement of Steady Flow

The experiment of steady flow has also been carried out. As shown in **Fig. 23-(a)**, the same water channel and girder model as bore wave are used. But different from bore wave experiment, the pump installed on water channel is applied to make a steady circular flow. The circular length is about 30m and the circular flow velocity is able to be controlled by the rotation speed of pump. In order to ensure the stability of steady flow, the seabed in bore wave experiment is removed. The max. flow velocity 120cm/s (8.5m/s) can be created. With the adjustment of crane (**Fig. 23-(b)**), the model can be put down into steady flow to measure wave force. The measurement by H6 at outside of side wall is applied to evaluate the steady flow depth at model location.

In the steady flow experiment, the author considered flow velocity is the significant parameter for wave force evaluation, and proposed the method of measuring flow velocity. Three propeller velocity meters are applied to measure flow velocity of steady flow. In the ideal steady flow condition, the average flow velocity happens near the central flow depth, thus the velocity meter V3 is set at the central depth of steady flow to manage the average flow velocity. Moreover, the velocity meters V1 and V2 are set at the same depth as model to measure the flow velocity that acts on model. V1 is set

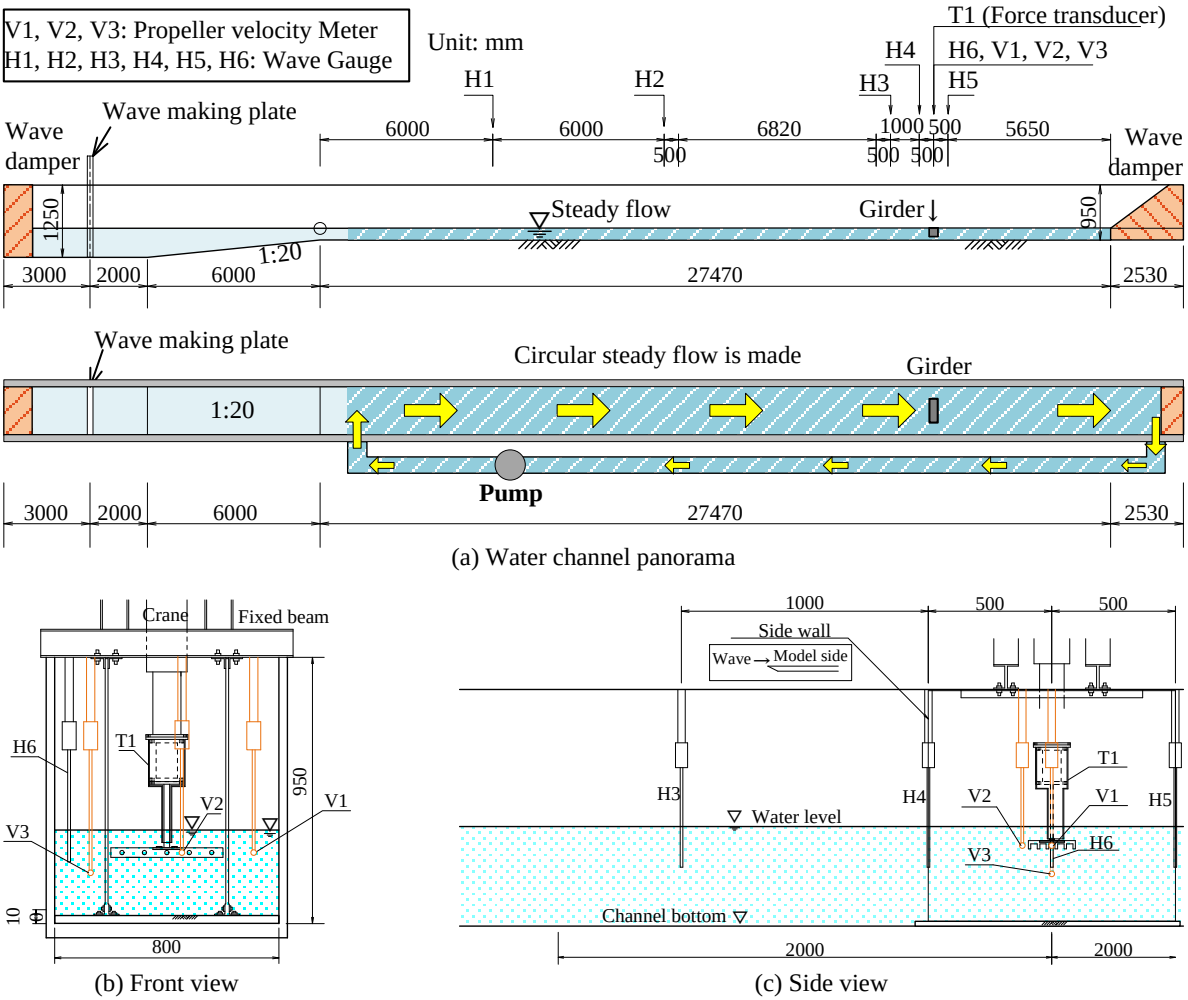

(a) Water channel panorama

(b) Front view

(c) Side view

Fig.23 Facility Condition (Steady flow, Unit: mm)

at outside of side wall while V2 is set right ahead of model (5cm far away from model front). Considering the measurement of V2 is affected due to the impact of flow and girder, V1 is used to evaluate flow velocity that acts on girder.

Evaluation for Steady Flow

In steady flow experiment, three types of parameters were considered: steady flow depth, flow velocity and model center height in steady flow. The steady flow depth and velocity of experiment are set based on the conditions of tsunami happened in Tohoku area. From the videos and photos that record tsunami conditions of Utatsu area, Koizumi area and Rikuzentakata area, it is known that the flow depth is between 10~20m, and the average flow velocity is about 6.0m/s[1)]. Therefore, the 35cm flow depth (17.5m) and 75cm/s flow velocity (5.5m/s) are set in the standard case (**Fig. 24**). And the Froude number Fr of standard case is calculated as 0.40. Besides, considering that the most stable flow condition happens in the middle depth, model center is set as Z1=14cm in standard case. Afterwards, another two types of flow velocities 50cm/s (3.5m/s) and 100cm/s (7.1m/s) are supplied flow velocity parameters. Furthermore, in order to understand the flow velocity and wave force variations in vertical direction, for

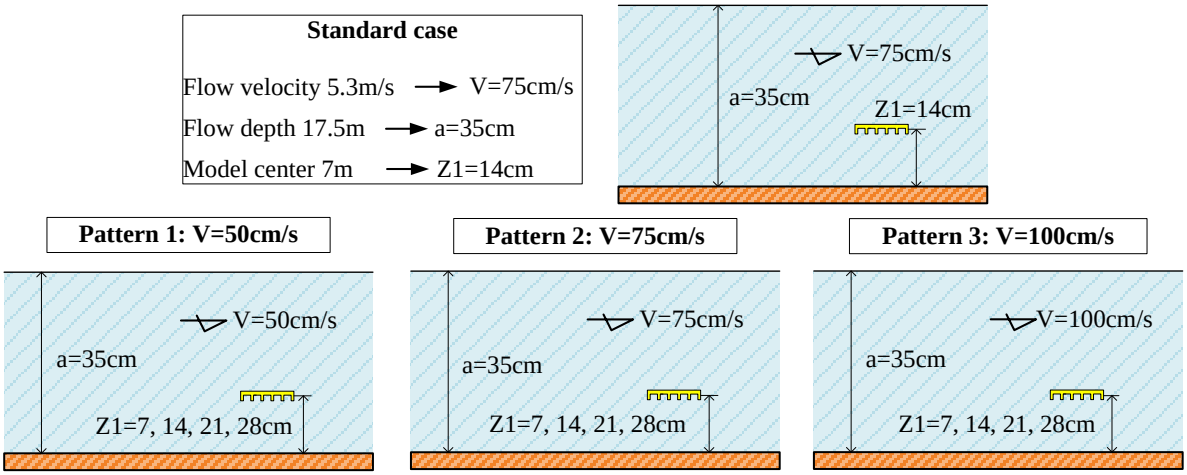

Fig.24 Parameters of Steady Flow Experiment

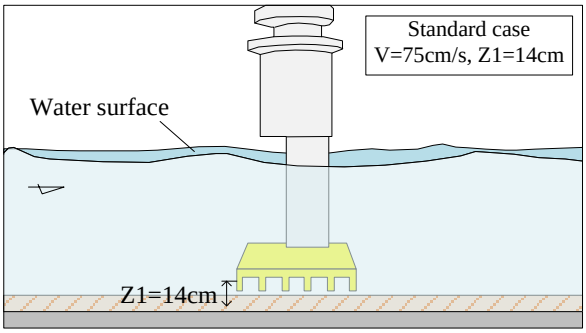

Fig.25 Shape of Steady Flow

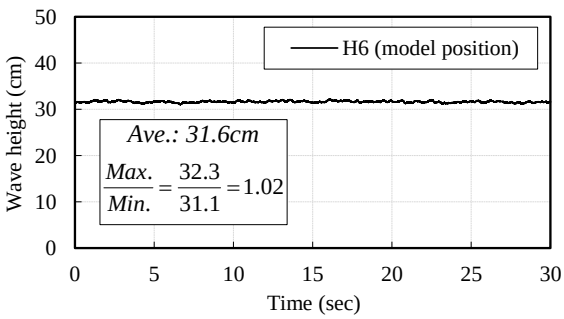

Fig.26 Wave Height (Standard Case)

each pattern of velocity parameter, the model central height in steady flow is set as another parameter (Z1=7, 14, 21, 28cm). Each case is conducted by three times to ensure the reasonability of measurement.

Above all, the experimental result of standard case is introduced. As shown in **Fig. 25**, drawn based on the video recording experiment, the flow condition of steady flow can be observed. It is notable that the water surface only shows small up-and-down motion, which is similar to the real tsunami condition in **Fig. 11**. Before creating steady flow, the static water depth is set as 35cm. Then the 35cm static water is driven by pump to make steady flow. From the wave height measurement (output interval: 1/1000s) by wave gauge H6 in **Fig. 26**, it is known that the flow depth at model became 31.6cm because a very small gradient happens on water surface after creation of steady flow by referring to the measurements by H1 (left end of steady flow, ave.: 34.5cm) and H6 (right end of steady flow, ave.: 31.6cm). Besides, the steady flow keeps stable condition approximately, because the difference between max. and min. wave height is only 2%.

With the management by velocity meter V3, the flow velocity in middle depth is adjusted as about 75cm/s. The flow velocity result by V1 is illustrated in **Fig. 27**. Different from wave height, the output of 1/1000s time interval generates great

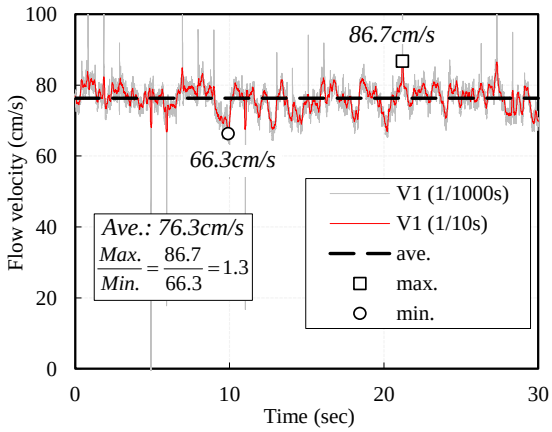

Fig.27 Steady Flow Velocity by V1 (Standard Case)

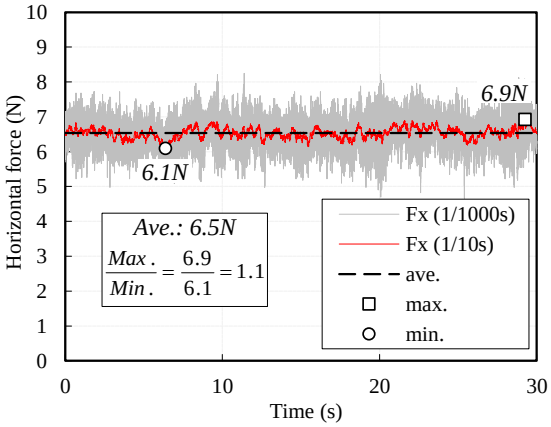

Fig.28 Wave Force (Standard Case)

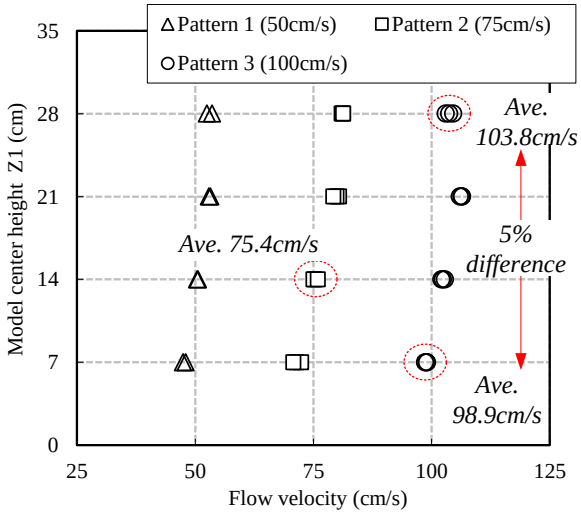

Fig.29 Flow Velocity Distribution (V1)

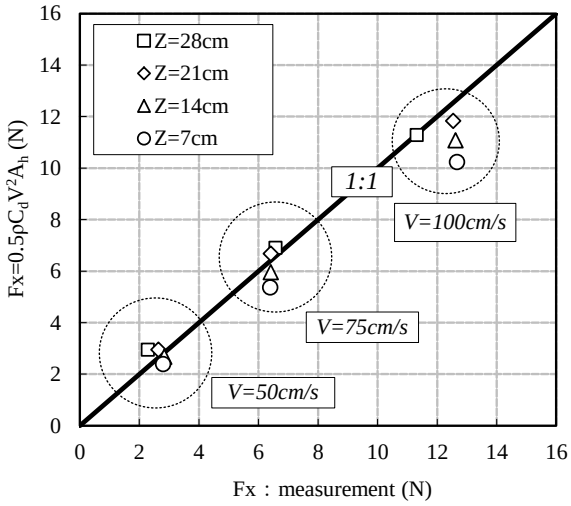

Fig.30 Comparison of calculating and measuring wave forces

vibration due to the electromagnetic noise. Therefore, the output by moving average of 1/10s time interval (called 1/10s average in the following content of this chapter) is applied to eliminate the vibration caused by electromagnetic noise. Although the difference between max. and min. flow velocities is about 30%, the average velocity after 1/10s moving average is 76.3cm/s, which is close to the objective 75cm/s and the 1/10s result 76.3cm/s is used for evaluation.

After that, the wave force is given in **Fig. 28**. Similar to velocity, the output of 1/1000s time interval is disturbed by electromagnetic noise, so the result of 1/10s average is applied for evaluation. From result of 1/10s average, it is obtained that the difference between max. and min. wave forces is 10% and both the max. and min. wave forces are close to ave. value, so the ave. wave force 6.5N can be used for evaluation.

By the same evaluation method of flow velocity as **Fig. 27**, the ave. velocity of

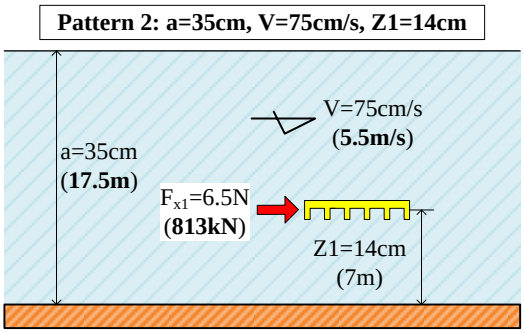

Fig.31 Wave Force of Prototype of Steady Flow

other cases are obtained. In **Fig. 29**, the flow velocities of all cases (including results of repeated measurements) are plotted. For each case, the deviation of repeated measurements is minor, so the reappearance of velocity measurement is good. For all the three patterns, from flow surface to bottom, the velocity decreases slightly. For example, to Pattern 3 (the greatest 7.1m/s steady flow is simulated), the ave. velocity from flow surface to bottom only decreases 5%. Therefore, the stable steady flow condition can be confirmed. After that, according to the research[2)], it is known that the wave force is mainly correlated with flow velocity and is able to be evaluated by the following Eq. (2), in which, wave force is the function of flow velocity and drag coefficient:

$$Fx = \frac{1}{2}\rho_w C_d v^2 A_h \tag{2}$$

Where, Fx is the wave force (kN); ρ_w is the sea water density (1.03g/cm^3); C_d is the drag coefficient (1.54, calculated by the Japanese Specification[3)]); v is the tsunami velocity (m/s); A_h is the effective projected area on girder (m^2).

For steady flow condition, the reasonability of Eq. (2) can be checked based on the experimental result. The calculation of wave force by standard case is shown as an example. By substituting the average flow velocity measured by three times with V1 (76.3cm/s in **Fig. 27**), into Eq. (2), the wave force is able to be calculated as 6.0N. On the other hand, the wave force is measured as 6.5N (**Fig. 28**), so the difference between calculation and measurement is 7%. Furthermore, the wave forces of all other cases are also calculated and the comparison between calculation and measurement is illustrated in **Fig. 30**. As a consequence, it is apparent that the calculation and measurement show the same level for all three patterns. In summary, the wave force of steady flow is proportional to the square of flow velocity and has no relationship with flow depth.

By converting the standard case “a=35cm, V=75cm/s, Z=14cm” to bridge prototype, as shown in **Fig. 31**, the 5.5m/s (ave. tsunami flow velocity in Tohoku region) steady flow with 17.5m tsunami inundation depth causes 813kN force on girder. After that, the difference of wave force between bore wave and steady flow with similar tsunami inundation depths can be understood by comparing **Fig. 31** and **Fig. 22**. As mentioned in **Fig. 22**, by converting the case “h=15cm, a=25cm, Z=12cm” to prototype ,

it is known that, with 20m inundation depth, the 12.5m broken bore wave causes 5300kN force on girder at most. Therefore, with similar inundation depths (broken wave: h+a=20m, steady flow: 17.5m), the wave force of 12.5m broken wave is about 6.5 times greater than the wave force caused by 17.5m steady flow (5.5m/s), which is a big difference. Thus, in the condition of tsunami with 10~20m inundation depth, if design wave force on basis of bore wave, the wave force may be overestimated.

Conclusions

From the photo/video analyses and experimental tests of bore wave and steady flow, the following conclusions are summarized:

(1) From the video and photo recording tsunami along Kesen River, it is concluded that the tsunami long wave shows steady flow shape generally. Besides, 1~3m small waves can be found at the surge front and water surface of steady flow.

(2) By the experiment of broken and un-broken wave, it is summarized that with the same heights, the max. wave force of broken wave is about twice greater than un-broken wave. Besides, the max. wave force of bore wave occurs when model position is set at the half of wave height (Z1/a=0.5).

(3) From steady flow experimental result, both the flow velocity and wave force almost do not change for different girder model positions. From the comparison of calculated and measured wave forces, it is found that the wave force is proportional to the square of flow velocity.

(4) If converting broken wave case “h=15cm, a=25cm, Z=12cm” to prototype, it is known that the 12.5m broken wave causes 5300kN force on girder at most. If converting steady flow case “a=35cm, V=75cm/s, Z=14cm” to prototype, it is found that the steady flow (17.5m, 5.5m/s) causes 813kN force on girder. Thus, it is concluded that although with similar inundation depths (broken wave: 20m, steady flow: 17.5m), the max. wave force of broken bore wave is about 6.5 times greater than the wave force of steady flow.

References

1. Fu, L., Kosa, K., Shimizu, H., and Zheng, Y., “Damage to Structures due to Tsunami and Evaluation of Tsunami Velocity in Shizugawa”, Proc. of JCI, Vol.34, No.2, pp.805-810, 2012.

2. Kosa, K., Nii, S., Shoji G., Miyahara K., “Analysis of Damaged Bridge by Tsunami due to Sumatra Earthquake”, Journal of Structural Engineering, Vol.55A, pp.456-460, 2010.

3. Japan Road Association, “Specifications for Highway Bridges Part Ⅰ Common”, pp.52, 2002.3.

Recent Changes to Seismic Design Practice in California

Mark Yashinsky[1]

Abstract

Caltrans Seismic Design Criteria requires bridges to have columns that can form plastic hinges and that have sufficient ductility for even unexpectedly large earthquakes. Most of these bridges are cast-in-place, post-tensioned box girder structures with integral bent caps. Caltrans engineers have been working to make other types of bridges conform to the same seismic criteria. Designing for other seismic hazards, improving analysis procedures, developing new retrofit procedures, better reinforcement details, and developing criteria for earthquake resistant elements other than ductile columns have been the source of considerable effort on the part of Caltrans Office of Earthquake Engineering in recent years.

Introduction

The typical bridge in California is a monolithic, cast-in-place, post-tensioned box girder structure. This type of bridge came to dominate California's highways as contractors accumulated formwork and as Caltrans developed experience and confidence in this kind of bridge. Caltrans' Seismic Design Criteria (SDC) (Caltrans, 2013) with its emphasis on columns that form plastic hinges is due to Caltrans large inventory of monolithically constructed bridges with moment resisting frames.

However, this type of bridge may be on its way out in California. There is a push by the Federal Highway Administration (FHWA) for Accelerated Bridge Construction (ABC) and the Next Generation of Bridges (NGB) to speed bridge construction without disrupting existing traffic. Also researchers are testing bridges that can remain relatively undamaged and can be put back into service soon after an earthquake. Caltrans Office of Earthquake Engineering (OEE) is helping to write the AASHTO Seismic Guide (AASHTO, 2011) for the use of other states with its emphasis on other types of bridges. It may be convenient to eventually adopt this Guide in California. All of these influences may eventually change California's inventory of bridges with accompanying changes to Caltrans SDC.

[1] Senior Bridge Engineer, Caltrans Office of Earthquake Engineering

CHANGES TO BRIDGE CONNECTIONS

Fixed Connections

Much effort has been spent on designing strong reliable connections between bridge members. Caltrans philosophy of capacity-protection relies on fixed column connections that won't be damaged by joint shear due to column plastic hinging. The current joint shear criterion requires the engineer to determine the principal stresses in the joint. If the stresses are low than just some additional reinforcement is required but if the stresses are high the joint must be made larger. Confinement reinforcement must continue from the column to the top mat of reinforcement in the bent cap and the bottom mat in the pile cap. The main column reinforcement must be fully developed into the top and bottom joints. This can be a problem since large diameter reinforcement requires deep caps to fully develop. The use of 'T' headed main reinforcement, dropped bent caps, or smaller diameter longitudinal reinforcement would be required for joints with a small depth.

Pinned Connections

Caltrans prefers fixed connections for bridge columns but sometimes a pinned connection is required. Caltrans uses pins for outrigger bent connections. A pin may also be required if the column diameter is bigger than the superstructure depth. Multicolumn bents have pinned connections at the bottom of the columns to reduce the size of foundations, a major cost for bridges. Reliable pinned connections that can handle service loads and aren't damaged by earthquakes are a subject of continuing research at UN Reno (Saiidi, 2010). Poorly designed pins resulted in the collapse of a mile long section of the Cypress Viaduct during the 1989 Loma Prieta Earthquake. Caltrans uses pipe pins and reduced section reinforcement pins to connect columns to caps. The pins typically require some kind of replaceable bearing surface and adequate transverse reinforcement to protect the concrete around the pin.

Splices

Caltrans has strict rules about the use of reinforcement splices. No splices are allowed in plastic hinge zones (PHZ) and only pre-approved ultimate splices can be used outside the PHZ of ductile members. Most capacity-protected members require ultimate splices while the reinforcement for remaining portions of the bridge can have a service or lap splice. Caltrans seldom uses spiral reinforcement in columns anymore, but when they do the spiral splice must be an extra 180° lap with a diagonal hook through the concrete core. Most columns use hoops, which require an ultimate splice. Caltrans seismic philosophy relies on an abundance of continuity and development to hold things together during earthquakes. Unfortunately,

reinforcement typically comes in 60 ft (18 m) lengths. Therefore rules about 'no splices' sometimes require exceptions for long or tall bridges.

Seats

The superstructure to substructure connection at abutments and bents is often a seat. Caltrans will sometimes eliminate the seat in favor of end-diaphragm abutments and integral bent caps, especially in regions of high seismicity. However, very long bridges usually require an in-span hinge seat to accommodate temperature, prestressed shortening, and other longitudinal displacements. Caltrans requires these seats to be longer than the Square Root Sum of the Squares (SRSS) of the displacements of the adjacent frames (plus creep, shrinkage, etc.) but not less than 24 inches (600 mm). Shear keys are provided at the left and right ends of abutment and bent cap seats to prevent transverse displacement (and bearing damage) from smaller earthquakes. Recent research (Bozorgzadeh, 2007) has shown these shear keys are stronger than anticipated and so a new modular shear key has been designed that will fail before more important bridge members can be damaged. For in-span hinge seats, double strong steel pipes are sometimes placed through the joint to prevent transverse movement and to provide a longer seat.

CHANGES TO BRIDGE MEMBERS

Foundations

At the bottom of a column is a spread footing, a pile cap, or large diameter shaft. Caltrans uses two kinds of shafts to support bridge columns. A Type 1 shaft is about the same diameter as the column and is designed to form a plastic hinge below the ground surface. Caltrans likes Type 1 Shafts because of their high ductility and long plastic hinge length. Testing at UCLA (Wallace, 2001) showed a 1.8 m (6 ft) diameter shaft had a 20% drift ratio. A Type 2 shaft has a larger diameter than the column to form a reliable plastic hinge above the ground.

The construction of shafts can be difficult and rules for construction and for earthquakes are sometimes in conflict and have to be resolved. For instance, the column reinforcement developed into the Type 2 Shaft should be as short as possible to make it easier for Construction to put a cold joint in the shaft that doesn't require special safety equipment for workers going down into the hole to clean the joint. Currently testing is being done at UC San Diego (Shing, 2012) to determine the bond-slip behavior of these large-diameter bars. This is the first time that very large diameter rebar has been tested and special equipment was needed to provide the pull-out force and special details were need to securely grab the rebar. Construction would also like to maintain a five-inch (130 mm) window between longitudinal and

transverse reinforcement in a shaft for the effective flow of wet concrete. Also, construction requires at least two PVC pipes in the shaft to check for anomalies in the concrete. This can interfere with a rule for less than eight inches between the main reinforcement. It’s hard to make a shaft that meets all of these requirements. Also, Construction doesn't like to pour shafts in wet conditions. This has made the use of large diameter Cast in Steel Shell (CISS) shafts much more popular.

The design of foundations depends on soil conditions and requires good communication between the geotechnical and the bridge engineer. Caltrans formed a committee to study the behavior of pile groups in competent and poor soil. They found that in good soil, the piles were essentially axial members and inexpensive standard piles could be used with pinned connections. However, in poor soil the piles must be have good ductility and fixed connections to the pile cap.

Spread footings are allowed to support abutments and bents on good material in areas of low to moderate ground shaking. Designers sometimes attach tie downs to spread footings to prevent overturning during earthquakes. Recent research (Deng, 2010) suggests that these spread footings could be allowed to rock, even for very large earthquakes (see section on EREs). However, there is a natural hesitancy to allow a bridge to rock back and forth. One can only too readily imagine the bridge rocking over.

Substructures

Caltrans prefers flexible columns to rigid pier walls, but they still allow them to be built. The SDC philosophy of plastic hinge elements and capacity-protected adjacent elements cannot be followed with pier walls, which are stronger than the foundation and can’t form a plastic hinge in the transverse direction. Caltrans requires pier walls to be designed as shear elements for the peak spectral acceleration of the Design Spectrum (times a safety factor). Pier walls are reinforced with stirrups and ties that can come loose during a large earthquake. Caltrans requires a cross tie with alternating 135 degree hooks at one end and 90 degree hooks at the other end wherever vertical and horizontal bars come together in a pier wall.

CHANGES TO TYPES OF BRIDGES

Caltrans is working to make more types of bridges fit the classification of ‘Ordinary Standard Bridge’ that can be designed using the SDC.

Slab Bridges

Slab bridges are designed using charts that had been recently updated for Load and Resistance Factor Design (LRFD). The charts provide the slab depth, reinforcement details, and pile spacing based on span length. Slab bridges are easy to design and cheap to build and so there is some reluctance to change the design to make them meet the requirements in Caltrans SDC. However, research at UN-Reno (Sanders, 2009) showed that well-designed piles with a fixed connection could result in joint shear damage in the slab. Also, the standard piles/shafts used to support the slab used wire for transverse reinforcement that can't form a plastic hinge with sufficient ductility. Caltrans formed a subcommittee, which is trying to develop a seismic design procedure that retains the use of the existing design charts (except in areas of very high seismicity). However, there is not a lot of slab reinforcement to meet the capacity-design requirements in the SDC.

The new criteria would require the columns (shaft/pile extensions) that support slab bridges to be at least 0.5 meters (18 inches) in diameter and have #13 metric (#4 US) hoops/spiral reinforcement. There are (at least) four ways for slab bridges to meet the requirements in Caltrans SDC with the stronger, more ductile columns.

1. Increase the slab depth until slab capacity overcomes top of column capacity.
2. Create a reduced column section between the slab and the top of column.
3. Provide a pin to reduce the top of column moments.
4. Augment slab reinforcement and/or incorporate a drop cap.

The subcommittee is currently performing analyses of slab bridges designed using the charts to see when the slab reinforcement cannot meet the capacity-protection requirements for the better columns (shaft/pile extensions).

Precast Bridges

Caltrans began designing precast girder bridges to meet all the SDC requirements in 2000 on the San Mateo Hayward Bridge widening. This 7.5 km (4.7 mile) long bridge supports precast girders on bent caps designed to provide full continuity of all the reinforcement to meet the joint shear requirements for the column plastic moment. Once construction commenced, they were able to build over 30 m. (100 ft.) of bridge every day despite the complicated connections between the girders and the bent cap.

There have been several recent tests of the seismic resistance of precast girder bridges with emphasis on the bent cap (Veletzos, 2006) (Snyder, 2011). These tests included inverted 'T' bent caps supporting different types of precast girders. Caltrans

OEE would prefer to have positive girder reinforcement through the bent since this most closely matches the SDC requirements and ensures that all damage occurs in the column plastic hinge. A design that Caltrans is exploring with Prof. Sritharan at Iowa State University. The girders would sit on the inverted 'T' bent cap and the bottom prestressing tendons would wrap around the four # 11 (#36 metric) rebars.

Another alternative that Caltrans is exploring with UN Reno (Saiidi, 2013) are Next Generation Bridge (NGB) Components for Accelerated Bridge Construction (ABC). This project, which started in 2007, has compared the performance of precast columns attached with couplers to the foundation to the performance of Caltrans standard cast-in-place (CIP) column and foundation. So far, five configurations have been tested: (1) the CIP column, (2) precast column attached to upset headed coupler without pedestal (HCNP), (3) precast column attached to ductile cast-iron grout-filled sleeve without pedestal (GCNP), (4) precast column attached to upset headed coupler with a pedestal (HCPP), (5) precast column attached to ductile cast-iron grout-filled sleeve with a pedestal (GCPP). The precast columns are hollow shells that are filled with self-consolidating concrete after they are attached to the foundations. The pedestal is to move the connection above the plastic hinge zone. So far the tests have been encouraging. The HCNP had better displacement capacity but the GCNP was easier to assemble. The tests will continue. Eventually, Caltrans hoped to test a complete assembly of precast footings, precast columns, precast bent cap, and precast girders. A serious issue for Caltrans is to make sure that these precast elements not only give good seismic performance but are practical to construct and don't become a maintenance problem.

Steel Bridges

Steel Girder Bridges can be quickly constructed with minimum interference to traffic, which make them an important bridge type for Accelerated Bridge Construction. The seismic design of steel bridges is addressed in Caltrans Steel Bridge Seismic Design Criteria (Caltrans, 2001). The seismic design of steel girder bridges is addressed in Caltrans SDC. The challenge is to design the connections for these bridges to be capacity protected.

Long-Span Bridges

Projects like the East Spans of the San Francisco Oakland Bay Bridge have given Caltrans a chance to reflect on issues related to long span structures. The towers need to remain in service after large earthquakes and so shear links between the tower legs were designed to act as a fuse and protect the towers from damage. However, this ERE hasn't been extensively tested and issues such as the welds, anchorage,

replacement after earthquakes, etc. need to be studied before shear links become standard equipment for bridge towers.

Caltrans requires a ductility capacity of at least three as a safety factor in case the primary ERE were to fail or if an unexpectedly large earthquake were to occur. Therefore, Caltrans has ductility and post yield performance requirements of hollow columns and towers on long-span bridges. Recent tests of hollow columns have shown promise, but nothing like the ductility of solid columns with closely spaced large diameter hoops. It seems illogical to accept less strength and ductility for the columns of more expensive bridges. Caltrans recommends that hollow rectangular columns have large compression members in the corners connected with very strong diaphragms so the whole section is fully engaged during the earthquake. The compression members should extend beyond the diaphragms so that bending is taken by the compression members rather than the diaphragms. Other requirements include:

1. **Cross ties with 180 degree hooks and 9 diameter heads.**
2. **Columns must have 900mm (3') minimum wall thickness for tall towers.**
3. **#24 metric (#8 US) inner bars.**
4. **#43 metric (#14 US) outer bars.**
5. **Number of inner bars must be at least 50% the number of outer bars.**
6. **Main reinf. > 1% includes inner and outer bars based on solid section.**
7. **200 mm (8") min. bar spacing, with stirrups at vertical bar.**

CHANGES TO SEISMIC DESIGN FOR OTHER HIGHWAY STRUCTURES

Caltrans is beginning to design other highway structures (besides bridges) for earthquake loads. Caltrans typically addresses 'life safety' for the seismic design of bridges and that has also been the focus for the seismic design of retaining walls, tunnels, and other highway structures.

Retaining Walls

For the past few years there has been considerable debate on how to design retaining walls for earthquake loads. Some engineers advocated applying the earthquake force (P_{AE}) at a height of H/2 or at H/3, while others argued that we should be designing retaining walls for a displacement similar to what we do for bridges. Currently, Caltrans uses designs retaining walls using KAE which is function of 1/3 of the Peak Ground Acceleration (PGA) for designing retaining walls but that could be a very large load since Caltrans PGA > 1.0g at many locations. Also, there is concern about having to design every retaining wall for earthquakes. This would require a lot of resources that may not be required when life safety is the main concern. Caltrans has pre-designed cantilever and gravity retaining walls on spread

footings and piles in the Standard Plans that have been checked for the reduced seismic acceleration of 0.33(PGA ≤ 0.6g). Caltrans concern is for sites in California where PGA ≥ 0.6g.

Tunnels

Caltrans has been building a lot of tunnels recently (Doyle Drive, Devil's Slide, Caldecott, etc.) and so tunnel seismic design criteria has been developed. The seismic design philosophy is the same as for bridges. The walls (or liner) are designed to be ductile and the crown and invert are designed to be capacity protected. During large earthquakes the tunnel is able to displace in a controlled manner (as long as P-Δ is small).

NEW EARTHQUAKE RESISTANT ELEMENTS (ERES)

Caltrans would like engineers to be able to choose from a variety of EREs depending on the bridge and the seismic hazard. We have already discussed column plastic hinges, ductile steel end diaphragms (for steel girder bridges), and shear links for bridge towers.

Abutment Embankments

An ERE that is commonly used for Ordinary Standard Bridges is yielding of the soil behind the abutment. The soil has an initial stiffness K_i =28.7 KN/mm per m of backwall (Ki=50kips/in per ft of backwall). The abutment stiffness, K_{abut} is K_i times the area of the backwall, and the effective stiffness, K_{eff} is adjusted for the gap in seat type abutments. The backwall is assumed to yield when the passive pressure reaches 239 kPa (5.0 ksf) times the backwall area. The structure's period is obtained from its mass and stiffness and the Design Spectra is used to obtain the acceleration and/or displacement. R_A equals the computed displacement divided by Δ_{eff} (the displacement when the backwall yields). Then the final stiffness of the abutment (K_{res}) is adjusted depending on the value of R_A.
If $R_A \leq 2$: The abutment controls the displacement $K_{res} = K_{eff}$.
If $R_A \geq 4$: The abutment contribution is small, reduce stiffness $K_{res} = 0.1K_{eff}$.
If $2 < R_A \leq 4$: The abutment stiffness is adjusted between $0.1K_{eff}$ and K_{eff} based on R_A.

Isolators

An ERE that shows promise are isolators such as lead rubber and friction pendulum bearings (AASHTO, 2010). They yield at a smaller force than column plastic hinges so the foundations can be made smaller and they prevent column damage so the bridge can be returned faster to service. A subcommittee was formed

to develop design criteria for Ordinary Standard Bridges using isolators and other EREs. The goal is to require similar behavior so that the bridge has the same level of safety no matter which ERE is chosen.

1. **Isolated bridges shall meet the requirements in Caltrans SDC.**
2. **Isolated bridge displacement is determined using AASHTO Isolation Guide.**
3. **Hazard is determined using Appendix B of the SDC (reduced for damping).**
4. **Isolators are designed with a safety factor of 1.25 times displacement demand.**
5. **All the substructure elements must have about the same stiffness and mass.**
6. **All the isolators must have the same stiffness and displacement capacity.**
7. **Bridge columns are designed to remain elastic for lateral isolator forces.**
8. **Bridge columns are designed for $V_u \geq 1.2*F_{1.25\Delta D}$ (1.2 times the lateral force).**
9. **Bridge column lateral capacity > 0.15g (0.15 times dead load reaction)).**
10. **Bridge columns must have a displacement capacity (beyond yield) > 3.0.**

Rules were developed to provide enough strength in the isolators to handle service and wind loads or shear keys should be provided to protect isolators from service and wind loads. Seats or catcher blocks are also required just in case the isolator breaks. No special requirements are made for expansion joints, which are allowed to break (and be quickly repaired) for the Design Earthquake.

Dampers

At one time Caltrans was hoping that viscous dampers would prove to be an effective ERE until they began leaking on several bridge retrofit projects. Because of the cost of having to replace these big dampers, Caltrans Structures Maintenance is reluctant to put them on any more state bridges. Recent retrofit projects (such as the Forest Hills Bridge) have used Buckling Restrained Braces (BRB) with good results. Also, there is hope that liquid-silicone filled dampers can be used instead of oil-filled dampers without all of the maintenance problems. Caltrans has funded research on shape memory alloys that may one day be used as bridge dampers.

Rocking

Caltrans is currently writing procedures that will allow rocking as an acceptable ERE for new bridges. Caltrans has always allowed rocking for bridge retrofits, but the seismic performance requirements for new bridges is higher. Caltrans has funded several research projects on rocking and the results are positive enough to begin discussions on allowing rocking for short bridges where Geotechnical Services recommends spread footings (Kutter, 2010) (Panagiotou, 2014). Similar to isolation bearings, bridge foundations that rock reduce the seismic force, require smaller footings, and should return the bridge to service more quickly.

Self-Centering Columns

Researchers are testing bridges that can remain relatively undamaged and can be put back into service soon after an earthquake. The University of Washington, Stanford University, and the University of California at Berkeley are all doing research into precast columns with a hole in the center for post tensioning cables that automatically re-center a bridge after an earthquake (Cohagen, 2009) (Lee, 2009) (Jeong, 2008). Since these columns would be quicker to assemble, this would meet Caltrans goal of accelerating bridge construction. However, Caltrans still has concerns about the ductility, the constructability, and maintenance of these columns.

Ductile Steel Elements

We have already touched on a few steel earthquake resisting elements. Shear links were constructed on the tower of the new East Bay Bridge in San Francisco Bay. These are similar to the eccentrically braced frames that are sometimes used in steel buildings. The use of ductile end cross frames on steel girder bridges also holds promise (Bahrami, 2010). After the 1999 Duzce, Turkey Earthquake the almost completed Bolu Viaduct suffered major damage to crescent moon-shaped steel dampers placed between a central hub and outer ring. Although the dampers performed well during an earlier earthquake, the Duzce earthquake caused very large displacements that the dampers could not handle.

IMPROVED ANALYSIS METHODS FOR SEISMIC HAZARDS

Caltrans has developed new methods of obtaining the seismic demands on bridges due to ground shaking, surface faulting, lateral spreading, and tsunami hazards. Depending on the bridge site some of these hazards need to be combined in the analysis.

Ground Shaking Hazard

In 2007, Caltrans began taking the envelope of the largest deterministically derived and probabilistically derived ground motion at the bridge site. The probabilistically derived ground motion was the largest ground shaking that had a 5% probability of occurring in 50 years from nearby faults. This hazard level (a 1000 year return period) was agreed upon by the members of the AASHTO T3 Committee after several years of study and it was used in the AASHTO Guide Specifications for LRFD Seismic Bridge Design and in Caltrans Seismic Design Criteria. A third ground motion due to an earthquake on a M6.5 fault that is 12 km from the bridge site

is included as the Minimum Deterministic. Caltrans spectra can be obtained for any bridge site in California at (http://dap3.dot.ca.gov/ARS_Online/index.php).

The demands due to the ground shaking hazard are currently obtained using the Equivalent Static Analysis (ESA) Method, the Elastic Dynamic Analysis (EDA) Method, or the Nonlinear Time History Analysis (NTHA) Method. No matter which method is used, the input ground motion comes from response spectra provided on the ARS Online website (and described in Appendix B of Caltrans SDC). Caltrans plans to move to using only probabilistically-derived ground motion by 2016.

At a recent meeting of Caltrans Seismic Advisory Board, Professor Ed Wilson spoke critically of the EDA Method. He said:

- EDA Method is only exact for SDOF systems.
- It produces only positive numbers for displacement and member forces.
- Results are maximum probable values that occur at an unknown time.
- Short and long duration earthquakes are treated the same.
- Demand/Capacity ratios are always overly conservative.
- EDA Method does not provide insight into bridge dynamic behavior.
- Results are not in equilibrium.

Caltrans would like to introduce procedures to perform a nonlinear time history analysis for Standard bridges. The problem is providing sufficient probabilistically-derived time histories of ground motion that are as statistically reliable as a response spectra. There is currently research at the PEER Center on ground motion selection and scaling for nonlinear analysis (Rezeaeian, 2010), which Caltrans will be incorporating into their new analysis procedure. The plan is to create sufficient synthetic time histories for the characteristics of the bridge site, scale the time histories to the probabilistic response spectra at the fundamental bridge period(s), and analyze the bridge using these scaled time histories at increments of 30° to obtain the maximum demands on bridge members.

Similarly, when engineers use the EDA method, Caltrans now requires that the CQC3 method shall be used to obtain the maximum ground shaking demands on bridge members in their local axis (Menum, 1998). Currently, the same ground motion is applied in two orthogonal directions, but the use of CQC3 will provide the correct demands if different response spectra are applied in different directions.

Surface Faulting Hazard

Surface faulting hazards are obtained from Holocene Epoch faults based on the California Geological Survey (CGS) Alquist-Priolo Maps as well as from site investigations and literature reviews. Similar to the ground shaking hazard, the deterministically-derived fault offset is obtained based on fault characteristics using Wells and Coppersmith or other empirical relationships (Wells, 1994). The

probabilistically-derived offset is obtained using a report by the San Francisco Public Utility Commission (Abrahamson, 2008).

Once the fault is located and the offset is obtained, the bridge foundations are moved into the offset position and the column displacements are obtained from a 3D model of the bridge. Then the ground shaking displacements are obtained for an elastic version of this bridge in a similarly deformed state (Chopra, 2008).

More information on determining surface fault hazards is provided in Caltrans Memo to Designers (MTD) 20-8 and MTD 20-10 (Caltrans, 2012).

Tsunami Hazard

Tsunami hazards were obtained through a research contract between the Pacific Earthquake Engineering Research (PEER) Center and URS Corporation (Thio, 2010). Seismic sources around the Pacific Ocean were identified and a finite difference model was developed to obtain the wave heights and velocities along the coast of California. Similar to other seismic hazards the 1000-year tsunami wave is being considered for use in design. Information on designing for tsunami is provided in Caltrans MTD 20-13. Recent research by Solomon Yim at Oregon State University (Yim, 2013) will be used to update MTD 20-13 and give designers equations for determining the tsunami wave forces based on the wave height and velocity at their bridge site. Caltrans is also working with other western coastal states on tsunami design guidelines.

Liquefaction and Lateral Spreading Hazard

Caltrans Geotechnical Services is currently developing standard methods for evaluating seismic hazards in the 'Geotechnical Manual,' which will be completed in 2014. http://www.dot.ca.gov/hq/esc/geotech/geo_manual/manual.html.

A new procedure has been written for determining demands on bridges due to lateral spreading, based on research funded by Caltrans (Shantz, 2012) (Ashford, 2010). Caltrans MTD 20-14 and MTD 20-15 provides designers with simple procedures for designing bridges for liquefaction and lateral spreading, but these memos may need to be revised based on new information and procedures.

Conclusion

After the 1989 Loma Prieta Earthquake Caltrans greatly increased its funding for seismic research, mostly directed at retrofitting Caltrans existing bridges. As the retrofit program neared completion, Caltrans changed its focus from research on existing bridges to the seismic design of new bridges. In 1999 Caltrans Seismic Design Criteria was first published, based on lessons learned from earthquakes and from Caltrans research program. Despite not having any damaging earthquakes in a number of years, Caltrans still supports a great deal of earthquake-related research.

References

AASHTO, *Guide Specifications for Seismic Isolation Design*, 3rd Edit., 2010.

AASHTO, *Guide Specifications for LRFD Seismic Bridge Design*, 2nd Edit., 2011.

Abrahamson, N., *Appendix C, Probabilistic Fault Rupture Hazard Analysis*, San Francisco PUC, General Seismic Requirements for the Design on New Facilities and Upgrade of Existing Facilities, 2008

Ashford, S., Boulanger, R., and S Brandenberg, *Recommended Design Practice for Pile Foundations in Laterally Spreading Ground*, Pacific Earthquake Engineering Research (PEER) Report 2010

Bahrami, H., Itani, A. M., I. G. Buckle. *Guidelines for the Seismic Design of Ductile End Cross Frames in Steel Girder Bridge Superstructures*, Report No. CCEER 09-04, Center for Civil Engineering Earthquake Research, University of Nevada, Reno, July 2010

Bozorgzadeh, A. et al. *Seismic Response of Sacrificial Exterior Shear Keys in Bridge Abutments*, UCSD Report No. SSRP–04/14, October 2007.

Caltrans. *Guide Specifications for Seismic Design of Steel Bridges*, 1st Edition, California Department of Transportation, Sacramento, CA, 2001

Caltrans. *Seismic Design Criteria*, Version 1.7 California Department of Transportation, Sacramento, CA. 2013.

Caltrans. *Memo to Designers Section 20 – Seismic*, California Department of Transportation, Sacramento, CA.

Chopra, A.K., and R.K. Goel, *Analysis of Ordinary Bridges Crossing Fault-Rupture Zones*, Earthquake Engineering Research Center University of California at Berkeley Report No. UCB/EERC-2008/01, 2008

Cohagen, L. S., Pang, B. K., Stanton, J. F., and M. Eberhard, *A Precast Concrete Bridge Bent Designed to Re-center after an Earthquake*, Research Agreement T4118, Task 05 Rapid Construction TNW 2008-09 TransNow Budget No. 61-5915, 2009.

Deng, L., Kutter, B., and S Kunnath. *Centrifuge Modeling and Numerical Studies of Rocking Shallow Foundations for Ordinary Bridges*, Report No.UCD/CGM-10/01, Department Of Civil & Environmental Engineering, College of Engineering, University of California at Davis, June 2010

Jeong, H. I. L., Sakai, J., and S. A. Mahin. *Shaking Table Tests and Numerical Investigation of Self-Centering Reinforced Concrete Bridge Columns*, PEER 2008.

Kutter, B.L., Jeremiac, B, and J.A. Ugalde, *Rocking Response of Bridges on Shallow Foundations*, PEER 2010/101, April 2010.

Lee, W. K. and S. L. Billington. *Simulation and Performance-Based Earthquake Engineering Assessment of Self-Centering Post-Tensioned Concrete Bridge Systems*, PEER 2009/109, 2009.

Menun, C. and A. Der Kiureghian, *A Replacement for the 30 %, 40%, and SRSS Rules for Multicomponent Seismic Analysis, Earthquake Spectra, Vol. 14,* Number 1, February 1998.

Panagiotou, M., et al. *Analytical and Experimental Development of Bridges with Foundations Allowed to Uplift during Earthquakes*, Ongoing Research at UC Berkeley, UC San Diego, and UC Davis (Agreement Number 65A0487), 2014

Rezaeian, A., and Armen Der Kiureghian, *Stochastic Modeling and Simulation of Ground Motions for Performance-Based Earthquake Engineering*, PEER 2010/02

Saiidi, M.S., and A Zaghi. *Seismic Design of Pipe-Pin Connections*, Report Number CCEER-10-01, University of Nevada at Reno, 2010.

Saiidi, M., Sanders, D., and Z. Haber. *Seismic Performance of Next Generation Bridge (NGB) Components for Accelerated Bridge Construction (ABC)*, http://wolfweb.unr.edu/homepage/saiidi/caltrans/NextGen/PDFs/ResearchNotes.pdf

Sanders, D., and M. Ayoub. *Specimen Design and Testing Piles Extension Connection to Slab Bridges*, University of Nevada, Reno FSRCC24-Experiment Summary. June, 2009.

Shantz, T., *Guidelines on Foundation Loading and Deformation due to Liquefaction Induced Lateral Spreading*, Caltrans, January 2012

Shing, P.B., and J. Mucia-Delso. *Bond-Slip Behavior Of Large-Diameter Reinforcing Bars*, UCSD 2012.

Snyder, R., Vander Werff, J., Thiemann, Z.,Sritharan, S., and J. Holombo. *Seismic Performance of an I-Girder to Inverted-T Bent Cap Connection*, Submitted to the California Department of Transportation Caltrans Project: 05-0160 Sept. 2011

Thio, H.K., *Probabilistic Tsunami Hazard in California*, PEER 2010

Veletzos, M. J., Resrepo, J. I., and F Seible. *Structural Systems Research Project Seismic Response of Precast Segmental Bridge Superstructures*, Report No. SSRP–06/18 Final, December 2006.

Yim, S. C. and M. Azadbakht, *Tsunami Forces on Selected California Coastal Bridges*, School of Civil & Construction Engineering, Oregon State University, Final Report No. CA13-1983, 2013

Wallace, J.W., et al. *Cyclic Large Deflection Testing of Shaft Bridges. Part I-Background and Field Test Results*, Report to California Department of Transportation, December 2001

NUMERICAL ASSESSMENT OF TSUNAMI-INDUCED EFFECT ON BRIDGE BEHAVIOR

Hisashi Nakao[1], Guangfeng Zhang[2], Toru Sumimura[3] and Jun-ichi Hoshikuma[4]

Abstract

This paper discusses the mechanism of tsunami-induced behavior of the superstructure through a series of flume test and analysis. In the flume tests, 1/20-scaled models of the superstructure were employed and effects of the fairing attached to superstructure and existence of service load bridge spanning adjacently parallel to highway bridge are examined. The result of flume test showed that the fairing effectively reduced the tsunami-induced horizontal and vertical forces applied to bearing supports. Service road bridge also reduced the tsunami-induced force if it survived the tsunami effect. Furthermore the analytical procedures were verified through comparison with the flume test results and it was found that the analytical air-pressure model should be considered for the estimation of the hydrodynamic pressure.

Introduction

Many bridges were severely damaged by tsunami in the 2011 Great East Japan Earthquake (e.g. NILIM & PWRI, 2011). Recovery of a function for bridges with severe damage including washed-away of the superstructures generally requires long time, which affects the post-earthquake emergency activities due to the missing link of highway network. In Japan, large interplate earthquakes including the Tokai earthquake, the Tonankai earthquake and the Nankai earthquake were predicted with high possibility of occurrence in next few decades, therefore researches on countermeasures for the tsunami effect on bridges has been urgently required.

Seismic design specifications for highway bridges were revised in 2012 based on lessons learned from 2011 Grate East Japan Earthquake and the tsunami effect has been required to consider into the design of bridges which are constructed in the tsunami inundation area. In order to develop the design method for the tsunami effect, the mechanism of bridge behavior subjected to the tsunami-induced force should be studied. Based on the hydrodynamic interaction mechanism, the bridge behavior due to the tsunami will be affected by the characteristic of the superstructure (configuration of cross-section, number of girder, length of overhang slab, etc), the property of tsunami (configuration of wave, tsunami wave height, tsunami velocity, etc), the geographical condition around the bridge (bathymetry, initial water level, etc), etc. Therefore, the tsunami effect on bridges should be studied with consideration of those interaction parameters.

[1] Research Specialist, Bridge and Structural Engineering Research Group, PWRI, Japan
[2] Former Researcher, Bridge and Structural Engineering Research Group, PWRI, Japan; Technical Development Division, Highway Technology Research Center, Japan
[3] Collaborating Researcher, Bridge and Structural Engineering Research Group, PWRI, Japan
[4] Chief Researcher, Bridge and Structural Engineering Research Group, PWRI, Japan

Table 1. Experimental Parameters of Flume tests

characteristic of superstructure / property of tsunami		model 1		model 2		model 3		model 4		model 5		model 6		model 7			model 8		
initial water level (converted to full scale)	targete tsunami height (converted to full scale)																		
10cm (2.0m)	15cm (3.0m)	✓	✓	✓	✓	✓	✓	✓	✓	✓	✓	✓	✓	✓	✓		✓	✓	
	20cm (4.0m)	✓		✓		✓	✓	✓	✓	✓	✓	✓	✓	✓	✓		✓	✓	
	35cm (7.0m)	✓	✓	✓	✓	✓	✓	✓	✓	✓	✓	✓	✓	✓	✓		✓	✓	
15cm (3.0m)	10cm (2.0m)	✓		✓	✓	✓		✓		✓		✓		✓	✓		✓		
	15cm (3.0m)	✓		✓		✓		✓		✓		✓		✓	✓		✓		
	20cm (4.0m)																		
	35cm (7.0m)			✓	✓									✓	✓				
20cm (4.0m)	5cm (1.0m)	✓		✓		✓		✓		✓		✓		✓			✓		
	10cm(2.0m)	✓		✓		✓		✓		✓		✓		✓			✓		✓
	15cm(3.0m)	✓		✓		✓		✓		✓		✓		✓			✓		
	20cm(4.0m)																		
30cm (6.0m)	5cm (1.0m)																✓		

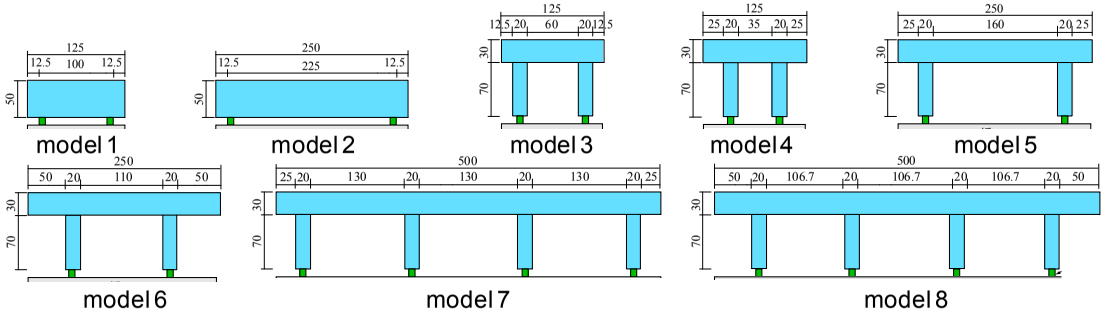

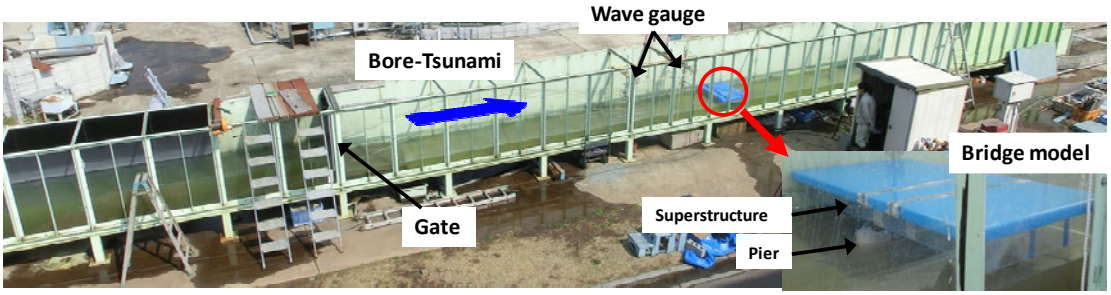

(a) Panorama view of flume test

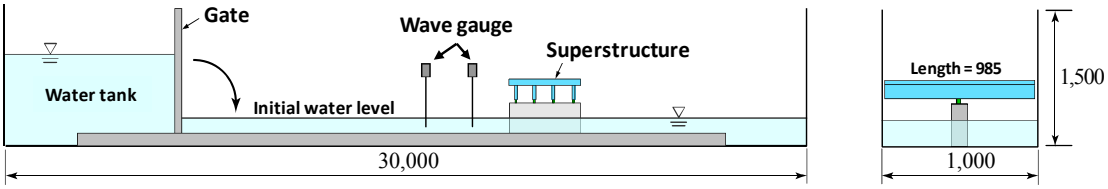

(b) Setup of flume test

Fig. 1 Setup of flume test

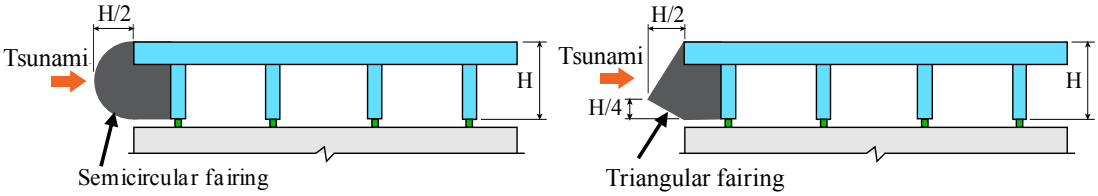

(a) Fairing models (Left: Semicircular faring, Right: Triangular fairing)

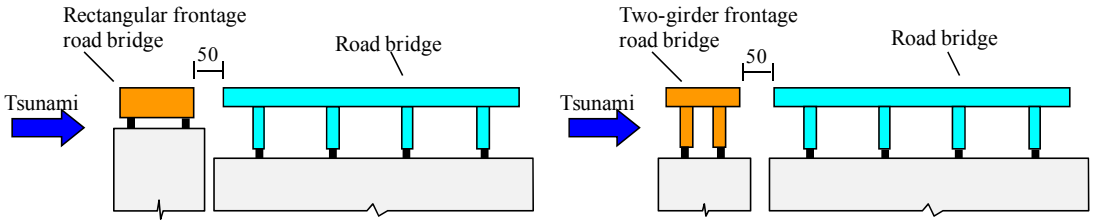

(b) Service road bridge models

(Left: Rectangular service road bridge, Right: 2-gider service road bridge)

Fig. 2 Details of fairing models and service road bridge models

It has been found from previous studies based on damage observation of washed-out bridges due to the tsunami that the behavior mode of those bridges can be categorized into two types, namely hydrodynamic-forces-dominant mode and buoyant-forces-dominant mode. The hydrodynamic-forces-dominant mode is generally caused by the tsunami bore, while buoyant-forces-dominant mode will be observed when the tsunami velocity is low at a bridge site and thus the water level rises gradually. It is also found from a previous experimental study conducted by authors that the buoyancy can be estimated based on the volume and the air in the structure. However, the tsunami-bridge interaction in hydrodynamic-force-dominant mode is more complicate than the buoyant-force-dominant mode in terms of impact on the

tsunami-induced behavior of bridges. Therefore, this paper discusses the mechanism of tsunami-induced behavior of the superstructure through a series of flume test and analysis. This research focuses on the mechanism of bridge behavior in the hydrodynamic-forces-dominant mode.

Flume Tests

Authors have conducted a series of test to study the behavior of bridge subjected to the tsunami-induced force. Experimental parameters the flume test and the test cases performed in this research are checked in Table 1. The flume tests were planned to examine effects of configuration of the superstructure, shape of the fairing attached to the superstructure and existence of a service road bridge spanning adjacently paralleled to a main bridge.

A large flume with 30.0m long, 1.0m width and 1.0m deep was employed in the test program as shown in Fig. 1. Recent researches by Yulong, Kosa (2013) have reported that the tsunami velocity observed around the site of washed-away bridges was estimated to be at most 8.0m/s based on several video records. In order to generate the simulated tsunami with the velocity of 8.0m/s in the flume test, a scale factor was determined as 1/20 and thus bridge models were designed with 1/20 scale in length.

In the flume test, the tsunami bore was generated by rapidly opening the gate of the water tank as shown in Fig. 1, where the tsunami velocity was controlled by initial water level and tsunami wave height.

Flume tests for eight bridge models as listed in Table 1 are introduced in this paper. In each model, reaction forces applied to bearing supports in both horizontal and vertical directions due to the tsunami-induced force were measured by biaxial load cells. Simultaneously, the hydrodynamic pressures at some points in the superstructure were measured by pressure gauges. The fairings were designed with semicircular and triangular shapes as shown Fig.2 (a). Details of the triangular fairing were determined based on a previous experimental research by authors. The service road bridge model was designed with the rectangular and the two-girders as shown Fig 2 (b). The clearance between the main bridge model and the service road bridge model is set as 50mm which corresponds with 1.0m in the real scale. An elevation of deck face of two bridges was set with the same level. In this test program, the fairing was attached to the ocean side of superstructure, because this research focuses on the mechanism of superstructure subjected to the tsunami-induced force.

Mass of the superstructure model employing in the test is not scaled the mass of real superstructure precisely based on principle of similitude. However, the purpose of this flume test is to examine the horizontal and vertical force to bearing supports induced by the tsunami, and the mass of the superstructure doesn't generate the tsunami-induced force. Therefore, it can be assumed in the test program that the effect of the mass of superstructure on the reaction force in bearing supports can be negligible.

The hydrodynamic pressures observed at the bottom of overhang slab and the web plate of girder are shown in Fig. 3,where the engineering value converted to full scale. Distribution of the hydrodynamic pressure observed for the case of low tsunami velocity exhibits a substantially uniform and variation of the hydrodynamic pressure is small. On the other hand, distribution of the hydrodynamic pressure for the case of high

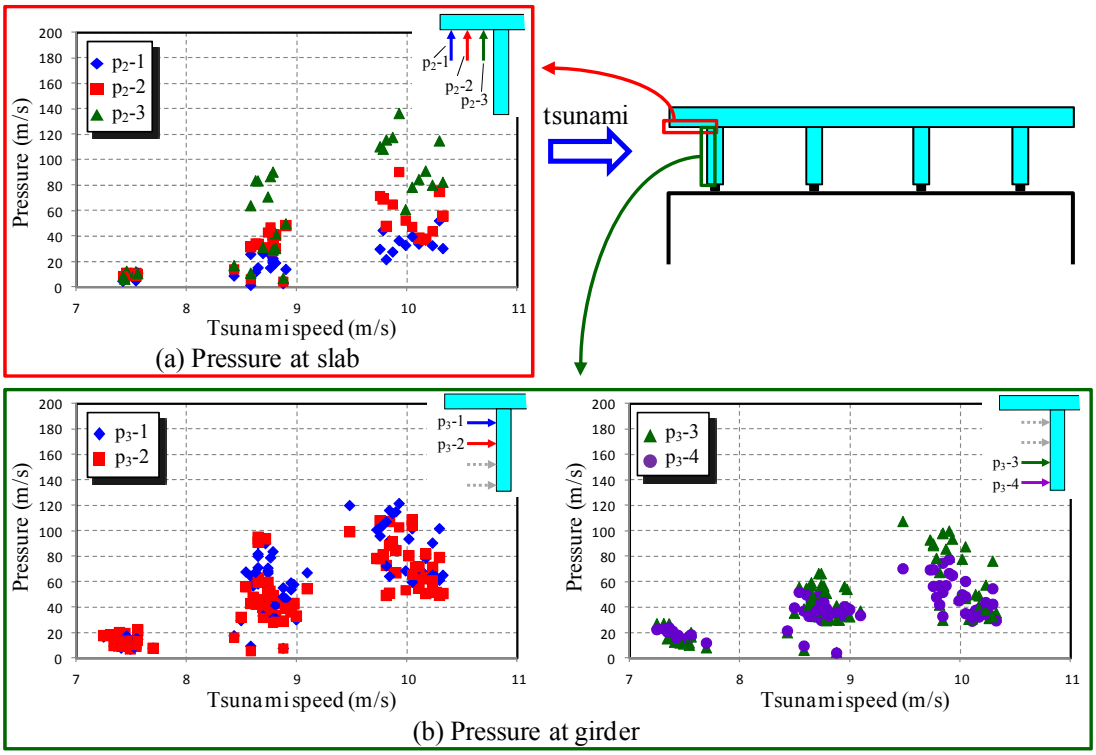

Fig. 3 Distribution of hydrodynamic pressure

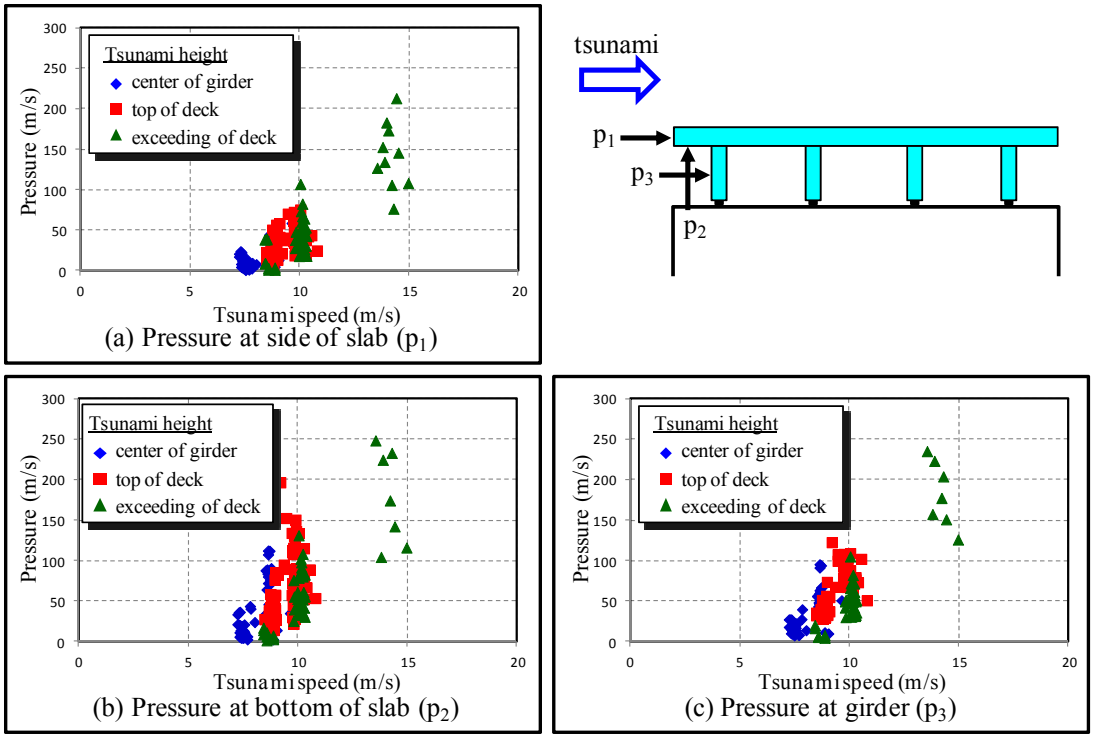

Fig. 4 Relation between hydrodynamic pressure and tsunami speed

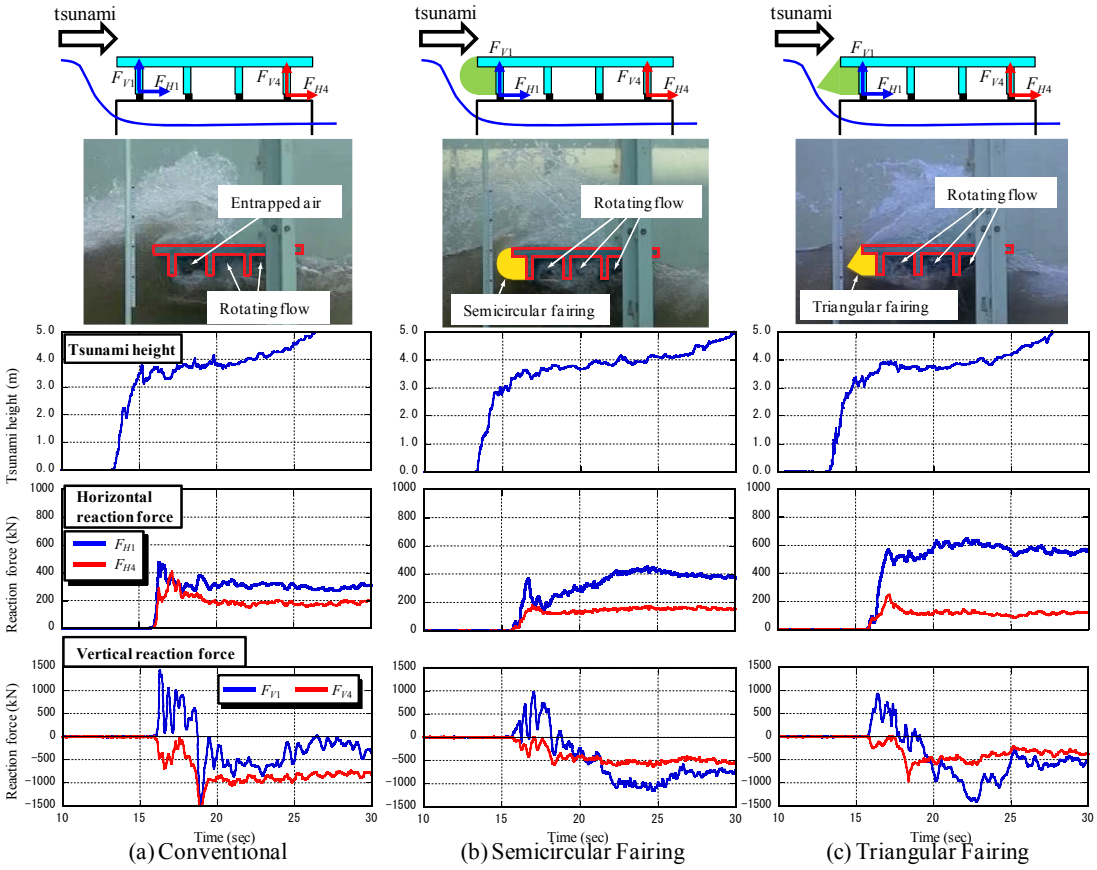

(a) Conventional (b) Semicircular Fairing (c) Triangular Fairing

Fig. 5 Time histories of reaction force in bearing (effect of fairing)

tsunami velocity seems to be uneven, and large pressure is measured at the top of the web plate.

Fig. 4 shows relation between the hydrodynamic pressure to superstructure and the tsunami velocity measured in the flume test, which seems to indicate that the relation exhibits roughly parabolic curve.

Fig. 5 and 6 show the time-historical responses of the reaction force to the bearing supports for the test case of the fairing and the service bridge, respectively. Wave height was measured at 1.0m ahead of the bridge model. The effect of the fairing on the reaction force to bearing supports is shown in Fig. 5, where the plotting data were obtained in the test case of the targeted tsunami velocity of 10m/s, the initial water level of 4.0m and the targeted tsunami height of 2.0m. As shown in Fig. 5, the fairing effectively reduced the tsunami-induced horizontal and verticals force applied to bearing supports.

The effect of existence of the service road bridge on the reaction force to bearing supports is shown in Fig. 6, where the plotting data were obtained in the test case of the targeted tsunami velocity of 7m/s, the initial water level of 4.0m and the targeted tsunami height of 2.0m. Fig. 6 indicated that existence of the service road bridge reduced the tsunami-induced horizontal and vertical forces applied to bearing supports of the main bridge if the service road bridge survived after impact of the tsunami.

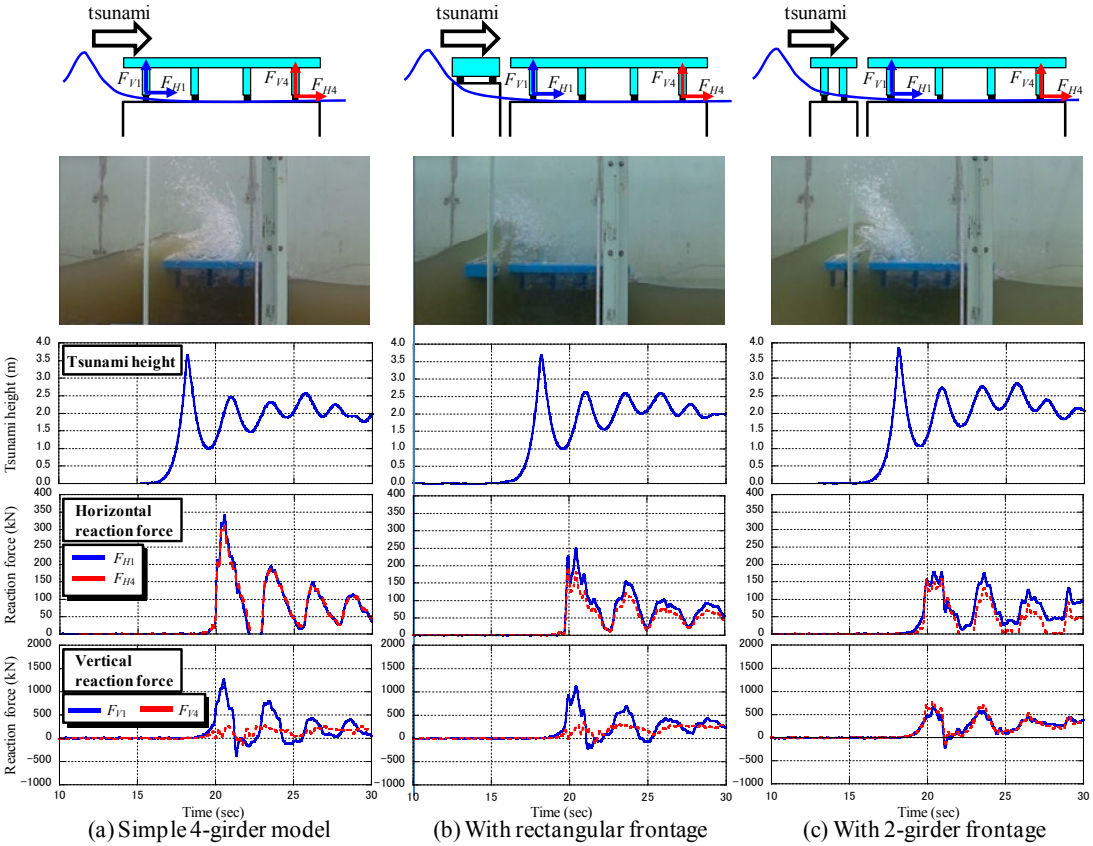

(a) Simple 4-girder model (b) With rectangular frontage road bridge model (c) With 2-girder frontage road bridge model

Fig. 6 Time histories of reaction force in bearing (effect of service load bridge)

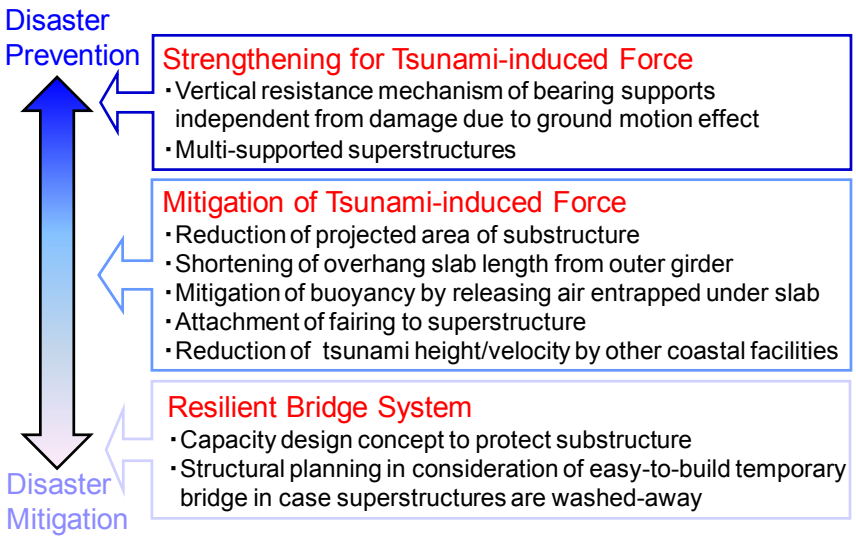

Fig. 7 Ideal Structure for Girder Bridges Subjected to Tsunami-induced Force

Ideal Bridge Structure Subjected to Tsunami Effect

Based on findings from experimental researches conducted by authors and the mechanism of the tsunami-induced force transmitted to bearing supports in bridges, an

ideal planning of bridge structure is proposed as shown in Fig. 7, where options are listed in terms of “disaster prevention” and “disaster mitigation”.

Numerical Analysis of The Flume Test

In order to examine the applicability of an analytical model for the bridge subjected to the tsunami-induced force, numerical analyses employing the numerical wave flume by the CADMAS-SURF/3D (Super roller flume for computer design of maritime structure) were conducted for test cases described above. This numerical analysis employs the Volume of Fluid Method (VOF method) which can simulate free

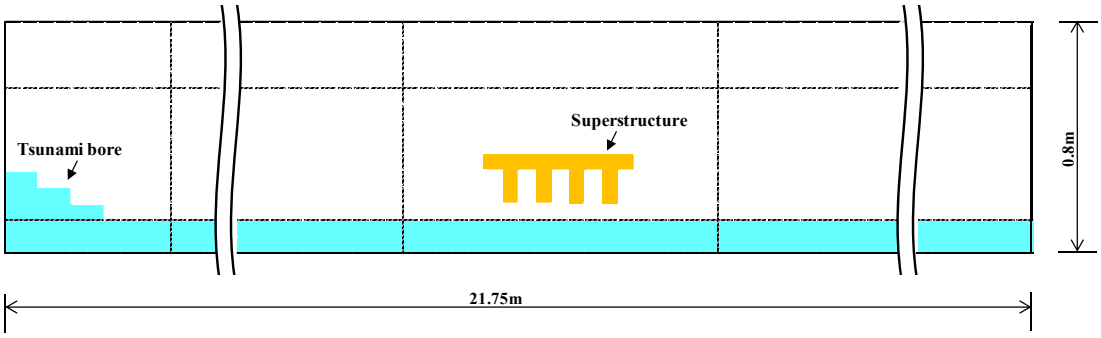

Fig. 8 Analytical model of flume test

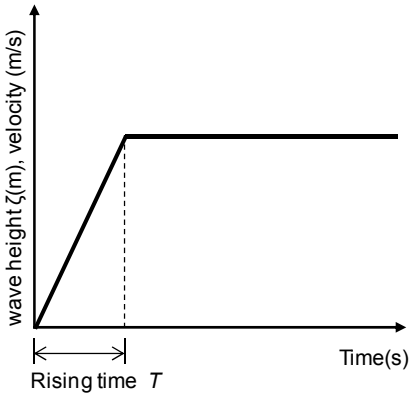

Fig. 9 Model for wave generator

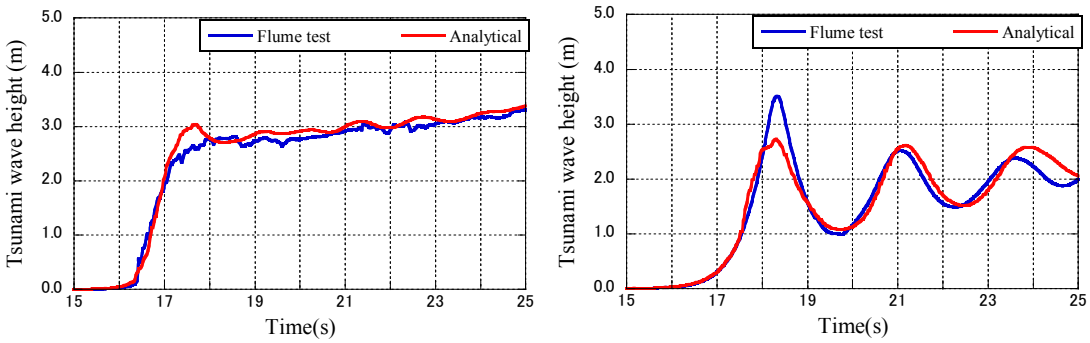

(a) Initial water level of 150mm (b) Initial water level of 200mm

Fig. 10 Time histories of tsunami wave height

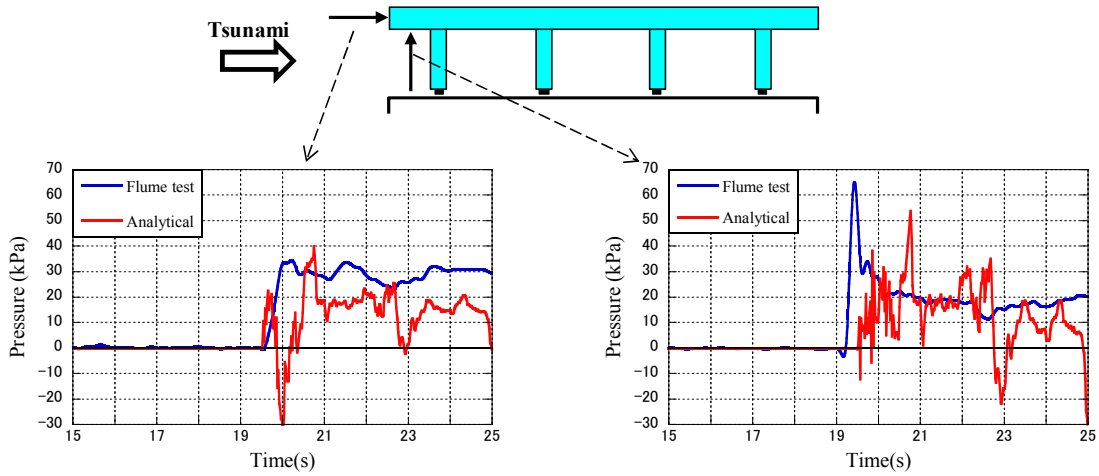

(a) Hydrodynamic pressure at overhang slab

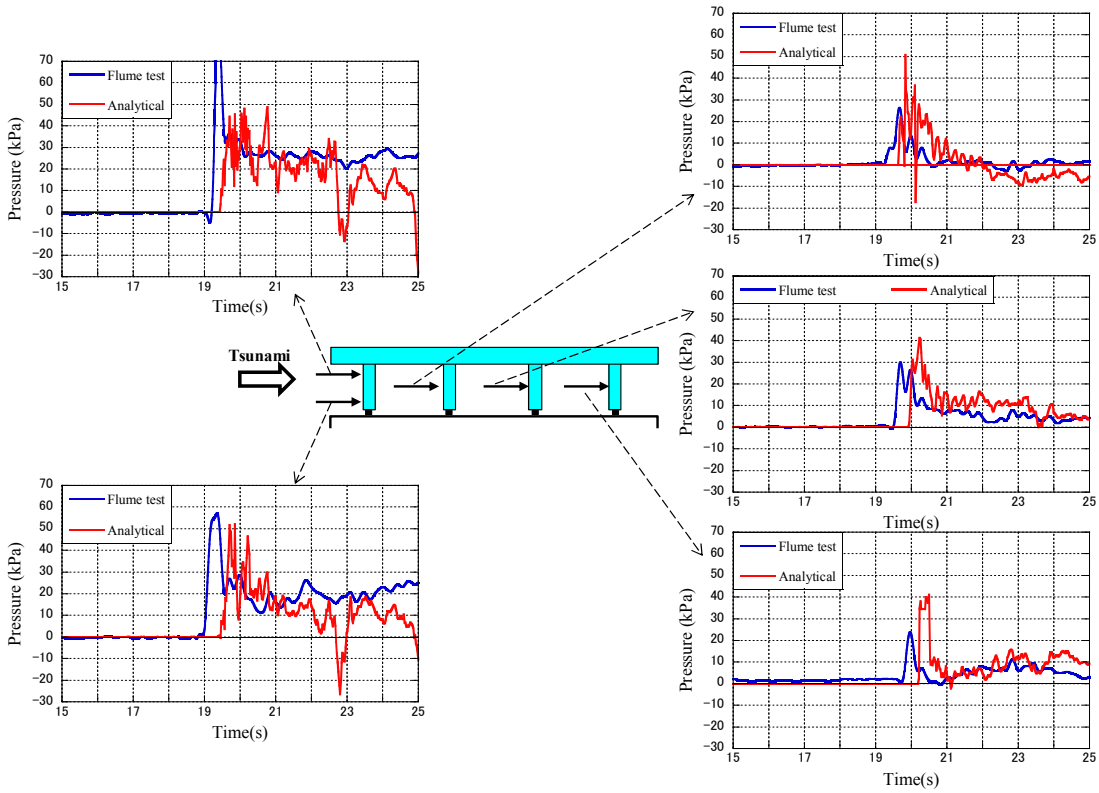

(b) Hydrodynamic pressure at web plate of girders

Fig. 11 Time histories of hydrodynamic pressure (initial water level of 150mm)

surface with high accuracy and high analytical speed.

Fig. 8 shows the two-dimensional analytical model of the flume tests described in previous section. The length of the flume model was set as 21.25m, to simulate the tsunami bore generated in the flume test. Superstructures with 4-girders model and rectangular slab model employed in the flume test were analyzed in this research. Tsunami wave was generated by using the wave model as shown in Fig. 9, where the rising time T is influenced by configuration of tsunami wave. Tsunami velocity U was calculated from the wave height and the initial water level as,

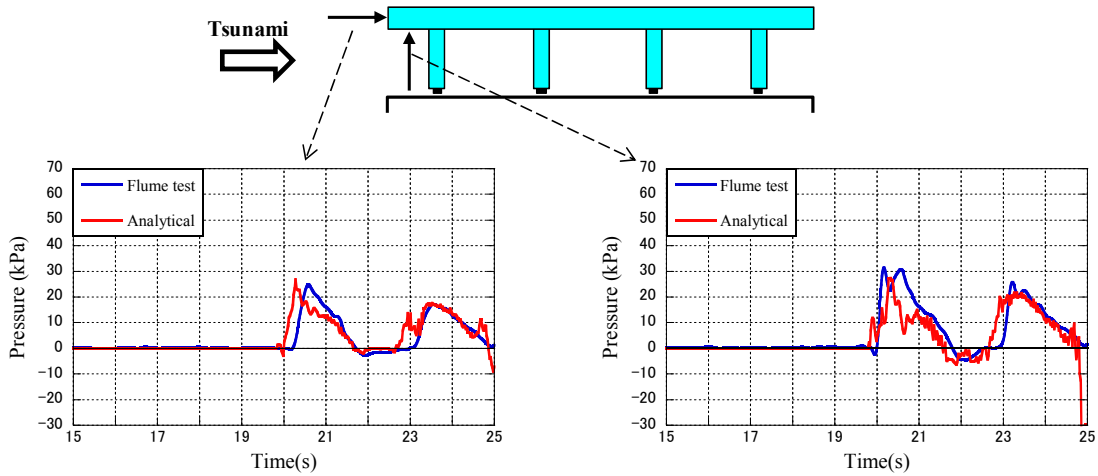

(a) Hydrodynamic pressure at overhang slab

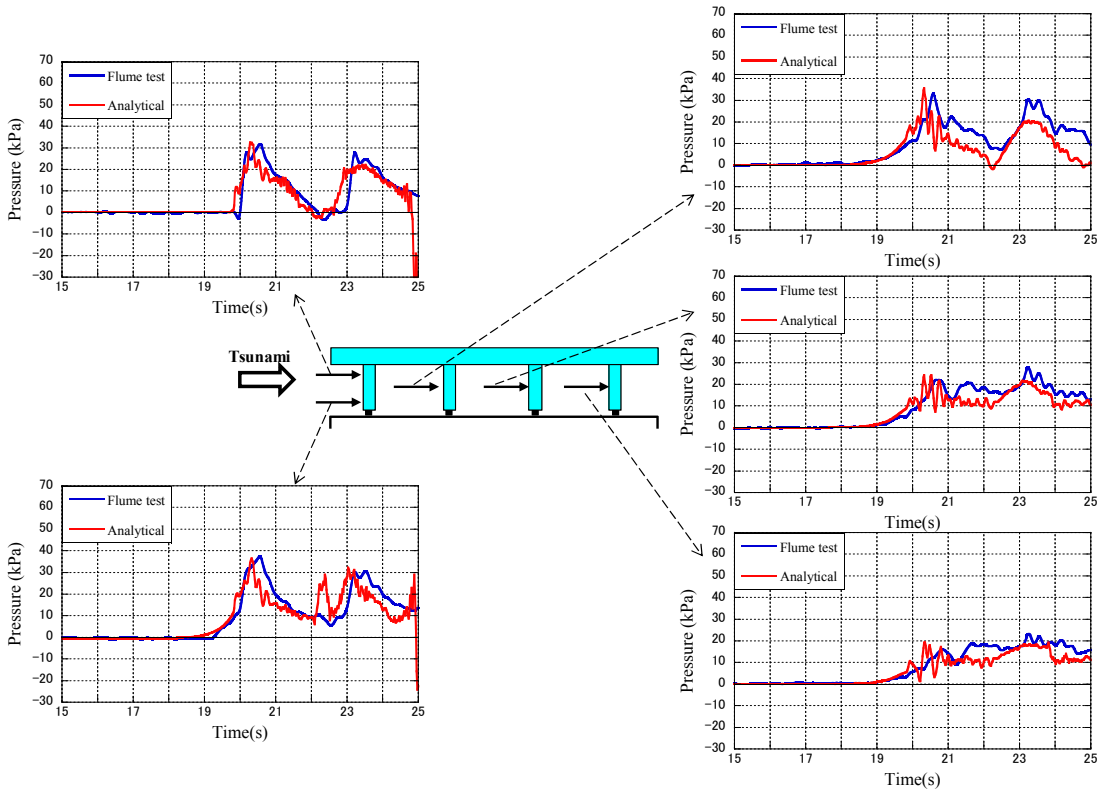

(b) Hydrodynamic pressure at web plate of girders

Fig. 12 Time histories of hydrodynamic pressure (initial water level of 200mm)

$$U = \frac{\zeta}{h+\zeta}\sqrt{\frac{g(h+\zeta)(2h+\zeta)}{2(h+\zeta-\eta\zeta)}} \tag{1}$$

where, h is the initial water level, ζ is the wave height, η is the resistance coefficient (assumed to be 1.03 by Fukui, 1962) and g is the gravitational acceleration. Tsunami wave can be controlled by these parameters (tsunami wave height ζ, initial water level h and rising time T). Two cases of the initial water level of 150mm and 200mm were set

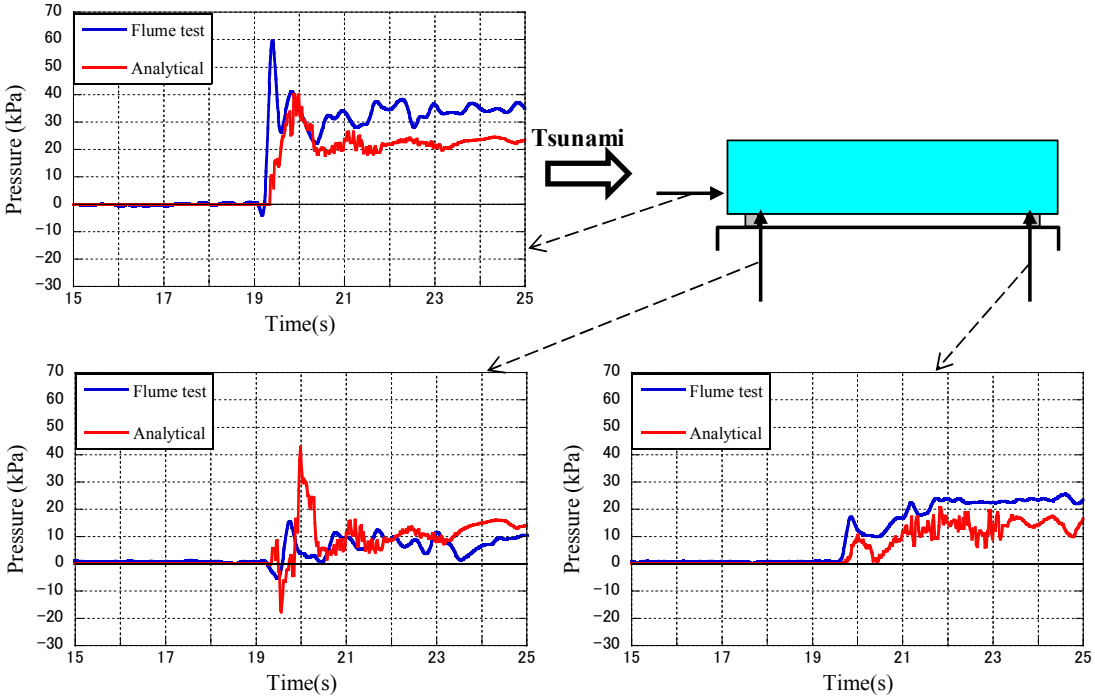

(a) The initial water level of 150mm

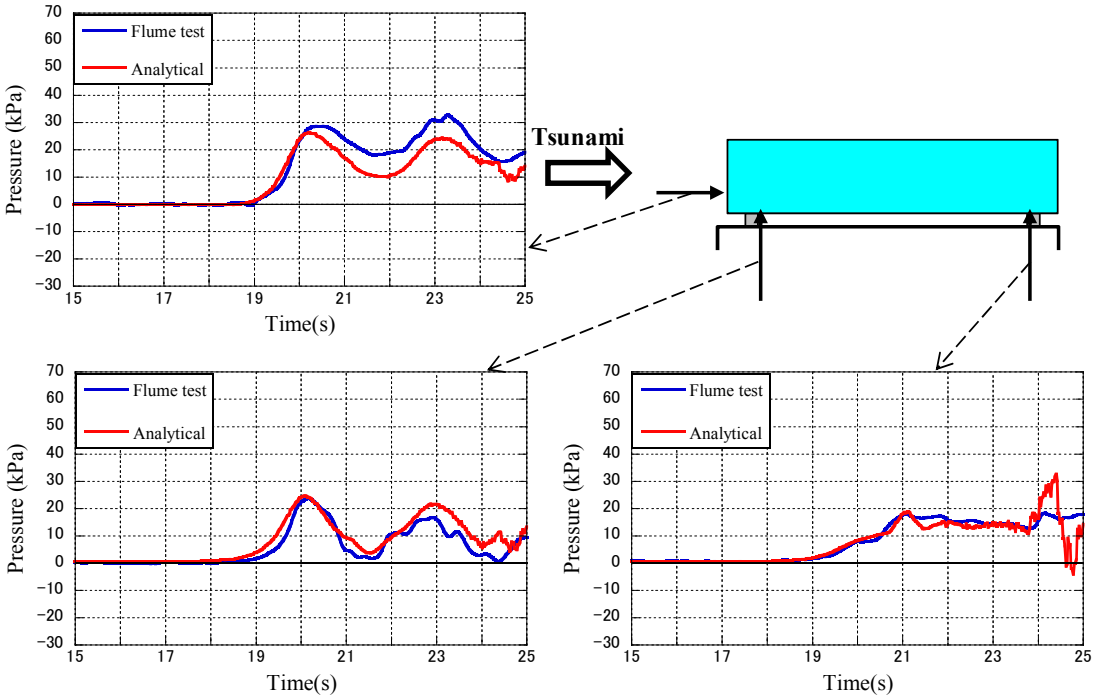

(b) The initial water level of 200mm

Fig. 13 Time histories of hydrodynamic pressure at side and bottom of rectangular model

in the analysis so as to generate tsunami with the wave height as high as deck face of superstructure models.

Fig. 10 shows time the historical wave height at the position of 1.0m ahead of

the model. The tsunami wave height analyzed by the model coincides well with the results of flume test in all case.

Figs.11 and 12 show the time historical hydrodynamic pressure at the bottom of overhang slab and the web plate in the model of 4-girders superstructure. For the case of the initial water level of 150mm as shown Fig. 11, the hydrodynamic pressures at the bottom of overhang slab acting immediately after the tsunami impact are smaller than the result of the flume test, and large variation of the hydrodynamic pressure is observed. The hydrodynamic pressures at the web plate of girder roughly coincide with the result of flume test. For the case of the initial water level of 200mm, the hydrodynamic pressures at the bottom of the overhang slab and the web plate of girder agree well with the result of flume test as shown in Fig. 12.

Fig. 13 shows the time history of the hydrodynamic pressure at side and bottom of rectangular superstructure model. It is noted that the hydrodynamic pressures do not agree well with the experimental data in the case of initial water level of 150mm. This may be because the tsunami velocity is so fast that the tsunami becomes breaking wave, which will cause complicate interaction with superstructure. On the other hand, in the case of initial water level of 200mm, the hydrodynamic pressure coincides with the result of flume test.

Conclusions

This paper discussed the tsunami-induced behavior of the superstructure through a series of flume test and analysis.

Based on findings from experimental researches conducted by authors and the mechanism of the tsunami-induced force transmitted to bearing supports in bridges, an ideal planning of bridge structure was proposed as shown in Fig. 7. Analytical procedures for estimating the hydrodynamic pressure to superstructure were introduced and an applicability of the method was shown through a comparison between analytical result and the large-scale flume test.

Furthermore, experimental and analytical results showed that the fairing effectively reduced the hydrodynamic pressure and thus reduced the tsunami-induced horizontal and vertical forces applied to bearing supports. The existence of the service bridge also reduced the tsunami-induced horizontal and vertical reaction forces applied to the main bridge, if the service bridge could survive after impact of the tsunami.

References

National Institute for Land and Infrastructure Management (NILM), Public Works Research Institute (PWRI): Quick Report on Damage to Infrastrucures by the 2011 off the Pacific coast of Tohoku Earthquake, Technical Note of National Institute for Land and Infrastructure Management, No.646, Technical Note of Public Works Research Institute, No.4202, 2011.

Hoshikuma, J. : Damage of Highway Bridges due to the Great East Japan Earthquake, Proc. 27th US-Japan Bridge Engineering Workshop, 2011.

M. Lee Marsh, Ian G. Buckle, W. Phillip Yen, Shideh Dasti, David Frost, Eric Monzon: Bridge Performance during the Great East Japan Earthquake of March 11, 2011, Proc. 27th US-Japan Bridge Engineering Workshop, 2011.

Japan Road Association. "Design Specification for Highway Bridges, Part V: Seismic Design." 2012 (in Japanese).

Yulong ZHENG, Kenji KOSA, Tatsuo SASAKI: Evaluation of Bridge Outflows due to Great Tsunami, Proceedings of the Japan Concrete Institute, Vol.35, Jul. 2013, pp. 841-846

Fukui, Y., Shiraishi, H., Nakamura, A. and Sasaki, Y.: Study of tsunami(Ⅰ)–for wave velocity of tsunami bore-, The Journal Coastal Engineering, Vol.9, 44-49, 1962.

HYBRID TESTING OF A PRESTRESSED GIRDER BRIDGE TO RESIST WAVE FORCES

Christopher Higgins[1], Jora Lehrman[2], Christopher Bradner[2], Thomas Schumacher[2], and Daniel Cox[1]

Abstract

This paper describes hybrid tests to characterize the structural performance of connection details for prestressed girder bridges subjected to hurricane wave loading. Full-scale specimens were tested under dynamic cyclic forces using measured force time-histories from hydraulic tests of a 1/5 scale model of a highway bridge spanning a coastal embayment. The wave load effects included combined dynamically applied horizontal and vertical forces on the connections. Test results showed none of the connections considered would be capable of resisting newly specified vertical wave forces for large wave heights when significant air is entrapped under the bridge.

Introduction

The US has many bridges located in coastal regions that are susceptible to wave forces. Many of these bridges were not designed to resist the lateral and vertical forces from large wave loading. This has been demonstrated by recent strong hurricanes that have caused significant damage to the transportation infrastructure. Damage to bridges is of particular concern because these critical assets limit capacity of the transportation system and can delay rescue, recovery, and rebuilding efforts after an event.

Post disaster surveys by Douglass *et al*. (2006), Padgett *et al*. (2008), Robertson *et al*. (2007), and Chen *et al*. (2009) among others described the failure modes, costs, and the wave conditions surrounding the failed superstructures. Failures were attributed to storm surge allowing the surface waves to strike the superstructure and overcome the capacity of the anchorages. Subsequent waves pushed the superstructures off of the supporting substructure. Chen *et al*. (2009) and Douglass *et al*. (2006) both developed models to hind-cast the conditions along the Gulf Coast, determine the surge height, maximum significant wave height, wave period, and estimated the total forces acting on the bridge superstructures.

Previous experimental research regarding wave loads on structures (Denson.(1980), Bea *et al*. (2001), and Cuomo *et al*. (2007) has focused on off-shore drilling platforms which differ significantly from near-shore bridge superstructures. More recent experimental work was conducted by Marin and Sheppard (2009) utilizing a 1:8 scale model of the I-10 bridge over Escambia Bay, Florida. The study

[1]Professor and [2]Former Graduate Student, School of Civil and Construction Engineering, Oregon State University, Corvallis, OR 97330

experimentally determined inertia and drag coefficients for wave loads, and developed predictive equations for wave induced loading. These equations were the basis of the AASHTO *Guide Specification* (2008) for bridges vulnerable to coastal storms. While typical wave loading on bridges as well as the global failure modes have been investigated, the behavior of the individual structural connections between the superstructure and substructure has not been examined and realistic multi-axis force interactions have not been considered.

Research Significance

Presently, no data are available that characterize the structural performance of connections between the bridge superstructure and substructure under hurricane-induced wave loads. These are the connections that were reported to have failed in previous storms and thus may control survival of low-lying coastal bridges. The present research combines hydraulic tests of a 1:5 scale model of a real highway bridge located in Escambia Bay, Florida to measure the wave forces on the bridge. The research developed for the first time an innovative laboratory setup that allowed the test specimen to simulate the dynamic response of the superstructure. The measured wave force histories on the large-scale hydrodynamic model were converted into the vertical and horizontal force components at the connections. The force histories from the large-scale hydrodynamic model were increased to prototype scale and then applied dynamically to full-size connection elements to characterize the structural performance. This approach represents a new technique in hybid testing to investigate fluid-structure interactions and is applicable to tsunami research.

Hydrodynamic Model Test

The hydraulic experiments were conducted in the Large Wave Flume (LWF) at the O.H. Hinsdale Wave Research Laboratory at Oregon State University. The LWF is 104 m (342 ft) long, 3.66 m (12 ft) wide and 4.57 m (15 ft) deep. For these experiments, the bathymetry was comprised of an impermeable 1:12 slope, followed by a horizontal section approximately 30 m (98 ft) in length, and then another 1:12 slope to dissipate waves and minimize reflection off the beach. The specimen was located in the horizontal section, approximately 18 m (59 ft) landward of the offshore sloped bathymetry, and 46 m (151 ft) from the wavemaker as illustrated in Fig. 1.

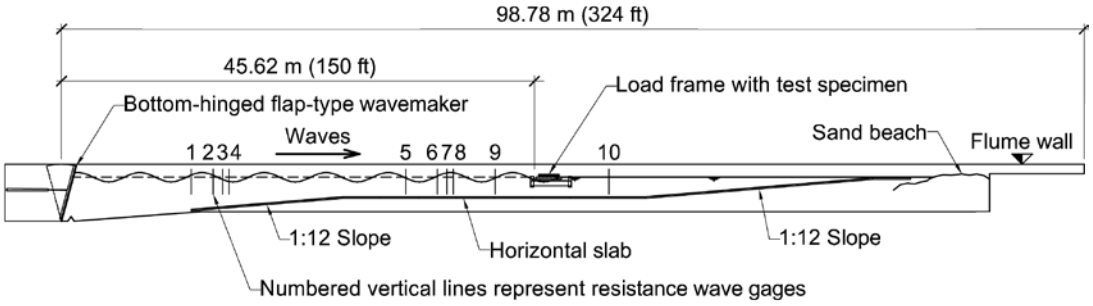

FIG. 1 – ELEVATION VIEW OF LARGE WAVE FLUME WITH SETUP.

The test specimen was based on prototype dimensions taken from Florida Department of Transportation drawings of the I-10 Bridge over Escambia Bay. Six scaled AASHTO Type III girders including the full complex cross-sectional geometry were constructed and connected with twin steel rods through four diaphragms spaced along the span. An analysis of the bridges damaged during Hurricane Katrina found that the individual spans failed independently, with little interaction between adjacent spans (NIST, 2006). This independent failure facilitated the testing of a single superstructure section. A geometric scale of 1:5 (undistorted) was chosen to allow the largest possible test specimen with a representative length to span the width of the wave flume. The total span length, S, of the model was 3.45 m (11.3 ft), the width, W, 1.94 m (6.36 ft), and the overall height, (h_d), 0.28 m (0.92 ft). Table 1 lists the model and prototype dimensions and weight. The deck was fastened to the girder and diaphragm sub-assemblage using 13 mm (0.5 in.) diameter threaded rods. Prior to installing the specimen in the wave flume, the gaps between the deck and supporting girders and diaphragms were sealed with caulking to replicate the air-tight integrity of the monolithically-cast prototype superstructures. Figure 2 shows the test specimen beams and diaphragms before attachment of the deck.

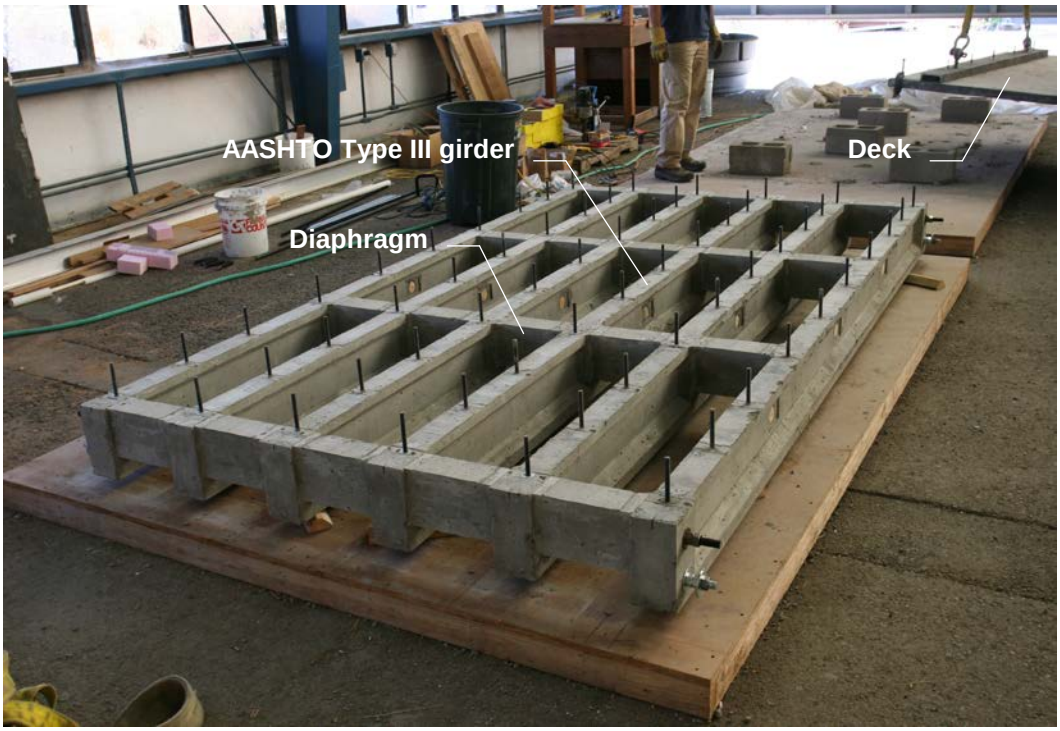

FIG. 2 – SPECIMEN ASSEMBLAGE OF GIRDERS AND DIAPHRAMS BEFORE PLACEMENT OF DECK.

Table 1. Properties of model test specimen (without guard rail) and corresponding prototype bridge.

Test parameter	Symb.	Model (1:5)	Prototype (1:1)
Water depth	H	1.60 - 2.17 m (5.25 – 7.12 ft)	8.0 – 10.9 m (26.2 – 35.6 ft)
Bottom girder clearance to SWL	d_c	± 0.279 m (± 0.92 ft)	±1.4 m (± 4.6 ft)
Wave height [1]	H	0.25 - 1.0 m (0.82 to 3.28 ft)	1.25 - 5.0 m (4.1 to 16.4 ft)
Significant wave height [2]	H_s	0.375 - 1.0 m (1.23 to 3.28 ft)	1.9 - 5.0 m (6.2 to 16.4 ft)
Wave period [1]	T	2.0 - 4.5 s	4.5 – 10.1 s
Peak wave period [2]	T_p	2.0 - 3.0 s	4.5 – 6.7 s

[1] For regular wave trials [2] For random wave trials

To simulate the dynamic response of the superstructure, a unique reaction frame was designed to permit the test specimen to move freely along the axis of wave propagation. The specimen was supported by two HSS7x5x1/2 steel members representing the bent caps. Each bent cap was then supported by two load cells mounted in line with the external offshore and onshore girders to measure vertical forces at these points. The four load cells were mounted on high-precision ball bearing rollers that allowed low friction motion of the load cells, bent caps and specimen along linear guide rails attached to the top flange of two W18x76 steel profiles (h = 0.50 m) bolted to each side of the flume wall. To measure horizontal forces, load cells were mounted between the offshore end of the bent caps and end anchorage blocks that were bolted to the flume wall. The specimen and reaction frame were mounted in the wave flume so that the bottom of the girders was located 1.89 m (6.2ft) above the horizontal bed to correspond with typical mudline-to-superstructure distances of the failed bridges. A drawing of the setup can be seen in Fig. 3

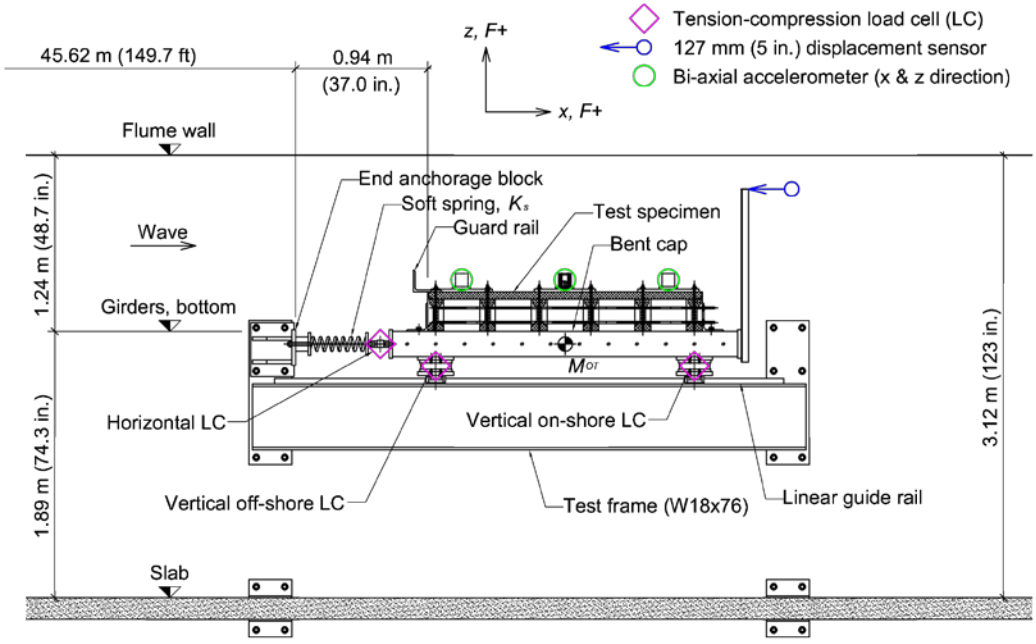

FIG. 3 - ELEVATION VIEW OF TEST SPECIMEN (FLEXIBLE SPRING SHOWN).

To investigate the influence of substructure flexibility on the wave loading response, an adjustable dynamic setup was developed and integrated into the reaction frame. The flexibility of the prototype substructure was modeled by a pair of elastic springs installed between the bent caps and the end anchorage blocks. To determine the required spring stiffness for the model, a finite element (FE) analysis was performed on a prototype-scale bridge similar in design to the test specimen. Two sets of springs were investigated. The first set was designed to be relatively soft in order to deliberately exaggerate displacements. The second, stiffer set of springs was chosen to realistically represent the bridge substructure. The two sets of springs selected for this project had spring constants of 107 kN/m (612 lb/in.) and 458 kN/m (2614 lb/in.) which produced fundamental periods of 0.95 s and 0.46 s, respectively.

The hydraulic experiments were divided in three phases. Phase 1 simulated a rigid structure. The test specimen was bolted to the bent caps and each bent cap was then connected to an end anchorage block via a load cell. Phase 2a and 2b simulated a flexible substructure using the previously described medium and soft springs, respectively. The springs were added to the bent cap-end anchorage block linkage described above, allowing the specimen and bent caps to vibrate along the rail guide (see Fig. 3). Phase 3 was designed to simulate the response of the bridge span upon failure of the bent cap connections. For this phase, the bent caps were rigidly connected to the end anchorages as in Phase 1, but the test specimen was disconnected from the bent caps with only the specimen self-weight and the resulting friction providing resistance.

Wave conditions and water levels were designed to simulate realistic conditions found at coastal bridges along the Gulf of Mexico during extreme events. Typically

these bridges are located in shallow water of 3-10 m (10-33 ft) and are somewhat protected by shoals and barrier islands. As a result, waves at these bridges are considerably smaller in height and length relative to ocean waves. Even during catastrophic events such as Hurricane Katrina, numerical modeling by Chen, et al. 2009) estimates a relatively small maximum significant wave height of 2.6 m (8.5 ft) and a peak period of 5.5 s at the U.S. 90 Bridge over Biloxi Bay. Similar conditions have been reported for Hurricane Ivan at the I-10 Bridge over Escambia Bay. Using the conditions hindcast by these models as a guide, a realistic range of water levels, wave heights, and wave periods was developed. To simulate storm surge, the water depth, h, at the specimen was adjusted from 1.61 m (5.3 ft) to 2.17 m (7.1 ft) in increments of 0.14 m (5.5 in.) which is equal to one-half the specimen height. The resulting SWL ranged between 0.28 m (11 in.), below the bottom of the girders to even with the top of the deck. A non-dimensional parameter, $d^* = (h-z_d)/h_d$, that represents the SWL elevation relative to the bottom of the girders, where z_d is the elevation of the bottom flange above the mudline and h_d is the height of the bridge deck. For these experiments, values of d^* ranged from -1.0 to +1.0 in increments of 0.5. For each of the five water depths, regular and random wave conditions were tested. For the regular wave trials, target wave height (H) and period (T) ranged from 0.25 to 1.0 m (0.8 to 3.3 ft) and 2.0 to 4.5 s respectively. Random wave trials consisted of a series of approximately 300 waves with a TMA spectrum (γ = 3.3). Target significant wave height (H_s) and peak period (T_p) ranged from 0.375 to 1.0 m (1.2 to 3.3 ft) and 2.0 to 3.0 s respectively. In all, 428 trials were conducted and the test variables are shown in Fig. 4.

The sensor suite was designed to measure wave conditions, forces and pressures acting on the specimen, and the response of the specimen as shown in Fig. 5. To measure water surface elevation, 10 surface piercing resistance wave gages (WG) were placed along the length of the flume (see Fig. 1). Gages 1-8 were arranged into two arrays of four and positioned offshore of the specimen to resolve incident and reflected waves at two locations. Gage 9 was placed approximately 4 m (13 ft) offshore of the specimen to measure water surface elevation in the vicinity of the specimen and Gage 10 was located 6 m (20 ft) onshore of the specimen. Six tension-compression load cells were deployed to measure overall forces on the model. Four ±89 kN (±20 kip) capacity load cells were mounted between the bent caps and rollers on the linear guide rail to measure vertical forces. The remaining two load cells were ±44 kN (±10 kip) capacity load cells that measured horizontal forces acting at mid-height of the bent caps. All six load cells were calibrated in the actual test configuration. To measure pressure distribution, 13 pressure transducers were installed in the specimen. Steel mounting plates were cast into the concrete so that the sensors could be securely flush-mounted to the surface of the specimen, minimizing the disruption of flow as well as the sensor response due to vibration. Pressure sensors were mounted in the offshore face of the deck, the webs of the front and interior girders, and along the underside of the deck between the girders.

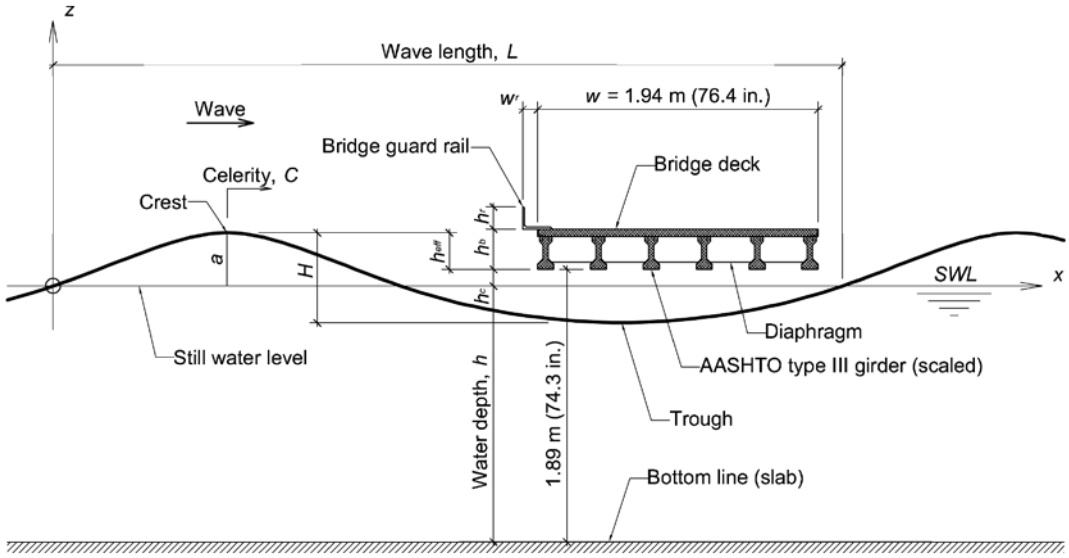

FIG. 4 - ELEVATION VIEW OF THE TEST SPECIMEN ACROSS TANK WITH TEST VARIABLES.

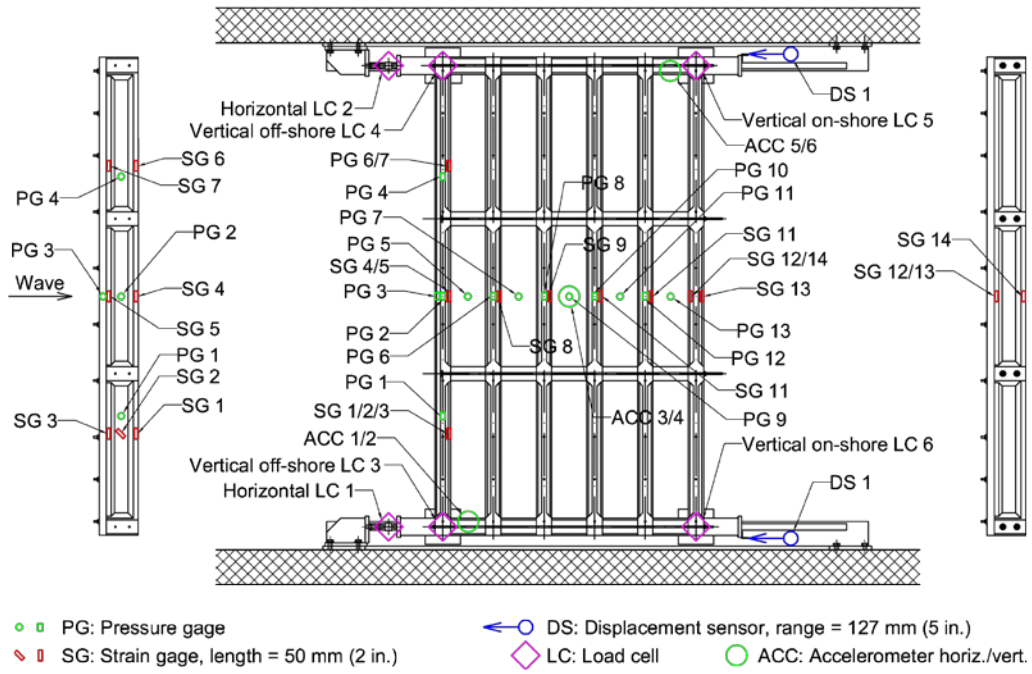

FIG. 5 – PLAN VIEW OF THE TEST SPECIMEN WITH SENSOR DETAILS.

Presented subsequently are example data that were collected for a water depth h of 1.89 m where the still water level is even with the bottom flange of the girders, i.e. $d^* = 0$. Some of the biggest forces are found under these conditions. The waves used in the following examples were regular with target wave period and height of 2.5 s and 0.625 m, respectively. The left side are Phase 1 while the right side are from Phase 2b.

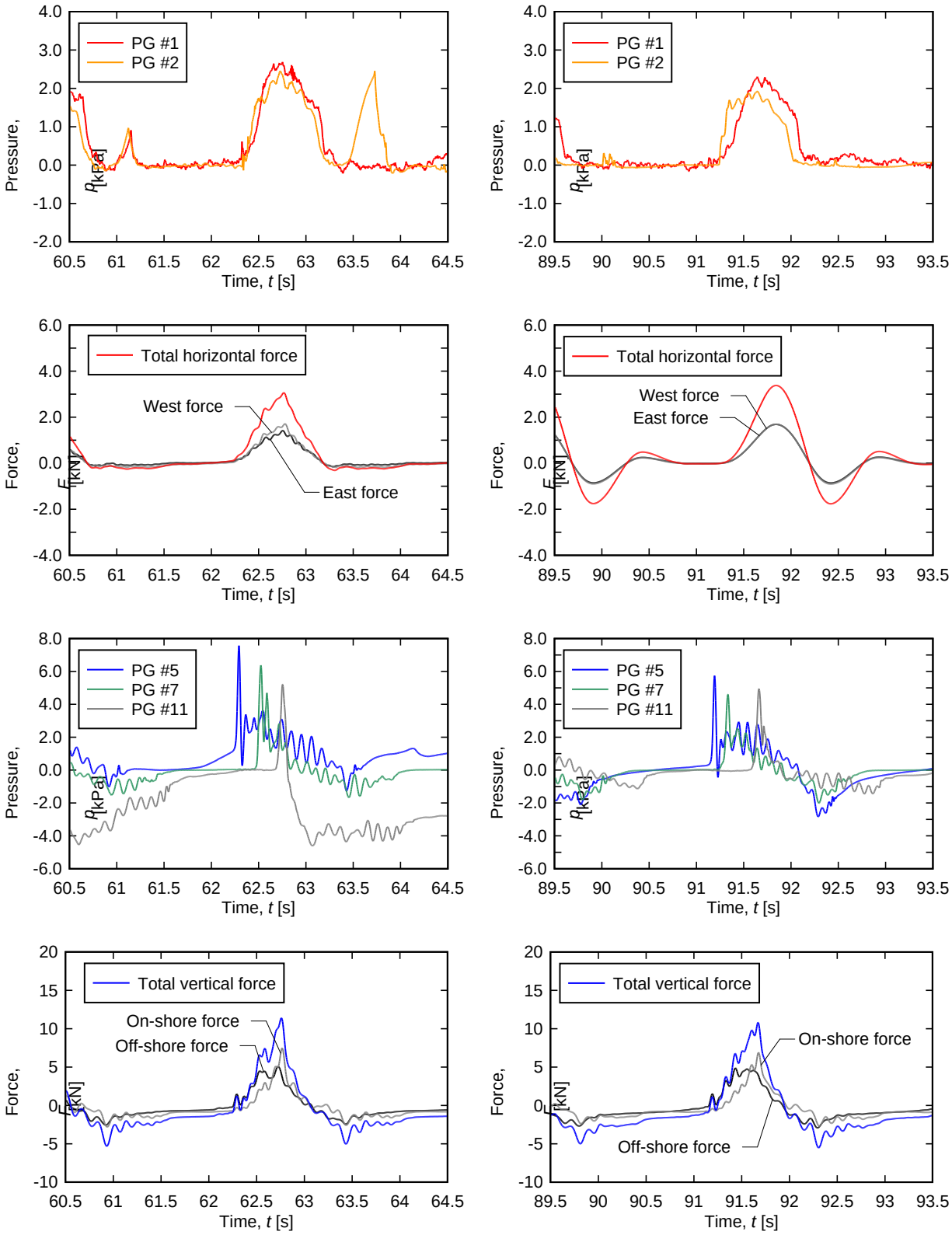

FIG. 6 – EXAMPLE MEASUREMENT FOR PHASE 1 (LEFT COLUMN) AND PHASE 2B (RIGHT COLUMN)

It was observed that the substructure flexibility resulted in higher vertical and horizontal forces than the rigidly attached bridge as summarized in Fig. 7.

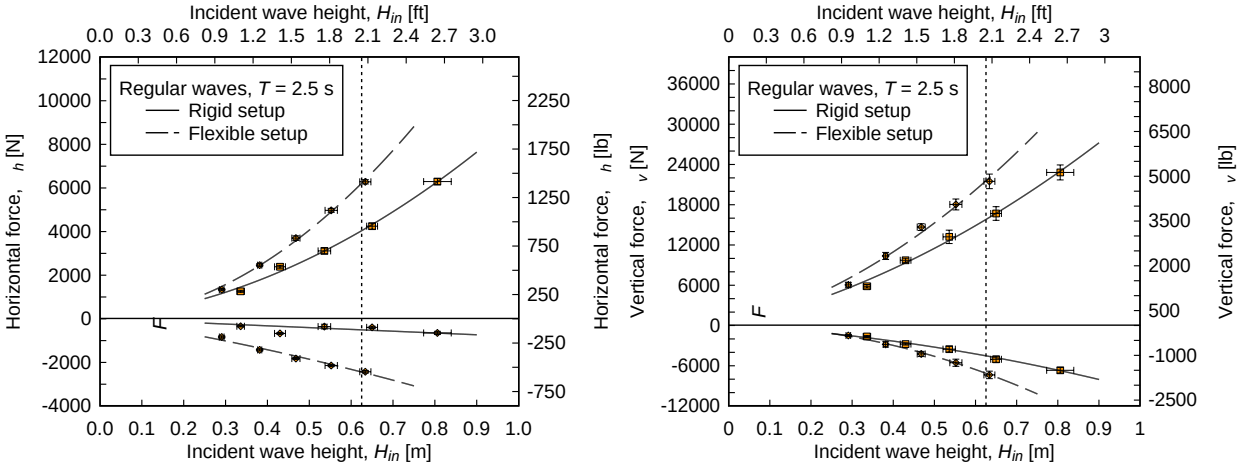

FIG. 7 - MEAN AND ONE STANDARD DEVIATION OF MAXIMUM AND MINIMUM MEASURED FORCES VS. INCIDENT WAVE HEIGHT (HORIZONTAL FORCE ON LEFT SIDE, VERTICAL FORCE ON RIGHT SIDE)

The vertical and horizontal force histories measured on the model were extracted from the ransom wave conditions that represented hurricane wave load conditions similar to Hurricane Katrina in Biloxi Bay, MS as reported by Chen (2009). These were applied to full-scale models of the connections that attach the bridge superstructure to the substructure as described subsequently.

Full-Scale Connection Tests

Wave force effects on the bridge model produced dynamic cyclic uplift with cyclic lateral loads that must be resisted by the connections that anchor the AASHTO type III bridge girders to the pile cap substructure. The simulated wave forces were applied to full-scale test specimens in the laboratory using a novel hybrid-testing method described here.

Prestressed girders have standardized dimensions and were widely used in past practice. The girder specimens were detailed according to in the Florida Department of Transportation plans for the Escambia Bay Bridge. The plans called for two groups of prestressing strands: (18) 13 mm diameter stress relieved straight strand pulled to 112 kN each (6) 13 mm diameter stress relieved double harped strand pulled to 112 kN each. The bursting steel stirrups consist of two L-shaped bars that extend the height of the girder and below the prestressing strand. Fig. 8 shows the reinforcing details at the end of the girder. The length of the specimens was designed to allow both ends of the specimen to be tested separately. The development length of the strand was conservatively assumed to be 0.91 m, and the beam was designed to be 3.05 m, or

approximately three transfer lengths. Thus, if one end of the beam was damaged during a test, there was a middle section of at least one transfer length to fully anchor the strand to enable testing of the opposite end for the second test.

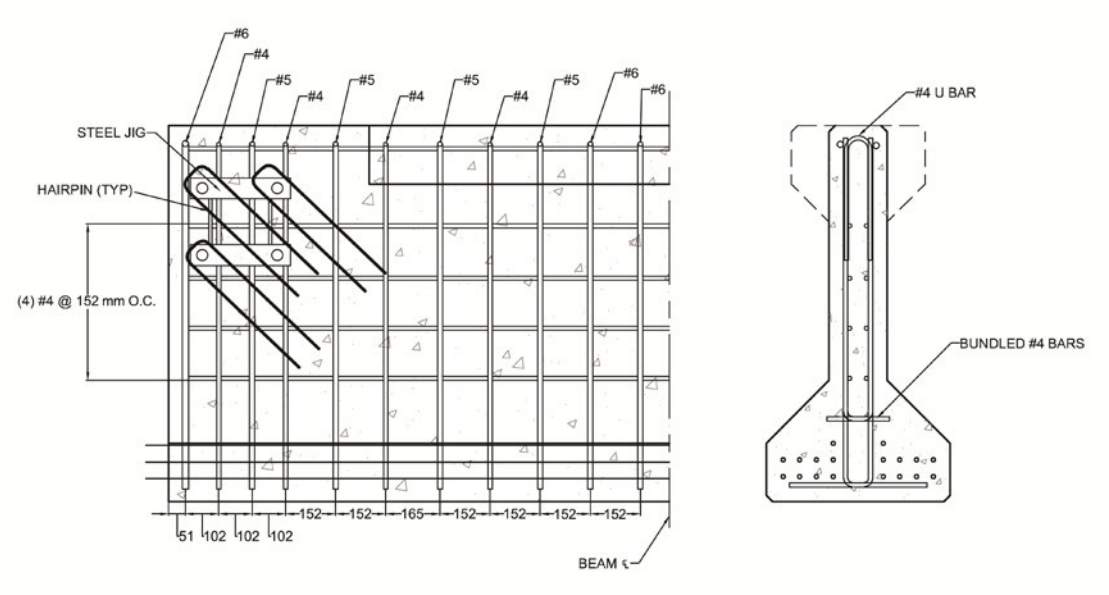

FIG. 8 – ELEVATION VIEWS OF FULL-SCALE GIRDER FOR CONNECTION TEST.

Three commonly used anchorage designs were used in this study. They were: 1) Threaded Insert/Clip Bolt Anchorage (CB), Headed Stud Anchorage (HS), and the Through-Bolt Anchorage (TB). These are shown in Fig. 9. The headed stud anchorage (HS) detail was used at the Escambia Bay, Florida site and failed under hurricane Ivan in 2004. In the case of Escambia Bay, only the exterior girders were detailed with this anchorage.

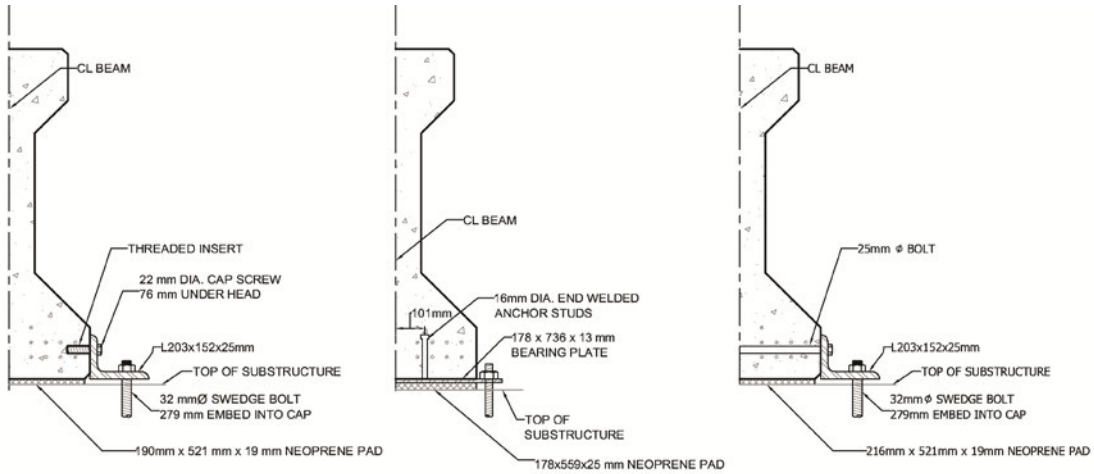

FIG. 9 –CONNECTION DETAILS TESTED (LEFT TO RIGHT: CB, HS, TB).

The specimen loading history was produced by taking the hydraulic model force

histories and scaling them up to prototype scale (the specimen full scale) using Froude similitude, time was multiplied by a factor of $\sqrt{5}$ and force was multiplied by 53. Data taken from the regular wave trial "reg1603" (conditions similar to Hurricane Katrina in Biloxi Bay, MS, reported in Chen (2009)) were used in the present study as the input forcing functions. The wave heights were 0.5 m and 2.5 m for the model and prototype, respectively. The wave periods were 2.68 s and 5.99 s for the model and prototype, respectively. The model data, scaled to prototype scale, were used as the analog input command signal to the hydraulic controllers. When a specimen did not fail at the 100% level, the force magnitudes were increased in 20% increments until failure occurred. Because uplift forces act, the bridge dead load had to be included in the loading history. Using the Escambia Bay Bridge as a prototype, a bridge self-weight load of 178 kN (negative sign) was initially imposed on the girder. This initial applied force represents the tributary weight of components and wearing surface for the exterior girder at the support reaction. Therefore in the data presented subsequently, vertical force values above zero are tensile (when the self-weight precompression is overcome).

The responses shown in this section are for the last imposed time history which produced failure in the connections. The CB connection exhibited the lowest strength of the connection types and failed during the 100% Katrina conditions. The horizontal and vertical load deformation response for the CB anchorage is shown in Fig. 10a and Fig. 11a, respectively. The girder sustained damage around the connection including cracking surrounding the inserts, followed by spalling of the concrete around the inserts, exposure of the outermost prestressing strands along the transfer length. The HS connection exhibited the highest strength of the connection types, failing at 180% of the measured load amplitude under the Katrina conditions. The vertical and horizontal load deformation response for the HS anchorage is shown in Fig. 10b and Fig. 11b, respectively. Failure of the connection was characterized by tensile fracture of the steel headed studs, and large plastic deformations of the connection plate. The damage to the concrete was limited to cracking around the reentrant corners of the plate interface. The TB connection failed at 160% of the measured load amplitude under the Katrina conditions. The vertical and horizontal load deformation response for the TB anchorage is shown in Fig. 10c and Fig. 11c, respectively. Cracking of the girder was observed at 100% Katrina conditions, making the strand susceptible to corrosion. The damage sustained by the girder at failure was extensive. The girder exhibited a large crack across the width of the cross section following the prestressing banding, and once that crack propagated across the entire length, a new crack around the bottom layer of prestressing appeared. The bottom layer of prestressing strand was pulled down and away from the girder as the vertical force produced uplift of the girder.

The test results were compared to the required demands from the recently published AASHTO *Guide Specifications for Bridges Vulnerable to Coastal Storms* (2008). Fig. 12 shows the vertical wave load demands for a bridge span of the type considered in the present research. The vertical load was calculated from the *Guide Specification* and includes the bridge self-weight for a range of maximum wave heights. The calculated maximum load is based on 12 anchorage points per span (one on each end of the girders). Also noted on the figure is the prototype scaled maximum

measured wave induced load from the hydraulic model. Assuming the maximum amount of trapped air, none of the three anchorage designs had sufficient strength to resist the expected vertical loads for wave heights exceeding 3.6 m. In service, bridges with the TB and CB anchorages generally have every girder connected to the pile cap while the Escambia Bay Bridge, with the HS detail, was only anchored at the exterior girders. While anchoring every girder increased the overall bridge resistance, it would not be sufficient to resist the vertical forces prescribed for large wave heights if air is trapped below the bridge deck.

All anchorage types have sufficient strength to resist the horizontal forces if all girders are anchored. The Escambia Bay Bridge, although connected only at the exterior girders with the HS anchorages, would have sufficient strength to resist the prescribed horizontal loads. While the horizontal force component of the wave loading is not as large as the vertical force components, when combined these forces can act in concert to sweep bridges from the substructure upon connection failure dominated by the vertical loading.

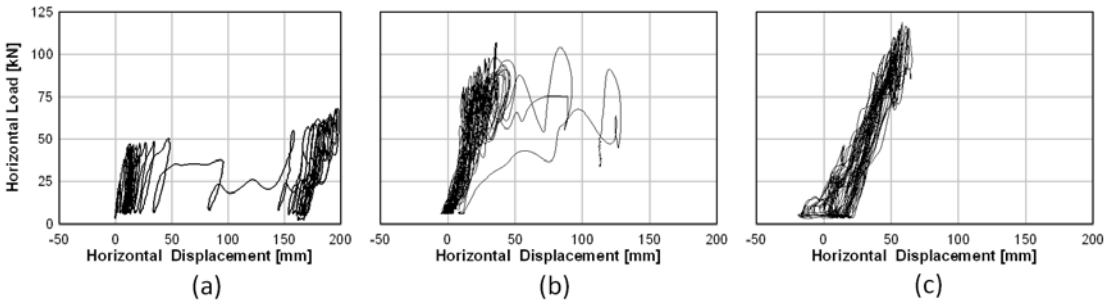

FIG. 10 - HORIZONTAL FORCE-DEFORMATION RESPONSE (LEFT TO RIGHT CB, HS, TB)

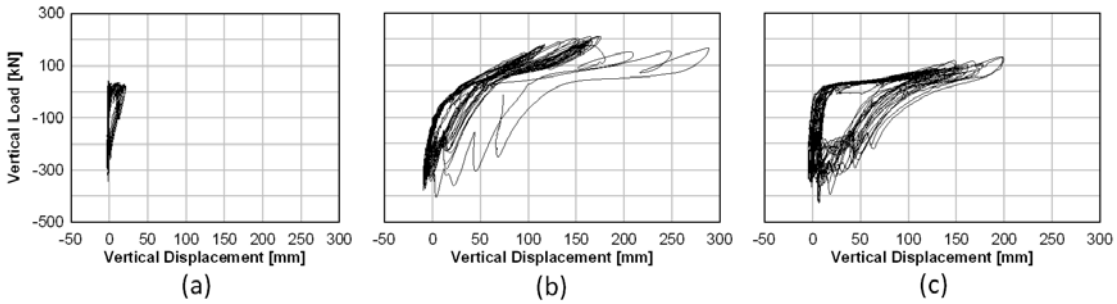

FIG. 11 - VERTICAL FORCE-DEFORMATION RESPONSE (LEFT TO RIGHT CB, HS, TB)

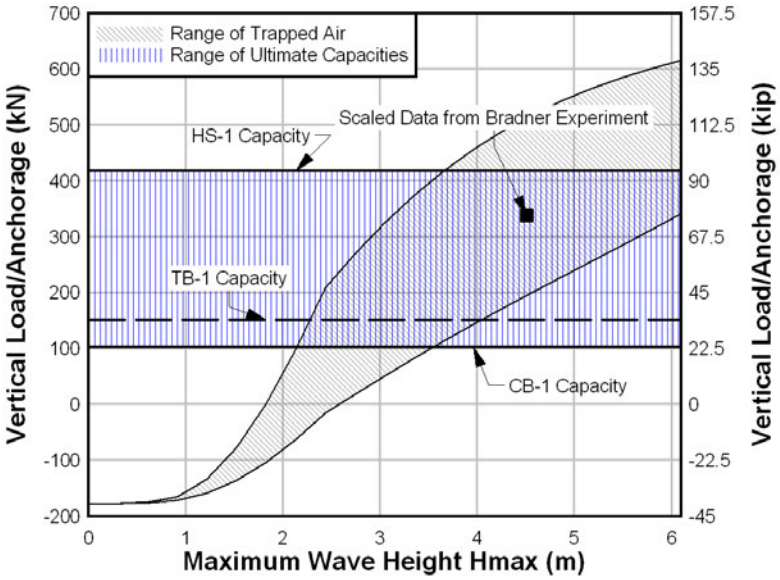

FIG. 12 – VERTICAL LOAD PER ANCHORAGE REQUIRED BY AASHTO GUIDE SPECIFICATION AND RELATIVE ANCHOR CAPACITIES.

Conclusions

Hydro-dynamic tests of a 1:5 scale model of a real highway bridge located on Escambia Bay, Florida were conducted to measure the wave forces on the bridge. The model used an innovative laboratory setup that allowed the test specimen to simulate the dynamic response of the substructure. The flexible substructure produced larger forces on the bridge than if it were rigid. The measured wave force histories on the large-scale hydrodynamic model were converted into the vertical and horizontal force components applied to the connections that join the superstructure to the substructure. The force histories from the large-scale hydrodynamic model were increased to prototype scale and then applied to full-size connection elements to characterize the structural performance. Three commonly used connection details were tested. The wave loading produced damage in the girders and the capacity of the connections would not be sufficient to resist the vertical loads prescribed by the AASHTO *Guide Specification* for the bridge configuration considered when wave heights exceeded 3.6 m and significant trapped air is present. The testing methods developed represent a new technique in hybid testing to investigate fluid-structure interactions. Additional details can be found in Lehrman *et al*. (2012) and Bradner *et al*. (2011)

Acknowledgments

This research was funded by Oregon Transportation Research and Education Consortium (OTREC) and the National Science Foundation with grant CMMI 0800822 of the Hazard Mitigation and Structural Engineering program. Dr. Keith Kaufman of Knife River in Harrisburg, OR, Mr. Robbie Chambless of the Alabama Department of Transportation, Mr. Artur D'Andrea of the Louisiana Department of Transportation, and Mr. Rick Renna of the Florida Department of Transportation provided helpful

suggestions. The findings, conclusions and recommendations presented are those of the authors and do not necessarily reflect the views of the project sponsors or individuals acknowledged.

References

American Assoc. of State Highway and Transp. Officials (2008). "Guide Specification for Bridges Vulnerable to Coastal Storms." 1st Ed., Washington, DC.

Bea, R. G., Iversen, R., and Xu, T. (2001). "Wave-in-Deck Forces on Offshore Platforms." J of Offshore Mechanics and Arctic Eng. , Vol. 123, Feb. 2001, 10-21.

Bradner, C., Schumacher, T., Cox, D., and C. Higgins (2011). "Experimental Setup for a Large-Scale Bridge Superstructure Model Subjected to Waves." J. Waterway, Port, Coastal, Ocean Eng., 137(1), 3–11.

Chen, Q., Wang, L., & H. Zhao, (2009). "Hydrodynamic Investigation of Coastal Bridge Collapse during Hurricane Katrina," J. of Hydraulic Eng., 135 (3), 175-186.

Cuomo, G., Tirindelli, M., and Allsop, W. (2007), "Wave-in-deck loads on exposed jetties." Coastal Engineering, Vol. 54, Issue 9, September 2007, 657-679.

Denson, K. H. (1980). Wave Forces on Causeway-Type Coastal Bridges: Effects of Angle of Wave Incidence and Cross-Section Shape, Water Resources Research Institute, Mississippi State University.

Douglass, S., Chen, Q., & J. Olsen (2006). "Wave Forces on Bridge Decks - Draft Report," Coastal Transportation Engineering Research and Education Center. University of South Alabama

Lehrman, J., Higgins, C., and Cox, D. (2012). "Performance of Highway Bridge Girder Anchorages under Simulated Hurricane Wave Induced Loads." J. Bridge Eng., 17(2), 259–271.

Marin, J., & M. Sheppard, (2009). "Storm Surge and Wave Loading on Bridge Superstructures," Proceedings of Structures Congress, Austin, TX. pp. 557-566.

Padgett, J., DesRoches, R., Nielson, B., Yashinsky, M., Kwon, O., Burdette, N., and Tavera, E. (2008). "Bridge Damage and Repair Costs from Hurricane Katrina." J. Bridge Eng., 13(1), 6–14.

Robertson, I., Riggs, H., Yim, S., and Y. Young, (2007). "Lessons from Hurricane Katrina Storm Surge on Bridges and Buildings," J. of Waterway, Port, Coastal, and Ocean Engineering, 133 (6), 463-483.

STUDY ON TSUNAMI WAVE FORCE ACTING ON A BRIDGE SUPERSTRUCTURE

Hidekazu Hayashi[1]

Abstract

In this study, we conducted waterway experiments to clarify properties that tsunami wave force affects a bridge superstructure which is generally applied to expressway bridges. In the waterway experiment, some tsunami waves which have maximum 10m height and 6.4m/sec flow velocity in actual scale were generated and applied to 1/50 scale bridge model to measure reaction forces by tsunami wave. Behaviors of tsunami wave after attacked scale bridge model were observed. We also estimated tsunami wave forces by comparing other experiment carried out and using the maximum wave forces converted in actual scale level.

Introduction

A number of bridges were washed away by tsunami caused by the-2011 Off-the-Pacific-Coast of Tohoku Earthquake. Though bridges of expressways managed by NEXCO were not damaged, arterial highways were washed away and made impassible at locations, and transportation of people and supplies for relief and restoration of infrastructures were delayed. Learning from the disaster, we now more deeply recognized the importance of the role that roads and bridges play in the recovery from large-scale disasters caused by tsunami.

There are routes with along the shore among expressways managed by NEXCO (Fig.1). We are afraid that some bridges may be washed away or collapsed if tsunami accompanying powerful earthquakes, such as the highly probable Nankai trough earthquake, occurs in the future. We need to provide expressway services even in the event of such disasters so that relief vehicles to transport people and supplies may pass. Expressways are designated as emergency transport routes and are necessary to rescue inhabitants and restore infrastructures.

Fig.1 A bridge along the shore in expressways

[1] Researcher, Road Research Department Bridge Division, Nippon Expressway Research Institute Co Ltd., Tokyo

In the study on tsunami wave force acting bridges, many experimental examinations have been performed. However, the calculation method for tsunami load isn't established in the current design standards in Japan. It is extremely important for a road manager to be able to recognize if the size of tsunami external force can be tolerated by reinforcement and correctly evaluate the damage of bridges caused by tsunami to minimize possible damage and to work hard to maintain the network of expressways.

We measured tsunami wave force using waterway experiment for standard superstructures adopted for bridges of expressways. We also conducted a numerical analysis using a general-purpose fluid analysis code with the VOF method and confirmed the integrity of the analysis results with the experimental results. The result of the experiments is only described in this report.

Waterway experiment

In this report, we measured tsunami wave force acting on a standard PC box-girder bridge with 2 traffic lanes that may be damaged by tsunami caused by the expected Nankai trough earthquake. The experiment model was a partial 1/50 scale model shown in Fig.2. The width and height are each 233mm, 64mm (11.64m, 3.18m at the actual scale). The wall handrail of the Florida model was also reproduced in this model. We assumed that tsunami height of 10m (experimental value 20cm) and flow velocity 6.4m/s (experimental value 0.91m/s) at the maximum, acted on a bridge girder. These values were decided referring to the tsunami height estimated for the Nankai trough earthquake, and the flow velocity was calculated by the speed of floating wreckage during a tsunami invasion.

Dimensions of the waterway with one side fitted with glass are 20m in length, 0.7m in width and 1.0m in height (Fig.3). The waves were generated using a slide board. The tsunami height and flow velocity were changed by adjusting movement distance, speed and the static depth. We selected the soliton wave as the form of wave pattern to confirm the basic characteristics of tsunami action on a bridge girder. The model was connected to a component force meter fixed to the beam positioned over the waterway through model support beams. The model's height from the static water surface to the girder bottom is 100mm (5m at the actual scale).

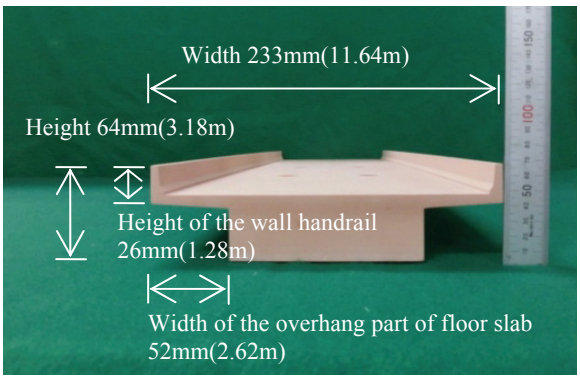

Fig.2 The experiment model
(( ): The dimension in the actual scale)

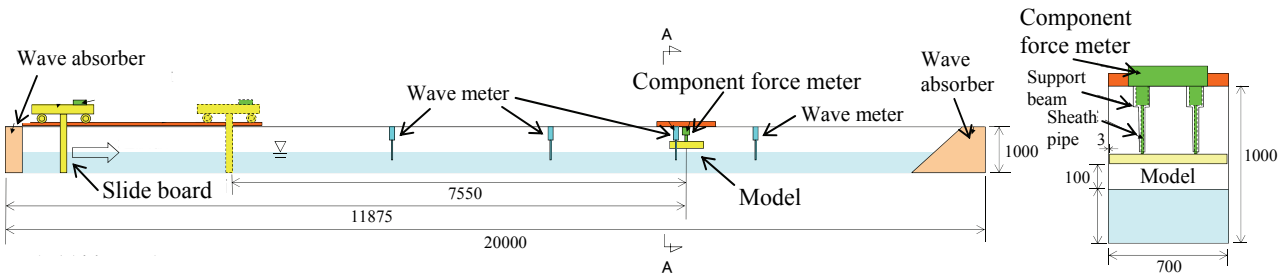

Fig.3 The equipment of the waterway experiment

We measured horizontal wave force, vertical wave force and moment, using set tsunami height, flow velocity and cross slope as parameters. We carried out experiments for 11 cases, as shown Table 1. The experiments were carried out for three tsunami heights as described in Fig.4 and with three flow velocities for each tsunami height. Before this experiment, we performed a wave-making test and confirmed that tsunami height and flow velocity for the experiment can be reproduced by controlling the speed of the slide board and the static depth (Fig.5). Fig.5 shows the measuring results of tsunami heights measured at the center of the model.

Table 1 The cases of experiments

Case	Tsunami height h_a (cm)	Flow velocity v_a (m/s)	Cross slope (%)
1	20	0.91	0
2		0.83	
3		0.80	
4	13	0.88	
5		0.78	
6		0.60	
7	11	0.79	
8		0.59	
9		0.53	
10	20	0.91	2.5
11			5.0

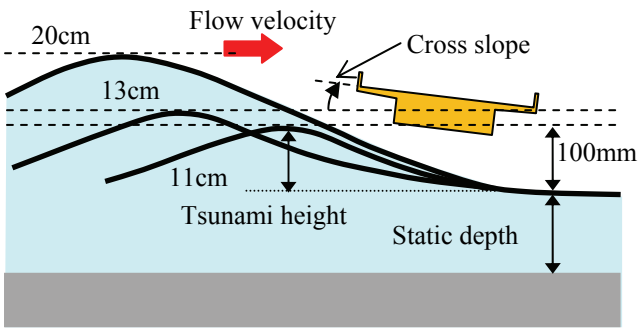

Fig.4 Tsunami height in the experiment

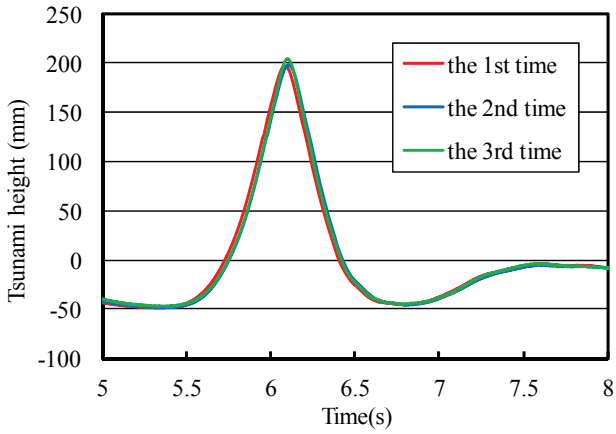

Fig.5 The confirmation of tsunami height before the experiment (case1)

Measurement procedure for wave force and flow velocity

Wave forces were measured using a component force meter attached to the model's upper part, and wave forces that act only on the model were measured by covering the model's support beams with sheath pipes. Measurements were taken three times for each case to improve the reliability of the collected data. The sampling frequency was set at 1,000Hz to measure the momentary power that act on the model. The vibration of the model caused noise, and therefore, we processed the measured data using a low-path filter, which cuts components more than the natural frequency (27Hz) of the model, and smoothed the wave pattern.

The law of similarity applying the Froude number was used, as the influence of frictional resistance and surface tension of water is generally small in waterway experiments reproducing tsunami, and the viscous effect is smaller than gravitational effect.

$$F_r = \frac{v_p}{\sqrt{gH_p}} = \frac{v_m}{\sqrt{gH_m}} \qquad (1)$$

At this point,

v : flow velocity

g : gravity acceleration

H : inundation depth

p and m express quantities for the actual bridge and the model.

The measurement procedure used for the flow velocity is PIV (Particle Image Velocimetry) and was carried out without the model. PIV is a method to estimate speed and speed vector from movement distance and time of individual particulates or particulate groups photographed as images by mixing identifiable particulates in the flow. We photographed images of waves at photography speed 0.001-0.002 seconds using PIV camera with 1,600*1,200 resolutions.

The flow velocity in the direction of the wave travel was measured at the center of the model and at 100mm from the static surface in the height direction (Fig.6). Fig.7 shows an example of horizontal and vertical distribution of the flow velocity. The mean

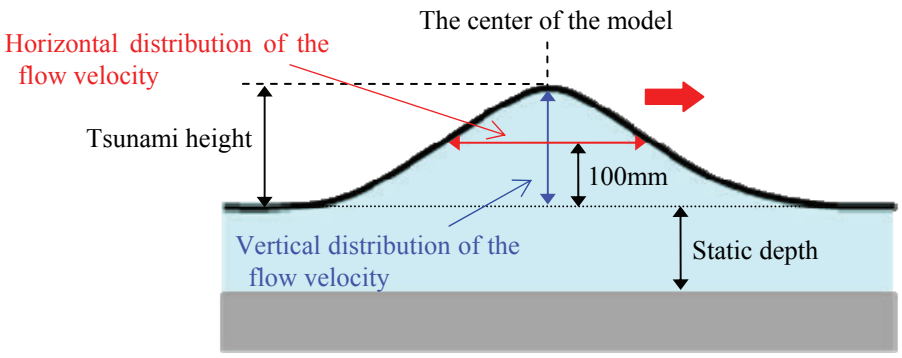

Fig.6 The location of measurement of velocity of flow

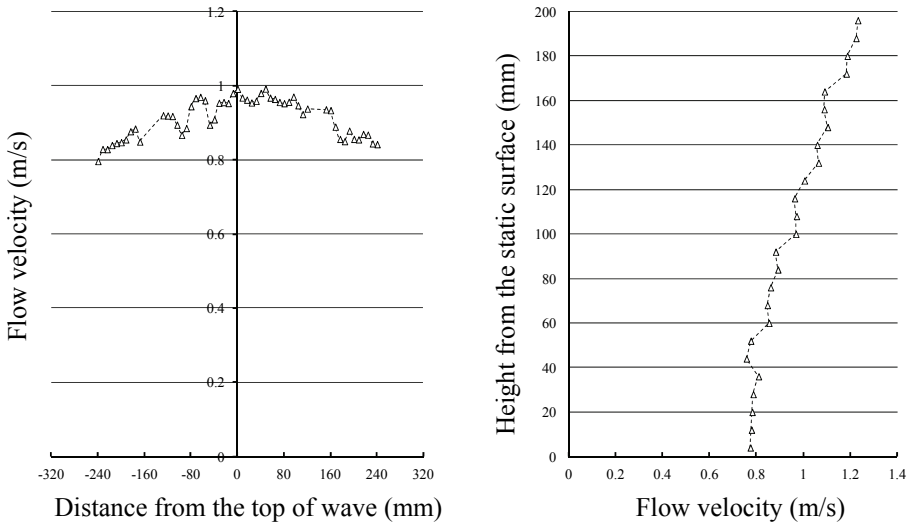

Fig.7 The horizontal and vertical distribution of the flow velocity (case1)

of horizontal distribution of flow velocity at height 100mm from the static surface is defined as the flow velocity for this experiment.

Measurement results of wave force

1. Horizontal wave force

Fig.9 shows a time history waveform of the horizontal wave force. We have indicated the first measurement in each case in Fig.9 because the results of the three measurements were similar in each case as can be seen Fig.8. The vertical axis is wave force and the direction of flow is plus. Zero second at the cross axis is defined as follows: when the slide board begins to move in Fig.8 and when waves impact the model in Fig.9.

The peak of the horizontal wave force was only once for tsunami height 11cm and 13cm. On the other hand, peaks occurred two times for tsunami height 20cm (case1-3) though the second peak didn't appear clearly like in case 3. We assume from the state of flow in Fig.12 that the first peak occurred because waves acted on the wall handrail and web side, and the second peak occurred because a mass of water launched from the upstream wall handrail side and fell to the downstream wall handrail.

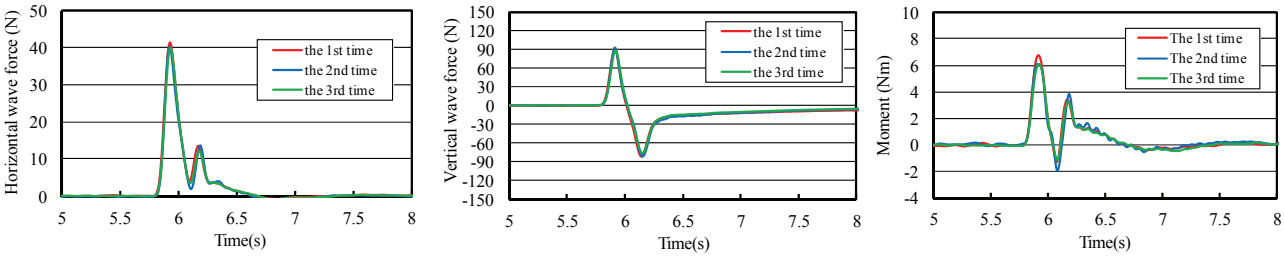

(a) Horizontal wave force (b) Vertical wave force (c) Moment

Fig.8 The time history waveform (case1)

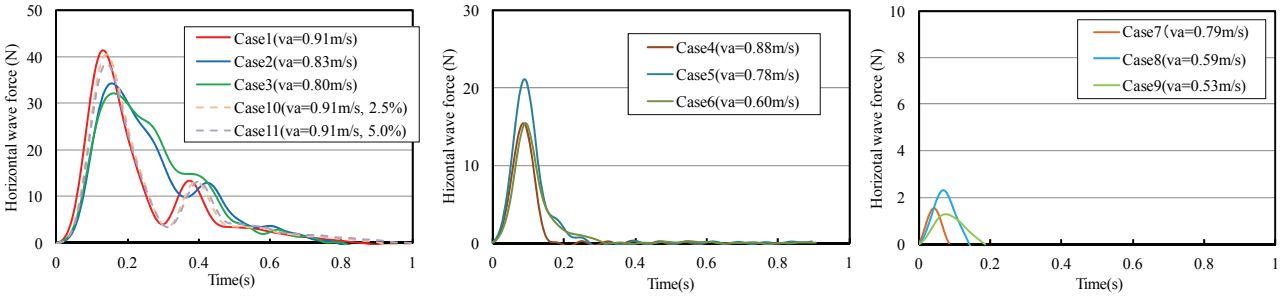

(a) Tsunami height 20cm (b) Tsunami height 13cm (c) Tsunami height 11cm

Fig.9 The time history waveform of horizontal wave force

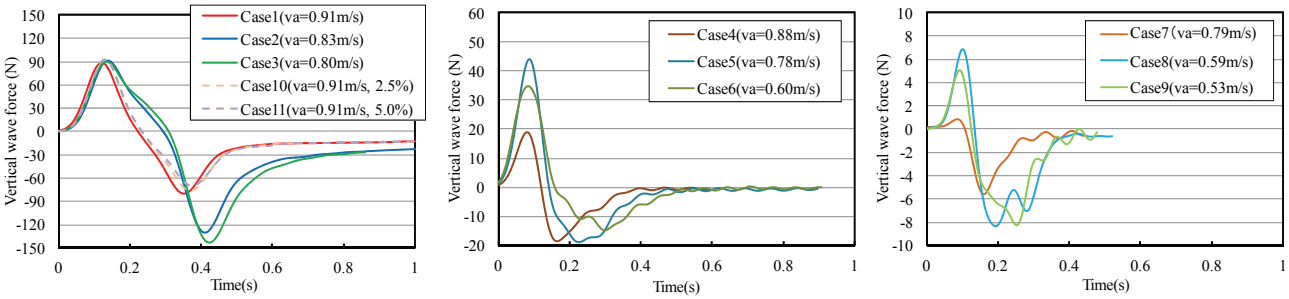

(a) Tsunami height 20cm (b) Tsunami height 13cm (c) Tsunami height 11cm

Fig.10 The time history waveform of vertical wave force

2. Vertical wave force

Fig.10 shows a time history waveform of the vertical wave force. The upward direction of the force is plus and the definition of the time is the same as Fig.9.

Vertical wave force peaked twice in each case. We assume that waves invaded from the undersurface of lower flange, entered the overhang part of floor slab, and lifted the girder in the first peak as shown in Fig.10. We assume that the mass of water falling to the surface of floor slab, and negative pressure caused by the separation of flow at the upstream and downstream undersurface of lower flange influenced the downward force acting in the second peak.

The behavior of case 4 is similar to that of case 1. We assume that waves acted on the undersurface of lower flange at the first peak and that the downward force occurred by the action of negative pressure (Fig.13).

3. Moment

Fig.11 shows a time history waveform of moment. The clockwise rotation is plus and the definition of the time is the same as Fig.9.

The peaks generally occurred twice except for tsunami height 11cm. We assume that the first peak occurred in case1, judging from the state of flow shown in Fig.12, when waves acted on the overhang part of floor slab and the side of the upstream wall handrail. In addition, we assume that the second peak occurred because the mass of water launched from the upstream wall handrail acted on the downstream wall handrail. In the case of tsunami height 13cm, we believe that the peak of positive moment occurred because the wave acted on the undersurface of lower flange and that the peak of negative moment was caused by negative pressure generated by the separation of flow at the undersurface of the upstream and downstream lower flange (Fig.13). From these results, we assume that the moment shows that the behavior of wave force is similar to the vertical wave force.

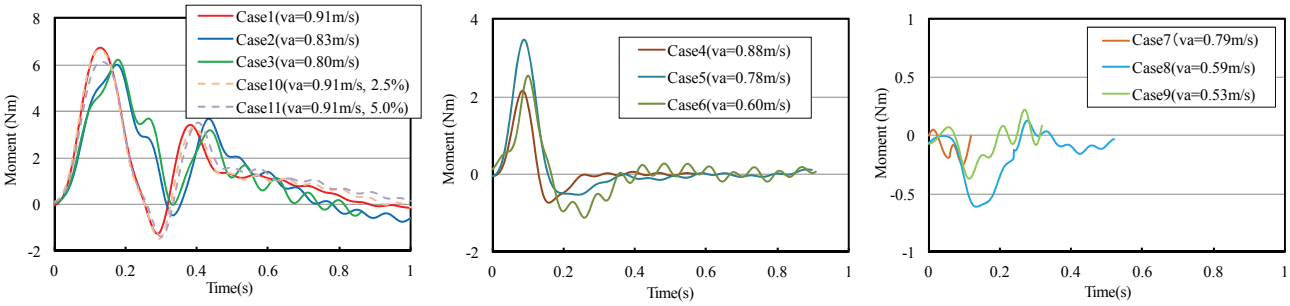

(a) Tsunami height 20cm (b) Tsunami height 13cm (c) Tsunami height 11cm

Fig.11 The time history waveform of moment

<u>The characteristic of tsunami wave force</u>

We have sorted out and displayed the data collected on the influence of the changes in the flow velocity, tsunami height and cross slope in Table 2-4 to estimate the characteristics of tsunami wave force. The largest wave force shown in Table 2-4 is the mean of the three maximum measured three times in each case.

First, we compared the influence of flow velocity at tsunami height 20cm in case 1-3. The horizontal wave force had a tendency to increase as flow velocity increased (Table 2). On the other hand, the downward absolute value of the vertical wave force decreased with increase of flow velocity; nevertheless, the upward wave force was almost constant regardless of flow velocity. We assume that the differences in the flow and volume of water mass launched caused by the different flow velocities influenced the results. The moment was constant regardless of flow velocity, as seen with the upward vertical wave force. Therefore, as for moment, we assume that the vertical component of moment is dominant. The size of the upward vertical wave force was around 2-3 times that of the horizontal wave force.

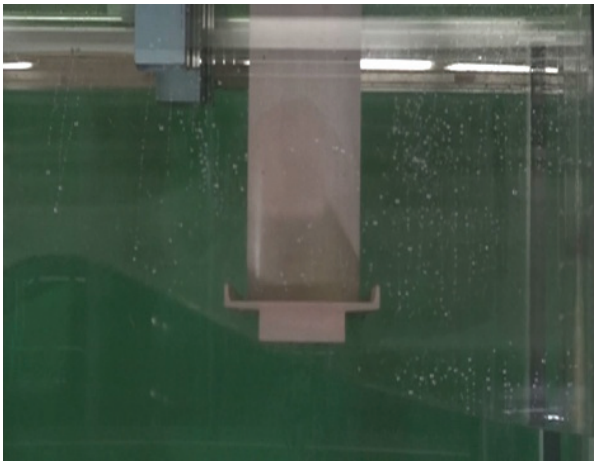

(a) Before collision (5.8sec)

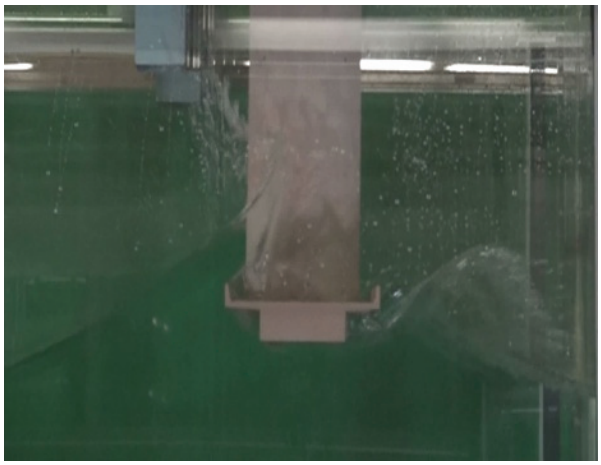

(b) The first peak (5.95sec)

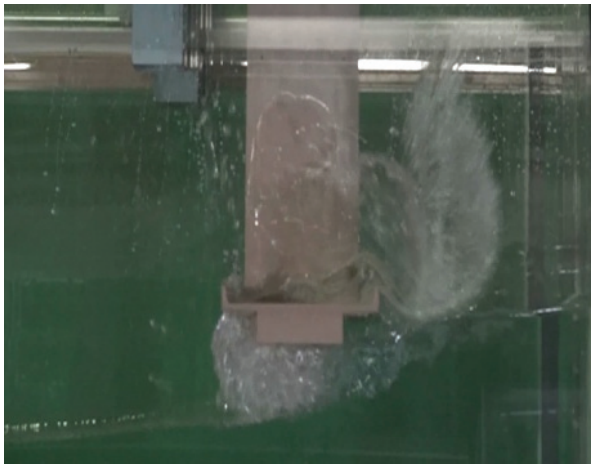

(c) The second peak (6.1sec)

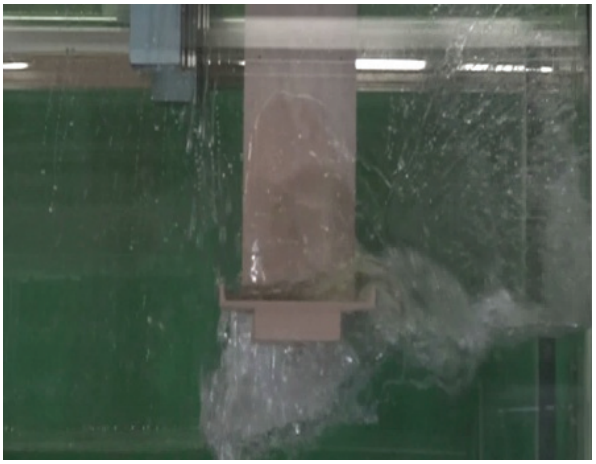

(d) After passage (6.25sec)

Fig.12 The state of flow (case1)

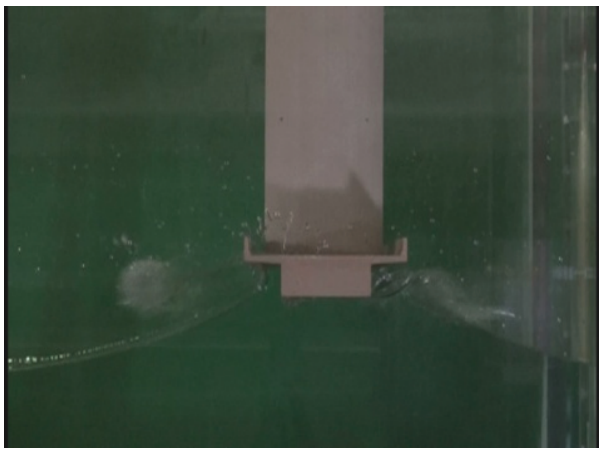

(a) The first peak

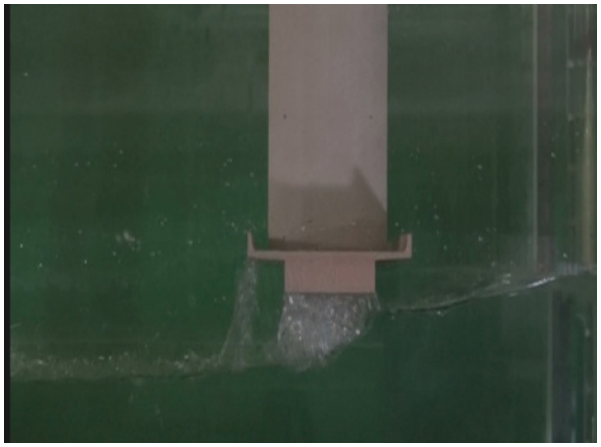

(b) The second peak

Fig.13 The state of flow (case4)

Next, we compared the influence of tsunami height in three cases (case 3,5 and 7) when flow velocity was about 0.8m/s (Table 3). The horizontal wave force, the vertical wave force and the moment increased as tsunami height grew. The relations of the horizontal wave force and the upward vertical wave force were around 2-3 times, as seen in the influence of flow velocity.

We compared the influence of cross slope in three cases (case 1, 11 and 12). The horizontal wave force and the vertical wave force each showed a tendency to increase by around 6% and 2%, respectively, when cross slope was 5.0% (Table 4). The downward vertical wave force decreased by around 7% because the decrease of the wave force caused by the cross slope was comparatively large. We assume that the volume of the wave launched decreased because the quantity of water mass dropping on floor slab decreased as the wall handrail height increased owing to the crossing slope. The cross slope didn't influence the moment.

Table 2 The maximum wave force (Tsunami height=20cm)

Flow velocity (m/s)		0.80	0.83	0.91
Horizontal (N)		32.3	33.8	40.5
Vertical (N)	Upward	91.1	89.6	89.5
	Downward	-142.1	-129.7	-79.7
Moment (Nm)		6.2	6.0	6.3

Table 3 The maximum wave force (Flow velocity=0.8m/s)

Tsunami height (cm)		11	13	20
Horizontal (N)		2.0	20.8	32.3
Vertical (N)	Upward	1.3	43.1	91.1
	Downward	-6.1	-18.6	-142.1
Moment (Nm)		0.2	3.5	6.2

Table 4 The maximum wave force (Tsunami height=20cm, Flow velocity=0.91m/s)

Cross slope (%)		0	2.5	5.0
Horizontal (N)		40.5	42.3	43.1
Vertical (N)	Upward	89.5	91.1	91.2
	Downward	-79.7	-77.2	-74.4
Moment (Nm)		6.3	6.3	6.2

Comparison with the results of other experiment

We compared the results with those of experiments carried out by Kosa. Kosa had carried out experiments by changing wave height, clearance of girder and form of wave on the "Lueng Ie bridge" where its girders had moved by tsunami caused by the earthquake off Sumatra in 2004. Of these experiments results, we compared our results with those of experiments conducted under the same condition as ours, which is without breaking wave. Table 5 shows a comparison of the experiment conditions. Fig.14 and Fig.15 show the comparison results (case 1-11) of horizontal wave force and vertical wave force. The vertical and cross axis are values made no dimension. The vertical axis is the value that divided the height of the center of girders in tsunami height, and the cross axis is the value that divided wave pressure in static pressure.

Here, we compared our experiments with Kosa's experiments, which was plotted in mark ◆, shown in the graph on the right side of Fig.14 and Fig.15.

The horizontal wave pressure was about 50% of the value measured in Kosa's experiments, and the vertical wave pressure was about 70% to the same level. These differences are considered to be caused by the differences in the experiment conditions, including cross-section and wave condition shown in Table 5. The vertical wave force was almost equal in the cases of tsunami height 20cm and 13cm.

Table 5 The comparison with the experiment conditions

		Our experiment	Kosa's experiment
Model	Type	Box girder	I-beam
	Cross section	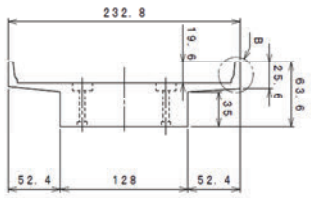	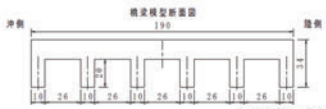
	Width	233mm	190mm
	Girder height	64mm	34mm
	Width/Height	3.64	5.59
Condition of wave	Tsunami height	200mm	110mm
	Static depth	400-550mm	150mm
	Velocity of flow	0.91m/s	About 1.5m/s
Wave force	Center of girder/Tsunami height	0.66	0.7
	Horizontal	41N	12N
	Vertical	90N	30N

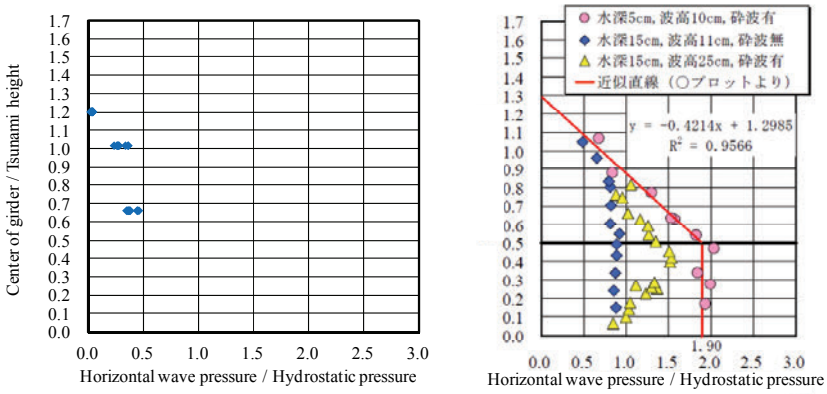

Fig.14 The comparison of horizontal wave force

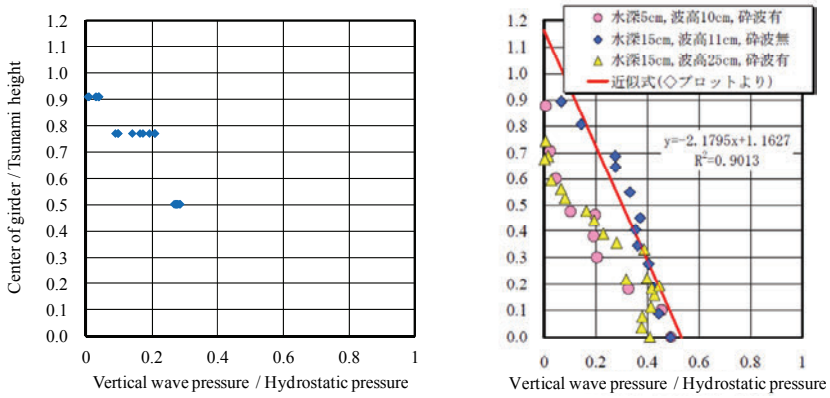

Fig.15 The comparison of vertical wave force

Reduced value of tsunami wave force on the actual bridge

We converted the maximum horizontal wave force and vertical wave force, measured in this experiment, into numbers at the actual bridge level and compared them with dead load of the girder (212kN/m) of the target bridge. The law of similarity of the Froude number was used for the conversion. Here, we made the conversion per unit length so that it may be adapted regardless of the span length of a bridge.

$$F_p = F_m / L_m \times n^2 \qquad (2)$$

At this point,

F_p : The wave force per unit length in the actual bridge
F_m : The wave force of the model
L_m : The length of the model (=0.694m)
n : The inverse of the scale of the model (=50)

Table 6 shows the maximum wave force converted to the actual scale level. Maximum wave force was generated at tsunami height 20cm (10m at the actual scale), and the upward vertical wave force of 2.2 times and the downward vertical wave force of 3.5 times acted on horizontal wave force. When we divided the reduced value of maximum wave force shown in Table 6 by the dead load of girder, it was confirmed that a force of about 0.7 times the dead load acted in the horizontal direction and about 1.5 times the dead load acted in the vertical direction.

Table 6 The maximum wave force converted into the actual bridge

		Maximum wave force (kN/m)	Maximum wave force/ Dead load
Horizontal		146	0.69
Vertical	Upward	328	1.54
	Downward	-512	—

Conclusion

In this experiment, we were able to confirm the characteristic of Tsunami wave force of soliton wave acting on a standard box-girder section of a bridge. We assume that it is appropriate to adopt an equivalent to the current standard for the horizontal wave force. This assumption was made by comparing the earthquake resistant design standard of bearing with the reduced value for the actual bridge in Tsunami wave force. On the other hand, it seems that we need a measure against uplift of the vertical wave force.

In this study, we carried out examinations of Tsunami wave force acting on a box-girder section for soliton waves. We'll carry out examinations for different waves, for example bore wave and long-period wave, and cross-sections, so that we may reflect this knowledge of Tsunami external force in the design.

Reference

Document of Cabinet Offices : Tsunami height, inundation area and damage assumption caused by the powerful earthquake of the Nankai trough earthquake, 2012

Kosa, K., Miyajima, M., Fujima, K., Shoji, M., Ono, Y., Shigeeda, M., Hirooka, A., Kimura, K. : Study on damage prediction of the road structure caused by tsunami and its reduction, New road technology meeting, 2010

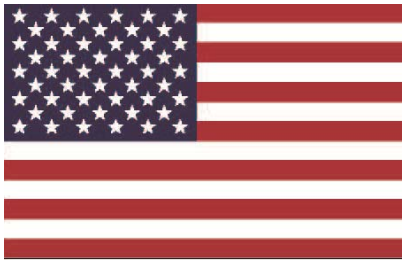

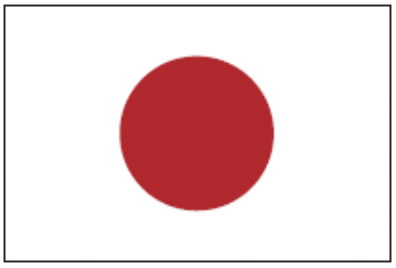

29th US-Japan

Bridge Engineering Workshop

Session 2

Maintenance

A COMPREHENSIVE BRIDGE PRESERVATION PROGRAM TO EXTEND SERVICE LIFE

Bruce Johnson[1]

Abstract

Bridges represent a large investment in highway systems. As highway systems age, agencies should optimize the methods used to preserve this high value portion of the infrastructure and extend its useful life. In the US funding for highway preservation and modernization is decreasing at a time when the largest age group of bridges is nearing the end of their expected service life. The cost of replacement and major rehabilitation with modern traffic mobility issues and environmental mitigation is excessive. Most agency budgets are insufficient to maintain service levels without a major shift in management to a preservation focus that maximizes the useful service life of highway infrastructure. This paper presents the key elements of a comprehensive preservation program and provides an introduction to tools used to assess, evaluate, prioritize, and carry out actions that can be shown to be cost effective methods to extend service life.

Introduction

More than 25 percent of the Nation's 600,000 bridges are rated as structurally deficient or functionally obsolete. More than 30 percent of existing bridges have exceeded their 50-year theoretical design life and are in need of various levels of repair, rehabilitation, or replacement. This issue is exacerbated by increasing travel demands, limited funding, and increasing costs of labor and materials. These circumstances have caused most bridge owners to become more reactive than proactive in their approach to managing and addressing their bridge program needs.

Bridge Preservation is a strategy which is intended to aid highway agencies in managing their bridge inventories at a critical stage where bridge needs are increasing and available funding is decreasing. In pavements, for example, a preservation strategy has been used which focuses on maintaining surface treatments in good condition in order to protect the highway substructure from costly damage. While bridges are more complex structures with greater variation in design- and damage can often result from conditions under the bridge as well as on upper surfaces- the intention of a well-managed and comprehensive bridge preservation program is both sound and timely.

Given that adopting a comprehensive bridge preservation program to extend service life to existing bridge inventory, much of which is close in age to its original design life is not without significant challenges and some limitations, it is possible to identify the components of an ideal system, while addressing the complications posed

[1] State Bridge Engineer, Oregon DOT (ODOT), Salem, Oregon, USA

by the “as is” conditions.

Even under ideal circumstances (e.g. starting with a new, rather than existing, bridge inventory), bridge preservation is just one component of successful bridge inventory management. Bridges will eventually require replacement and along the way, conditions may also necessitate major rehabilitation to address functional problems or deterioration based needs beyond what can be expected with typical preservation actions. However, even under less than ideal circumstances (e.g., existing inventory of predominantly advanced age), a comprehensive bridge preservation program has much to offer agencies in increasing the cost effectiveness of their bridge investments, maximizing the number of bridge needs addressed with a given level of investment and in prolonging the service life of the bridge inventory.

Bridge Preservation –Definition

Bridge preservation is defined as actions or strategies that prevent, delay or reduce deterioration of bridges or bridge elements, restore the function of existing bridges, keep bridges in good condition and extend their life. Preservation actions may be preventive or condition-driven.[2]

Effective bridge preservation actions are intended to delay the need for costly reconstruction or replacement actions by applying preservation strategies and actions on bridges while they are still in good or fair condition and before the onset of serious deterioration. Bridge preservation encompasses preventive maintenance and rehabilitation activities (refer to FIGURE 1).

An effective bridge preservation program:

1) Employs long-term strategies and practices at the network level to preserve the condition of bridges and to extend their useful life;

2) Has sustained and adequate resources and funding sources; and

3) Has adequate tools and processes to ensure that the appropriate cost effective treatments are identified and applied at the appropriate time.

2 Ahmad, Anwar, 2012

FIGURE 1, BRIDGE ACTION CATEGORIES, PRESERVATION ALTERNATIVES

Comprehensive bridge preservation program

One of the challenges facing many bridge program managers is transitioning existing bridge management organizational structures currently in use within agencies to align successfully with a new model in which bridge preservation plays a prominent role in bridge inventory management.

A successful bridge program seeks a balanced approach to preservation and replacement. A focus only on replacing deficient bridges, while ignoring preservation needs, will be inefficient and cost-prohibitive in the long term. A traditional "worst first" approach to managing bridge assets may result in lower performance measures. A "worst first" approach allows bridges in good condition to deteriorate into the deficient category, which generally is associated with higher costs and more complex projects.

Organizationally, the "worst first" model is fairly simple- a staff of bridge designers is focused primarily on bridge replacement and a relatively small, and often independent, bridge maintenance function takes care of the routine maintenance needs of the bridge inventory. Successful adoption of a comprehensive bridge preservation program will require a new organizational paradigm- one in which bridge staff of all disciplines- inspection, design, maintenance and programming, are more highly integrated and focused on bridge preservation. In addition to organizational staffing issues; existing funding categories, performance measurement systems and program decision making processing may all be affected by an increased focus on bridge preservation.

The objective of a good bridge preservation program is to employ cost effective strategies and actions to maximize the useful life of bridges. Applying the appropriate bridge preservation treatments and activities at the appropriate time can extend bridge useful life at lower lifetime cost.

Preservation activities often cost much less than major reconstruction or replacement activities. Delaying or forgoing warranted preservation treatments will result in worsening condition and can escalate the feasible treatment or activity from preservation to replacement. The latter will result in extensive work and higher cost. A viable alternative is timely and effective bridge preservation of sound bridges to assure their structural integrity and extend their useful life before they require replacement.

FIGURE 2 *illustrates the difference between the hypothetical deterioration of bridge with and without preservation actions*. Physical deterioration of an element is a gradual process as illustrated by the curve A-B. Timely application of preservation actions, perhaps even shortly after the element is put into service, can extend the life of some elements as illustrated by the curve A-C. If preservation action occurs after some deterioration as indicated by curve A-D, improvement in condition may occur (D-E) followed by subsequent deterioration as illustrated by E-F. It is often possible to apply multiple cycles of preservation action in extending the life of an element, timely painting and subsequent repainting of steel being a good example.

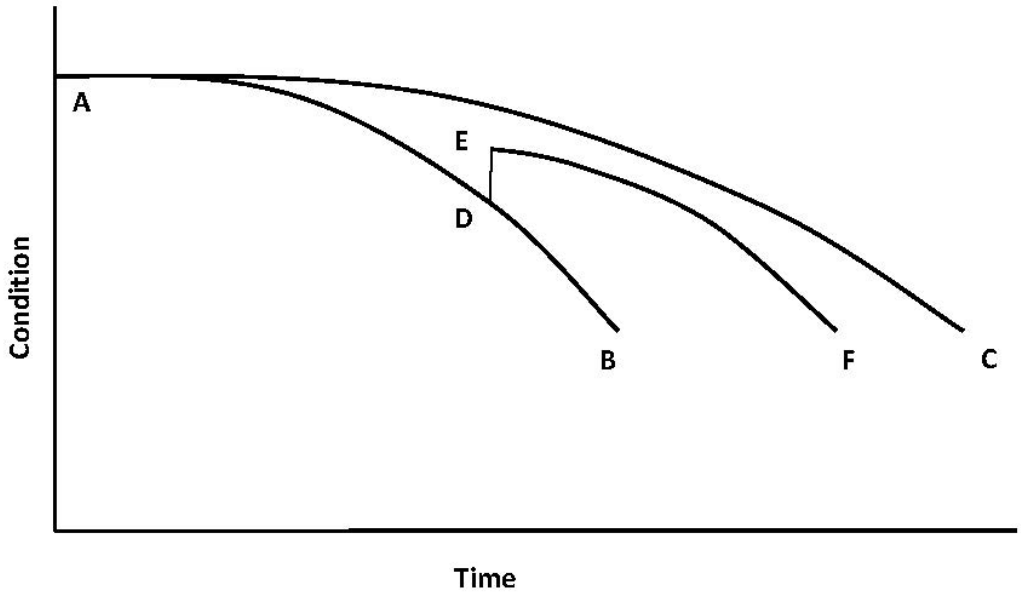

FIGURE 2, EFFECT OF PRESERVATION ON IDEALIZED CONDITION OVER TIME[3]

A successful bridge program is based on a strategic, systematic, and balanced approach to managing bridge preservation and replacement needs.

3 Johnston, David, 2013

Systematic Preventive Maintenance Program[4]

A systematic preventive maintenance program (SPMP) is one of the key processes in a comprehensive bridge preservation program. The following are features included in the SPMP.

FIGURE 3, THE SYSTEMATIC PREVENTIVE MAINTENANCE PROCESS[5]

Systematic Preventive Maintenance Programs include both cyclic and event-driven activities. Examples of cyclic activities are shown in TABLE 1.

Cyclical PM Activity Examples	Commonly Used Frequencies (Years)[4]
Wash/clean bridge decks or entire bridge	1 to 2
Install deck overlay on concrete decks such as: - Thin bonded polymer system overlays - Asphalt overlays with waterproof membrane - Rigid overlays such as silica fume and latex modified	 10 to 15 10 to 15 20 to 25
Seal concrete decks with waterproofing penetrating sealant	3 to 5
Zone coat steel beam/girder ends	10 to 15
Lubricate bearing devices	2 to 4

TABLE 1, EXAMPLES OF CYCLIC PREVENTIVE MAINTENANCE ACTIONS[6]

4 Ahmad, Anwar, 2012
5 Ahmad, Anwar, 2012
6 Ahmad, Anwar, 2012

Oregon Example Bridge Program Strategy and Management

In Oregon, bridge conditions are projected to significantly deteriorate over the next several decades because of a combination of factors including reduced funding for preserving state bridges and a significant number of bridges reaching the end of their service life. The largest portion of the existing inventory was built prior to 1970; 1,500 bridges will reach the end of their design life by 2020. Of these "end of design life" bridges, approximately 27% are currently just one point away from structural deficiency as defined by FHWA. In 2011, ODOT leadership recognized that alternative bridge management strategies was be necessary to manage the deterioration while maintaining public safety and preserving as much of the public's investment as possible. The consequences of reduced bridge funding were identified as including potential condition and weight restriction levels that are route based, and a shift away from bridge replacements. Preparation of ODOT's maintenance staff for additional responsibilities would also be needed.

Initially, bridge service life was analyzed using three categories of bridges, based on the period of construction and importance to the highway network. These categories are: 1) high value coastal, historic and major river crossings, and border bridges; 2) bridges built during the 1950s and 60s and 3) all others. The second group of bridges were typically designed with very low safety factors and for loads much less than allowed by state law since the mid-1980s. It is not cost effective to preserve this group of bridges because of their weak elements, but neither is there funding to replace them. More recent service life analysis in Oregon has begun to refine bridge categories by material, design and environment.

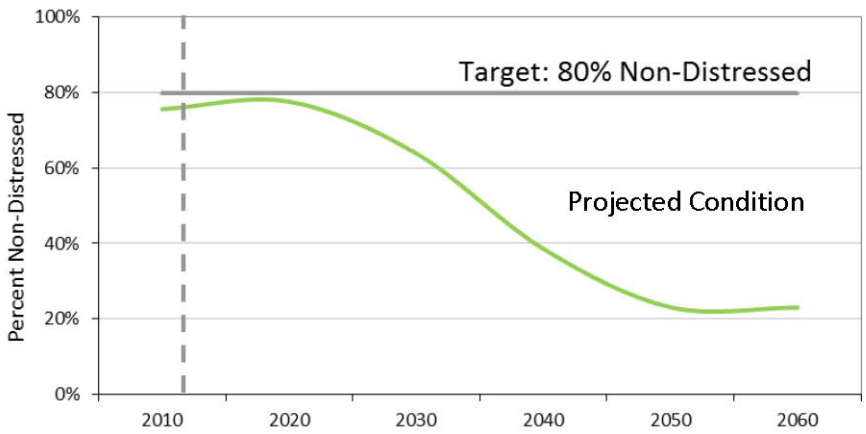

FIGURE 4, OREGON DOT PROJECTED BRIDGE CONDITION OVER 50 YEARS

ODOT adopted a bridge preservation strategy with seven goals. Chief among these are the following:

- Ensure the protection of high value coastal, historic and major river crossings, and border structures using timely preservation actions before cost becomes prohibitive.
- Give next priority to maintaining the highest priority freight corridors to ensure efficient freight movement.
- Develop a preventive maintenance program that will extend the service life of the deck and other structural components.
- Bring lower priority structurally deficient structures currently in Poor condition to Fair condition using a partial rehab scope of work.
- Use bridge inspection, health monitoring and improved deterioration prediction methods to anticipate future bridge conditions.

Although much work remains in Oregon to develop a comprehensive bridge preservation program, the groundwork has been laid. Most the rehabilitation work on the high value structures is being accomplished within our Statewide Transportation Improvement Program (STIP) using federal funds. Urgent and critical maintenance recommendations and work on low priority bridges in Poor condition are mainly addressed through Oregon's Major Bridge Maintenance (MBM) program, which is a smaller state-funded program. Other preservation activities, such as deck overlays, have been funded by both programs.

Current Research on Decision-Making for Bridge Preservation (NCHRP 14-23)

This promising research project seeks to begin to address many of the questions that arise in the implementation stage of a comprehensive bridge preservation program. It takes a pragmatic view of the key components that are needed to link existing systems and processes to the requirements of a successful bridge preservation program. The objective of the research under NCHRP Project 14-23 is to develop a handbook for possible adoption by AASHTO that will: 1) assemble a catalog of bridge element preservation actions; 2) quantify the benefits of bridge preservation actions; 3) provide decision-making tools to optimize bridge preservation actions; and 4) develop a method to determine appropriate levels of funding to achieve bridge agency selected goals and performance measure.

Current Research on Bridges for 100-Year Life (SHRP2 R19A)[7]

This long term study is already producing useful systems that will aid in the design for service life for a particular bridge element, system or subsystems. It suggests selecting feasible bridge systems and provides a method for analyzing these systems one at a time to identify the factors that influence the service life of bridge elements; identify failure modes and consequences; mitigation measures and assessment of risk through life cycle analysis. As an example TABLE 2 below shows

7 Azzizinamini, Atorod, 2013

the summary results of LCCA for four deck durability alternatives in an area of deicing salt use.

Alternative	Main Feature to address corrosion	Initial cost	Life cycle cost
AASHTO Base Design	N/A	$37,215	$774,676
1	Impermeable concrete using silica fume	$44,645	$277,550
2	Use of 316-stainless steel	$152,753	$152,753
3	Increasing concrete cover	$46,519	$691,114
4	Using membrane and overlay	$109,541	$172,252

TABLE 2, ALTERNATE DECK STRATEGIES FOR SERVICE LIFE SUMMARY[8]

Bridge Preservation Performance Measures

New performance measures are needed to support comprehensive bridge preservation programs. AASHTO and SCOPM have recognized the need for standard and consistent measures nationwide, but that provide adequate flexibility to states, local agencies and MPOs in setting performance targets and supporting the goals and communication needs of their own programs. As the sources of standard bridge data currently available are limited to NBI data, this data is the recommended source. Using NBI data to develop a "needs based" performance measure has been challenging due both to a lack of granularity and, in some cases, different divisions used as break points between categories. Below is an example of an NBI "needs based" performance measures illustrating the potential for target setting.

8 Azzizinamini, Arorod, 2013

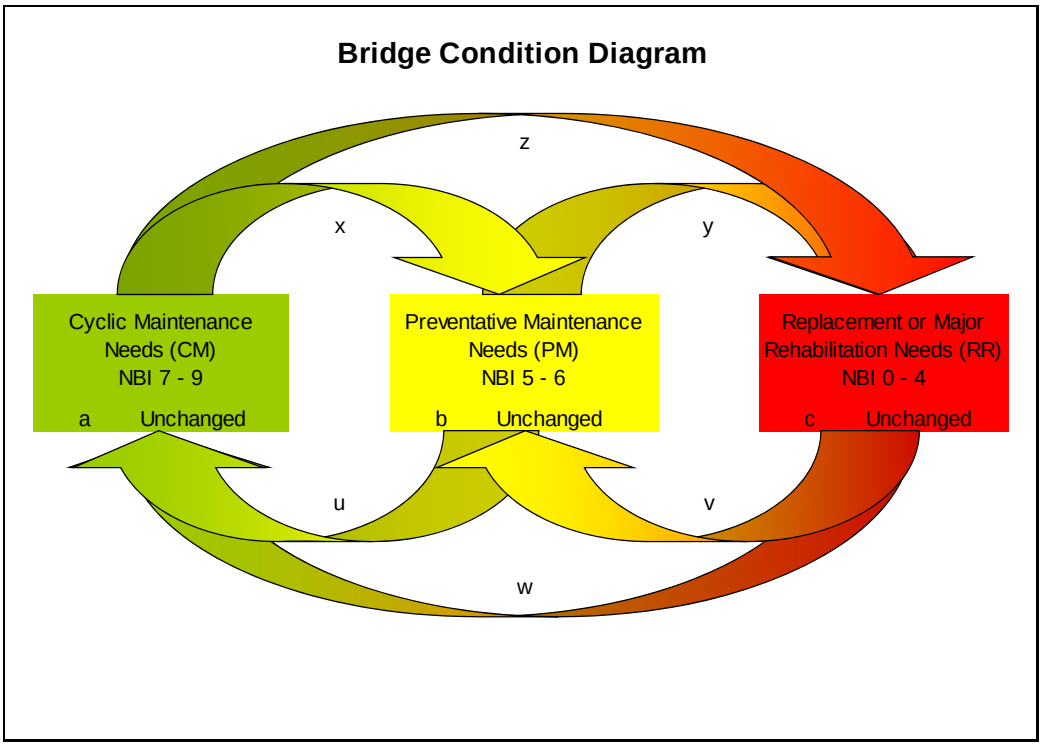

FIGURE 5, Measures can track for movement of bridge condition annually

Conclusions

A comprehensive systematic process is necessary to manage a large bridge inventory and to take full advantage of the service life extension potential of modern structures. Tools are currently available or are being developed to facilitate inspection, evaluation, selection of cost-effective preservation actions and monitoring performance of bridges and bridge elements. Tools are also available to estimate overall program funding levels to achieve a desired service level of highway bridges. Nevertheless, considerable challenge remains to bridge managers seeking to adopt a comprehensive bridge preservation program to achieve a best fit within an agency's overall bridge management system.

References

1. AASHTO, "Bridge Element Inspection Guide", 2013
2. Ahmad, Anwar, PE, FHWA "Bridge Preservation Guidelines", 2012
3. Azzizinamini, Atorod, PE, PhD, SRHP2 Project 19A Report and "Guidelines Design of Bridges for 100-year Life"
4. Bowling, Gary, PE, PLS, et al, "ODOT Inspection Manual", 2013
5. Bowling, Gary, PE, PLS, et al, "ODOT Bridge Inspection Coding Guide", 2013
6. Johnston, David, PhD, Michigan State University, personal communications and research in progress, 2013

INVESTIGATION AND COUNTERMEASURES FOR FATIGUE CRACKS THAT EMERGED ON THE FINGER JOINT OF THE CABLE-STAYED BRIDGE "TSURUMI-TSUBASA BRIDGE"

Tsuyoshi KOSUGI[1]
Masakatsu TAKANO[2]
Masanori TAKAHASHI[3]

Abstract

As a result of a follow-up investigation for fatigue crack damages of the finger joint of the Tsurumi-tsubasa Bridge in 2012, where emergency repair had been carried out from 2008 to 2010, 140 cracks were found along the root of the welded part of the face-plates. Due to analysis of tendency for crack causing, it was confirmed that weld detail at the time of fabrication was one of the factors for crack causing.

As for the blocks of the face-plates with serious damages, they were replaced by blocks having been installed under the road shoulders as an emergency measure before they were replaced by newly fabricated ones. For face-plates which could be re-used, they were repaired by shop welding.

Introduction

Tsurumi-tsubasa Bridge on the Metropolitan Expressway is a 3-span continuous steel cable-stayed bridge, approx. 1 km long in length. The average volume of daily traffic is more than 40,000 vehicles, and the percentage of over-sized vehicle traffic is more than 25%. As for the Tsurumi-tsubasa Bridge, fatigue cracks of the finger joint were found for the first time in 2004. Since then, cracks and fractures have been found intermittently. For these damages, exchange and/or replacement of blocks of the face-plates have been conducted so far. A lateral-view of the Tsurumi-tsubasa Bridge is shown in Fig.1 and a complete view is shown in Fig.2.

In the follow-up investigation for the finger joint of the Tsurumi-tsubasa

[1] Senior Staff of Third Management Division, Structural Management Department, Shutoko Engineering Co., Ltd.
[2] Manager of First Management Division, Structural Management Department, Shutoko Engineering Co., Ltd.
[3] Deputy Manager of First Maintenance Design Division, Kanagawa Operation Bureau, Metropolitan Expressway Co., Ltd.

Bridge intended for serial observation in 2012, 140 crack damages were found along the root of the welded part of the face-plates and it was affirmed that damages tended to increase. So, repair by shop welding was carried out as a practical measure against crack damages, by analyzing occurrence tendencies of the damages and weld detail in time of fabrication. In this script, crack investigation and countermeasures taken for the damages will be described.

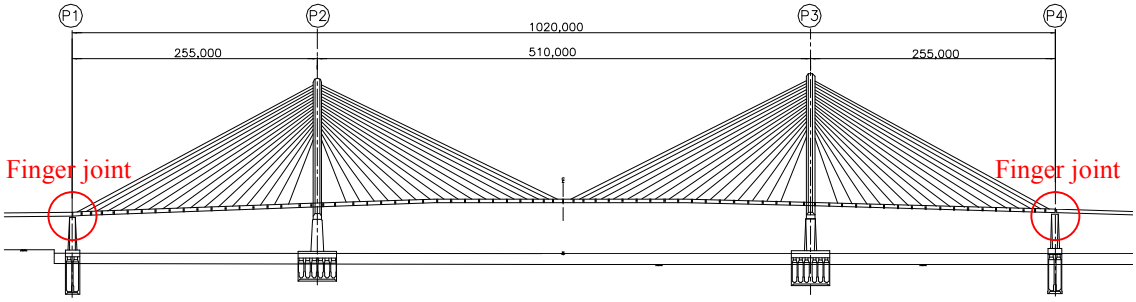

Fig.1 Lateral-view of the Tsurumi-tsubasa Bridge

Fig.2 Complete view of the Tsurumi-tsubasa Bridge

Structure of finger joints

As for the finger joint of the Tsurumi-tsubasa Bridge, joint clearance is 3220mm, the length of design movement is ±320mm on a steady basis, and ±700mm in times of an earthquake. The length of the finger joint is approx. 2000mm, and as the cantilevered length is long, approx. 1700, it is designed as a simple beam with an intermediate supporting beam. Structure of the finger joint is shown in Fig.3.

The face-plate block of the finger joint is composed of face-plates cut out

from thick steel plates and spacing-plates that are welded mutually. Weld structure of the face-plate block is shown in Fig.4. As for a the blocks of the face-plate, welding is done around the spacing-plate by fillet weld with the leg size of 9mm, but welding was not fully done in narrow spaces sandwiched between the face-plates, because it was physically difficult to weld in narrow spaces at the time of fabrication. Crack damage found during this investigation all generated from such parts.

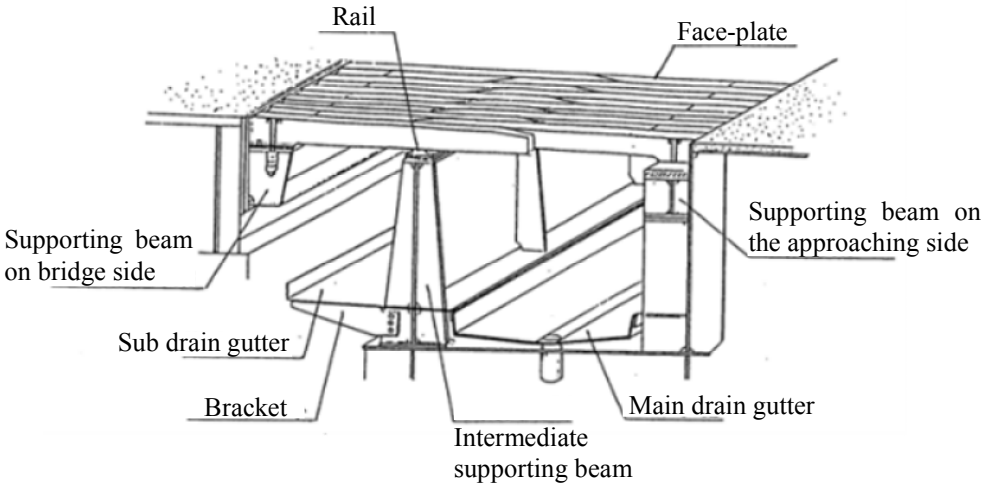

Fig.3 Structure of finger joint

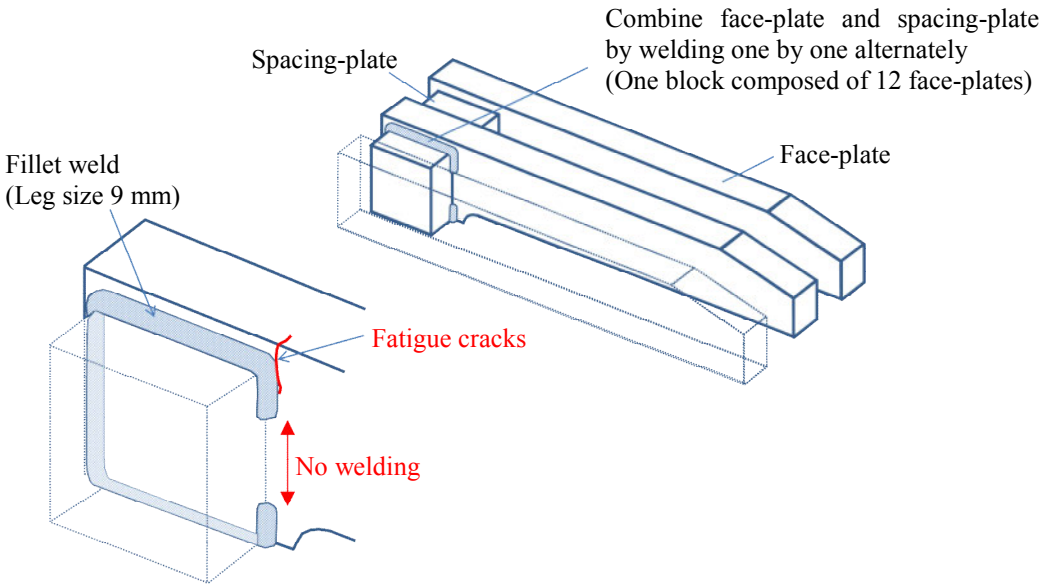

Fig.4 Weld structure of the face-plate block

Sequence of events so far

Fatigue cracks were found on the finger joint of Tsurumi-tsubasa Bridge for the first time during the inspection in 2004 (Fig.5). The cracks which could be observed visually generated from the parts welded to the root of the top surface of the face-plate. Subsequently, an emergency inspection was carried out for these parts, and approx. 80 cracks were found. As a countermeasure, removal of the cracks by machining and replacement of the face-plate blocks were implemented.

Since then, follow-up investigations and support for damages were carried out repeatedly, but a fracture of the face-plate occurred in 2010 (Fig.6). Fortunately, it did not affect traffic, because it was only one face-plate that fractured. The cause of this fracture was a new type of crack that generated from the corrosion part of the bottom surface of the face-plate (Fig.7). At that point, an emergency inspection was carried out against the corrosion part of the bottom surface of the face-plate and the same type of cracks generated from the corrosion part were found at approx. 10 points besides the fractured face-plate. This time as well, replacement of the face-plate blocks was carried out as a countermeasure.

Fig.5 Cracks from the root of the welded part of the face-plate found in 2004

Fig.6 Fracture of the face-plate that occurred in 2010

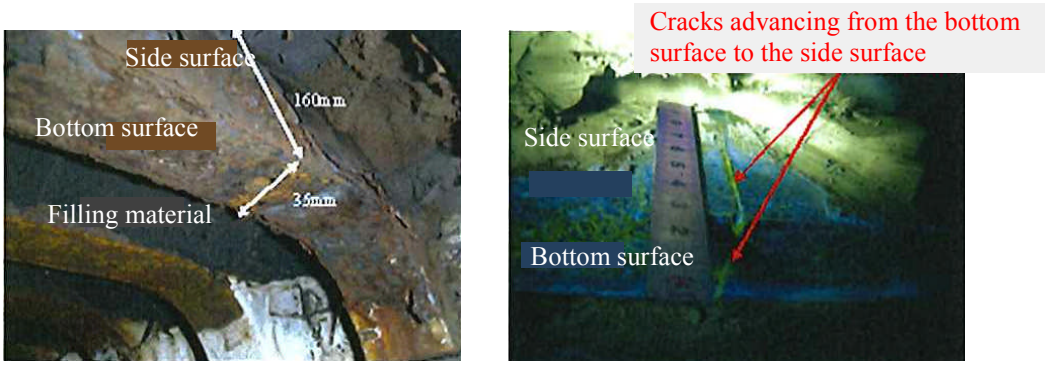

Fig.7 Cracks generated from the corrosion part of the bottom surface of the face-plate

Investigation of cracks

Content of investigation

In this follow-up investigation, magnetic particle examination for crack investigation was applied to the root of the top and bottom surface of the face-plates, where crack damages had been found up until then. Examinations were applied to all parts of welding done to the root of the top surface of the face-plates, except for those having been installed under the road shoulders, as well as the bottom surface of the face-plates where corrosion was remarkably serious and loading positions of the wheels of over-sized vehicles. In total, there were 1500 investigation points, including 1100 points on the top surface and 400 points on the bottom surface. Research status of the investigation is shown in Fig.8 and 9.

As for the corrosion of the bottom surface, it had not advanced or prevailed compared to the status when the inspection for the corrosion of the bottom surface was carried out two years ago, in 2010. This might be because cover plates on the bottom surface of the face-plates were removed during that inspection, and there was no place for water to gather.

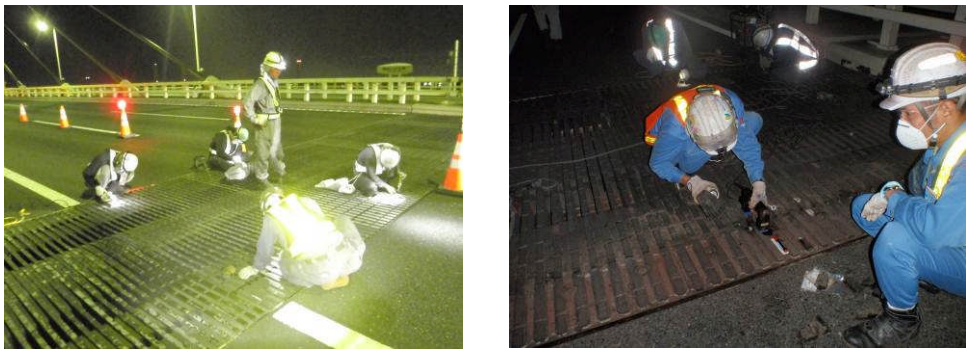

Fig.8 Research status of investigation for the top surface of the face-plate

Fig.9 Research status of investigation for the bottom surface of the face-plate

Results of the investigation

As a result of a magnetic particle examination conducted at 1500 points on the top and bottom surface of the face-plates, 140 cracks were found at the root of the welded part of the top surface. Genesis location of the cracks is shown in Fig.10 and the breakdown of the number of cracks is shown in Table.1. During this investigation, a flaw indicating pattern was not found on the bottom surface of the face-plates.

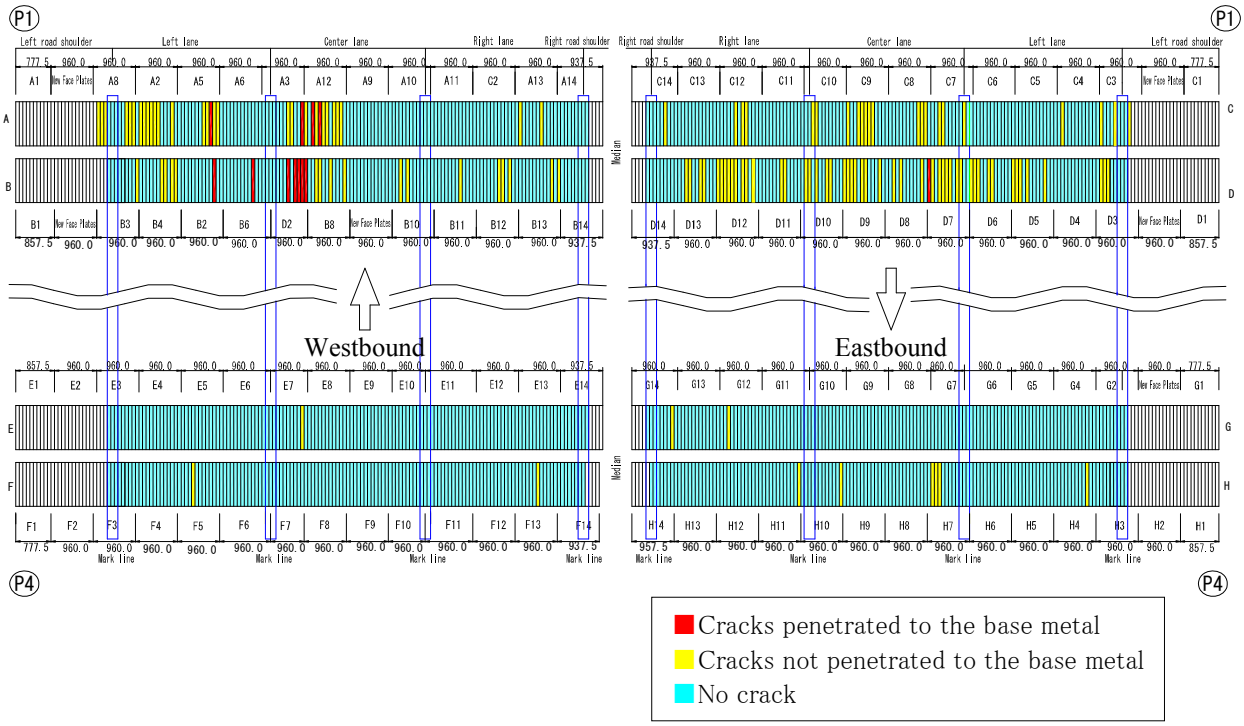

Fig.10 Genesis location of cracks

Table.1 Breakdown of discovered number of cracks

Place	Direction	Discovered number of cracks (Points)		Total
		Cracks penetrated to the base metal	Cracks not penetrated to the base metal	
P1	Westbound	11	45	56
	Eastbound	1	72	73
P4	Westbound	-	3	3
	Eastbound	-	8	8
Total		12	128	140

Most cracks which were found during this investigation generated at the finger joint on P1 pier. Of all 140 points, cracks penetrated to the base metal were found at 12 points, and cracks penetrated from the welded part of both sides of the face-plate to the base metal were found at 4 points, which could lead to fracture. The most severe damage is shown in Fig.11. As for the blocks of the face-plate with remarkably serious damages, they were replaced as an emergency measure by robust ones which had been installed under the road shoulders, and thereafter were replaced by newly fabricated blocks as a permanent measure.

In this investigation, an unprecedented number of cracks were found at 140 points, and it was confirmed that the number of cracks were continuing to increase. In particular, although substantial replacement of blocks had been carried out in 2010, more than 50 cracks were found at the face-plate blocks under the lane bound for west on P1 pier. So it is considered that the cracks in these places generated two to four years after the replacement. On the other hand, many cracks were found in other places where block replacement had not been carried out. Cracks also generated at the right lane where traffic of over-sized vehicles is light. This indicates exteriorization of accumulated damages at the finger joint of the Tsurumi-tsubasa Bridge, which has already passed 18 years since it was placed to service.

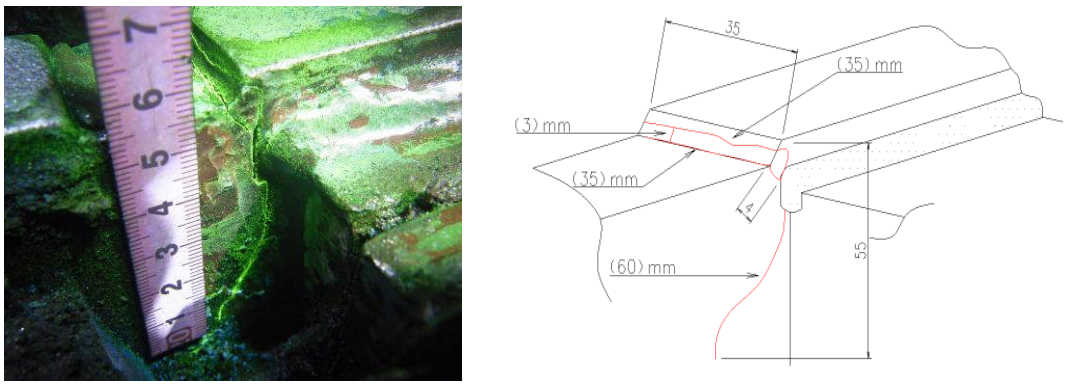

Fig.11 Cracks penetrated to base metal

Consideration

All cracks generated from the root of the welded part of the face-plate, and most of them generated from the weld toe. This type of crack tends to penetrate to the base metal if they remain untouched (Fig.12).

The finger joint on the P1 pier had an overwhelmingly larger number of crack damages compared to the P4 pier, which may be attributed to the difference of quality made by its fabricating companies. Furthermore, as abrasion was confirmed during the past inspections on the rail of the intermediate supporting beam installed under the face-plates, it can be considered that this abrasion is the cause of the increase of amplitude of the face-plates.

Focusing on traffic lanes, a large number of serious damage were found in the center lane among three. This may be because over-sized vehicles running at high speed on the center lane have recently increased.

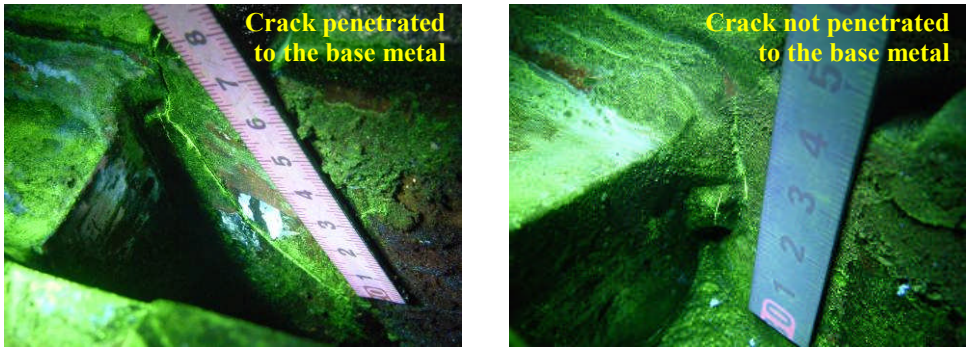

Fig.12 Cracks with (left) and without (right) penetration to base metal

Analysis of damage

Of all the 140 damages found during this investigation, 129 damages were found at the finger joint on P1 pier. By confirming detailed fabricating structure, difference of welding status of the finger joint on the two piers was identified, as shown in Fig.13, and an un-welded spot was left between face-plates on both piers. At the finger joint on P4 pier where there were few cracks, welding was done vertically within approx. 50mm from the corner of the spacing-plate. However, at the finger joint on the P1 pier where there were many cracks, welding was done only at the corner of the spacing-plate. Furthermore, finishing process or the weld toe on both piers was not conducted sufficiently. So, causing factors for the crack damages are considered as the following;

- A breakpoint was installed in the weld structure with an overlapping joint, and of

low fatigue durability.

- A start/end position of welding subject to damage was installed at the corner of the spacing-plate, a point of stress concentration where stiffness changes.
- Finishing process was not sufficiently provided at the weld toe.

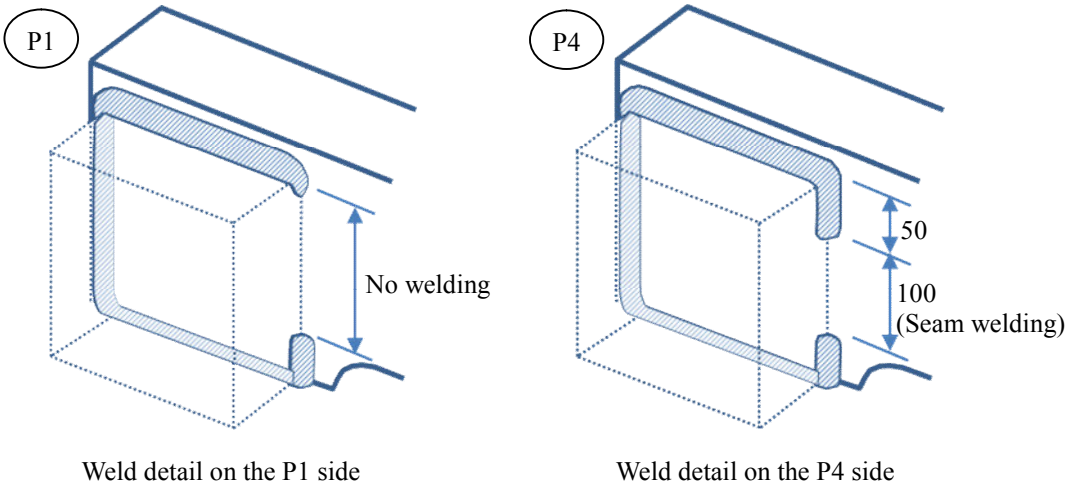

Fig.13 Weld detail of the root of the face-plate

Countermeasure for damages

Of the140 crack damages found during this investigation, as for the 12 damages which penetrated to the base metal of the face-plate, an emergency measure by replacing the blocks by robust ones that are installed under the road shoulders, was rapidly carried out from the aspect of ensuring safety for vehicles, then a permanent measure of replacing them by newly fabricated ones was applied.

On the other hand, concerning the points of crack damages without penetration to the base metal, as the number of blocks amounted to 37, fabrication of new blocks was not realistic from the view point of period of production time and cost. Blocks were temporarily removed and replaced one after another, and weld repair was carried out within the factory, not targeting restitution but bearing in mind improvement of fatigue durability, considering the causing factors for the crack damages, as the following.

- Remove all crack damages by machining, and restoring by fillet weld ensuring enough length of bead.
- Leaving no insufficient welded places, not-welded and/or seam-welded
- Not to leave the start/end position of welding.
- Conduct finishing process for the welded toe.

Details of the weld repairing work are described as follows.

Weld in narrow spaces

Welding repair for crack damages was restored by re-weld, after weld bead of the cracks were completely removed by machining, and at the same time, insufficient welded places were restored by welding ensuring enough leg length of the bead. As for the welding work, the finger joint was fixed upright and a downward stance of welding which causes less flaw was adopted. Also, coated arc welding was implemented for narrow spaces using a longer weld rod than usual. The welding status restored by this process is shown in Fig.14, and the restored weld bead is shown in Fig.15. As for start/end position of the restored weld bead, a new bead was welded onto the existing one and then was removed by a grinder.

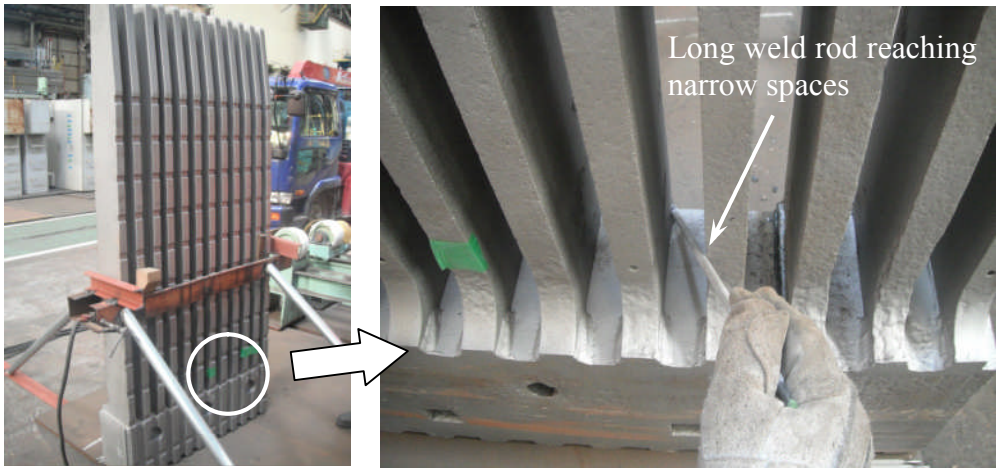

Fig.14 Working conditions and weld rod used for this work

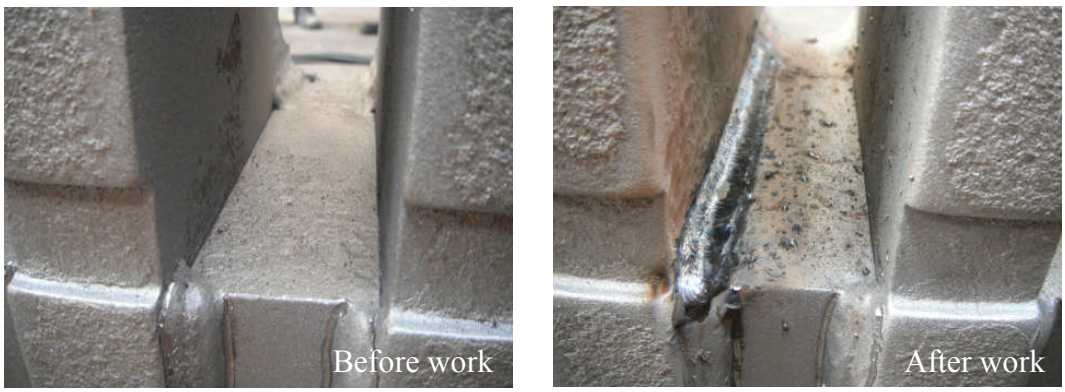

Fig.15 Restored status of welding for narrow spaces (before work, after work)

Process of weld toe

As for the processing the of the weld toe, welding start/end position in narrow spaces between the face-plates were finished by a grinder, and the scope within 50mm from the edge of the top surface of the spacing-plate was processed furthermore by peening. The status of processing the weld toe is shown in Fig.16.

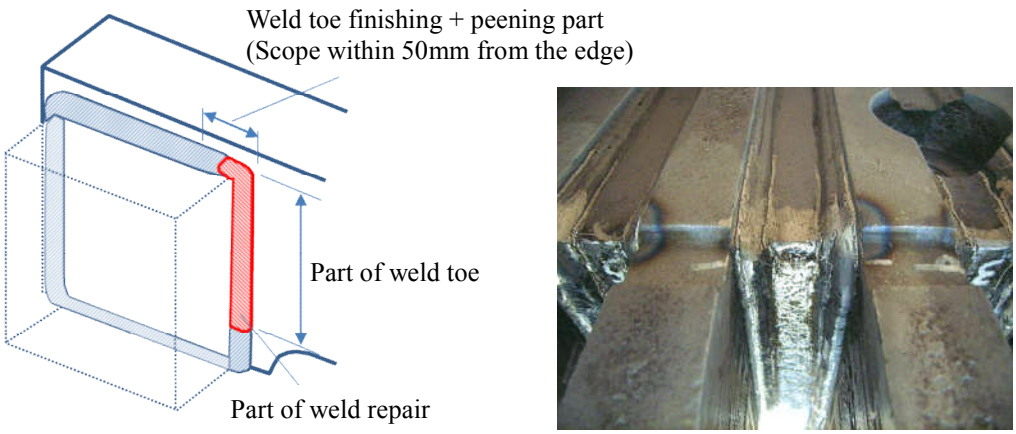

Fig.16 Status of processing the weld toe (final status)

Summery

Cracks of the face-plates which were found during this investigation generated from the welding point done to the root on the upper surface of the face-plate. Most cracks that generated from the weld toe tend to penetrate to the base metal over time.

Cracks on the face-plate were found more on P1 pier. As the length of the welded part of the root was different between on P1 pier and on P4 pier, it is considered that this is attributed to the difference of weld detail in time of fabrication.

In this investigation, cracks from the bottom surface of the face-plate were not found. The reason is considered that corrosion had not proceeded since the cover plate was removed from the bottom surface of the face-plate during the temporary inspection in 2010.

A countermeasure for crack damages generated in the finger joint was examined according to the degree of damages and a corresponding policy was determined. As for the blocks where cracks penetrated to the base metal, they were replaced by newly fabricated ones, because re-use of existing blocks was impossible. On the other hand, blocks without penetration to the base metal were temporarily removed, then weld repair was carried out at the factory, considering economical efficiency. In repairing the blocks, a welding method was devised in consideration for

the improvement of fatigue durability and such possibility was confirmed.

Conclusion

This follow-up investigation was carried out two years after the last investigation in 2010. As some critical damages were found this time, it was a significant result to discover damages of the face-plates before they might fracture.

The Metropolitan Expressway is now implementing a weld repair for these damages. It is considered that fatigue durability of the existing face-plates will be improved if an appropriate weld is applied, even if the face-plate is a re-used one. The weld repair has been completed approx. up to 60% at the end of August 2013, and the entire work is scheduled to be completed by the end of the year.

However, as for the finger joint on the P4 pier, its quality is relatively high, but it cannot be said that no damage has been caused until now, so periodical inspection is scheduled to be conducted after the repair.

Acknowledgments

We especially thank all members related to the maintenance management in the Metropolitan Expressway Co., Ltd. for their appropriate advice and guidance as well as their support throughout the entire process to complete this paper.

PRELIMINARY SEISMIC CONSIDERATIONS FOR PULASKI SKYWAY REHABILITATION PROJECT

Xiaohua H. Cheng[1]

Abstract

The 3.5 mile (5.63 km) long Pulaski Skyway is located in northern New Jersey, serving as a major connection from Newark to New York City. Built in 1932, the Skyway mainline consists of different types of superstructures supported on 108 piers and one abutment. Due to existing bridge condition and funding availability, the entire bridge is under plan and design for major rehabilitation. Seismic retrofit is one of the major rehabilitation actions under plan and has to be considered in conjunction with other rehabilitation actions. To achieve cost-effectiveness, feasibility assessment and preliminary site-specific seismic analysis are conducted. This paper presents background of the bridge rehabilitation plan, seismic considerations, assessment result, and geotechnical seismic vulnerability study that may lead to decision making.

Introduction

The Pulaski Skyway, completed in 1932 and opened to traffic in 1933, is the vital link in the northern New Jersey transportation network, linking Jersey City, South Kearny and Newark. It serves as an express link for car and bus traffic to and from the Holland Tunnel, via Rt.139, carrying ADT of 74,000. The 3.5 mile (5.63 km) long elevated structure is composed of a series of different types of bridges (118 spans in total: 108 for mainline and 10 for east approach) that carries Route 1 & 9 over the Hackensack River, Passaic River, New Jersey Turnpike (I-95), several railroads, local roads, and industry facilities (**Fig.1**).

The inspection reports (NJDOT, 2010) have shown that the Skyway is in need of major repair and rehabilitation due to deterioration that occurred over its lifetime. The bridges are structural deficient (SD) and functional obsolete (FO) that do not meet modern design and safety standards. NJDOT has developed long term strategy for improvement of the entire structure, anticipated to commence in 2015. Due to the high cost and complexity, this major project will be performed in several stages, and concept development and initial/feasibility assessment study are conducted to evaluate project alternatives and select the most cost-effective alternative to advance to the design.

Among many factors for the preservation and rehabilitation plan, structural systems and safety concerns are the major considerations. The objective is to bring the Pulaski Skyway into a good service condition and extend to another life cycle useful for 75 years by addressing structural deficiencies, mitigating vulnerability to seismic

[1] Principal Engineer, Bureau of Structural Engineering, Bridge Engineering and Infrastructure Management, New Jersey Department of Transportation (NJDOT), Trenton, NJ 08625, USA

hazard, modifying functional deficiencies, and improving the overall condition and operational safety of the roadway. This paper will provide brief information on the current structural condition, rehabilitation considerations, and seismic retrofit considerations, through initial site-specific assessment and geotechnical seismic vulnerability study.

Existing Bridge Conditions

The Pulaski Skyway consists of 108 spans (numbered east to west) of elevated bridge structures, including a series of superstructure (**Fig.2**): two 550 ft (168m) through truss main spans with 350 ft (107m) flanking truss spans over Passaic River and Hackensack River, three steel through trusses over railroads in Jersey City (east), deck trusses between the two through trusses, and deck trusses and girder bridges in the remaining spans. The foundation types along the mainline are complicated, including spread footings, pile foundations (concrete and timer), and concrete caissons. The bridge is 3.5 mile (3.63 km) long and 56.5 ft (17.2 m) wide (**Fig.2**) carrying 4 lanes. The original concrete deck slab still remains with several times of resurfacing along the service life, and will be replaced entirely in the near future. Note that ramps and approaches off the mainline will not be included in the discussion of this paper.

Based on the previous inspection reports and suggestions, a series of interim repairs and rehab have been implemented in 1978, 1983-1984 and 2008, such as deck repairs, deck overlay/resurfacing, partial widening, parapet/railing repairs, priority repairs to superstructure and substructure.

The current biennuial inspection report shows that the bridge overall physical condition is "Poor" due to superstructure condition, and overall condition is "Serious" due to low inventory ratings of some truss diagonal and steel girder members. The following is a summary:

- *Components* (**Fig 3** & **Fig.4**):
  - Deck: Poor (due to continued extensive deterioration of underdeck, and spalling of the top of the deck);
  - Superstructure: Poor
  - Substructure: Fair
- *Structurally Deficient* (SD): Poor ratings; Structural steel defects
- *Functionally Obsolete* (FO): Poor geometrics; Low vertical clearance

A further in-depth FEA rating of the entire structure is being performed and result is under evaluation to ensure the final load rating. A special assessment of the primary truss gusset plates was conducted to measure remaining sections and used in this in-depth structural analysis.

Deck and Joints The deck is in overall "poor" condition due to continued extensive deterioration of the underdeck (spalling and cracking with efflorescence), and continued spalling of the top of the deck (**Fig.3**). The loose concrete on the underside of deck has become a safety issue for roadway below. The slide plate and steel finger

expansion joints throughout the bridge are in "fair" condition with vertical profile mismatch from ¼" (~6mm) to 1" (~25mm) and one is frozen.

Superstructure The structure steel exhibits areas of moderate to severe rust throughout, with substantial pack rust and local areas of heavy section losses; Severe rusting occurs primarily at the truss lower chords and joints, and in all steel components below the open deck joints and floorbeam cantilever ends. The paint system has generally failed throughout the structure.

Concrete encasement for the stringers and girders typically exhibits minor to moderate deterioration. The on-going maintenance has performed to remove most of the existing encasement from the steel girders and expansion pier bents, both to prevent falling concrete onto roadways and ensure that hidden section losses at the joint areas can be discovered and repaired (**Fig.3**).

Typical deterioration of truss members in through trusses and deck trusses are shown in **Figure 3**. The rate and amount of localized deterioration represents a progressive structural distress that has continued since last biennial inspection.

The truss pin assemblies of upper and lower chords typically exhibit localized material loss due to wear around the exposed surface of the pin between the truss connection plates, or rust. UT testing of primary truss pins and accessible truss pins of other spans was performed. The observation indicated the presence of 3 small localized discontinuities which are acceptable due to corrosion pitting, etc.

Bearings Severe rust, minor section loss, missing nuts, and pack rust between vertical stiffeners are observed at fixed and expansion bearings, but evidence of normal movement are noted at all sliding bearing locations.

Substructure Pulaski Skyway mainline structure was constructed on different types of foundations depending on superstructure type, soil condition and foundation depth. They include spread footings, timber piles, CIP concrete piles, precast concrete square piles, concrete caissons (single or pair), columns/piers are of two types: concrete encased steel piers and reinforced concrete piers with pedestals (**Fig.4**),

The substructure is in "fair" condition. Most deterioration is concrete cracks with heavy efflorescence, spalling, delaminated concrete areas. Many of these defects have previously been repaired with concrete patches and epoxy crack sealant, which is deteriorated/cracked again. The previously added post tension rods and beam collars appear to be limiting crack propagation (typically for Piers 65 to 67 Main Truss over Hackensack River) (**Fig.4**).

Earlier underwater inspection report states that the submerged substructure components are in overall "fair" condition (east portion) due to cracks and spalls in the concrete, or satisfactory (west portion).

Rehabilitation Plan

Several remedial actions are recommended and implemented for interim repairs and short-term rehabilitation based on the biennial inspection report. The structure is on the National Historical Register and a full replacement is not economically feasible, so the final decision was made to rehabilitate Skyway in current configuration. With significant funding available recently, a comprehensive long-term rehabilitation plan has been developed by NJDOT, under the Pulaski Skyway Improvement Program, to ensure the bridge integrity and extend the bridge service life. The following major rehabilitation actions related to the entire bridge structure are planned:

- Deck replacement:
  - Using precast panels with stainless steel reinforcement, and using partially lightweight concrete;
  - Structural response to be monitored by sensors during different construction stages
  - Deck joint replacement and joint reduction/elimination; use of modular joints
- Superstructure rehabilitation:
  - Concrete encasement removal;
  - Replacement of severely corroded members;
  - Structural steel repairs for severely deteriorated members
  - Strengthening members rated low (under consideration dependent on FEA rating results)
- Substructure rehabilitation:
  - Repair of concrete columns/piers, bent caps/strut beams, pedestals and abutments
  - Retrofit of foundations/footings (dependent on seismic retrofit analysis)
- **Seismic retrofit**:
  - Bearing replacement with isolation bearings (under consideration);
  - Soil improvement (under consideration)
  - Other alternatives (seat length; restraints, Etc.)
- Re-painting:
  - Removal of existing lead paint
  - Re-coating

General Seismic Considerations in New Jersey

The seismic histories of New Jersey and New York, as documented by NJDEP, NYGS and USGS, show that many earthquakes have been recorded in the project region between 1973 and 2012. Although it makes NYC and northern NJ region among the highest in frequency of seismic activity in the country, the recent 100 year or so recorded maximum magnitude of earthquake in New Jersey was 5.0 in Richter Scale (VI and VII in MM Scale). Prior to 1990s, design and details of all highway bridges did

not take earthquake or security issue into account. This implies that most existing highway bridges, including Pulaski Skyway, have potential to be vulnerable to seismic damage during an earthquake event.

Now NJDOT requires that seismic design and seismic retrofit for standard or ordinary bridges to follow AASHTO "Guide Specifications for LRFD Seismic Bridge Design" (AASHTO, 2011) and FHWA "Seismic Retrofitting Manual for Highway Structures" (FHWA, 2006), respectively (NJDOT, 2009). All NJDOT bridges should initially be considered to be "standard" and designed for "life safety" performance objective considering a seismic hazard corresponding to 7% probability of exceedance in 75 years (approximately 1,000 year return period). However, consideration for increasing bridge Importance Category is permitted and should strictly be based on social/survival and security/defense factoring of the bridge location. If these factors clearly indicate the location's critical nature, increase of Importance Category and/or Performance Level may be considered. The foundation supporting a bridge structure shall be designed not to experience damage in an earthquake event to prevent from costly inspection and repair work after an earthquake event.

To obtain general seismic information for preliminary design reference purpose, a research was carried out on "Seismic Design Considerations" in New Jersey (Agrawal, Liu & Imbsen, 2011) and statewide Seismic Design Category (SDC) maps were developed for Standard Bridges using AASHTO/USGS 1,000 year hazard map, and Critical Bridges using USGS 2,500 year hazard maps (or using 1.5 time seismic hazard map of 1,000 year return Period), respectively. The SDC maps are developed based on AASHTO Guide Spec procedure, AASHTO/USGS seismic maps, and representative soil classes for each zip code location referring to NJDOT Geologic Survey (NJGS) boring log database (**Fig.5**).

Figure 6 shows the SDC maps for Standard/Ordinary Bridges and Critical Bridges in New Jersey. It can be seen that for standard/ordinary bridges, the SDC is "A" for almost all locations in New Jersey regardless of soil site classes (except some locations requiring site-specific investigation (blue area in the map)), while for critical bridges, SDC "B" possibly exists in some locations (green in Hudson County) due to low soil site classification "E" or "D" (purple or red in **Fig.5** soil site map). Coincidently Pulaski Skyway falls in this area.

In conjunction with the seismic hazard analysis of New Jersey, liquefaction hazard analysis was conducted to assess the liquefaction potential of each zip code. The analysis utilized the Standard Penetration Test (SPT) blow counts of soil and followed the approach by Youd et al. which is one of the approaches suggested by the AASHTO Guide Spec. (AASHTO, 2011). It can be seen from these maps that areas with higher liquefaction hazard are mainly in the northern part of New Jersey especially where the Pulaski Skyway is located. For 2,500 year event, compared to the hazard for 1000-year earthquake, the areas with "medium" liquefaction hazard are now classified as "high", and some areas with "low" hazard now have "medium" liquefaction hazard.

It is noted that the SDC maps and liquefaction hazard maps for standard or critical bridges are for preliminary design and reference purposes only, since critical or specially important bridges require site specific analysis and the maximum acceleration a_{max} at ground surface that is needed for liquefaction potential analysis that must be obtained using site-specific analysis.

Although Pulaski Skyway is a vital link between the Holland Tunnel/NYC and NJ turnpike, interstate highway and northern Jersey highway system, considering the highway redundancy in the area and high cost of seismic retrofit, it is very important to correctly evaluate the bridge vulnerability, risk of seismic damage and alternative comparison to achieve the most cost-effective solution.

It appears that Pulaski Skyway seismic analysis needs further site-specific analysis, because 1) From above general analysis, Pulaski is located in a relatively high seismic risk area of New Jersey as an important bridge; 2) The bridge is a historical signature bridge as a vital highway link; 3) Seismic retrofit for this existing bridge should follow FHWA Seismic Retrofitting Manual (FHWA, 2006; MCEER, 2006), instead of AASHTO Guide Spec. (AASHTO, 2011) despite their similar philosophy.

It is anticipated that the following questions be addressed from site-specific seismic analysis:

1) What seismic hazard level should be used for seismic analysis to achieve a cost-effective alternative?

2) What is the seismic retrofit demand for the selected seismic hazard?

3) What alternate measures are needed for seismic retrofit for superstructure and substructure?

4) What extensive seismic retrofit should be taken or avoided in conjunction with the entire rehabilitation plan, such as isolation bearings, subsurface soil improvement, pier and foundation retrofit, etc.

Initial Assessment for Seismic Design Criteria

Pulaski Skyway site-specific subsurface soil investigation was conducted, including P.S. Logging testing. Initial site-specific seismic response analysis was performed for three seismic hazard levels of 500, 1,000, and 2,500 year return period to preliminarily understand the seismic retrofit demand for the bridge. From site specific soil investigation result, site class is summarized as: Piers 1 to 41 – Class D; Piers 42 to 63 – Class E; Piers 64 to 98 – Class E; and Piers 99 to 108 – Class D.

Multi-mode response spectrum analysis was performed. The bridge period for main through trusses is 1.71 Sec. for Mode 1 and 1.49 Sec. for Mode 2. The recommended design response spectrum for Pier 64 to 98, covering two main through trusses and deck trusses between and beyond the two main trusses, is shown in **Fig. 8**.

To further investigate relative cost estimates for seismic retrofit, the effect of the three seismic hazard levels on the Capacity (C) to Demand (D) ratio, C/D, are analyzed.

The results for Piers 41 to 100 are plotted in **Figure 9**, presenting elastic moment C/D ratio for concrete pier pedestals (column bases). Pier column results are skipped herein. Most of the concrete piers were found to be deficient for the 2.500-year event, i.e. C/D is less than 1.0. The computed C/D ratio is as low as 0.16 for column (not shown herein) and 0.23 for pier pedestal (column base). According to available drawings, some original pier columns and pedestals appear to be unreinforced. In addition, some piers were subject to net uplift under 2,500 year event without capacity. It is clear that seismic retrofit required for 2,500 year event would be very extensive.

For the 1,000 year event, the computed C/D ratios are significantly higher than 2,500 year event, and most columns and pedestals are adequate (i.e. C/D is equal or greater than 1.0). The lowest C/D is 1.5 for pier column and 0.61 for pedestal, and none of them would be subject to net uplift for the 1,000 year event. Comparing to 2,500 year event, the seismic demand is greatly reduced and hence seismic retrofit required would be less extensive. It is noted that although seismic demand may be lower, due to exiting pier condition and soil site condition, the vulnerability to seismic damage does exist. For 500 year event, computed C/D ratios for pier columns and pedestal are greater than 1.0 for all piers from 41 to 100.

On the other hand, FHWA Seismic Retrofit Manual (FHWA, 2006) is used to find out seismic retrofit requirement for the Pulaski Skyway following the evaluation procedure provided in the Manual. Providing that Bridge Importance is "Essential", Anticipated Service Life is ASL-3 for 75 years (>50 years), and Upper Level Ground Motion is 1,000-year return period, the minimum performance level would require to be PL2 Operational, which is the performance level Pulaski Skyway bridge is expected. The initial Seismic Retrofit Category (SRC) evaluation comes up with Hazard Level II and SRC B for PL2 and SRC C for PL3 "Fully Operational".

Geotechnical Seismic Vulnerability Assessment

A comprehensive work (PB, 2013) has been performed for soil logging as deep as 100 ft. (30.5m), deriving shear wave velocity, site-specific seismic response analysis, liquefaction evaluation for 1,000 year return period, and evaluating foundation vulnerability (C/D).

Due to the lack of real earthquake records (acceleration time histories); selected seed histories (NYCDOT) were used for ground motion input in Pulaski Skyway site-specific ground motion analysis. Response spectrum scaling methodology was used to generate the synthetic spectrum-compatible ground motion time histories for site-specific response analysis. The design rock acceleration time histories for both transverse and longitudinal directions were developed for 1,000 year event. The 5% damped, spectrally-matched bedrock motions agreed closely with USGS probabilistic bedrock response spectrum after converting from time history to their corresponding response spectrum. The maximum spectral acceleration results (envelope) of all site response analyses were used to develop the recommended spectrum for design purposes to accommodate the uncertainties in differential soil stratigraphy. Site classes for

foundations along the Pulaski Sky are summarized as shown in last Section.

The existing foundations include: 1) Spread footing at Piers 1 to 41; 2) Precast and cast-in-place concrete files at Piers 45 to 63 and Piers 101 to 108 (except Piers 50 and 52) with various pile cap sizes; 3) Timber piles at Pier 42 to 44 and 99 & 100; 4) Batter piles at west abutment; and 5) Single caisson at Piers 64 to 87 & pair caisson at Piers 88 to 98.

The foundation seismic vulnerability evaluation was based on results of liquefaction analysis and foundation nominal resistance analysis for each pier location. These vulnerabilities consist of changes to foundation demand due to seismic loading and effects of liquefaction. Due to the expanded subsurface information obtained in this study, areas susceptible to liquefaction were better defined resulting in fewer piers considered vulnerable to liquefaction than identified during the feasibility assessment phase. Liquefaction effects analysis includes seismic-induced settlement, down drag on deep foundation, and lateral spreading for 1,000 year seismic event.

Capacity-Demand Ratios for each foundation type were summarized. Almost all spread foundations failed in eccentricity (C/D ranging from 0.01 to 1.87) while many failed in sliding (C/D ranging from 0.12 to 8.33). All group pile foundations except one are satisfactory. All deep caissons are satisfactory if no liquefaction effect (C/D >2.0).

Based on the results of the preliminary vulnerability analysis, several foundations exhibited the need for possible remediation, pending investigation with final loading conditions from final design phase.

Several alternative mitigation methods are considered for the existing bridge: 1) to improve the subsurface liquefiable soils around the existing foundations; 2) to retrofit existing superstructures, substructures, and foundations to accommodate the predicted liquefaction and related ground movement; 3) for hazard other than liquefaction in spread footings, to install isolation bearings to mitigate seismic displacement and moment in substructures; to increase footing sizes; to tie-down anchor bolts along each side of footing, and so on. FHWA Manual and other alternatives will be sought to achieve cost-effective solutions in final design.

Summary

The discussion recommends earthquake hazard level of 1,000 year return period to be used for seismic analysis for cost-effectiveness. Although seismic response is not high, the vulnerability to seismic damage does exist due to poor condition of existing bridge and soil condition on the bridge site, which may require a retrofit action. Further study is needed to address the seismic retrofit questions and move on to determine final seismic retrofit design criteria.

Acknowledgments

The author gratefully acknowledge Parsons Brinckerhoff, NJDOT Project Management, and Mr. Nat Kasbekar, Director of NJDOT Bridge Engineering and Infrastructure Management for the information on Pulaski Skyway seismic study.

References

American Association of State Highway and Transportation Officials (AASHTO), "Guide Specifications for LRFD Seismic Bridge Design", 2nd Edition, 2011

A. Arawak, H. Liu and R. Ibsen. "Seismic Design Considerations", FHWA-NJDOT Research Report Knox, 2011

Federal Highway Administration (FHWA), "Seismic Retrofitting Manual for Highway Structures: Part 1 – Bridges, Jan. 2006

T. Ho, R. Donikian, T. Ingham, C. Seim and A. Pan, "Seismic Retrofitting Guidelines for Complex Steel Truss Highway Bridges", Special Report MCEER-06-SP05, 2006

New Jersey DOT "Design Manual for Bridges and Structures", 5th Edition, 2009

NJDOT "Bridge Re-Evaluation Survey Report of the Rt. US 1 & 9 Pulaski Skyway over the Hackensack & Passaic Rivers, Local Roads and Railroads (Span A0 through A9 & 1 through 85)", Sept. 2010 (also Spans 85 through 108 & Newark Ramp)", Sept. 2010

Parsons Brinckerhoff (PB), "Geotechnical Seismic Vulnerability Report", June, 2013

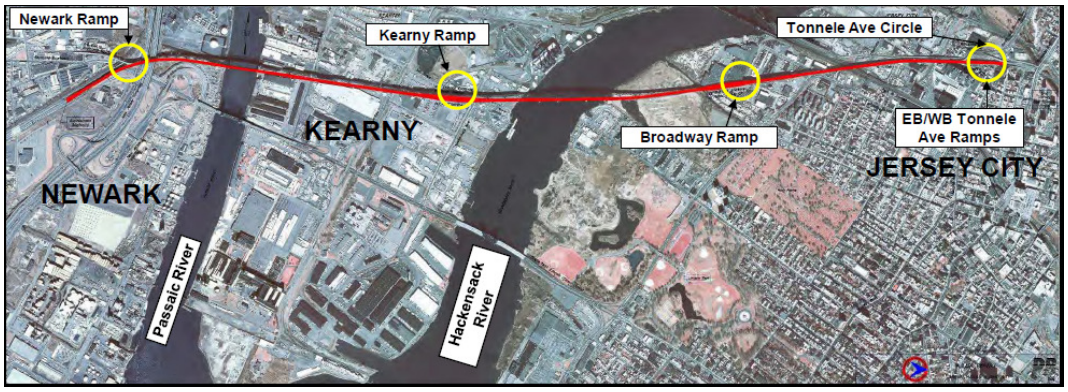

(a) Location of Pulaski Skyway (Up: North; Left: Newark; Right: Holland Tunnel)

(b) General View of Pulaski Skyway

Figure 1 Pulaski Skyway Location and Overall View

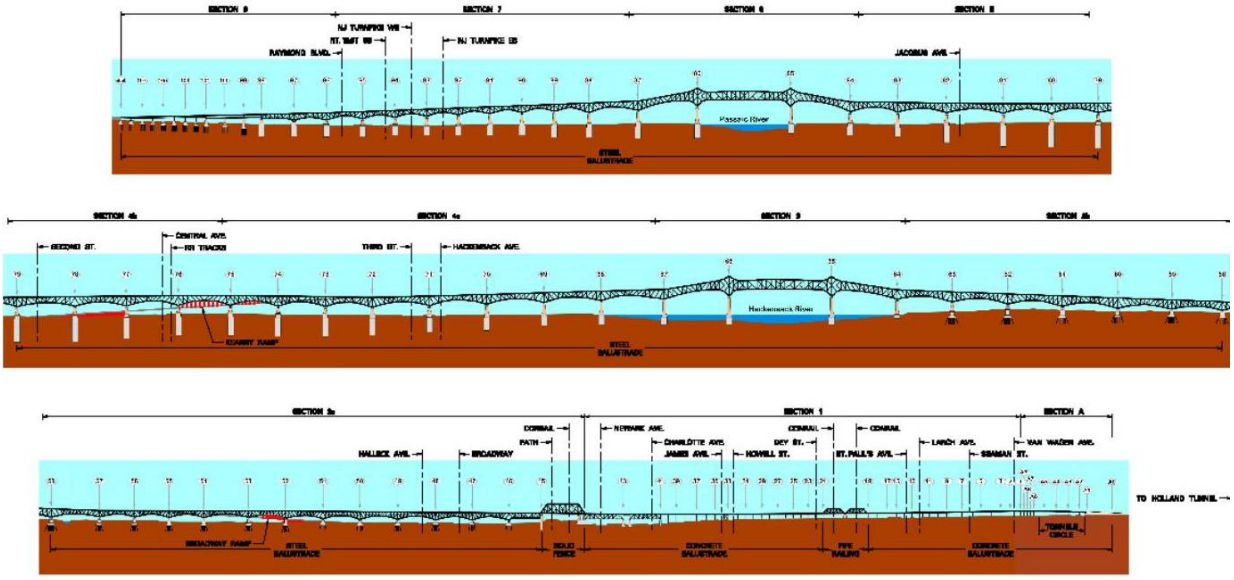

Elevation

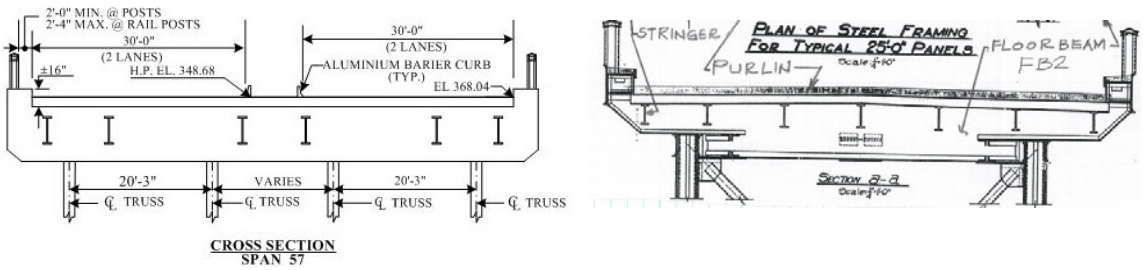

Typical Cross Section

Superstructure

Figure 2 Pulaski Skyway Bridge Elevation, Typical Cross Section and Different Superstructure

(a) Concrete Deck Spalling (underdeck): Left – Rebar exposure; Right – Cracking with efflorescence (chloride contamination)

(a) Encasement Loss in Stringer/Floorbeam and Steel Girder Encasement Removal

(b) Severe Rust and Section Loss of Truss Chord, Stringer and Floorbeam; Wear Pin Connection Hole and Pack Rust

Figure 3 Superstructure Deterioration Examples

(a) Severe Concrete Scaling with Efflorescence in Pier Column, and Chipped Concrete and Expose Rebar at Bearing Seat

(b) Wide Concrete Cracks and Efflorescence in Column Pedestal and Previously Added Post Tension Rods and Beam Collars; Concrete Encasement Cracking

Figure 4 Substructure Deterioration Examples

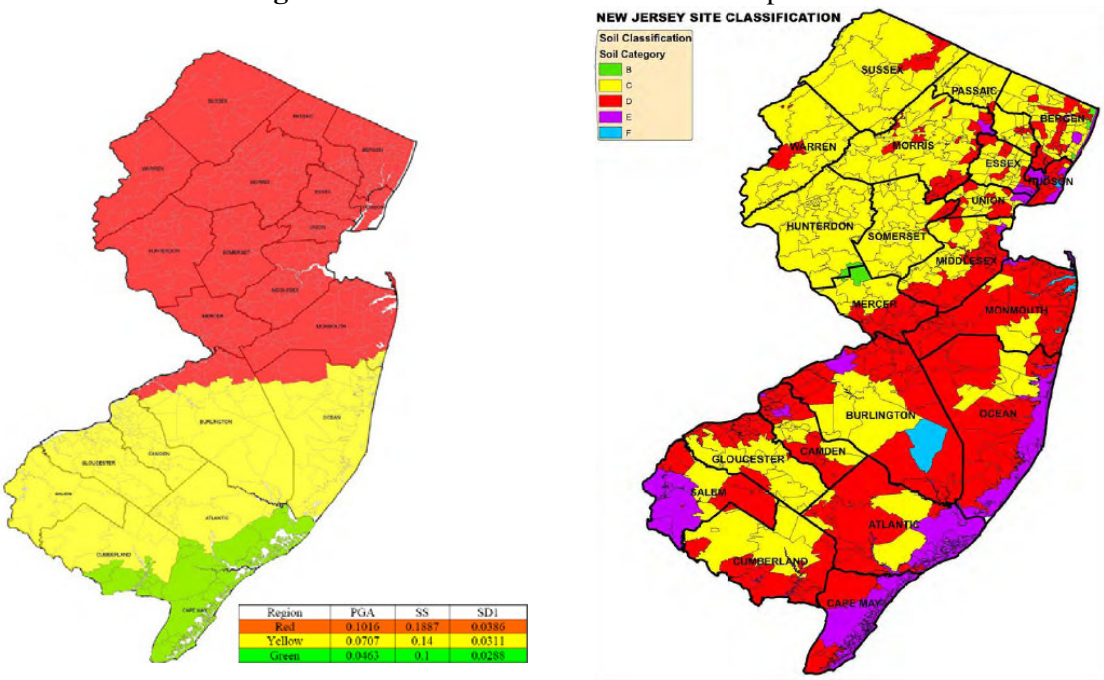

Figure 5 Seismic Map of New Jersey Using AASHTO/USGS 1,000 Year Return Period (left) and Soil Site Classification Map (right)

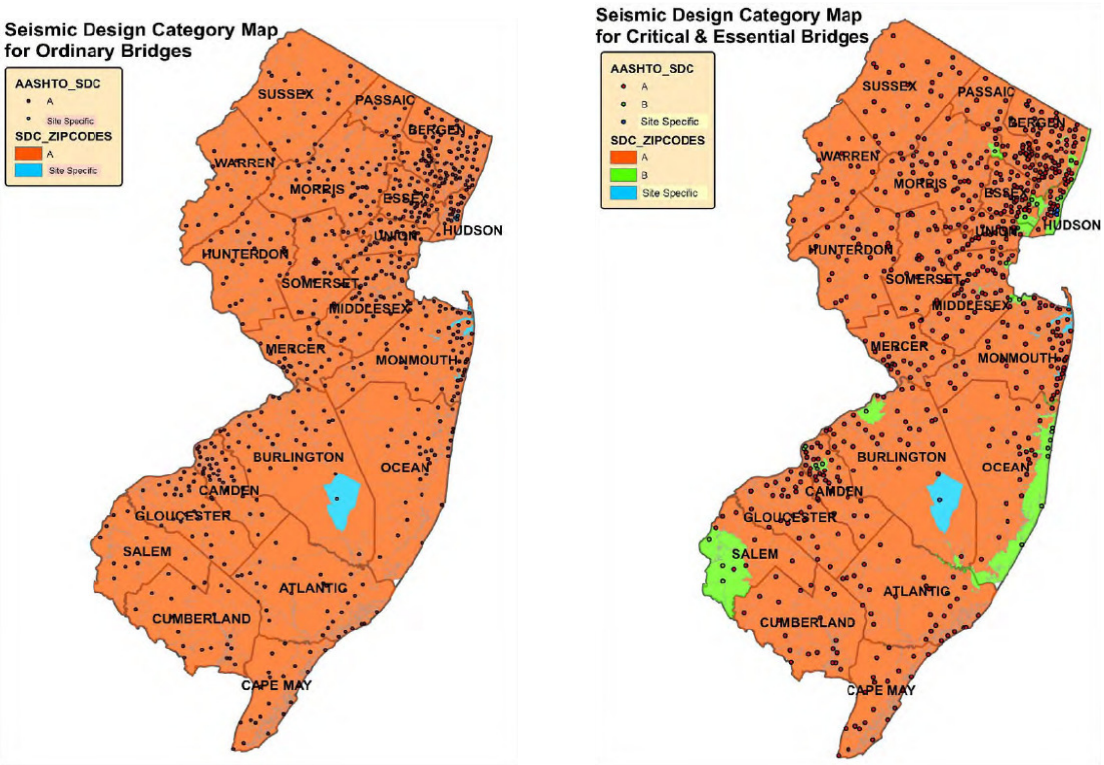

Figure 6 Seismic Design Category Maps for Standard/Ordinary Bridges and Critical/Essential Bridges in New Jersey

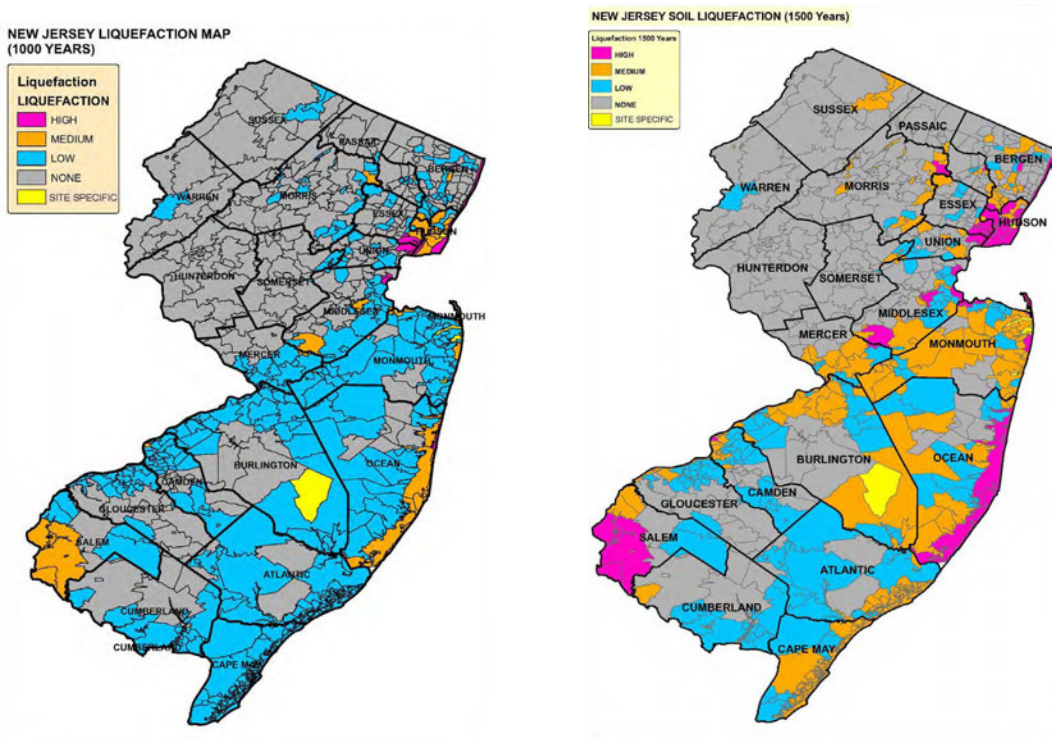

Figure 7 Liquefaction Hazard Map for Standard and Critical Bridges in New Jersey

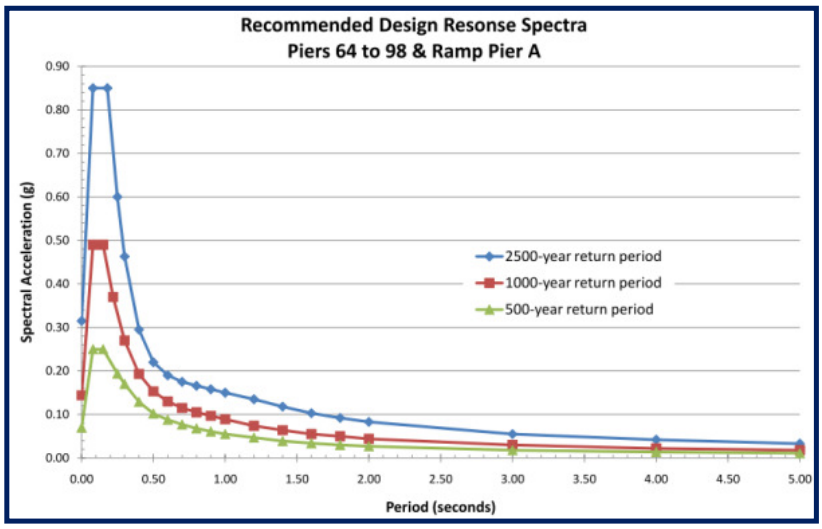

Figure 8 Recommended Design Response Spectrum for Piers 64 to 98

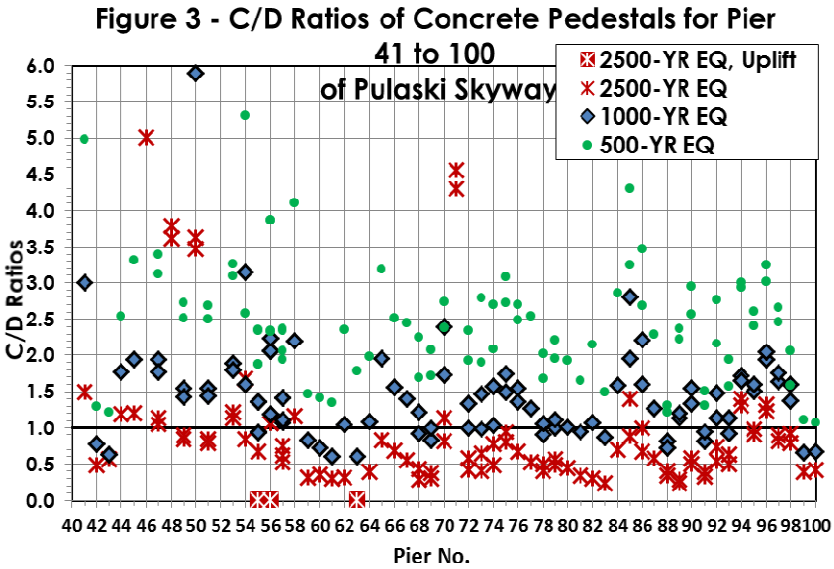

Figure 9 Seismic Capacity to Demand Ratio (C/D) Evaluation for Concrete Pedestals

DEVELOPMENT OF FAST ACCELERATED SET CONCRETE APPLICATION FOR REPAIRING THE DETERIORATED REINFORCED CONCRETE DECKS

Yuichi Ishikawa[1], Doyeon Kwak[2] and Mamoru Moriyama[3]

Abstract

Many reinforced concrete bridge decks in the Hokuriku Expressway, hereinafter called as RC decks, have been damaged by deicing salt attack. The delaminated RC decks have been repaired by patching and applying the ultra rapid concrete. However, ultra rapid concrete application requires a special type of vehicle for mixing concrete, which results in the considerable increase of the total repairing cost of the RC decks. This paper describes the development of a rapid hardening concrete named Fast Accelerated Set Concrete, hereinafter called as FACET. FACET is mixed directly with calcium aluminates and sulfate powder in a mixer truck, and it can develop the compressive strength greater than 24N/mm^2 in 6 hours. In this research work, a total deck area of about 1,000m^2 is investigated to confirm the workability and the supply capacity of the FACET system. A cost-effective and easy supply system of FACET for repairing delaminated RC decks is furthermore proposed.

Introduction

These days, many RC decks in the Hokuriku Expressway have been damaged by deicing salt attack. The delaminated RC decks are normally repaired through the patch of concrete material. In order to reduce the influence on traffics and logistics on the expressway, a quick repairing method is always requested. As a result, the ultra rapid concrete, whose a unique characteristic is quick setting to reach the concrete compressive strength of 24N/mm^2 in 3 hours has been applied. The ultra rapid concrete requires to be mixed on the site by using a stationary type or portable type, as shown in **Fig. 1**. The mixing cost on the site of this material is normally ten times higher than that in the plant. A more cost-effective concrete material is therefore required. This paper presents the development of the supply system for FACET. This FACET is mixed directly with powder of the calcium aluminates and sulfate in a mixer truck and enables to develop compressive strength greater than 24N/mm^2 in 6 hours, whereas maintain cost performance.

[1] Central Nippon Highway Engineering Nagoya Co. Ltd., Kanazawa, Ishikawa, Japan, y.ishikawa.a@c-nexco-hen.jp
[2] Taiheiyo Material Corporation, Sakura, Chiba, Japan,doyeon-kwak@taiheiyo-m.co.jp
[3]Central Nippon Highway Engineering Nagoya Co. Ltd., Kanazawa, Ishikawa, Japan, m.moriyama.aa@c-nexco.co.jp

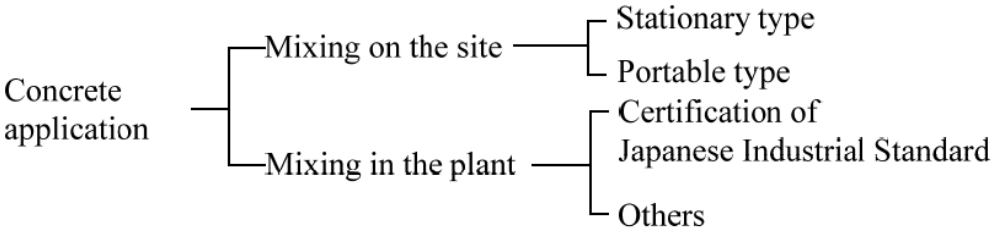

Fig.1 Concrete application types in Japan

The Problem in Repairing the Delaminated RC Decks

The Hokuriku Expressway began operating in 1970s. In winter season, deicing salts have been used on this expressway. The use of deicing salts have dramatically increased, as shown in **Fig. 2**, as a result of studded tires being banned in 1990 for heavy snowfall areas in Japan [1]. When the deicing salts (i.e. chloride ion) and water reach down the reinforcing bars, hereinafter rebars, an electrolytic action is started and causes the corrosion of rebars. As the corrosive particles build up, they expand against the concrete cover, eventually exceeding the tensile strength of the concrete. As presented in **Fig. 3**, this causes the horizontal cracks along the upper area of rebars, which results from the exceedance, can cause a delaminated area of concrete [2].

Delaminated RC decks are normally inspected by using the hammer tapping on the asphalt pavement, as given in **Fig. 4**. This inspection method is easy to be used and can detect fast the delaminated area. However, this method has low accuracy in estimating the area of delaminated RC decks, as addressed in **Table 1**. On the other hand, for the use of the conventional ultra rapid concrete application the good estimation of the repairing material volume is always require because if there is a mistake in the estimation of repairing area, mixing problem will occur, as depicted in **Fig.5**. Therefore, a development of a flexible supply system for the FACET is furthermore proposed.

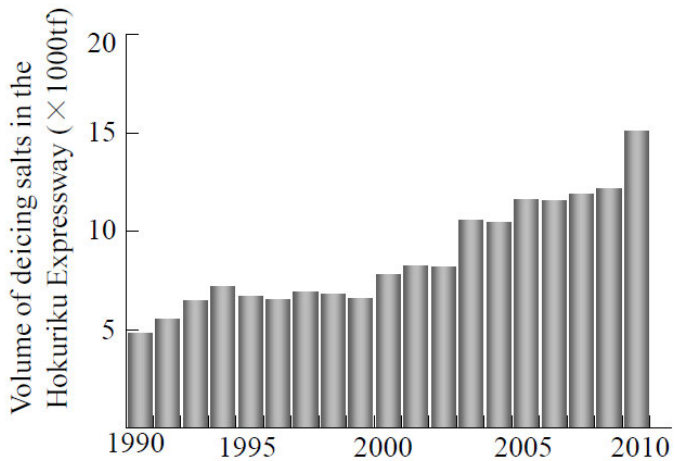

Fig.2 Volume of deicing salts in the Hokuriku Expressway

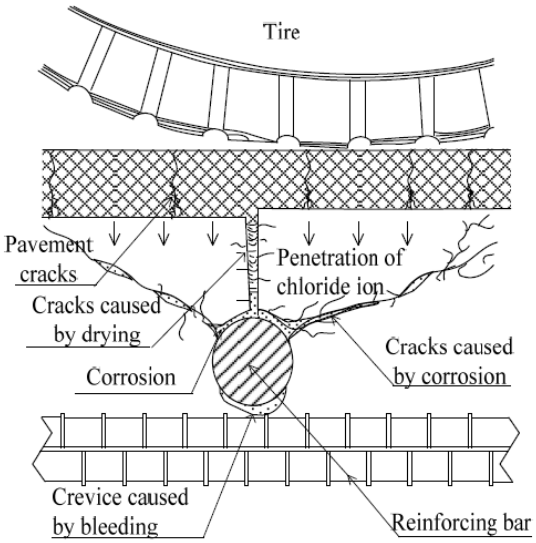

Fig.3 The delaminated RC decks caused by deicing

Table 1. Accuracy rate of hammer tapping

Method	Visual survey used on the concrete cores
Hammer tapping	88%

Fig.4 Typical investigation of RC decks

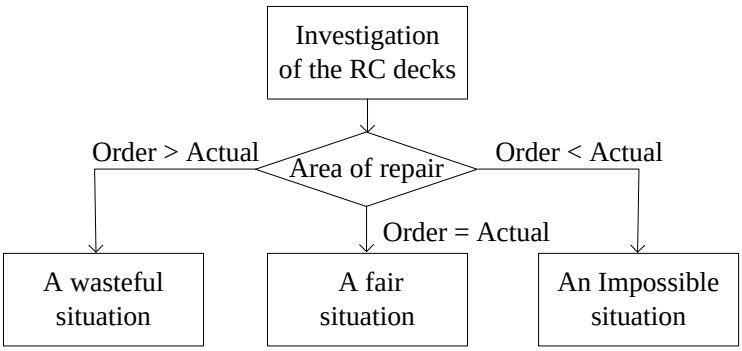

Fig.5 The problem of mixing concrete on the site

Characteristics of Facet

1. Outline

Mix of FACET applies a new manufacture concept. The ready mixed concrete, which doesn't harden yet, is supplied from a plant with a certification from Japanese Industrial Standard. FACET is made by mixing the ready mixed concrete with delaying agent solution, whose main chemical compound is called oxycarbonic acid, and then the powder of calcium aluminates and sulfate is added in a mixer truck. The typical mix proportion of the FACET is shown in **Table 2.** On the other hand, **Table 3** shows the comparison of FACET with the conventional ultra rapid concrete application. It shown from this table, the cost of using FACET is approximately half times cheaper than that of ultra rapid concrete. The mixing method of FACET also enables it to be a flexible supply system, which is expected if the repairing area is out of the estimation.

2. Material characteristics of FACET in fresh concrete condition

Fig. 6 shows the condition of the fresh FACET slump measured in accordance with the JIS A 1101. Because the FACET contains large amount of powder, the shape of slump measured is in viscosity condition. In addition, FACET has less bleed water on the concrete surface.

Fig.7 shows the measuring resistance of the penetration proctor in accordance with ASTM C 403. This result shows that the volume of delaying agent solution and temperature are influencing the setting time. Therefore, it is recommended that the material temperature should be measure and then an adjustment of the volume of delaying agent solution should be done to suit the concrete workable time.

Table 2. Typical mix proportion of the FACET (Unit: kg)

Water	Cement	Sand	Aggregate	Chemical admixture	Delaying agent		Admixing powder
					Chemical compound	Water	
168	350	744	1018	3.5	3.5	10	150

Table 3. Comparison of FACET with conventionally ultra rapid concrete application

	FACET Concrete	Ultra Rapid Concrete
Compressive strength	24 N/mm^2 in 6 to 12 hours	24 N/mm^2 in 3 hours
Starting of the mixed concrete setting time	More than 60 minutes	20 to 40 minutes
The place of mixing the concrete	In the concrete plant then add the powder on the site	On the site
Supplying ability	15 to 30 m^3/hour	15 to 30 m^3/hour
Price (×thousand yen)	120 to 180	250 320

Fig.6 The condition of FACET in accordance with slump test (JIS A 1101)

3. Material characteristics of FACET in hardening concrete condition

The compressive strength of FACET enables to be developed greater than 24 N/mm^2 in 6 hours and finally reached more than 70 N/mm^2 in 28 days, as shown in **Fig.8**. **Fig.9** shows the salt penetration depth of various concrete measured by Electron Probe Micro Analyzer ,hereinafter EPMA. The penetration of chloride ion in FACET is less than that in normal concrete. As a result, the high durability of FACET is confirmed.

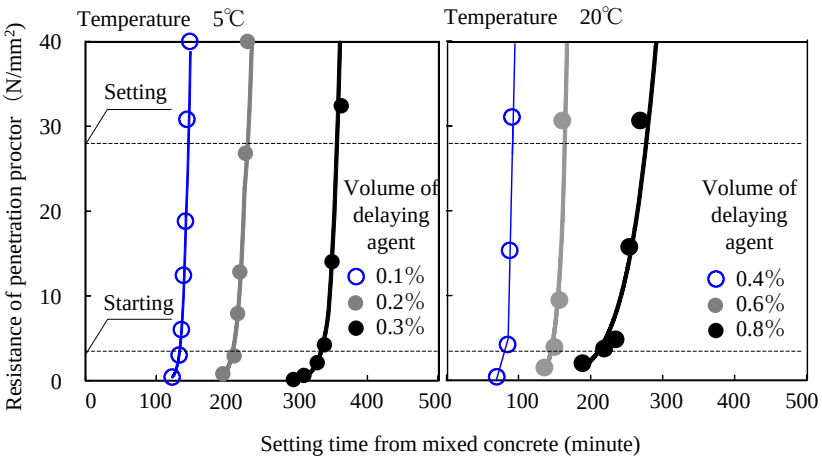

Fig.7 The measuring resistance of the penetration proctor of FACET

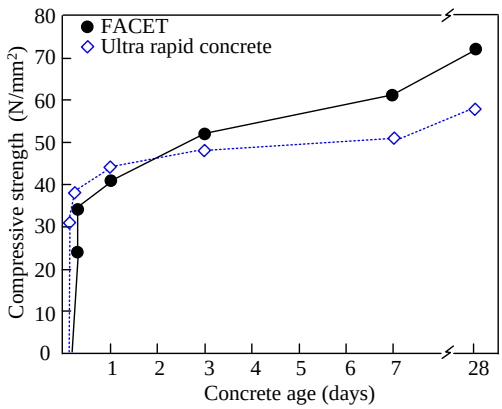

Fig.8 The compressive strength

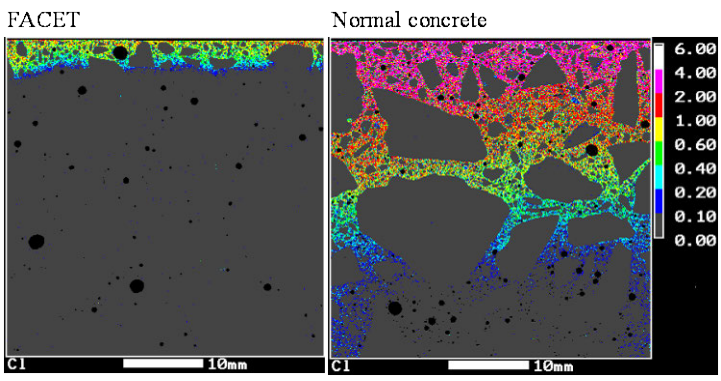

Fig.9 The salt penetration depth of various concrete measured by EPMA

Feasibility Test of Facet on the Construction Site

1. Feasibility test situation on the construction site

In order to repair the RC decks damaged by deicing salts in the Hokuriku Expressway, an experimental repair was performed on the total RC deck area of approximately 1,000 m^2. The production stages of FACET is shown in **Fig. 10**. First, as the concrete was brought to the construction site from the concrete plant by a mixer truck, the delaying agent solution was mixed with the concrete in high speed mixing for 15 seconds. Second, the fast accelerated admixture is added to the concrete mix in high speed mixing for 3 minutes. Before pouring the FACET, the degraded RC decks were removed with water jet, as shown in **Fig. 11**. Bleeding was not observed on the surface of the FACET. Therefore, it proves that a concrete with good quality was placed.

Furthermore, **Fig. 12** shows different curing method on the surface of the concrete which is resulting in different temperature of concrete. As shown in **Fig. 13**, the compressive strength of the concrete is gradually increasing. In addition, if the concrete surface is covered with a vinyl sheet the temperature of the concrete will be higher, especially at the early hours, compared with open-air curing, and the compressive strength will gradually increase over time by thermal insulation. Even though there are differences in the compressive strength before 6 hours on each curing method, but the compressive strength after 24 hours is almost the same.

2. The occurrence of initial cracks

The FACET can be effectively applied for repairing degraded RC decks. The experimental test of the repaired RC decks using FACET has been conducted for two years since 2012. However, only initial cracks with the average width of 0.2mm has been observe on about the area of 70m^2. Additionally, the initial cracks didn't form a directional cracks, as seen in **Fig. 14**. The crack densities are 3.3m/m^2 in the longitudinal direction, and 4.4m/m^2 in the lateral direction. It is noted that the grid density method counts the number of intersection and cracking grid lines drawn at 125mm intervals.

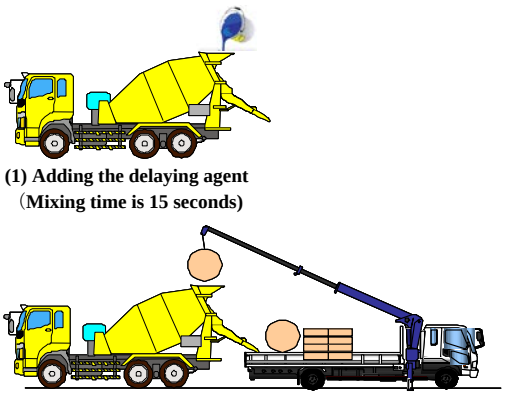

(1) Adding the delaying agent
（Mixing time is 15 seconds)

(2)Adding the powder(Mixing time is 180 seconds)

Fig.10 The addition of delaying agent solution and fast accelerated admixture

Fig.11 Removing the surface of RC decks with water jet

It is intended to quantify the crack density by dividing the total length of the grid. It therefore would be said that if FACET is applied the direction of crack can be detected easily.

Fig. 15 shows a schematic evaporation of water from the concrete surface and the effect of the presence or absence of curing sheet. The surface area of RC deck in contact with the outside air is large. Thus, the initial cracking is likely to occur due to moisture evaporation from the condensation, which happens before. Due to this reason, the concrete surface is covered with a curing sheet until the condensation of FACET ends. This method prevents the temperature change and moisture evaporation of rapid concrete, and therefore, becomes effective.

3. Experiments on the prevention of initial cracks in the FACET concrete

In order to prevent the occurrence of initial cracks on the surface of the FACET, the experiment of fresh concrete curing method and different troweling time have been performed. **Fig. 16** shows the sketch of the surface crack of the FACET concrete on a typical experimental condition. The specimens used in the experiment are 100mm thick with the size of 1320x840mm, and four specimens with the size of 560x350mm. In the case of applying the coating curing agent to the surface of the fresh concrete, the initial crack does not occur on the surface of the concrete. On the other hand, without applying the coating curing agent to the concrete surface, a countless fine cracks occurred on the surface of concrete. It turns out that it is important to prevent the moisture evaporation on the surface of FACET with a coating curing agent. Moreover, as a comparison without applying a coating curing agent, occurrence of an initial crack can be controlled by adjusting the right time to do troweling on the surface of concrete. There is a tendency that it is possible to remove the initial cracks, if the finishing of concrete surface is carried out at 60 to 90 minutes from mixing the FACET

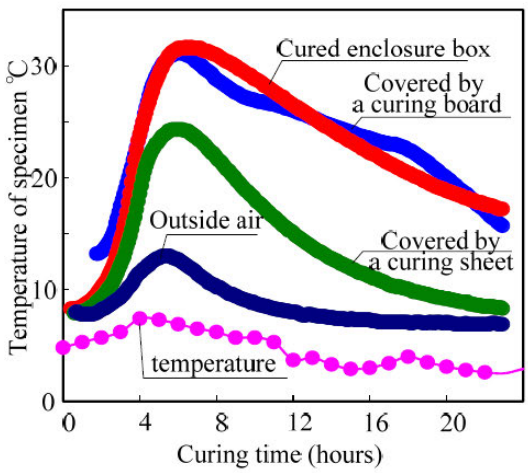

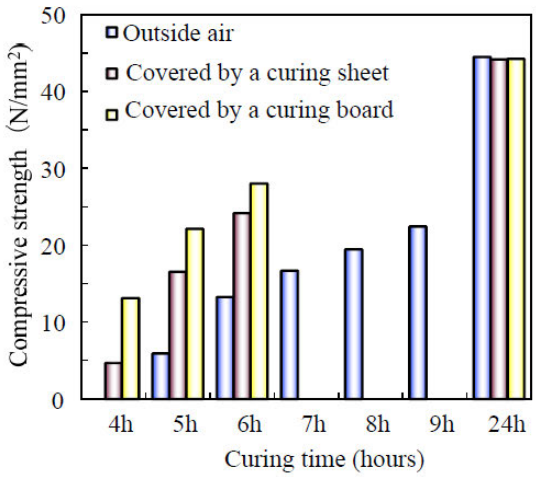

Fig. 12 The difference in the temperature change by different curing method

Fig.13 Changes in compressive strength due to temperature change

Therefore, when FACET is used for repairing RC decks, it is better to follow the following procedure. First the coating curing agent is applied and the surface of the concrete is tapped using the trowel. Then the curing method is conducted by covering a vinyl sheet on the concrete surface. This curing method will not make the hydration heat release rapidly by vaporization heat due to water evaporation of the concrete.

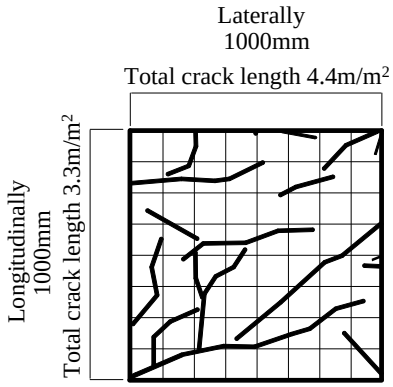

Fig.14 The initial cracks of FACET

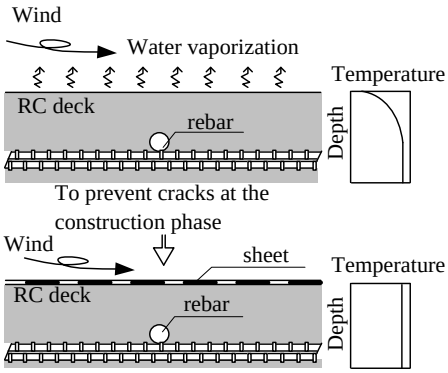

Fig.15 The reason of the concrete cracks

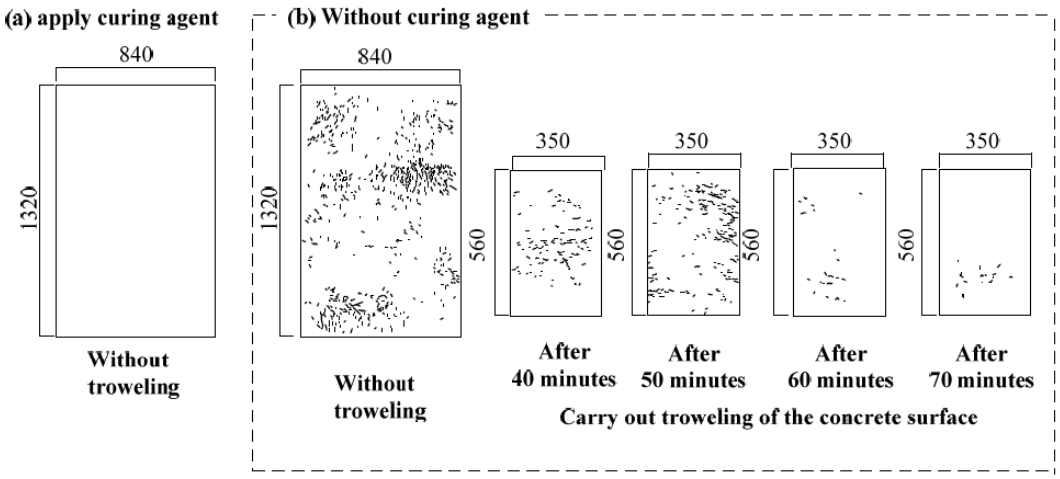

Fig. 16 The sketch of the surface crack of the FACET

Conclusions

This feasibility study confirmed the cost-effectiveness of the FACET. By adding the fast accelerated admixture and delaying agent solution in ready-mixed concrete, the practical application of the new concrete method is furthermore examined. The examination result confirmed that the proposed method can reduce up to half of the cost, in comparison with the use of the conventional ultra rapid concrete. As a result, the material cost of the repair concrete can be reduced significantly. The basic system of the material supply also can be developed from the ready-mixed concrete plant. This cost-effective supply system can cover the inaccuracy in the estimation of the delaminated RC decks, which is normally conducted by hammering.

Because FACET may have a little bleeding and tend to be influenced by the moisture evaporation of the concrete surface, it is suggested that the coating curing agent is applied to the concrete surface. Moreover, it is also proposed that the finishing of concrete surface is carried out at 60 to 90 minutes from mixing the FACET. This will prevent the occurrence of the initial cracks. In addition, it is important to cover the concrete surface with a vinyl sheet in order to prevent the hydration heat from releasing rapidly.

References

[1] Japan Concrete Institute Technical Report:'' Technical reports of damaged reinforced concrete structures due to de-icing salts", ISBN4-931451-17-2 C3050, 1999, (in Japanese)

[2] Y. Ishikawa, M. Aoyama, Y. Adachi and M. Nagai:"Damage assessment of reinforced concrete decks due to chloride-induced corrosion of reinforcing bars and fatigue, IABMAS, 2012.7

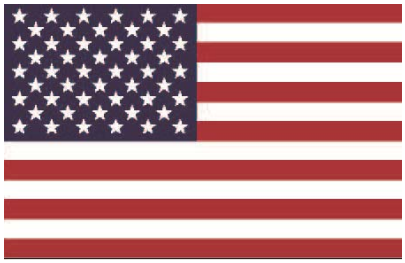

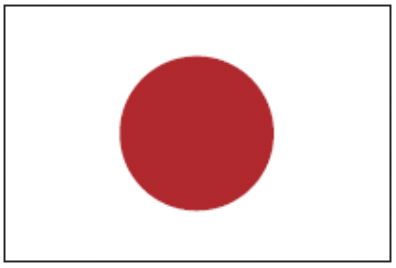

29th US-Japan

Bridge Engineering Workshop

Session 3

Inspection

BRIDGE INSPECTION STANDARDS IN JAPAN AND US

Masahiro Shirato[1] and Takashi Tamakoshi[2]

Abstract

Element-level bridge inspection has been developed in Japan and the US respectively. Conventional maintenance / rehabilitation urgency rating needs a diagnosis given by qualified engineers and is somehow subjective. In addition to that, the element data recording of damage state rated in an objective manner is a new trend. The present paper compares the histories and concepts of bridge inspection program in both countries and highlights some of the element-level inspection results in Japan. The results show that the accumulation and big data mining of objective element-level data has a huge potential to improve bridge management and design / inspection standards.

Introduction

Bridge inspection is primarily conducted to assess the structural safety and related maintenance urgency for individual bridges. Accordingly, bridge inspection demands a comprehensive engineering (or subjective) judgment for structural safety and maintenance urgency at the structural member level or component level or bridge level. However, recently collecting objective / scientific damage rating at element level has been widely accepted both in Japan and the US and executed in addition to the conventional inspection standards.

For example, the amendment of Road Law was approved in Japan in May 2013, clarifying that it is an obligation for all road administrators to inspect structures with consideration of preventive maintenance. It also empowers Minister for Land, Infrastructure, Land, Transport and Tourism to investigate road administrators' statuses for highway maintenance for the sake of technology development. In the US, MAP-21 (Moving Ahead for Progress in the 21st Century Act) was enacted in 2012. While the conventional national bridge inspection standards with a 0-9 scale rating continue to be executed for structural components of all bridges on public roads, now States are required to collect element level condition state data set of bridges on the National Highway System. With these backgrounds, both Japan and the US have established element-level bridge inspection standards these days, respectively. However, the definition of 'element' in bridge inspection is different between Japan and the US. It is not a problem of which is better or which is worse. It should be important to make the definition of element and data recording structure meet the aims of element level inspection, which may vary with bridge owner by bridge owner.

Accordingly, the present paper considers what should be considered to set out

[1] Senior Researcher (Bridge & Structures), National Institute for Land and Infrastructure Management, Ministry of Land, Infrastructure, Transport and Tourism
[2] Head, Bridge and Structures Division, ditto

the definition of ‘element’ or unit of condition rating or data collection structure in inspection. The present paper first reviews expected outputs from big-data mining in bridge inspection data in the era of scientific element level bridge inspection. Ministry of Land, Infrastructure, Transport and Tourism bridge inspection protocols and US NBIS (National Bridge Inspection Standards) are compared, pointing out the difference in the definition and unit of components and elements in bridge inspection (MLIT, 2004). Secondly, the details in MLIT’s ‘finite’ element level damage rating protocol are reviewed, in which the MLIT protocol is comprised of damage appearance ratings for ‘finite’ elements and maintenance urgency ratings for structural members., where the definition of ‘finite element’ will be explained later. Finally, the present paper shows some highlight scientific facts that are found out in the data of MLIT `finite’ element level bridge inspection and discusses the potentials of MLIT’s finite element level bridge inspection on promoting data-driven bridge maintenance and R&D in bridge engineering.

Brief histories of Element-level Bridge Inspection in Japan and the US

Bridge inspection protocols depend on the aims of inspection. Table 1 shows expected scientific / engineering achievements and administrative achievements in bridge inspection. The primary concern of bridge inspection is to secure the structural safety for passengers moving under and on bridges. Conventional bridge inspection programs both in MLIT and the US are stipulated mainly for evaluating the urgency for maintenance or other actions from the viewpoint of safety. In Japan, a model bridge inspection manual developed in 1988 by Public Works Research Institute (PWRI) of then Ministry of Construction and used to be recommended (legally non-binding). A single rating indicator was assessed for each structural member in each span, accounting for the extent of damage and the urgency of maintenance simultaneously. In the US, the Silver Bridge spanning the Ohio River collapsed in 1967 and NBIS was enforced in 1971. Inspection is mandatory for all bridges on public roads. Inspection frequency is two years in principle. States have collected overall condition data for components at the bridge level, where components are defined as superstructure, substructure, deck, and culverts. States also shall conduct monitoring the bridge when a critical finding is found during an inspection. NBIS was updated several times, learning bridge collapses and major failure events.

In 1990s-2000s, the importance of preventive maintenance was realized in both Japan and the US, respectively, for better bridge management. Table 2 shows the number of bridges and vehicle shares by owner in Japan. MLIT has and operates as many as 20,000 bridges on designated sections of national highways. The Japanese road network was intensively developed during the rapid economic growth of the 1970s, and the number of road bridges has now reached approximately 700,000 (bridge length ≥ 2 m). As shown in Figure 1, it is predicted that the number of bridges older than 50 years will account for almost half of bridges in 15 years. Fatigue in steel piers and deck plates, chloride ingress in prestressed concrete beams, alkali silica reaction (ASR) in concrete structures, and fatigue failure of concrete in reinforced concrete decks were widely reported. MLIT raised a preventive maintenance initiative and ordered National Highway Offices to implement the present once-in-5-year bridge

inspection protocol in 2004 (MLIT, 2004). Maintenance urgency rating for structural members is included, but damage appearance rating for more detailed units is also recorded. Damage appearance ratings are introduced because of expecting a scientific achievement of No. 2 in Table 1, data-driven systematic preventive maintenance. However, it is also designed to achieve data-driven updates and improvements in design specifications and inspection protocols as well as the understanding of needs in bridge preservation technology, corresponding to the expected scientific achievements Nos. 3 and 4 in Table 1.

Because preventive maintenance is required to reduce future maintenance costs, MLIT started a subsidy program in 2007 for local governments to establish long-term bridge maintenance programs. As a result, prefectures now have bridge inspection programs that follow the MLIT protocol and sometimes with some changes. Namely, bridges on arterial routes that carry a large part of traffic are now inspected periodically. However, some municipalities still do not inspect their bridges. Some conduct but inspection protocol and quality are not standardized.

In the US, several states started improving their bridge inspection program to obtain condition data for structural elements for bridge management system use. CoRe element data collection guide was developed in AASHTO for bridge owners to aim at better bridge preservation programs and performance-based budgeting. Most states started to follow it (AASHTO 2002). MAP-21 was enacted in 2012 and now all states will need to collect element level inspection data for bridges on NHS, following the reporting system of AASHTO Manual for Bridge Element Inspection (AASHTO, 2013). FHWA is also directed under MAP-21 to study cost-effectiveness, benefits and feasibility of collecting element-level data for non-NHS.

Summary of Bridge Inspection Protocol in Japan

Maintenance Urgency Rating

In both Japan and the US, bridge inspection protocols are comprised of the part for assessing structural safety and the part for collecting quantitative and objective damage data for elements. In terms of the structural safety part, there is no big difference in philosophy between the MLIT protocol and the US NBIS, except for the unit of assessment.

In the MLIT protocols, bridges with a span longer than 2 m are inspected once in every five years. Hands-on visual inspection is required. Tools and devices may be used with a limited amount to determine such as fatigue crack in steel members. For each structural member in each span, the condition is translated into either of the following maintenance urgency ratings:

A No repairs needed.
B No immediate repairs needed.
C Repair needed
E1 Emergency action is necessary from the viewpoint of structural safety

and stability

E2 Emergency action is necessary because of other factors.

M Repairs needed in the course of the regular maintenance work

S Further detailed investigations needed

Maintenance urgency ratings are diagnosis given by experienced engineers in a subjective manner, recommending to bridge owners the needs for action by the time of the next inspection. Engineers are required to interpret the maintenance urgency for each member, taking into account the damage appearance ratings in finite elements in the structural member, specific characteristics of the damage such as the direction of crack, the location of damage in the structural member, the function of the structural member, likely causes / sources of damage, interactions with other damage at other structural members and components in the bridge, earlier remedial work history, the deck / slab coating system, the drainage system, environmental factors such as traffic volume, deicing salt dumping volumes, the distance from the sea etc and so on. No numeric criteria like crack width and length are specified for maintenance urgency ratings.

In the US, each bridge is divided into four major parts for assessment: deck, superstructure, substructure and culvert. Inspectors give either of 0-9 ratings in a subjective manner of interpretation for damage. The rating scale for each part ranges from 0-9 depending on the severity of damage and urgency of action. Namely, four indices describe the extent of damage as a whole bridge.

Figure 2 shows a schematic diagram of deterioration curves. Deterioration rates have a huge variety and the variety increases with increase in the extent of damage. Figure 3 shows an example of test result for the fatigue of concrete in RC deck slabs. Wheel loading tests were conducted for two specimens, where a wheel subjected to a given axel load moved back and force on the specimen until the specimen collapsed. The test specimens were cut out of two different existing bridges and their crack widths and densities in concrete are very similar to each other. However, Specimen A in Figure 3 did not collapse at a wheel movement of 200,000 cycles while Specimen B collapsed at a wheel movement of 20,000 cycles, with 1/10 of the durability compared to Specimen A. This should be because some cracks had already penetrated through the entire depth of deck slab before the experiment as indicated by efflorescence marked with the red circle in Figure 3. As also well known, other factors such as water coming from the deck slab surface can accelerate the evolution of fatigue crack in deck slab concrete. Figure 4 shows cracks in steel members. The influence of cracks on the safety of bridges depends on crack locations and directions. Namely the maintenance urgency rating for cracks cannot be easily standardized as a function of crack widths and lengths and it should mislead engineers to set out any numeric criteria for maintenance urgency ratings such as a function of crack widths and other numeric parameters. Engineer’s diagnosis on site should go first.

(Finite) Element-Level Damage Appearance Rating

Preventive maintenance has been promoted in both Japan and the US in recent

years to reduce the future rehabilitation cost. Data-driven management has been expected to help bridge administrators seek a preferable timing and preventive remedial measure to provide for individual bridges. Quantitative distributions of different extents of damage within components are required to estimate future maintenance costs more precisely, because preventive maintenance is sometimes conducted span-by-span or portion-by-portion. In addition to bridge management use, the importance in data objectivity has been widely recognized to examine the long-term bridge performance and improve bridge design. However, the maintenance urgency rating does not necessarily equal the extent of damage appearance. It involves a subjective prediction by engineers regarding the time evolution in existing damage and related degradation in structural safety, calling for taking into account various factors such as the possible causes of damage.

Accordingly, an element-level data collection with scientific / objective damage condition ratings is required to capture the type and distribution of distress in components and monitor the exact extent of present damage at each distress and at the time of the inspection. Both element-level data collections in Japan and the US record objective, not subjective, standardized condition states for specific defects. However, as illustrated in Figure 5, there is a notable difference in the definition of 'element' and the data recording philosophies / structures between Japan and the US.

As specified in the AASHTO manual (AASHTO, 2013), elements in the US are breakdowns of components that are directly related to the load capacity such as the group of girders, the group of columns, the group of abutments, the group of fixed bearings and the group of movable bearings in a bridge. In addition, secondary components such as protective coating systems, wearing surfaces, and joints are also set out. The data structure is summarized as follows:

- Category of element
- Specific defects
- Damage ratings: good, fair, poor, and severe for each category of defect
- Quantities of each category of defect in feet, area, or each for enumerated elements for each category of defect and each damage extent.

Elements defined in the MLIT protocols are subdivided portions of individual structural members at individual spans. For example, as shown in Figure 5, every single girder for each span is subdivided into several parts at the position of floor beams in a span. Figure 6 illustrates examples of element categories and finite element meshing for damage appearance ratings in the MLIT protocol. In Figure 6, a line from dot to dot or an area from panel to panel is a finite element. Hereafter, 'element' in Japan will be referred to as 'finite element' in this paper in comparison of `element' in the US, because the geometry of elements and the inspection data structure are analogous to those of finite element analyses.

Figure 7 illustrates the data recording structure, in which:

- Individual damage ratings for 13 defect categories at maximum for each finite element. For example,

- ✓ A finite element of a steel beam has damage appearance ratings for #1 Corrosion, #2 Cracking, #3 Looseness / Falling, #4 Rupture, and #5 Deterioration of corrosion-proofing function, respectively
- ✓ A finite-element of a concrete beam has damage condition ratings for #6 Cracking, #7 Peeling and exposure of reinforcing bars, #8 Leakage and free lime, #9 Falling out of place, #10 Damaged concrete reinforcement, and #12 Lifting, respectively.

- Damage conditions are from "a" being no damage and "e" being the worst. Even the existence of no damage shall be recorded.
- Furthermore, in relation to the damage category #6, cracking, crack patters are also categorized as also shown in Figure 7.

As also shown in Figure 7, when choosing a span and an element category, you can see the layers of finite element damage rating maps as many as specified defect categories --- big data processing friendly.

Data objectivity is thought of crucial and a reference manual is published by NILIM, MLIT, to keep the data objectivity, showing sample photographs of each damage category of each damage rating. Inspectors are requested to record the existence and extent of damage as precisely as possible in a digital manner, 'a' being no damage and 'e' being the worst. They have to assign the damage appearance rating of 'a' to 'e' sort of automatically with no subjective translation, comparing sample photographs and some numeric criteria like crack width on the reference with what they see and measure on site. It is also worth noting that MLIT, in practice, has awarded the maintenance urgency rating inspection and damage condition rating inspection, separately. Both ratings are cross-checked by bridge administrators as sort of a quality assurance system.

Because data objectivity is secured and the distributions, categories, and ratings of damage at finite elements are digitized and clustered, MLIT's finite-element level inspection is expected to cover all aspects listed in Table 1.

Big Data Mining on the MLIT's Finite Element Level Bridge Inspection Database

To examine the effectiveness of the design for MLIT's finite element-level inspection protocol, some highlight findings processed from a big data of MLIT's finite element level bridge inspection are shown below. Since 2003 the finite-element level bridge inspection has been implemented for as many as 20,000 bridges under the jurisdiction of the national government. Most bridges have been inspected twice following the same finite element level inspection protocol and some bridges have been inspected three times. Damage appearance rating data obtained in FY2006-2010 are mainly used below.

Figures 8 and 9 are examples of showing the potential of the promotion of data-driven preventive maintenance using the finite element level inspection. Figure 8 shows the ratio of the number of spans with any damage at designated finite elements to the number of all finite elements inspected in terms of steel I-beam bridges. Figure 8 deals with corrosion of I-beam. Because of the finite element inspection, a tendency in

the distribution of damage extent in a girder or a span can be understood. Span-ends and outside girders are susceptible to damage compared with span-centers and inner girders. This may be attributed to the water that comes through expansion joints and stay around girder-ends and the supply of chlorides from the sea brought by wind or deicing salt from the road surface to outside girders. Because finite-element data is likely to show the difference in the distribution of distress in a structural member, we can expect to grasp the needs of new and better preventive maintenance techniques. For example, based on such findings, NLIM and MLIT highway offices have proposed a zone painting manual.

Figure 9 shows a stochastic transition in corrosion of steel girders. Using two batches of finite element data that covers 10 years, the change in damage condition rating for corrosion of the same finite elements is counted and the transition probabilities are calculated from a to a, b, c, d, e, respectively, from b to b, c, d, e, respectively, from c to c, d, e, respectively, and so on, resulting in a stochastic time evolution in corrosion of bridge girders with years. In this calculation, finite elements that were applied to some remedial work in the past such as the refurbishment of surface coating system were discarded. Different deterioration tendencies within a span and within a girder are found out, which should get involved in bridge management systems to limit the extent of overestimation or underestimation of deterioration in estimating the future total maintenance costs for bridges.

Figure 10 is an example of showing the potential of data-driven improvement of design specifications using finite element-level bridge inspection. Figure 10(a) describes the numbers of spans with specific crack patterns in post-tension PC T-beams. Crack patterns are categorized into twenty different identities in inspection as illustrated in Figure 10(c), where only major patterns are shown in the illustration. The result shown in the left-hand side of Figure 10(a) is based on all inspection results (3,874 spans in total), while the right-hand side of Figure 10(a) is only based on initial inspection results out of all inspections (136 spans in total), where in MLIT new bridges are inspected within two years after putting in service using the finite element level bridge inspection protocol. The data clearly shows that cracks evolve with years. Cracks along PC cables such as patterns #2 and #20 or along stirrups such as pattern #10 may indicate the corrosion of cables and reinforcement. Structural details of PC tendons and cover depths have been changed for almost the last twenty years and we would like to follow the inspection results to figure out the effectiveness of such changes. Figure 11(b) shows the comparison in crack patterns between post-tension and pre-tension PC beams. Cracks of Patterns #2 and #4 especially appear more in post-tension girders. More stringent construction quality controls can be required for post-tension beams.

Meanwhile, the existence of cracks with pattern #1 indicates that some flaw could exist in design practice. For example, the present design standards in Japan do not incorporate residual stresses accumulated during construction such as thermal stresses during concrete casting into stress calculations, while usually residual stresses due to welding are involved in setting the strength curve of steel beam and columns. Long-term loads such as shrinkage and creep of concrete and the related restrained

stresses due to the existence of reinforcement bars may be necessary to be examined. Cracks can give adverse effects on the long-term durability of concrete structures and violate the presumptions / theories to calculate stresses in cross-sections and strengths of prestressed concrete beams.

Figure 11 is an example of the potential of developing a more logical inspection protocol by conducting a big data analysis on the finite element level bridge inspection data. Figure 11 shows the number of steel I-beam spans and box-beam spans with or without any crack by age and by average daily large vehicles. Crack tends to appear either when a bridge is older than 20-30 years or when carrying more than 10,000 large vehicles a day. The result indicates that further analyses may clarify the needs for the introduction of special inspection programs by age and type of distress.

In conclusion, the results highlighted above show the effectiveness of finite element level bridge inspection to aim at all achievements listed in Table 1.

Concluding Remarks

We are seeing the advent of the use of big data in bridge inspection. Both Japan and the US just have changed laws in terms of bridge inspection and adopted finite element or element level inspection. Both countries are now considered to face a significant challenge to use the big data of bridge inspection wisely. To conduct data mining, data collection protocol should be carefully designed to make the data structure harmonize with big-data mining. The present paper shows that the MLIT's finite element level bridge inspection protocol is likely to do a good job in this regard. This paper especially points out potentials that finite-element level damage rating can be useful to figure out scientific facts that backup data-driven preventive maintenance, data-driven technology development in maintenance, and data-driven improvement / development in design specifications and inspection standards, with examples.

Data collection strategies can change with bridge administrators / owners' needs as summarized in Table 1 and there is no guidance for relevant assessment units (definition of 'element') and data collection structures. Accordingly, the authors hope to continue to exchange and share with each other between Japan and the US the information on:

- Benefits of detailed data collection such as best practices in the data-driven management of individual bridges or the data-driven coordination of network-level bridge preservation programs.
- Examples of things to be improved in design and construction based on scientific fact findings from the data
- Examples of data-driven technology development in bridge inspection and maintenance (e.g. Clarifying development targets and needs for non-destructive testing tools)

References

AASHTO (2002). Guide for Commonly Recognized (CoRe) Structural Elements,

CORE-1-I1. AASHTO, Washington, DC.
AASHTO (2013). Manual for Bridge Element Inspection, 1st Edition. AASHTO, Washington, DC.
Ministry of Land, Infrastructure, Transport and Tourism (2004). Bridge Inspection Manual.

Table 1. Relationship between aims of periodical bridge inspection and Japan and US bridge inspection standards

Expected scientific / engineering achievements	**Expected administrative achievements**	Ratings	Inspection units
1. Preservation of bridges - Leading to maintenance or other actions - Sending to detailed inspection	Securing safety for passengers under and over bridges	Maintenance urgency rating (Subjective)	Components in NBIS or Members in MLIT protocol
2. Data-driven systematic investment in preventive maintenance at network level and bridge level, respectively	Better funding scheme and performance measurement in management	Damage appearance rating (Objective)	Elements in AASHTO manual or Finite-elements in MLIT protocol
3. Data-driven "kaizen" or continuous updates in design specifications, inspection standards, retrofit guidelines etc	Technology development		
4. Data-driven technology development for maintenance			

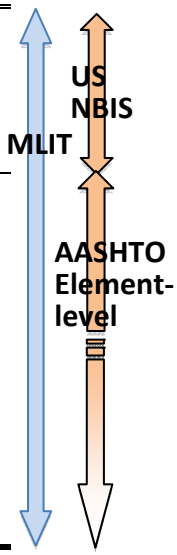

Table 2. Bridge Inventory in Japan (As of April 2013)

	Number of road bridges*	**Average 24-hour traffic numbers**** [**Large vehicle** / **total**]
National Expressways (Owned by MLIT and operated by expressway companies)	7,246 (1.1%)	9,068 / 27,884
National Highways --- Designated Sections **(Owned and operated by MLIT)**	**20,763 (3.1%)**	**3,326 / 16,641**
National Highways --- Other Sections (Owned and operated by Prefectures)	30,200 (4.4%)	1,127 / 8,120
Prefectural Roads	100,152 (14.7%)	568 / 4,941
Municipal Roads	521,173 (76.7%)	
Total	**679,534 (100%)**	---

*As of April 2013 ** Based on the 2010 road traffic census data

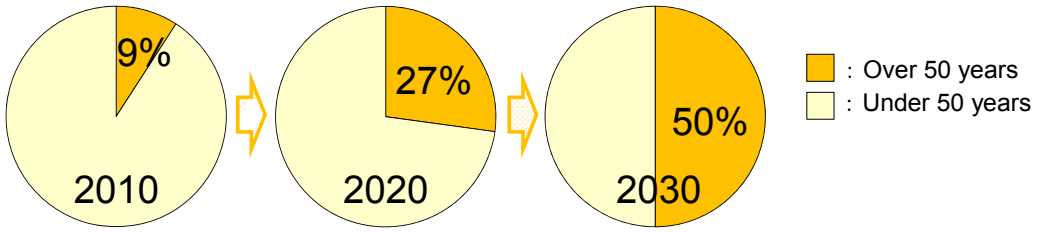

Figure 1. Percentages of bridges older than 50 years at present, in 10 years and in 20 years.

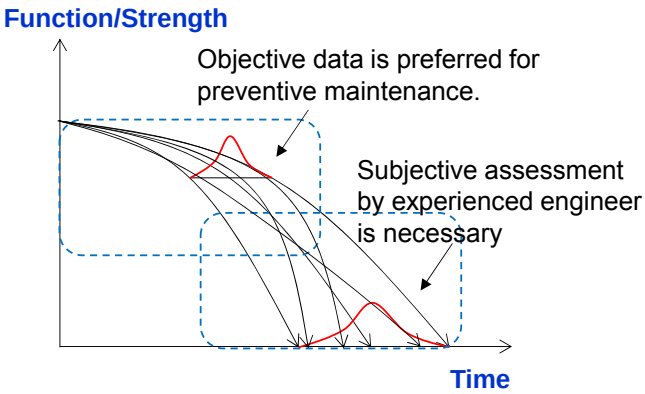

Figure 2. Schematic diagram of deterioration curves, showing the variation in deterioration rate becomes larger with increase in deterioration

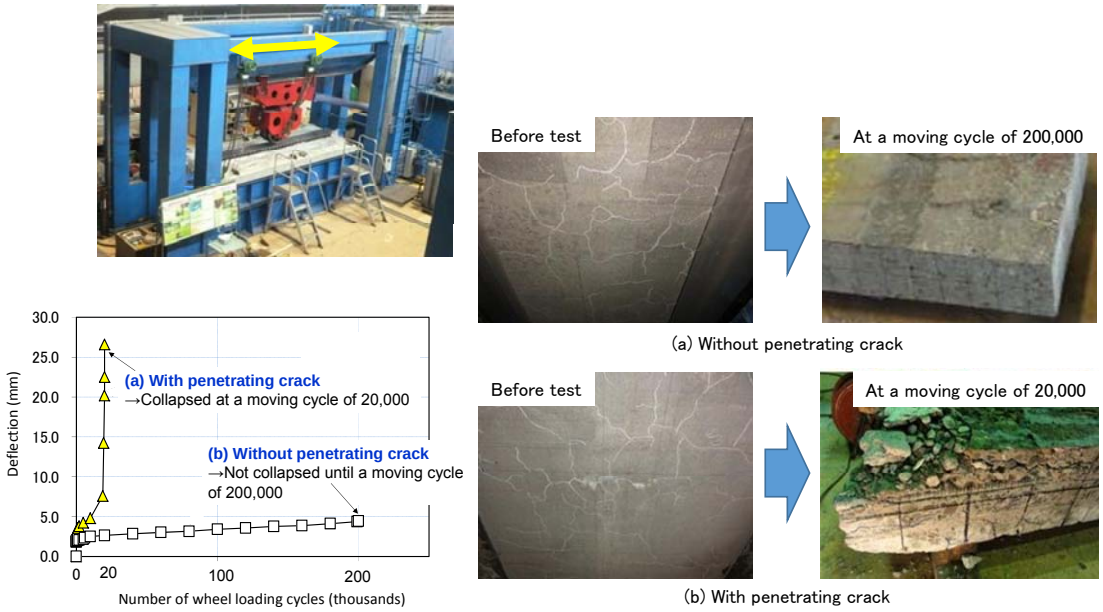

Figure 3. Example of moving wheel loading tests for fatigues in RC deck slabs having similar damage appearance states

(a) Joint of main girder and gusset (b) Sole plate (c) Cross frame

Figure 4. Cracks at different positions in steel superstructures

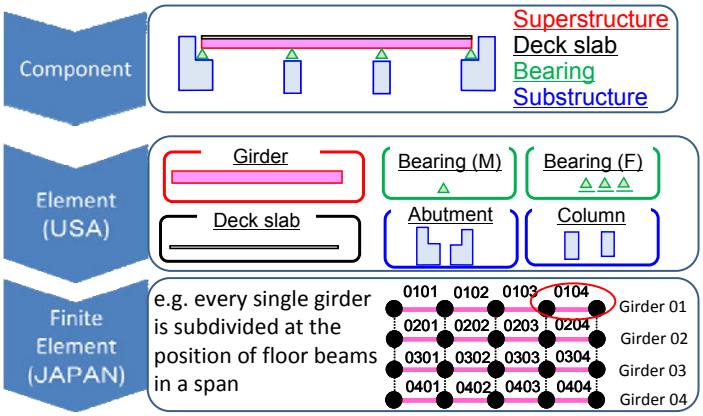

Figure 5. Difference in definition of 'element' in inspection between MLIT (Japan) and the US

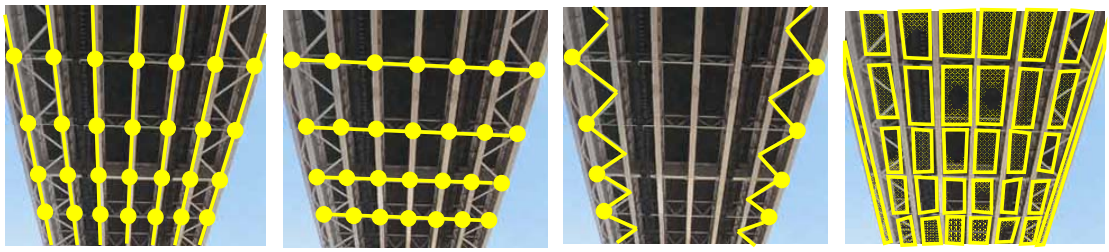

Girder beams Floor beams / Cross frames Lower laterals Deck slabs

Figure 6. Examples of element categories and finite element meshes in the MLIT's finite element level bridge inspection

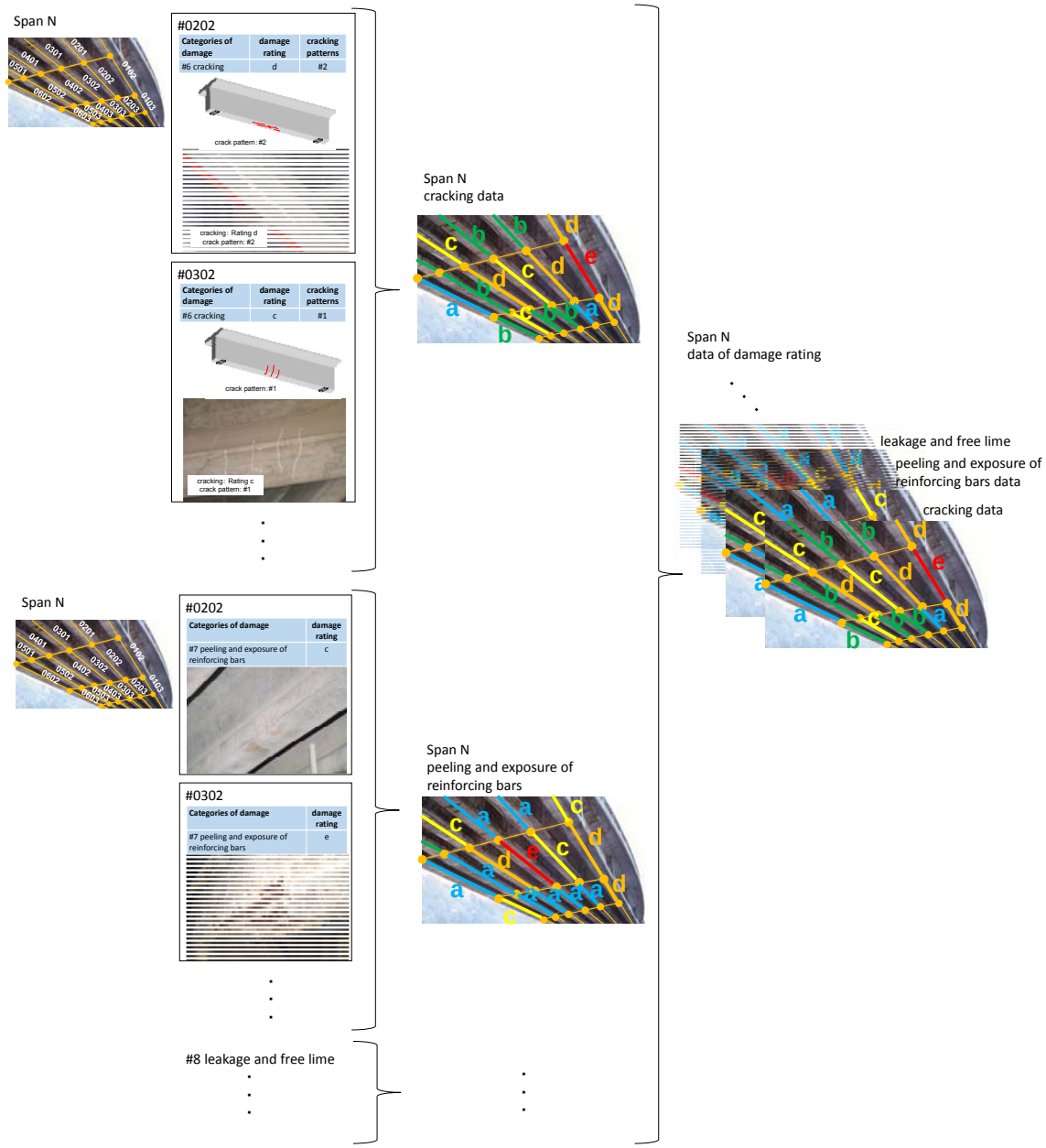

Figure 7. Data structures in finite element level bridge inspection of MLIT

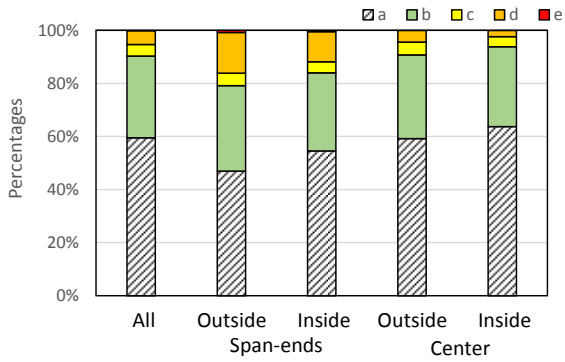

Figure 8. Percentages of finite elements in terms of corrosion in steel beams of steel I-beam bridges (“a” being no damage and “e” being the worst)

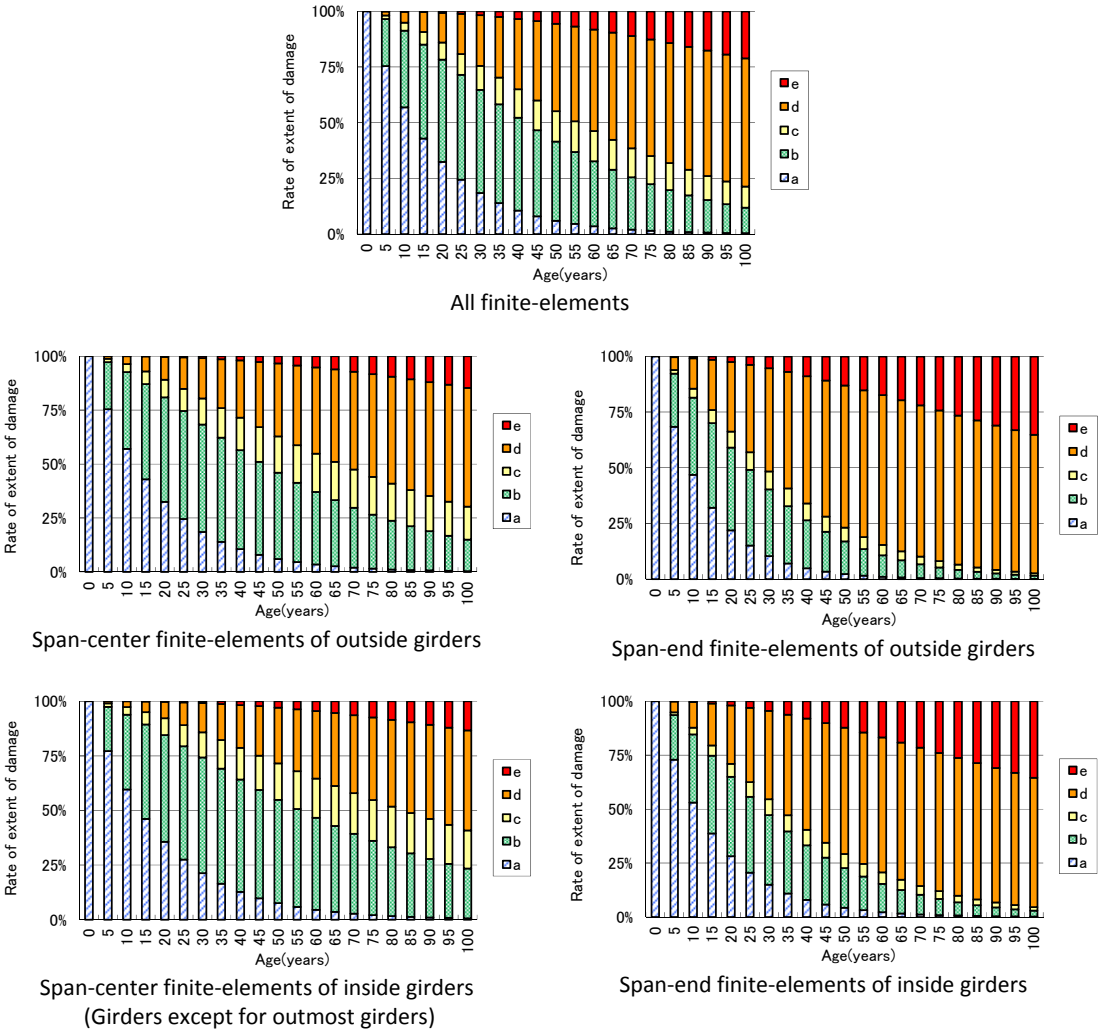

Figure 9. Stochastic time evolution in corrosion with years on steel beams of steel I-beam bridges (Based on the inspection data from FY2009 to FY2013)

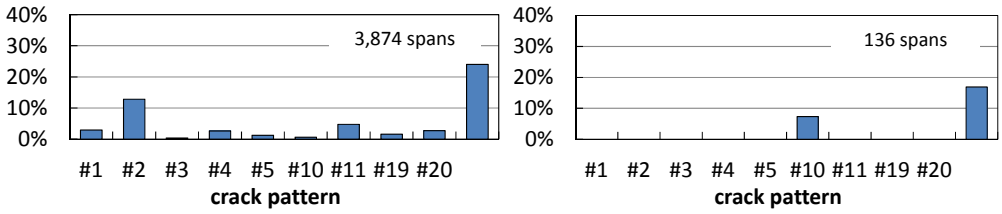

All inspection results

New bridges inspected within 2 years after putting in service

(a) Crack patterns in post-tension T-girders

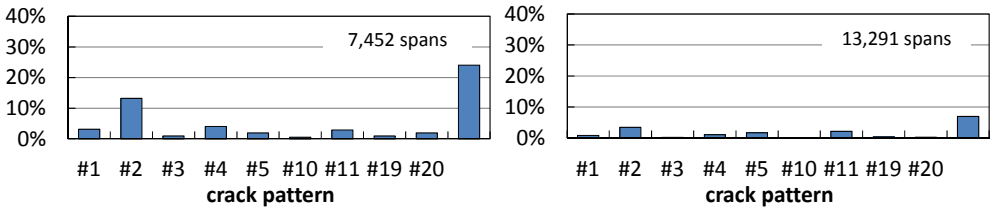

Post-tension PC girders

Pre-tension PC girders

(b) Comparison in crack patterns between post-tension girders and pre-tension girders

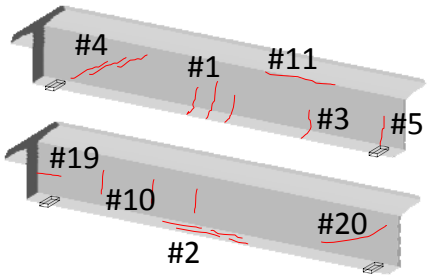

(c) Crack patterns in MLIT's inspection manual

Figure 10. Number of spans with one or more finite elements having individual patterns of crack regarding PC beams.

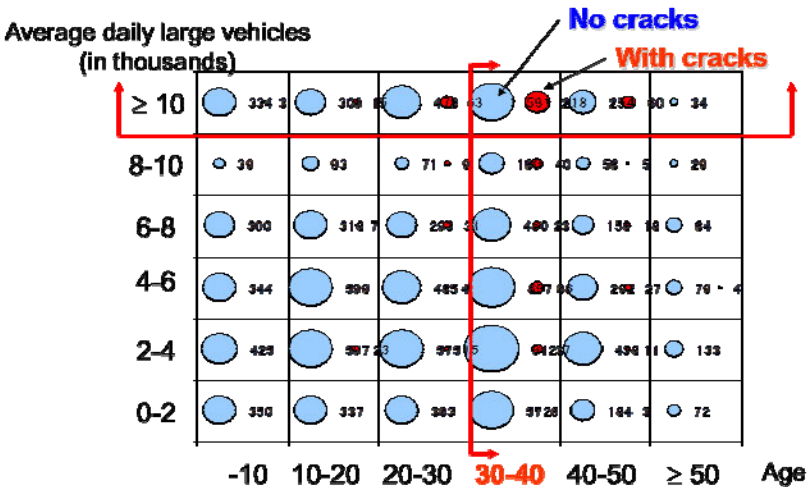

Figure 11. Number of spans with crack detected in steel I-beams and box-beams by age and average daily large vehicles

NON-DESTRUCTIVE MONITORING AND ACTIVE PREVENTION OF CORROSION IN SUSPENSION BRIDGE MAIN CABLES

Deeble Sloane, M.J.[1], Gatti, C.[1], Brugger, A.[2], Betti, R.[3] and Khazem, D.H.[4]

Abstract

In this paper, the results of a multi-year project that led to the development of a corrosion monitoring system to be embedded inside a main cable are presented. A variety of state-of-the-art sensing and non-destructive evaluation technologies have been considered and tested, using a full-scale specimen of a suspension bridge main cable. The selected sensors were then installed on a main cable of the Manhattan Bridge in NYC and temperature, relative humidity and corrosion rate measurements were recorded for almost one year, collecting very interesting information on the internal environment of the cable. Such a monitoring system is currently being used in testing the effectiveness of the practice of cable dehumidification: while this technology has already been installed on real bridges, there is no experimental validation of its effectiveness.

Introduction

In the maintenance and rehabilitation of cable suspension bridges that have been in service for many years, the issue of the assessment of the remaining strength of the main cables is still unresolved.

Currently, all state and local agencies responsible for the maintenance of suspension bridge cables base their maintenance plan mainly on previous experiences and on limited information from limited inspections. Usually, exterior covering of the cable are visually inspected biannually. If such inspections reveal some deterioration problems, main cables undergo “in-depth” inspections if the maintenance budget allows for such undertaking. The cable is then unwrapped at a few locations along the cable length and is wedged into its center. After this, a visual inspection of the wires’ conditions is performed and, in some cases, a few wires are cut and removed for laboratory testing. As a result of the NCHRP Project 10-57, guidelines for inspections have been developed so as to standardize such cable inspections.

In-depth inspections of cable systems in aging suspension bridges in the New York metropolitan area and in the North-East of the United States have shown that 1) there is often water trapped inside the cable, with a pH as low as 4, and 2) there are broken wires (in some cases up to 300 broken wires in between two cable bands) inside the cables and at the anchorages (Betti and Yanev, 1999), indicating brittle fractures and extensive corrosion (see Figure 1). These alarming findings are inexplicable and the reason of the presence of such broken wires must be found in the complex deterioration process within a main cable. In fact, while the effects of corrosion on ordinary structural steel can be mainly characterized by the loss of material and by the ensuing reduction of the cross sectional areas of members, the

failure of high-strength bridge wires manifests itself, in addition to the loss of material, in a number of related phenomena referred to as stress corrosion, corrosion cracking, corrosion fatigue, and hydrogen embrittlement. These phenomena appear to have a much more detrimental effect on the strength of wires than just the reduction of the wire's cross section area and play a fundamental role in the difficult task of determining the "actual" strength of bridge cables.

Figure 1: Broken wires in a suspension bridge main cable

Unfortunately, current visual inspections can provide neither an adequate amount nor sufficiently reliable data that can be used for an accurate estimation of the remaining strength of a deteriorated main cable. A natural progression towards the use of Non-Destructive Testing (NDT) methods and enhanced sensing technologies to assess a cable's remaining strength results from the downfalls of present inspection techniques. Sensing technologies measuring environmental variables directly related to high-strength steel corrosion, such as temperature and relative humidity, may provide engineers with an evolving portrayal of the cable's conditions and help them formulate a more "informed" assessment of the cable's condition and its maintenance needs.

In this paper, the results of a multi-year research project on the development of a corrosion monitoring system for main cables of suspension bridges and its application to assess the effectiveness of the cable dehumidification practice are briefly presented. This monitoring system has been tested on a full scale cable mock-up in the Carleton Laboratory at Columbia University as well as in service conditions on one of the main cables of the Manhattan Bridge in NYC.

Corrosion Monitoring System

To select the most appropriate technologies to be used in such a study, a complete survey of the available corrosion monitoring techniques and sensors was conducted. The goal was to find out about the state-of-the-art of the currently available sensor technologies, especially corrosion monitoring techniques, and to see whether these sensors/technologies could be applied to the monitoring of main cables in suspension bridges. Technologies were classified into two categories: 1) Indirect Sensing Technologies and 2) Direct Sensing Technologies. With the term "Indirect Sensing technologies", we indicate all sensors and technologies that measure quantities that can be either directly (e.g. corrosion rate) or indirectly (e.g. temperature) related to corrosion of the wires. Direct Sensing technologies, instead, represent those technologies that can directly measure the effect of corrosion on the cross-section of the cable (e.g. magnetic flux measurements can be directly correlated to the cross-section of the specimen).

Various types of sensors that satisfied criteria related to size, accuracy, resistance to compaction forces, environmental durability and sensitivity to environmental variables, etc. were selected and tested. First, such sensors were tested in an accelerated corrosion chamber and then placed inside the cable specimen. Among the sensors selected, there were HS2000V Precon sensors (to measure temperature and relative humidity levels), Analatom Linear Polarization Resistance sensors and the CorrInstruments Coupled Multiple Array and Bimetallic sensors (to measure corrosion rate). A total of 72 sensors was placed inside the cable specimen in an arrangement shown in Figure 2:

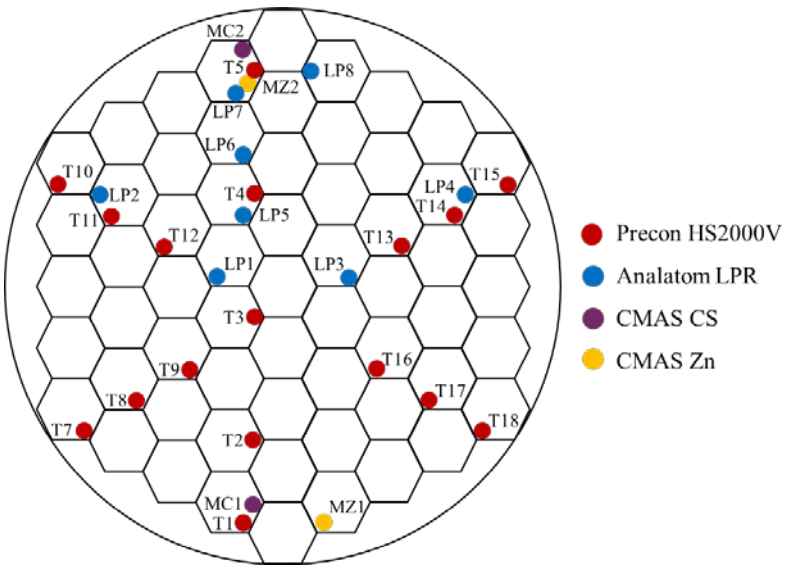

Figure 2: Schematic representation of sensor distribution inside the cable specimen

In order to test the effectiveness of the monitoring system, a full-size mock-up cable specimen was built and exposed to varying, controlled environmental conditions. The mock-up specimen was made with 73 hexagonally shaped strands, each consisting of 127-high strength steel wires, thus creating a cable with a 50.8 cm

diameter and a cross-sectional area composed of 9,271 wires. Of the 73 strands, 66 measured 6.10 m in length while the remaining 7 were 10.67 m long; these long strands were subjected to a tensile load that induced stresses in the wires up to 700 MPa so to highlight and eventually accelerate the phenomenon of stress-corrosion cracking. An environmental chamber was built around the mock-up cable specimen so to expose the cable to controlled environmental conditions (simulated rain, heating and cooling) in order to assess the functionality of the sensor network. Figure 3 shows the full-scale cable specimen with the environmental chamber.

Figure 3: Cable mock up and environmental chamber

Results from Laboratory Testing Program

After the cable mock-up was built, a long series of cyclic corrosion tests was planned with the purpose of testing the sensors that were part of the proposed corrosion monitoring system. These tests consisted in subjecting the cable specimen to cycle of rain, heat and cooling of different duration: each experiment lasted for many days and, at the end of each test, measurement data were analyzed and, if necessary, changes of the test conditions were made. The total duration of this experimental phase lasted about a year.

During each test, the temperature, relative humidity and corrosion rate were recorded at various locations in the cable cross-section so to have an experimental image of the distributions of temperature, relative humidity and corrosion activity within the cable. Figure 4 shows the recorded measurements of the temperature inside the cable specimen along a vertical radius during a test consisting of a series of 4-hour rain-heat-air conditioning cycles (Sloane et al. 2013). From these measurements, it was concluded that, with greater distance from the heat source, the

temperature variations within the cable's cross-section diminish with respect to the outside temperature. Maximum temperatures within the cable did not reach levels as high as those recorded in the chamber and temperature fluctuations decreased with increased distance from the heat source. The upper outer region showed substantial temperature fluctuations whereas near monotonic increases in temperature occurred in the center of the cable. Average temperature gradients found during the heating phase of each cycle prove that the cable heated evenly with maximum heating rates being obtained at central vertical locations. Lastly, the time to which the cable interior was affected by temperature fluctuations increased with greater cable depth.

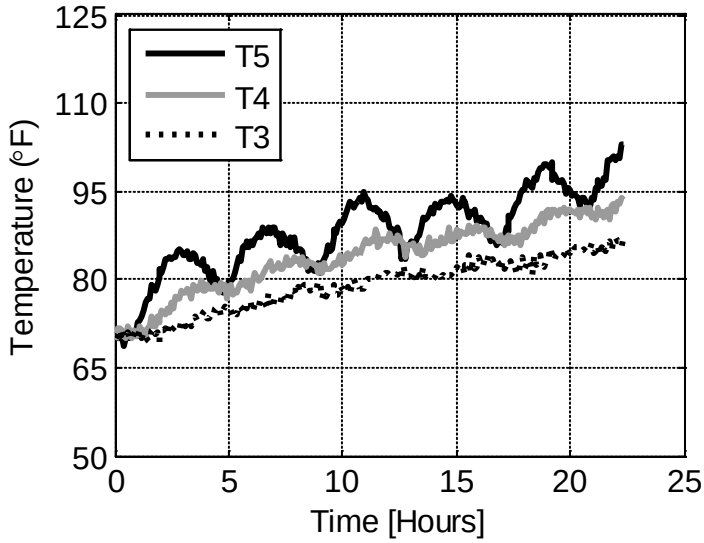

Figure 4: Temperature vs. time plot along the vertical radius

Much more complex is the interpretation of the relative humidity data because, while the temperature data lends itself to a collective analysis, general trends are not as identifiable in the relative humidity data. This is because water can penetrate inside the cable from many different locations and can find many different paths to spread in between the many wires and reach the sensors at different times. However, some "very general" trends can still be found and provide useful information on the good functioning of certain sensors.

Looking at the data recorded by all the various sensors, it can be concluded that increased levels of relative humidity results in increased levels of corrosion activity, as recorded by different types of corrosion sensors. Statistical analyses showed that the experimental dependence of corrosion rate values, as recorded by LPR sensors, on temperature was strongly linear.

With regard to the Direct Sensing technologies tested (Main Flux and Magnetostrictive technologies), none of them showed to be ready for field applications, even though some have great potential for future applications. In the specific problem in question, the size of the main cable is the main road block for their immediate applicability, tied to logistical (large magnetic fields) and sensitivity (detection of small wire breaks) constrains.

System Installation in one of the Main Cables of the Manhattan Bridge

Once the laboratory testing phase was completed, the entire system was installed inside two cable panels of the Manhattan Bridge in New York City. Built in 1912, this suspension bridge is one of the main traffic arteries between Manhattan and Brooklyn. Spanning over a length of 2089 m. with a central span of 448.1 m., this bridge carries a daily traffic flow of over 72,000 vehicles per day. There are 4 main cables, each made of 37 strands of 256 wires each, for a total of 9,472 wires bundled in a cable of a 21-in. diameter. The number of wires and the corresponding cable diameter of one of the Manhattan Bridge cables are quite close to the number of wires and cable diameter of the cable mock up tested in this study.

In each of the two panels, the main cable was wedged at 4 groove positions along the circumference and 19 sensors per panel were installed inside the cable. These sensors consist of temperature/relative humidity sensors and of three types of corrosion rate sensors. The data collection lasted about 11 months, at the end of which, the monitoring system was removed.

The data collected by the 38 sensor network provided a quite unique, real time picture of the internal environment of the cable, which is an important key to understanding corrosion in suspension bridge cables and can help develop a cost effective mitigation strategies. For example, it was extremely interested to see the variation of the temperature and relative humidity inside the cross-section of the cable in service conditions. Figure 5 shows the distribution of the maximum and minimum temperature and relative humidity over the entire cable cross section recorded on different days during the year. These maps show clearly that the distribution of temperature and humidity is not uniform across the cable cross section and that the bottom and shaded side portions of cable are likely to retain higher levels of humidity than the upper portion. Moreover, there are higher temperature and lower humidity during the day. In addition, when comparing the humidity levels between summer (August) and winter (January), it confirms that the internal relative humidity level is higher in the winter months than during summer months. An interesting observation is that, during the spring months when the temperature range is between 49°F and 60°F and the relative humidity between 40% - 95%, the internal cable environment is the most conducive to corrosion, with high level of humidity and with daily temperature cycles between day and night.

With regard to the corrosion rate sensors (Analatom LPR, CorrInstruments CMAS and Bi-metallic), all the sensors provided some useful and consistent measurement of corrosion activity. For example, all sensors showed that no corrosion activity was detectable when the relative humidity was below 45%.

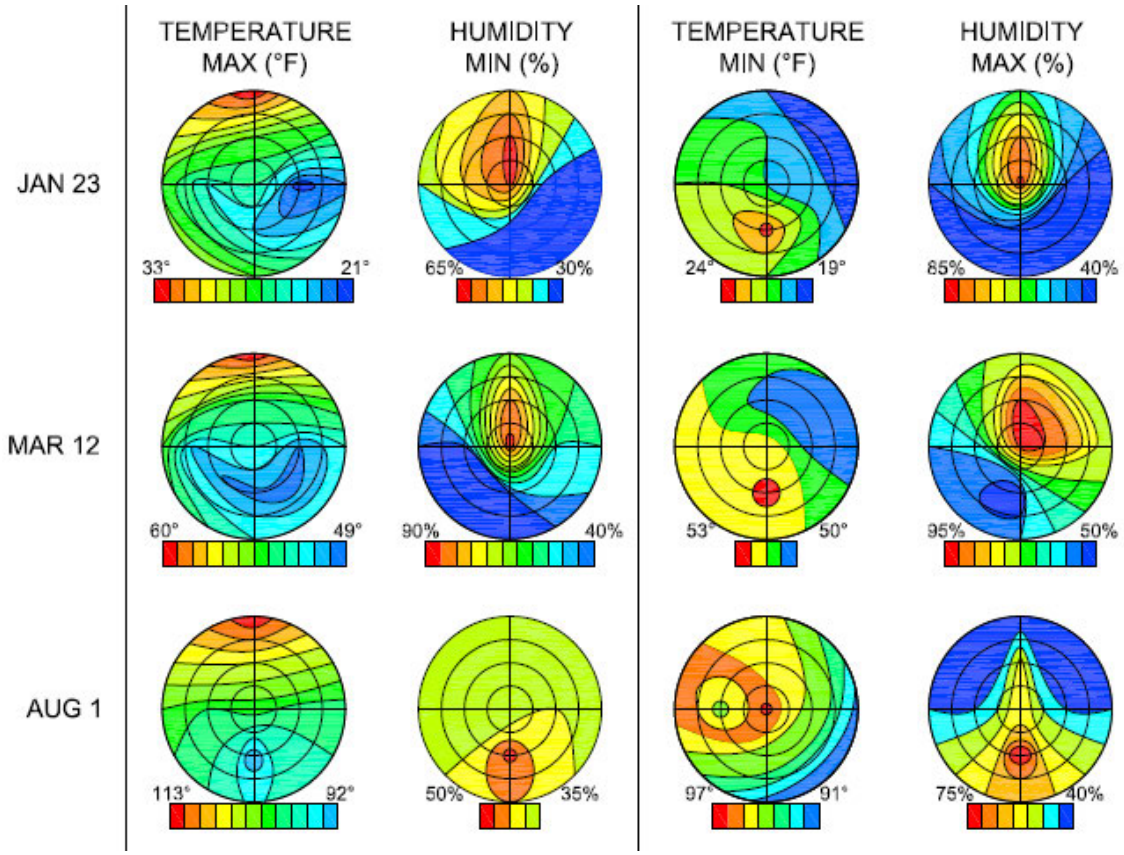

Figure 5: Distribution of Temperature and Relative Humidity inside a Main Cable

Testing the Effectiveness of the Dehumidification "Practice"

Having a monitoring system that can measure the distribution of temperature and relative humidity inside a cable allows us to test how effective the current practice of cable dehumidification is. Today, there is a trend of installing dehumidification systems that, when needed, inject dry air inside the cable, with the goal in mind to keep the humidity level inside the cable below 40%. The need for the system's activation is regulated by measuring the humidity of the outflow air at some specific locations along the length of the cable: such a measurement, based on the results obtained from the field investigation presented before, could be misleading. In fact, this measurement could not be representative of the complex humidity pattern inside the cable (see Figure 5).

To study how effective the dehumidification system is, the full-scale cable mock-up has been redesigned (Figure 6) so to accommodate a cable dehumidification system and a new series of tests have been planned.

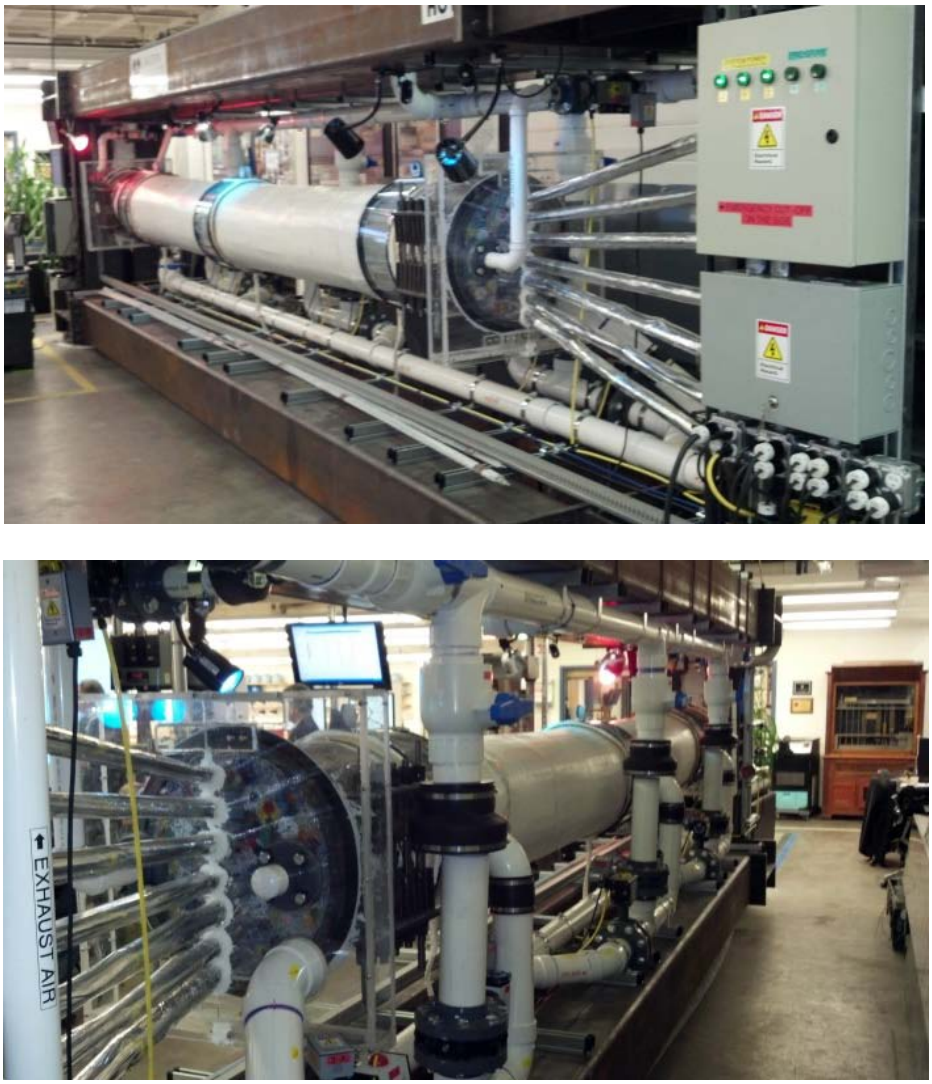

Figure 6: Front and Back View of the Cable Mock-up with Dehumidification System

In each test, first, the level of the relative humidity is elevated to a high value (above 90%) practically constant over the entire length of the cable specimen, and then dry air is injected inside the cable through a set of injection ports.

The cable specimen has been enclosed through a combination of D.S. Brown's Cableguard® Elastomeric Cable Wrap System and custom made PLEXIGLAS ports and end boxes manufactured in the Carleton Laboratory at Columbia University. Inlet/outlet ports have been placed at the center as well as at each end of the cable specimen so to allow for different injection-exhaustion configurations. The cable system has been humidified by two Nortec RH2 Space humidifiers, blowing humid air through Direct-Drive Corrosion-Resistant 10" duct fans with airflow 620 cfm @ 1/8" static pressure and 565 cfm @ 3/8" static pressure, and dehumidified by pumping dry air from a Honeywell DH150 Dehumidifier (with the flow also boosted by the Direct-Drive Corrosion Resistant 10" duct fans). Figure 7 shows a schematic representation of the humidification/dehumidification system set up.

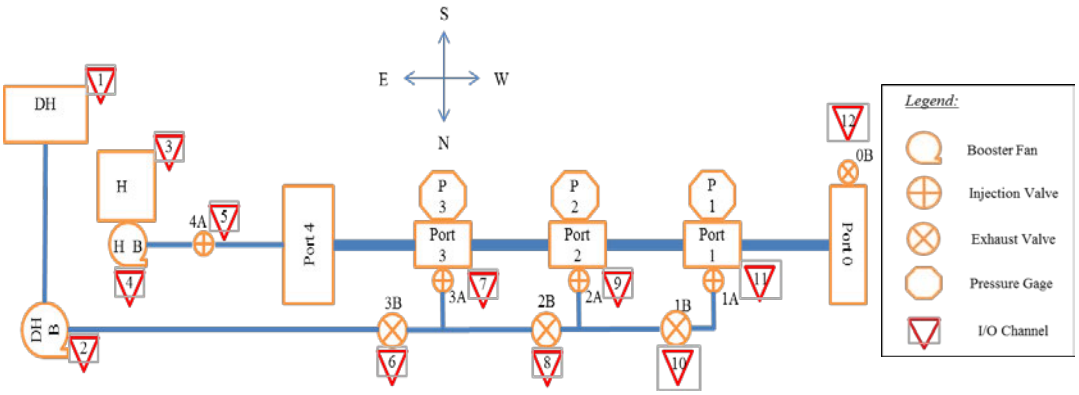

Figure 7: Schematic representation of Humidification/Dehumidification System

The monitoring system consists of 39 temperature and relative humidity sensors placed at three locations along the length of the cable specimen (center and both ends). At each location, the 13 sensors have been placed along three diameters, spaced at about 180° from each other, so to have a overall picture of the distribution of temperature and relative humidity over the entire cable cross-section.

Preliminary Results from Dehumidification Tests

At the time of the writing of this paper, the series of the dehumidification tests is still ongoing and the data are still being analyzed. However, there are some preliminary data worthy of our attention that could lead to interesting results.

Figure 8 shows the time variations of the relative humidity recorded at different depth along the vertical diameter (just below the cable surface (A1), at the center of the cross-section (A3) and at the bottom of the cross-section (D1)) for the three different cross-sections where the sensors are (Figure 8a at the injection port, Figure 8b at the center of the cable's length and Figure 8c at the exhaust port).

These results seem to confirm some of the expectations the dehumidification system is supposed to provide. First of all, as expected, there is a time lag, among the three cross-sections, for the time at which the relative humidity is dropped below 40%: from almost constant level of 90% relative humidity over the length of the cable, the system very rapidly reduces the humidity level at the injection port (less than 15 minutes) but it takes almost an hour to reach the same level at the farthest cross-section. It is also interesting to see the pattern in which dehumidification occurs within cable cross-sections: in the injection port, the outer areas of the cable are dehumidified faster than the core of the cable. This is expected because, at the injection port, the dehumidified air can freely move around the cable, affecting first the outer areas and then the center. However, once the dry air is in the cable, it is pushed by the ventilation system along "preferential" routes that depend on factors like cable compaction, wire misalignment, presence of corrosion products, etc.. These effects change the pattern with which the cross section is dehumidified: in fact, for the other cross sections (at mid length and at the other end), it appears that the core

is dehumidified first and then the surroundings (in Figure 8(c), sensors A3 shows a faster drop of relative humidity with respect to the outer sensors (A1 and D1)).

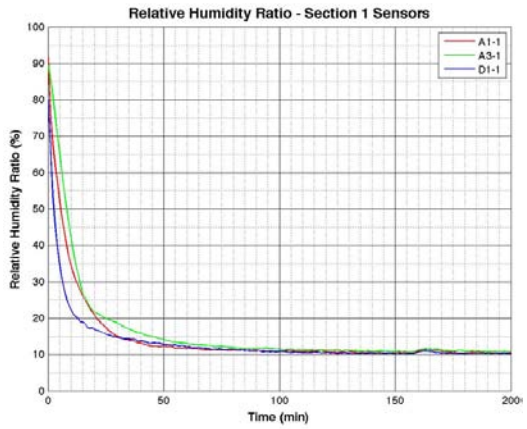

(a)

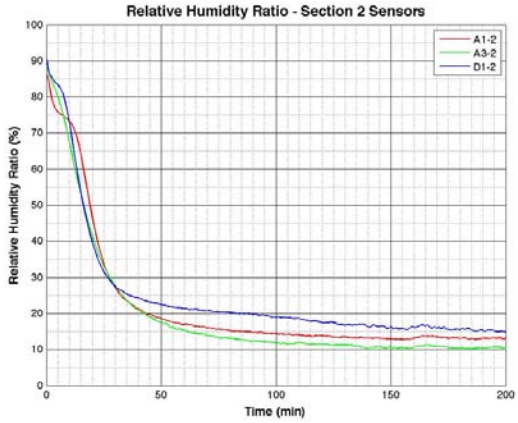

(b)

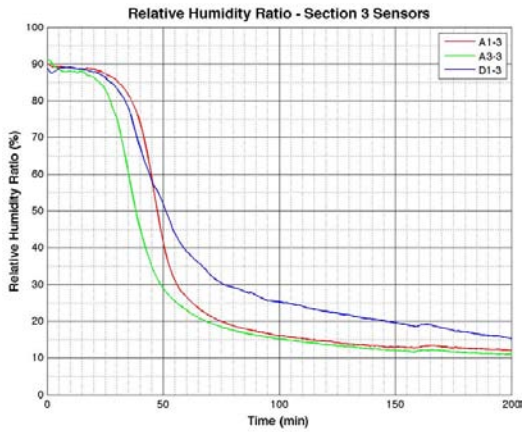

(c)

Figure 8: Plots of Relative Humidity vs. Time: Input in Port 1 and Exhaust in Port 3

These different patterns are a clear indication that the assumption of uniform dehumidification of the cross-section should be taken quite loosely, since the pattern is affected by factors that are quite different to quantify a priori. Even within a cross-section, as shown in Figure 8(c), different locations in a cross-section could reach the same level of humidity at different times: for example, the center and the lower portion of the cross-section reach the same 40% relative humidity threshold with a time lag of 20 minutes over a 1 hour test.

Another interesting aspect that needs further attention is concerning about the effectiveness of the dehumidification practice at low temperatures. When the system operates at much lower temperatures, the effectiveness seems to be drastically reduced. Figure 9 shows the same relative humidity-time diagram for same test conditions as in Figure 8(a) but conducted at a lower temperature (around 0°C).

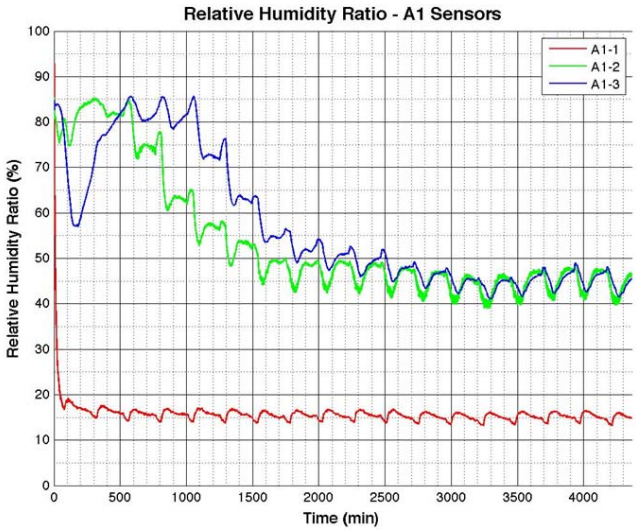

Figure 9: Relative humidity vs time at the injection port during a low temperature test.

Here, the plots of the relative humidity vs time recorded at the top sensors along the length of the cable specimen are presented and a puzzling result appears. From a preliminary analysis, it seems that the dehumidification system is not capable of bringing the relative humidity level down below 40% for cross-sections different from the injection one. While the system is very effective, as expected, in decreasing the level of relative humidity at the injection location, the dry air cools off when moving along the length of the cable and is not as effective as before in reducing the level of humidity away from the injection point. This could have implication on how to run a dehumidification system during the winter season. However, these are just preliminary results of a test program that is currently ongoing and general recommendations will be provided at a later time.

Conclusions

In conclusion, this study demonstrates that it is possible to measure corrosion activity inside the main cables of suspension bridges. The selected sensor network system was successful in providing information on the interior environment of a suspension bridge's main cable, helping understanding the conditions in which main cables of suspension bridges operate. The information provided by such a system can be used to make more reliable estimation of the safety factor and remaining service life of such important structural elements as well as to help bridge engineer in conducting more efficient and cost-effective inspections. The sensor system developed in this study represents a unique tool for testing the effectiveness of the cable dehumidification practice, practice that, although implemented already, has no experimental validation.

Acknowledgements

The authors would like to acknowledge the Federal Highway Administration (Dr. Ghasemi and Dr. Virmani), the Metropolitan Transportation Authority (Dr. Paskova) and the Port Authority of New York and New Jersey (Mr. Webber) for providing the necessary support to this project. The authors would also like to acknowledge the support and useful suggestions by Dr. B. Yanev, New York City Department of Transportation.

References

Betti, R., and Yanev, B. (1999). "Conditions of Suspension Bridge Cables: The New York City Case Study." *TRB*, 1654, 105-112.

Deeble Sloane, M.J., Betti, R., Marconi, G., Hong, A.L., Khazem, D. (2013). "Experimental Analysis of a nondestructive corrosion monitoring system for main cables of suspension bridges." *ASCE J. Bridge Eng.*, 18(7), 653-662.

SOUNDNESS EVALUATION OF PRESTRESSED CONCRETE STRUCTURES BY VIBRATION MEASUREMENT

Hidetaka Homma[1], Yoshitomi Kimura[1], Akiko Hiroe[1]

Abstract

Prestressed concrete (PC) structures are advantageous in terms of durability. However, even they deteriorate as they age. We conducted a study of soundness evaluation by vibration measurement for existing PC bridges demolished due to obsolescence, remarkable defects or other reasons.

This paper describes the result of vibration measurement of an existing PC bridges. The levels of damage that engineers want to evaluate by vibration measurement vary depending on maintenance levels. Therefore, we conducted vibration measurement and examined possibility of anomaly detection as to various damage cases of PC bridges. From the result, when subjected to significant damage, it was found that the frequency is reduced by about 30% relative to healthy values.

Introduction

Since prestressed concrete (PC) structure can control cracking by the use of prestressing, it is advantageous in respect of durability. However, even these PC structures deteriorate throughout in-service years. As shown in Figure 1, deterioration has been seen in some PC bridges at stages earlier than their service life due to defective grout filling or other reasons. Therefore, effective estimation of remaining strength of a deteriorated PC structures would be the challenge in the maintenance of PC bridges.

Based on the above-mentioned background, "Public Works Research Institute" and "Japan Prestressed Concrete Contractors Association" have been jointly conducting clinical studies by using demolished bridges to enhance the evaluation technology for PC bridges. Measurement of the vibration characteristics of a PC bridge before its demolition was performed as part of the clinical study. Since vibration measurement has the advantage that it is a nondestructive testing and simple approach, whether it can be applicable for the estimation of the remaining strength of the deteriorated existing PC bridges is evaluated.

Figure1. Corroded and Broken Cables in Precast Segment Box Girder Bridge

The PC bridge which greatly suffered the dynamic damage

[1] Center for Advanced Engineering Structural Assessment and Research, PWRI

Fudai floodgate maintenance bridge suffered severe damage due to the attack of gigantic tsunamis generated by the 2011 Great East Japan Earthquake.

Figure 2. Fudai floodgate maintenance bridge (after Tsunami)

As shown in Figure 2 ,two spans of the bridge collapsed totally due to failure at their mid span and another two spans survived with large vertical residual deflections. Especially in the 3rd. span, maximum deflection of 300mm and bending cracks with the maximum width of 5mm were observed. Therefore, it was considered that the span might collapse anytime. On the other hand, in the 4th. span, the maximum deflection was 80mm.

As shown in Figure 3, we have measured the vibration by excitation in the weight falling method with nine accelerometers evenly spaced between end crossbeams.

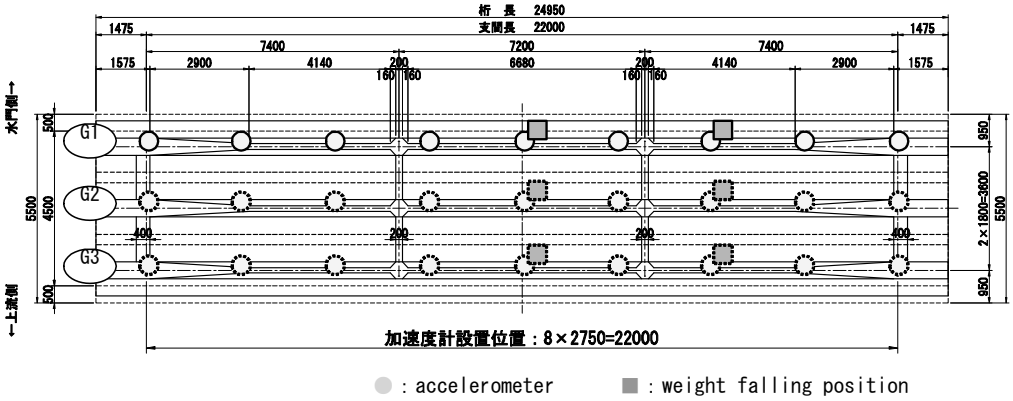

Figure 3. Measurement position and excitation position

Figure 4 shows the result of measurement. A slight difference was observed in each of the main girder vibration frequency. Compared with the analysis result of intact model, frequencies of 3rd. span are 20 to 30 percent lower and those of 4th. span are 10 to 20 percent lower than that of intact state. Tendency of reduction of vibration frequencies was consistent with extent of damage. It was confirmed that it is possible to detect the load-bearing performance degradation by measuring the vibration of the member, if the PC member is subjected to large

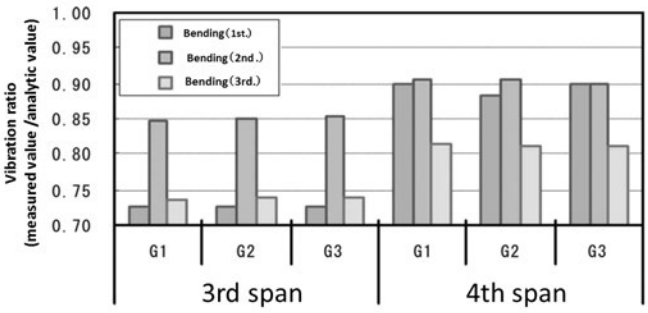

(analytic value：1st. 4.22Hz ,2nd. 16.88Hz , 3rd. 37.98Hz)

Figure 4. Vibration frequency ratio for the analytic value

mechanical damage. Reduction rate of the second bending mode in the 3rd. span was small compared to the first bending mode and the third bending mode. The reason of this difference is that the portion of the maximum amplitude of the 1st and 3rd modes coincides with the severely damaged portion of the girders as shown in figure 5. Moreover, in the 4th. span, reduction of vibration frequency of higher mode was remarkable.

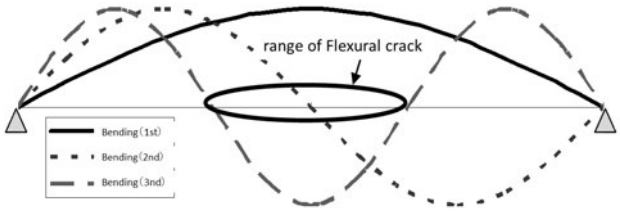

Figure 5. Bending vibration mode of the simple

Transition of vibration characteristics during loading tests

The transition of vibration characteristics was investigated during loading tests of the decommissioned girders. These investigations were conducted during two different loading cases. The investigation during the bending loading test and the shear loading test assumed the damage of whole girder and the damage of a part of the girder respectively.

Transition of vibration characteristics during bending load tests

Bending load tests were conducted on the girders sampled from decommissioned bridges. One was a pre-tensioned girder from Nakagawa Bridge and another was a post-tensioned girder from Aimigawa Bridge. Vibration measurements were conducted as follows. Velocimeters or accelerometers were set on the upper surface of PC girder as shown in Figure 6. After reaching each loading step, we unloaded to zero and we gave excitation by a plastic hammer (impact excitation method) and measured the dominant vibration frequencies.

The result of vibration measurement of the pre-tensioned girder is shown in Figure 7. The decreasing ratio of the frequencies of the first and second modes are plotted in the figure. The deformation was measured at the maximum deflection point, not at the measurement points of vibration. Before the bending cracks appeared (loading step 4), decrease of frequencies was observed for the first and second modes. But they did not change very much after the appearance of the bending cracks. And finally at step 8 at which applied load was higher than the design bending strength of 80kN and the girder considerably deformed, decrease of the

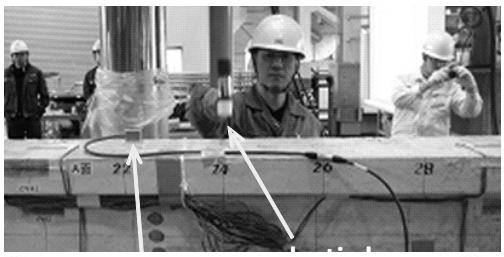

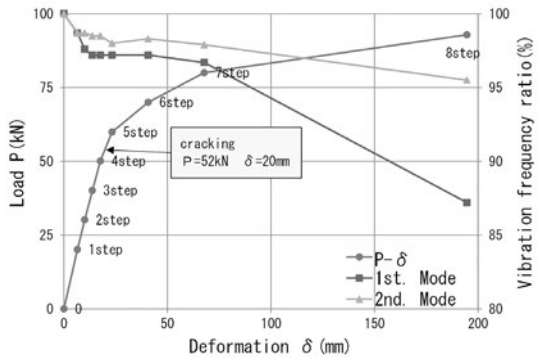

Figure 7. Transition of vibration frequency(pre-tensioned girder)

frequencies reached approximately 13% and 5% for the first and second modes respectively.

The result of vibration measurement of the post-tensioned girder is shown in Figure 8. The steps at which the girder was unloaded and the vibration measurement was conducted were set after the appearance of the bending cracks. From the figure, it was found that the frequencies did not decrease much between the appearance of cracks and the yield of steel members, although that of the first mode decreased significantly between the beginning of the loading and the appearance of the cracks.

On the other hand, the decrease of the frequency was approximately 30 % at the primary bending mode and approximately 20 % at the secondary bending mode in Step 4 which is the final point of the member after reaching the maximum load.

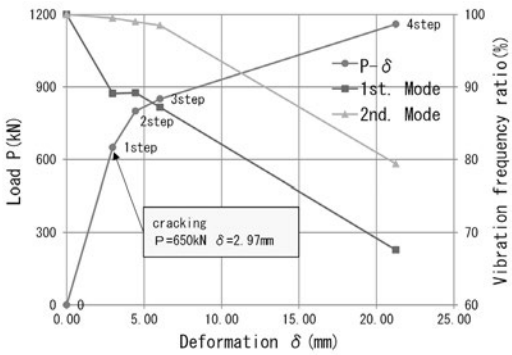

Figure 8. Transition of vibration frequency(post-tensioned girder)

It can be considered that one reason of the decreasing of the frequency in the early loading stage is that the supports were not stable enough at the beginning of the loading. From the above, it was verified on both pre-tensioned and post-tensioned girder that the frequency decrease significantly when the member is close to the ultimate state, while the frequency did not change remarkably around the load level of the appearance of the flexural cracks or that of the yield of members. This reason can be conceived that on PC members, the cracks closed by the restoring force after unloading and the stiffness of member was recuperated.

Transition of vibration characteristics during shear loading tests

A shear loading test was conducted at the post-tensioned girder (Aimigawa Bridge). The vibration measurement was conducted before and after loading tests. In the test, the girder was loaded until the yield of the steel members. The latter vibration measurement was conducted in unloaded condition. The impact excitation method by a sandbag and the ambient vibration method were adopted.

Table 1. Result of the vibration measurement during shear loading tests

mode	Loading test	natural frequency (Hz)	
		ambient vibration method	impact excitation method
bending (1st.)	before	6.694	6.378
	after	6.458	6.353
	ratio	0.95	1.00
bending (2nd.)	before	21.301	21.276
	after	21.130	21.047
	ratio	0.99	0.99
bending (3rd.)	before	Undeterminable	57.363
	after	Undeterminable	52.953
	ratio	—	0.92

Table 1 represents the result of the vibration measurement. Regarding the ambient vibration measurement method, the higher-order-mode of vibration could not be measured but some decreasing of the frequency could be found in each dominant vibration mode. Regarding the impact excitation method, the frequency tended to decrease when the order of mode was high. This is because, for the third bending, the partial damage near the shear loading point corresponds with the antinode of vibration

mode. Which coincides with the previous studies.

Vibration characteristic of deteriorated bridge

The PC bridge at which the vibration measurement was performed is shown in Figure 9. The structural type is a five-span simple PC T-section girder bridge. It was constructed in 1967 and served more than 40 years. Since the bridge was constructed on the coast of Japan Sea and therefore severely damaged by chloride attack, repairs had been performed more than once as damages of concrete or corrosion of steel were identified. However, because of confirmation of re-deterioration due to corrosion and breakage of PC wires as shown in Figure 10, rebuilding of the bridge was planned, and its service was terminated in September, 2010. Before its demolition, the vibration test was performed by vehicle falling method, weight falling method, and ambient vibration method as shown in Table 2. Excitations were applied at 1/2 and 1/4 points of the span on the G3 girder, and measurements were performed at points that divide the G1 and G5 girders equally into 8 segments. (Shown in Figure 11) The measurement condition is shown in Figure 12. Examples of spectra obtained in the vibration test performed by using vehicle falling method, weight falling method, and ambient vibration method are shown in Figure 13.

Figure 9. PC bridge

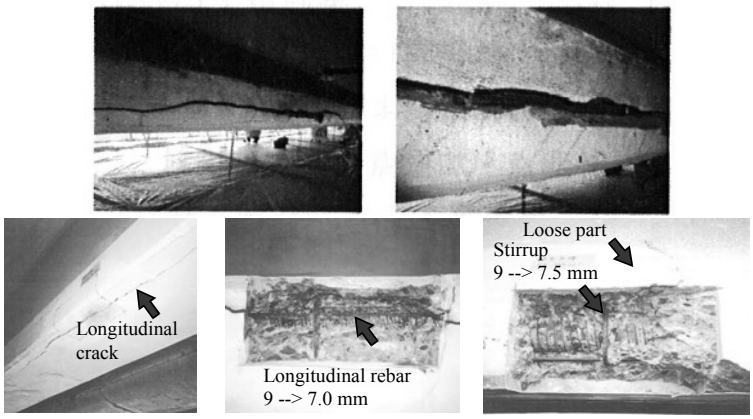

Figure 10. Deterioration of PC bridge

Table 2. Methods of excitation

	Vehicle drop method	Weight drop method	Ambient vibration method
Excitation method	4 rear wheels of a vehicle of 111 kN weight are dropped from a step of 130 mm high to provide forced excitation to the bridge.	A weight of 0.245 kN mass is dropped by free fall from a height of 1.0 m to provide forced excitation to the bridge. The shock excitation force is about 30 kN.	The ambient vibration during a calm period when there is no traffic on the adjacent temporary bridge is measured. * Because microtremor exists around the bridge due to natural and artificial causes, the bridge is continuously subject to random and micro vibration.
Advantages	No special excitation equipment other than testing vehicle is required. Relatively large excitation force can be obtained.	When a small size weight is used, vibration can be applied by human power. Relatively constant excitation force can be applied.	No excitation needs to be applied, and measurement can be performed easily even for a bridge which is currently in-service.
Disadvantages	The weight of vehicle sometimes cannot be negligible as an added mass. Also, the characteristic vibration of the vehicle (e.g. 3 Hz for a damp truck) can sometimes dominate as an excitation force.	Depending upon the mass of weight, there can be cases that adequate excitation force cannot be obtained.	A vibration measurement equipment with high precision is necessary. It may sometimes be influenced by noise, etc. and/or the process method because of small amplitude.

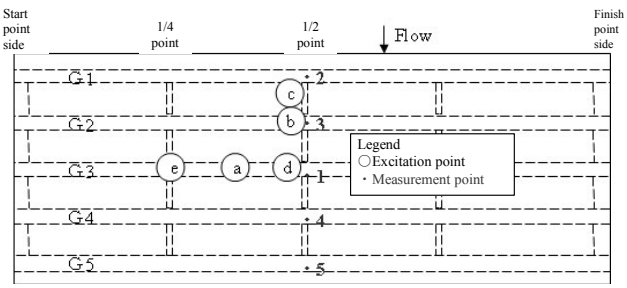

Figure 11. Excitation point and the measurement point

Vehicle falling method

Weight falling method

Figure 12. Excitation methods

The Figure shows results obtained in the 1st. span with excitation point located at 1/4 point of the span and measurement at 1/2 point of the G3 girder span. Dominant frequencies have been concentrated near 4Hz in the all method. Additionally, dominant frequencies in the range of 20 Hz ~ 40 Hz were found in the weight falling method. Also, for the weight falling method in which the third through fifth dominant frequencies (20 Hz ~ 40 Hz) were

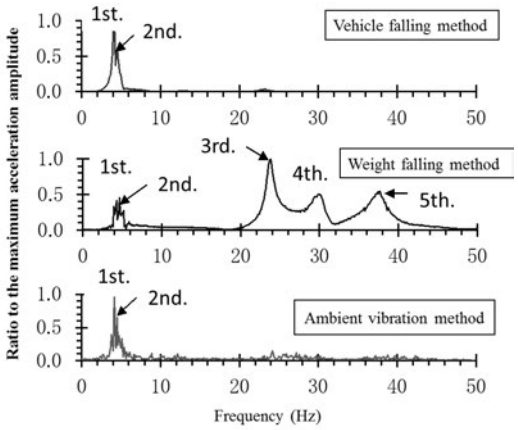

Figure 13. Measured spectra

found, dominant frequencies of the 1st. span, where damage was severe, and the 2nd. span, where damage was minor, were shown in Table 3. According to the inspection data of the past, section loss of concrete and breakage of PC cable by chloride attack has been found in the 1st. span. Deterioration of the 1st. span was severe while that of the 2nd. span was comparatively minor. For higher modes, frequencies of the 1st. span were much smaller than those of the 2nd. span. As mentioned in the shear loading test, it may be possible to grasp the deterioration by measuring the high-order vibration modes.

In this bridge, it was possible to find a difference of the frequencies because

Table 3. Comparison of frequency (1st. Span1, Span 2)

Mode number	Dominant frequency(Hz)		f1/f2	Mode of vibration
	Span 1	Span 2		
	f1	f2		
First	4.3	4.3	1.00	First bending
Third	23.7	25.2	0.94	Unknown
Fourth	30.2	31.5	0.96	Third bending
Fifth	37.1	40.8	0.91	Unknown

the deterioration levels of each span differs. However, this method may not be applied to the most of the bridges. For the general cases, it is better to measure the value when intact state and compared it when the bridge deteriorates.

CONCLUSION

From the result of this study, the following conclusions can be drawn:

(1)When the PC Bridge suffered severe damage, there is possibility of detecting deterioration by vibration measurement.

(2) For PC members, reduction of vibration frequency is small because of the restoring force induced by the prestress.

(3) It may be possible to detect the damage of PC bridges comparing the vibration characteristics in sound state and those in current state.

Acknowledgments

CAESAR's research activity utilizing decommissioned bridges was able to be conducted using demolished bridges provided from municipalities along with cooperation agreement with the Japan Prestressed Concrete Contractors Association (JPCCA). We thank them for their corporation.

CONCRETE BRIDGE DECK CONDITION ASSESSMENT USING ROBOTIC SYSTEM RABIT

Nenad Gucunski[1], Ali Maher[2] and Hamid Ghasemi[3]

Abstract

Development and implementation of RABIT (Robotics Assisted Bridge Inspection Tool) in condition assessment concrete bridge decks is described. The system uses multiple nondestructive evaluation (NDE) technologies in characterization of three most common deterioration types: rebar corrosion, delamination, and concrete degradation. The system implements four NDE technologies: electrical resistivity (ER), impact echo (IE), ground-penetrating radar (GPR), and ultrasonic surface waves (USW), and advanced vision to complement traditional visual inspection. The associated platform for the enhanced interpretation of condition assessment in concrete bridge decks is comprised of data integration, fusion, and deterioration and defect visualization. The data visualization platform facilitates intuitive presentation of the main deterioration and defects.

Introduction

The Federal Highway Administration's (FHWA's) Long Term Bridge Performance (LTBP) Program initiated development of a robotic system for condition assessment of concrete bridge decks named RABIT (Robotics Assisted Bridge Inspection Tool). Based on the discussions with State Departments of Transportation (DOTs) and bridge expert groups, the Program included the concrete bridge deck performance as one of the key bridge performance issues. To create knowledge about the deck performance, the LTBPP team has been conducting periodical manual data collection using multiple NDE technologies (Gucunski et al., 2012 and 2013), visual inspection and physical sampling and testing. While the manual NDE data collection provided high quality information, it was also a labor intensive, expensive and a relatively slow process. As the Program is entering a new phase, with the need to assess the condition of decks on hundreds of bridges, a data collection that is rapid, economical and consistent became an imperative for the success of the LTBP Program. In addition, to fully benefit from the application of multiple NDE technologies, there was a need for interpretation techniques that can effectively integrate data from different NDE technologies and perform inferences that may not be possible from a single technology. While the development of the RABIT system was triggered by the needs of the LTBPP, potential benefits to State DOTs were also considered.

---

[1] Professor and Chair, Department of Civil and Environmental Eng., Rutgers University
[2] Director, Center for Advanced Infrastructure and Transportation, Rutgers University
[3] Team Leader, Turner-Fairbank Highway Research Center, Federal Highway Administration

From the technical point, the RABIT system was designed with two main objectives in mind. The first objective was to develop a system that would enable automated NDE data collection. The NDE technologies included those already implemented and proven within the LTBP Program, in particular: impact echo (IE), ultrasonic surface waves (USW), electrical resistivity (ER) and ground penetrating radar (GPR). The operation of the robotic platform was designed to collect data at rates four or more times faster than the current manual data collection that requires a team of five or more people, as for example it is illustrated in Figure 1. The second objective was to create a platform for enhanced interpretation of condition assessment in concrete bridge decks through data fusion, and deterioration and defect visualization. While the system provides a near real-time preliminary condition assessment of the bridge deck, the interpretation and visualization platform specifically addresses data integration and fusion from the four NDE technologies. It integrates survey results and facilitates intuitive presentation of the main deterioration caused by corrosion, delamination, and concrete degradation. The following sections describe the main components of the robotic platform and the control system for data collection monitoring and analysis.

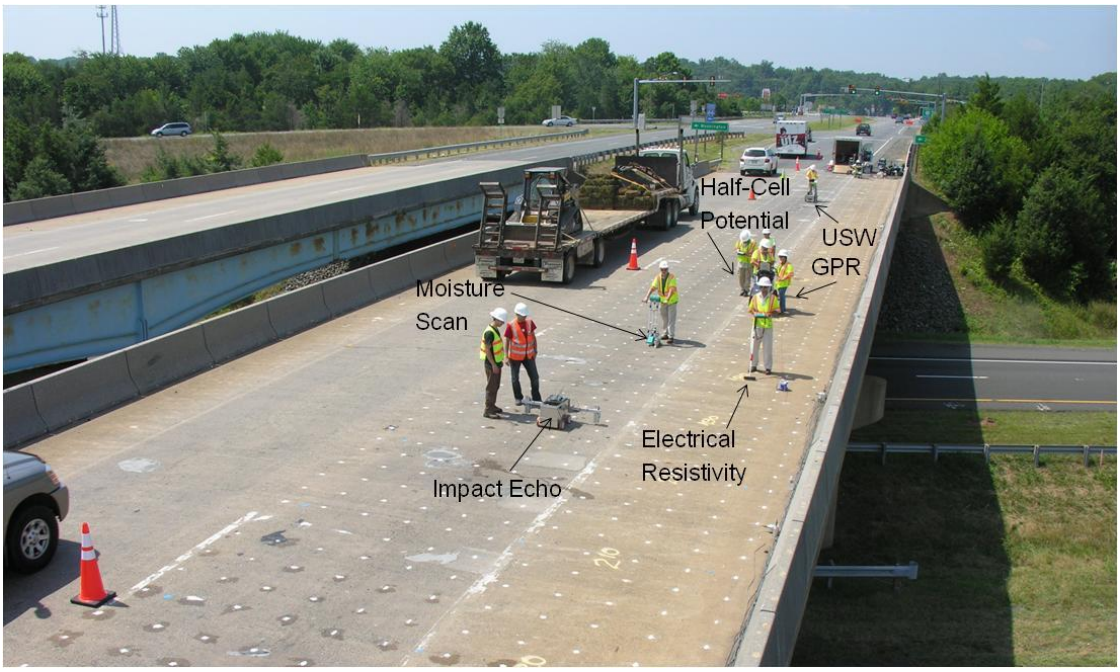

Figure 1. Condition surveys of a bridge deck using multiple NDE technologies.

Benefits of Condition Assessment Using NDE

The primary benefits from the condition assessment using NDE technologies stem from the quantitative nature of the information collected. That information can be described in terms of condition maps, describing the location and severity of deterioration, and calculated condition indices, describing the overall condition of the deck of a bridge or a section of a bridge. As an illustration, a set of typical results of the NDE based condition assessment of deck using four NDE technologies is shown in Figure 2. In all maps the areas marked in hot colors describe progressed deterioration

or condition favorable for fast progression of deterioration. On the other side of the spectrum are zones plotted in cold colors, describing good conditions.

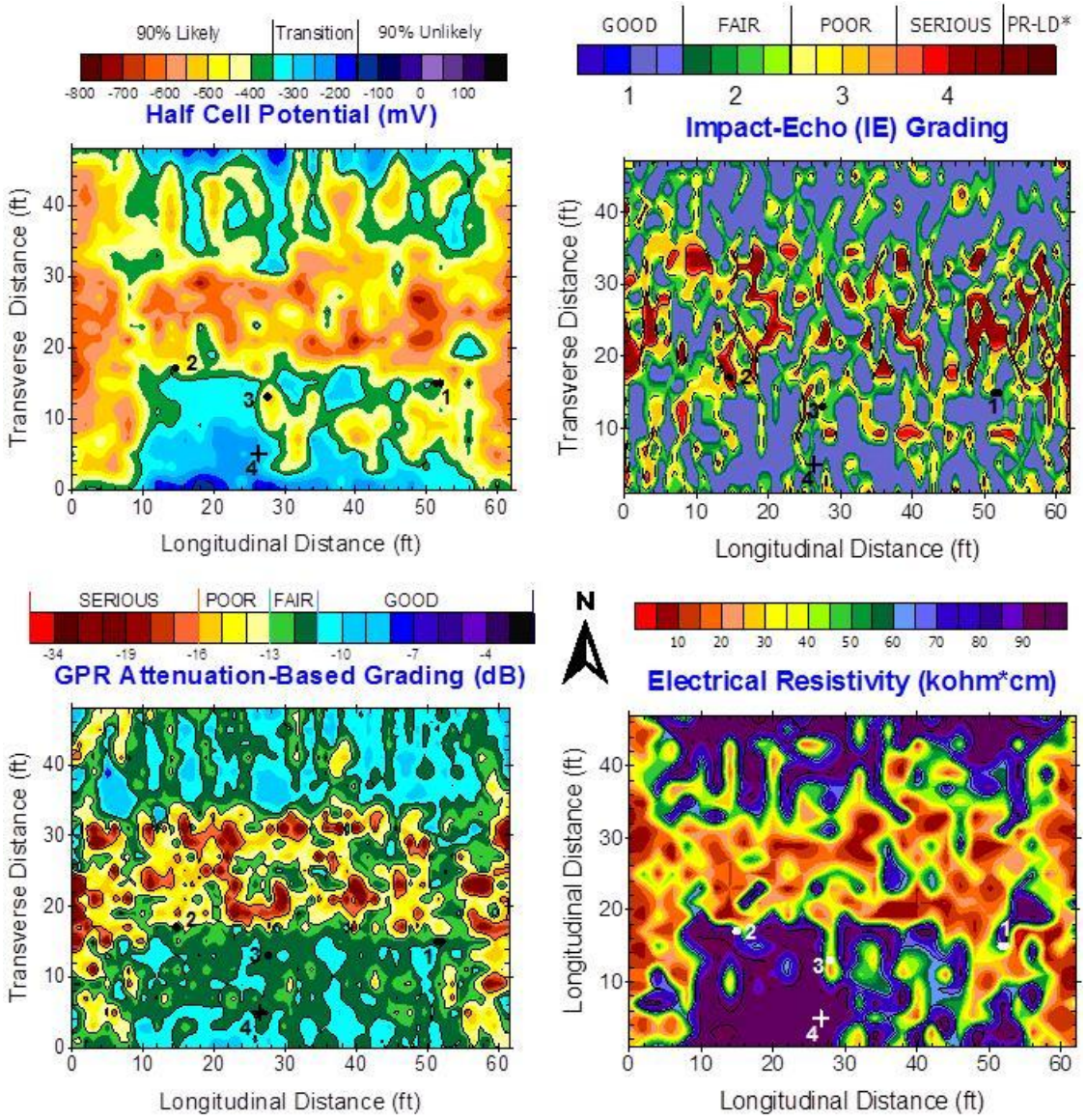

Figure 2. Conditions maps from half-cell potential, impact echo, GPR and electrical resistivity surveys.

The condition maps shown in Figure 2 demonstrate the ability of different technologies to detect and define the boundaries of deterioration, and to describe their severity. It was also demonstrated during the first phase of the LTBP Program that the NDE technologies have ability to monitor deterioration progression. As an illustration, condition maps from ER surveys conducted in 2009 and 2011 are shown in Figure 3. The maps clearly describe progression of the aggressiveness of the corrosive environment during the two year period in both the extent and severity level. Similar ability of other NDE technologies was demonstrated.

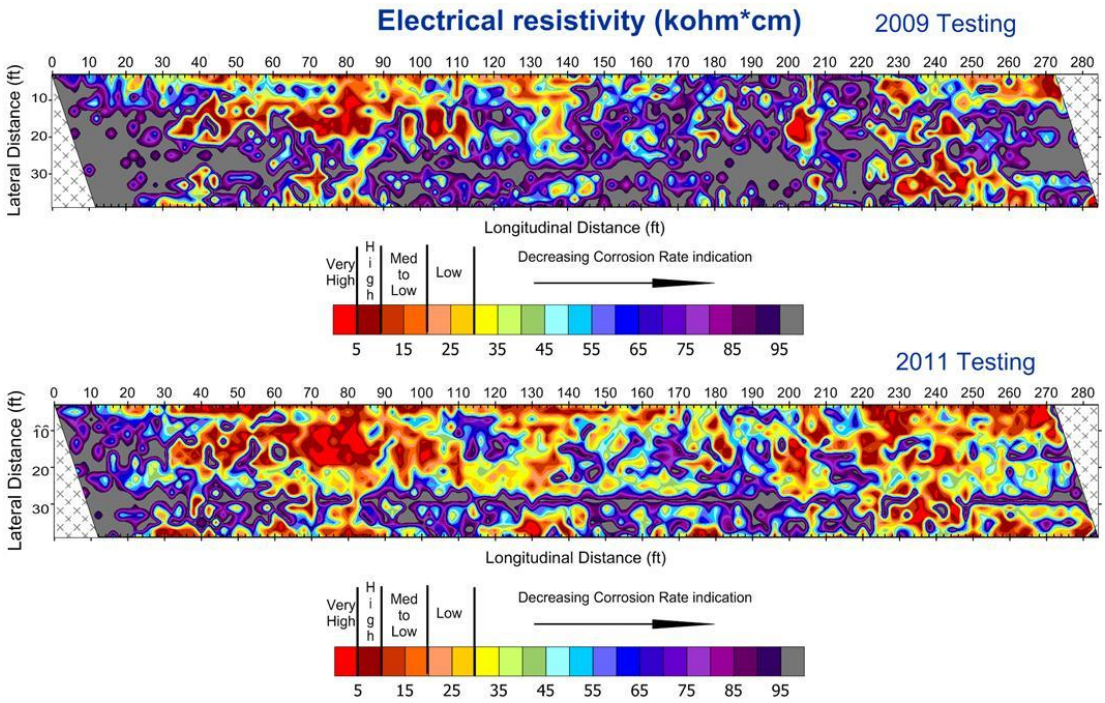

Figure 3. Assessment of progression of aggressiveness of corrosive environment using electrical resistivity.

The quantitative nature of NDE data can be also exploited for a more objective condition rating of deck and to more precisely quantify deterioration progression. It can be also used, in combination with bridge deck segmentation, to identify bridge sections with higher deterioration. Condition rating with respect to each of the deterioration or defect types is calculated using a weighted area approach. For example, the rating with respect to delamination, on a scale of 0 (worst) to 100 (best), is calculated from a weighted average of percentages of the areas falling into the three delamination conditions. The area described as sound (no delamination) is assigned a weight factor of 100. The area described in the state of initial delamination (fair to poor grade) is assigned a factor 50, and the area in the state of severe delamination a factor 0. Condition ratings with respect to delamination, corrosion and concrete degradation for a bridge are illustrated in Table 1. The progression of deterioration in all three cases can be observed. Condition ratings on the network level or sections of larger bridges can be utilized to identify the areas of faster deterioration progression and or the ones that should have priority in maintenance or rehabilitation.

Table 1. Condition Ratings for a Bridge Deck

	2009	2011
Active Corrosion	39.4	28.1
Delamination Assessment	70.0	57.2
Concrete Degradation	48.1	35.3
Combined Rating	52.5	40.2

Description of the Robotic Platform

The robotic system for condition assessment of bridge decks, with its main components marked, is shown in Figure 4. The robotic platform is a Seekur robot from Adept Mobile Robot Inc. The robot itself is approximately 1.4 m long, 1.2 m wide and 1.1 m tall. It has four omni-directional wheels. which enable the robot to move laterally and to turn at a zero radius. These wheels also allow fast movement from one test location to the next one in any direction. The primary navigation system is a differential GPS, for which the robot uses two Novatel antennas mounted on the robot, and the third one on a tripod, the base station. The information from the GPS systems is fused with the information from an on board inertial measurement unit (IMU) and a wheel encoder using Kalman filter. It is sufficient to take GPS coordinates at three points on the deck to fully define the robot movement path. The sensor arrays are 1.8 m wide, enabling the robot to assess half of a lane width in a single pass.

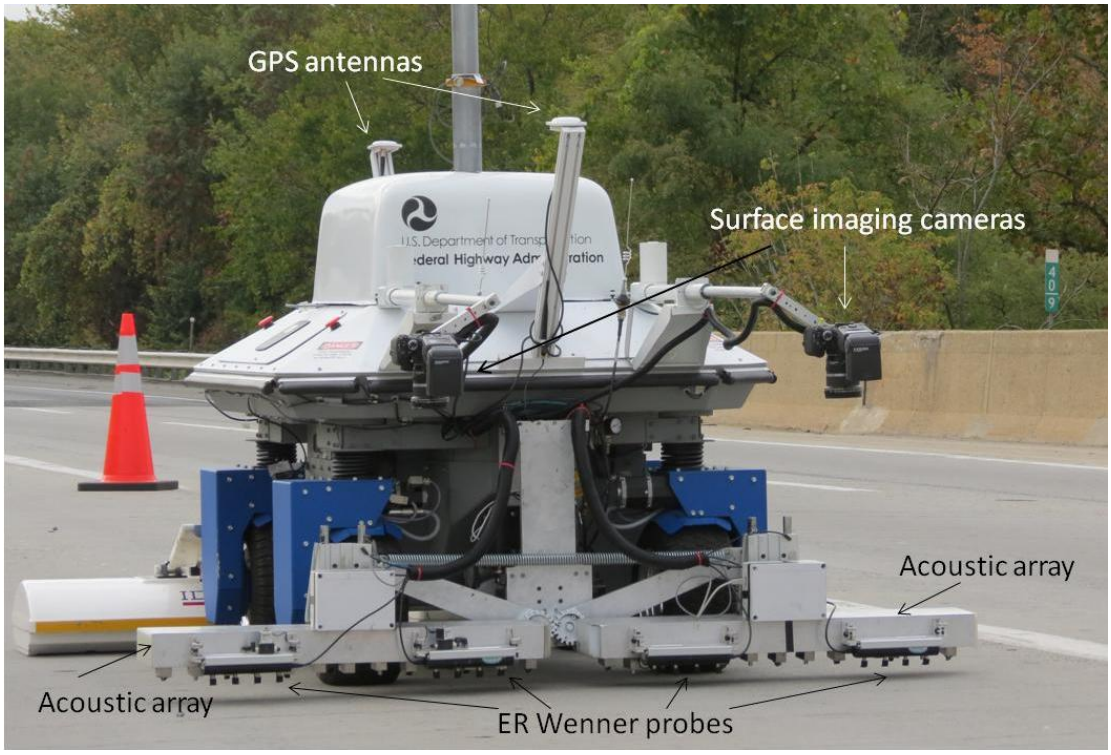

Figure 4. Front end of RABIT with NDE and navigation components.

The system is equipped with the sensors for the four previously described NDE technologies, and three digital cameras for high resolution bridge deck surface imaging and panoramic imaging of the test location surrounding. As shown in Figure 4, there are two acoustic arrays on the front end of the robot. Each of the arrays has four impact sources and seven receivers (accelerometers), enabling multiple IE and USW tests to be conducted. The sources and receivers are coupled to the deck surface pneumatically. The primary purpose of IE testing is to determine the extent and severity of delamination, while the USW testing is used to describe the concrete quality by

measuring the concrete modulus. Also, attached to the acoustic array boxes are four ER Wenner types probes. Each of the probes has small diameter water supply lines that spray water on the probe's electrodes to establish the electrical contact between the electrodes and concrete surface. The ER measurements are conducted to assess the corrosive environment, which is primarily affected by the presence of moisture, salts, chlorides, etc. Finally, there are two high resolution cameras on the front end, each of them taking an image of approximately 0.7 m by 1.0 m area of the deck surface. All the images are stitched into a single high resolution image of the bridge deck.

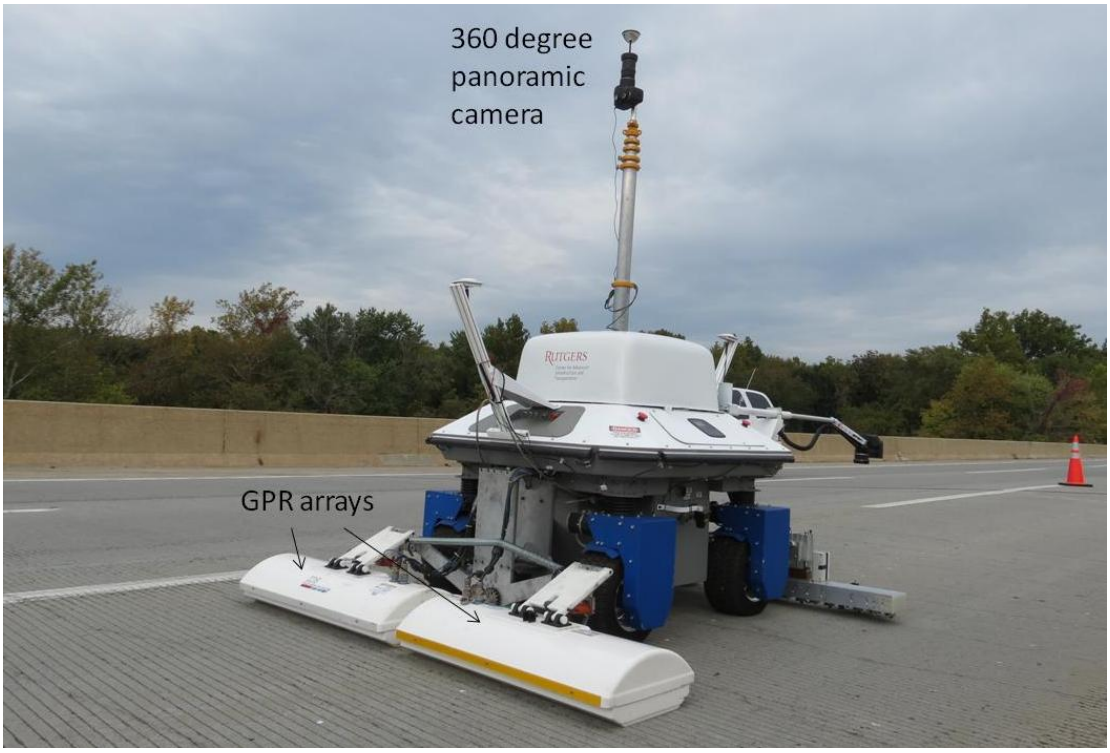

Figure 5. Rear side of RABIT with GPR arrays and panoramic camera.

The GPR arrays marked on the rear side of RABIT in Figure 5 have primary purpose to do rebar mapping, to measure the concrete cover, and to contribute to the assessment of the corrosive environment, concrete degradation and likelihood of delamination. Each of the two IDS Hi-Bright arrays has sixteen antennas, or two sets of eight antennas of dual polarization. Finally, there is the third digital camera mounted on a mast in the middle of the robotic platform. The mast can lift pneumatically the camera to a 4.5 m height to take 360 degree panoramic images of the bridge deck.

All the collected data are wirelessly transmitted from the robot to the "command van" as they are collected. All the data being collected can be monitored in the van. The data are analyzed as received, and some of the results are presented in near real time. For example, the impact echo records are analyzed to create a delamination map, the surface wave data are analyze to create a concrete quality map, a corrosion rate map is created from correlations to the resistivity data, etc. The robot operator can control and

monitor data collection and analysis on four main monitors in the van. As an illustration, a screen describing the collection of GPR data for a single antenna, a time history and spectrum for one of the impact echo devices, deck surface imaging, and electrical resistivity from two ER probes are shown in Figure 6. In addition, the operator can monitor the robot movement and position on the deck based on the transmitted GPS coordinate, as illustrated in the figure.

Figure 6. Screen of one of the monitors in the "command van."

Conclusions

The robotic system RABIT, with its integrated multiple NDE technologies and vision, fully autonomous and rapid data collection, and associated data analysis and interpretation, opens new ways in the condition assessment of concrete bridge decks. The complementary use of four NDE technologies: electrical resistivity, impact echo, ground-penetrating radar, and ultrasonic surface wave testing, enables detection and characterization of corrosion, delamination, and concrete degradation with higher spatial resolution and confidence level. The associated platform for enhanced data integration and visualization facilitates more complete review of the collected data and more intuitive presentation of the main deterioration and defect types. While the system will find its first use in the data collection for the FHWA's LTBP Program, it has high potential for implementation by transportation agencies and bridge owners in their daily operations.

Acknowledgments

This publication was supported by a subcontract from Rutgers University, Center for Advanced Infrastructure & Transportation (CAIT), under DTFH61-08-C-00005 from the U.S. Department of Transportation – Federal Highway Administration (USDOT-FHWA). A large number of individuals from Rutgers' School of Engineering working within the Center for Advanced Infrastructure and Transportation (CAIT) have contributed to various aspects of the robotic system development, construction and implementation. The authors gratefully acknowledge contributions of: Professors Basily Basily, Jingang Yi and Kristin Dana, Research Associates Drs. Hung La and Seong-Hoon Kee, Research Engineers Hooman Parvardeh and Ronny Lim, and graduate students Parneet Kaur and Prateek Prasanna.

References

Gucunski, N. Romero, F., Imani, A. and Fetrat, F.A., "Nondestructive Evaluation-Based Assessment of Deterioration Progression in Concrete Bridge Decks," Proceedings of the 92nd Annual Transportation Board Meeting, Washington, D.C., January 13-17, 2013, on CD.

Gucunski, N., Maher, A., Ghasemi, H., and Ibrahim, F., "Segmentation and Condition Rating of Concrete Bridge Decks using NDE for More Objective Inspection and Rehabilitation Planning," the 6th International Conference on Bridge Maintenance, Safety and Management - IABMAS 2012, Stresa, Lake Maggiore, Italy, July 8-12, 2012, on CD.

Disclaimer

Non-Destructive Bridge Deck Assessment using Image Processing and Infrared Thermography

Masato Matsumoto[1]

Abstract

Traditionally, highway bridge conditions have been monitored by visual inspection with structural deficiencies being manually identified and classified by qualified inspectors. However, the quality of inspection results depends on the individual inspector's subjective judgment based on his/her knowledge and experience. Under these circumstances, innovative non-destructive bridge condition assessment technologies using infrared thermography and digital concrete surface imaging have been developed and applied to the highway bridge structures in Japan. This paper describes the results of integrated high-end infrared thermography and line sensors to obtain bridge deck defects and delamination with on-site applications for sample bridges in the state of Florida.

Introduction

Condition ratings of bridge components in the Federal Highway Administration (FHWA)'s Structure Inventory and Appraisal (SI&A) database are determined by bridge inspectors in the field for bridge deck, superstructure and substructure. This information has been used by bridge owners as a basis for decisions on bridge maintenance, rehabilitation, and replacement. The condition ratings also influence a bridge's Sufficiency Rating (SR), as well as whether the bridge may be classified as "structurally deficient".

However, the determination of bridge condition ratings is generally subjective depending on individual inspectors' knowledge and experience, as well as varying field conditions. For the evaluation and documentation of concrete deterioration (cracks, potholes, delamination, spalls, etc.) and changes over time, the current practice can be lacking in accuracy and completeness, as well as time consuming and costly if road closures are required for the inspection (Fig.1). Recent advancements in imaging technologies have made their applications practical and possible in more detailed bridge inspections. The technologies can overcome some shortcomings of human subjectivity and are intended to improve and complement, but not to replace, human inspections. The innovative technologies presented herein will be able to make bridge inspections more objective, more consistent, more scientific, and more efficient. The need for utilization of thermography has been advocated especially for detecting subsurface defects using low-cost hand-held infrared cameras by Washer et al. These thermal imaging cameras are intended to be used by the state DOT personnel using while they are conducting their conventional visual inspections and walk-throughs (Washer, et. al, 2009). Guideline requirements developed for the effective application

[1] Executive Vice President, NEXCO-West USA, Inc.

of the technology in the field using the hand-held cameras are also described along with application of the technology for the detection of deterioration in a typical highway bridge (Washer, et. al, 2010). In this paper, the authors present the integrated use of high-end infrared thermography (IR) and line sensors to obtain bridge deck cracks, defects and delamination at a very rapid and high resolution for structural assessment and decision making. The authors present that the integrated system can scan a network of bridges with a special design truck running at 50 mph (without any lane closure) with excellent detail in a matter of couple days. In order to validate the effectiveness of the new inspection technologies, a pilot inspection project was conducted through a joint research effort with the University of Central Florida (UCF). The objective of the research project was to investigate the technologies on the selected bridges to objectively characterize these deteriorated bridges with a university-government-industry collaboration, by exploring the use of novel image based technologies in a way that the information generated through these technologies will provide useful data for the inspection and evaluation of civil infrastructure systems.

Fig.1: Current Bridge Inspection Practice

Innovative Imaging Technologies for Bridge Deck Inspection

The new imaging technologies for bridge inspection described in this paper include the following:

- Line Sensor Camera for deck top surface defects such as cracks and potholes
- IR (Infrared thermography) for subsurface defects such as delamination (detecting possible future potholes)

From November 12th to 14th, 2012, several reinforced concrete bridge decks carrying I-4 in Central Florida area were scanned while driving 50mph by line sensor cameras and an infrared camera mounted on the truck (Fig.2). No lane closures of any kind were needed during the field data collection. The system scanned approximately 13-ft of deck width from each run.

Before visiting the bridge site, detectable crack width was calibrated by scanning a large crack width ruler (Fig.3) at the campus of UCF (University of Central Florida). It was verified that cracks with 1/64” or greater can be successfully detected

by the line sensor camera system.

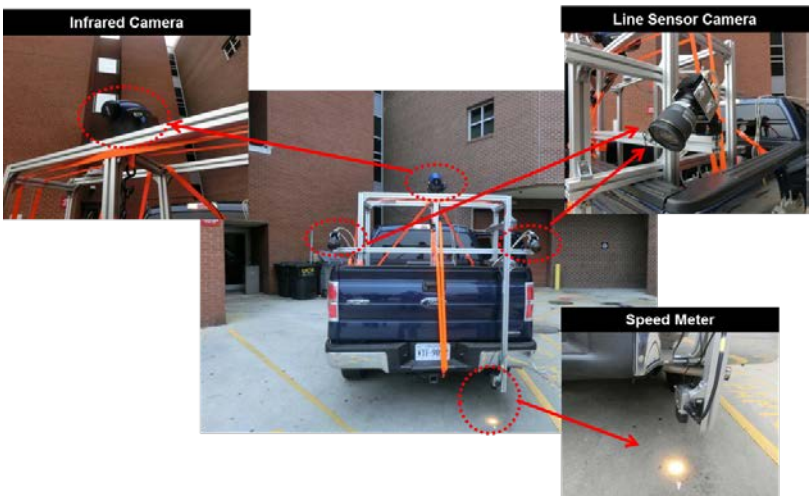

Fig.2: Truck-Mounted Line Sensor Cameras and Infrared Camera

(A Large Crack Width Ruler)

Fig. 3: Calibration of Detectable Crack Width by the System

<u>The pilot Project</u>

During the pilot application, 10 bridges carrying I-4 in Central Florida area were scanned by the system. Fig.4 is the photo of a scanned bridge located in downtown Orlando. The bridge includes 3 spans carrying 4 lanes of the traffic. The 4th (left) lane has been added to the existed three lanes during the recent bridge widening project. Fig.5 depicts the overall condition and defects on the deck surface. Small potholes with the size of 5”-10” and cracks with longitudinal and transversal direction were detected from the scanned visual images obtained by the line sensor camera system. Some of the cracks make hexagonal shape and causing delamination/potholes within the cracking areas. The detected cracks were typically 1/64” (0.3mm) in width. According to the Bridge Inspectors Field Guide (Florida Department of Transportation, 2008), cracks should be classified into three categories as shown in Table 1, and the NBI (National Bridge Inventory) specified “Distressed Area” is calculated for the rectangular area

including “Moderate,” or “Severe” cracks. Most of the detected cracks on this bridge deck shall be categorized as ‘Insignificant’, and these cracks could not be detected by the traditional visual inspection that is typically performed by the bridge inspectors overviewing the deck surface defects from the shoulder. The infrared thermography camera successfully detected the possible delamination in deck concrete as shown in Fig.5 (hatched in pink colour). In order to find such deck subsurface defects traditional technique using chain dragging method (Fig.1- left) requires lane closure during the inspection period.

Fig.4: A Scanned Bridge in Downtown Orlando, FL

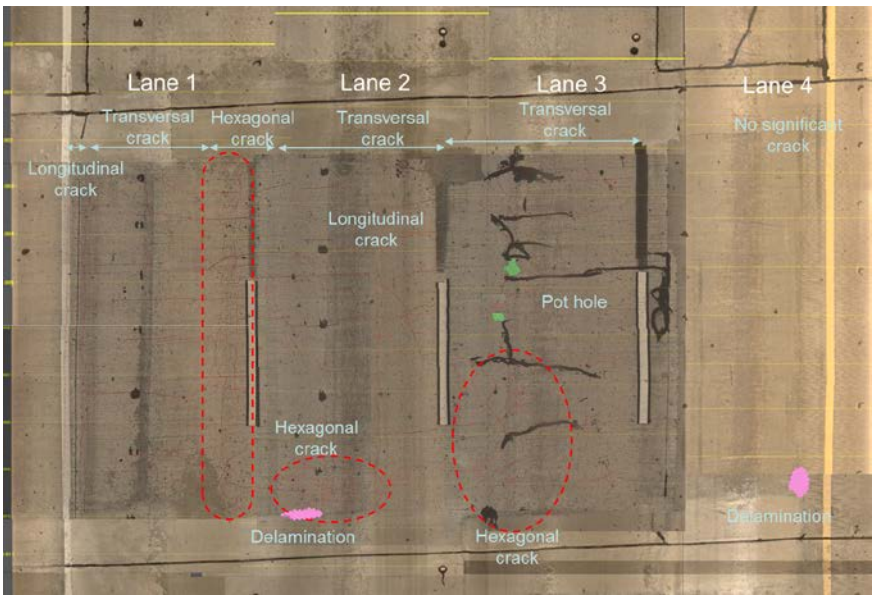

Fig.5: Overall Condition of the Deck at Downtown Orlando

In this study, a sophisticated IR camera was used, which is currently used in industry for delamination detection. The Infrared camera (FLIR 5600) has the shutter speed of 1/1400, enabling the bridge deck scanning team to drive 50mph while collecting the high quality IR images for analysis (where the conventional IR inspection uses lower standard IR camera with only 1/125 shutter speed). The uncooled detector which is used in the conventional IR inspection works by the change of resistance,

voltage or current when heated by infrared radiation, thus requiring longer exposure time to take the IR image. In this study, raw infrared images were further analyzed based on algorithm developed and tested in Japan on many bridges. The proprietary IR software applied in this project can classify the damage rate into three categories; the classification categories being “Critical” (crack caused by delamination reaches on concrete surface and immediate attention is required), “Caution” (crack exists within 2cm from the concrete surface and close monitoring is recommended) and “Indication” (Currently satisfactory) (see Fig.6). Raw infrared (IR) image data is filtered and rated into three categories by the software to indicate and evaluate the severity of the subsurface defects in concrete structures. The real time monitor shows the raw thermal image and filtered/rated images at the field (Fig.7). Fig.8 is an example of the thermal image and software output for a scanned bridge in downtown Orlando.

Table 1: Categorization of Crack Size (FDOT, 2008)

	Insignificant	Moderate	Severe
Crack Size	<1/16”	1/16”-1/4”	>1/4”

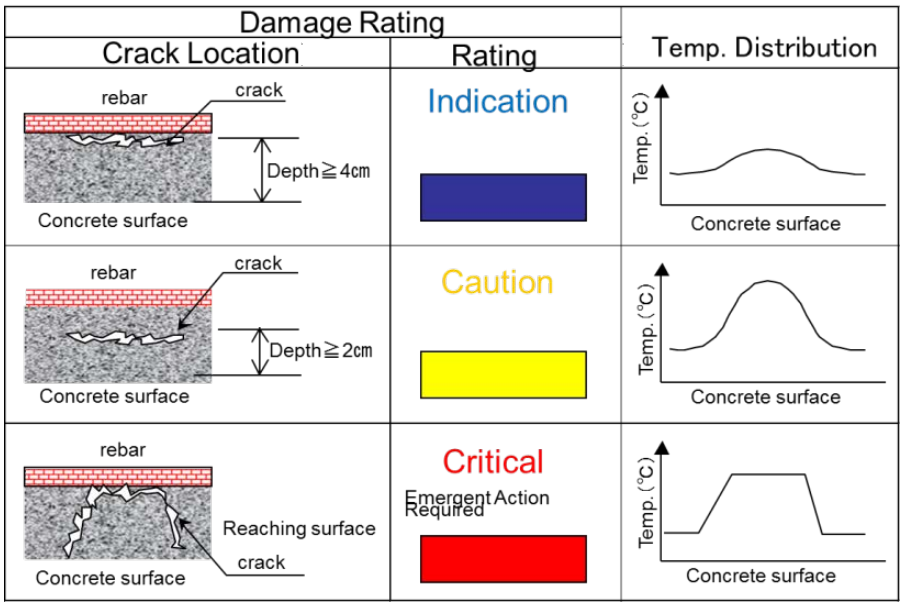

Fig.6: Damage Rating by Infrared Imagery Software

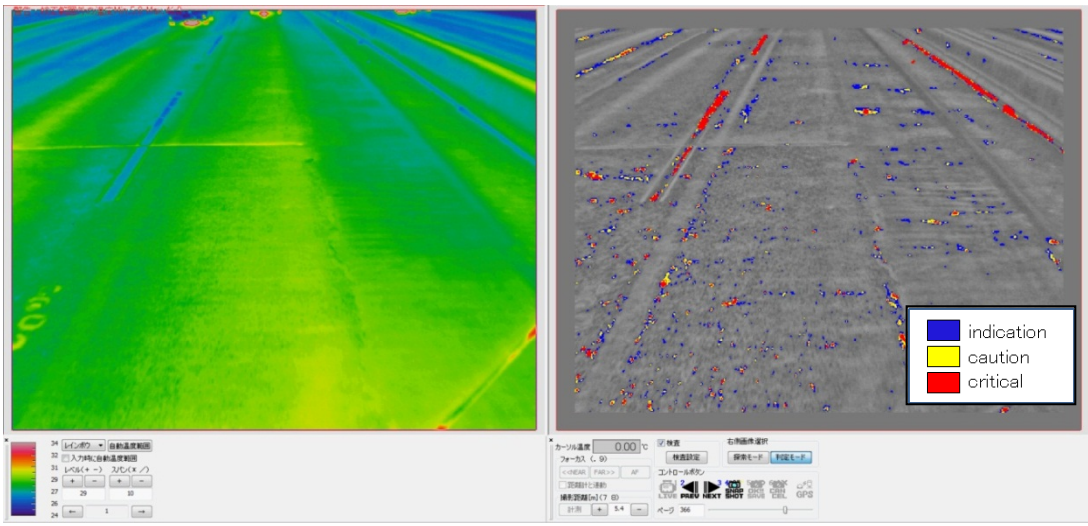

Fig.7: The Real Time IR Monitor (Thermal Image (left) and IR Software Output (right))

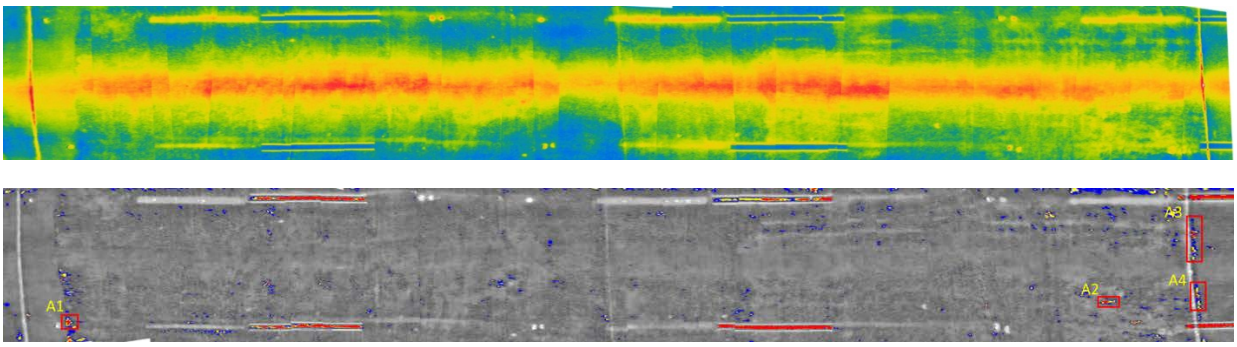

Fig.8: Thermal Image and IR Software Output for the Scanned Bridge

Fig.9 shows an example of detected pothole and possible delamination. Typically, perimeter of the pothole becomes vulnerable to further cracking and delamination due to the concentrated loading, causing the pothole area expanding to the surrounding area. Patching the potholes before it starts growing is a good maintenance strategy to increase the level of safety to the motorists and reduce the total maintenance cost for the bridge owner. Fig.10 shows the visual image and infrared software output at the third lane of the bridge deck. Some potholes and possible delaminated areas were found along the longitudinal construction joint between the widened and existed decks, especially at the shear key locations. Fig.11 shows an example of the visual image and infrared software output close to the expansion joint. Delaminated areas in concrete were found at the boundary of existing deck concrete and the concrete placed after the settlement of expansion joint. These ‘boundary’ areas between the concrete placed in different time period can be the possible weak spots to initiate potholes and delaminated areas.

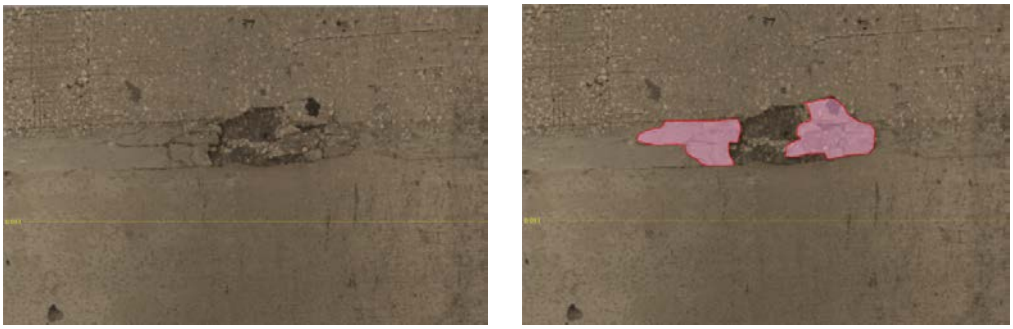

Fig.9: Detected Pothole and Possible Delamination

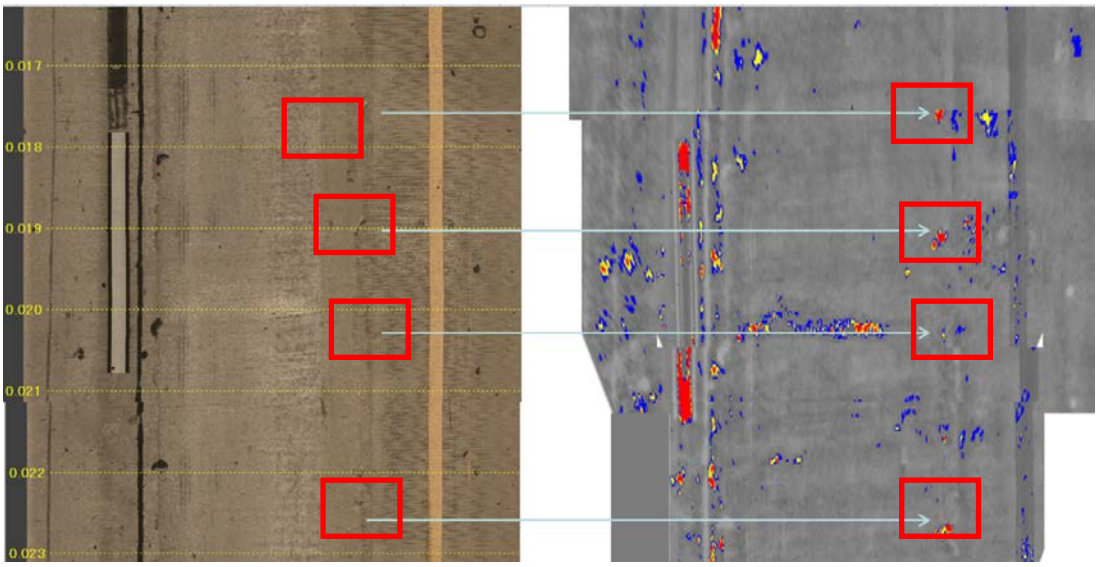

Fig.10: Visual Image (left) and IR Software Output (right) at Longitudinal Construction Joint

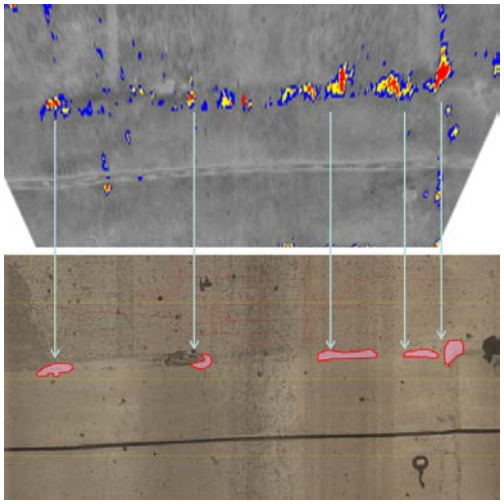

Fig.11: Visual Image (bottom) and IR Software Output (top) at Expansion Joint

Table 2 describes the four condition states defined in the AASHTO Guide Manual for Bridge Element Inspection (AASHTO, 2011). Based on the AASHTO Manual, the condition states for each span/lane of the bridge deck were determined and summarized in Fig.12. Cracking significance and patterns varies for each span/lane of the bridge deck. If we could apply this deck scanning system to the corridor level inspection and determine the condition state for each span/lane of each bridge in the network, the bridge owner can use this information to prioritize the bridge deck repair/rehabilitation program and efficiently allocate the limited budget to obtain the maximum return on investment for the network level bridge management.

Table 2: Standard Condition States for Defects in Bridge Elements (after AASHTO, 2011)

Condition State #	Condition State
1	Good
2	Fair
3	Poor
4	Severe

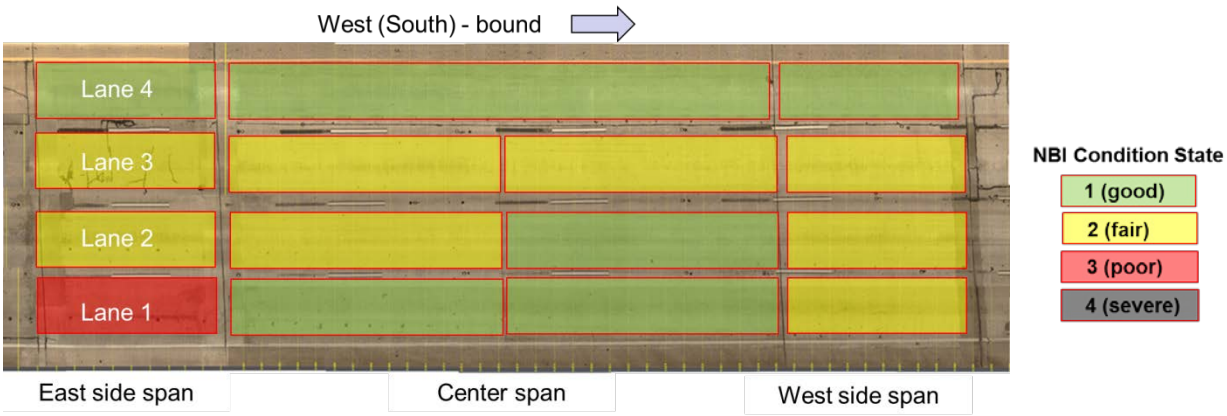

Fig.12: Determining the Condition States for Each Span/Lane of the Bridge Deck

Fig.13 shows an example of potholes with corroded rebar exposed on the deck top for another bridge on I-4. The cause of the spall in deck top concrete could be lack of cover thickness and/or corrosion of rebar. The infrared software shows some potential delamination around the spalled concrete and other potential deck subsurface delamination as shown in Fig.14, indicating the possible rebar corrosion and occurrence of future pothole. The red line in Fig.14 is estimated re-bar location on the deck top side (interval of rebar estimated to be approximately 8” from the two exposed rebar shown in Fig.13).

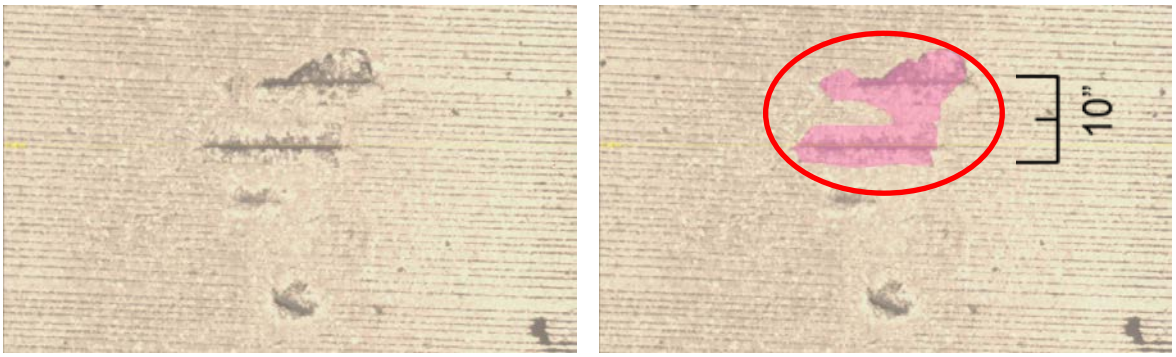

Fig.13: An Example of a Pothole with Corroded Rebar Exposed

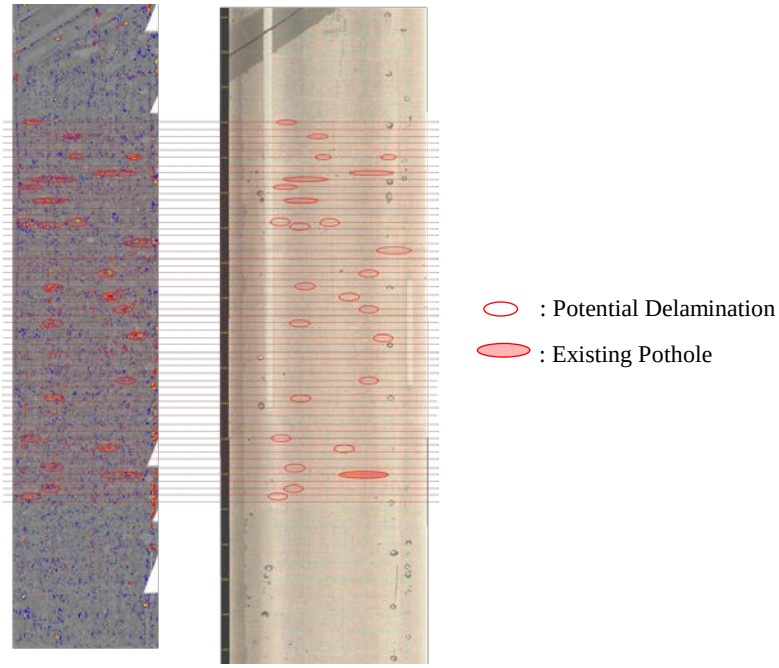

Fig.14: Visual Image (right) and Infrared Software Output (left)

Application to the Corridor Level Inspection

Bridge decks with some possible symptom of deterioration detected by overviewing the scanned images require further intensive analysis using the combination of high resolution digital image and the results of infrared thermography. The deck scanning system can calculate the distressed deck surface area in terms of cracking and delamination. The percentage of distressed area for the total deck surface can be used as a quantitative index to determine the degree of deterioration for each span/lane of the bridge. If we could apply this deck scanning system to the corridor level inspection and determine the condition state for each span/lane of each bridge in the network, the bridge owner can use this information to prioritize the bridge deck repair/rehabilitation program and efficiently allocate the limited budget to obtain the

maximum return on investment for the network level bridge management.
Fig.15 depicts the recommended flowchart for phase-by-phase corridor level bridge deck inspection. The purpose of the first phase of corridor level inspection is to collect the high resolution digital image and infrared inspection results in the field without any lane closure. The Phase 1 inspection generates the edited video image for deck top scanning results with potholes and major crack location identification. The scanned image of the structural members can be used to locate the areas of cracking and delamination and quantitatively summarize the distressed deck areas and determine the condition state for each span/lane of the bridge (Phase 2). Based on the quantitative summary of percentage of distressed deck surface area, the span/lane of the bridge with distressed areas over pre-determined threshold value can be 'flagged' and lined up in the list of 'candidates' for bridge repair/rehabilitation program. Threshold values for percentage of distressed area in determining the AASHTO element level inspection is proposed in Table 3 (edited from the reference, Minnesota Department of Transportation, 2011). The threshold values and decision making indices can be tailored based on the need and requirements of different bridge owners. The outcome of the Phase 2 inspection can be used to pre-screen the bridges possibly being deteriorated or showing symptom of future deterioration, and support the bridge inspection engineers to determine the priority for repair/rehabilitation program in a quantitative matter. Moreover, the new inspection technology provides additional benefits by increasing the level of safety for both inspectors and motorists and storing historical inspection data for the monitoring of crack/delaminated area propagation. In addition, deck underside scanning (Matsumoto, et. al, 2013) may be recommended for selected spans of the bridge deck requiring additional information to further investigate the cause and/or degree of deterioration (Phase 3). The digital record taken by the deck top scanning system can contribute to monitor the progress of damage over time, allowing the bridge owner to monitor the long-term bridge performance and predict the future condition of the bridge deck that would support the better decision on bridge maintenance and management.

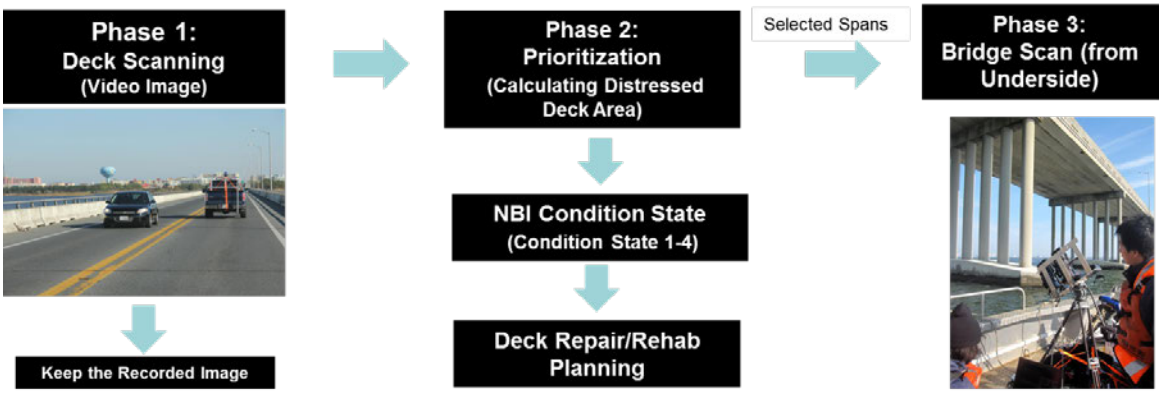

Fig.15: Recommended Flowchart for Phase-by-Phase Corridor Level Inspection

Table 3: Proposed Threshold Values in Determining the Condition States
(edited from MnDOT, 2011)

Condition State	Description
Condition State 1	The combined area of unsound wearing surface (spalls, delaminations, delaminated temporary patches) is 2% or less of the total deck area
Condition State 2	The combined area of unsound wearing surface (spalls, delaminations, delaminated temporary patches) is more than 2% but not more than 10% of the total deck area
Condition State 3	The combined area of unsound wearing surface (spalls, delaminations, delaminated temporary patches) is more than 10% but not more than 25% of the total deck area
Condition State 4	The combined area of unsound wearing surface (spalls, delaminations, delaminated temporary patches) is more than 25% of the total deck area

Summary and Conclusions

(1) The field data collection by deck top scanning system using line sensor cameras and infrared camera was successfully finished without any kinds of lane closure. Cracks with 1/64” (0.3mm) or greater in width and possible delaminated areas were successfully detected by the system.

(2) Combination of line sensor cameras and IR camera system (Deck Top Scanning System) will provide complete information on surface and subsurface conditions of concrete bridge decks and contribute to find a symptom of possible future deterioration in its early stage, allowing the bridge owner to proactively take an action to make a batter decision on repair/rehabilitation planning.

(3) The phase-by-phase corridor/network level bridge inspection described in this paper can efficiently pre-screen the bridges with potential problems and need more detailed analysis to determine the NBI condition states for each span/lane of the bridge deck.

(4) Periodic collection of the data will allow consistent and accurate documentation of structural condition changes over time. For example, temporal subtraction of crack map will present changes of crack widths and lengths, as well as other surface features, between specific times in a concise and scientific manner. This function of the scanning system can replace the ‘in-situ monitoring’ of crack length/width and deformation of the structure.

(5) Selected imaging data and results of periodic temporal subtractions can be prepared in any file format and integrated into the Bridge Management System (BMS), such as Pontis® or bridge inventory database system to provide complete and objective information for better bridge management decisions.

References

American Association of State Highway and Transportation Officials (AASHTO, 2011): “AASHTO Guide Manual for Bridge Element Inspection,” First Edition

Florida Department of Transportation (2008): Bridge Inspectors Field Guide Structural Elements

Matsumoto, M., Mitani, K. and Catbas, F. (2013): Bridge Assessment Methods Using Image Processing and Infrared Thermography Technology: On-Site Pilot Application in Florida. Compendium of Papers of the 92nd Annual Meeting of the Transportation Research Board. Transportation Research Board, National Research Council, Washington, DC.

Minnesota Department of Transportation (2011): Bridge Inspection Field Manual. Minnesota Department of Transportation: Oakdale, MN.

Washer, G.A., Fenwick, R.G., Bolleni,N.K., and Harper, J. (2009), “Effects of Environmental Variables on the Infrared Imaging of Subsurface Features in Concrete Bridges,” Transportation Research Record 2108: Journal of the Transportation Research Board, Washington, D.C., pp. 107-114.

Washer, G., Bolleni, N.K., Fenwick, R.(2010), “Thermographic Imaging of Subsurface Deterioration in Concrete Bridges,” Transportation Research Record: Journal of the Transportation Research Board, No. 2201Washington, D.C., pp. 27-33.

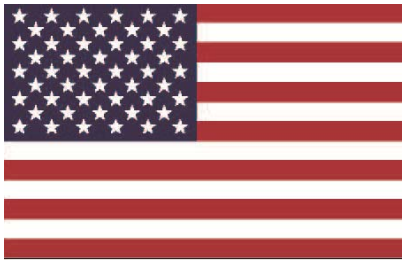

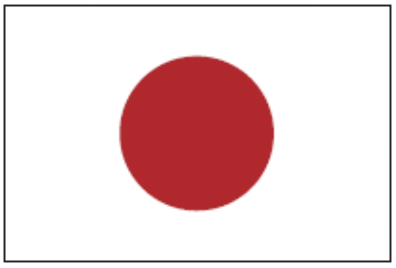

29th US-Japan

Bridge Engineering Workshop

Session 4

Retrofit and Repair Work

The Skagit River Bridge Collapse and Recovery Plan

Bijan Khaleghi[1]

Abstract

The Skagit River Bridge in Interstate 5 in Burlington Washington was struck by an oversize-load vehicle and the northern truss span of the bridge collapsed into the into the river. Emergency responders at Washington State Department of Transportation (WSDOT) and partnering agencies mobilized immediately and, thankfully, no lives were lost.

The WSDOT recovery plan to reconstruct the Skagit River Bridge comprises of three contracts: 1) installing a temporary bridge to reconnect the Interstate 5; 2) Replace the permanent span using the accelerated bridge construction technics, and; 3) Rehabilitate the remaining trusses to the current functionality standards.

Introduction

On May 23, 2013 the evening commute was just ending along a four-lane stretch of the Interstate 5 corridor, which lies between the Canadian Border and Seattle. At roughly 7 p.m., a semitruck heading southbound and carrying a permitted oversized-load struck the first portal and several subsequent sway members along the steel truss section of the bridge. The northern truss span of the bridge collapsed into the Skagit River. While the semi-truck made it across hitting several more sway frames along the way, several vehicles didn't and the occupants had to be rescued. No one was killed in the collapse.

The Washington State Patrol (WSP), the Washington State Department of Transportation (WSDOT) and local agencies responded immediately, setting up and manning detour routes both east and west around the bridge.

WSDOT immediately responded with bridge engineers to assess the damage and begin plans for both emergency and permanent repairs, while communication staff responded to the media sent out updates and Freight Alerts region wide. Traffic engineers worked through the night to refine the detour routes for the roughly 71,000 vehicles that were detoured through the city streets of Burlington and Mount Vernon.

Within 24 hours a contractor was hired under an emergency contract to remove the collapsed span, and began working with WSDOT engineers to install a temporary span to get the Interstate back open. As the work was being done to temporarily restore I-5 traffic, WSDOT engineers began assembling contract documents for a permanent span repair.

[1] State Bridge Design Engineer, Washington State Department of Transportation, Bridge and Structures Office

Bridge Type Selection for Replacement Span

Within hours of the collapse, discussions were underway at WSDOT about how best to replace the collapsed span, and how to restore traffic as quickly as possible. Time requirements, vertical clearance requirements, and superstructure dead load limitations quickly became the primary guiding factors in designing the span replacement.

Minimizing traffic disruptions dictated the installation of side-by-side single lane temporary modular truss bridges (supplied by ACROW, and subsequently replaced with the permanent span). For navigational purposes, vertical clearance to the river below had to be equal to or greater than that provided by the original truss span. And, importantly, to minimize any additional seismic inertial loads to the existing bridge substructure, the dead load of the replacement span could not exceed the dead load of the original truss span by more than 5%.

Three options were investigated for permanent span replacement; a steel through-truss (a near duplicate of the original span), a steel plate girder span with concrete deck, and a prestressed concrete girder span with concrete deck. The steel through-truss, though light in weight and aesthetically consistent with the original bridge, was thought to be too time-consuming to fabricate and erect. The project was advertised for Proposal with the assumption that the most-likely structure types for Proposal were going to be the steel or concrete girder options.

Four Design-Build Teams submitted Proposals for the Permanent Span Replacement. Two of the Proposals included steel girder replacement spans, and the remaining two Proposals included prestressed concrete girder span options. WSDOT selected the best value proposal, which utilized a prestressed concrete girder deck bulb tee replacement span. Lightweight concrete was specified for the girders, diaphragms and barriers, to stay within the stipulated span dead load limitations. The concrete girder Proposal chosen offered competitive initial costs, low overall life-cycle costs, the shortest girder procurement time, and the minimum closure time required to replace the temporary span with the permanent span.

Replacement Span Design

The WSDOT recovery plan to reconstruct the Skagit River Bridge consisted of constructing the permanent replacement span using the accelerated bridge construction technics. The permanent replacement span, composed of deck bulb tee girders made of lightweight aggregate with concrete overlay, was built adjacent to the bridge and its temporary span as shown in Figures 1 and 2. The roadway was closed to traffic for a period of 19 hours while the temporary span was moved out and permanent replacement span was moved into position.

Figure 1. Conceptual Truss Span Replacement with Prestressed Concrete Girders

Figure 2. Conceptual Temporary Bridge and Setup for Span Replacement

The new permanent bridge was analyzed and designed using the current LRFD Bridge Design Specifications and the WSDOT BDM. The WSDOT Bridge and Structures Office provided over the shoulder reviews of the design, shop drawings, and construction submittals.

In order to limit the weight of superstructure, the girder spacing of 2.316 m was considered to keep the replacement structure as light as possible. Using 2.316 m girder spacing eliminated one line of girders to reduce the total superstructure weight. The total weight of new superstructure including the lightweight concrete traffic barriers and concrete overlay was 915 tons, within the limit required by the contract. Figure 3 shows the headed bars of deck bulb tee girders at the fabrication plant.

Figure 3: Headed bars at closures

Differential camber and reflective cracking are the two performance challenges involved with use of deck bulb tees for long spans. In order to minimize the reflective cracking the superstructure design required 1) use of 38 mm of concrete overlay instead of HMA for this project, 2) use of high strength concrete closure and overlapping bars instead of welded ties.

The differential camber was adjusted using the leveling beams prior to casting concrete at the closures. The predicted camber for lightweight deck bulb tee girders was 6.5”, and the measured girder cambers were slightly above the predicted camber. The Span to depth ratio of 29.5 for the new superstructure met the LRFD Bridge Design criteria for deflection. Figure 4 shows the variation between measured and predicted cambers.

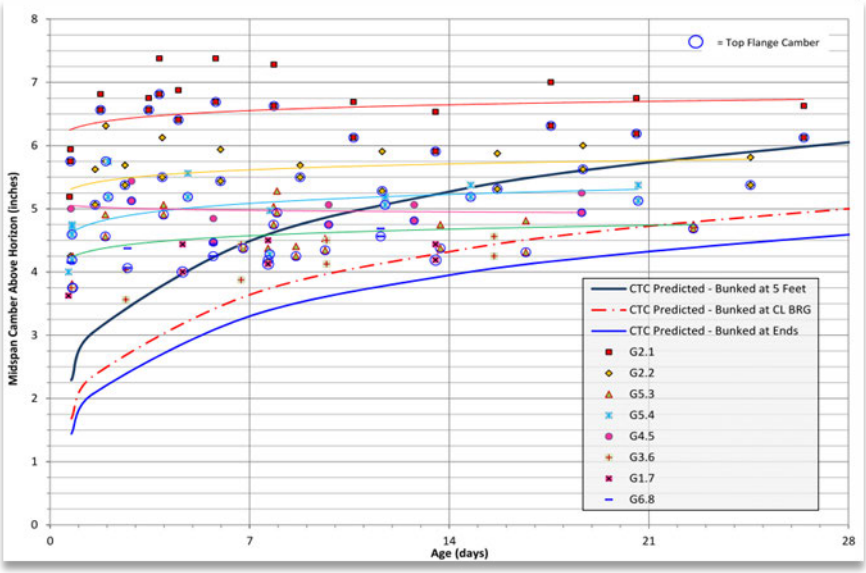

Figure 4: Measured and predicted cambers.

The design compressive strength of lightweight concrete used for the deck bulb tees was 62mPa, with a compressive strength of concrete at transfer of prestress of 48 mPa. The unit weight of lightweight concrete mix was 1952 kg/m^3, with unit weight of girder of 2128 kg/m^3 for design and dead load calculations. A total of 48-15mm diameter strands was used for design of girders.

Two temporary supports at 6 m from the end of girders were provided at intermediate diaphragms locations to accommodate bridge move. Temporary strands in top flange of girders were provided to compensate stresses due to negative moment at the temporary supports.

Replacement Span Construction

The Design-Build method was used with the goal of rapid construction. The project's scope of work included construction of the new span adjacent to the bridge's two temporary spans, then removal of the temporary spans and placement of the single, permanent span.

The permanent superstructure was constructed on a steel piling and bents, just downstream of the temporary spans as shown in Figure 5.

Figure 5: Permanent superstructure constructed on a steel piling and bents downstream of the temporary spans

The girders were set using a 500 ton crane on the river's dike and a 200 ton crane on a Flexifloat barge system. The crane picks were quite detailed. Each pick required 19 specific moves, including passing the end of the girder from the dike to the barge crane, tucking the girder under the boom of the barge crane - while re-ballasting the barge system - and finally re-ballasting the barge as the girder was placed on the temporary bent.

A time lapse series of the entire girder setting operation can be found at this link (www.youtube.com/watch?v=-IdUap4_IvY)

A separate row of piling and bents were built to support a rail system that would be used to slide the temporary spans out, and slide the new span into place as shown in Figure 6.

Figure 6: Supports for slide of the new span into place

To complete the bridge, the girders were tied together with closure pours between the girders and end diaphragms. This was followed by pouring the traffic barrier and a 38 mm micro silica deck overlay. A separate intermediate set of diaphragms or jacking beams were also installed using reinforced cast-in-place concrete. Figure 7 shows the placement of deck bulb tee girders.

Figure 7: Placement of deck bulb tee girders

A vertical and horizontal jacking system was concurrently installed using a rail system supported by temporary piling and bents as shown in Figure 8.

Figure 8: Jacking system for Bridge Slide

To complete the installation of the new span, first the temporary spans were lifted off the existing substructure and slid off onto the temporary bents upstream of the bridge. The new span was moved in a similar fashion, with the exception that it needed to be shifted a half inch to fit into place. Figure 9 shows the slide of the temporary Bridge.

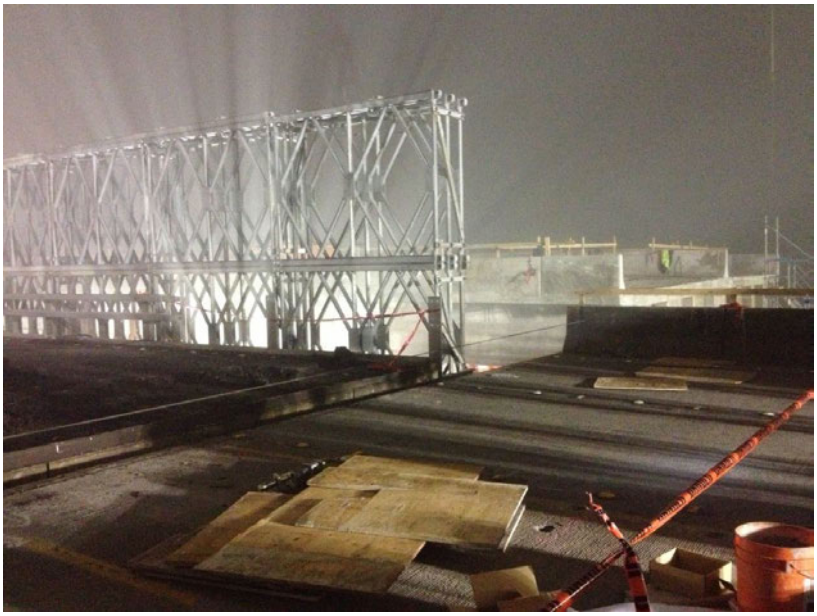

Figure 9: Temporary Bridge Being Slide Out

The overall construction started on July 12 and the new span was opened to traffic on September 15. It took just under 19 hours to swap the spans and open the freeway to traffic as shown in Figure 10.

Figure 10: Completion of Span Replacement

To finish up the work, the temporary spans were disassembled onto the Flexifloat barge system and all of the piling was removed from the river as shown in Figure 11.

Figure 11: Dismantling of Temporary Bridge on Flexifloat Barge and Removal of piling

Conclusion

Successful as the replacement of the collapsed bridge was (the number of closed days totaled only 28), there is little rest for the designers and contractors. With the permanent replacement span in place, attention turns to the remaining sway-frame truss sections and their vertical clearances. While truckers are responsible for their over-height loads, states are prudent to examine over-height hits and apply mitigation if possible. In this case that means removing and replacing the lowest height elements of the trusses, increasing the vertical clearance across the two outside lanes, helping to extend the already long-life of the I-5 Skagit River Bridge.

Repair Works on a Composite Girder Cable-Stayed Bridge damaged by Ship Collision (Binh Bridge in Vietnam)

Tomonobu Tokuchi, Shinji Kaifuku, Satoshi Kawabata, Tatsuya Idani

Abstract

The Binh Bridge, a 3-span cable-stayed bridge with composite girders and a center span of 260m, was opened to traffic in 2005. In 2010, 3 ships swept upstream by a typhoon collided with the bridge, resulting in serious damage to the main girder and several cables. Repair and rehabilitation works on the bridge were awarded to IHI Infrastructure Asia Co., Ltd.

The complexity of repairing a composite girder cable-stayed bridge required the utilization of innovative methods in the analysis, planning and execution of the repair works. The repair works included, cutting of the damaged steel girders and on-site welding of new plates and stay cable replacement utilizing the adjacent stay cables in temporary hanger system that reduced erection loads during repair works.

Introduction

Binh Bridge, located in Haiphong City, Vietnam, is a 3-span cable-stayed bridge with composite girders and a center span of 260m that was completed in 2005. Figure 1 shows a complete view of the Binh Bridge at completion. In July 17th 2010, three cargo ships that had been moored for repair at a shipyard near the Port of Haiphong were carried approximately 600 m upstream by typhoon No. 1 and collided with the composite girder of the Binh Bridge. Fig. 2 shows a general view of one of the ship's bridge stuck onto the composite edge girder after collision.

Figure 1 Binh Bridge at Completion

Figure 2 Ship Collision of Main Girder

In response to a request from the Binh Bridge Management Company, IHI Corporate Research & Development, IHI Infrastructure Systems Co., Ltd. (IIS) and IHI Infrastructure Asia Co., Ltd. (IIA) working together as the IHI Group, initiated investigations and evaluations of the degree of damage immediately after the accident. A damage report was submitted together with a proposal of the repair method. The works were classified as part of the ODA (Official Development Assistance) emergency assistance program and in March 2012, IHI Group was given awarded the repair works of the bridge.

The Binh Bridge is designed as a cable-stayed bridge with a composite girder of 2 steel edge girders and a concrete deck slab, making the stress conditions in the main girder to be influenced by the bridge's construction steps. Accordingly, to evaluate the stress levels in the damaged sections, it was necessary to faithfully simulate the construction stages in an analytical model. By conducting these analyses particularly carefully, the repair of the girder and replacement of the stay cable were performed without incident.

This may have been the first attempt in the world to repair the main girder of a composite-girder cable-stayed bridge. In addition, replacing the cables of a cable-stayed bridge was a first experience for IHI, and only a small number of cases have been reported in the world. It is for these reasons that we are reporting on this valuable experience.

Damage Outline

The main areas of damage were; lower-flange of the main girder (22.5m), two stay cables, the guard railing and a navigation sign board in downstream side. (Figure 3)

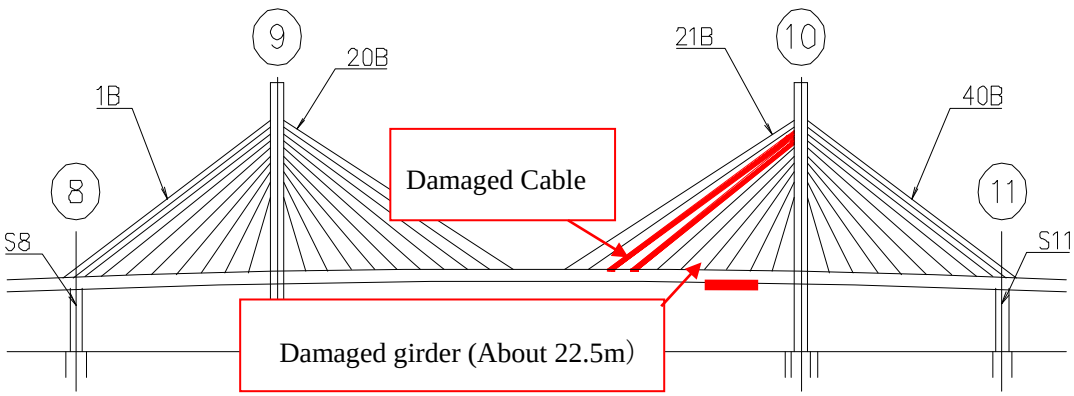

Figure 3 Damage locations on bridge

The main girder lower-flange was deformed in the out-of-plane direction with the vertical stiffeners exhibiting complete buckling. Figure 4, 5 show the damaged edge girder. However, the floor beams and concrete deck slabs were undamaged and sound.

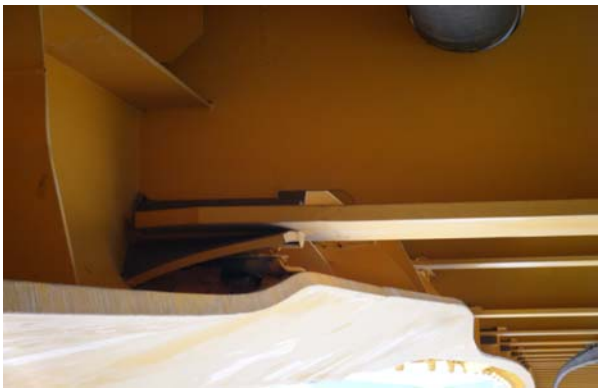

Figure 4 Damaged Edge Girder (Inner side)

Figure 5 Damaged Edge Girder (Outer side)

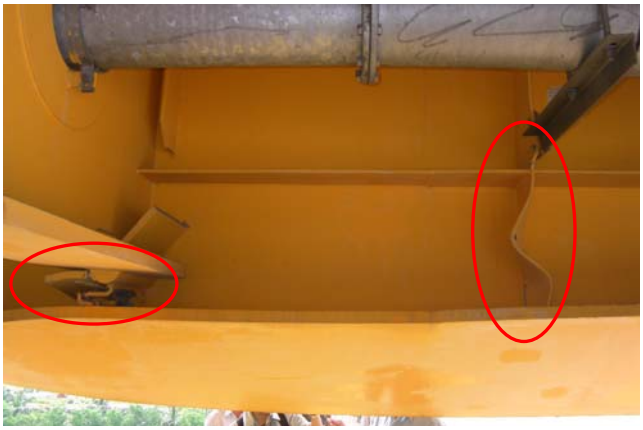

Figure 6 Buckled Stiffeners

Figure 7 Cable Damage

The polyethylene cover(PE cover) of the two stay cables was peeled off completely exposing the wire strands which had partial damage to the galvanizing cover. Figure 7 shows the damaged cable. “White rust” of the zinc coating was also observed. From the damage condition, it was obvious that salty water had gone into the stay cable and thus the stay cable would require replacement.

Traffic Control

After the accident, we restricted traffic until safety was confirmed. Only one of the lanes out of the four lanes was open to traffic (upstream side). This lane was opened as a two-ways lane for use by two-wheeled vehicles.

Subsequently, we conducted analysis on the assumption that the lower half of the cross section of the main girder was damaged. It was thus confirmed that the main girder would have a slight margin of stress, so we eased the traffic control to allow passenger cars with a mass of 20 kN or less to pass through one lane and the sidewalk on the upstream side.

Our repair work started in May 2012, and in order to use heavy machines such as construction cranes, passenger cars were restricted crossing the bridge all day to constrain the traffic of heavy objects other than construction machines and materials for the repair work. Automobiles crossing the river were asked to use a temporarily operated ferry or another bridge located 5 km upstream during the period of this traffic control.

Evaluation of Damage to Girder

The main girder was significantly bent on the bottom flange side by the collision and had residual plastic deformation. A web was pulled by the bottom flange until it developed out-of-plane deformation. Webs had cracks in places near cable anchorages and were shifted by a distance nearly equal to the plate thickness (20 mm) in an out-of-plate direction. Stiffeners on the inner side of the main girder were pushed upward by the bottom flange until they were buckled, and it was impossible to replace the stiffeners. Figure 6 shows the buckled stiffeners.

We conducted evaluation in terms of the strain of the plates with the aid of Expression (1) below. In the evaluation, we used cold bending radius 5t (ε = 10%) that is stated in the Specifications for highway bridges as a guide, in order to achieve Charpy absorbed energy higher than or equal to the required performance[(2)] of steel materials from the viewpoint of ensuring the toughness of steel plates. Figure 8 shows the surface curvature of bent plate being measured.

$\varepsilon = t/(2R)$ …… (1)

t: Plate thickness

R: Surface curvature

Figure 8 Surface curvature of bent plate

The simple strain evaluation by this method revealed that most portions had a strain of 3% (corresponding to a load of 15t) or lower. The strains were at levels that would not cause problems. However, we determined to replace portions with cracks and those with apparent residual deformation anyway. The bridge portion that would be replaced is approximately 22.5 m long in the longitudinal direction and 1050 mm

from the bottom of the main girder, which is slightly higher than half of the girder height. Figure 9 shows the portion that would be replaced in the main girder.

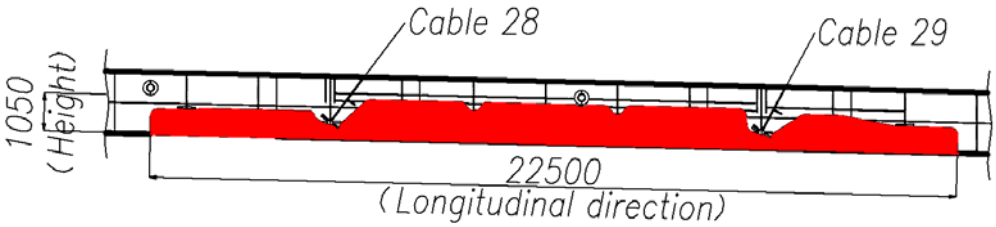

Figure 9 Replaced main girder range

Evaluation of Damage to Cables

Since the wires of the damaged cables were not broken, we judged that their tensile strength was not degraded. The durability of a cable is affected by scratches and corrosion on the surface of its wires. This is because their fatigue strength varies depending on scratches and corrosion. For cable-stayed bridges, the durability of their cables means the durability of the bridges. Accordingly, measures to repair damage to cables need to be taken as quickly as possible.

In this investigation, damage to PE cover, scratches on cable wires, damage to galvanized paint on the wires, and development of white rust were observed. These types of damage pose severe problems for cables.

Influence of Scratches of wire

Scratches deep enough to catch a fingernail were observed on parts of the surfaces of element wires that were exposed to the atmosphere with PE covers removed. The scratches were formed in the axial direction, making it easy to see that a steel material slid axially along the surfaces of the element wires.

Since the scratches on the surfaces of the element wires were small, it was presumed that the static strength of the wires had not been degraded. The fatigue strength of the wires, however, varies depending on the shape of the scratches, and even a scratch as long as 100 μm may cause strength degradation. Accordingly, the fatigue strength of damaged element wires should be regarded as degraded. However, it was presumed that only the element wires on the outermost layer of the steel wire bundles were scratched and that the element wires in the inner layers were sound. Therefore, we concluded that cable fatigue evaluation with the influence of corrosion ignored should be performed on the premise that loads acting on the cable will be supported only by inner-layer element wires.

Influence of Corrosion of wires

White rust developed on the surfaces of element wires that were exposed to the atmosphere as their PE covers had been stripped away. This fact suggests that after the PE covers had been stripped away, the surfaces of the element wires were exposed to rainwater. Accordingly, it is presumed that rainwater permeated the steel wire bundles and accumulated in the bottoms of the cables.

The zinc layers (minimum: 300 g/m^2) of galvanized steel wires immersed in seawater will likely corrode until they completely disappear in as little as one year. In addition, after the zinc has been lost, the corrosion of steel wires will progress which degrades the fatigue strength.

The Binh Bridge is located near an estuary that is exposed to sea breezes. Accordingly, the rainwater collecting in cables presumably contains salt. Therefore, there was the possibility that in the rainwater-holding portions of the third (No. 23) and fourth (No. 24) cables from the top, zinc on the surfaces of element wires would be lost in as little as one year and that the cable fatigue strength would start to degrade.

It was difficult to accurately evaluate the durability of the damaged cables, so it was impossible to guarantee their quality for the future. Therefore, we determined to replace the damaged cables with new cables.

Cable Socket Portions

In three cable socket portions of other cables, abrasion that seems to have been made due to contact with a steel material was found. In the main bodies of some of these sockets, indentations were found in the corner portions at their ends, but no abnormalities were found at the anchorages, which are the most important parts. Some of the anchor caps were partially deformed and had damaged bolts.

No cracks were found in the painting at the member boundary portions between cable sockets and shim plates and between shim plates and washers. This indicates that the cable sockets did not rotate or move in the accident. Therefore, we judged that the three anchors that had scratches on their cable sockets would function soundly such that cable replacement would not be required.

Repair and rehabilitation works

After long detailed investigation by the Employer, IHI was awarded this repair and rehabilitation works on the Binh Bridge in March 2012. These works included all of the repair and rehabilitation works (Edge Girder, Stay Cable, Railing, concrete deck slab and so on).

Repair of Girder

Before partially replacing the damaged portion of the main girder, we first examined section forces by analysis with consideration given to continuous composition performed at the construction stage of the bridge and thereby investigated the stresses exerted in the present state of damage. Since the bridge consists of a composite girder, the stress check was performed by adding the stresses exerted before the composition and those exerted after the composition. This process allowed us to estimate the stress condition before the accident. However, it was difficult to estimate the stiffness degradation of the portion damaged by the accident and to examine stress redistribution due to the stiffness degradation. Consequently, we were not able to accurately ascertain the stress condition after the accident.

Therefore, as our reinforcement policy, we determined to provide additional reinforcement ensuring sectional performance higher than or equal to the section stiffness of the main girder in a sound state, so that when the main girder was undergoing partial cutting, the section force of the cut portion and fluctuating loads would be supported. We decided to cut and replace the damaged portion under these conditions.

In addition, we designed reinforcements for supporting the section force according to the following policy. We assumed that after the accident, the bottom flange and web of the damaged girder were also supporting stresses occurring in a sound state. We also assumed that stresses released by cutting the damaged portion on the above assumption would be redistributed to the reinforcements and the remaining portion of the girder. Based on these assumptions, we designed the required section of the reinforcements.

Side view

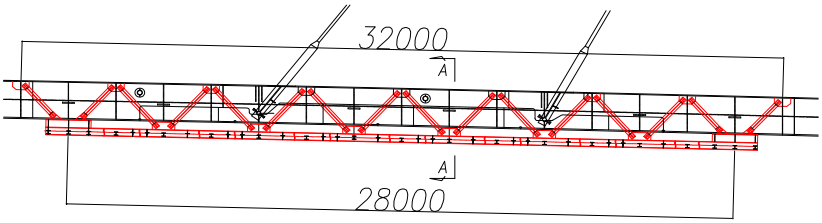

A-A Section

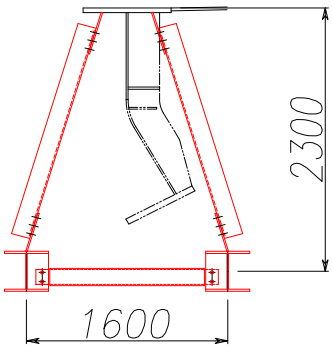

Figure 10 Temporary Bypass Truss (Drawing)

In order to partially cut the main girder and remove the cut portion to replace it with a new member, it was necessary to first attach reinforcements for supporting the section force. A large crane was not able to be placed immediately above the damaged portion, so we were only able to place a hydraulic crane with a lifting capacity of 1000 kN. Moreover, in order to perform the repair work, we needed to pass the boom of the crane through the space between existing stay cables. It would be impossible to transfer very large members through the space. Since we could only use limited equipment to reinforce the bridge and with limited space, we determined to perform the reinforcement work by using a truss structure (Temporary Bypass Truss). Figure 10 illustrates the structure of the truss.

Figure 11 Temporary Bypass Truss

Repair of main girder

In the process of installing scaffolds and the temporary bypass truss, the main girder was first marked with girder cutting lines and reference lines. We arranged rails consisting of channel steels with rollers on the scaffolds and the temporary bypass truss in order to allow members to be transferred horizontally.

Figure 12 Cutting of the damaged parts

By cutting a web of the damaged portion, the remaining side of the web would form a free end, and stress would be released. There was a possibility that the released stress might be redistributed near the free end causing the web to develop local buckling. Accordingly, before cutting the damaged member, we added a horizontal stiffener near the portion that would become the free end of the web in order to reinforce the portion.

In order to compare the actual stresses with those calculated for design, we attached a uniaxial strain gauges to the upper and bottom flanges of the main girder and the temporary bypass truss and measured the stresses and strains at each construction stage to confirm safety. We also measured the elevation of the main girder at each major construction stage to confirm that no abnormal values were observed.

Cutting girder and groove making were performed on site. Dismantled girder was cut to approximately 2m pieces for easier handling when transferring the pieces from under bridge to over the deck slab easily.

After exact measurement of the remaining girder piece, the new girder member was fabricated the factory of IHI Infrastructure Asia.

Figure 13 Fabrication of new parts

Figure 14 Installation of new parts at site

Replacement of damaged Stay Cable

The cable adjacent and above the damaged cable was used as a Temporary Hanger System. This system reduced the sag of the cable being removed and the one being installed, resulting in efficient installation works. This replacement work's procedure is shown in the following figure.

The installation step details are as follows

1) Install the scaffolding around cable anchorage of pylon side and girder side.

2) Center-hole Jack and tension rod are installed on the anchorage of girder side.

3) Winch for lifting up or down device is installed.

4) Pulleys to be able to move on the cable are installed on the Stay Cable adjacent and above the damaged cable. Temporary hanger System is hanged from pulleys.

5) Band of Temporary Hanger System is fixed to replacement cable to support the self-weight of replacement cable with tensioning by Temporary Hanger System.

6) At the anchorage of girder side, the tension of existing stay cable is un-load by Center-Hole jack.

7) Remove the socket from the anchorage of girder side.

8) Remove the socket form the anchorage of pylon side.

9) Replacement cable with pulleys is lifting down by Winch.

In case of installation of new stay cable, opposite works of abovementioned procedure is performed.

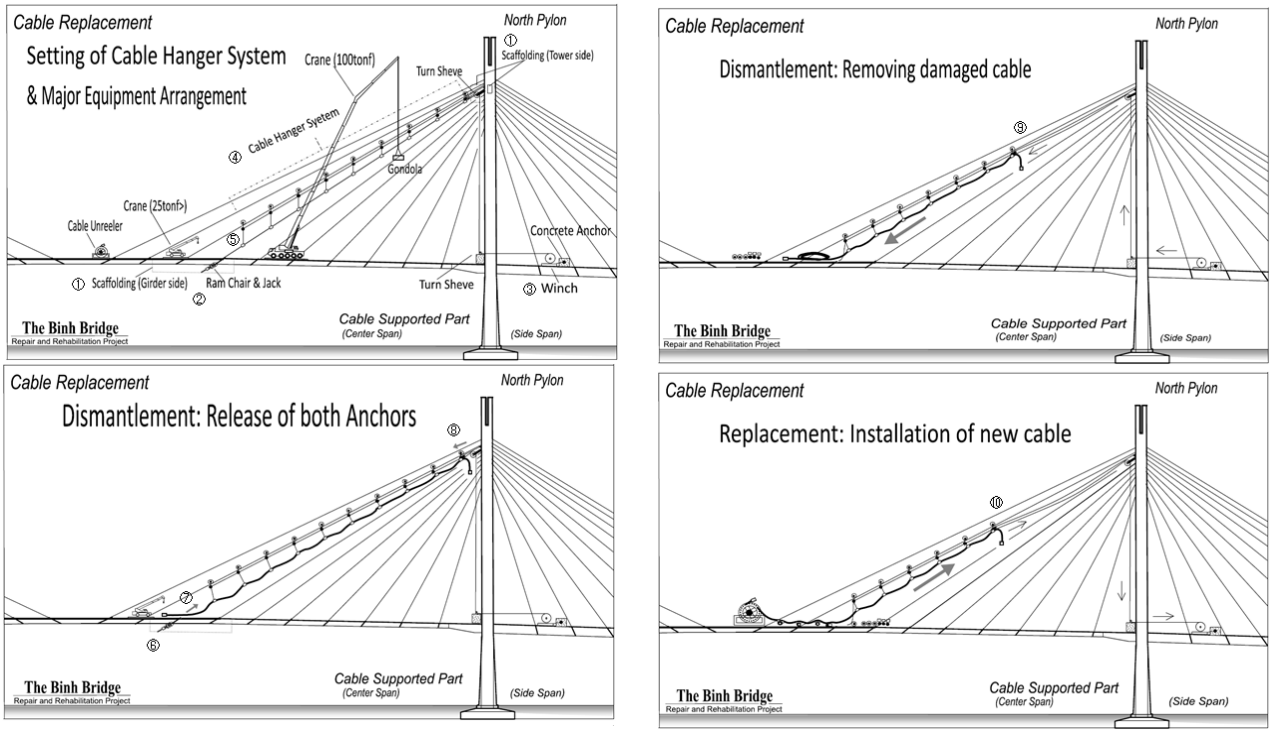

Figure 15 Dismantle and Installation of Stay Cable

Figure 16 Installation of new stay cable

Design and analysis

We designed an analytic model by incorporating the Temporary Bypass truss into a three-dimensional frame model of the entire cable-stayed bridge. We used it to conduct a sequential analysis for examining fluctuating loads in each construction step to sum the section forces and evaluated the total section force. Figure 25 illustrates the three-dimensional frame model.

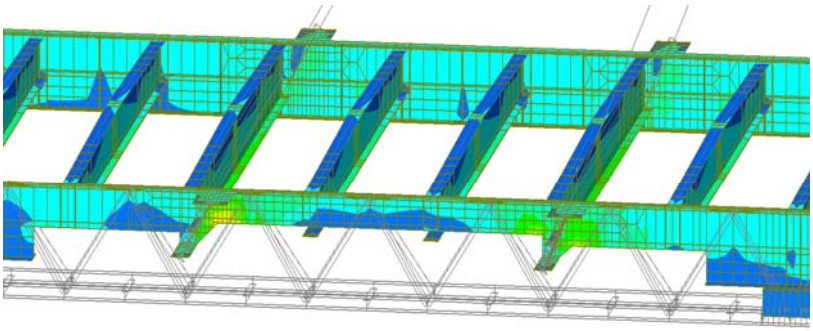

Figure 17 FEM Model for checking local stress

The local influence of factors such as the shape of the cut portion of the girder, and the structural influence of factors such as the effective width of the slab, cannot be accurately taken into consideration by performing only a stress check based on section forces obtained by the frame analysis. Accordingly, for the replacement portion of the girder, we also designed a Finite Element Method (FEM) model with consideration given to cable anchorages and the Temporary Bypass truss and applied the section forces obtained from the above frame model to the FEM model to evaluate local stress intensity. In this process of using the FEM model, we also simulated the sequential steps to confirm safety.

Stress Monitoring

To confirm the validity of the analysis result and the safety of construction, we also monitored stress by using strain gauges attached to the upper and lower flanges and the Temporary Bypass truss. The monitoring was performed at the following four stages with respect to stress values observed

Step 1: Installation of Temporary Bypass Truss

Step 2: Cutting of the damaged Girder

Step 3: Welding of the new girder

Step 4: Dismantling the Temporary Bypass Truss

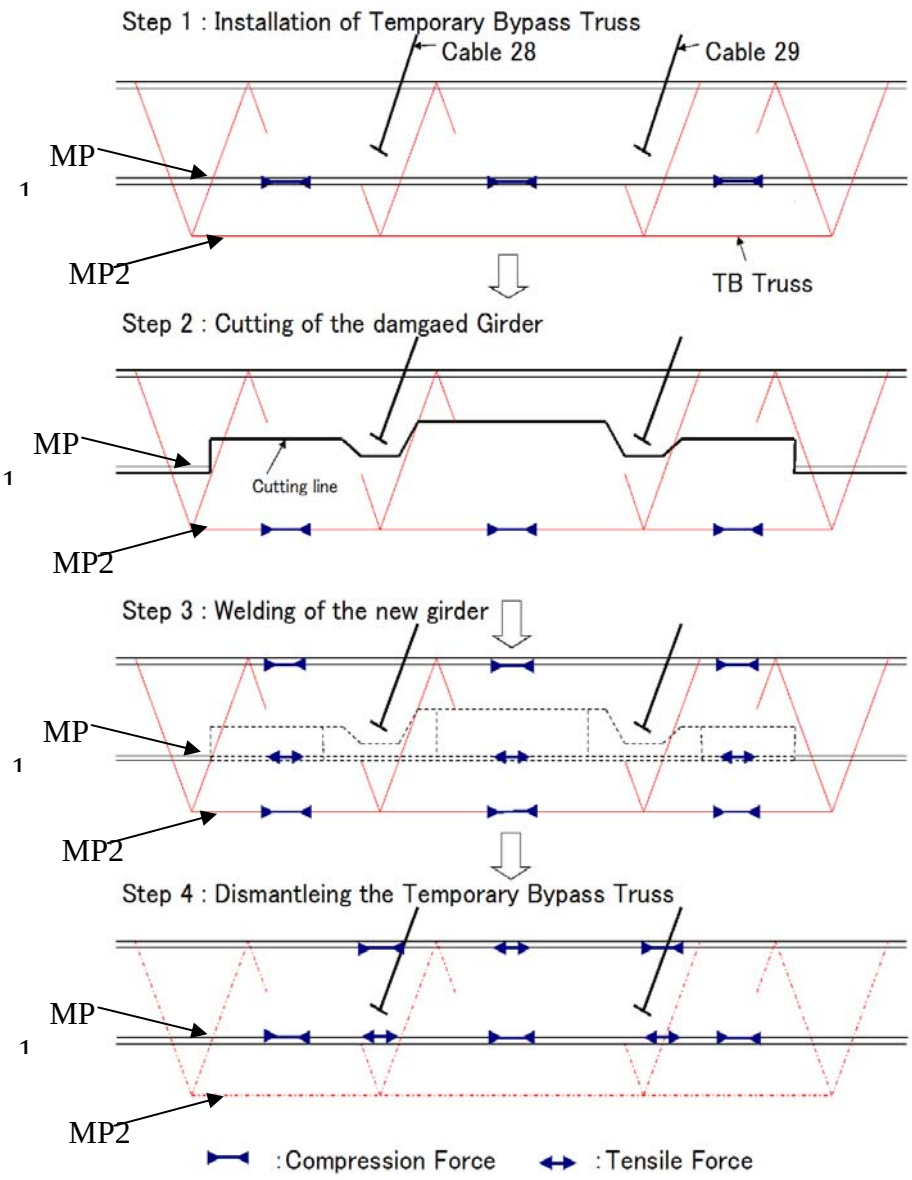

Figure 18 Stress monitoring for each construction step

In the figure 18, load flow transferring to lower flange and Temporary Bypass Truss during repair is shown. In the figure 19, the result of monitoring measuring point (MP)1 and 2 is shown by graph. For the vertical axis of this graph acting force is shown and for the horizontal axis construction step is shown. Regarding vertical bar of this graph, the changing force of lower flange and Temporary Bypass Truss per each construction step is shown. And Regarding polyline of this graph the sum total of that is shown.

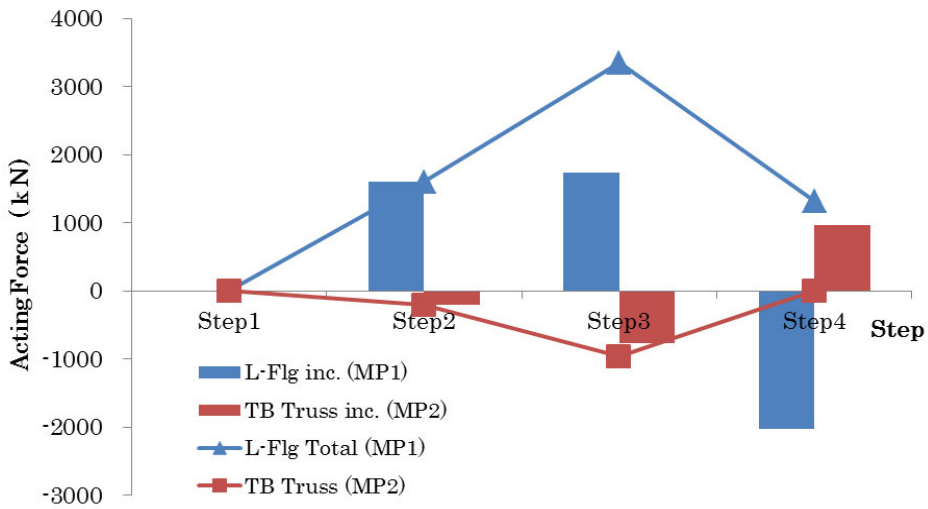

Figure 19 Force changes during construction

When cutting the lower flange deformed in the out-plain direction, the residual stress is released and the behavior which be back to non-deformed condition was confirmed. In the measuring result of monitoring, stress difference between edge girder of upstream side and that of downstream side due to out-plain deformation of edge girder was confirmed.

In the measuring result, the average value between the stress on edge girder of upstream side and that of downstream side is plotted to remove the influence of out-plain deformation.

When Temporary Bypass Truss was installed on the girder, there is not stress in this Temporary Bypass Truss but compression force is acted on the edge girder (Step1). When cutting damaged edge girder, Temporary Bypass Truss is compressed due to re-distribution of compression force of cut edge girder (Step 2). When welding of newly parts of edge girder, Temporary Bypass Truss is compressed because of welding shrinkage. Also welded newly part of edge girder is tensioned (Step3). When dismantle the Temporary Bypass Truss, due to release of compression force acted on Temporary Bypass Truss, this force is distributed to edge girder and concrete deck slab (Step 4). Finally distributed acting force on the Lower Flange is approximately 1000 kN (for the stress, approximately 22 N/mm2 (Section 900mm x 60mm)) including residual stress due to welding.

From the above result, we concluded that because Temporary Bypass Truss was transferred from the compression force acted on damaged edge girder, it is very efficient for this repair work.

Opening Investigation of damaged Stay Cable

After replacement the damaged Stay Cable, we performed the opening investigation for corrosion situation of wire of Stay Cable 24B. About 5.7m position from cable socket was into the guide pipe of Cable Anchorage and stay cable cover of about 7.6m position apart from there was damaged and wire of stay cable was exposed. Stay Cable was exposed in the rain due to typhoon and 4 days later temporary cover of Stay Cable is covered.

In our investigation, about 1.7m area from the socket including 1.5m portion cowered with polybutadiene rubber was peel. Opening investigation result is shown in Figure 20.

As a result, regarding wire from the edge of cable to 1.2m position some area is same as new product partially but the white rust could be found over the top of cable. Also in slight area the red rust could be found. As above mentioned, nevertheless it is difficult to evaluate the effect of corrosion; the replacement of damaged stay cable was decided in consideration to safety of long span. In our internal investigation, it was confirmed that wire was corroded two years later after damage Cover of Stay Cable. So if the cover of Stay Cable is damaged, the water invader should be prevented as soon as possible.

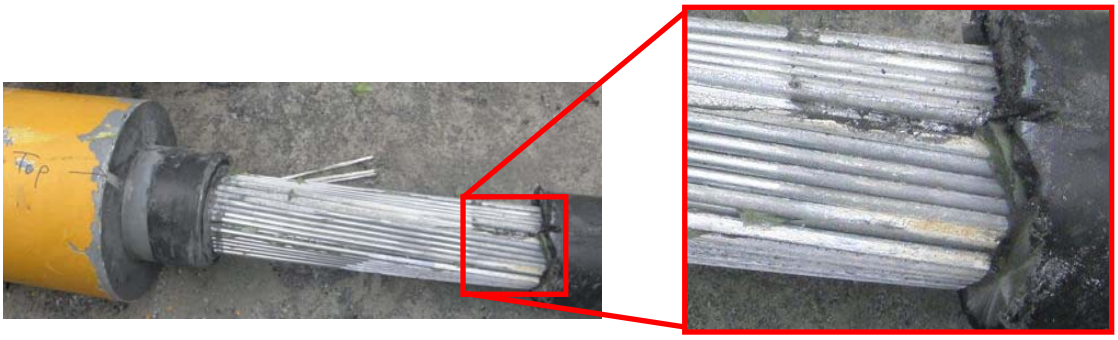

Figure 20 Opening investigation result of damaged stay cable

Conclusions

Large cargo ships, which do not normally pass under the Binh Bridge, were pushed along by a typhoon until they collided with the bridge damaging the main girder and stay cables of the bridge. No one ever expected such a severe accident resulting in damage to the main girder and part of the stay cables to happen to this two-main-composite-girder cable-stayed bridge. Fortunately, however, its slabs and floor beams were sound, and consequently, the redundancy of the bridge allowed it to

deliver performance far beyond expectations and not collapse.

This repair work is characterized by the following aspects.

(1) The repair of the girder was performed by the temporary bypass truss method using trusses with a triangular cross section. This method allowed us to safely complete cutting of the old girder and installation and welding of a new girder.

(2) The stress behavior and displacement behavior of the complex structure of the bridge were examined by performing assembly calculations faithfully simulating each construction step with the aid of both frame analysis and FEM analysis, which allowed us to safely complete the repair work.

(3) During the repair work of the girder, we performed computerized construction by conducting stress monitoring for safety confirmation.

(4) In order to replace some cables contained in the cable plane, we used a temporary hanger system using pulleys able to move along a cable and were thus able to replace cables in a safe and accurate manner. This method will also be able to be used for various types of construction, such as cable replacement for aging cable-stayed bridges.

〔Reference〕

(1) Construction Report for “Binh Bridge “in Vietnam, Kenji Matsuno, Yuichi Yamamoto, Masaaki Nakayama, Atsushi Oyama, Syusaku Ueshima, Masashi Yabuno Bridge and foundation Engineering Vol. 40 2006/9 pp18-23

(2) A STUDY ON STRAIN AGING OF COLD WORKED STRUCTURAL STEEL AND ALLOWABLE COLD WORKING RADIUS, Koji HOMMA, Chitoshi MIKI, Isao SOYA, Hideya SASAO, Taketo OKUMURA, Shuuichi HARA, Journal of JSCE No. 570/I-40 1997. 7 pp153-162

INCORPORATING BUCKLING RESTRAINED BRACES (BRB) AS PART OF THE AUBURN-FORESTHILL BRIDGE SEISMIC RETROFIT

Mark L. Reno, P.E.[1]

Martin N. Pohll, S.E.[2]

ABSTRACT

The Foresthill Bridge was built by the Bureau of Reclamation in 1973. The 2,428 ft. long bridge is comprised of three spans and sits 730 ft. above the North Fork of the American River. The parabolic haunched deck truss bridge has fracture critical, high-strength steel members. Under the California Department of Transportation's Local Agency Seismic Retrofit Program, Placer County embarked on the seismic retrofit design of this bridge, which incorporates the use of large Buckling Restrained Braces to improve the performance of the bridge during large seismic events while not affecting the current daily performance of the structure.

[1] Principal, Quincy Engineering, Inc., Sacramento, CA

[2] Senior Bridge Engineer, Quincy Engineering, Inc., Sacramento, CA

INTRODUCTION

The Auburn-Foresthill Bridge is a steel deck truss type bridge that links the towns of Auburn and Foresthill, California. The bridge was built by Kawasaki Heavy Industries for the Bureau of Reclamation and first opened to the public on September 3, (Labor Day) 1973. The bridge is currently owned and maintained by Placer County.

The 2,428 ft. long bridge is comprised of three spans (639 ft. – 862 ft. – 639 ft.) and sits 730 ft. above the North Fork of the American River and would have spanned the reservoir created by the proposed, but never constructed Auburn Dam. The center 502 feet of span two is a suspended span. The reinforced concrete bridge deck is composite and provides two 20 ft. wide roads, separated for the entire length of the truss spans by a 16 ft.-8 inch wide opening. The bridge was designed for a future median widening that could be accomplished by the installation of new stringers and a concrete slab.

Two slender, hourglass-shaped piers provide support for the main span. These piers are 403 ft. in height, 60 ft. wide at the top and bottom, and tapered to a 25 ft. wide neck. The main piers have hollow cores extending 207 ft. from the 85-ft. square base. The bridge truss depth at each end and at the center is 50 ft. and increases to 100 ft. at the main piers, thus forming a pleasing parabolic shaped bottom chord. A photo of the Foresthill Bridge is shown in Figure 1 below.

FIGURE 1. AERIAL VIEW OF FORESTHILL BRIDGE LOOKING NORTH

As part of the California Department of Transportation's Local Agency Seismic Retrofit Program, Placer County embarked on the seismic retrofit design of this bridge. This project has taken many of the concepts and design methodologies that were developed during the retrofits of the California Toll Bridge Program and then added more innovation. The project tasks included Seismic Assessment, Retrofit Strategy, and Final Design and Construction. The Design Team completed the Final Design (PS&E) in August 2009. The construction contract was awarded to Golden State Bridge in December 2010 with a bid of $ 58,374,849. The Hanna Group is providing project management/construction management services during construction, which is expected to be completed in early 2014.

DESIGN INFORMATION

Quincy Engineering, Inc. (QEI) developed the Auburn-Foresthill Bridge Seismic Retrofit Design Criteria as a living document that evolved along with the project. This concept also followed the design methodologies used on the California Toll Bridge retrofits, because of the unique features and aspects attributed to those structures. QEI's project specific design criteria followed a similar format of the major toll bridge crossing retrofit projects previously completed in California and was reviewed and approved by a Project Peer Review Panel and by Caltrans.

The criteria included seismic performance requirements, loads and combinations, analysis methods, foundation design requirements, nonlinear foundation springs, steel and concrete material properties, as well as component design parameters.

The criteria documents the seismic hazards and the existing faults in the vicinity of the project. The criteria also discusses how the three ground motions were generated by modifying actual earthquake records with a spectrum matching technique such that the modified time histories would have the same shaking level as the ARS design curves adopted for the design.

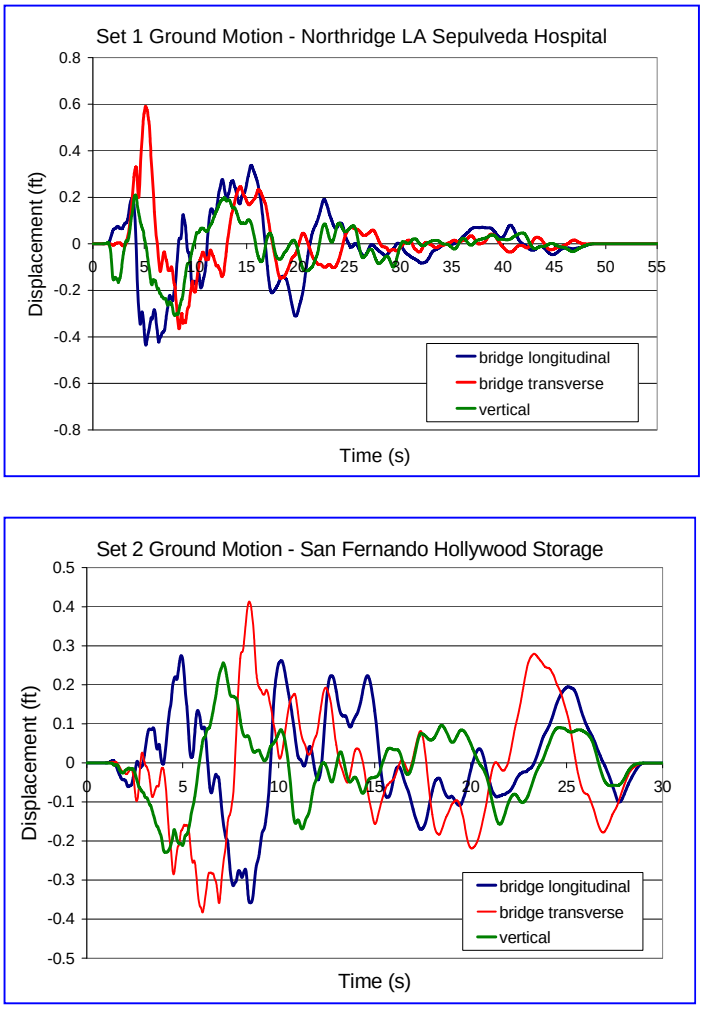

FIGURE 2. SEISMIC GROUND MOTIONS

The final design utilized the enveloped demands of all three motions as shown in Figure 2 to ensure the structure met the performance requirements. The performance goal was to limit seismic damage to the elements and locations that were inspectable and repairable to allow full service to be restored within months.

FINITE ELEMENT MODEL

A detailed three-dimensional model of the bridge was constructed by SC Solutions using the general purpose finite element program ADINA as shown in Figure 3. The finite element (FE) model included material and geometric nonlinearities. Nonlinear plastic beam elements (moment curvature elements) were used to simulate the behavior of superstructure and pier elements.

These nonlinear plastic beam elements captured nonlinear axial and bending member behavior, as well as global buckling of the superstructure elements. The concrete abutment structures were completely independent of the main bridge structure and were not included in the model.

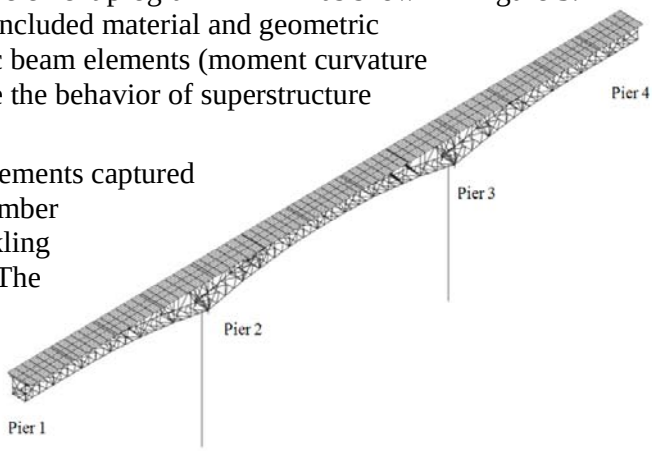

FIGURE 3. ADINA MODEL

At Piers 1 and 4 the bridge is resting on fixed vertical bearings and is anchored in the longitudinal direction with longitudinal anchors modeled with nonlinear elastic truss elements with calculated tensile and compressive capacities. In the retrofit model, buckling restrained braces (BRB) were added and modeled with nonlinear plastic elements with kinematic hardening. The fixed vertical bearings were modeled with nonlinear-elastic vertical-compression-only springs. The bridge was also restrained in the transverse direction by transverse anchors at Piers 1 and 4 in the vertical and transverse translational directions.

Input ground motions in the form of synchronous displacement time-histories were applied to the ground nodes at each boundary location. For retrofit, the transverse anchors were removed and replaced with two transverse keys modeled with non-linear spring elements. In the retrofit model, transverse ground motions at Piers 1 and 4 were applied only at the new transverse keys.

FIGURE 4. PIER 2 BEARING

The existing truss bears on top of Piers 2 and 3 and was not restrained in longitudinal translation. The pier top rocker bearings were modeled explicitly with rigid compression-only vertical spring elements and rigid linear elastic transverse spring elements. The rocker bearings shown in Figure 4 allowed a maximum displacement of ±12 inches.

In the as-built model, longitudinal translation was assumed to be unrestrained. For retrofit, longitudinal translation was assumed to be unrestrained up to a displacement of ± 11 inches, where a non-linear spring representing the friction/sliding of the bearing was engaged.

LONGITUDINAL ANCHOR RETROFIT

The truss superstructure is anchored to Piers 1 and 4 in the longitudinal direction with longitudinal anchors (as shown in Figure 5), and consists of two 2 inch x 12 inch ASTM A441 anchor plates embedded into the concrete foundation. The anchor plates are connected to each of the main truss gussets with two 1.50 inch x 18 inch ASTM A441 link plates and 6.0 inch diameter pins. The link plate capacity is stronger than the anchor plate capacity.

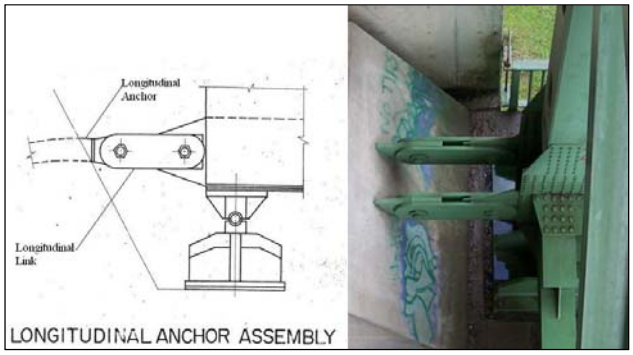

FIGURE 5. LONGITUDINAL ANCHOR

Time history results show that the anchor plates will experience forces exceeding their capacity. Without these anchors holding the bridge in the longitudinal direction, the superstructure may impact the abutment walls or drift away from the concrete seats during seismic loading, resulting in loss of vertical support. The capacity of the anchor plates used in the time history analysis limits the magnitude of the forces transmitted to the truss superstructure. Retrofit schemes that increase the capacity of the longitudinal anchor system could increase the force levels transmitted to the truss and thus the amount of required truss strengthening. Strain time history demands on the anchor plates show that the plates will have strains close to the ultimate strain limit of the steel members and failure of the members is possible. The stronger component, the link plates, remains elastic for the duration of the time history analysis.

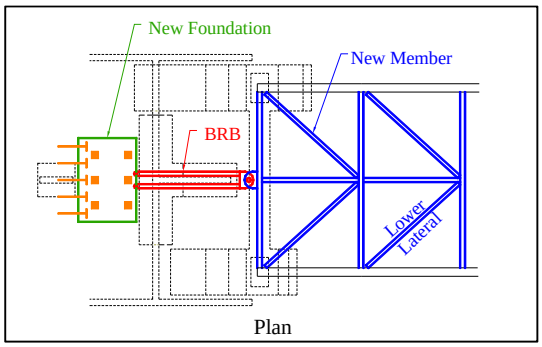

FIGURE 6. BRB LAYOUT AT PIER 1 AND 4.

To provide longitudinal stability after link plate yielding, a seismic response modification device, buckling restrained braces (BRB), was installed as shown in Figure 6 to ensure that forces transferred to the superstructure do not exceed acceptable levels while still providing longitudinal stability.

BRB have the advantage of providing a ductile system to restrain the longitudinal movement of the trusses while limiting the forces transmitted to the trusses. The devices are anchored to a new longitudinal strut at Piers 1 and 4, and to new separate foundations constructed under the approach spans. The BRBs are relatively maintenance free with only periodic painting required. They can be easily inspected after a seismic event and can be readily replaced if the BRB experiences large seismic strains. Longitudinal anchors are retrofitted by slightly reducing the capacity of the link plates to insure that yielding occurs in elements that can be inspected and repaired after a significant seismic event.

The retrofitted link plate shown in Figure 7 at right was specified to have controlled yield properties to closely define when the BRB's would be engaged.

The BRB system was installed at the centerline of the bridge so the truss is free to rotate about a vertical axis and forces from rotational restraint will not magnify the required longitudinal anchorage forces.

FIGURE 7. RETROFIT.

BUCKLING RESTRAINED BRACES

Buckling restrained braces are generally constructed of a cruciform or rectangular steel core surrounded by a debonding material and encased in a steel hollow tube filled with grout. The steel core carries the axial load while the outer tube, via the concrete, provides lateral support to the core and prevents global buckling. The core is free to yield in tension and compression.

Three BRB manufacturers that were known to manufacture BRB that could be utilized on this project were contacted to determine the design parameters for the time-history analysis and to make sure that design requirements could be met by the vendors. They included:

- Core Brace, West Jordan, UT
- Star Seismic,Park City, UT
- Nippon Steel Engineering Company, Tokyo, Japan

These manufacturers were extremely helpful in providing guidance on their manufacturing capabilities. Each manufacturer had a preferred end connection that included welded, bolted, or pinned connections and provided suggested connection details. The manufacturers also suggested that the strain should be limited to 2%. The manufacturer also provided guide specifications and suggested force tolerances for testing, since previous testing protocols for devices of this size and magnitude had not been developed.

The BRB were modeled in the non-linear time-history model using a non-linear plastic link element (with kinematic hardening) to model the yielding portion of the

brace and with elastic end elements to model the non-yielding ends. The following are the anticipated parameters of the BRBs as shown in Figures 8 and 9:

Yield Length = 171 inch End Length = 12 inch

Yield Area = 48.0 in^2 End Area = 61.32 in^2

Yield Stress = ± 42 ksi Yield Force = 2,000 kips

Tensile Plastic Stiffness = 3.5% Elastic Stiffness

Compressive Plastic Stiffness = 4.5% Elastic Stiffness

FIGURE 8. BRB FORCE VS. DISPLACEMENT.

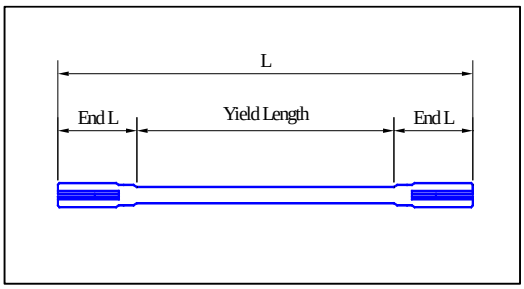

FIGURE 9. BRB YIELD LENGTH.

The longitudinal anchor elements are removed from the system when their strains exceed 4%. Following the rupture of all longitudinal anchors elements, longitudinal ground motions at Piers 1 and 4 are only applied through points where the BRB system anchors to the foundation. The lower lateral chevron bracing members near Piers 1 and 4 have strain demands exceeding criteria. The lower laterals were replaced with new members and a new longitudinal member was added to transfer the BRB forces into the bracing system as shown in Figure 6. The new members and the BRB connections have been designed to the BRB forces corresponding to 1.5 times the maximum BRB strains reported in the time-history analysis. The installation of the new bracing system required a detailed construction sequence so that the wind load resisting system of the structure remained intact at all times.

DESIGN PROCESS

During the design process SC Solutions provided time-history analysis results (as shown in Figure 10 on the next page) that included:

- Force-Displacement plots to provide a measure of the forces that would be required to be transferred;
- Time vs Strain plots to insure the strain did not exceed 2% as recommended by the manufacturers;
- Time vs Accumulated plastic strain to provide a measure of energy absorbed and to insure that the accumulated plastic strain did not exceed 200 times the yield strain; and

- Time vs Displacement plots of Relative Displacements between the Truss and Piers and Expansion Joint at Node U15 to insure that the available displacement capacities were not exceeded.

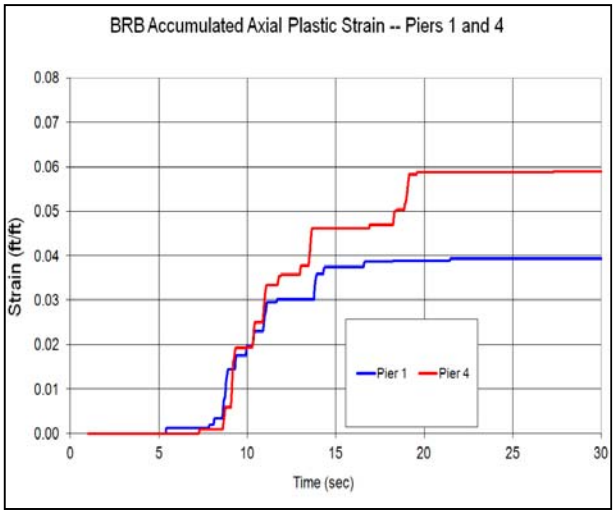

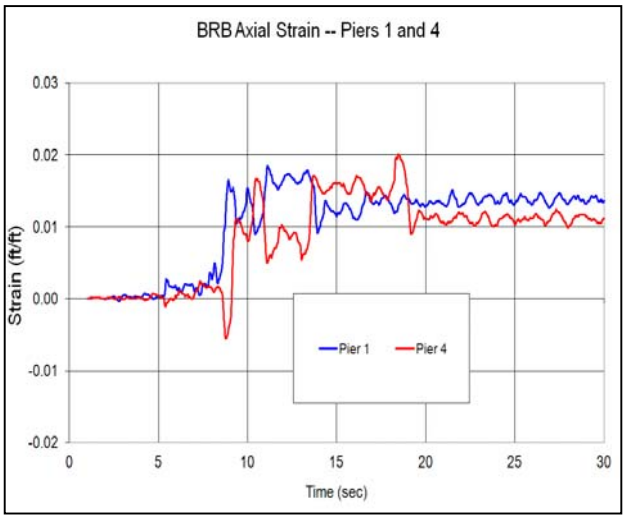

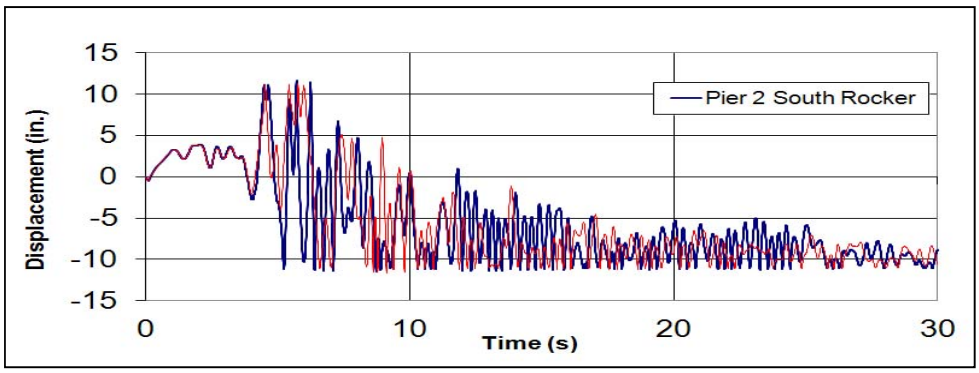

FIGURE 10. BRB MODEL RESULTS.

The yield capacity of the BRB's was kept to maximum of 1000 kips so that prototype testing could be accomplished within the limits of the UCSD facility, and the maximum strain was limited to 2% to keep within the limits of the BRB manufacturers. The yield length of the BRB used in the model was adjusted during the design process to limit the strain but was kept within the available length of specimens that could be tested at the UCSD facility. Ultimately, the testing limitations and protocol for these devices limited the size and magnitude of the BRBs.

PROJECT PLANS AND SPECIFICATIONS

The project plans defined the performance characteristics of the BRB in the form of a plot, as shown in Figure 11 below. Bolted or pin connections were permitted to accommodate the standards of various manufacturers, and both types of connections were designed and incorporated into the plans.

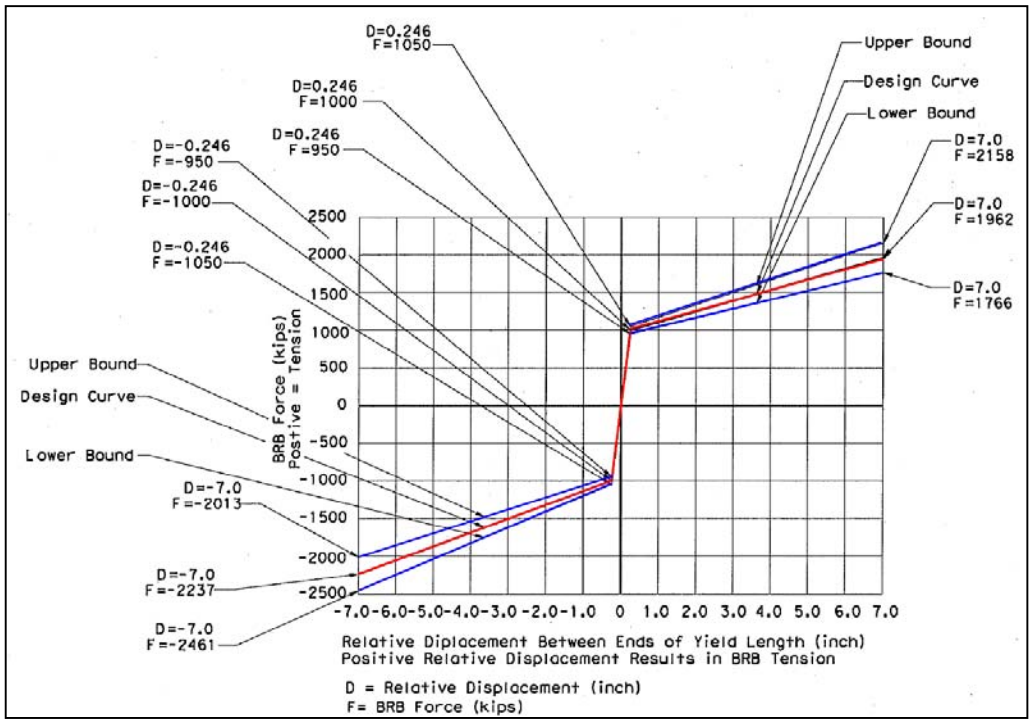

FIGURE 11. BRB CHARACTERISTIC CURVE.

BRB manufacturers bidding on this project were limited to those manufacturers that have successfully tested BRB's similar to the proposed BRB in the project plans. The contractor was allotted twenty-eight (28) weeks to produce working drawings and calculations, provide results of testing on two prototype specimens, and to produce final working drawings, a quality control program, and a maintenance manual for these devices. Stress-strain test results were required for the production of the prototype BRB's to be tested and the steel materials used for the BRB's shipped to the site were required to be fabricated from plates cast from the same heat used for the fabrication of the prototype BRB. Connections of the BRB to the brackets on the

structure were required to be designed by the manufacturer for a force resulting from a displacement of 1.5 times the design displacement and were designed not to slip at the yield force.

BRB SUPPLIER

Golden State Bridge, the General Contractor that won the bid selected Nippon Steel Engineering Company, Tokyo, Japan to provide the BRB's for the project. The BRB's were manufactured by Yajima USA in Reno, Nevada and were provided at a cost of $90,378 for four braces to be installed, plus two braces required for prototype testing. The braces have an overall length of 276 inches and a yield length of 171 inches. The cruciform steel section was fabricated from ASTM A36 steel that was tested for stress-strain properties. The yielding section is housed in an outer tube fabricated from HSS 16x16x0.3125. The end connections utilized 16-1.25 inch diameter ASTM A490 bolts as shown in Figure 12 above.

FIGURE 12. BRB CONNECTION

PROTOTYPE TESTING

Testing was conducted by the University of California, San Diego at the Seismic Response Modification Devices (SRMD) Testing Facility in July 2011 as shown in Figure 13. The testing cost of $29,742 was paid for by the Contractor and the cost of the testing at UCSD was quoted in the project specifications. At the time that this project was advertised for bid, UCSD was the only facility capable of testing to the required demands; and the facility has previously tested BRB devices. The facility has limitations on the test length of BRB specimens, which influenced the selection of the yield length. Because of the numerous demands on this testing facility for other projects, scheduling an available time for testing, that met the needs of the Contractor, required constant communication with UCSD and the Contractor for over a year.

FIGURE 13. UCSD TESTING.

Both Caltrans whom had a lot of the lab time tied up with their experiments and UCSD were very cooperative in scheduling this testing around their other commitments.

Two specimens were tested in accordance with the project specifications that were based upon the AISC 341-05 protocol (as shown in Figure 14) except that the test displacements were 1.50 times the following design displacements*:*

- Axial Displacement = 3.42 inch (2% strain)
- Horizontal Axis Rotation = 0.003 radians
- Vertical Axis Rotation = 0.005 radians

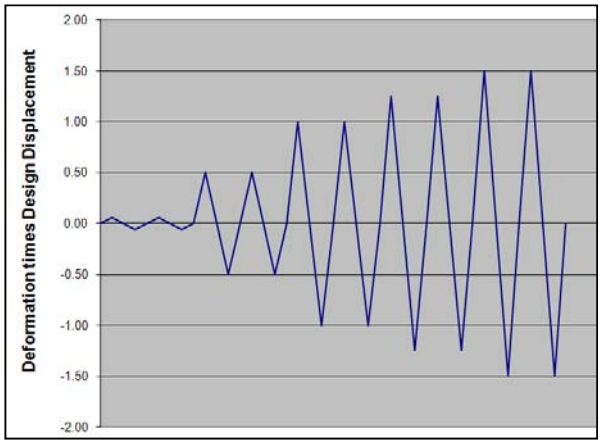

FIGURE 14. TESTING PROTOCOL.

The tests satisfied the following requirements, which were outlined in the project specifications:

- The two prototype tests shall display dynamic characteristics within 5% of each other.
- Test results shall display force-displacement characteristics within the upper and lower bound envelope shown on the plans. See Figure 15 below for results.
- The force-displacement hysteresis loops shall exhibit stable, repeatable behavior with positive stiffness and no pinched hysteretic behavior for all cycles.
- The BRB's shall show no signs of distress up to an inelastic axial deformation of 200 times the yield deformation. The tests results showed accumulative plastic strains of 828 and 1055 ε_Y.

The testing protocol required additional final cycles to failure, but for reasons of safety and difficulties in the performance of the testing machine, the specimens could not be tested to failure. The original intent was to test these devices to failure.

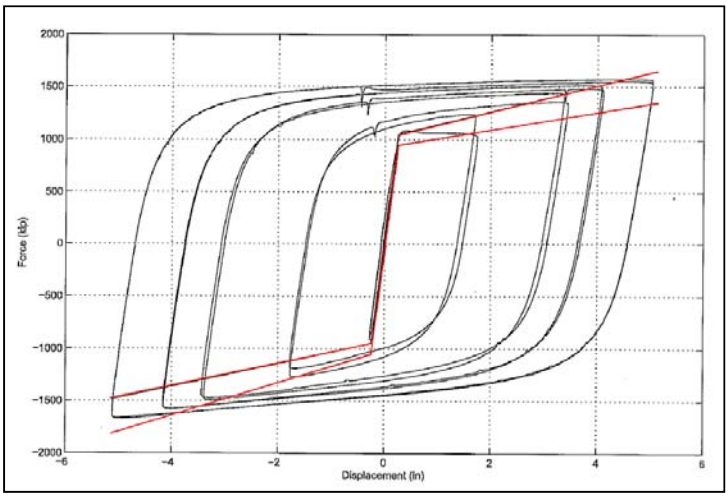

FIGURE 15. FORCE-DISPLACEMENT TEST RESULTS.

CONSTRUCTION

The erection of the BRB was similar to the installation of other structural steel members and did not involve any additional substantial equipment beyond what was already being utilized. In fact, the erection of the BRB did not amount to the largest hoists during this project. At this time, all of the structural retrofit work has been completed on the project. The BRBs at both ends of the bridge have already been placed. The only work that remains on the project is to complete installation of modular joint seal, as well complete the re-coating of the entire bridge. There were no significant construction change orders during the structural retrofit work including the BRBs. See Figure 16 for installation.

FIGURE 16. BRB INSTALLATION

CONCLUSION

The seismic retrofit of the Foresthill Bridge posed many challenges. These challenges were met by using the latest analysis tools and by innovative criteria and seismic modification devices. The BRB's allowed the designers to solve a stability issue with a passive device that allowed the service behavior of this truss to remain unchanged. The BRB's will not be activated until a large seismic event occurs, so that service level cycles will not impact the BRB. This eliminated any concerns that service loads and their affect on the bridge would be altered. Utilization of the BRB reduced a significant amount of additional steel retrofit of the truss and subsequent connections and thereby reduced the overall project costs substantially.

ACKNOWLEDGEMENTS

The authors would like to thank the staff at the Placer County Public Works Department for their assistance and oversight during the course of the project; in particular, Sherri Berexa, Matt Randall and Kevin Ordway. The Project Specific Peer Review Panel, consisting of Ahmad Itani with University of Nevada Reno, Steve Thoman with David Evans & Associates, John Hinman with CH_2M Hill, Frieder Seible with University of California San Diego and Geoff Martin with University of Southern California, provided comments that proved invaluable. The staff at the Caltrans SRMD Test Facility made the testing phase of the project proceed without issue. Golden State Bridge, Inc. provided the heavy lifting to make the project a success. The comments by Caltrans as well as their involvement also added to the success of the project.

The authors wish to acknowledge the contributions of the project sub-consultants, CH_2M Hill, SC Solutions, David Evans & Associates, Fugro, Earth Mechanics, Inc. and Cadre Design Group for their contributions to the project.

UNITS CONVERSION

1 inch = 25.4 mm	1 ksi = 6.895 megapascal
1 foot = 304.8 mm	1 kip = 4.448 kilonewton

LOAD-CARRYING CAPACITY OF CORRODED END CROSS-GIRDER

Eiki Yamaguchi[1], Hiroyuki Tsuji[2]

Abstract

An end cross-girder plays an important role when the steel girder bridge is subjected to seismic loading. But, located near the girder end, it is often found corroded, which could degrade the load-carrying capacity. Therefore, it is of a practical significance to investigate the seismic performance of a corroded end cross-girder. To this end, the present study conducts nonlinear finite element analysis of end cross-girders with various corrosion patterns under horizontal load. It is observed that not only the degree of corrosion but also the corrosion pattern influences the degradation of the load-carrying capacity. It is also found whether or not the lower flange is connected to the main girder makes a large difference in the load-carrying capacity

Introduction

Bridges without cross girders at the ends of main girders have been constructed in Chile. Many of them were badly damaged in the 2010 Chile Earthquake (Chen et al. 2010). The end cross-girder in the steel bridge is thus an important member under seismic loading. The seismic design code in Japan indeed requires that end cross-girders shall possess rather large cross sections (Japan Road 2012b).

Needless to say, corrosion decreases cross sectional area, leading to the degradation of the load-carrying capacity. Main cause for the replacement of steel bridges is said to be corrosion (Japan Road 2012a). Corrosion is thus one of the crucial phenomena to be dealt with in the maintenance of steel bridges, and the issue of corroded steel girders has attracted many researchers (for example, Liu et al. 2011). Nevertheless, much remains to be done since corrosion patterns are numerous.

Corrosion is most serious at the end of a main girder, as water comes in through an expansion joint and there are many members in the neighborhood of the girder end that may deteriorate corrosion environment. Hence, the corrosion problem is often investigated in association with the girder end (for example, Khurrama et al. 2012).

The end cross-girder is susceptible to corrosion and found corroded frequently. The corroded girder may not perform as expected during earthquake. However, so far, study has not been taken from this viewpoint so that the influence of the corrosion on the

[1] Professor, Dept. of Civil Engineering, Kyushu Institute of Technology, Kitakyushu
[2] Graduate Student, Dept. of Civil Engineering, Kyushu Institute of Technology, Kitakyushu

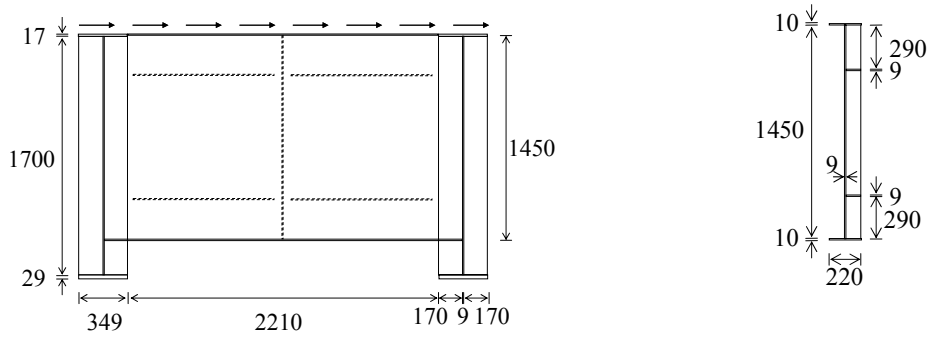

(a) Side view (b) Cross section

Figure 1 End cross-girder model

load-carrying capacity of the end cross-girder under seismic loading is yet to be well understood.

The objective of the present study is to reveal the influence of corrosion on the seismic resistance of the end cross-girder. The study is carried out by nonlinear finite element analysis.

End Cross-Girder Model

Referring to a bridge in the design example of Japan Bridge (2005), the steel end cross-girder shown in Figure 1 is employed in the present research. The model consists of a cross girder and parts of main girders, 220 mm long. Young's modulus E of the steel is 2.0×10^5 N/mm^2, Poisson's ratio 0.3 and the yield stress 235 N/mm^2. The elastic-plastic behavior of the steel is assumed to be of Mises type and the uniaxial behavior in tension is described by two lines. The intersection of the two lines is the yield point and the slope of the second line is E/100.

To simulate the seismic behavior, horizontally distributed load is applied to the upper flange of the cross girder model. The load is monotonic so as to capture the basic performance under seismic loading. The upper flange is supposed to be connected to a concrete slab, which prevents the deformation of the upper flange and due to which the displacement of the upper flange in the bridge-axis direction (out-of-plane displacement) is assumed neglected in the analysis.

Figure 1(a) is the side view of the model. This figure is the view from the parapet and the horizontal load is applied toward right as indicated by the arrows. The web of the end cross-girder model has two longitudinal stiffeners and one transverse stiffener. The stiffeners are indicated by the dotted lines as they are installed on the opposite side of the web. The stiffeners and the main girders form two panels, Panel L and Panel R. The two

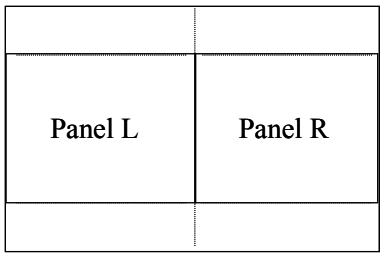

Figure 2 Panels L and R in web

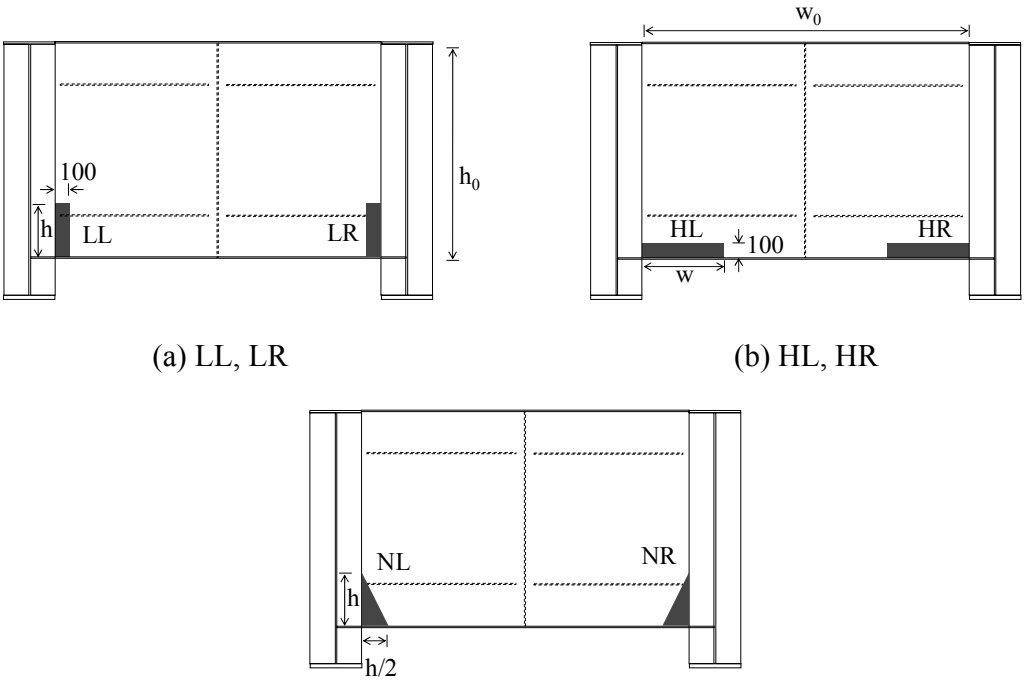

(a) LL, LR

(b) HL, HR

(c) NL, NR

Figure 3 Corrosion model

panels are indicated by pink and blue, respectively, in Figure 2.

Corrosion Model

Based on the study of corrosion development in steel girders in the literature (for example, Liu et al. 2011), six corrosion models are constructed in the present study. They are illustrated in Figure 3: all the corrosion models in Figure 3(a) have the size of h-by-100 mm; all the corrosion models in Figure 3(b) the size of 100 mm-by-w; and all the corrosion models in Figure 3(c) the size of h-by-h/2.

To study the influence of the corrosion size on the load-carrying capacity of the end cross-girder, various values of h, w and Δt are considered in each model: h/h_0, w/w_0 = 25%, 50%, 75%; Δt =2 mm, 4 mm, 6 mm. Herein Δt is the reduction of the plate thickness due to corrosion. The combination of these parameters requires 54 analyses. In addition, the analysis of the original girder (no corrosion) is conducted.

Outline of Analysis

Initial imperfections of the steel girder can influence its strength significantly. Therefore, initial deformation and residual stress need be taken into account in the analysis. To find the relevant initial deformation, the eigenvalue analysis is conducted first to obtain buckling modes. The initial deformation mode is made identical to the mode of the smallest buckling strength. The initial deformation is then constructed so as to have the maximum displacement within the range of the fabrication tolerance specified in Japan Road (2012a).

Several models of residual stress distribution are available in the literature by Usami (2005). In the present study, the residual stress distribution used in our previous study (Yamaguchi and Akagi 2012) is employed. Since the residual stress distribution is in a state of self equilibrium, the residual stress is given to the analysis model by conducting thermal stress analysis. The analysis is done by assuming temperature distribution so as to insert the stress distribution desired. The relevant temperature distribution is found by a trial-and-error method.

All the analyses are conducted by ABAQUS (2008). The finite element model of the cross girder utilizes 4-node shell elements for the entire body.

Numerical Results and Discussion

The same type of the corrosion model is considered at the left and right bottom corners of the web. Since actual seismic loading is cyclic, only one of them is considered to be significant herein, the one that leads to a larger reduction in the load-carrying capacity. Therefore, although all the 54 corroded girders were analyzed, only the significant cases are reported in what follows. The significant corrosion models turn out to be LL, HL and NL.

Numerical results are presented in Table 1 and Figures 4 to 6, in which P_{max} is the maximum load of a corroded cross girder and P_0 is the maximum load of the original cross girder. The color in Figure 4 indicates the out-of-plane displacement.

In the original cross girder, shear buckling occurs in both panels, Panels L and R, and the diagonal-tension field, a region that undergoes out-of-plane displacement and is located diagonally, is developed before the maximum load is reached.

In LL, the diagonal-tension field forms in each panel, but the directions of the

Table 1 Load-carrying capacity

Corrosion model	Δt (mm)	h/h_0	P_{max}/P_0	Corrosion model	Δt (mm)	h/h_0 (w/w_0)	P_{max}/P_0
LL	2	0.25	0.997	NL	2	0.25	0.983
		0.50	0.984			0.50	0.963
		0.75	0.993			0.75	0.949
	4	0.25	0.984		4	0.25	0.971
		0.50	0.968			0.50	0.923
		0.75	0.972			0.75	0.887
	6	0.25	0.954		6	0.25	0.958
		0.50	0.923			0.50	0.850
		0.75	0.911			0.75	0.788
HL	2	0.25	0.997				
		0.50	0.995				
		0.75	0.996				
	4	0.25	0.986				
		0.50	0.987				
		0.75	0.989				
	6	0.25	0.980				
		0.50	0.979				
		0.75	0.849				

out-of-plane displacements in the two panels are opposite unlike in the original model. Out-of-displacement takes place also near the left upper part of Panel L. LL reduces the load-carrying capacity by up to 9%.

Deformation characteristics of HL model are virtually the same as those of the original cross girder and strength reduction is very little, as long as corrosion development is not so severe. In HL with w/w_0=75% and Δt=6 mm, however, the deformation mode is very different: out-of-plane displacement occurs at the right bottom part of the web while no clear diagonal-tension field in Panel L is observed; and the load-carrying capacity reduces by 15%.

In NL, each panel forms a diagonal-tension field, but the one in Panel L is larger in area and displacement. 21% reduction of the load-carrying capacity is found with h/h_0=75% and Δt=6 mm.

The average load-carrying capacity is shown in Figure 5. Simple average values of all P_{max} / P_0 are 0.965, 0.973 and 0.919 for LL, HL and NL, respectively. The relationship between the

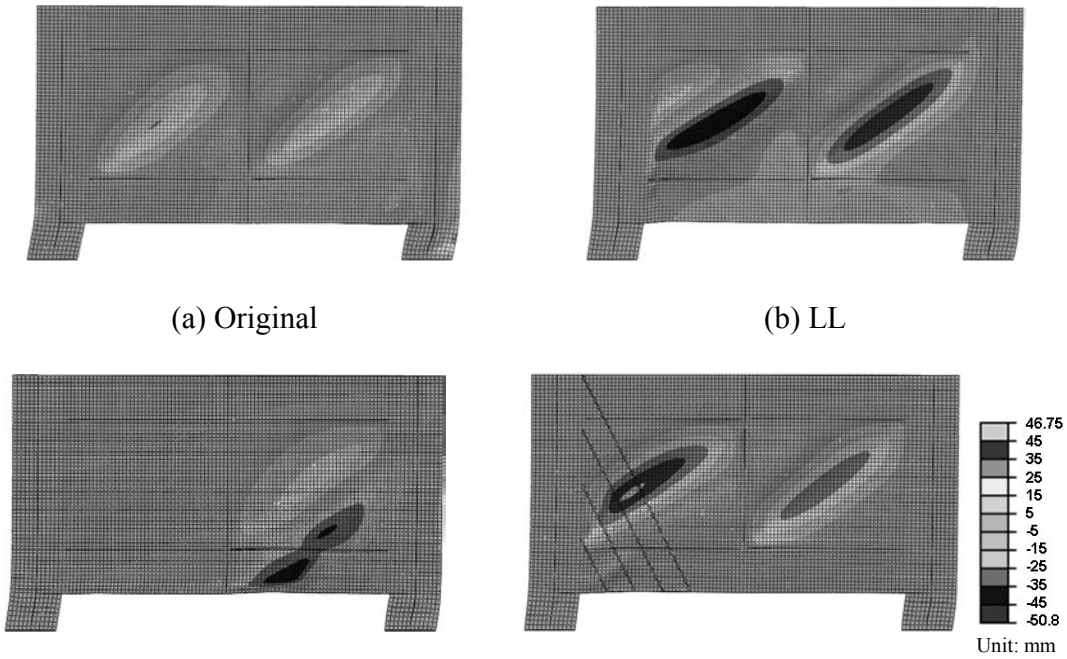

(a) Original (b) LL

(c) HL (d) NL

Figure 4 Deformation at maximum load (w/w_0=75%, Δt=6 mm for (b)-(d))

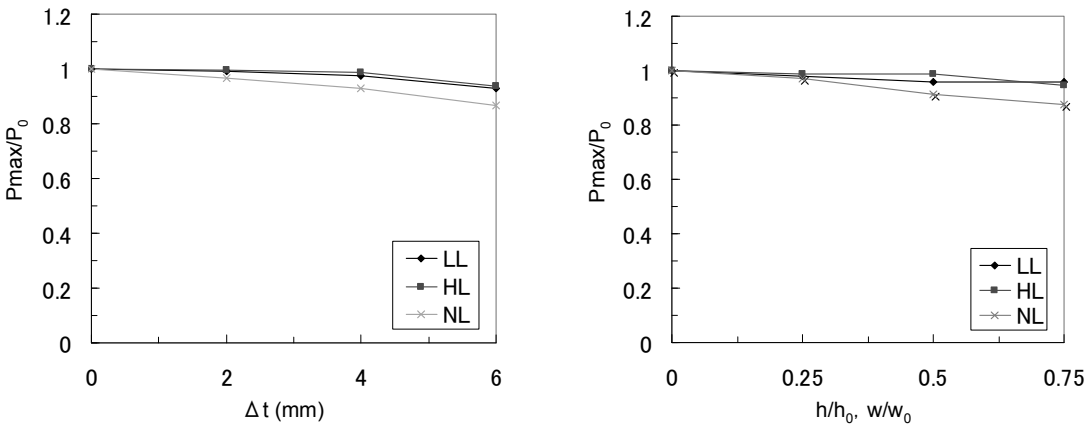

(a) Variation with Δt (b) Variation with h or w

Figure 5 Average load-carrying capacity

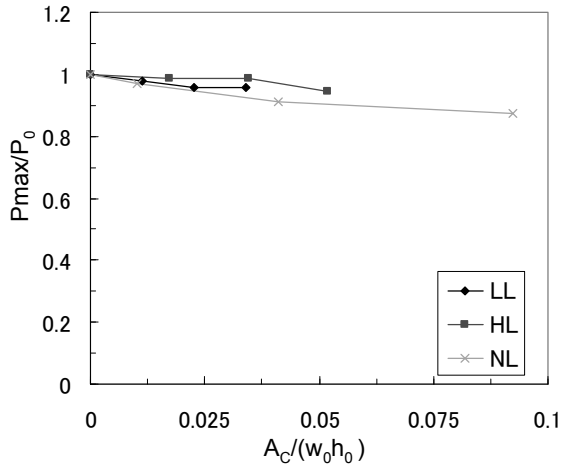

Figure 6 Variation of load-carrying capacity with corroded area

corroded area A_C and P_{max} / P_0 is investigated and plotted in Figure 6. In all theses figures, NL yields the lower bound, indicating NL has the largest influence on the load-carrying capacity.

The lower flange of the cross girder is connected to the main girder by bolts. The design requirement for the strength of the connection is not clear and may not survive under a large seismic load. Separating the connection. The original girder and LL with w/w_0=75% and Δt=6 mm are analyzed. The separation reduces the load-carrying capacity of the original girder by 11% and that of LL by 20%: P_{max} / P_0 of LL reduces to 0.73, while it is 0.91 if the lower flange of the cross girder is connected to the main girder. The result here reveals the importance of the connection, the design of which should be examined carefully.

Concluding Remarks

An end cross-girder of a steel bridge plays an important role during earthquake. However, it is often found corroded as it is located in the neighborhood of a girder end. The corrosion can reduce the load-carrying capacity. Against this background, the present study investigated the influence of the corrosion on the performance of the end cross-girder under horizontal load.

The end cross-girder undergoes shear buckling and forms diagonal-tension field before it reaches the maximum horizontal load. This basic deformation characteristic changes when it is corroded. As the degree of the corrosion becomes bigger, the load-carrying capacity decreases more. The way the corrosion influences is dependent on the corrosion type: NL is found to have the largest influence.

The connection between the lower flange of the end cross-girder and the main girder has been found significant. Once disconnected, the end cross-girder performs very differently and the load-carrying capacity decreases greatly. The present design of the connection needs more attention so as to ensure the adequate performance of the end cross-girder during earthquake.

Acknowledgments

Grant-in-Aid for Scientific Research (C) (KAKENHI, No. 23560570) is gratefully acknowledged.

References

ABAQUS: User's Manual, ABAQUS Ver. 6.8, Dassault Systemes Simulia Corp., 2008.

Chen, G. et al.: 2010 Chile Earthquake implications to the seismic design of bridges, Proceedings of the 26th US-Japan Bridge Engineering Workshop, pp.203-216, 2010.

Japan Bridge Association: Design Example and Commentary of Composite Girder, 2005.

Japan Road Association: Specifications for Highway Bridges Part 2 Steel Bridges, 2012a.

Japan Road Association: Specifications for Highway Bridges Part 5 Seismic Design, 2012b.

Khurrama, N., Sasaki, E. et al.: Analytical demonstrations to assess residual bearing capacities of steel plate girder ends with stiffeners damaged by corrosion, Structure and Infrastructure Engineering, pp.1-11, 2012.

Liu, C., Miyashita, T. and Nagai, M.: Analytical study on shear capacity of steel I-girder with local corrosion nearby girder ends, Journal of Structural Engineering, JSCE, Vol. 57A, pp. 715-723, 2011.

Usami, T. (Editor): Guidelines for Stability Design of Steel Structures, 2nd ed., JSCE, 2005.

Yamaguchi, E., Akagi, T.: Influence of corrosion of transverse stiffener at support on load-carrying capacity of steel girder, Proceedings of the 28th US-Japan Bridge Engineering Workshop, pp.137-147, 2012.

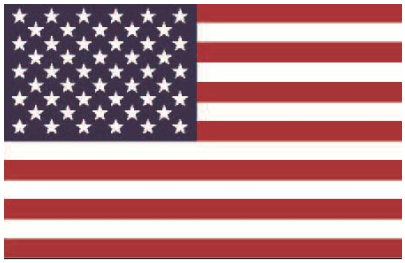

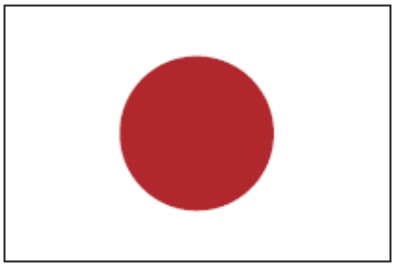

29th US-Japan

Bridge Engineering Workshop

Session 5

Design1

WHICH UNCETAITY (OR ERROR) IS THE MOST CRITICAL IN GEOTECHNICAL DESIGN

Yusuke Honjo[1] and Yu Otake[1]

Abstract

The author has been proposing a reliability based design (RBD) scheme for practicing geotechnical engineers. Results of RBD on some structures are presented in this paper to highlight the characteristics of the geotechnical RBD. Based on the results, some discussions are made to identify the major issues geotechnical RBD is facing. It is concluded that spatial variability of soil properties is only one of the sources of uncertainty. In many design problems, statistical estimation error, design calculation model error and transformation error associated have higher uncertainty. It is important to recognize these aspects in developing the geotechnical RBD to the next and the higher stage..

Introduction

Needs for carrying out reliability analysis (RA) for complex geotechnical design problems are increasing due to the introduction of the limit state design worldwide. On the other hand, in the current practical design of geotechnical structures, many sophisticated calculation methods, *e.g.* commercially available user friendly FEM programs *etc.*, are employed. These methods become more and more user friendly, and can be used with very small efforts for preparing input data and summarizing calculation results.

It takes quite amount of effort for people to combine these programs with RBD. To connect these design tools to RBD tools is not an easy task. Furthermore, to understand and become proficient with these RBD tools need quite amount of time and efforts.

Considering these situations, the author has been proposing a new RBD scheme for geotechnical design. The essence of the issue that makes geotechnical engineers difficult to practice RBD, as I see, is the mixing of geotechnical design tools with RBD tools in the existing RBD procedure. Furthermore, if we mix them together, one tends to lose intuitive understanding to the design problem at hand, which is very important in geotechnical design to make engineering judgements in the course of design.

The RBD scheme we are proposing here attempts to take into account of characteristics of geotechnical design as much as

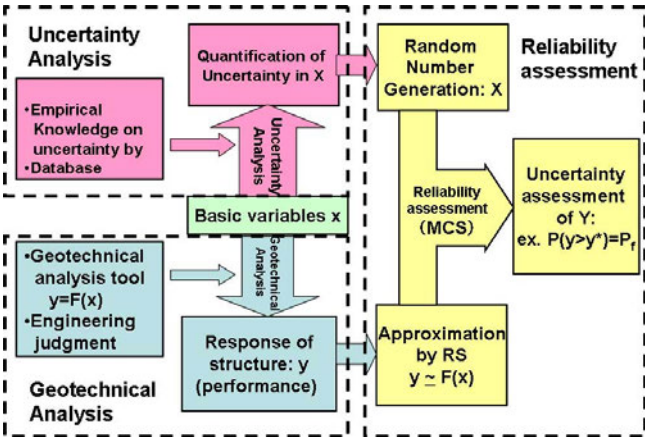

Figure 1 Proposed RBD scheme

[1] Department of Civil Engineering, Gifu University, Gifu, Japan

possible. The scheme is for geotechnical engineers who are proficient in various aspects of geotechnical design but not very familiar with RBD tools.

In this presentation, only the overall outline of the scheme is described. The concept of the methodology is more focused, but details are not very well explained. For the details of the methodology, readers are requested to see papers listed in the reference list. I

It is also a purpose of this paper to identify the major sources of uncertainty that are important in geotechnical RBD through four examples. It may be generally recognized that the spatial variability of soil properties is the most important source of uncertainty in geotechnical RBD. However, from the results presented in this paper, it is only one of the sources of uncertainty. In many design problems, statistical estimation error, design calculation model error and transformation error associated with estimating soil parameters (*e.g.* friction angle) from the measured quantities (*e.g.* SPT N-values) exhibit higher uncertainty.

PROPOSED SCHEME FOR GEOTECHNICAL RBD

Outline of the Scheme

The basic concept of the scheme is illustrated in Figure 1. The scheme starts with the basic variables. The basic variables include all variables concerned in design: Various actions, environmental effects, geotechnical parameters, other material properties, configuration and size of structure and supporting ground, boundary conditions are all included in the basic variables.

The scheme proposed here is separated to three parts: (I) geotechnical design, (II) uncertainty analysis of basic variables and (III) reliability assessment.

Geotechnical design, (I), is almost the same as usual design procedure for geotechnical structures. The response of the structure (safety factor etc.), y, is obtained from the basic variables, x, by the design calculations. In some cases y can be related to x by a relatively simple performance function. In other cases, the response surface (RS) method can be used to relate x to y by a regression analysis (Box & Drepper, 1987).

The uncertainty analysis of basic variables, (II), is the main part of RA. Statistical analysis plays the major role in this analysis. Some basic knowledge on probability theory and statistical analysis are required in this step. Much accumulated knowledge in geotechnical reliability design is employed in carrying out the analyses. The author is recommending use of R language in this step which can make the analysis very easy and efficient. Actually, all the uncertainty analyses and reliability analyses presented in this paper are done by R.

The reliability assessment, (III), is carried out based on the results of the uncertainty analyses and the performance function by simple Monte Carlo simulation (MCS). MCS is recommended due to the following reasons:

(1) MCS is a very straight forward reliability analysis procedure that does not require detailed background knowledge of the probability theory in most cases.
(2) Since the performance function (or the response surface) introduced in the RBD calculation is simple, they do not require much calculation time. Therefore, it is not necessary to introduce any sophisticated reliability analysis methods that save the number of calculations of the performance function.

Classification of Uncertainties and Their Treatment

A classifications of the uncertainties encountered in geotechnical RBD is given in this section together with brief description how they are generally treated in this study. Not all the uncertainties classified here need to be considered in all geotechnical RBD. They need to be chosen according to the needs and the conditions of each design problem. It is assumed in this paper that the uncertainties on actions are separately given.

Measurement error

It is error involved in measurements in investigations and tests. In the traditional error theory, the measurement error is assumed to independently and identically follow a normal distribution. On the other hand, this error may include biases caused by the equipments and the operators. However, this error is usually ignored in geotechnical RBD because the influence of it may not be large compared to other uncertainty sources. Furthermore, it is very difficult to separate measurement error from observed spatial variability. Thus, the observed spatial variability may also include the measurement error.

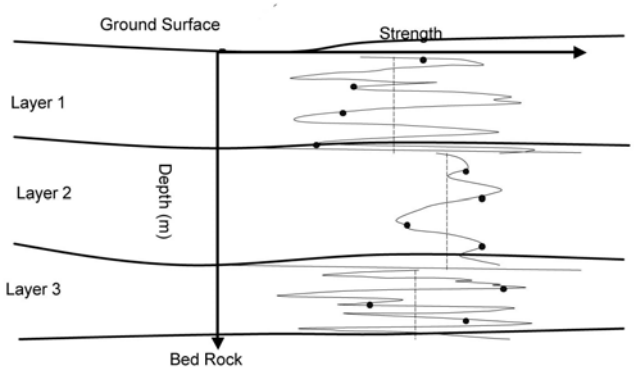

Figure 2 Modelling soil profile by random field

Spatial variability:

The spatial variability of geologically identical geotechnical parameters are conveniently (or fictitiously) modelled by the random field (RF) theory in geotechnical RBD. The geotechnical parameters are determined by themselves and already exist at each location. However, because of our ignorance (*i.e.* lack of knowledge or Epistemic uncertainty (Baecher and Christian, 2003)), we model them using RF for our convenience. It is a simplification and an idealization of the problem.

It is a general procedure to model soil profile that belongs to a geologically identical layer by superposition of the trend and the random components (Lumb, 1974; Vanmarcke, 1977; Matsuo, 1984; Phoon and Kulhawy, 1999a *etc.*). The trend component gives a general overall behavior of the soil property, whereas the random component describes discrepancy of each observation from the trend (Figure 2):

$$z(x) = f(x|\beta) + \varepsilon(x|\sigma,\theta) \qquad \varepsilon \sim N(0,\sigma^2,\theta) \tag{1}$$

where

x : spatial coordinate vector (x_1, x_2, x_3), $f(x|\beta)$: a function showing the trend component

β : trend parameter vector, $\varepsilon(x|\sigma,\theta)$: the random component

σ^2 : variance of the random filed, θ : autocorrelation distance vector $\theta = (\theta v, \theta_h)$

θ_v : autocorrelation distance in vertical direction, θ_h : autocorrelation distance in horizontal direction

The random component $\varepsilon(\boldsymbol{x})$ is assumed to consist a stationary (=homogeneous) random filed (RF). The stationarity assumed in this study is that in a weak sense, which implies the RF can be described by the following three statistics:

$$\begin{aligned} &\mu_z(x_1, x_2, x_3) = 0 \\ &\sigma_z^{\ 2}(x_1, x_2, x_3) = \sigma^{\ 2} \\ &\rho_z(x_1, x_2, x_3) = \rho(\Delta x_1, \Delta x_2, \Delta x_3) \end{aligned} \tag{2}$$

The first equation states that the mean is a constant, *i.e.* independent of the coordinate $\boldsymbol{x}=(x_1, x_2, x_3)$. In the present context, this mean value is assumed to be 0. The second equation expresses that the variance is also constant. Finally, the third equation states that the autocorrelation function is given not by the absolute coordinate but by the relative distance between the two coordinate positions.

In addition to the above assumptions, the form of autocorrelation function is specified in this study. Due to the deposition process of soil layers, it is generally assumed that autocorrelation structure for the horizontal direction, *i.e.* x_1 and x_2, and for the vertical, *i.e.* x_3, are different. We assume that the autocorrelation function has separable property as suggested by Vanmarcke (1977):

$$\rho_\varepsilon(\sqrt{\Delta x_1^{\ 2} + \Delta x_2^{\ 2}}, \Delta x_3) = \rho_{\varepsilon h}(\sqrt{\Delta x_1^{\ 2} + \Delta x_2^{\ 2}}) \cdot \rho_{\varepsilon v}(\Delta x_3) \tag{3}$$

The exponential type autocorrelation function is assumed in this study

The typical values of these statistics for various types of soil are summarized, for example, in Phoon and Kulhawy (1999a and 1999b).

Statistical estimation error

Errors associated with the estimation of parameters of RF are termed the statistical estimation error. It further includes estimation error for parameter values estimated at a certain point in space by, say, Kriging. RF theory is used as a platform to evaluate statistical estimation errors.

In evaluating statistical estimation error, the author believes it very important to distinguish between the two cases below (Honjo and Setiawan,2007; Honjo, 2008).

General Estimation*:* The relative position of investigation location and of a structure to be built <u>is not taken into account</u> in soil parameter estimation. For example, if a large container yard to be designed, the bearing capacity of the ground at an arbitrary location may be evaluated considering general property of ground condition obtained in the whole area.

Local Estimation*:* The relative position of investigation location and of a structure to be built <u>is taken into account</u> in soil parameter estimation. Therefore, there would be considerable reduction in the estimation error if the two locations are very close. A straightforward example of this case is that if one wants to design a foundation for a house and made a detailed soil investigation at the spot, one need to consider very little uncertainty to ground condition.

The situation described here as General and Local estimation are rather common situations encountered by geotechnical engineers. The engineers surely have treated these conditions in an implicit way, and modified their design. These are a part of so called *engineering judgement* in the traditional geotechnical engineering. The difference here is that we explicitly take into account these situations and try to quantify the uncertainty.

Honjo and Setiawan (2007) has given formulation for these two cases for a particular situation. Honjo (2008) has discussed this problem in connection with actual design. A recent paper by Honjo et al. (2011) gives a general formulation for the general estimation, which is employed in the examples of this paper as well. For the local estimation in this paper, block Kriging is employed (*e.g.* Wachernagel, 1998).

The author believes that a general statistical theory need to be developed for these two situations based on RF theory. It is like the normal population theory gives a general theory for the mathematical statistics. Although any real situation do not exactly satisfy the simplified and idealized assumptions made in the theory, it can contribute quite a lot to give a basic platform for the evaluation of the statistical estimation error in geotechnical parameter estimation and geotechnical RBD.

Transformation error

Errors associated with the transformation of measured geotechnical parameters by a soil investigation to geotechnical parameters used in the design calculation are termed transformation error. There are usually both biases and scatters in the transformations.

Readers will see the examples of the transformation errors in the examples of this paper. The most comprehensive reference for this problem is a manual provided by Kulhawy and Mayne (1990), which gives considerable amount of quantitative information on this problem.

Design calculation model error

This is error associated with prediction capabilities of simplified and idealized design calculation models on the real phenomena. In geotechnical engineering, the tests and experiments closer to real structure scales (*e.g.* pile load tests, plate loading tests *etc.*) are more commonly performed, and many failure cases are available especially on earth structures such as embankments, cut slopes and excavations. These facts make it easier for us to evaluate the model errors in a quantitative manner in geotechnical design.

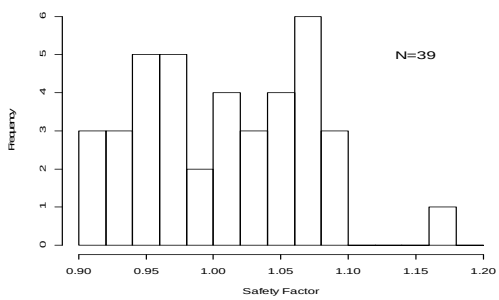

Figure 3 Error in Swedish circular slop analysis (Matsuo and Asaoka, 1976)

For example, the model error of the Swedish circular slip method in stability of embankment on soft cohesive soil is analyzed in detail by Wu and Kraft (1970) and Matsuo and Asaoka (1976). The latter has analyzed failed embankments on soft ground, and concluded that by the cancellations of many factors involved in the stability analysis, the final safety factors calculated follows an uniform distribution that lies between 0.9 and 1.1 (Fig.3). This conclusion is essentially in accordance with a comprehensive review on this problem by Wu (2009), where he stated that the combined uncertainty for limit equilibrium analysis with circular slip is estimated to be mean 1.0 (i.e. no bias) with COV 0.13-0.24.

By over viewing the uncertainties encountered in geotechnical design, most of uncertainty sources are Epistemic uncertainty (*i.e.* lack of knowledge) rather than Aleatory uncertainty (*i.e.* pure randomness) (Beacher and Christian, 2003). We are like playing cards with the ground where we peep through their cards by some investigations. (In this game, fortunately, the nature does not have any intention to circumvent us.) An example of sequence of uncertainties entering into geotechnical RBD is illustrated in Figure 4.

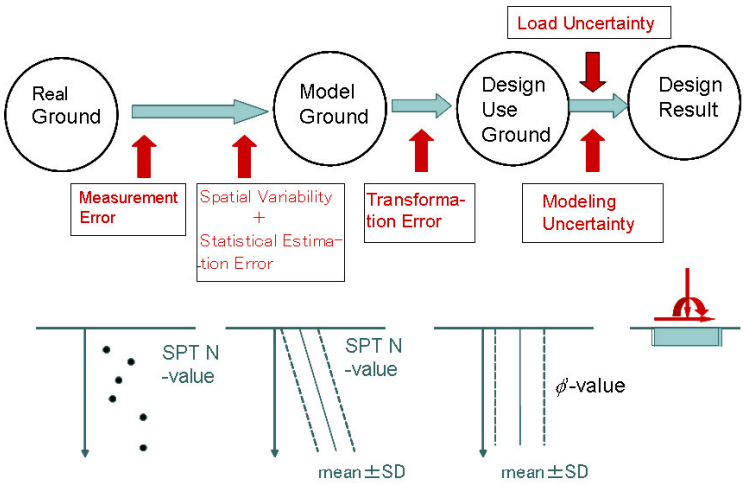

Figure 4 An example of a procedure for geotechnical RBD

Local Average and Reliability Assessment

There is a description on the characteristic value of a geotechnical parameter in Eurocode 7 (CEN,2004) as follows:

> *'The zone of ground governing the behaviour of a geotechnical structure at a limit state is usually much larger than a test sample or the zone of ground affected in an in situ test. Consequently the value of the governing parameter is often the mean of a range of values covering a large surface or volume of the ground. The characteristic value should be a cautious estimate of this mean value' (CEN EN1997-1, 2.4.5.2 (7)).*

The same fact has been pointed out much earlier by Vanmarcke (1977) that it is the local averages (LA) of soil properties that are important in controlling behaviour of geotechnical structures, such as piles, shallow foundations and slopes.

In geotechnical RBD, it is necessary to take the weighted average of geotechnical parameters to obtain the resistance. For example, the shaft resistance of a pile is integration of the soil strength along the pile shaft, resistance moment of a slip surface is integration of soil strength along the slip arc, and settlement of a pad foundation may be controlled by the average stiffness of a certain size of soil mass right under the foundation.

The local average (LA) of the geotechnical parameter for vertical direction over a length L is defined:

$$\bar{Z}_L = \frac{1}{L}\int_0^L Z(x)dx \tag{4}$$

It is apparent that the mean of the LA coincides with the original mean of the RF, μ. Furthermore, the variance reduction of the local average from the original variance of the RF has extensively studied by Vanmarcke (1977 and 1983), where he has derived

so called the *variance function*, $\Gamma^2(L)$. If the autocorrelation function is of the exponential type, s_L^2, can be obtained by the variance function as,

$$s_L^2 = E\left[\left\{\frac{1}{\mathrm{L}}\int_0^L Z(x)dx - \mu\right\}^2\right] = \sigma^2\Gamma^2\left(\frac{L}{\theta}\right) = \sigma^2\left(\frac{\theta}{L}\right)^2\left[2\left(\frac{L}{\theta} - 1 + \exp\left(-\frac{L}{\theta}\right)\right)\right] \tag{5}$$

Vanmarke has further extended the theory to multidimensional space, and found that if the autocorrelation function is separable, the variance of local average over an area or a volume can be obtained by multiplying the variance functions for each dimension.

In this study, the resistance is calculated based on the local average of a certain soil mass that is controlling the behaviour of a geotechnical structure. Thus the uncertainty of resistance is a reflection of the variance of the local average of the geotechnical parameter.

GEOTECHNICAL RELIABILITY BASED DESIGN BY EXAMPLES

The proposed RBD scheme has been applied to several cases. 4 examples are chosen here to illustrate the procedure and highlight the characteristic of the method. Based on the results, some discussions are made to identify the major issues geotechnical RBD are challenged.

The first three examples are problems set by ETC10 for the purpose of a comparative study of the national annexes of Eurocode 7. The problems are relatively straight forward but not excessively simplified to lose the essence of real geotechnical design problems. Due to the limitation of the space, the details of RBD are not described. One should see Honjo et al. (2010, 2011) for the details.

The fourth problem is based on Otake et al. (2011) submitted to this conference. It is a reliability assessment of a 14 km long irrigation channel for liquefaction during expected Tokai-Tonankai earthquake. The difference between the general and the local estimation of the soil parameters on the results are emphasized.

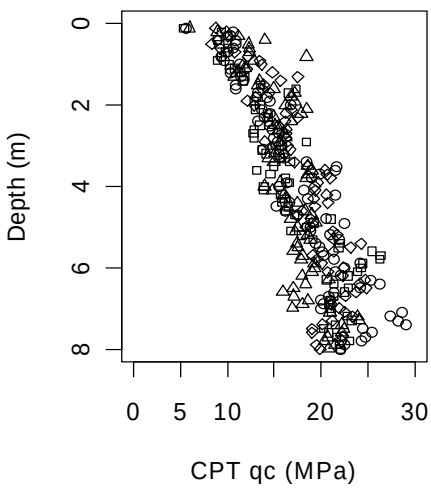

Figure 6 4 CPT q_c results

Pad foundation on sand (ETC10 EX2-1)

The problem is to determine the width of a square pad foundation on a uniform and very dense fine glacial outwash sand layer of 8 (m) thick on the underlying bedrock (Figure 5). It is requested that the settlement should be less than 25 (mm)

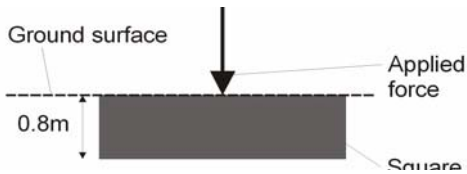

Figure 5 The pad foundation on sand

(SLS) and stability should be secured (ULS). The design working life of the structure is 50 years.

It is specified that the pad foundation is to be built at embedded depth of 0.8 (m), and vertical permanent and variable loads of the characteristic values 1000 (kN) (excluding the weight of foundation) and 750 (kN) respectively are applied. The unit weight of the concrete is 25 (kN/m^3). No horizontal loading is applied.

There are 4 CPT tests within 15 (m) radius from the point the pad foundation is to be constructed and digitized q_c and f_s values of 0.1 (m) interval are given to 8 (m) depth from the ground surface (Figure 6). The groundwater is 6 (m) below the ground surface. The unit weight of sand is 20 (kN/m^3).

Uncertainty analysis

There are two limits states to be examined: SLS where the settlement should be less than 25mm, and ULS where the stability should be secured.

For the SLS, the CPT q_c values are used to model the spatial variability of the ground. A linear model is used to describe the trend and the residuals follow a normal distribution. The vertical autocorrelation distance of 0.4 m is estimated. The horizontal autocorrelation distance of 4 m is assumed.

The general estimation is employed and estimation error is evaluated. Also reduction of the variance by taking the local average between the depth of 0.8 to 1.8 m is taken into account. The overall reduction of SD of CPT q_c value is estimated, where SD of 2.28 MPa reduced to 1.66 MPa.

Table 1 List of basic variables for Ex.2-1 SLS settlement

Basic variables	Notation	mean	SD	Distribution type
Estimation error and local average variance of q_c	I_E is proportional to I_{qc}	qc=10.54+1.66x_3 (MPa)	7.2(MPa) COV=0.13(1) at z=1.5(m)	Normal
Transformation error on E' from q_c	δ_E	1.14	0.94	Lognormal
Permanent load	δ_{Gk}	1.0	0.1	Normal(2)
Variable load	δ_{Qk}	0.6	0.35x0.6=0.21	Gumbel distribution(2)

(Note 1) COV has been obtained by Eq.(3). (Note 2) Based on JCSS (2001) and Holicky et al. (2007).

Table 2 List of basic variables for Ex.2-1 ULS stability

Basic variables	Notation	Mean	SD	Distribution type
Spatial variability	ϕ'_{tc}	42.8 (degree)	0	Deterministic variable
Transformation error from q_c	ϕ'_{tc}	42.8 (degree)	2.8 (degree)	Normal
R_u model error	δ_{Ru}	0.894	0.257	Lognormal
Permanent action	δ_{Gk}	1.0	0.1	Normal
Variable action	δ_{Qk}	0.6	0.35x0.6=0.21	Gumbel distribution

The transformation of CPT q_c values to Yong's modulus is done considering the transformation error. The mean and SD of the error is estimated to be 1.14 and 0.94 respectively. This is considerably large error.

The uncertainty associated with the permanent and the variable loads are taken from Holicky et al. (2007). . These quantities are used in the code calibrations of the structural Eurocodes rather widely. The uncertainties evaluated are listed in Table 1 for SLS.

For the ULS, the CPT q_c values are first converted to internal friction angle in a equation proposed by Kulhawy and Mayne (1990). The converted internal friction angle had very small variance, which made the spatial variability of this quantity null. The transformation error in this conversion is given in the same literature.

The model error in the bearing capacity calculation form the internal friction angle is obtained from a recent literature which compares the calculated values with the results of the plate loading test. The evaluated uncertainties are listed in Table 2 for ULS.

Geotechnical analysis and performance function

As for SLS, 3D PLAXIS is used to obtain the relationship between the settlement and the foundation size, B at the mean values of Young's modulus and the loads. It is found that the settlement has a linear relationship with $log(B)$. Since the ground is assumed to be a elastic body, the settlement is doubled if Young's modulus is half or the load is doubled. These relationships are taken into account, and a performance function is obtained:

$$s = \frac{(17.0 - 9.73\log(B))}{I_E \cdot \delta_E}\left(\frac{\gamma \cdot D_f \cdot B^2 + G_k\delta_{Gk} + Q_k\delta_{Qk}}{\gamma \cdot D_f \cdot B^2 + G_k + Q_k}\right) = \frac{(17.0 - 9.73\log(B))}{I_E \cdot \delta_E}\left(\frac{20 \cdot B^2 + 1000\delta_{Gvk} + 750\delta_{Qvk}}{20 \cdot B^2 + 1750}\right) \quad (6)$$

The performance function for ULS is given as follows:

$$M = Ru(B,\ \phi'_{\mathrm{tc}}) \cdot \delta_{Ru} - G_k \cdot \delta_{Gk} - Q_k \cdot \delta_{Qk} \quad (7)$$

Where R_u is a classic bearing capacity formula, and M is the safety margin. The definitions of other notations are given in Table

Reliability assessment and results

Simple Monte Carlo simulation is employed to carry out the reliability analysis. The uncertainty listed in Table 1 and Eq.(6) are used to evaluate the probability that the settlement exceeds 25 mm for SLS. The same procedure is taken to evaluate the failure probability of the pad foundation based on Table 2 and Eq.(7).

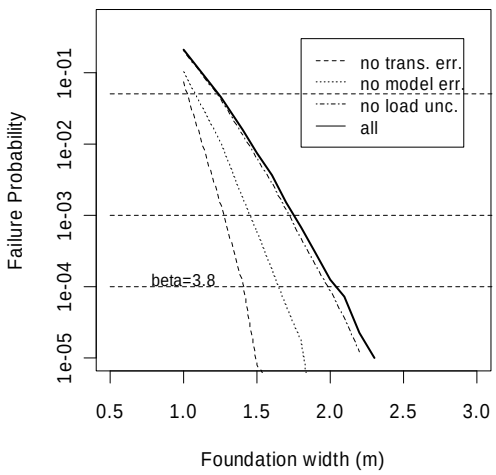

Figure 7 The results of MCS on the stability of the pad foundation.

Figure 7 shows the results of MCS on ULS of the pad foundation. The MCS is repeated several times by removing each uncertainty sources to see the impact, which the results are also presented in the figure. The necessary width of the foundation based on the result for both SLS and ULS are presented in Table 4.

Table 4 summary of the results for the pad foundation

Limit state	Target β for 50 years design working life. (P_f)	Required width (m)
S.L.S.(s < 25 mm)	1.5 (0.067)	B > 2.4 (m)
U.L.S.(stability)	3.8 (10^{-4})	B > 2.2 (m)

Table 5(a) contribution of each uncertainty source for settlement analysis (B=1.0 m)

Uncertainty sources	All uncertainties Considered	transformation error	spatial variability	load uncertainty
β and β_{-i}	0.595	2.804	0.623	0.590
contribution	100 %	92 %	8 %	0 %

Table 5(b) contribution of each uncertainty source for stability analysis (B=1.0 m)

Uncertainty sources	All uncertainties considered	transformation error	model error	load uncertainty
β and β_{-i}	0.811	1.443	1.261	0.840
contribution	100 %	51 %	44 %	5 %

The influence of each uncertainty source is listed in Table 5(a) and (b). An approximation method to estimate the contribution of each factor is explained in Appendix A. A discussion will be made on these resu;ltss in the latter section of this paper.

Pile foundation in sand (ETC10 EX2-6)

Problem description

The problem is to determine pile length L (m) of a pile foundation of a building. The pile is a bored pile (D = 0.45 m) embedded entirely in a medium dense to dense sand spaced at 2.0 (m) interval (Figure 8). Each pile carries a characteristic vertical permanent load of 300 (kN) and a characteristic vertical variable load of 150 (kN). The soil profile includes Pleistocene fine and medium sand covered by Holocene layers of loose sand, soft clay, and peat (see Table 6).

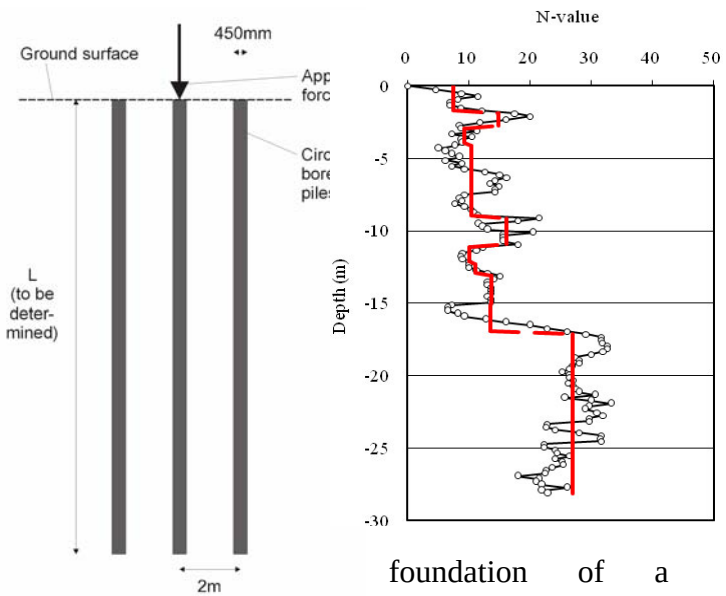

Figure 8 The configuration of the bored pile and soil profile by SPT N-value transformed from CPT q_c value.

There is one CPT (q_c measurement only) close to the spot to determine the strength profile of the ground. The water table is about 1.4 (m) below the ground level.

Uncertainty analysis

The bearing capacity estimation equation for pile the author used is based on SPT N-value. Thus CPT q_c value is converted to SPT N-value by a equation given in

Kulhawy and Mayne (1990). This transformation equation has the transformation error of mean 1, COV 1.03 and follows a log normal distribution.

Since there is only one CPT test result, and the layer have quite complex structure, the soil profile is modeled by 10 layers and the mean and the SD of each layer is estimated from the CPT test result.

The model error in the empirical bearing capacity estimation equation used widely in Japan is obtained from a literature which is based on the results of a number of pile loading test results. The model error for estimating shaft resistance and pile tip resistance are given separately as shown in Table 6.

Table 6 Statistical properties of the basic variables

Basic variables	Notations	Mean	SD	Distribution	Note
uncertainty on characteristic value of permanent load	δ_{Gk}	1.0	0.1	Normal	G_k = 300 (kN) (1)
uncertainty of characteristic value of variable load	δ_{Qk}	0.6	0.21	Gumbel	Q_k = 150 (kN) (1)
uncertainty of estimating pile shaft resistance	δ_f	1.07	0.492	Log Normal	Okahara *et.al* (1991)
uncertainty of estimating pile tip resistance	δ_{qd}	1.12	0.706	Log Normal	Okahara *et.al* (1991)
uncertainty of transformation from CPT q_c to N	δ_t	1	1.03	Log Normal	Kulhawy & Mayne (1990)
Layer 1 Clay with sand seams	$N1^{(2)}$	7.51	3.66	Normal	Depth 0.0 - 1.9 (m)
Layer 2 Fine sand	$N2^{(2)}$	14.80	4.58	Normal	Depth 1.9 - 2.9 (m)
Layer 3 Clay with sand seams	$N3^{(2)}$	9.24	1.44	Normal	Depth 2.9 - 4.0 (m)
Layer 4 Fine silty sand	$N4^{(2)}$	10.33	3.22	Normal	Depth 4.0 - 9.0 (m)
Layer 5 Fine silty sand with clay & peat seams	$N5^{(2)}$	16.17	3.31	Normal	Depth 9.0 - 11.0 (m)
Layer 6 Clay with sand seams	$N5^{(2)}$	10.08	1.45	Normal	Depth 11.0 - 12.3 (m)
Layer 7 Clay with peat seams	$N7^{(2)}$	11.14	1.51	Normal	Depth 12.3 - 13.0 (m)
Layer 8 Clay with peat seams	$N8^{(2)}$	13.68	0.54	Normal	Depth 13.0 - 15.0 (m)
Layer 9 Fine sand	$N9^{(2)}$	13.56	7.24	Normal	Depth 15.0 - 17.0 (m)
Layer 10 Fine sand	$N10^{(2)}$	26.98	3.71	Normal	Depth 17.0 (m) below

（Note 1）Based on Holicky, M, J. Markova and H. Gulvanessian (2007). (Note 2) Unit of soil ayers are SPT N-values

The uncertainties on permanent and variable loads are taken from the same literature used in the previous example, and given in Table 6.

Geotechnical analysis and performance function

The performance function employed in this example is given as follows:

$$M = U\delta_f \sum_{i=1}^{n} \delta_{ti} f_i(\delta_t N_i) L_i + \delta_{qd} q_a(\delta_t N_n) A_p - \delta_{Gk} G_k - \delta_{Qk} Q_k \tag{8}$$

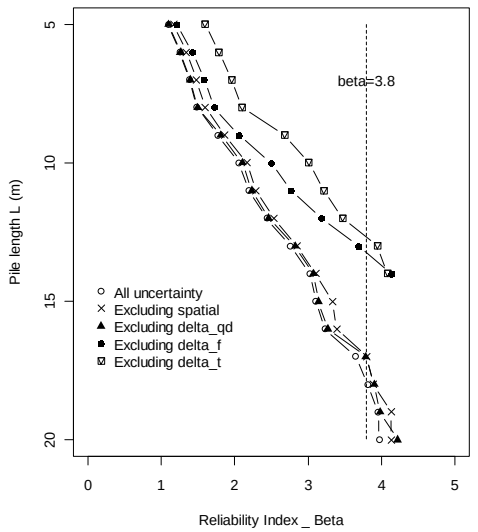

Figure 9 The results of MCS on the stability of the pile foundation.

where, U: perimeter of the pile (m), f_i: maximum shaft resistance of each soil layer (kN/m2), L_i: thickness of each soil layer (m), N: standard penetration test (SPT) blow count, q_d: ultimate pile tip resistance intensity per unit area (kN/m2), and other notations are listed in Table 6. The details of f_l and q_d is given in SHB (2002).

Reliability assessment and results

Monte Carlo simulation using R language is carried out for different pile length L (m) to obtain the reliability index (or probability of failure). In this analysis, the number of random numbers generated for each case is 500,000 sets. The obtained reliability index for different pile length is shown in Figure 9.

Since the case considered is the ultimate limit sate, the reliability index, β, of more than 3.8 may be required. The pile length of more than 18 (m) is necessary.

In order to investigate the contribution of each uncertainty sources, reliability analyses are carried out by removing each uncertainty source at a time. These results are shown in Figure 9 as well. The rate of contribution of each source is further presented in Table 7 The contributions are estimated based on the approximation method explained in Appendix A. The result of this table will be discussed later.

Table 7 contribution of each uncertainty source for a pile bearing capacity (at L=13 m)

Uncertainty sources	All uncertainty	Spatial variability	Pile tip resistance	Pile shaft resistance	Transformation error
β and β_{-i}	2.75	2.85	2.82	3.69	3.94
contribution	100 %	6 %	5 %	41 %	48 %

Embankment on peat ground

Problem description

An embankment is to be designed on a soft peat ground whose final height should be 3 (m) above the ground surface (Figure 10). The problem here is to determine the first stage embankment height. The inclination of the embankment slope is 1:2, whereas the crest width 1 (m). The unit weight, γ, of the embankment soil is 19 (kN/m^3) and the friction angle ϕ'_k=32.5 (degree).

The ground surface is horizontal. The ground consists of a few dm of topsoil and normally consolidated clay (γ=18 (kN/m^3) and γ' = 9 (kN/m^3)) on a 3 to 7 (m) thick peat layer with γ' =2 (kN/m^3) overlaying Pleistocene sand of γ' =11 (kN/m^3) and ϕ'_k =35 (degree). 5 filed vane test (FVT) results are given whose testing interval is 0.5 (m) in the vertical direction and the length varies between 2.5 and 7.0 (m).

Only ultimate limit state needs to considered and no variable loads have to be taken into account.

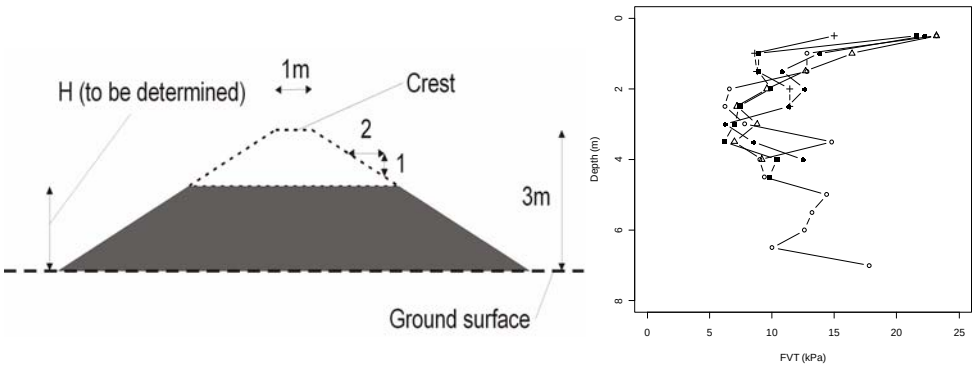

Figure 10 The configuration of an embankment on peat and the results of 5 FVT..

Uncertainty analysis

The five FVT results are plotted in Figure 10. It is observed that s_u at surface layer of about 0.5 (m) is considerably larger than the bottom peat layer indicating different soil layer. It is determined to separate these data, and group them as topsoil. The trend component of the underneath peat layer is obtained as a quadratic curve, and the residual random component fits to a normal distribution with a constant variance of 2.40^2 (kPa^2).

The statistical estimation error for estimating the local average of peat layer is obtained, whose SD is estimated to be 0.528 (kPa), whereas the variance reduction by local averaging for 4 m depth makes SD of spatial variability to be 1.12 (kPa). The resulting SD for the local average of the peat strength is $\sqrt{0.528^2+1.12^2}=1.24$ (kPa).

The uncertainty concerning the thickness of the top soil is introduced, so as the undrained shear strength, s_u. They are all listed in Table 8.

The design calculation model error is obtained based on Matsuo and Asaoka (1976), where an uniform distribution of [-0.1, 0.1] is introduced.

Table 8 Basic variables of embankment on peat

Basic variables	Notations	mean	SD	Distribution
Topsoil s_u	$s_{utopsoil}$	21.04 (kPa)	3.44	Normal
	$(I_{topsoil})$	(1.0)	(0.163)	
Peat s_u	s_{upeat}	14.73-3.51z +0.536z^2 (kPa)	1.20	Normal
	(I_{peat})	(1.0)	(0.13)(1)	
Topsoil thickness	D_t	[0.5, 1.0] (m)		Uniform(2)
Uncertainty of ϕ'=0 method	δ_{Fs}	[-0.1, 0.1]		Uniform(3)
Unit weight of embankment	γ_f	19.0(kN/m^3)	—	Deterministic
Friction of embankment	ϕ_f	32.5 degree	—	Deterministic
Unit weight of topsoil	γ_c'	9.0(kN/m^3)	—	Deterministic
Unit weight of peat	γ_P'	2.0(kN/m^3)	—	Deterministic
Friction of sand	ϕ_s	35 degree	—	Deterministic
Unit weight of sand	γ_s'	11.0(kN/m^3)	—	Deterministic

(Note 1) s_{upeat} (at z=4.0(m)) = 14.73 - 3.5x4.0 + 0.53x4.0^2 = 9.27, COV=1.24/9.27=0.13

(Note 2) It is assumed that the boundary of the topsoil and the peat layer lies somewhere between z = 0.5 to 1.0 (m).

(Note 3

Geotechnical analysis and performance function

A response surface (RS) that relates embankment height, h, s_u of the topsoil layer, s_u of the peat layer, the thickness of the topsoil, D_t, and the safety factor, F_s, is obtained by a regression analysis based on the results of the stability analysis of 75 combinations of these parameters. Swedish circular method is employed for the stability analysis. In order to make the response surface equation simple, s_u of the peat layer and the topsoil layer are normalized at their mean values

$$I_{peat} = s_u/(\text{mean of } s_u \text{ of the peat layer})$$
$$I_{topsoil} = s_u/(\text{mean of } s_u \text{ of the topsoil}) = s_u/21.04 \qquad (9)$$

Based on the obtained response surface, a performance function is obtained as follows:

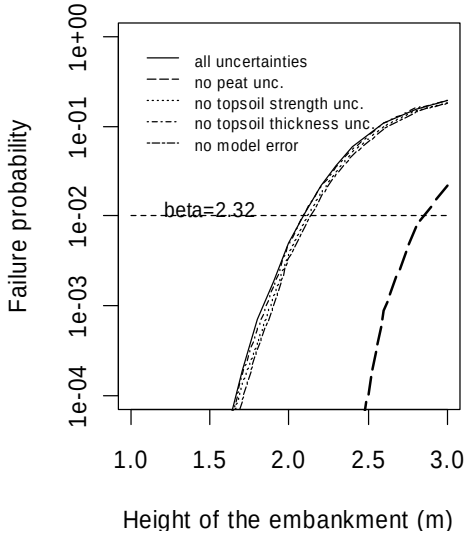

Figure 11 An embankment on peat MCS results.

$$Fs = 1.783 - 1.351\,h + 0.213\,h^2 + 1.156\,I_{peat} + 0.272\,I_{topsoil} + 0.091\,D_t + \delta_{Fs} \qquad (10)$$

where the notations are given in Table 8.

Reliability assessment and results

The performance function obtained in Eq.(10) is employed to evaluate the failure probability of embankment, Prob[$Fs \leq 1.0$], by MCS. The uncertainties considered in the analysis are listed in Table 8.

The MCS results are plotted in Figure 11. It is difficult to determine what level of reliability is required in this structure. If the failure probability of 1 %, which is β = 2.32 is chosen as a target, the height of the embankment for the fist stage may be 2.1 (m). The safety factor by the Swedish method is about 1.4 if the mean values of soil parameters are used in the stability calculation

The failure probability is evaluated by removing each uncertain source to find out the impact of each source. These results are also presented in Figure 11. The contribution of each source is approximately estimated by the method explained in Appendix A, where the results are listed in Table 9. In this case, the peat soil strength is the dominant source of uncertainty which is followed by the model error.

Table 9 The rate of contribution of each uncertainty source for embankment stability

Uncertainty sources	All uncertainty	Peat strength	Top soil strength	Top soil thickness	Model error
β and β_{-i}	2.27	4.58	2.38	2.29	2.44
Contribution	100 %	75 %	9 %	2 %	13 %
Notes		Statistical: 14 % Spatial: 61 %			

Discussions

It is also one of the purposes of this paper to identify some of the major issues geotechnical RBD is challenged based on the results of the examples. The important sources of uncertainty in geotechnical RBD can be found by carefully discussing the results presented in Tables 5(a), 5(b), 7, 9 and 11. The following observations are

possible for RBD of SLS and ULS of the pad foundation, the pile foundation and the embankment on peat:

- It is found from SLS design of the pad foundation that uncertainty is quite large which makes necessary size of the foundation massive (Table 4). This is due to the large uncertainty in transforming CPT q_c to Young's modulus, which can be seen from the results in Table 5(a) that 92% of the uncertainty comes from this transformation error. It is well recognized among geotechnical engineers that estimating stiffness characteristics of ground from the penetration type investigations such as SPT and CPT is not reliable, and the result is ascertaining this fact. Traditionally, therefore, SLS is not checked in the shallow foundation design, and fairly large safety factor, *e.g.* 3, is introduced in ULS design to secure the performance for SLS.
- In stability problem of the foundation, *i.e.* ULS of the pad foundation and the pile foundation, the transformation error and the design calculation model error dominate the uncertainty. In both examples these two uncertainty sources contribute about 40 to 50 % of all uncertainty in the RBD respectively that they are actually controlling the results of the design (Tables 5(b) and 7). The transformation error in the pad foundation design is estimating ϕ' from q_c, whereas in the pile foundation design from q_c to SPT N-value. The model errors of the design calculation equations for the both examples are obtained by comparing the calculated results to the observations (i.e. the results of plate loading tests and pile loading tests). If the author was familiar with the pile capacity calculation formula based on q_c, the transformation error in the pile design may have been considerably reduced. The spatial variability of the soil property in the two examples are small because (1) the variance reduction by the local averaging, and (2) very small fluctuation of ϕ' in the pad foundation example.
- Only in the embankment example, the soil spatial variability is the major source of the uncertainty (Table 9). The spatial variability of the peat and top soil undrained shear strength occupies 70% of the total uncertainty. The statistical estimation error and the design calculation model error contribute 14 and 13 % respectively. This consequence comes partly from the accuracy of the design calculation formula, i.e. Sweetish circular slip method, as presented in Fig. 3. The model error in this example is much smaller compared to the former examples.

CONCLUSIONS

All the examples exhibited in this paper, the description is orders in "*problem description*", "*uncertainty analysis*", "*geotechnical analysis and performance function*" and then "*reliability assessment*". The uncertainty analysis part does require some knowledge in statistical analysis. However, other parts need only small knowledge on probability and statistics. It is anticipated that the readers are able to perceive some engineering judgments introduced in geotechnical analysis part, such as some geotechnical interpretation of the transformation equation from q_c to ϕ' in the pad foundation ULS example, the introduction of top soil layer thickness into embankment stability example.

Through these examples, it may be understood that it is not necessarily soil properties spatial variability that controls the major part of uncertainty in many geotechnical design problems. The error in design calculation formulas, transformation

of soil investigation results (*e.g.* SPT N-values, FVT, CPT q_c) to actual design parameters (*e.g.* s_u, ϕ', resistance values), and statistical estimation error are more important sources in some cases.

All the statistical and reliability calculations carried out in this paper are done by R language. Due to the restriction of space, it was not possible to explain the superiority of this language in this paper. By using R language, these operations become much user friendly and less time consuming.

REFERENCES

Baecher, G. B. and J. T. Christian (2003). Reliability and statistics in geotechnical engineering. New York: John Wiley & Sons.

Box and Draper(1987) : Empirical Model Building with Response Surface , John Wiley.

CEN (2004). *Eurocode 7: Geotechnical design - Part 1: General rules, EN 1997-1:2004 (E), (F) and (G), November 2004*, European Committee for Standardization: Brussels.

ETC 10: Evaluation of Eurocode 7, Design Examples 2, 2009,

Honjo, Y. and K. Kuroda (1991). A new look at fluctuating geotechnical data for reliability design, Soils and Foundations, Vol.31, N0.1: 110-120.

Honjo, Y. & Setiawan B. (2007), General and local estimation of local average and their application in geotechnical parameter estimations, Georisk, 1(3), 167-176.

Honjo, Y.(2008): General vs. Local Reliability Based Design in Geotechnical Engineering, a keynote lecture at APSSRA'08, Structural Reliability and Its Application (eds. L.S. Katafygiotls, Limin Zhang, W.H. Tang and M. Cheung) pp.41-52.

Honjo, Y., T. Hara and T.C. Kieu Le (2010): Level III reliability based design by response surface: an embankment, Proc. 17th Southeast Asian Geotechnical Conference, Vol.2 pp203-206, Taipei.

Honjo, Y., T. Hara and T.C. Kieu Le (2010): Level III reliability based design by response surface: pad foundation, Proc. 17th Southeast Asian Geotechnical Conference, Vol.2 pp.207-210, Taipei.

Holicky, M., Markova, J. & Gulvanessian, H. (2007). Code calibration allowing for reliability differentiation and production quality. Applications of Statistics and Probability in Civil Engineering. Kanda, Takada & Furuat (eds).

Kulhawy, F.H. & Mayne, P.W. (1990). Manual on estimating soil properties for foundation design. Report EL-6800, Electric Power Research Inst., Palo Alto, 306 p.

Jounel, A.G. and Huijbregts, C.J. (1978). Mining Geostatistics: Academic Press.

Lumb, P.(1974): Application of statistics in soil mechanics, 'Soil Mechanics - new horizons', pp.44-111, Newness Butterworths, London, 1974.

Matsuo, M & A. Asaoka (1976). A statistical study on conventional “safety factor method”, *Soils and Foundations*, 16(1), 75-90.

Okahara, M., Takagi, S., Nakatani, S., and Kimura, Y. (1991). A study on bearing capacity of a single pile and design method of cylinder shaped foundations, Technical Memorandum of PWRI, 2919.

Phoon, K.K. and F.H.Kolhawy (1999a). Characterization of geotechnical variability, Canadian Geotechnical J., 36: 612-624.

Phoon, K.K. and F.H Kolhawy (1999b). Evaluation of geotechnical property variability, Canadian Geotechnical J., 36: 625-639.

SHB (2002) Specifications for highway bridges, Japan Road Association..

Vanmarcke, E.H. (1977). Probabilistic modeling of soil profiles, Journal of the. Geotechnical Engineering Division, ASCE, Vol.103, No.GT11, pp.1227-1246.

Vanmarcke, E.H.(1983), Random Field: Analysis and Synthesis, The MIT Press, Cambridge, Massachusetts.

Wachernagel, H. (1998). Multivariate Geostatistics: second completely revied edition: Springer.

Wu, T.H. and Kraft, L.M. (1970). Safety Analysis of Slopes, *Journal of Soil Mechanics and Foundations, ASCE*, 96(2), 609-630.

Wu, T.H. (2009), Reliability of geotechnical predictions, *Procs of The Second International Symposium on Geotechnical Risk and Safety*, CRC Press, p3 – 10.

2010 MAULE CHILE EARTHQUAKE WALL PERFORMANCE AND ITS APPLICATION TO IMPROVEMENT OF THE AASHTO LRFD SEISMIC WALL DESIGN SPECIFICATIONS

Tony M. Allen, P.E.[1]

Abstract

The 2010 Maule Chile earthquake provided a natural full scale laboratory to investigate the seismic performance of walls designed using the AASHTO design specifications (AASHTO 2002). Examples of wall performance in Chile during that earthquake and lessons learned, as well as wall performance observations from other earthquakes and seismic research, were used to develop the first major update of the AASHTO specification seismic wall design sections in almost 20 years. Specification improvements described include a no seismic design option, recommendations for wall design and construction details to improve seismic performance, and a revised seismic earth pressure design approach, resulting in more cost effective wall designs.

Introduction

On February 27, 2010, a magnitude 8.8 earthquake occurred just off the coast of the Maule region in central Chile, affecting the central valley and coastal areas, and strongly affecting Chile's two largest cities, Santiago and Concepción. This was a major subduction zone earthquake, a type of earthquake that is not uncommon in Chile. A reconnaissance team (including the author) organized by the US Federal Highway Administration (FHWA) investigated the performance of Chile's transportation infrastructure shortly after the earthquake (Yen, et al., 2011).

This paper summarizes the performance of the retaining walls in that earthquake and identifies lessons learned. Considering the magnitude of this earthquake and the observed good performance of walls, even those close to the epicenter, it was decided to use the information gained to help evaluate the potential for developing improvements to the AASHTO LRFD Bridge Design Specifications regarding seismic wall design. This paper also describes how this information, seismic wall performance information from other earthquakes, and seismic research was used to develop the first major revision to the AASHTO LRFD seismic wall design specifications (AASHTO 2012) in almost 20 years.

2010 Maule, Chile Ground Motions

Ground motions from this earthquake were felt strongly from Santiago (335 km NE of the epicenter) to the Arauco Peninsula over 100 to 150 km south of the epicenter. Peak ground accelerations ranged from 0.17g to 0.3g at good soil sites, but to as high as 0.56g in poor soil sites, in the Santiago vicinity and in the central valley. In Concepción on the coast, peak horizontal and vertical ground accelerations of 0.6g or

[1] State Geotechnical Engineer, Washington State Department of Transportation

more were observed. One of the most notable features of this earthquake was its duration. Figure 1 provides an example ground motion in the Concepción area and illustrates its duration. The ground motions experienced in Chile in this earthquake are likely to be similar to what the coastal areas of Washington and Oregon in the USA could experience in the future and represent the design level event for that area.

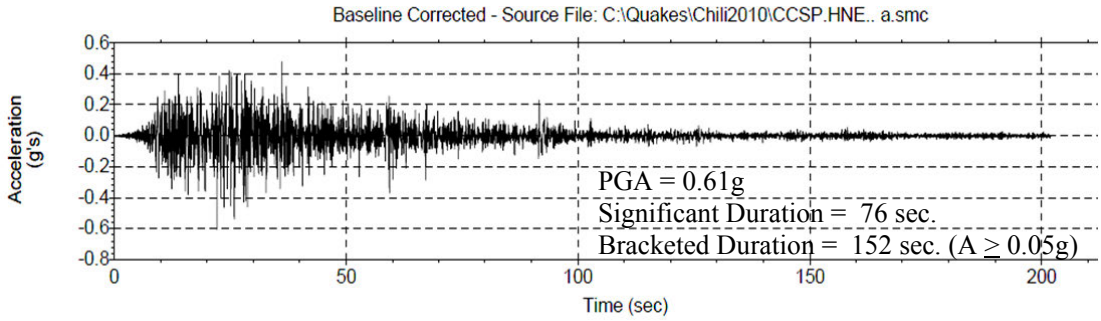

Figure 1. Example Ground Motion from San Pedro De La Paz, Concepción (after Yen, et al. 2011).

Wall Design in Chile

Transportation infrastructure walls in Chile have been designed using the AASHTO Standard Specifications for Highway Bridges (AASHTO 2002) since the mid-1950's. Therefore, this earthquake provided an excellent opportunity to evaluate how walls designed using the AASHTO specifications could perform in a design level earthquake in the Pacific Northwest of the United States (US).

As is true for bridges, design peak ground accelerations (PGA's) for walls in Chile were only 0.12g before 1985, increasing to 0.15g after 1985, and increasing again in 2001 to 0.4g on the coast and 0.3g in the central valley (Yen, et al. 2011). The design acceleration is reduced to 50% of the PGA for gravity walls, allowing some movement of the wall to occur, though for reinforced soil walls, this reduction in the acceleration was not allowed.

Wall Performance in Chile

Wall performance in the 2010 Chile earthquake was observed at 14 sites, and each site typically had multiple walls. Wall types evaluated included panel and concrete block faced reinforced soil walls, concrete gravity walls, and anchored walls. Wall heights ranged from a few meters to over 12 m. Backfill soil for most walls was granular, ranging from fine uniform sands to well graded gravels. Overall, wall performance was very good, with only limited damage, and no walls collapsed. The first three figures (figures 2 through 4) show examples of walls that performed well. The next four figures (figures 5 through 8) illustrate walls that suffered damage but that did not collapse.

Figure 2(a) shows two walls retaining the approaches to the Americo

Vespucio/Independencia Bridges in Santiago, built in 2004. The wall to the left in the figure is a high density polyethylene (HDPE) geogrid reinforced wall with a dry cast concrete block facing, and the one on the right is a steel reinforced soil wall with concrete precast panels. Both walls are approximately 6 to 7 m in height. Figure 2(b) shows the bridges at the same interchange, which did sustain some damage that required the bridge to be shored until repairs could be made. Other than some toppling of facing blocks at the top of the block faced wall due to poor connection and coping details, the walls showed no signs of damage due to the earthquake.

Figure 2. The Americo Vespucio/Independencia Interchange Showing (a) Bridge Approach Walls, and (b) the Bridges and Abutments.

Figure 3 shows an exceptionally large (i.e., approximately 12 m high) concrete faced gravity wall supporting the Maipu River Railroad Bridge just south of Santiago. Both the wall and bridge were not damaged and were fully operational after the earthquake, yet parallel bridges at this site did suffer significant damage, but without collapse.

Figure 4(a) shows one of the dry cast concrete block faced HDPE geogrid reinforced soil walls that form the bridge abutments for the Avenida Independencia Bridge at Estribo Francisco Mostrazal between Santiago and Rancagua in the central valley. These walls, 7.4 m in exposed height, directly support the bridge abutment footing load of approximately 210 kPa at each abutment, the typical maximum allowed footing loading in the AASHTO design specifications. The walls were designed using the 2002 AASHTO Standard Specifications (Tensar Earth Technologies 2003). For seismic design, the acceleration coefficient used was 0.3g. Though ground motion data was not available at this particular site, based on ground motion data in the general vicinity, actual PGA's were likely in the range of 0.3g to 0.5g. Reinforcement spacing varied from 0.2 to 0.4 m, and reinforcement length varied from 80 to 100% of the wall height. Most of the reinforcement layers had an ultimate tensile strength of approximately 130 kN/m. Good quality crushed stone backfill (42° design friction angle) was used for the walls.

As can be seen in the figure, the abutment walls showed no sign of damage or permanent deformation. However, the bridge superstructure was damaged, but still functional, as shown in Figure 4(b). The bridge superstructure has both significant skew and a significant longitudinal downward slope. The combination of slope and

skew caused the bridge superstructure to move downslope and toward the acute angle in the bridge skew, resulting in the damage, yet the walls were unaffected. This case history is a testament to the ability of reinforced soil wall structures to resist large earthquake loading.

Figure 3. Abutment Wall Supporting the Maipu River Railroad Bridge South of Santiago.

Figure 4. Avenida Independencia Bridge Geogrid Reinforced Soil Walls at Estribo Francisco Mostrazal (a) West abutment, and (b) East Abutment.

Figure 5 shows one of the first reinforced soil walls built in Chile, in 1995. This wall is located in Concepción, near one of the hardest hit areas in that location. The site is underlain by 6 to 7 m of loose sand and silt with a high water table, and some sand boils (evidence of liquefaction) were observed. One of the older bridges at the site collapsed, and the other bridges were significantly damaged (Yen, et al. 2011). The wall shown in the figure is approximately 10 m high where it makes contact with the severely skewed Via Elevada railroad undercrossing bridge abutment wall. The severe skew restricted the length of the steel soil reinforcement (bar mats) attached to the wall facing panels closest to the bridge abutment wall. Furthermore, the vertical joint between the reinforced soil wall and the bridge abutment wall was not tied together to prevent movement and separation at the vertical joint, though in all other respects, the wall was designed in accordance with the AASHTO bridge design specifications available at that time, but using a higher seismic design acceleration (0.4g) than required by Chilean design standards at that time (W. Neely, Aug. 30, 2010 personal communication). The backfill used for the wall was a uniform medium river sand. Based on testimony from the wall supplier (W. Neely, personal communication), the backfill soil used was very difficult to maintain compaction, causing difficulties in

keeping the facing panels aligned during wall construction. As can be seen in Figure 5, the wall top moved outward about 0.3 m, likely the result of the lack of connection at the vertical joint combined with the medium uniform sand backfill.

Figure 5. Abutment and Reinforced Soil Wall at the Via Elevada Railroad Undercrossing.

The other walls at the bridge shown in Figure 5 and other bridges at this interchange exhibited similar performance problems where the reinforced soil walls joined with the bridge abutment walls. An example of the walls at these other bridges is shown in Figures 6 and 7. In this case, the lower wall moved outward over 0.3 m, due to a combination of lateral sliding and outward rotation. It is possible that liquefaction induced weakening of the soil below the wall contributed to this movement. However, of all the walls observed in Chile, this is the only wall that exhibited what appeared to be a sliding failure. In all other cases, when wall movement occurred, it was due to rotation of the wall, or liquefaction induced displacement. As the wall moved outward, a large gap formed due to the lack of connection across the vertical joint, allowing much of the sand backfill to flow through the opening.

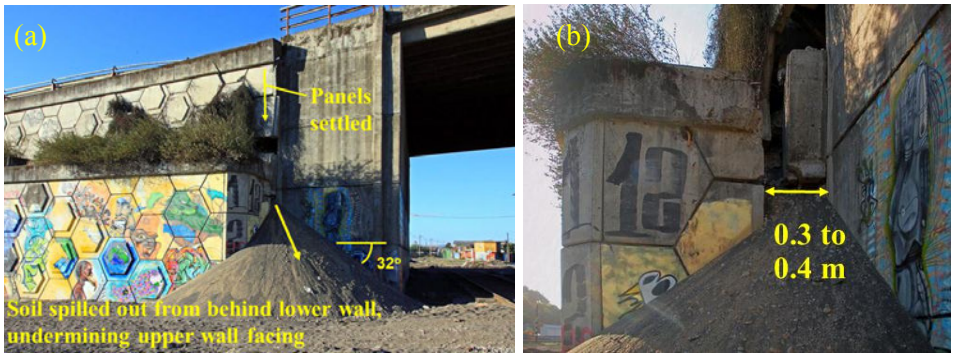

Figure 6. Tiered Walls at the Via Elevada Railroad Crossing (a) Overall View of Walls, and (b) Close-up Showing Movement of Lower Tier.

Figure 8 shows one of the four dry cast concrete block faced HDPE geogrid walls built in 2009 that retain the approach fills for this railroad undercrossing near Talca in the central valley, almost directly east of the earthquake epicenter. PGA's in

this area were likely in the range of 0.5g, based on ground motion records in the general area (e.g., Curico) and its relatively close proximity to the epicenter. The walls have a maximum height of over 9 m plus a 2 m high surcharge. Another important feature of these walls is the very tight curve in the wall alignment. Based on construction photos, geogrid strips were placed throughout the curve, requiring the geogrid strips to overlap one another through the curve. It was not clear if some soil was placed between the overlapping geogrid strips to ensure good pullout resistance, and how well the geogrid connected with the facing blocks within the curve in the wall alignment.

Figure 7. Wall Shown in Figure 6, but from Back Side Showing Exposed Junction between Reinforced Soil Wall and Bridge Curtain Wall.

As can be seen in this figure, the wall shown did exhibit significant deformation, primarily through tilting, as no sliding of the wall at its base was observed. The tilting of the wall resulted in the formation of 45° shear bands (see especially Figure 8c) in the facing blocks, especially transverse to the bridge centerline and in the vicinity of the tight radius curve in the wall alignment. Some deformation and shearing also was present in the other four walls at this site, but not as severe as the wall shown in the figure.

Summary of Wall Performance in Chile and Lessons Learned

Overall, very few walls within the region affected by the 2010 Maule earthquake exhibited even minor damage, and no wall actually collapsed (Yen, et al. 2011). This observation applied to reinforced soil walls, concrete gravity walls, anchored walls, and soil nail walls (Yen, et al. 2011). Of the walls that did exhibit some damage, as illustrated in the previous figures, the damage typically consisted of a few toppled facing blocks, separation of vertical joints between the wall and adjacent structure, tilting of the facing, though generally less than 0.2 to 0.3 m, and in one case, shearing of the facing blocks. With the exception of the walls that were subjected to liquefaction effects, most of the wall performance problems observed were due to marginal or inadequate design details that could be improved. Walls generally did not exhibit basal sliding or settlement unless the soil below the wall exhibited liquefaction, and even in that case, no wall collapse was observed. This may indicate that sliding resistance is much greater than assumed in design. This finding is similar to that described by Koseki, et al. (2006) with regard to observations from model walls in shake table studies.

Figure 8. Muros Talca Railroad Crossing with Dry Cast Concrete Block Faced HDPE Geogrid Walls (a) Ground View, (b) View of Wall from Bridge, and (c) Close-up of Wall Face Showing 45° Shear Bands.

A lesson learned from the performance of walls in Chile is the importance of using good details for wall design and construction. Specifically, the following should be considered for future design of walls in seismically active areas:

- Avoid uniform sand backfill, especially if it lacks angularity. While uniform sand is well drained, it can be unstable with regard to reinforced soil wall backfill, allowing soil reinforcement to slip and facing panels to separate. A more well-graded mix of soil, but with low silt/clay content, is preferred.

- The top facing blocks or panels should be tied together well to prevent toppling. This can be accomplished through the use of good coping details, and possibly connecting and grouting the top few blocks or panels together.

- Wall corners and tight radius curves in the wall alignment tend to exhibit damage more often than relatively straight sections of wall. If wall corners are not properly joined together, they can open up and allow backfill to spill through during shaking. In severe cases, shearing of panels or facing blocks can occur. Special details may be necessary at corners or sharp turns in the wall alignment to prevent separation of panels and to address the three dimensional aspects of the corner or tight radius curve.

- Full height joints in walls can come apart during shaking. These joints should

be structurally tied together adequately to prevent separation during shaking, but not so tight that the joints attract load and differential settlement issues cannot be addressed.

- For reinforced soil walls, a minimum reinforcement length of 70% of the height or more, especially in upper part of wall, appears to prevent excessive lateral deformation of wall face. This is especially important for heavily skewed bridges where the reinforced soil wall joins the curtain wall or abutment wall.

Application of Lessons Learned to Improve the Seismic Wall Design Specifications

Recognizing the very good performance of walls in the 2010 Maule earthquake, considering the severity of the ground motions, a reasonable next step is to re-evaluate the seismic wall design provisions of the AASHTO design specifications. To make sure such specification changes are broadly applicable, wall performance in other earthquakes and seismic wall research were considered. Furthermore, research conducted at the request of the AASHTO Bridge Subcommittee (Anderson, et al. 2008) was considered, as it was the Subcommittee's intention to use the research results provided in that report as the basis for updating the seismic wall design portions of the AASHTO LRFD Bridge Design Specifications. The AASHTO T-15 Technical Committee took the lead in implementing this research plus the lessons learned from Chile to complete the revisions needed. Since the AASHTO specifications are national in nature, national (i.e., US) input from the voting members of the Bridge Subcommittee (i.e., all state transportation departments), academia, and the wall industry was obtained, including review of draft design specification changes. Only the development background for some of the key changes made to the seismic wall design articles in the AASHTO Specifications are described herein due to paper length restrictions. Specifically, the following are addressed: (1) the development of no seismic analysis provisions for walls, (2) improvements to the approach used to estimate seismic earth pressure, and (3) the development of recommended wall details for improved seismic performance.

The concept of a no seismic analysis option was initially developed by Anderson, et al. (2008). The criteria they recommended were very simple, considering the peak ground acceleration and slope above the wall. This was used as a starting point. To establish a no seismic analysis provision for walls, key criteria to determine whether or not a no seismic analysis is allowed for a given wall were needed. Criteria selected to be developed for this purpose are as follows: (1) the maximum acceptable PGA, (2) potential for liquefaction or presence of sensitive clays, (3) the wall application, and (4) total wall height.

Regarding the first criterion, maximum PGA, the concept is to require wall seismic design only for cases in which there is a risk of poor wall performance. Opinions varied widely among the US states regarding the maximum allowed PGA, as the value selected defines which US states must do seismic design of walls. Recommendations from various researchers regarding the value selected also varied. Even as early as 1970, Seed and Whitman (1970) concluded that "many walls

adequately designed for static earth pressures will automatically have the capacity to withstand earthquake ground motions of substantial magnitudes and in many cases, special seismic provisions may not be needed," and further indicated that this applies to gravity walls with PGA's up to 0.25g. Anderson, et al. (2008) recommended using a PGA of 0.2 to 0.3g, depending on the soil slope above the wall. More recently, Bray, et al. (2010) and Lew, et al. (2010a, 2010b) indicate that lateral earth pressure increases due to seismic ground motion are likely insignificant for PGA's of 0.3g to 0.4g or less, indicating that walls designed to resist static loads (i.e., the strength and service limit states) will likely have adequate stability for the seismic loading case. Figure 9 shows the results of centrifuge modeling of walls under seismic loading conducted by Al Atik and Sitar (2010) that illustrates seismically induced lateral earth pressure does not become significant until the PGA exceeds 0.4g.

A PGA criterion can also be developed empirically from wall performance in past earthquakes, such as the 2010 Maule Chile earthquake. Clough and Fragaszy (1977) assessed damage to floodway structures, consisting of reinforced concrete cantilever (vertical) walls structurally tied to a floor slab forming a continuous U-shaped structure, due to the 1971 San Fernando earthquake. They found that no damage was observed where PGA's along the structures were less than 0.5g (see Figure 10). However, damage and wall collapse was observed where accelerations were higher than 0.5g or where the structures crossed the earthquake fault, though in the latter case damage was quite localized. They noted that while higher strength steel rebar was used in the actual structure than required by the static design, the structure was not explicitly designed to resist seismic loads. Gazetas, et al. (2004) for concrete gravity walls in the 1999 Athens earthquake and Lew et al. (1995) for tieback shoring walls in the 1994 Northridge earthquake observed that wall performance was good for peak ground accelerations up to just under 0.5g even though the walls were not specifically designed to handle seismic loads. AASHTO (2012) provides a more complete summary of wall seismic performance in Appendix A11.

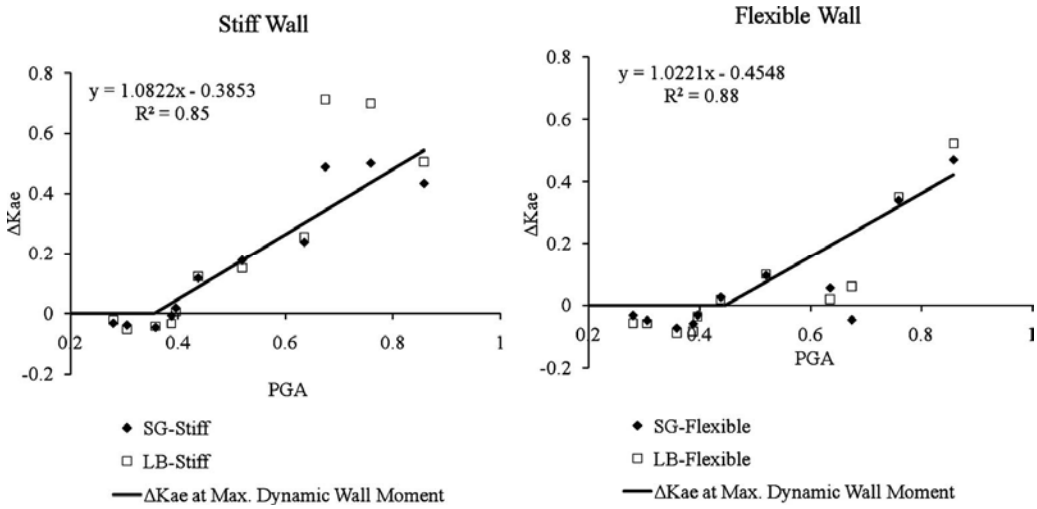

Figure 9. Centrifuge Wall Modeling Results Illustrating when Dynamic Earth Pressure (ΔK_{ae}) Becomes Measurable (after Al Atik and Sitar, 2010).

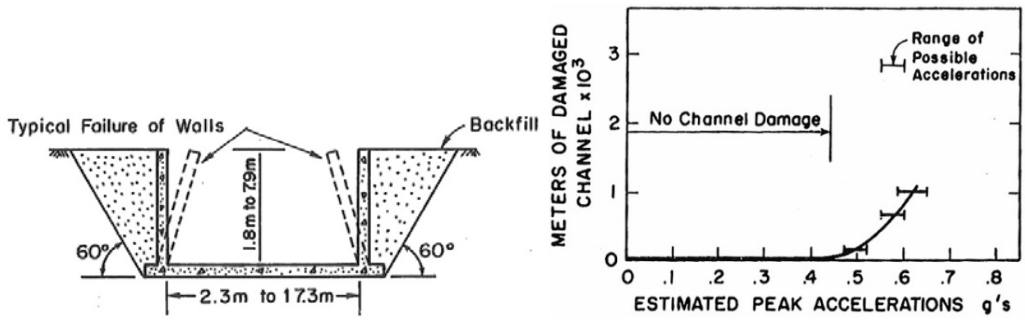

Figure 10. Floodway Walls in the 1971 San Fernando Earthquake, (a) Floodway Wall Configuration and Failure Mechanism, and (b) PGA versus Length of Walls Damaged (after Clough and Fragaszy 1977).

While there have been some notable wall failures in past earthquakes, those failures were for situations where more severe ground motions that noted above occurred, severe liquefaction occurred, or for much older walls that did not come close to even meeting current design standards for static loading. For example, Seed and Whitman (1970) indicated that severe displacement or collapse occurred for some concrete gravity walls and quay walls in the great Chilean Earthquake of 1960 and in the Niigata, Japan Earthquake of 1964 due to severe liquefaction. But at sites where the water table was deeper, severe wall damage or collapse was an infrequent occurrence. Tatsuoka, et al. (1996) indicated that collapse occurred for several of the very old (1920's to 1960's) unreinforced masonry gravity walls and concrete gravity structures exposed to strong shaking (e.g., as high as 0.6g to 0.8g) in the 1995 Kobe Japan earthquake, likely due to the presence of weak foundation soils or the presence of a very steep sloping surcharge (e.g., 1.5H:1V) combined with poor soil conditions.

As summarized previously, wall performance in the 2010 Maule earthquake was very good, even for relatively high long duration earthquake ground motions, though in most cases those walls were designed for seismic loading. If problems did occur, it was typically due to wall details that could be improved to ensure good seismic performance. Furthermore, some of the tallest walls did suffer more significant damage, but without collapse.

Therefore, from these observations combined with available research, the following can be concluded with regard to a wall no seismic analysis provision:

- Setting the limit at 0.4 g for a no seismic analysis provision represents a reasonable compromise between observations from laboratory modeling and full scale wall situations (i.e., lab modeling indicates seismic earth pressures are very low below 0.4g, and walls in actual earthquakes start to have serious problems, including collapses even in relatively good soils, when the acceleration is greater than 0.5g and the wall has not been designed for the seismic loading).
- Liquefaction can contribute to severe wall damage, displacement, and possibly collapse. Therefore, if significant liquefaction can occur, a seismic analysis

should always be conducted. This also applies to walls supported on sensitive or otherwise already weak cohesive soils.

- If wall damage occurs, it appears more likely to occur with taller walls, say 10 m or more in height. Therefore, seismic analysis should normally be conducted if the wall height is approximately 10 m or more.
- Walls that are in critical applications, such as those that support other structures, should always be evaluated for seismic loading, considering both the stability and performance of the wall itself, and the effect the wall performance has on the structure it supports.
- The wall details are important for obtaining good seismic performance, especially how abrupt changes in wall geometry and vertical joints are tied together, and how the top facing elements are tied together (e.g., with the coping). In 2010, the AASHTO specifications did not have much information on what are considered good seismic details for walls. Therefore, good seismic details should be a condition of use of the no seismic analysis option for walls.

Considering the good performance of walls typically observed in even the largest and most damaging of earthquakes, it is likely that the methods currently in use to estimate the seismically induced lateral earth pressures on walls are conservative. Therefore, factors contributing to design conservatism in the seismic earth pressures used for design are investigated. The Mononobe-Okabe (MO) method to estimate seismic earth pressure has been in use for many years and is likely one source of this conservatism, especially in certain situations (Koseki, et al. 1998; Nakamura, 2006). The MO method, while simple to use, also has limitations in its applicability, and due to lack of alternative design tools, has been used in situations for which the method was not intended (AASHTO 2012). Anderson, et al. (2008) developed an alternative Generalized Limit Equilibrium (GLE) Method that could be applied, with greater accuracy, to a wider range of situations, such as layered soils, high ground water, and the presence of soil cohesion. This method will yield similar results to the MO Method for the simpler situations for which the MO Method was developed, as the theoretical basis for both methods still results in flattening of the failure surface and increase in failure mass due to seismic acceleration, contributing to conservative predictions from both methods (Koseki, et al. 1998). However, the GLE Method can be used to advantage to account for factors the MO Method is not capable of addressing, reducing the level of conservatism in those situations. Therefore, the Anderson, et al. (2008) alternative procedure is now included in the AASHTO design specifications and the limitations of the MO Method are described. While this is a step in the right direction, the MO analysis method improvements to seismic earth pressure prediction developed in Japan (Koseki, et al. 1998) should, however, be considered in the future for the AASHTO seismic wall design specifications.

Another source of conservatism in the prediction of seismic earth pressure is the treatment of the active soil mass behind the wall during shaking as a rigid body (Koseki, et al. 2006). This affects how wall deformation during shaking affects the seismically induced forces in the wall and the soil mass and the assumption that the seismic forces act simultaneously on the wall and the backfill. In the past, this issue has been crudely addressed through reduced acceleration theoretically calculated using

Newmark analysis, and in some cases with discounting a portion of the seismic active earth pressure when combined with the wall inertial force, at least for reinforced soil walls (AASHTO 2002). Anderson, et al. (2008) partially addressed this though a recommended wave scattering factor and improvements to prediction of seismic earth pressure reduction as a function of sliding deformation. While these improvements are still somewhat dependent on the rigid body assumption, they do reduce some of the conservatism in the prediction of seismic earth pressure. These recommended improvements are now included in the new (AASHTO 2012) design specifications. Refinements, based on Nakamura (2006), in how seismic earth pressure forces are combined with wall mass inertial forces to account for phase differences in these forces have also been developed and included in the AASHTO specifications.

The location of the seismic earth pressure resultant can be another source of conservatism in assessing the seismic stability of walls. Mononobe and Matsuo (1929) originally suggested that the resultant of the active earth pressure during seismic loading remain the same as for when only static forces are present (i.e., H/3, where H is the wall height). However, theoretical considerations by Wood (*1973*), who found that the resultant of the dynamic pressure acted approximately at mid-height, and empirical considerations from model studies summarized by Seed and Whitman (1970), resulted in increasing the height of the resultant location above the wall base to H/2, which has been used for many years in US design practice. Back analysis of full scale walls in past earthquakes, however, indicates earth pressure resultants located higher than H/3 will overestimate the force, resulting in a prediction of wall failure when in reality the wall performed well (Clough and Fragaszy, 1977). This appears to be consistent with observations of walls in Chile. Recent research also indicates the location of the resultant (static plus seismic) should be at H/3 based on centrifuge model tests on gravity walls (Al Atik and Sitar, 2010, Bray, et al., 2010, and Lew, et al. 2010). However, Nakamura (2006) also indicates that the resultant location could be slightly higher, depending on the specifics of the ground motion and the wall details. A reasonable approach is to assume that for routine walls, the combined static/seismic resultant should be located at the same location as static earth pressure resultant, but no less than H/3. However, a slightly higher resultant location (e.g., 0.4H to 0.5H) should be considered for walls in which the impact of failure is very high.

With regard to wall details that can help to ensure good seismic wall performance, the lessons learned from the 2010 Maule Chile earthquake provided previously herein can be used directly, as well as used in principle to apply to details used in current proprietary wall systems to address, for example, wall corners and vertical joints in the wall facing. Hence, the AASHTO LRFD Bridge Design Specifications (AASHTO 2012), specifically articles 11.6.5.6 and 11.10.7.4, now include recommendations for wall design and construction details that will help to improve wall seismic performance.

Concluding Remarks

The 2010 Maule Chile earthquake provided a natural full scale laboratory to investigate the seismic performance of walls designed using the design code that has

been used in US transportation infrastructure design, the AASHTO Standard Specifications for Highway Bridges (2002). Lessons learned from the wall performance observed in that earthquake, as well as wall performance observations from other earthquakes and recent seismic research, were useful for developing the first major update of the AASHTO seismic wall design specifications in almost 20 years. Overall, the updated wall design specifications are less conservative than what has been used in the past, improving the cost effectiveness of wall designs in seismically active areas. Yet, the addition of recommendations for improved wall design and construction details in the AASHTO specifications will help to obtain more consistent seismic performance of walls in the future.

Highlighted herein is the development background for some of the key changes recently implemented in the AASHTO LRFD Bridge Design Specifications. The improvements made to the estimation of seismic earth pressure are a good first step. However, it is recommended that the Koseki, et al. (1998) improvements to MO analysis be considered for future AASHTO specification improvements. There are other significant changes to those design specifications that could not be discussed in detail due to space limitations, such as, the use of soil cohesion in seismic design situations, and an improved internal seismic stability design procedure for reinforced soils walls. The AASHTO specifications, Section 11 and Appendix A11, (AASHTO 2012) should be consulted for additional background on these changes.

Acknowledgments

The assistance of Chile's Ministry of Public Works in getting to the wall sites and in obtaining background information on the walls is gratefully acknowledged.

References

AASHTO. 2002. *Standard Specifications for Highway Bridges*. American Association of State Highway and Transportation Officials (AASHTO), 17th ed., Washington, D.C.

AASHTO. 2012. *AASHTO LRFD Bridge Design Specifications*, American Association of State Highway and Transportation Officials, Sixth Edition, Washington, D.C., USA.

Al Atik, L. And Sitar, N., 2010, "Seismic Earth Pressures on Cantilever Retaining Structures," *ASCE JGGE*, October 2010, pp. 1324-1333.

Anderson, D.G., Martin, G. R., Lam, I. (P.), and Wang, J. N., 2008, *Seismic Analysis and Design of Retaining Walls, Slopes and Embankments, and Buried Structures*, NCHRP Report 611, National Cooperative Highway Research Program, 137 pp.

Bray, J. D., Travasarou, T., and Zupan, J., 2010, "Seismic Displacement Design of Earth Retaining Structures," *Proceedings of the ASCE Earth Retention Conference 3*, Bellevue, WA, pp. 638-655.

Clough, G. W. and Fragaszy, R. F. 1977. "A Study of Earth Loadings on Floodway Retaining Structures in the 1971 San Fernando Valley Earthquake." *In Proc., 6th World Conference on Earthquake Engineering*. pp. 7 37–7 42.

Gazetas, G., Psarropoulos, P. N., Anastasopoulos, I., and Gerolymos, N. (2004). "Seismic behavior of flexible retaining systems subjected to short-duration moderately strong excitation." *Soil. Dyn. Earthquake Eng.*, 24, 537–550.

Koseki, J., Tatsuoka, F., Munaf, Y., Tateyama, M., and Kojima, K., 1998, "A Modified Procedures to Evaluate Active Earth Pressure at High Seismic Loads," *Soils and Foundations*, Special Issue on Geotechnical Aspects of the January 17 1995 Hyogoken-Nambu Earthquake, Vol. 2, pp. 209-216.

Lew, M., Simantob, E., and Hudson, M. E. (1995). "Performance of shored earth retaining systems during the January 17, 1994, Northridge earthquake." *Proc., 3rd Int. Conf. on Recent Advances in Geotechnical Earthquake Engineering and Soil Dynamics*, Vol. 3, St. Louis.

Lew, M., Sitar, N., and Al Atik, L., 2010a, "Seismic Earth Pressures: Fact or Fiction," *Proceedings of the ASCE Earth Retention Conference 3*, Bellevue, WA, pp. 656-673.

Lew, M., Sitar, N., Al Atik, L., Pouranjani, M. and Hudson, M. B., 2010b, "Seismic Earth Pressures on Deep Building Basements," *SEAOC 2010 Convention Proceedings*, pp. 1-12.

Mononobe, N. and Matsuo, M., 1929, "On the Determination of Earth Pressures During Earthquakes," *Proceedings, World Engineering Congress*, Vol. 9.

Nakamura, S., 2006, "Reexamination of Mononobe-Okabe Theory of gravity Retaining Walls Using Centrifuge Model Tests," *Soils and Foundations*, Vol. 46, No. 2pp. 135-146.

Seed, H. B., and R. V. Whitman. 1970. "Design of Earth Retaining Structures for Dynamic Loads." *In Proc., ASCE Specialty Conference on Lateral Stresses in the Ground and Design of Earth Retaining Structures.* American Society of Civil Engineers, NY, pp. 103–147.

Tatsuoka, F., Koseki, J., and Tateyama, M., 1996, "Performance of Reinforced Soil Structures during the 1995 Hyogo-ken Nanbu Earthquake," *IS Kyushu '96 Special Report, Earth Reinforcement*, Ochiai et al. eds., Balkema, pp. 1-36.

Tensar Earth Technologies, 2003, *MESA Wall Design Calculations for Ruta H-10 San Francisco de Mostazal*, 10 pp.

Yen, W. P., Chen, G., Buckle, I., Allen, T. M., Alzamora, D., Ger, J., and Arias, J. G., 2011, *Postearthquake Reconnaissance Report on Transportation Infrastructure Impact of the February 27, 2010 Offshore Maule Earthquake in Chile*, FHWA Report No. FHWA-HRT-11-030, Washington, DC, 214 pp.

THE STRUCTURAL DESIGN OF PILE FOUNDATIONS BASED ON LRFD FOR JAPANESE HIGHWAYS

Hideaki Nishida[1],Toshiaki Nanazawa[2], Masahiro Shirato[3] ,
Tetsuya Kohno[4], and Mitsuaki Kitaura [5]

Abstract

One of the motivations for applying reliability-based design to geotechnical engineering is to confirm that more reasonable and cost-effective design results will be obtained when owners and designers invest in more detailed geotechnical investigations. In this paper, we propose load and resistance factor design for the structural design of piles in pile foundations for Level 1 earthquake situation. The proposed load factors in the study are a function of the chosen soil investigation/testing and piling method, which is applied to the bending moment in piles. Therefore, better choices of soil investigation/testing and high quality piling method will result in more reasonable design results.

Introduction

Reliability-based design approaches, such as load and resistance factor design (LRFD) and partial factor design have been widely accepted in structural design. These design methods are also applied to several foundation design codes. One of the motivations for applying reliability-based design in geotechnical engineering is to confirm that more detailed geotechnical investigations will result in more reasonable and cost-effective design. For example, the standard penetration test (SPT) is conducted for every project and almost all design parameters can be derived using empirical transformation equations based on SPT-N values, though other soil investigations are carried out less frequently. However, the uncertainty in the Young's modulus of soil depends on the adopted geotechnical measurement, testing method and soil types.

As shown in Fig. 1, the peak bending moments at the pile top and underground govern the structural design of piles. For example, when the surrounding soil is relatively soft or when the number of pile rows is relatively large, a sway deformation mode prevails and the pile-top bending moment should be the (absolute) maximum bending moment. On the other hand, when the surrounding soil is relatively hard or when the number of pile

[1] Senior Researcher, CAESAR PWRI
[2] Chief Researcher, CAESAR, PWRI
[3] Senior Researcher, NILIM
[4] Researcher, CAESAR, PWRI
[5] Former Exchange Researcher, CAESAR, PWRI

rows is relatively small, a rotation or inclination deformation mode prevails, and the underground peak bending moment should be the maximum bending moment. This indicates that the variation in stiffness of surrounding soil or axial resistance of piles is a major source of uncertainty in the calculated bending moment in piles.

However, load and resistance factors for the structural design of foundation structural members are usually the same as those used in typical structural design and they have no relationship with geotechnical aspects.

This study proposes a structural LRFD concept for piles of foundation considering the difference in reliability of geotechnical testing/investigation methods and piling methods so that design codes can support the effort to achieve more reasonable soil investigations and piling methods.

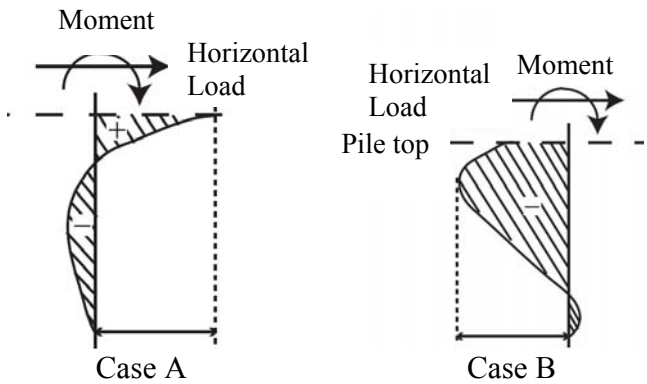

Figure 1 Bending moment distribution in a pile

Variation in the Coefficient of Horizontal Subgrade Reaction

A horizontal load test database of piles is available in PWRI with boring log data. The observed coefficient of subgrade reaction at a displacement level of 1% of the pile diameter can be estimated using the beam-on-Winkler foundation theory, assuming a uniform coefficient of horizontal subgrade reaction, where 1% of the pile diameter is defined as the reference displacement level to estimate the coefficient of subgrade reaction in the Japanese Specifications for Highway Bridges. The average coefficient of horizontal subgrade reaction for the subsoil layers can also be calculated using typical empirical equations shown in the Japanese Highway Bridges Design Specifications. The coefficient of horizontal subgrade reaction is a function of Young's modulus of soil. Whereas the Japanese Highway Bridges Design Specifications shows that the Young's modulus of soil, E, is based on the secant modulus of an unloading-reloading cycle obtained by a plate loading test, an alternative empirical equation to derive the Young's modulus of soil from an SPT-N value is also provided as $E = 2{,}800N$ (kN/m^2), because soil testing other than SPT is not often conducted. Accordingly, the model error in estimating the coefficient of

the subgrade reaction can be derived by comparing the observed and calculated values for the case in which SPT-N values are used to estimate the Young's modulus of soil.

The ordinate indicates the ratio of the observed value to the calculated value of the coefficient of horizontal subgrade reaction. The abscissa indicates the average SPT-N value, N_{ave}, for the subsoil layers over the characteristic pile length, η,

$$\eta = [(kB) / (4E_pI_p)]^{1/4} \quad (1)$$

where k is the coefficient of subgrade reaction, B is the foundation width (i.e., pile diameter), and E_pI_p is the bending rigidity of the pile. The governing soil classification for the subsoil layers within the characteristic pile length is indicated by different symbols. For subsoil layers having an SPT-N value smaller than 5, even the bias, λ_k, ranges from 1 to 4. For subsoil layers having an SPT-N value not smaller than 5, the bias, λ_k, is approximately 1.0 and the coefficient of variation, COV_k, is 0.60 for sandy soils and 0.70 for cohesive soils.

The model error in the estimation of the coefficient of subgrade reaction, k, is comprised of the model error in the estimation of the Young's modulus of soil, E, and the transformation error from the Young's modulus of soil, E, to the coefficient of subgrade reaction, k. The bias λ_k and the coefficient of variation COV_k of the subgrade reaction, k, are given as follows:

$$\lambda_k = \lambda_E \times \lambda_T \quad (2)$$

$$COV_k^2 = COV_E^2 + COV_T^2 \quad (3)$$

where λ_E and COV_E are the bias and COV of the Young's modulus of soil, E, and λ_T and COV_T are the bias and COV of the transformation error from E to k. Accordingly, the uncertainty in k is a function of the uncertainty in E that depends on the choice of soil investigation and testing method as well as soil classification.

The PWRI database indicates that the empirical equation of $E = 2800N$ (kN/m^2) has a bias, λ_E, and coefficient of variation, COV_E, of approximately 1.0 and 0.55 for sandy soils, where the data for cohesive soils is not available. Finally, based on Eq. (3), we can approximate the COV of the transformation error from E to k, COV_T as 0.25. This value is considered independent of the soil investigation method.

Based on a study by Phoon and Kulhawy, the uncertainty in estimating the Young's modulus of soil, λ_E and COV_E, is modeled as shown in Table 1 for several soil investigation and testing methods. Finally, using Eq. (3), the values of λ_E and COV_E shown in Table 1 and the transformation error from E to k, λ_E = 1.0 and COV_E = 0.25, the uncertainty in the coefficient of subgrade reaction can be set as listed in Table 2 as a function of soil investigation methods and soil classification.

Table 1 Uncertainty in the Young's modulus of soil

Soil investigation / testing	Uncertainty in E_{PMT} or E_{Lab}	
	λ_E	COV_E
Pressure meter test (PMT, Direct)	1.0	0.30
Laboratory test (Lab, Direct)	1.0	0.30
SPT-N (Transformation)	1.0	0.55

Table 2 Uncertainty in the coefficient of subgrade reaction

Soil investigation / testing	Prevailing soil condition	Uncertainty in k	
		Bias	COV
Pile load test	—	1.0	0.25
Pressure meter test or laboratory test	—	1.0	0.45
Only SPT	Sandy	1.0	0.60
	Cohesive	1.0	0.70
	$N_{ave} < 5$	1.0	1.00

Variation in the Axial Pile Spring Constant

In the current Japanese design specification, axial pile spring constant which installed at the pile top is modeled as function dependent on the rigidity of pile and pile length. However, the estimation accuracy is low especially the case of short pile or high rigidity pile.

In order to improve estimation accuracy of Kv, estimation equation is newly proposed. Displacement at pile top depends on not only the rigidity of pile but also the deformation of the tip of the pile. Therefore, displacement at the top of the pile can be expressed by the sum of pile deformation and displacement at the tip of pile shown this equation, and Kv is expressed as Eq(4).

$$K_V = \frac{1}{\frac{L}{2EA}\left(1+\gamma_y-\zeta\right)+\xi\frac{4\gamma_y}{\pi D_p^{\,2}k_v}} \qquad (4)$$

Where,

γ_y : Estimated tip transmitting ratio which the pile is yield at the top of pile ($0 \leqq g_y \leqq 1$) . It is assumed as $\gamma_y = X\gamma_{10d}$

γ_{10d} : Estimated tip transmitting ratio which the displacement of the top of pile is reached at 10% of pile diameter. It is assumed as $\gamma_{10d} = R_p / R_{Nu}$

R_p : Ultimate bearing at the tip of pile estimated by using bearing

estimation equation ($=q_d \cdot A$)

R_{Nu} : Ultimate Bearing estimated by using bearing estimation equation

X : Modification coefficient to estimate tip transmitting ratio which the pile is yield at the top of pile shown in Table 3

ζ : Modification coefficient to estimate deformation of pile shown in Table 3

ξ : Modification coefficient to estimate displacement of the tip of pile shown in Table 3

Table 3 Modification coefficients

Pilling Method	X	ζ	ξ	
			Sandy, Gravel	Cohesive
Driven pile method	0.89	0.08	0.22	0.42
Vibro-hammer method	0.98	0.23	0.46	-
Cast-in-place RC pile Method	0.62	0.19	0.63	0.47
Bored pile method	0.76	0.09	0.30	-
Steel pipe soil cement pile method	0.72	0.38	0.31	-
Screwed steel pile method	0.78	0.28	0.40	-
Pre bored pile method	0.69	0.02	0.20	-

This equation includes three modification coefficients, X, ζ and ξ. These coefficients were adjusted to estimate the Kv values obtained by vertical pile loading test results. Fig.2 shows the comparison of estimated and measured Kv in case of cast-in-place RC pile. It is found that the improved Kv estimates the measured one well in comparison with the conventional one.

Table 4 shows the statistic of uncertainty of model error of the Kv. The characteristic point is that the each bias of proposed Kv is approx.1.0. This means that the proposed Kv is estimated the average of Kv well.

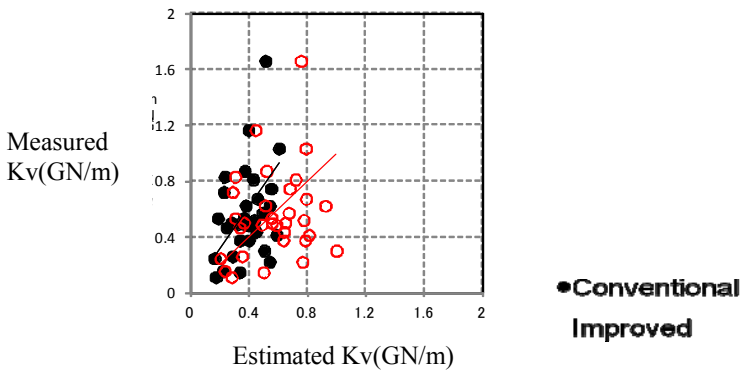

Figure 2 Estimated and Measured Kv relationships (Cast-in-place RC pile)

Table 4 Uncertainty of model error of axial pile spring Constant K_v

	Conventional			Proposed		
Piling Method	Bias	COV	Data	Bias	COV	Data
Driven pile method	1.29	0.39	90	0.99	0.37	29
Vibro-hammer method	1.11	0.14	4	0.97	0.33	4
Cast-in-place RC pile Method	1.40	0.64	59	1.14	0.60	33
Bored pile method	1.12	0.36	87	0.97	0.37	33
Steel pipe soil cement pile method	1.12	0.27	24	1.00	0.26	12
Screwed steel pile method	1.38	0.38	20	1.03	0.34	20
Pre bored pile method	0.78	0.29	39	0.98	0.30	13

Design Equation

In allowable stress design, both the tensile stress in reinforcement and the compressive stress in concrete are checked. Accordingly, the present study proposes the following LRFD equations for the pile bending moment:

$$\Psi \ M_{cal} \leq \Phi_Y M_Y \qquad (5)$$
$$\Psi \ M_{cal} \leq \Phi_U M_U \qquad (6)$$

where Ψ is the load factor or modifier that considers the uncertainty in the calculated pile bending moment in the pile, Φ_Y and Φ_U are the resistance factors for yield and maximum bending moment strengths, respectively, M_{cal} is the calculated pile bending moment in the pile, and M_Y and M_U are the yield and maximum bending moment strengths of the pile, respectively. The yield bending moment strength, M_Y, agrees with the bending moment at which a reinforcement bar becomes plastic and the maximum bending moment strength, M_U, agrees with the bending moment at which the bending strain in concrete reaches the compressive collapse strain. Based on above considerations, it is expected that the load factor, Ψ, that is applied to the calculated bending moment in piles becomes a function of the soil investigation/testing method and soil classification, because the distribution of the pile bending moment in the depth direction varies with the uncertainty in the coefficient of subgrade reaction, as stated above.

Code Calibration

1) Prototype foundations

A code calibration will be conducted for two prototype highway bridge foundation of piers for each piling methods using FOSM. The prototype highway bridge substructures are designed by Japanese Highway Bridges Design Specifications and are checked for allowable stresses for concrete and reinforcement with factors of safety. In this study, we deal with seismic design of pile foundations for the Level 1 (or frequent scale) Earthquake

Design situation. The combination of all dead loads and seismic inertial force from the superstructure is considered, and these loads are also considered as given conditions with no uncertainty. The design calculation is conducted using a typical beam-on-Winkler-foundation model. A schematic diagram is shown in Fig. 3. The axial resistance of a pile subjected to vertical loads is expressed using a spring arranged at the pile top.

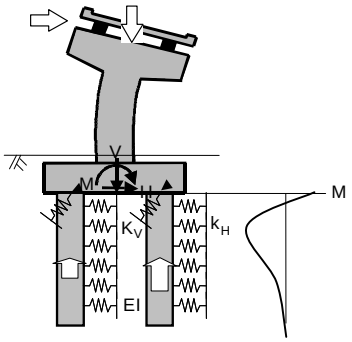

Figure 3 Design calculation model

In this paper, we basically introduce the cast-in-place RC piles (Drilled shaft) cases. The prototype highway bridge substructures are shown in Fig. 4. Because of simplicity, in consideration of the variation in the Young's modulus of soil, a uniform subsoil layer overlaying the bearing layer is assumed for both cases. The Case A foundation is designed so that the maximum bending moment in the piles will appear at the top of pile. The Case B foundation is designed so that the maximum pile bending moment will appear deep underground.

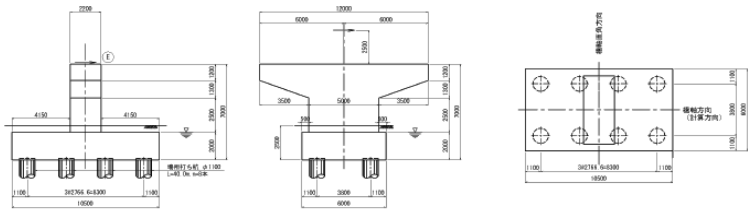

Case A (E_{PMT} = 1,400 kN/m^2, K_V, = 580,000 kN/m, Pile diameter, B, = 1,100 mm)

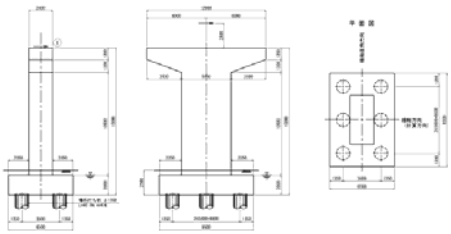

Case B (E_{PMT} = 8,400 kN/m^2, K_V, = 687,000 kN/m, Pile diameter, B, = 1,350 mm)

Figure 4 Prototype highway bridge substructures (cast-in-place RC piles)

2) Monte Carlo simulation for estimating the uncertainty in the calculated pile bending moment

The Monte Carlo simulation is conducted to estimate the variation in the calculated pile bending moment. The model uncertainties considered in the Monte Carlo simulation are listed in Tables 2, 4, and 5. All of the parameters are assumed to follow a lognormal distribution. The model uncertainty in the bending rigidity of the pile is estimated separately using a Monte Carlo simulation for the designed cross-sections considering the model uncertainty in the material property such as the Young's modulus of reinforcement and the unconfined strength of concrete that is cast underwater.

Monte Carlo simulation was conducted for different prototype design cases and different soil investigation or testing cases or piling methods. The calculation error is estimated by dividing the (absolute) maximum bending moment calculated in the Monte Carlo simulation by the (absolute) maximum bending moment obtained in the prototype design calculation.

Table 5 Model uncertainty in the material property of drilled shafts

Items	Nominal value	Bias	COV
Concrete strength, f_{ck}	24 N/mm^2	1.40	0.18
Young's modulus of concrete	Given as a function of f_{ck} in the Japanese Specifications for Highway Bridges and modeled to be deterministic in this study		
Yield strength of reinforcement (SD345)	345 N/mm^2	1.14	0.04
Young's modulus of reinforcement	2.00×10^5 N/mm^2	(constant)	(constant)

3) Monte Carlo simulation for estimating the uncertainty in the bending strength of the pile

A separate Monte Carlo simulation is conducted for the bending strength of a pile for the cross section of prototype structures. The material uncertainties in concrete and reinforcement are as listed in Table 5. The bending strength of a pile changes with the axial force on the pile with increasing seismic force. In other words, the increment in the axial force during an earthquake has an uncertainty because of the model error of the typical design calculation model, such as the coefficient of horizontal subgrade reaction and the axial spring of the pile. The variation in the axial force of the tensile pile can be estimated from the numerical results obtained in the previous Monte Carlo simulation for the uncertainty in the calculated bending moment, in which the structural design of the pile is governed by the design of the tensile piles. As a result, the uncertainty in the increment of the axial force during an earthquake is estimated to have a bias of 1.0 and a COV of 0.10.

The uncertainty in the yield bending moment strength, M_Y, and the ultimate bending moment strength, M_U, considered in this study is used based on the Monte Carlo

simulation's result shown in Table 6.

Table 6 Uncertainty in M_Y and M_U (Cast-in-place RC pile)

Bias	1.15
COV	0.10

4) Load and resistance factors obtained by FOSM

FOSM is used to obtain the load and resistance factors. First, the reliability indexes of the prototype foundations are estimated. Table 7 shows the example of reliability indexes of Cast-in-place RC pile designed by current Japanese highway design specification for L1 Earthquake. It is found that β for positive side is more sensitive than for negative side by the difference of soil investigation methods. Additionally, beta value evaluated by SPT test which N value is less than 5 is smaller than the other cases. These results indicated that reliability of piles depend on the soil investigation methods, especially maximum bending moment appears at the head of pile.

Target Reliability index β_T is set based on evaluated reliability indexes of the typical types pile foundation designed by current design specification. Soil investigation method is assumed as SPT on sandy soil. Typical types pile foundations are assumed as following 3 types of pile foundations; Cast-in-place RC pile, Steel pipe pile by driven pile construction method and by embedding method by an inner excavation construction. Accordingly, we finally use the target reliability indexes of β_T = 1.8 and 3.1 for the yield and ultimate bending moment strengths, M_Y and M_U, respectively.

Table 7 Reliability indexes of Cast-in-place RC pile designed by current design specification for L1 Earthquake

		Yield Bending moment M_Y		Maximum bending moment M_U	
Soil investigation / testing		Positive	Negative	Positive	Negative
Pile load test		1.84	1.50	4.08	2.59
Pressuremeter test or laboratory test		1.54	1.50	3.54	2.59
Only SPT	Sandy soil	1.31	1.50	3.07	2.59
	Cohesive soil	1.20	1.50	2.85	2.59
	$N_{ave} <$ 5 (bias =1.0)	0.86	1.50	2.27	2.59

Basically, load factor and resistance factor are set separately. However, we found that resistance factor was not sensitive, so resistance factor puts together in loading factor like Eq.(7) in this study. Moreover, new loading factor divides into two factors shown in Eq(8).

One is a loading factor considering the difference of pile types and piling methods. The other is a loading factor considering the difference of soil investigation or load tests. By this modification, we are able to clarify a merit to introduce the LRFD more clearly. These factors divided though trial and error method.

$$\Psi' = \Psi / \Phi \qquad (7)$$

$$M_d = \Psi_1 \cdot \Psi_2 \cdot M \qquad (8)$$

Where,

M_d : Design bending moment of piles

M : Calculated Bending moment of pile

Ψ_1 : Load factor considering the difference of pile types and piling methods

Ψ_2 : Load factor considering the difference of soil investigation / load tests

Finally, the load factors are obtained as summarized in Table 9 and Table 10. As for the load factor considering the difference of pile type and piling methods Ψ_1, the load factor of cast-in-place RC pile tends to be larger than the others. It is assumed because the COV of Kv of this pile type is larger than the others. As for the load factor considering the difference of soil investigation and load testsΨ_2, it is found that it is to enable reasonable design by detailed soil investigation or load test.

Table 9 Load factor considering the difference of pipe type and piling method Ψ_1

Pile type and Piling Method	Yield Bending Moment M_Y		Maximum bending moment M_U	
	Positive	Negative	Positive	Negative
Cast-in Place RC Pile	1.80	2.05	1.90	3.75
Steel Pipe Pile(Drilled pile)	1.40	1.50	1.70	2.40
Prestressed High strength Concrete Pile(Drilled pile)	1.60	1.75	1.85	2.70
Steel Pipe Pile (embedding method by an inner excavation construction)	1.50	1.50	1.55	2.40
Prestressed High strength Concrete Pile(embedding method by an inner excavation construction)	1.75	1.70	2.00	2.90
Steel Pipe Soil Cement Composite Pile	1.30	1.25	1.55	1.70
Steel Pipe Pile (Screwed Steel Pile Method)	1.45	1.45	1.55	2.10
Preboring Pile Driving Method	1.65	1.60	1.95	2.60

Table 10 Load factor considering the difference of soil investigation and load testsΨ_2

Soil investigation / testing		Positive	Negative
Pile load test		0.90	1.00
Pressuremeter test or laboratory test		0.95	1.00
Only SPT	Sandy soil	1.00	1.00
	Cohesive soil	1.05	1.00
	$N_{ave} < 5$	1.15	1.00

Concluding Remarks

We proposed the load factors to verify the bending moment of pile of pile foundation for Level 1 earthquake based on LRFD design concept. However, the number of test calculations is not enough to finalize these load factors. We confirm validity of proposed load factors from these results and are going to revise them as needed.

References

[1] Shirato, M., Fukui, J., and Matsui, K. “Present situation regarding geotechnical investigations and the determination of geotechnical parameters in Japan," Proc. of Int. Workshop on Foundation Design Codes and Soil Investigation in view of International Harmonization and Performance Based Design (eds. Honjo et al.), 2002, Balkema, pp. 237-243

[2] Japan Road Association. Specifications for Highway Bridges, 2012.

[3] Phoon, K.K. and Kulhawy, F.H. “Characterization of geotechnical variability,” Canadian Geotechnical Journal, 36, 1999, pp. 612-624

[4] Kouno, T., Nakaura, T., Shirato, M., and Nakatani, S. “An evaluation of the reliability of vertically loaded shallow foundations and grouped-pile foundations,” Geotechnical safety and risk (eds. Honjo et al.): 2nd Int. Symp. on Geotech. Safety (IS-Gifu), 2008, Taylor and Francis Group, London, pp. 177-184

[5] Shirato, M., Kouno, T., and Nakatani, S. "Geotechnical criteria for serviceability limit state of horizontally loaded deep foundations," Geotechnical safety and risk (eds. Honjo et al.): 2nd Int. Symp. on Geotech. Safety (IS-Gifu), 2008, Taylor and Francis Group, London, pp. 119-126

EFFECT OF DECK PLATE THICKNESS OF ORTHOTROPIC STEEL DECK ON FATIGUE DURABILITY

Jun Murakoshi[1], Shu-ichi Hirano[2], Hideaki Harada[3]

Abstract

The effect of thickness of deck plate on fatigue durability of OSDs was also discussed from experimental and analytical results to improve fatigue durability of the structural details for the deck plate cracks. Wheel running fatigue tests were performed for full-scale test specimen with combination of 16/19mm thickness deck plates and 6/8 mm thickness ribs. Finite element analyses were also conducted in order to clarify the effect of thickness of deck plate on local stress at rib-to-deck welded joints.

Introduction

Orthotropic steel deck (OSD) bridges have been widely used for long-span bridge and urban viaducts for reducing dead load. OSDs consist of many thin steel plates, stiffened by a series of closely spaced longitudinal ribs supported by transverse floorbeams (see Fig. 1). As they support vehicle wheel loads directly as deck system, considerations for fatigue has to be supposed to be required in the design of OSDs. With rapid increase of vehicle weight and traffic volume in Japan, various types of fatigue cracks shown in Fig. 2 have recently been observed in existing OSDs under severe traffic condition, resulting from the complicated welded details combined with local stresses that can be difficult to quantify in the design. Among such fatigue damages, two types of severe cracks have been observed at the rib-to-deck welded joints. They initiate at the root of the one-sided fillet weld. One type of them propagates into the deck plate and finally reaches its surface (deck plate cracks), while the other propagates through the weld (bead cracks). Among them, the deck plate cracks have potential to threaten safety of traffic due to cave-in of road surfaces if they reach a certain length. Focusing on the two types of cracks, especially the deck plate cracks, the research projects have been conducted for the following objectives:

1) Identification of the causes of fatigue cracking and proposal of appropriate structural details to improve fatigue durability for newly constructed bridges
2) Development of an ultrasonic inspection method which can detect invisible cracks initiating in the weld root
3) Performance evaluation of applicability of steel fiber reinforced concrete (SFRC) overlays as a measure to retrofit existing damaged OSDs

[1] Chief researcher, Center for Advanced Engineering Structural Assessment and Research(CAESAR), PWRI
[2] Senior researcher, CAESAR, PWRI
[3] Research specialist, CAESAR, PWRI

Fig. 1 View of orthotropic steel deck box girder bridge

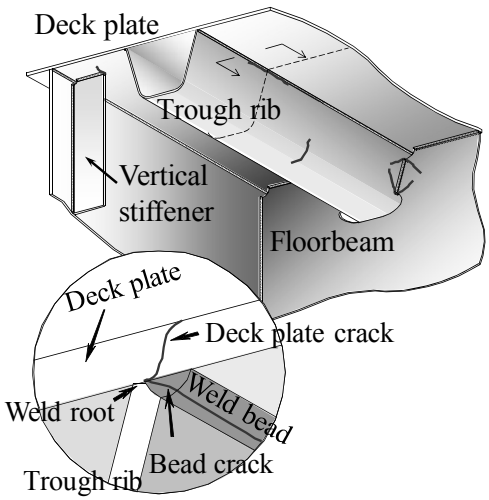

【Section of the rib-to-deck weld connection】

Fig. 2 Major fatigue cracks observed in OSDs

Major findings of the research were summarized in PWRI Technical notes. In this paper, the experimental and analytical results regarding the first objective were discussed based on results.

Features of Deck Plate Cracks

Fig. 3 shows detailed inspection for a deck plate crack. According to investigation of existing damaged OSDs, the tendencies of deck plate cracking are listed below.

1) Cracks have been observed in about 10 to 30 years after construction under heavy traffic route. In terms of cumulative traffic volume of heavy vehicles estimated roughly by multiplying the current volume of heavy vehicle traffic and service years, cracks have been detected when it exceeded around 12million vehicles/lane.
2) Cracks have been observed both at the rib-to-floorbeam (RF) connections and the other parts in the rib-to-deck (RD) weld line under the wheel running position, initiating in the weld root.

(a) Visual observation of deck surface after removal of asphalt layer

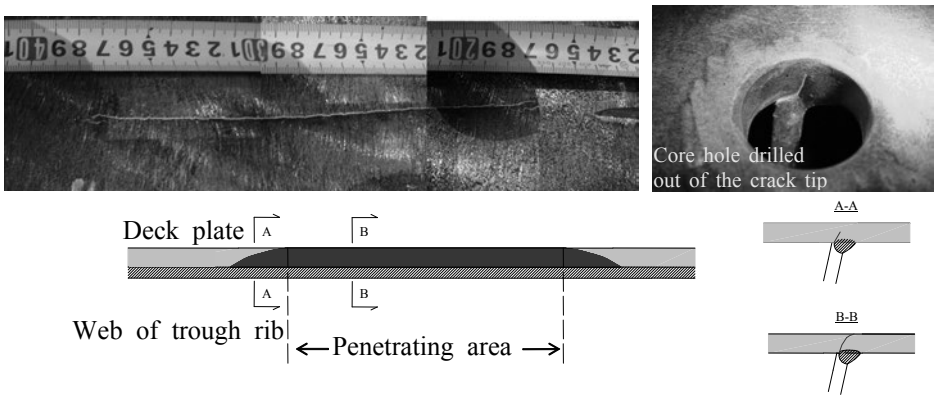

(b) Description of observed crack

Fig. 3 Detailed inspection for deck plate crack

3) While the thicknesses of the damaged deck plate were mostly 12mm and the floorbeam spacings were 2.0 to 2.85mm and the thicknesses of the rib were 6 or 8mm, the tendency of cracking is not clear in relation with detailing dimensions except for the deck plate thickness.

Current Fatigue Design

Fatigue Design Guideline for Steel Highway Bridges was issued in 2002. Requirement for standard structural details of OSDs is specified to ensure fatigue resistance. In the Fatigue Design Guideline, the minimum deck plate thickness is 12mm. As to the RD one-sided fillet weld, 75 percent minimum penetrations of rib thickness are required for preventing weld bead cracks. After identifying deck plate cracks, from long-term performance point of view, the minimum deck thickness has been increased to 16mm at wheel load running position in case of use of closed ribs in the latest design code, which was revised in 2012. The results of the present research were reflected in the revision.

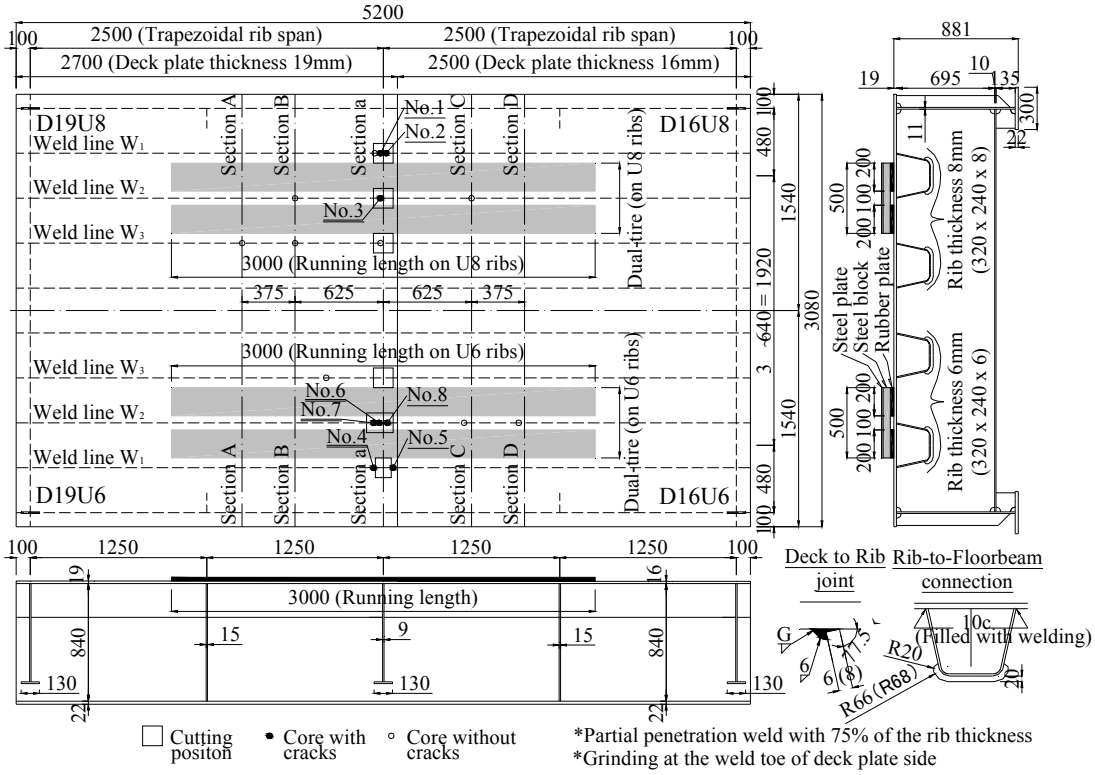

Fig. 4 Structural dimensions of the full-scale test specimen

Fig. 5 View of testing by wheel running test machine

Wheel Running Test

Specimen Description and Test Configuration

Wheel running tests of full-scale OSD test specimen were conducted in order to observe crack propagation behavior and evaluate fatigue durability improvement by increasing deck plate thickness. Structural dimensions of the specimen are shown in Fig. 4. D#U# in the figure denotes combination of the thickness of deck plate and rib. It has four trapezoidal ribs with the rib-span of 2500mm. The deck thickness is 16mm at one span and 19mm at another including the rib-to-floorbeam connection. In

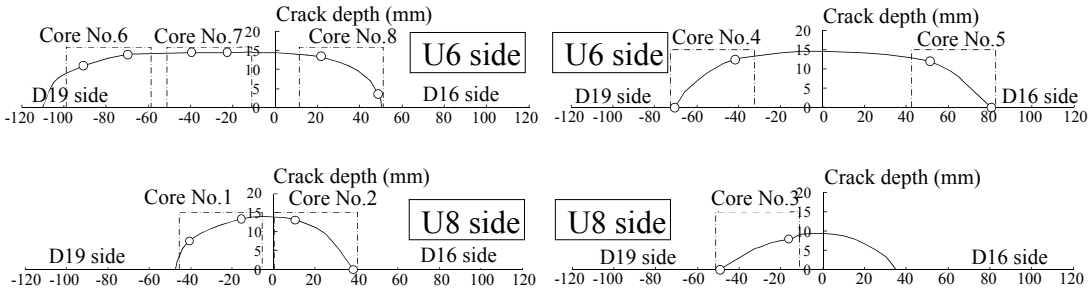

(a) Weld line W_1 (b) Weld line W_2

Fig. 6 Shapes of deck cracks in the weld root at the rib-to-floorbeam connections(D19)

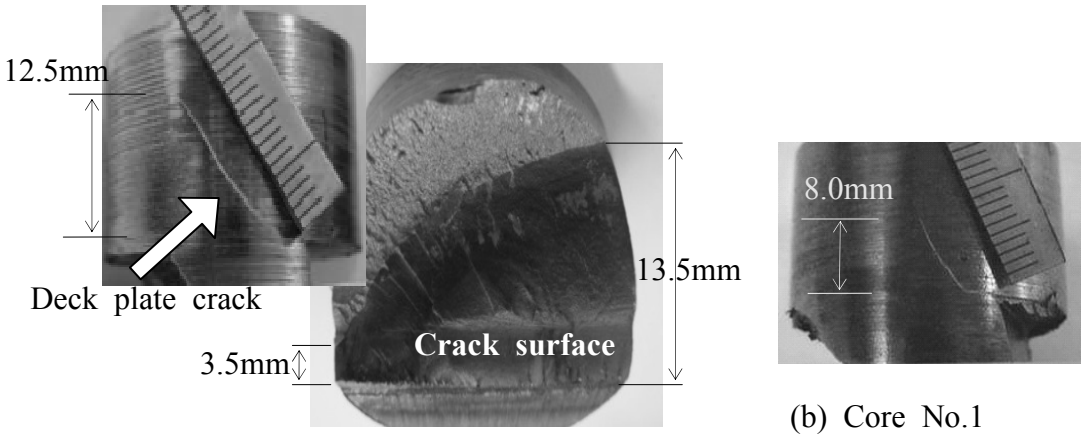

(a) Core No.4 on the U6 side

(b) Core No.1 on the U8 side

Fig. 7 Cracks observed on the core surfaces

addition, two trapezoidal ribs with thickness of 6mm and the other two with thickness of 8mm, four in total, were used to investigate the effect of difference of rib thickness. Therefore, wheel running test can be conducted for different details at a time under two loading cases. Steel grade is SM490Y. Structural details were designed by the Fatigue Design Guideline. The partial penetration of 75% rib thickness was ensured for the RD weld. One-pass CO_2 gas shielded arc welding was applied with natural groove for U6. Two-pass CO_2 gas shielded arc welding was applied with 35° groove and 2mm edge for U8.

The test was conducted at 4million cycles each on U6 and U8 rib side of the test specimen. The wheel running test machine owned by PWRI was used for the test (see Fig. 5). Wheel load was set to 150kN based on the measured truck axle load observed in the past field measurements, referred to the Fatigue Deign Guideline. Running length of wheel load was set to 3m, two rubber sheets with the width of 200mm and the thickness of 22mm were set on the deck surface to simulate rubber dual-tire wheel load. Above them, steel blocks with the width of 500mm and the length of 200mm were set along longitudinal direction, and a steel plate with the width of 560mm and the thickness of 16mm was placed over them for running the steel wheel of the test machine.

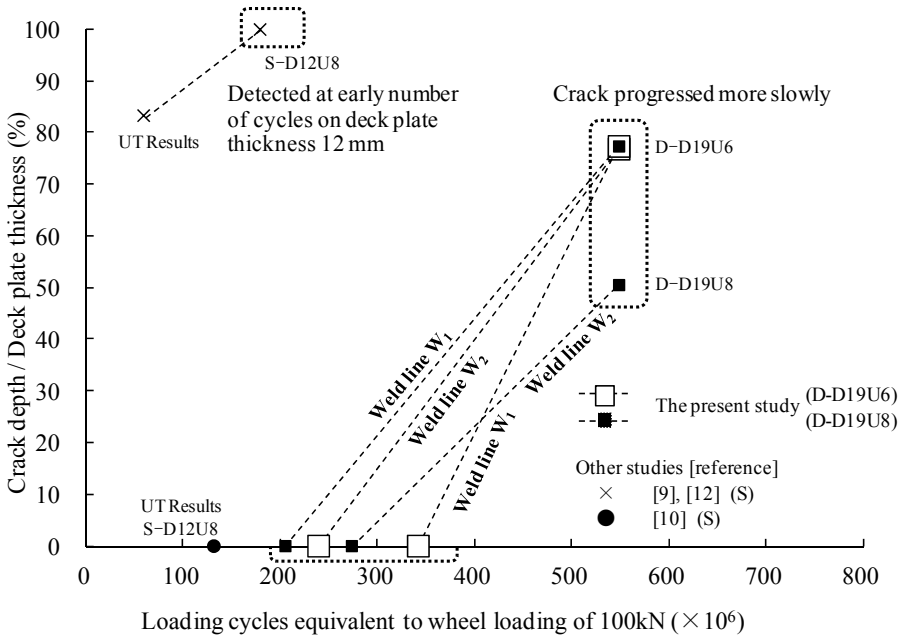

(a) Cracks in weld parts of RD connections at rib-to-deck weld

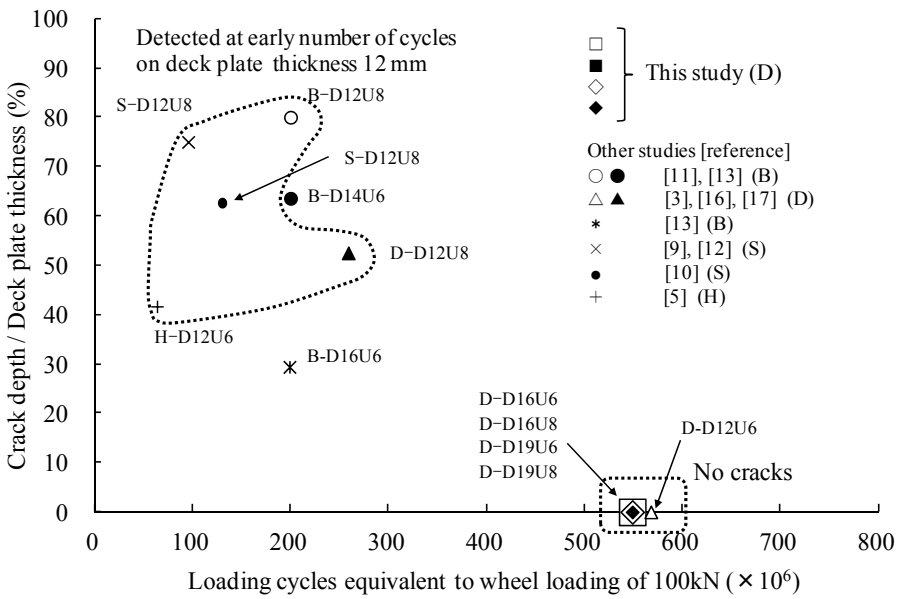

(b) Cracks in other parts at rib-to-deck weld

Fig. 8 Ratio of crack depth to deck thickness versus loading cycles equivalent to 100kN wheel load

Ultrasonic testing (UT) was performed every 0.25million cycles during the test. In order to observe directly the initiation and propagation behavior of cracks after the test, drilled cores were taken with the diameter of 40mm locations showing a large change of measured strains or those where high ultrasonic echoes were measured by UT.

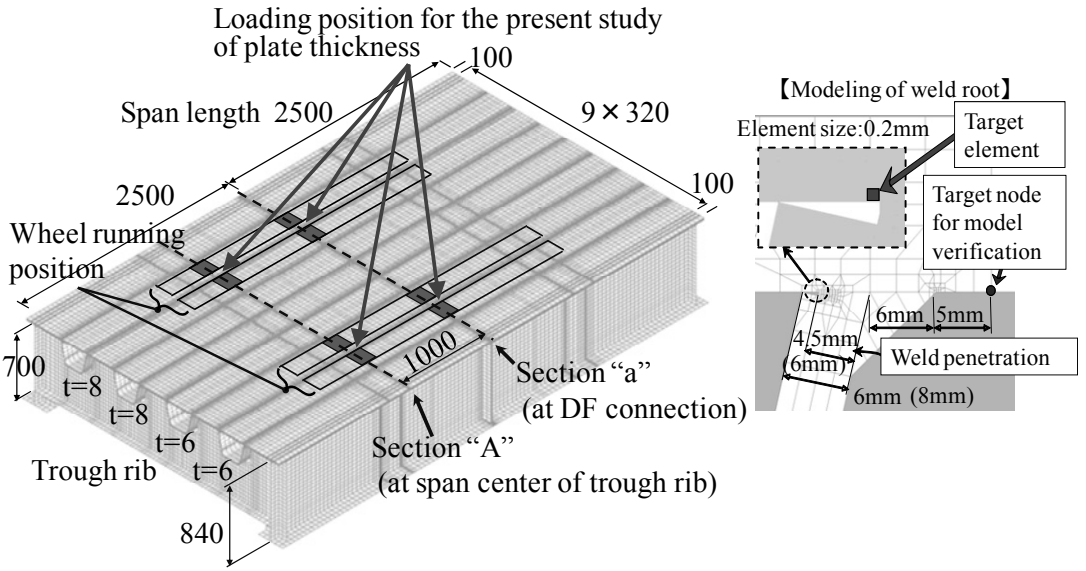

【Dimension of model】

Deck plate thickness	12 mm, 14 mm, 16 mm, 19 mm
Span of ribs	2500 mm (x 2 spans)
Detail of ribs	320 x 240 x 6 x R40 (2 ribs), 320 x 240 x 8 x R40 (2 ribs)
Web of main girder	Thickness 11mm, Hight 840 mm
Web of floorbeam	Thickness 9mm, Hight 700 mm
Vertical Stiffener	Thickness 15mm, Width 135 mm
Properties of material	Elastic modulus 2.06 x 10^6 N/mm^2, Poisson's ratio 0.3
Constraint condition	Integrity constraint of the lower surface of main girder
Load condition	Dual-rire 150 kN

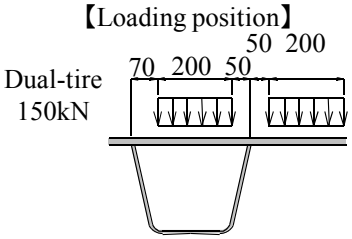

Fig. 9 Analysis model of test specimen

Test Results

Locations of drilled cores taken from the deck plate were shown in Fig. 4. Black symbols and white symbols in the figure denote cores where crack were detected or not respectively. As results of UT conducted during the test, cracks were observed only at four locations of RF connections of weld lines W_1 and W_2 both on U6 and U8 sides. Fig. 6 shows shapes of all observed cracks initiating in the weld root. Intersections of the crack tip and the core surface are also shown with white symbols in the figure. Fig. 7 shows photos of cracks observed on the surface of core No.4 on the U6 side and the core No.1 on the U8 side. Cracks initiated in the weld root and propagated semi-elliptically at an angle of approximately 50 degrees to the deck plate surface. The direction of crack is similar to that of actual cracks in damaged OSD bridges. As the results, progress of deck plate cracks is possible even if the deck thickness is increased to 19mm.

Fig. 8 shows the relation between the ratio of crack depth to deck thickness and the number of loading cycle equivalent to 100kN wheel load. The results by the authors and those by other studies are plotted in the figure. The equivalent loading cycles were calculated based on the linear cumulative damage rule (m=3). Crack depths estimated from UT are also plotted. Although the variation in data is large, crack growth tended to progress relatively slowly with increase of the deck thickness.

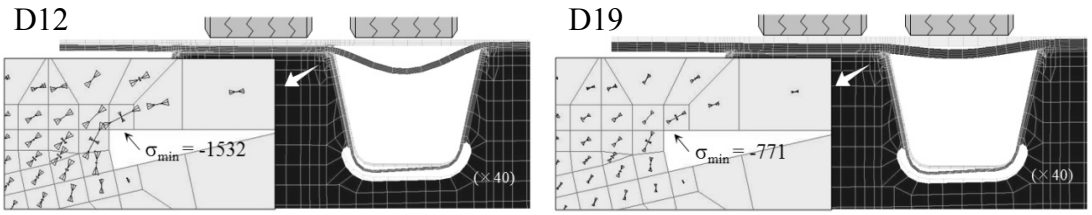

(a) Cross section "a" (at rib-to-deck connection)

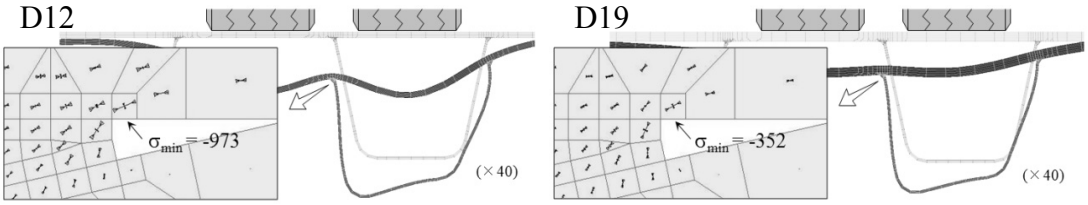

(b) Cross section "A" (at span center of the trough rib)

Fig. 10 Deformation and principal stress vector diagrams for D12U6 and D19U6

Finite Element Analysis on Local Stress of Structural Details

Analysis Method

FE analyses were conducted for the full-scale test specimen focusing on the local stresses in the weld root where cracks initiated. Fig. 9 shows outline of the analysis model. In modeling, the minimum dimensions of elements of the target weld root were set to 0.2mm×0.2mm×0.5mm. Although local stresses of the weld root are affected by element dimensions in the analysis model, relative comparison of local stresses by using the same detail modeling is considered to be appropriate. The elastic modulus of E and Poisson's ratio ν for steel material were set as E=206,000N/mm^2 and ν=0.3, respectively. The contact point between the bottom surface of deck and the inner surface of rib at the RD connection was modeled as separated node. Dual-tire wheel loads of 150kN were applied above RD weld line, same as that in the wheel running test. Especially in this paper, the results of loading patterns at section "a" at DF connection and section "A" at span center of trough rib were discussed.

Analysis Results

Fig. 10 shows the deformation and the principal stress vector diagrams for the combination of D12U6 and D19U6 at cross section of "a" (rib-to-deck connection)" and "A" (span center of the trough-rib). Relative high peak compressive stresses occurred at the weld root due to local bending of deck plate. Deformation of the deck and the rib and local stress of target element in the weld root decreased with increase of the deck thickness. Absolute values of the minimum principal stress are larger than those of the maximum principal stress in the weld root. As to target element, the direction of minimum (compressive) principal stress corresponds almost perpendicularly to the direction of crack propagation.

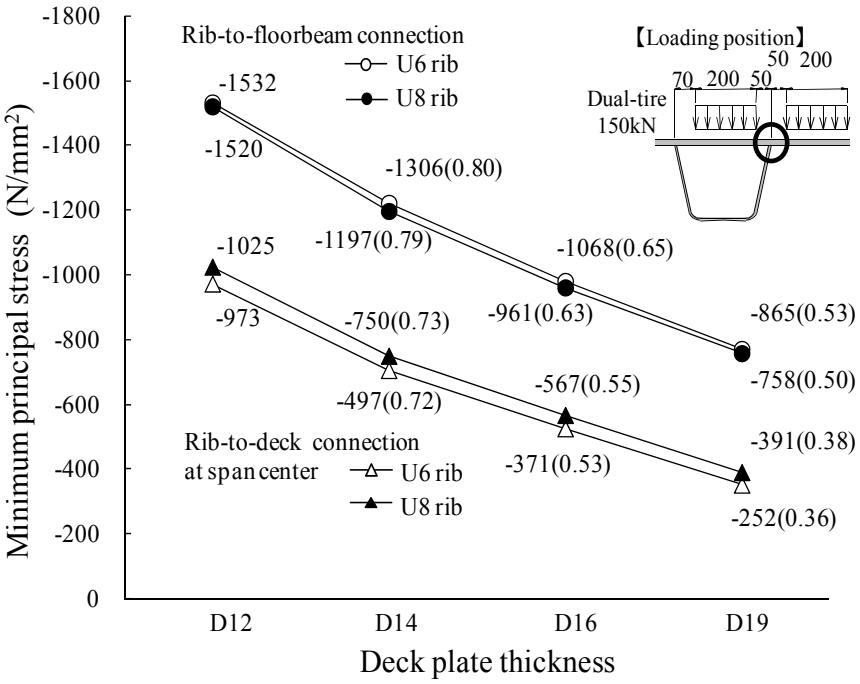

Fig. 11 Minimum principal stress versus deck plate thickness

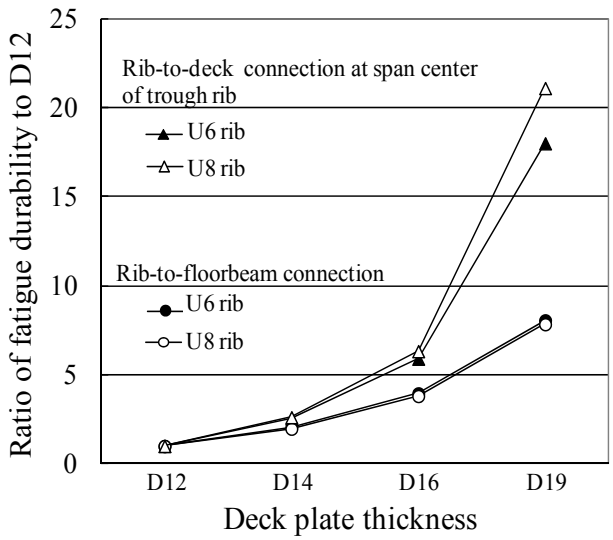

Fig. 12 Ratio of Fatigue durability to D12 versus deck plate thickness

Fig. 11 shows the minimum principal stress for the target element in the weld root by deck thickness. The ratios to the stresses for D12 are indicated in parentheses. The effect on fatigue durability of deck thickness was evaluated on the basis of relative comparison of minimum principal stress since compressive principal stress is dominant in the local stresses at the weld root under wheel loading. Increase of deck thickness can significantly reduce the minimum principal stress. The minimum principal stress at RF connection part for D19 is larger than that at RD connection part at the span center of the trough rib for D16 and D19, which corresponds to tendency

of fatigue cracking observed in the test. Rib thickness does not significantly affect the local stresses in the weld root.

Fig. 12 shows the relative comparison of fatigue durability by deck plate thickness. Fatigue durability was assessed based on the local stresses in the weld root by cumulative damage rule. As to the weld root at RF connection, where is under more severe fatigue condition, estimated fatigue durability for OSD with D14, D16 and D19 against local stress are about 2, 4 and 8 times as long as that with D12, respectively.

Conclusions

Wheel running fatigue tests were performed for full-scale test specimen with combination of 16/19mm thickness deck plates and 6/8 mm thickness trapezoidal ribs. Finite element analyses were also conducted in order to clarify the effect of thickness of deck plate on local stresses in the weld root at the rib-to-deck connections. The major findings are summarized as follows.

1) Deck plate cracks occurred at the rib-to-floorbeam connections even in the deck thickness 19mm. However, based on the test results of the present study and other studies, the crack growth tended to progress relatively slowly with increase of deck plate thickness.

2) Relative high peak stresses occurred at the weld root due to local bending of deck plate. The extent of reduction of the stresses in the weld root was evaluated for increase of the deck plate thickness.

Acknowledgment

Wheel running tests of the full-scale OSD test specimen and some portions of the FE Analyses in the present study were conducted as a part of the joint research with NILIM, MLIT and Japan Bridge Association, "Joint research on structural improvements with damage evaluation for orthotropic steel deck" (2006-2008). Special appreciation is extended to their collaboration.

References

[1] Japan Road Association (JRA), “Specification for highway bridges, part II steel bridge”, 2002. (in Japanese)
[2] JRA, “Guideline for fatigue design of steel highway bridges”, 2002. (in Japanese)
[3] Japan Society of Civil Engineering, “Fatigue of orthotropic steel bridge deck”, Steel Structures Series No.19, pp.63-75, 2010. (in Japanese)
[4] Murakoshi, J., Yanadori, N. and Ui, T., “Study on fatigue damage and retrofit methods in existing orthotropic steel bridge decks”, Proceedings of the

Symposium on Steel Structures and Bridges, Vol.10, pp.19-37, 2007. (in Japanese)
[5] NILIM, MLIT and Japan Bridge Association, “Cooperative research on durability of the steel members on bridge - survey on the inspection method of the orthotropic steel decks - ”, Technical note of NILIM, No.471, 2008. (in Japanese)
[6] Kikuchi, T., Kodama, T. and Goto, K., “Replacement of pavement with SFRC to improve fatigue characteristic in Shonan Ohashi bridge”, Proceedings of the Symposium on Steel Structures and Bridges, Vol.10, pp.1-10, 2007. (in Japanese)
[7] NILIM, MLIT, PWRI and Japan Bridge Association, “Research on structural improvements with damage evaluation for orthotropic steel deck”, Technical note of NILIM, No.608, 2010. (in Japanese)
[8] NILIM, MLIT, “Experimental study on durability of orthotropic steel decks and deck plate thickness - effect of plate thickness of trough rib and deck plate on the through crack formation - ”, Technical note of NILIM, No.558, pp.62-116, 2008. (in Japanese)
[9] PWRI, “Study on effects of deck plate thickness of orthotropic steel deck on deck plate cracks”, Technical note of PWRI, No.4224, 2012. (in Japanese)
[10] Takada, Y., Hirano, T., Sakano, M. and Matsui, S., “Characteristic on fatigue cracks and experimental study on fatigue analysis of existing the orthotropic steel bridge deck in Hanshin Expressway”, Proceedings of 5th Symposium on Decks of Highway Bridges, pp.253-258, 2006. (in Japanese)
[11] Shimozato, T., Kamiki, T., Inaba, N., Tomita, Y. and Ono, S., “Wheel running fatigue test on orthotropic steel deck”, Proceedings of the 60th JSCE Annual Meeting, pp.795-796, 2005. (in Japanese)
[12] Shimozato, T., Wakabayashi, N., Inaba, N., Tomita, Y., Ono, S. and Watanabe, M., “The fatigue durability verification test after SFRC reinforcement on orthotropic steel decks with fatigue damage”, Proceedings of the 62nd JSCE Annual Meeting, pp.839-840, 2007. (in Japanese)
[13] Ono, S., Hirabayashi, Y., Shimozato, T., Inaba, N., Murano, M. and Miki, C., “Fatigue properties and retrofitting of existing orthotropic steel bridge decks”, Journal of JSCE A, Vol.65, No.2, pp.335-347, 2009. (in Japanese)
[14] Inokuchi, S., Uchida, D., Hirayama, S. and Kawabata, A., “Evaluation method for fatigue life of welding joint between deck plate and U-shaped rib in orthotropic steel decks”, Journal of JSCE A, Vol.67, No.3, pp.464-476, 2011. (in Japanese)

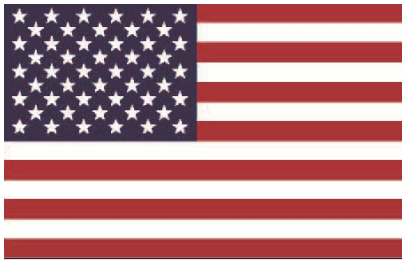

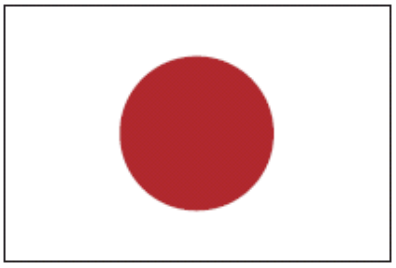

29th US-Japan

Bridge Engineering Workshop

Session 6

Seismic and Tsunami 2

Concepts for Tsunami-Resistant Design Criteria for Coastal Bridges

Yoshiteru Yokoi[1], Takashi Tamakoshi[1], Shuhei Kawami[1], and Masahiro Shirato[1]

Abstract

This paper discusses ideas on the basic concept of highway bridge design for tsunami and examines a mathematical formula for estimating tsunami forces on highway bridges. The present paper first reviews restoration case histories of highway bridges that underwent tsunami impact in the 2011 Earthquake off the Pacific Coast of Tohoku and on-going studies by road management authorities to develop post-tsunami response to bridge damage. Based on the reviews, this paper proposes controlling the bearing strength to fail at a designated scale of tsunami and prevent the tsunami force onto the superstructure from exceeding the expected level. Second the present work proves that hydraulic mathematical formulas are quite effective to calculate drag and uplift forces due to tsunami loads, with identifying bridges that suffered washout of superstructures and those that did not suffer in the 2011 tsunami using the formulas.

Introduction

In March 2011, a magnitude 9.0 earthquake occurred off the Pacific Coast of Japan's Tohoku Region (hereafter referred to as the 2011 Tohoku Earthquake). The epicenter was at the edge of the oceanic plate in the coastal waters of Tohoku. One of the largest tsunami in history struck the length of the coastline from the Tohoku Region down to the Kanto Region of Japan. As shown in Figure 1, National Highways 45 and 6 were major arterial roads that ran along the Pacific coast. Bridges on these highways seemed to sustain no major damage during the earthquake tremor itself. However, the tsunami run-up after the earthquake washed out the superstructures and/or the soil behind the abutments, as shown in Photo 1 and most towns and roads on the costal line were also inundated and tons of debris was left [1] [2]. Immediate restoration efforts began to secure access to the disaster-stricken region, with a 97% recovery in length of National Highways 45 and 6 achieved within seven days of the disaster. However, the wash-out bridges impeded the full recovery of the routes.

Large tsunami are predicted to hit at the long coastal lines of Japan in the expected the Tokai, Tonankai and Nankai Earthquakes [3]. The Japanese Ministry of Land, Infrastructure, Transport and Tourism (MLIT) of Regional Development Bureaus (RDB) at the respective regions are currently studying tsunami countermeasures to maintain their wide-area road networks for post-event emergency response to reach tsunami run-up zones [4][5]. Two concepts are typically considered in their studies. One is, to enable logistics of massive relief supplies, constructing new roads in locations that appear unlikely to be impacted by the tsunami. Another is securing bridges on existing bare-essential national highways running along the costal areas and communities to distribute the relief supplies. In terms of the latter efforts, the RDBs

[1] Researcher, Head, Visiting Researcher, and Senior Researcher. Bridge & Structures Division, National Institute for Land and Infrastructure Management, Ministry of Land, Infrastructure, Transport and Tourism

have studied to develop construction methods for temporary bridge and embankment structures and a comprehensive plan to stock construction material reserves to the ends.

However, because no practical guidance is available to predict the possibility in bridge failure due to tsunami forces or to design a countermeasure to minimize the damage to bridges due to tsunami loads, the RDBs' plans somehow end up presuming the situation that all existing bridges are likely to be inundated and out of commission after the tsunami. For this reason, the National Institute for Land and Infrastructure Management (NILIM), MLIT, and Center for Advanced Engineering Structural Assessment and Research (CAESAR) are engaged in a joint study to establish a preliminary guideline for bridges subjected to tsunami. NILIM's Earthquake Disaster Prevention Division has been studying to set out the design tsunami height and flow velocity at any bridge locations and the Bridge and Structures Division has been studying bridge performance requirements including the translation formula to estimate the design tsunami forces on bridges from the given design tsunami height and velocity and the limit state demands of each structural components. CAESAR, meanwhile, has been studying methods to estimate and design the ultimate strength of bearings to the horizontal and uplift tsunami forces transferred from the superstructure, as well as bridge superstructure proportions and special device installations on superstructures to mitigate tsunami impacts.

Of such research efforts, this paper discusses the basic concepts of tsunami design criteria for highway bridges. First, the paper proposes the concept of damage control design that focuses on facilitating traffic recovery for post-event emergency response. An understanding of the tsunami remedial measures for bridges now being studied by the road management authorities is as crucial as an analysis of actual bridge damage and restoration measures taken after the 2011 Tohoku Earthquake in the present work. In particular, the present paper discusses the effectiveness of accepting superstructure washouts. The idea is aimed at reducing tsunami forces transferred on substructures from superstructures, with the intent of preventing loss of substructures. Secondly, hydraulic formulas are examined to estimate tsunami forces on bridges. For 85 bridges that had typical superstructures and were inundated during the 2011 Toshoku Earthquake tsunami, the present paper calculates horizontal and uplift hydraulic forces on bridges and evaluates whether the superstructure would be washed out or not, comparing the actual damages to those bridges.

Overview of On-going Tsunami Countermeasure Works

To prepare for the predicted mega-earthquakes, road management authorities have been studying measures to secure post-event road networks for emergency transport. For arterial roads along the coastline, each road management authority has been predicting tsunami run-up areas and potential availability of detours to plan access routes to communities in their jurisdictions. Their study is typically comprised of two major works: seeking locations of new roads that are unlikely to be impacted by tsunamis and strengthening existing arterial routes that run along the tsunami run-up costal areas and communities.

Figure 2 summarizes the plan of tsunami countermeasures for the coastal region of Kii Peninsula [5]. A wide span of the Kii Peninsula coast is predicted to be hit if a tsunami generated from the Nankai Trough, a known potential mega-earthquake

subduction zone where multiple epicenters over an extended area could interact in a conjunct series. National Highway 42, the arterial coastal road of the Kii Peninsula, has as many as 20 bridges likely to be inundated in the tsunami. The Kinki Regional Development Bureau, MLIT, has been studying emergency recovery operations to resume the National Highway 42 for emergency transport, presuming all those bridges could become unusable. Table 1 shows temporary restoration measures now being considered to counter bridge washouts along the coastal zones. When a bridge is short, a temporary replacing structure can be built using H-girders and steel plates for example. For sites with slightly longer bridges, the required bridge length can be shortened by temporarily filling the approach embankments on both sides with sandbags, on top of which a temporary bridge of H-girders and steel plates can be installed. When a much longer bridge is required, the plan is to install corrugated pipe culverts covered with sandbags as fillings for a temporary road. These measures have been tested on site, and the road management authorities are planning to stock the reserve materials and equipment needed to implement these temporary restoration works.

Based on these measures by the road management authorities, the following points can be made:

- Even at the worst-case scenario, it should not be necessary to protect a whole bridge structure from a tsunami for the quick restoration after a tsunami washout.

Therefore, the focus is not only to protect the bridge against tsunami; there is also need to study design criteria from the perspective of controlling structure damage levels to facilitate quick emergency restoration of transportation.

Case Study of Emergency Restoration after the 2011 Earthquake off the Pacific Coast of Tohoku

Photos 2(a) and (b) highlight two examples of emergency bridge restorations damaged due to the tsunami in the 2011 Tohoku Earthquake. Photo 2(a) shows an example of emergency restoration that was achieved relatively quickly. Neither the superstructure nor the substructure of this bridge underwent critical damage. However, the soil behind the bridge abutment did wash out. A prefabricated bridge kept in reserve at another location was transported and assembled on site. Since the existing bridge could be served as a foundation for the emergency bridge, the bridge was opened to traffic only 0.5 month after the disaster.

On the other hand, Photo 2(b) is an example that required a longer restoration period. This bridge experienced the wash-out of not only the superstructure but also one of the substructures. With part of the substructure washed out, it was suspected that the remaining substructures also suffered significant damage, meaning that a detailed underwater and underground survey was needed to estimate the reliability of the remaining parts. In this case, a temporary bridge was constructed next to the original bridge. It took 3.5 months after the earthquake to open the temporary bridge to traffic.

Based on these case histories, we learned that:

- Even if the soil behind the bridge abutment is washed out, as long as the superstructure and the substructure remain intact, emergency measures to

restore movability can be achieved quickly.

- If the superstructure is washed out but the substructure is in usable condition, emergency measures to restore movability can be achieved quickly.
- Emergency measures are likely to become time-consuming when the substructure is washed out or is tilted.

These experiences indicate that tsunami design criteria need to be studied not only from the perspective of protecting all bridges against tsunamis, but also from the standpoint of controlling the damage so as to facilitate restoration.

Concept on Tsunami Design Criteria for Bridges

Based on on-going efforts by the RDBs and earlier experiences in the 2011 Tohoku Earthquake, the present paper discusses the three options shown below as tsunami design criteria for bridges:

Choice 1: For design earthquake motions and tsunami, the required design goal is to limit the level of damage to both superstructure and substructure so that both of them can remain usable for emergency transport. For given design tsunami, the superstructure and substructure shall be designed to have a sufficient strength so that the designated tsunami does not cause the washout, overturning or tilting of the bridge.

Choice 2: For design earthquake motions, the bridge shall be designed to ensure that the substructure, at least, will remain in a reusable condition for emergency measures to restore movability. For tsunami, bearings shall be designed to have a relevant breaking strength to allow for the superstructure to wash out at the designated tsunami scale, thereby reducing the impact to the substructure and keeping the substructure in an acceptable condition for the re-use in the emergency relief transport.

Choice 3: The design goal is to keep both the superstructure and substructure usable for emergency transport after any tsunami of any scale. Design a special bridge shape or special devices and attachments to smooth the tsunami flow around the bridge and minimize tsunami impacts on the bridge.

During a rare-scale earthquake, bearings and bridge piers are subjected to cyclic loads. In terms of Choice 1, a plastic hinge is induced at the bottom of bridge piers to dissipate the seismic energy through the cyclic plastic deformation during the earthquake, while bearings are designed to remain thriving. When the tsunami hits at the bridge after the earthquake tremor, the bearings and bridge piers are subjected to external pushover forces that will continue for some extended seconds. If the design allows the plasticization of a structural component under a pushover force, a significant residual displacement in the single direction can be accumulated. Accordingly, the bridge should have to be designed so that both bridge piers and bearings remain elastic. The corresponding design criteria can be given as follows:

$$\text{(Bearing Strength)} / \text{(Design Tsunami Forces to the Superstructure)} > 1.0$$

(Remaining Pier Strength) / (Design Tsunami Forces to both Super and Substructures) > 1.0

For simplicity, safety factors are omitted in the above equations. For Choice 1, however, the accuracy of design tsunami height and flow and corresponding design tsunami forces will greatly affect the reliability in design. Furthermore the bridge condition becomes uncontrollable when the tsunami goes beyond the scale the design assumes.

In terms of Choice 2, the design policy for earthquake motions is the same as Choice 1. For tsunami, the design allows bearings to break at the given design tsunami force, so that tsunami forces transmitted from the superstructure on the substructure will not exceed the design tsunami force even when tsunami with a scale larger than the scenario comes. This idea ensures that the bridge pier will not wash out or result in critical damage. While the seismic design for a rare-scale earthquake anticipates energy dissipation in the plastic hinge at the bottom of pier and keeps bearing response within the elasticity range, the tsunami design allows bearings to break, thereby dispersing the energy to keep the bridge pier within the range of elastic response. Design criteria can be written as follows:

(Bearing Strength) / (Design Tsunami Force to the Superstructure) = 1.0

(Remaining Pier Strength) / ($\Phi \times$ Bearing Strength + Design Tsunami Force to the Substructure) > 1.0

where Φ = the overstrength factor to the bearing strength. The flow velocity, wave height and approach angle of the tsunami may depend on the minute topographic boundary conditions of the surrounding areas. Use of flow velocity and wave height to estimate the external forces acting on the bridge therefore involves a great deal of uncertainty. With Choice 2, however, regardless of the scale of tsunami in reality, the design load becomes equal the bearing failure load, which to some extent can be controlled artificially. For this reason, Choice 2 offers a better prediction of damage to bridges and hence is more beneficial than Choice 1 from the perspective of road management and disaster relief operation planning. The challenge for Choice 2 is the development of a bearing structure that allows for the quantitative evaluation of overstrength factor Φ with as a small error as possible.

Choice 3, if technically achievable, is the most favorable option since it is less impacted by the uncertainty in tsunami force estimation, and offers a usable superstructure against any scales of tsunami. Study on superstructure shapes and devices that can minimize the impacts of the tsunami is awaited. Research and development of such technologies is currently underway at CAESAR, Public Works Research Institute (PWRI) [6][7].

Study on the Feasibility of Superstructure Washout Assessment Using Hydraulic Formula to Estimate Tsunami Forces

In Choice 1 and Choice 2 above, the estimation of design tsunami scale and tsunami force is key to make the washout assessment of superstructures practical. A common method to estimate tsunami forces for a given design tsunami flow is to obtain the hydrodynamic horizontal and uplift forces by substituting the given flow velocity and height into hydraulic formulas.

Tsunami forces on bridges can vary depending on multiple factors such as the superstructure type, existence of other structures in the vicinity, and local topography. Bridges that experienced washout in the tsunami of the 2011 Tohoku Earthquake had different superstructure types, materials, shapes, and sizes. As shown in Photo 1, the damage characteristics were also different from bridge to bridge, including the washout of superstructure, the collapse and washout of bridge pier, and the washout of abutment backfill. In some cases, the type and extent of the damage differed greatly among bridges located close to each other. Different bearing types were used in these bridges, the behavior of which may have affected the superstructure washout. Considering all these factors and examining the damage case histories observed in the 2011 Tohoku Earthquake, a feasible and practical method is sought herein to estimate tsunami forces on bridge superstructures.

Bridges Selected for Feasibility Study

Out of all bridges inundated by the tsunami in the 2011 Tohoku Earthquake, 85 bridges were selected for the present study, categorized into typical steel I-girder bridges, concrete T-girder bridges, and concrete slab bridges. These bridges were selected as follows:

1. First, bridges were chosen if the bridge type, structural dimensions could be confirmed through original drawings or post-earthquake site visits.
2. Of those chosen in the first step, bridges were excluded if they were located at sites where a minute difference in site conditions had likely change the tsunami flow velocity, direction, wave height, etc., greatly, such as those located immediately behind flood gates.

Table 2 summarizes the number of washouts by bridge type and Figure 3 shows a breakdown of the bearing types for each bridge type. Four types of bearings were used: rubber pad bearings, direct placement, line bearings and rubber bearings.

Analysis Method

As illustrated in Figure 4(a), a two-dimensional plotting is used in the present study in terms of the inverses of the safety factors, F.S., for horizontal washout and vertical washout (uplift), respectively. If the inverses of both safety factors are less than 1.0 for both the horizontal and vertical directions, the superstructure was theoretically supposed not to wash out. If the inverse of one of the safety factors exceeds 1.0 for either direction, the bridge was notionally supposed to washout. As shown in Figure 4(b), if a set of the inverses of the safety factors of a bridge is plotted above the 1:1 line, it means the uplift force should be prevalent, while the plot below the 1:1 line indicates the prevalence of the horizontal force rather than the uplift force.

The inverses of the safety factors for the horizontal and vertical directions are calculated using the following formulas:

1 / F.S. = (Horizontal Tsunami Force) / (Horizontal Bearing Resistance)

1 / F.S. = (Uplift Tsunami Force) / (Superstructure Weight)

Calculation methods for the tsunami horizontal and uplift forces, as well as for the horizontal bearing resistance, will be described in later sections.

Calculation of Tsunami External Forces Using Hydraulic Formulas

In the wake of widespread tsunami damage to bridges in the 2004 Sumatra-Andaman earthquake and 2011 Tohoku Earthquake, the reaction force on bridge structures due to tsunami waves has been studied in bridge engineering. For example, Kosa et al [8] have conducted wave flume tests and proposed experimental equations to calculate the horizontal and uplift forces for scaled model bridges during tsunami, incorporating factors such as the tsunami flow velocity and height at site. Hoshikuma et al. [6] have conducted water flume tests to examine tsunami forces on scaled-bridge girders, measuring the transmission force between bearings and abutments. They have shown that the response of bridge girders to tsunami can change with the difference in the shape of girders. For example, their test results have indicated that bridges having a simple rectangular shape can be exerted by downward forces while T / I-beam girder bridges can be uplifted and then overturned initiating at the side facing directly to the incoming tsunami. Kataoka et al. [9] and Ezura et al. [10] have simulated the tsunami run-up from the epicenter of the 2011 Tohoku Earthquake up to 10 to 20 bridges at different sites. They have compared simulated and observed bridge wash-out case histories, showing that the tsunami simulation can reproduce tsunami impacts with a reasonable accuracy. Namely these previous works indicate the following aspects:

- It is necessary to consider both horizontal and vertical forces when assessing the influence of tsunami on bridges.
- Hydrological lift and drag formulas may work accurately to some extent when the tsunami velocity and height at site are given.
- Tsunami run-up simulations can estimate the velocity and height of the tsunami at a particular site with an acceptable accuracy including the propagation process from a tsunami source.

In accordance with these findings, the present study will hypothesize the tsunami forces as noted below. The total horizontal tsunami force on superstructures is a superposition of hydrostatic and dynamic pressures. The hydrostatic pressure can be imbalanced at the time or just after the time when the tsunami hits the girders and depends on water elevation. The hydro dynamic force is assumed to account for the compensation of total water pressure on superstructure in addition to the static one.

$$P = P_1 + P_2 \tag{1}$$

$$P_1 = \rho_s \cdot g \cdot b \int_{z_2}^{z_1} (h' - z) dz \quad (2)$$

$$P_2 = \frac{1}{2} \rho_s \cdot C_d \cdot A \cdot \upsilon^2 \quad (3)$$

whereas,

P_1 = hydrostatic pressure force on the bridge seaward surface,

P_2 = hydrodynamic pressure force on the bridge surface facing the tsunami travelling from the offshore,

ρ_s = seawater density = 1030 kg/m^3,

g = gravitational acceleration = 9.8 m/s^2,

b = girder length (m),

h' = height of the tsunami crest from the static water level or the ground level (m),

z = height from the static water level or the ground level (m),

z_1 = height of the girder bottom from the static water level or the ground level (m),

z_2 = height of the top of the curb blocks on the deck from the static water level or the ground level (m),

A = area subjected to pressure (m^2),

v = horizontal flow velocity of the tsunami (m/s), and

C_d = resistance factor.

C_d should be calibrated to account for tsunami forces based on damage case histories and experiments. As a starting point, the present paper simply employs the following formulas that are used in the Japanese Specifications for Highway Bridges to calculate wind load, although further study is needed for the value of C_d in the future:

$$C_d = 2.1 - 0.1\, B / D \qquad \text{if } 1 \le B / D < 8 \quad (4)$$

$$C_d = 2.1 - 0.1\, B / D \qquad \text{if } 8 \le B / D \quad (5)$$

whereas,

B = total width (m),

D = superstructure height (m) (height from the base of the main girder to the top of curb blocks).

Vertical force U is given as the sum of U_1 (buoyancy force in the inundation area) and U_2 (lift pressure caused by the flow), assuming the water fills up surrounding the bridge. It is calculated using the following formula:

$$U = U_1 + U_2 \tag{6}$$

$$U_1 = \rho_s \cdot g \cdot V \tag{7}$$

$$U_2 = \frac{1}{2}\beta \cdot \rho_s \cdot C_d \cdot A' \cdot \upsilon^2 \tag{9}$$

whereas,
$V =$ volume of the superstructure (m^3),
$C_L =$ lift coefficient, and
$A' =$ footprint of the bottom of the superstructure (m^2).

A lift coefficient of 0.50 was assumed in the present paper. Numerical wave simulations using a software of CADMAS-SURF were separately conducted for a rectangular cross-section object located at different heights in a two-dimensional (2-D) channel, counting the total value of upward water pressure distributions on the cross-section. CADMAS-SURF is based on the non-compressive fluid theory and the Navier-Stokes formula as the basic equations and employs the VOF (Volume of Fluid) method to deal with the free surface of the fluid.

In practice, tsunami horizontal flow velocity (v) and height (h') could be given via tsunami hazard maps and other sources. However better accuracy is needed for the purpose of the present analysis. The horizontal flow velocity and wave height at each bridge site in the 2011 Tohoku Earthquake tsunami is therefore estimated via a tsunami run-up simulation with CADMAS-SURF separately. The Fujii-Satake model Ver.4.6 is employed as the tsunami generation model.

Figure 5 compares tsunami heights at sites between the simulation and post-tsunami measurement, where the actual tsunami height records at bridge locations are shown in the literatures [11] [12]. The difference between the simulation and post-tsunami measurement is generally within 30%, but greater discrepancies are observed at some locations.

Bearing Resistance

The horizontal resistance is the sum of the shear strengths of the bearing anchor bolts of all bearings. The shear strength of each anchor bolt is calculated using the following formula:

$$R_{SH} = A \cdot \sigma_u / \sqrt{3} \tag{10}$$

whereas,
$A =$ effective cross sectional area of the anchor bolt (mm^2), and
$\sigma_u =$ nominal tensile strength of the anchor bolt (N/mm^2).

Detailed drawings of bearing did not exist for eight bridges and the present study

designed them again following the standards at the time when they were originally designed to predict their horizontal resistances.

The vertical resistance involves the weight of the superstructure and typical design forces of bearing described in design guidance books in the past which equaled 0.30 times the bearing reaction forces for dead loads for rubber bearings and 0.10 times of that for other bearings. Resistances provided by unseating prevention restrainers are also neglected for both horizontal and uplift forces for the sake of simplicity.

Analysis Results

The inverse numbers of the safety factors for 26 steel plate girder bridges are plotted in Figure 6(a). Hereafter in Figures 6(a) to (c), the black dots indicate bridges washed out in the actual tsunami; the white dots indicate bridges that were not washed out in the actual tsunami. The bridges that were washed out in the actual tsunami are plotted in the region where the inverse of the safety factor exceeds 1.0 (i.e., safety factor is below 1.0) in either the horizontal or uplift direction. Some bridges that did not wash out in the actual tsunami are plotted in the region where the inverse of the safety factor exceeds 1.0 in either direction, indicating the present tsunami force formula can give tsunami impact forces on the conservative side. These results show that tsunami external force formulas can be based on hydrodynamic forces to calculate tsunami forces on bridges.

As indicated in Figure 6(a), the inverse of the horizontal safety factor is greater than the inverse of the uplift safety factor (i.e., the uplift safety factor is smaller) in some of the bridges. This is likely because steel plate girder bridges are relatively lightweight.

The inverse numbers of the safety factors for the 24 concrete T-girder bridges are plotted in Figure 6(b). Almost all of the bridges washed out in the actual tsunami are plotted in the region where the inverse of the safety factor exceeds 1.0 (i.e., safety factor is below 1.0). Most of the concrete T-girder bridges were not vertically fixed tightly in the calculation and the bridges that were actually washed out are plotted in the lower right region of the graph, indicating that they were impacted greatly by the horizontal wave force. This is likely because the concrete T-girder bridges are relatively heavy.

Seven black dots of bridges that were actually washed-out were plotted in the region with an inverse of the safety factor below 1.0 in both directions. For six out of the seven, the inverse of the safety factor was close to 1.0 in the horizontal direction. Calculation of the wave force and bearing strength can contain errors, and bridges with an inverse of the safety factor ranging between 0.80 and 1.00 are more likely to be affected by such error. To improve the calculation precision of the wave force and bearing strength, there is need for more accurate tsunami estimates and more accurate evaluation of the bearing strength, all of which require further research.

The remaining two bridges are indicated in Figure 6(b) by ovals marked ‘A’. Calculations show that the inverse of the safety factor for these bridges is smaller than 0.50 (i.e., safety factor of 2.0 or greater). Even with the additive safety factor, the calculations fail to explain the actual tsunami damage experienced. The tsunami travel and run-up simulations for the two bridges show a tsunami flow velocity of 0.6 m/s and

2.1 m/s, respectively, which seems too small to wash bridges out. This is under 50% of the smallest flow velocity calculated for the washed-out concrete T-girder bridges in reality. These discrepancies can likely be improved by reviewing of the setting of the surrounding conditions in the tsunami travel and run-up simulations.

The inverse numbers of the safety factors for the 35 concrete slab bridges are plotted in Figure 6(c). The three bridges indicated by ovals marked 'B' in Figure 6(c) were actually washed out, but had very small inverse of horizontal and uplift safety factors by calculation. The tsunami travel or propagation and run-up simulations for the three bridges show a flow velocity of less than 2.0 m/s. This is approximately 60% the lowest velocity calculated for the other concrete slab bridges that were actually washed out.

In Figure 5, the bridges marked with A and B in Figure 6 are also designated, in which, as mentioned above, the tsunami flow velocities were slower than 2.1 m/s at those bridges in the calculation which is considered too slow to wash the superstructure out. The corresponding tsunami heights are clearly underestimated in two out of those five bridges. Thus we can neglect the analysis results for the bridges marked with A and B to evaluate the effectiveness of Equations (1) through (9). Overall, we consider that the calculation results agree with the actual bridge damage in general and, if the tsunami flow velocity and wave height at the bridge location are provided, standard hydraulic formulas can be used to calculate the horizontal and uplift forces that act on the bridge with sufficient precision.

Conclusions

This study yielded the following results:

1. Experiences from the tsunami recovery efforts after the 2011 Tohoku Earthquake backs up a damage control design philosophy to protect the substructure by intentionally allowing the superstructure to be washed out as one of design objectives.
2. The case-history analysis for 85 bridges hit by the 2011 Tsunami shows that typical hydraulic equations works in practice both in the horizontal and uplift behavior.
3. A factor of safety of 1.2 or 0.80 should be considered to predict the horizontal and uplift Tsunami forces or the design bearing strength, respectively. However, the authors believe that the accuracy should be improved by calibrating drag coefficients more relevantly based on damage case histories and experimental results.

References

[1] Building Research Institute, National Institute for Land and Infrastructure Management (NILIM), Ministry of Land, Infrastructure and Transport: Survey Report on Damages from 2011 Earthquake off the Pacific Coast of Tohoku, NILIM Reference Material No. 674, Building Research Reference Material No. 136, 2012.

[2] Tokuyama, H. Learning from Japan's Ordeal. Public Roads, Vol. 75, No. 6. Publication Number: FHWA-HRT-12-004. 2012.

[3] Government of Japan Cabinet Office Website:

http://www.bousai.go.jp/jishin/nankai/nankaitrough_info.html
[4] Committee on Disaster Management and Earthquake Disaster Countermeasures Website, Chubu Regional Development Bureau, Ministry of Land, Infrastructure, Transport and Tourism: http://www.cbr.mlit.go.jp/road/kanri-bunkakai/
[5] Kinki Regional Development Bureau, Ministry of Land, Infrastructure, Transport and Tourism: http://www.kkr.mlit.go.jp/plan/bousairenraku/index01.htm
[6] Nakao, H., Cho, K., Sumimura, T., and Hoshikuma, J.: How the Section Characteristics of the Superstructure Affects Tsunami Action on the Bridge. Japan Society of Civil Engineers (JSCE) Journal A1 (Structural and Geotechnical Engineering) Vol. 69, No. 4 (Geotechnical Engineering Journal Vol. 32), I_42-I_54, 2013.
[7] Sumimura, T., Nakao, H., and Hoshikuma, J.: Experimental Study on Resistance Characteristics of Steel Bearings Against Tsunami Action on Bridges. JSCE Journal A1 (Structural and Geotechnical Engineering) Vol. 69, No. 4 (Geotechnical Engineering Journal Vol. 32), I_102-I_110, 2013.
[8] Shimizu, H., Kosa, K., Sasaki, T., and Takeda, S.: Analysis of Tsunami Damage of Highway Bridges. JSCE Structural Engineering Journal, Vol. 58A, 2012.
[9] Kataoka, S., Kaneko, M., Matsuoka, K., Nagaya, K., and Unjoh, S.: Replication Analysis of Earthquake and Tsunami Damage on Highway Bridges that Suffered Washout of Superstructure and Bridge Pier. JSCE Journal A1 (Structural and Geotechnical Engineering) Vol. 69, No. 4 (Geotechnical Engineering Journal Vol. 32), I_932-I_941, 2013.
[10] Ezura, Y., Shoji, G., and Hiraki, Y.: Estimation of Tsunami Fluid Pressure Acting on a Wash-away Bridge Deck by the 2011 Off the Pacific Coast of Tohoku Earthquake Tsunami. JSCE Journal B2 (Coastal Engineering) Vol. 68, No. 2, I_411-I_415, 2012.
[11] The 2011 Tohoku Earthquake Tsunami Joint Survey (TTJS) Group: The 2011 off the Pacific coast of Tohoku Earthquake Tsunami Information. http://www.coastal.jp/ttjt/
[12] Haraguchi, T., and Iwamatsu, A.: Detailed Maps of the Impacts of the 2011 Japan Tsunami: 167. Koko Shoin Publishers Ltd. Tokyo. 2011.

Table 1. Examples of post-event recovery plans for bridges

Type	Type1	Type2	Type3
Conditions	Narrow rivers	Wider rivers	Very wide rivers
Restoration Method	H-steel + Cover plates	Sandbags + H-steel + Cover plates	Sandbags + Cover plates + Corrugated pipes
Schematic Diagram	Cover plates 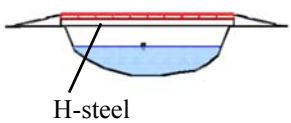 H-steel	Cover plates Sandbags 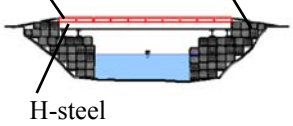 H-steel	Cover plates Sandbags 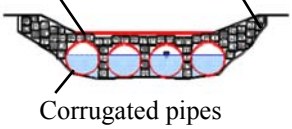 Corrugated pipes

Table 2. Numbers of bridges in total, wash-out and no wash-out by girder type

Girder type	Number of bridges		
	Total	Wash-out	No wash-out
Steel I-beam	26	14	12
Concrete T-beam	24	13	11
Concrete slab	35	18	17

Photo 1. Examples of damaged bridges due to the 2011 Tohoku Earthquake Tsunami (From Left to Right: Washout of superstructure, Collapse of piers, and Washout of backfill behind abutment)

(a) Opened to traffic in 14 days of the tsunami strike

(b) Opened to traffic in 3.5 months of the tsunami strike

Photo 2. Examples of emergency restoration for wash-out bridges after the 2011 Tohoku Earthquake Tsunami

Figure 1. Major arterial roads along the Pacific Coast in the region of Tohoku

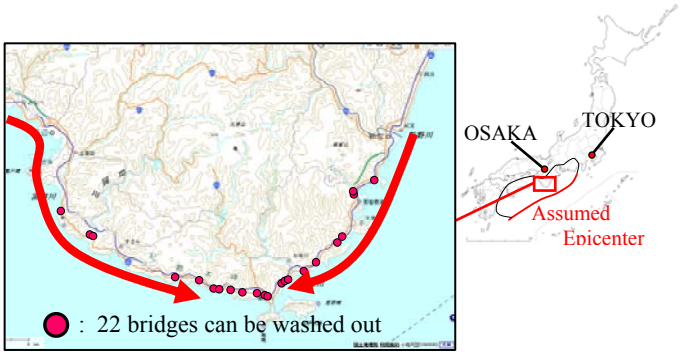

Figure 2 Bridges located on the major national highway in the predicted tsunami run-up zone along the Kii Peninsula Coast

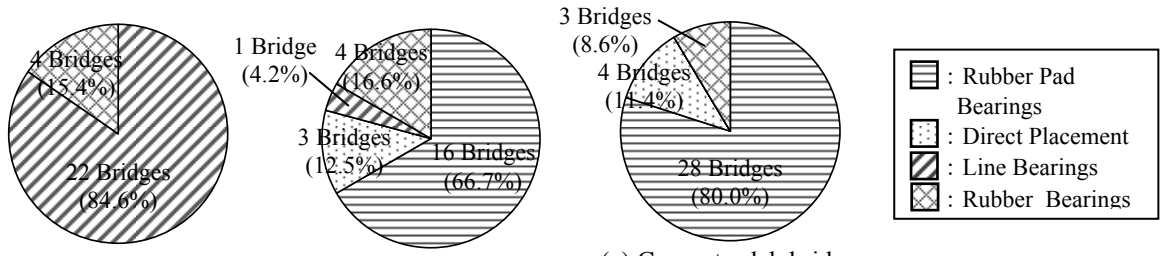

(a) Steel I-beam bridge (b) Concrete T-beam bridges (c) Concrete slab bridges

Figure 3. Types of bearing used in the bridges chosen in Table 2

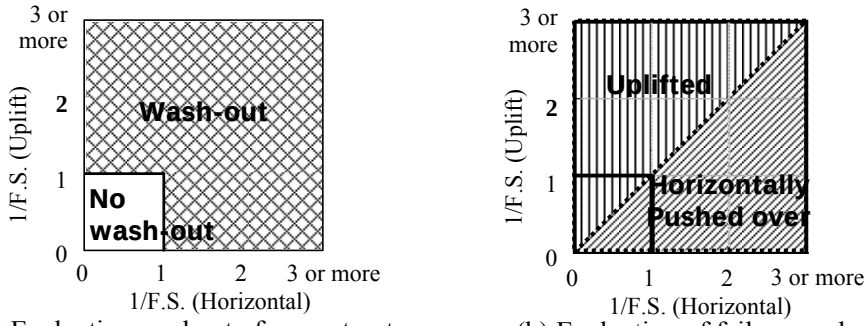

(a) Evaluation washout of superstructures (b) Evaluation of failure mode

Figure 4. Illustrative understandings used in the present analysis

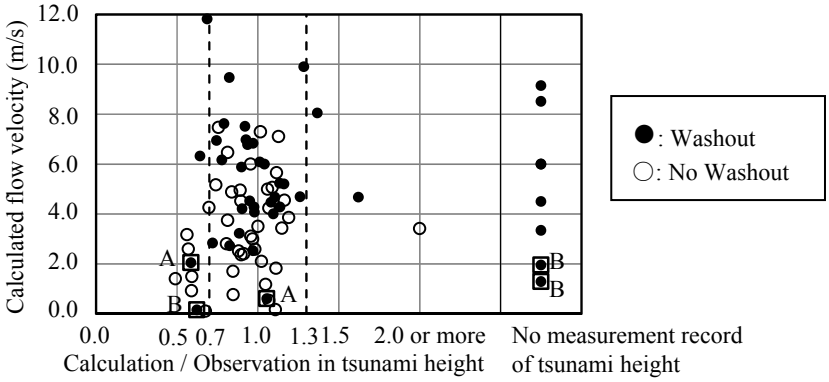

Figure 5. Calculated tsunami flow velocities and comparison in tsunami height at bridge site between the calculation and post-event measurement

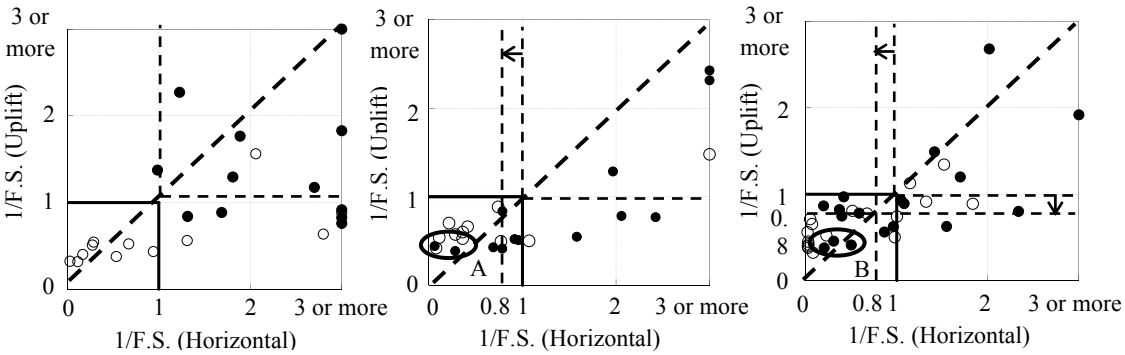

(a) Steel I-beam bridges (b) Concrete T-beam bridges (c) Concrete slab bridges

Figure 6. Inverse values of safety factor in horizontal and uplift directions (Black dots: Wash-out bridges, White dots: Not washed-out)

QUANTIFYING THE SEISMIC RESILIENCE OF HIGHWAY NETWORKS USING A LOSS-ESTIMATION TOOL

Ian G. Buckle[1] and Stuart D. Werner[2]

Abstract

Today *life-safety* is no longer the sole requirement of a highway system subject to a major earthquake. *Resilience* has been added to the list of requirements to ensure rapid recovery and minimal impact on the socio-economic fabric of modern society. In qualitative terms, a resilient system recovers quickly, whereas a non-resilient system does not. It is more difficult to express resilience in quantitative terms, yet it is important to try to do so. If resilience can be quantified, we can understand why some systems are more resilient than others. In this paper REDARS, a loss-estimation tool for highway systems, is used to identify factors affecting resilience and, by way of a demonstration application, show that column retrofitting and modest improvements in mobilization rates, can improve resilience by factor of 4 for a small-moderate sized city.

Introduction

Earthquakes remain one of the world's major problems. They occur frequently, without warning, and result in high death tolls, thousands of injuries, and crippling economic losses.

For many years earthquake engineering research around the world has focused on saving lives and minimizing the number of injuries, but, we now recognize that the protection of human lives is a necessary but not sufficient goal to minimize the social and economic impacts of a major earthquake. Recent data from U.S. natural disasters show that, despite the advances in earthquake engineering and other natural hazards, economic losses due to these disasters are escalating at an alarming rate, particularly over the last 25 years in the U.S.

The time has come to focus on controlling the economic and social losses from future earthquakes, in addition to life-safety, to prevent a socioeconomic catastrophe. It is the hypothesis of this paper (and others in this field) that these losses can be greatly reduced by building resilience into our infrastructure systems, and in this paper we explore the application of this concept to highway systems.

Resilience

Technically, *resilience* is the ability of a body to bounce back and recover its original shape after being subjected to stress. In societal systems, resilience is the ability of these systems to recover rapidly from a shock or disturbance. Fig. 1 shows schematically the effect of resilience on the response of a system, measured by the

1 Professor, Dept. Civil and Environmental Engineering, University of Nevada, Reno NV, 89577, USA
2 Principal, Seismic Systems and Engineering Consultants, Oakland CA, 94611, USA

quality of service over time. In this figure an event occurs at time t_1 and there is an immediate loss of service from Q_0 to Q_1 (for example the number of passenger-miles traveled on a highway system) followed a period of recovery such that by time t_2, full service has been restored. Bruneau et al (2003, 2004) have used this framework to define loss of resilience, but in this paper we use Fig. 1 to quantify resilience and identify those factors that lead to resilient systems. If we are able to quantify resilience we are then be able to understand why some systems are more resilient than others. We would also be able to develop incentives for owners and decision makers to make infrastructure systems more resilient and measure progress towards developing resilience to natural disasters.

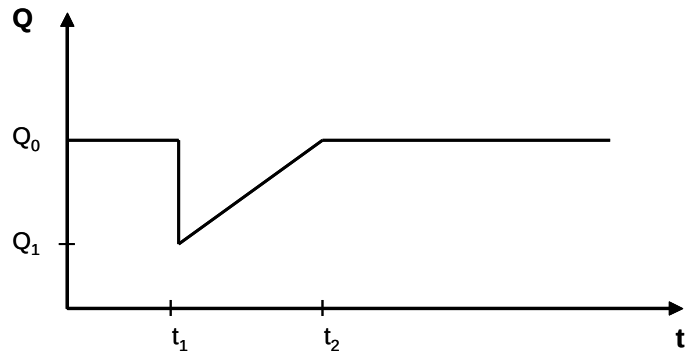

FIGURE 1. IMPACT OF AN EARTHQUAKE ON QUALITY OF SERVICE, Q (BRUNEAU ET.AL. 2003, 2004)

Quantifying Resilience

In Fig. 2 the initial impact of the event is the loss of service $\delta Q = Q_0 - Q_1$. This loss is the direct result of the vulnerability of the system to the event and the more fragile the system (the more vulnerable) the greater δQ. The rate of recovery (r) from Q_1 is assumed to be constant over time for the purpose of illustration, leading to a full recovery at time t_2. The recovery time (T) is a measure of the resilience of the system (Fig. 3); the smaller T, the higher the resilience; the higher T, the lower the resilience.

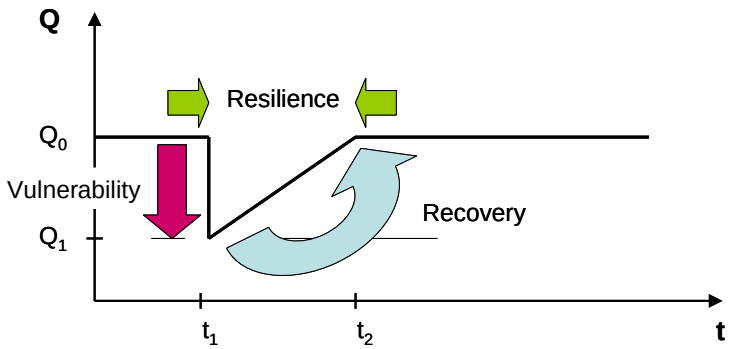

FIGURE 2. RESILIENCE AS A FUNCTION OF VULNERABILITY AND RATE OF RECOVERY (BUCKLE and LEE, 2006)

It follows that resilience is inversely proportional to recovery time T, and that

T is given by:

$$T = (t_2 - t_1) = \delta Q / r$$

Consequently, reducing vulnerability improves resilience. Likewise increasing the rate of recovery improves resilience, but doing both at the same time produces the most resilient systems.

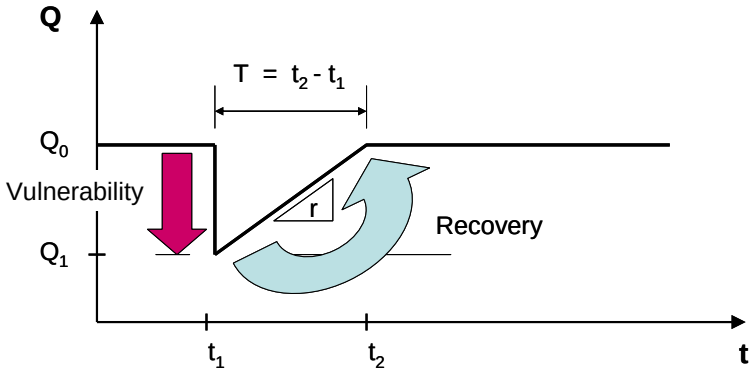

FIGURE 3. MEASURE OF RESILIENCE: TIME TO RECOVER TO PRE-EARTHQUAKE QUALITY OF SERVICE, T

As noted above, improving resilience can be achieved by reducing vulnerability and this may be done by building structural systems with capacity for extreme loads, retrofitting existing systems, adding redundancy, relocating co-located systems, reducing the interdependence of infrastructure systems, and avoiding the potential for cascading failures. However the cost of this mitigation (reducing vulnerability) can be prohibitive and an intelligent approach is necessary which balances expenditure of resources against likelihood of damage and the consequences of damage (impact on recovery time).

Also as noted above, resilience can be improved by increasing the rate of recovery and this can be achieved by empowering community response and resourcefulness, building emergency response capacity (not just at the local level but also regionally and nationally), anticipating needs and identifying resources ahead of time. New tools are now available for selected infrastructure systems that enable pre-event planning to be undertaken. These tools are based on system loss-estimation models and can be used to calculate system performance parameters (e.g. traffic flows) for either deterministic or probabilistic-based event scenarios. They therefore offer a methodology to estimate recovery times (e.g. T_{80}) and may therefore be used to quantify the resilience of such systems.

One such tool is REDARS (Werner et. al., 2000), which has been recently modified (REDARS 3) to allow the resilience of highway systems to be specifically studied (Werner et. al., 2013).

Resilient Highway Systems

The post-earthquake resilience of a highway system can be measured deterministically or probabilistically in the following ways, all of which are accommodated in REDARS 3:

- ***System-Wide Resilience*** -- is a single value of the time at which aggregated travel times or trip demands throughout the entire highway system achieve their pre-earthquake values.

- ***Location-Specific Resilience*** -- represents the time at which travel times and trip demands to/from any user-selected location achieves their pre-earthquake values. This enables the resilience to be assessed of travel to/from various locations that are vital to a region's emergency response and economic recovery, such as: (a) major medical centers; (b) airports and water ports; (c) government centers; (d) major centers of commerce; and (e) population centers.

- ***Route-Specific Resilience*** – represents the time at which travel times along any user-selected route within the highway system achieve their pre-earthquake values. This enables the resilience of travel to be assessed along various key routes within the system such as: (a) non-redundant and heavily traveled routes to/from centers of population or commerce; (b) lifeline routes that must accommodate emergency travel almost immediately after an earthquake; (c) routes for travel to/from emergency response facilities; and (d) major routes for interstate travel.

The resilience of a highway system can be affected by a variety of factors related to: (a) the highway system and surrounding region; (b) the reparability of the earthquake damage; and (c) post-earthquake traffic-management. These factors are discussed in the following sections.

System and Regional Factors

Factors related to the highway system and surrounding region that affect resilience, include:

- Size, redundancy, and traffic-carrying capacities of the highways and arterials
- Trip demands on the system and the resulting degree of pre-earthquake traffic congestion experienced by the system, and
- Proximity of centers of commerce and population to the earthquake damage.

Damage and Repair Factors

Factors related to the extent of damage to the system and the rate at which this damage is repaired, that affect resilience, include:

(a) Earthquake-induced Damage

The following factors affect the potential for earthquake damage to the components of a highway system (bridges, roadways, approach fills, tunnels, embankments, etc.) which, in turn, affect post-earthquake downtimes and system resilience.

- ***Seismic Risk Reduction Measures***. Whether or not seismic risk reduction measures have been implemented affects the potential for earthquake damage to the system components. Such measures include seismic design/retrofit of bridge structures, and soil improvement measures along the system's roadways, bridges, slopes, and embankments.

- ***State of Maintenance.*** Whether or not the various components are well maintained affects their performance during an earthquake. If components have deteriorated due to weathering and other factors, their seismic performance will be adversely affected.

- ***Soil Conditions.*** Highway components located on potentially-liquefiable soils or along unstable slopes that could slip during ground shaking, are more prone to earthquake damage and disruption than will components located on competent soils and slopes.

- ***Geologic Hazards.*** The proximity of the highway system to active faults affects the geologic hazards to which the system is subjected during an earthquake. Any element of the system that happens to cross a shallow fault that undergoes surface rupture could be damaged by the resulting relative ground displacement. Also, the level of ground motion hazard to which the highway system is subjected depends on the distance of the system to active faults in the region.

(b) Component Attributes

Bridge attributes affecting seismic performance include material of construction, span-support conditions, skew angle, whether they have been seismically designed, and if not, whether they have been retrofitted. Tunnel attributes affecting seismic performance include the tunnel radius, material of construction, construction type (cut-and-cover vs. drilled), and whether they have been seismically designed. Approach fill attributes affecting seismic performance include extent of compaction and type of fill.

(c) Damage Repair

The rate at which highway system damage can be repaired strongly affects system resilience. The damage repair rate will depend on the following factors:

- ***Bridge Damage Accessibility.*** Bridge repairs are slowed, if a damaged bridge crosses a river or other waterway, or is in close proximity to other roadways or structures that limit access to the damage.

- ***Repair Resource Mobilization.*** The time needed to mobilize repair resources affects total downtimes. This mobilization time depends on: (a) whether design of the repairs is needed; and (b) whether damage is widespread throughout the highway system and extends to other elements of the region's built infrastructure. If repair resources are scarce, mobilization times will be seriously affected. Stockpiling of emergency repair resources beforehand can reduce post-earthquake mobilization times.

- ***Geologic Hazards.*** Experience from past earthquakes has shown that earthquake-induced landslides can block highways, and that earthquake-induced failures of slopes or embankments can damage nearby highway components. In addition, earthquake-induced liquefaction of soils that support a bridge can severely damage both the foundations and substructure. Each of these geologic-hazard-related sources of highway damage can lead to extensive repair downtimes which slow recovery and decrease the resilience of the system.

- ***Accelerated Repairs.*** Accelerated repairs of key elements of a highway system can substantially reduce downtimes and improve resilience. An accelerated program for the repair of severely damaged freeways in Los Angeles after the Northridge Earthquake was particularly successful. It greatly reduced the downtime for affected sections of the freeway and reduced regional indirect losses due to the freeway damage. Network resilience was markedly improved.

Traffic Management Strategies

Traffic-management strategies can improve the resilience of a highway system. Such strategies can include:

- ***One-Way Traffic Strategies.*** Changing traffic flow directions from two-way to one-way on roadways near the system damage.

- ***Increased Traffic Capacities.*** Removal of parking lanes along major roadways near the damage can improve traffic flows and increase the recovery times in the vicinity of the damage.

- ***Staggering of Traffic Demands.*** The staggering of work hours among major employers in a region with severe highway damage can spread traffic demands over time and improve traffic mobility while the damage is being repaired. This will reduce congestion and improve repair times leading to faster recovery of the highway system.

Demonstration Application

This section presents a demonstration application of the REDARS 3 software to the quantification of seismic resilience of the highway system in Shelby County, Tennessee. This application consists of a deterministic analysis of system resilience after an earthquake of M_w 7.7 that simulates a repeat of the 1811-1812 New Madrid, Missouri events. These earthquakes caused strong shaking throughout the Midwest and were felt over much of the eastern United States. The analysis includes the response of bridges to ground motions, but does not include the effects of other hazards (liquefaction, landslide, etc.) nor does it include response of roadways and other highway components to this shaking. Ground motions from this earthquake are estimated using ShakeMap procedures (Wald et al., 2006).

Shelby County is located in the southwest corner of Tennessee, just north of the border between Tennessee and Mississippi. It includes the city of Memphis which had a population of over 655,000 in 2010. The Shelby County highway system is shown in Fig. 4. It includes a beltway of interstate highways that surrounds Memphis, major crossings of the Mississippi River along Interstates 40 and 55, and various arterials roadways. The system includes 466 bridges, of which 137 were constructed during or after 1990 and therefore are assumed to have been seismically designed, and 84 bridges that have been seismically retrofitted. The remaining 245 bridges have neither been seismically designed nor retrofitted.

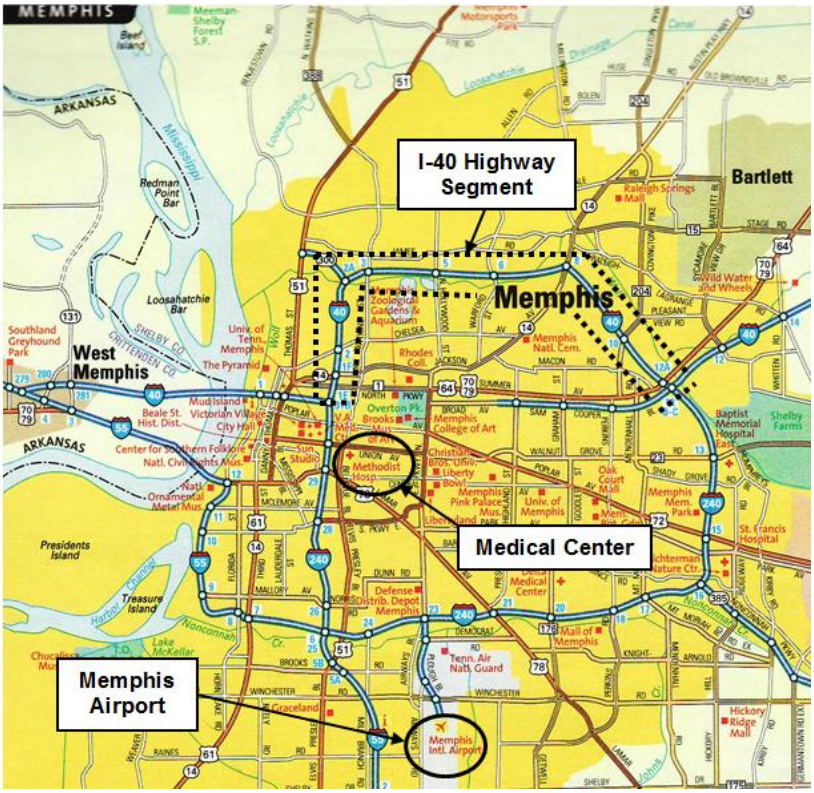

FIGURE 4. SHELBY COUNTY, TN, HIGHWAY SYSTEM SHOWING LOCATIONS AND ROUTE SEGMENT FOR RESILIENCE STUDIES

Analysis Procedure

The REDARS-3 methodology estimates (a) earthquake damage states for every bridge in the Shelby County highway system for the given ground motion, and (b) the cost and downtime for repair of each damaged bridge. These downtimes form system states at various post-earthquake times, i.e. network links that are closed due to bridge damage at various post-earthquake times.

Link closures will require drivers to detour around the damaged bridges and use alternative routes. This will cause traffic congestion that can be severe if many links throughout the system are closed at a given time. REDARS applies a transportation network analysis procedure to each system state, in order to estimate the extent of this congestion and how it affects travel throughout the highway system. The end results of the analysis for each post-earthquake system state represents the effects of this congestion in two ways: (a) travel times will be increased - i.e., it will take longer for travelers to get from their origin to their destination; and (b) trip demands on the system will be reduced - there will be a reduced propensity to travel because of the congestion. (i.e., trip demands on the system will be reduced).

The final phase of the analysis uses these increased travel times and reduced trip demands to determine system resilience.

As noted previously, resilience will strongly depend on the estimated downtimes of the damaged bridges while they are being repaired. Downtimes are estimated by a model that has been developed for bridges in the Central and Southeastern United States (CSEUS). The model uses component-based fragility functions which enable better estimates to be made of downtimes than previously possible. However, downtime estimates are uncertain, and these uncertainties should be kept in mind when reviewing the resilience results given in this paper. Default repair parameters developed by Werner et al. (2013) are used to estimate the downtimes in this application.

In addition to downtimes during repairs, additional time will be needed to mobilize repair resources at the sites of the damaged bridges before the repairs can proceed. Estimation of this mobilization time is uncertain, because it depends on factors that cannot be anticipated beforehand. For example, if existing repair resources in a region are insufficient to address damage to the entire built infrastructure in the region (in addition to the highway system), there may be competition for these resources until additional emergency resources arrive. The bridge repair model used in this application, invokes a mobilization time scale factor that depends on the earthquake magnitude, in order to roughly account for the effect of additional infrastructure damage on mobilization time. For the major earthquake (M_w=7.7) considered in this application, a mobilization time scale factor of 1.30 was used, and applied to the repair downtime of each bridge to obtain a total downtime for that bridge. Since the damage to the built infrastructure in the region due to such a large earthquake could be severe, a mobilization time scale factor of 1.30 does not seem unreasonable. It is noted that, for

this earthquake magnitude, a value of 1.30 corresponds to the default value built into REDARS 3. This factor can be overridden by the user.

The major crossings of the Mississippi River by Interstates 40 and 55 are not included in this application because component-based fragility functions for these complex bridges have not yet been developed.

Analysis Results

To illustrate the usefulness of the REDARS software tool, the results of three cases are given below:

1. Resilience of the highway system in its current state for each of the resilience definitions described above (system-wide, location-specific, and route-specific). In the results presented below, this case is the 'Baseline Scenario'.

2. Improved resilience of the highway system if the remaining number of non-seismically designed bridges, that have not yet been retrofitted, were retrofitted with steel jackets (245 bridges). In the results presented below, this case is the 'Bridge Improvement Scenario'.

3. Improved resilience of the highway system if repair times were reduced by (a) reducing the mobilization time scale factor from 1.30 to 1.15, and (b) repair times were reduced by 20% over those used in the baseline case (No. 1 above). In the results presented below, this case is the 'Repair Efficiency Scenario'.

(a) <u>Effect of Different Scenarios</u>

Comparison of the resilience curves in Figs 5 to 8 show how various resilience definitions (i.e., system-wide, location-specific, and route-specific travel time and trip demand measures) are affected by the different scenarios. These figures show the following trends:

- For all resilience definitions, the repair-efficiency and bridge-improvement scenarios improve the resilience throughout the Shelby County region for both measures of resilience: travel time and trip demand.

- The bridge-improvement scenario leads to the largest improvement in resilience. This improvement is greatest for the route-specific resilience, for which the time to reach 100% of pre-earthquake performance is less than 150 days, as compared to over 600 days for the baseline scenario.

- The bridge-improvement and repair-efficiency scenarios improve the rate of recovery for the system-wide and location-specific travel-times at virtually all post-earthquake times.

- The repair-efficiency scenario has little effect on the recovery of the I-40 route-specific travel-time until about 400 days or so after the earthquake. After this time, this scenario substantially improves the rate of recovery relative to the baseline scenario.

- For all scenarios (including the baseline scenario), the trip-demands recover much faster than the travel times. The bridge-improvement and repair-efficiency scenarios give additional improvements in these recovery rates.

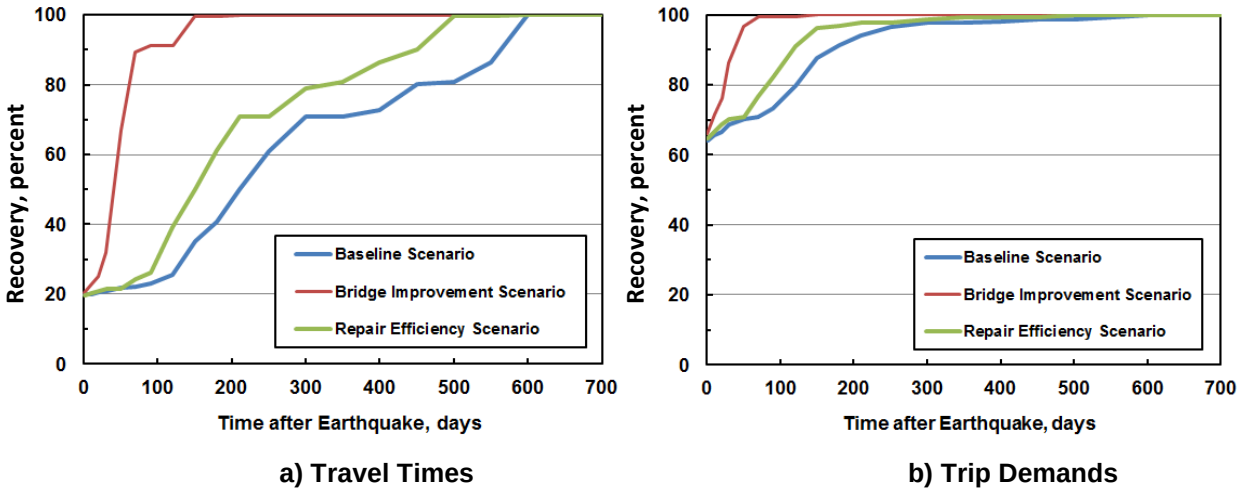

FIGURE 5. EFFECT OF VARIOUS SCENARIOS ON RESILIENCE OF SYSTEM-WIDE TRAVEL

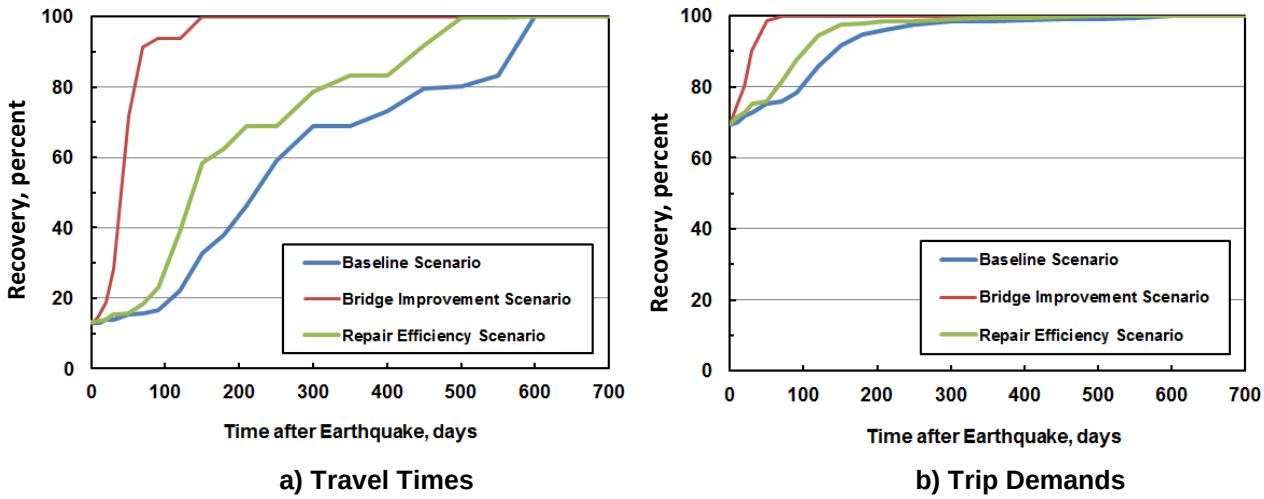

FIGURE 6. EFFECT OF VARIOUS SCENARIOS ON RESILIENCE OF LOCATION-SPECIFIC TRAVEL (TO/FROM MEDICAL CENTER)

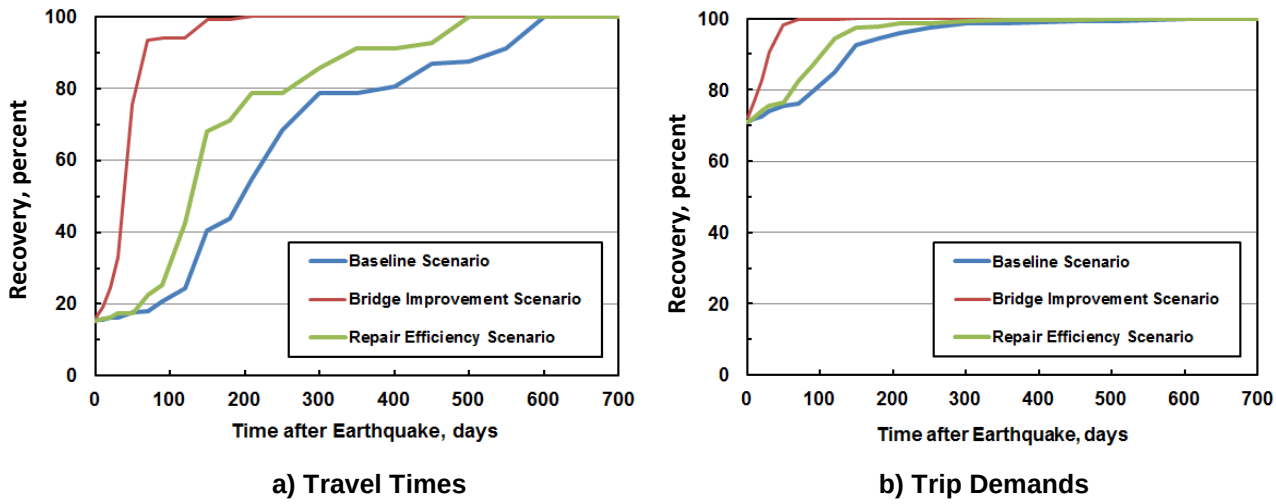

FIGURE 7. EFFECT OF VARIOUS SCENARIOS ON RESILIENCE OF LOCATION-SPECIFIC TRAVEL (TO/FROM MEMPHIS AIRPORT)

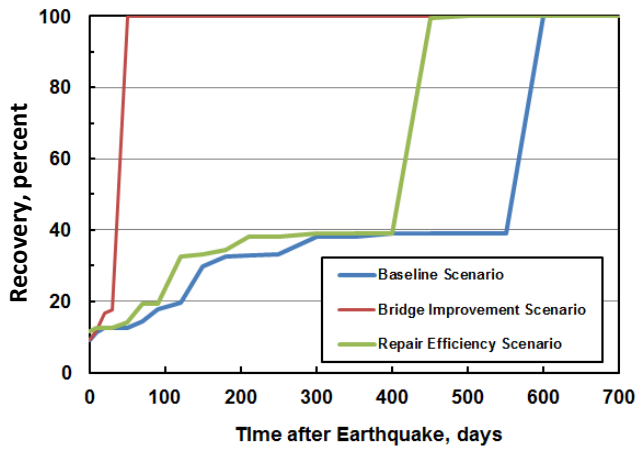

FIGURE 8. EFFECT OF VARIOUS SCENARIOS ON RESILIENCE OF ROUTE-SPECIFIC TRAVEL TIMES (I-40 SEGMENT)

(b) <u>Effect of Different Resilience Definitions</u>

Computed system-wide, location-specific, and route-specific travel-time resiliencies for each scenario are compared in Figs 9 to 11. These figures show that:

- The different resilience definitions can produce very different resilience values. These different values strongly depend on whether the baseline, location-specific, or route-specific scenarios are being applied.

- The travel times to/from the Memphis Airport are slightly more resilient than the system-wide travel times, and are also slightly more resilient than the Medical Center travel times. The recovery of the system-wide travel times and the Medical Center travel times are nearly identical.

- Comparison of route-specific and system-wide travel-time recovery times are scenario-dependent. These different rates of recovery are similar to the bridge-improvement scenario. Under the baseline and repair-efficiency scenarios, the recovery of the system-wide travel time typically exceeds that of the route-specific travel-time.

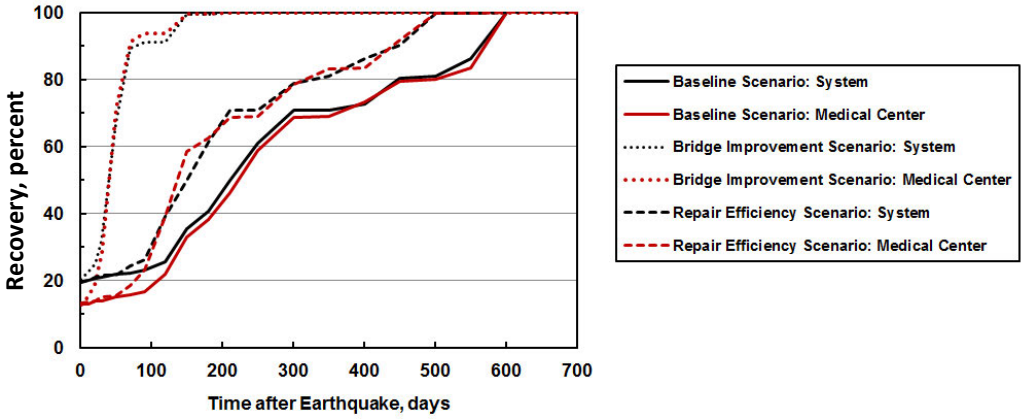

FIGURE 9. COMPARISON OF TRAVEL TIME RECOVERY: SYSTEM-WIDE AND LOCATION-SPECIFIC (MEDICAL CENTER)

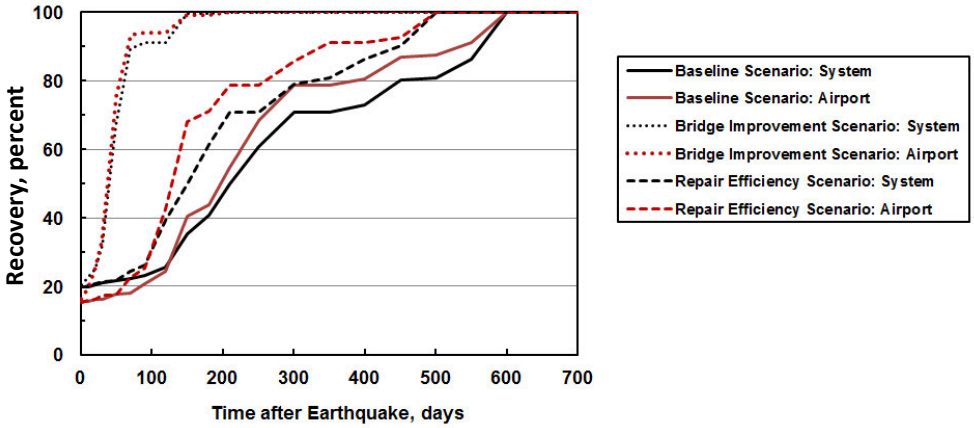

FIGURE 10. COMPARISON OF TRAVEL TIME RECOVERY: SYSTEM-WIDE AND LOCATION- SPECIFIC (MEMPHIS AIRPORT)

Figure 12 compares recovery rates based on trip-demand for the entire system and the Medical Center. The figure shows that like the recovery in travel-time, trip-demand recovery is scenario dependent. For the baseline scenario and the repair-efficiency scenario, the trip demands to/from the Medical Center are slightly more resilient than the system-wide trip demands. However, when the bridge improvement scenario is in place, the resilience of the trip demands for the Medical Center is very high. Similar results were found for the Memphis Airport location.

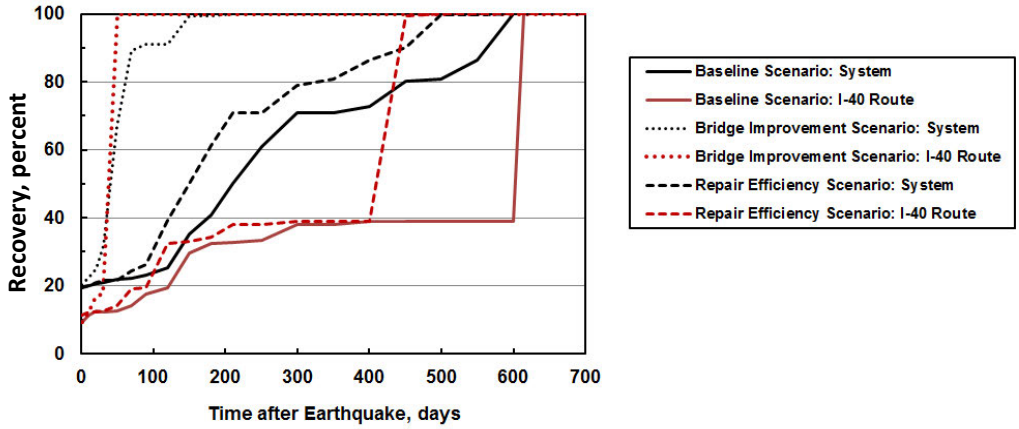

FIGURE 11. COMPARISON OF TRAVEL TIME RECOVERY: SYSTEM-WIDE VS. ROUTE SPECIFIC (I-40 ROUTE)

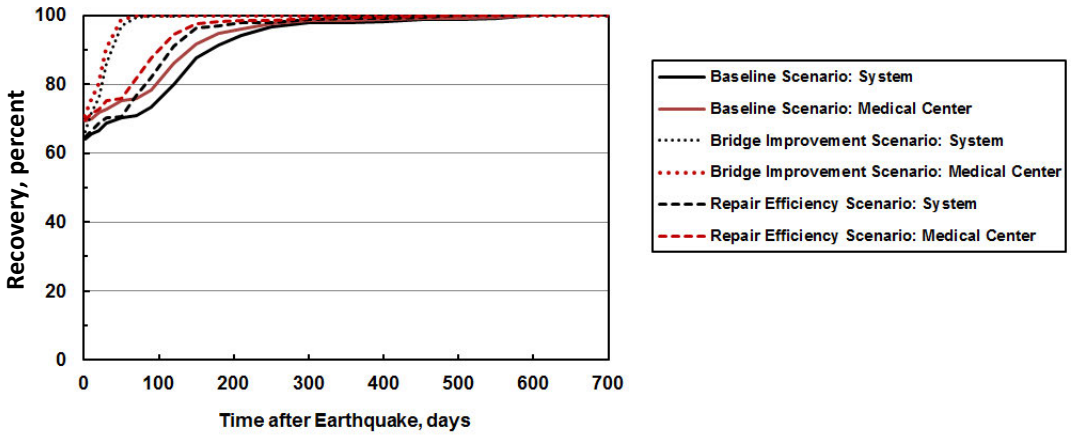

FIGURE 12. COMPARISON OF TRIP DEMAND RECOVERY: SYSTEM-WIDE VS. LOCATION-SPECIFIC (MEDICAL CENTER)

Conclusions

Today *life-safety* is no longer the sole requirement of a highway system subject to a major earthquake. *Resilience* has been added to the list of requirements to ensure rapid recovery and minimal impact on the socio-economic fabric of modern society. In qualitative terms, a resilient system recovers quickly, whereas a non-resilient system does not. It is more difficult to express resilience in quantitative terms than qualitative ones, yet it is important to try to do so. If resilience can be quantified, we can understand why some systems are more resilient than others.

It is shown that factors affecting resilience include: system and regional factors, damage and repair factors, and traffic management strategies. Furthermore it is helpful to distinguish between system-wide resilience, location-specific resilience, and route-specific resilience.

From the results of a demonstration application, it may also be concluded that REDARS, a loss-estimation methodology for highway systems, is also a useful tool for quantifying resilience. For example, it has been shown that column retrofitting and modest improvements in the mobilization rates, can improve resilience for a small-to-moderate sized city by factor of four.

Acknowledgments

The authors wish to acknowledge ZhengHui Hu and Charles Hyuck of ImageCat, Long Beach, CA, for their assistance programming REDARS 3 and running the analyses reported in this paper. This research was performed as part of an ongoing project at the University of Nevada Reno related to 'Improving the Seismic Resilience of Highway Systems,' funded by the Federal Highway Administration under Contract DTFH61-07-C-00031. Expert guidance was provided by the COTR, Wen-huei (Phillip) Yen, Principal Engineer, FHWA Office of Bridge Technology, Washington DC.

References

Bruneau, M., Chang, S. E., Eguchi, R. T., Lee, G. C., O'Rourke, T. D., Reinhorn, A. M., Shinozuka, M., Tierney, K., Wallace, W.A., and von Winterfeldt, D.A., 2003. *A framework to quantitatively assess and enhance the seismic resilience of communities*, 19 (4) Spectra, Jl. Earthquake Engineering Research Institute, Oakland, CA, pp 734-752.

Bruneau, M., and Reinhorn, A., 2004. *Seismic resilience of communities-conceptualization and operationalization*, Proc. International Workshop Performance-Based Seismic Design, Bled.

Buckle, I.G., and Lee, G.C., 2006. *Improving the resilience of highway systems to major earthquakes*, Proc. 100th Anniversary 1906 San Francisco Earthquake Conference, Earthquake Engineering Research Institute, Oakland CA.

Wald, D.J., Worden, B.C., Quitoriano, V., and Pankow, K.L., 2006. *ShakeMap Manual: Technical Manual, Users Guide, and Software Group, Version 1.0*, Website http://earthquake.usge.gov/shakemap, United States Geological Survey, Menlo Park CA, June 19.

Werner, S.D., Taylor, C.E., Moore, J.E., Walton, J.S., and Cho, S., 2000. *A risk-based methodology for assessing the seismic performance of highway systems*, Technical Report MCEER-00-0014, Multidisciplinary Center Earthquake Engineering Research, Buffalo, NY 265pp.

Werner, S.D., Hu, Z-H., Huyck, C., 2013. *Research to develop highway system resilience analysis procedure and new bridge model, and to program REDARS 3 and REDARS LITE Software*, Technical Report submitted to UNR Center for Civil Engineering Earthquake Research, Seismic Systems & Engineering and ImageCat Inc.

Seismic requirements for laminated elastomeric bearings and test protocol for verification

Masatsugu Shinohara[1], Junichi Sakai[2] and Jun-ichi Hoshikuma[3]

Abstract

Laminated elastomeric rubber bearings have been widely used after 1995 Kobe, Japan, earthquake, and no severe damage had been observed before the 2011 earthquake. However, some of laminated elastomeric rubber bearings, including those designed according to the post-1995 design specifications, suffered severe damage such as rupture or deep crack into rubber by the 2011 earthquake. Considering the significance of the damage of laminated elastomeric rubber bearings during the 2011 Great East Japan earthquake, the seismic design specifications for highway bridges, which were revised in spring, 2012, included requirements for seismic structural members including bearings. This paper introduces the requirements for seismic structural members and the test protocols, which were recently proposed by the authors, for laminated elastomeric rubber bearings in order to verify the requirements.

Introduction

The 2011 Great East Japan earthquake caused the catastrophic damage by the huge tsunami and the strong ground shaking in the Tohoku and Kanto regions. Although many road bridges were washed away in the coastal areas by the tsunami, structural damage caused by the strong ground shaking was relatively less. This is because the seismic retrofit projects have been performed to highway bridges and the retrofitted bridges performed well under the strong ground excitation. Relatively old but unretrofitted bridges suffered relatively larger damage.

In terms of damage of bearings caused by the 2011 earthquake, steel bearings of bridges that were designed according to pre-1980 design specifications but had not been retrofitted suffered severe damage. Failure of side stopper of fixed bearings, failure of side blocks, fracture of set bolts were observed after the event as shown in Photo 1. On the other hand, minor damage, which did not have significant effect on its structural function, was observed in steel bearings designed according to post-1995 design specifications.

Laminated elastomeric rubber bearings have been widely used after 1995 Kobe, Japan, earthquake, and no severe damage had been observed before the 2011

[1] Senior Researcher, Center for Advanced Engineering Structural Assessment and Research, PWRI
[2] Senior Researcher, Center for Advanced Engineering Structural Assessment and Research, PWRI
[3] Chief Researcher, Center for Advanced Engineering Structural Assessment and Research, PWRI

earthquake. However, some of laminated elastomeric rubber bearings, including those designed according to the post-1995 design specifications, suffered severe damage such as rupture or deep crack into rubber by the 2011 earthquake as shown in Photo 2. Although neither deck unseating nor collapse of bridges occurred due to this damage, this had a significant impact on the reliability of the rubber bearings.

(a) Movable bearing (b) Fixed bearing

Photo.1 Damage of steel bearings designed according to pre-1980 design specifications

(a) Rupture of rubber bearing (b) Crack of rubber bearing

Photo.2 Damage of laminated elastomeric rubber bearings designed according to post-1995 design specifications

Although the causes of this damage have still been under investigation, one of the causes could be the insufficient original capacity of the rubber bearing. In fact, not only the seismic performance of design level excitation but also the behavior up to failure had not been verified through a series of experiments considering seismic loading before the 2011 earthquake.

Considering the significance of the damage of laminated elastomeric rubber bearings during the 2011 Great East Japan earthquake, the seismic design specifications for highway bridges, which were revised in spring, 2012, included requirements for seismic structural members including bearings. In particular, seismic isolation bearings in seismic isolation bridges (Menshin bridges) have fundamental functions to ensure the seismic performance of the bridges, and thus, the isolation bearings are one of the most important members in Menshin bridges.

This paper introduces the requirements for seismic structural members and the test protocols, which were recently proposed by the authors, for laminated elastomeric rubber bearings in order to verify the requirements.

Requirements for seismic structural members

The 2012 seismic design specifications for highway bridges require experimental verification for members which are significantly affected by the seismic effect as followings:

1) Failure mode shall be clear, and sufficient safety margin for the failure should be ensured,

2) Stable behavior under cyclic loading for the design level ground motion shall be ensured, and

3) An analytical modeling of mechanical properties such as nonlinear force versus displacement relation shall be clarified.

The conditions for application, such as range of temperature, axial force, structural details, etc., shall also be determined based on the conditions of the corresponding experiment. These requirements are intended to be used to verify newly developed material, structural design, structural members, devices, etc. in order to encourage the introduction of these new technologies in the performance-based design concept.

For bearings, the following is also required in addition to the above listed requirements.

4) Bearings shall be simple in mechanism to ensure its full function under seismic excitation.

This is because manufactured bearings consist of various parts for various functions such as transmitting loads to substructure, flexibility for displacement of superstructure, resisting uplift force, etc., and thus, complicated mechanism might be likely developed.

Experimental protocol for verification of mechanical properties of laminated elastomeric rubber bearings

The experimental verification is employed not only for verification of the requirements but also for determination of the design limit values. For such purpose, it is necessary to determine an experimental protocol and verification methods for the requirements described in previous chapter. Quasi-static cyclic loading tests are selected as a standard experimental method in this purpose because they are suitable to examine the damage progress due to increment of deformation, dynamic strength, ductility and energy dissipation capacity, and the effects of number of cycles on cyclic behavior.

For laminated elastomeric rubber bearings, the design limit strain shall be determined based on experiments verifying the requirements of items 1) and 2) listed in previous chapter, which verifies the ultimate failure mode and stable behavior under seismic excitation.

To verify the ultimate failure mode, a cyclic loading of 2 cycles with amplitude

of the ultimate limit displacement (as plotted A in Figure 1) is required, and a safety factor of 1.2 shall be considered to determine the design limit strain from the displacement at Point A. After this loading, a monotonic loading is performed up to the deformation in which the bearing loses its function due to rupture or buckling of the bearing.

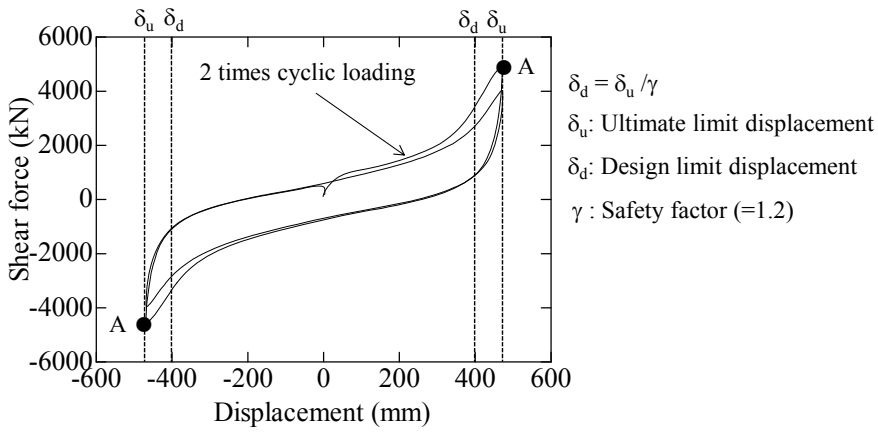

Fig.1 Hysteretic loop at the ultimate limit displacement

To verify the stable behavior under seismic excitation, a cyclic loading of at least 5 cycles with amplitude of the design limit displacement is required as shown in Figure 2. The degradation of equivalent stiffness and energy dissipation capacity is evaluated through the cyclic loading test.

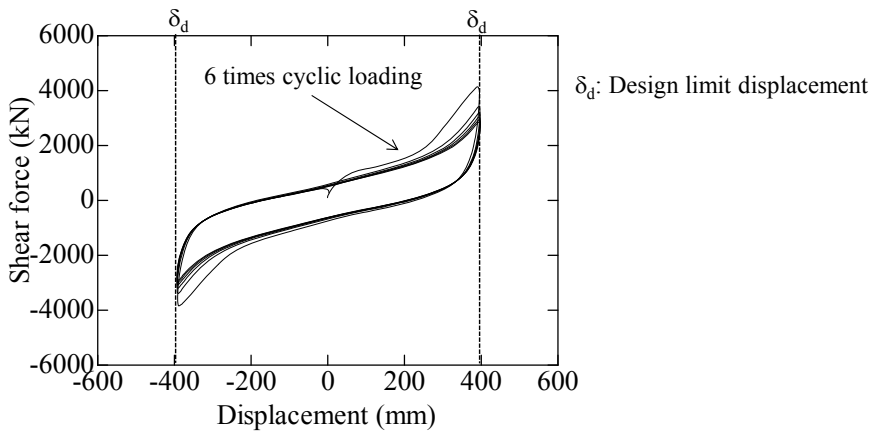

Fig.2 Hysteretic loop at the design limit displacement

The number of cycles in the loading test employed for verifying the stable behavior of the bearing was determined based on the analytical seismic response of bridges with isolation bearings or elastomeric bearing under design ground motions. A series of nonlinear dynamic response analyses was conducted with input ground motions for both the interplate earthquake and the near-fault earthquake. Figure 3 shows the number of times exceeding 90% of the maximum response displacement.

For both the bridges with isolation bearings and those with elastomeric bearings, the maximum number of times exceeding 90% of the maximum response displacement is 4, and thus, by considering 5 as the number of cyclic loading in the experimental verification, the stable behavior of the bearings can be ensured during seismic response of the bridge under a strong excitation.

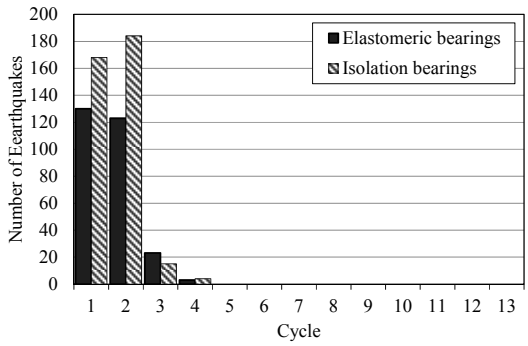

Fig.3 The number of times exceeding 90% of the maximum response displacement

Figure 4 shows an example of lateral force versus displacement relation and plots of the degradation of equivalent stiffness and energy dissipation capacity. As cyclic loading is applied with the same displacement, equivalent stiffness and energy dissipation capacity decrease, but the degree of decrement at each cycle decrease, which means behavior of bearing becomes more stable under cyclic loading. Table 1 summarizes the requirements for verifying the stable behavior under cyclic loading. The virgin loading can be ignored in this evaluation because the hysteresis of virgin loading excursion shows apparently different behavior from the hysteresis of the 2nd and the following cycle.

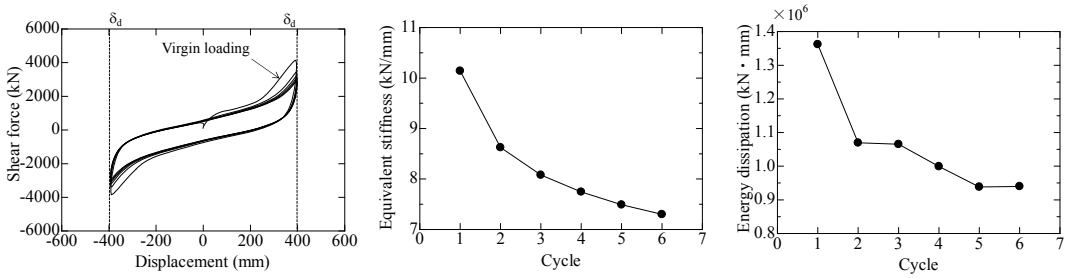

(a) Hysteretic loop at the design allowable displacement

(b) Equivalent stiffness at each cycle

(c) Energy dissipation at each cycle

Fig.4 Example of lateral force versus displacement relation and plots of the degradation of equivalent stiffness and energy dissipation capacity

Table 1 Requirements for the stable behavior of laminated elastomeric rubber bearing under cyclic loading

Items	Engineering indexes for evaluation	Criteria
1	Degradation ratio of equivalent stiffness at the 6th cycle loading to the 2nd cycle loading	Less than 30%
2	Degradation ratio of energy dissipation capacity at the 6th cycle loading to the 2nd cycle loading	Less than 30%
3	Degradation ratio of equivalent stiffness in each loading cycle (2nd to 6th cycle loadings)	Less than 10%
4	Degradation ratio of energy dissipation in each loading cycle (2nd to 6th cycle loadings)	Less than 15%

Modeling method of mechanical properties of laminated elastomeric rubber bearings

It is essential to model mechanical properties such as nonlinear force versus displacement relation appropriately because the accuracy of seismic response evaluated by not only nonlinear dynamic analyses but also nonlinear static analyses highly depends on the reliability of the idealization of mechanical properties. In particular, since seismic isolation bearings in Menshin bridges have fundamental functions to ensure the seismic performance of the bridges as described above, the accurate idealization of mechanical properties of isolation bearings is needed.

The design specifications recommend employing an appropriate analytical model of lateral force versus lateral displacement relation based on a series of cyclic loading tests. As shown in Figure 5, lateral force at the maximum displacement decreases as cyclic loading is repeated with the same displacement, which suggests that the analytical model shall be set to represent the behavior of the 5th cycle loading at the design limit displacement as shown in Figure 5. This is because the model developed based on this concept results in conservative estimation of the seismic energy dissipation and the seismic response of bridge.

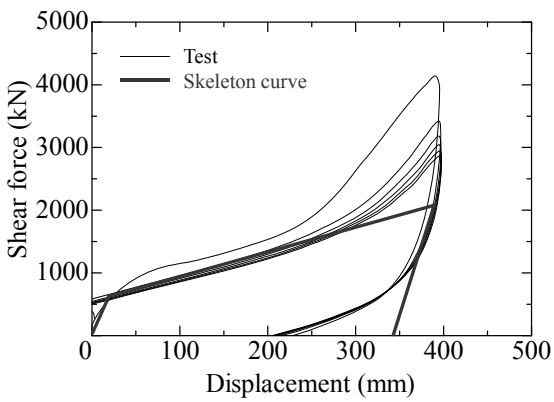

Fig.5 Hysteretic loop and skeleton curve at the design limit displacement

The hysteresis of 1st cycle of laminated elastomeric rubber bearings shows quite different from those after 2nd cycle as shown in Figure 5. Lateral force of 1st cycle at the maximum displacement is 21% larger than that of 2nd cycle. This large lateral force could cause damage at its attachment of bearings. Therefore, this large lateral force shall be considered into the design of the attachment and the member attached with bearing.

Example of experimental verification for laminated elastomeric rubber bearings

This chapter exemplifies results of the lateral loading test of lead rubber bearing conducted for verification of the seismic requirements. Table 2 shows dimensions and properties of the test specimen. The dimension of the rubber is 1020 mm, the layer thickness of rubber is 39mm, the shear stiffness is 1.2N/mm^2, the primary shape factor is 5.99, and the secondary shape factor is 6.41. The bearing contains 4 circular lead plugs with diameter of 144mm.

The lateral loading test was conducted with vertical pressure of 6N/mm^2. The test specimen was loaded at laboratory temperature with the loading rate of 15mm/sec.

Table 2 Dimensions and properties of test specimen

Specimens dimension	Longitudinal		A	mm	1020
	Lateral		B	mm	1020
	Total rubber height		T	mm	314
Design dimension	Plane Dimension	Longitudinal	a	mm	1000
		Lateral	b	mm	1000
	Laminated-rubber	Layer thickness	t_e	mm	39
		Number of Rubber layers	n	—	4
		Total layer thickness	Σte	mm	156
	Lead shape	Lead diameter	DP	mm	144
		Number of lead plug	NP	—	4
Properteies	Primary shape factor		S1	—	5.99
	Secondary shape factor		S2	—	6.41
	Rubber Shear Modulus		G	N/mm^2	1.2
	Vertical stiffness		E	N/mm^2	324

Table 3 lists a series of loading sequence of the experimental verification. Step 1 is the test conducted for quality control. 11 times cyclic loading at effective design displacement, which corresponds to 0.7 times design limit displacement, was applied to the specimen in Step 1. In this test, the effective design displacement was determined to be 280mm.

Table 3 Series of loading sequence of the experimental verification

STEP	Displacement	Number of times to repeat	Purpose
1	Effective design displacement（0.7×δa）	11	Quality control
2	Design limited displacement（δa）	6	Verification of stable behavior
3	Ultimate limited displacement（1.2×δa）	2	Verification of behavior at the ultimate limit state
4	Rupture displacement	Monotonic loading	Verification of safety margin for failure

Step 2 is the test for verification of stable behavior at the design limit displacement. 6 times cyclic loading was applied to the specimen in Step 2. The amplitude of this loading is 400 mm. Step 3 is the test for verification of behavior at the ultimate limit state. 2 times cyclic loadings at the ultimate limit displacement (480 mm), which corresponds to 1.2 times design limit displacement, was applied to the specimen in Step 3. And then, monotonic loading was applied up to the deformation in which the bearing loses its function due to rupture or buckling in Step 4.

Table 4 shows shear force versus displacement relation at each step and photos at maximum shear deformation. Figure 6 shows change of equivalent shear stiffness and energy dissipation capacity, respectively.

Table 4 Shear force versus displacement relation at each displacement

Step and Conditions	Shear force versus displacement relation	Photo at maximum deformation
Step1: Effective design displacement Shear strain: 175% Cyclic times: 11times	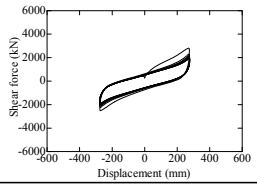	
Step2: Design limit displacement Shear strain: 250% Cyclic times: 6times	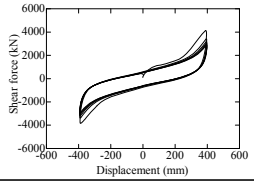	
Step3: Ultimate limit displacement Shear strain: 300% Cyclic times: 2times	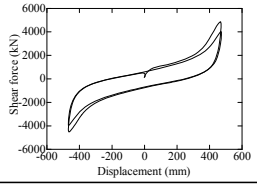	
Step4: Up to rupture Shear strain: 370% Monotonic loading	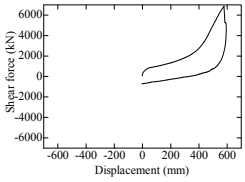	

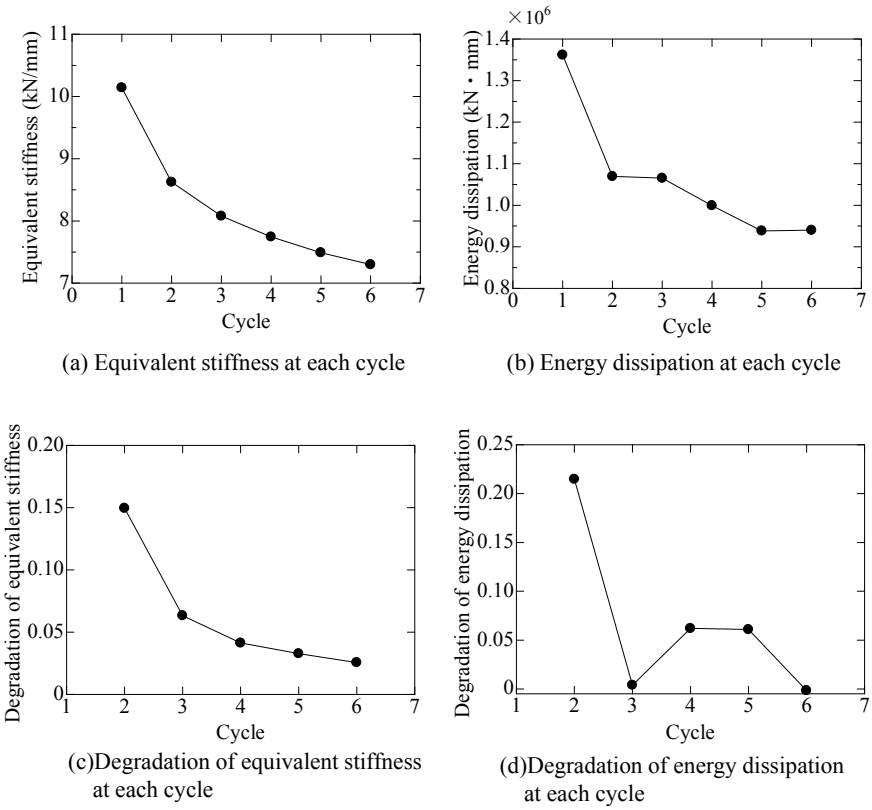

Fig. 6 Change of equivalent shear stiffness and energy dissipation capacity

Although the lateral force at the 1st cycle is significantly large, stable behavior after the 2nd cycle can be observed during cyclic loading at the design limit displacement. In the cycles at the ultimate limit displacement, stable behavior can be still observed although noticeable hardening behavior can also be observed. After loading at Step 3, lateral displacement was applied monotonically and the force increased up to 6852kN, which corresponds to 1.7 times larger than the lateral force at the design limit displacement, and finally ruptured.

Concluding remarks

This paper summarized the seismic requirements for bearings of bridge and test protocols for verification for the limit state and stable behavior under cyclic loading were proposed, so that mechanical properties such as the nonlinear relation between force and displacement were appropriately modeled in the seismic analysis of bridge.

It has been over 15 years since laminated elastomeric bearings widely used. Stock of old laminated elastomeric bearings will increase in the near future. On the other hand, though only 15 years passed, damage of laminated elastomeric rubber bearings are observed due to seismic force or deterioration due to environmental effects. Therefore, PWRI has just kicked off a collaborative research project with highway companies on investigation of change of mechanical and material properties of not only laminated elastomeric bearing but also steel bearings in order to evaluate

mechanical properties, residual capacity and diagnostic technic of existing bearings in bridges.

References

National Institute for Land and Infrastructure Management (NILM), Public Works Research Institute (PWRI): Quick Report on Damage to Infrastructures by the 2011 off the Pacific coast of Tohoku Earthquake, Technical Note of National Institute for Land and Infrastructure Management, No.646, Technical Note of Public Works Research Institute, No.4202, 2011.

HOSHIKUMA, J.: DAMAGE OF HIGHWY BRIDGES DUE TO THE GREAT EAST JAPAN EARTHQUAKE, Proc. 27th US-Japan Bridge Engineering Workshop, 2011.

SAKAI, J., HOSHIKUMA, J., and KATAOKA, S.: Revisions of Japanese Seismic Design Specifications for Highway Bridges Based on Knowledge Derived from Recent Earthquakes and Research Accomplishments, Seventh National Seismic Conference on Bridges & Highways, Oakland, California | May 20-22, 2013.

Earthquake Engineering Research Team, Earthquake Disaster Prevention Research Group, Public Works Research Institute: Draft Guidelines for Experimental Verification of Seismic Performance of Bridges (Quasi-Static Cyclic Loading Tests and Shake Table Tests for Bridge Columns), Technical Note of Public Works Research Institute, No.4023, August 2006.

CYCLIC LOADING PROTOCOL FOR BRIDGE COLUMNS SUBJECTED TO SUBDUCTION MEGA EARTHQUAKES

Ramiro Bazaez[1] and Peter Dusicka[2]

Abstract

Current structural design philosophies rely on the inelastic capacity of structures for resisting seismic excitations. In order to assess such capacity, cyclic loading protocols have been used as a common practice. However, analytical and experimental results have shown that the rotation capacity of columns is highly influenced by the loading. For that reason, quasi-static loading protocols that reflect the increase in inelastic demands on reinforced concrete bridge columns subjected to subduction mega earthquakes are developed and their influence on bridge columns is examined.

Introduction

All structural components have limited capacity. For that reason, understanding their behavior under strong ground motion excitations has always been a major objective of earthquake engineering. One method to assess the performance of structural components is via experimental evaluations utilizing quasi-static cyclic loading. The relatively slow application of the load in quasi-static tests allows experimentalists to relate structural metrics such as top displacement, chord rotation, drift, strains, etc. to visual damage of specimens (e.g. first cracking, spalling of the concrete, buckling of longitudinal reinforcement). Current earthquake design procedures for structural components have been established based on experimental results utilizing quasi-static cyclic tests. Moreover, design codes are trending to a relatively new design methodology called "Performance-based seismic design" (PBSD). In this methodology, a number of performance levels, which are frequently defined in terms of acceptable levels of damage, need to be satisfied under different levels of seismic hazards.

Under this design methodology the assessment of different structural components plays a fundamental role. Numerous experimental and analytical studies have been conducted in order to assess structural components, define limit states and acceptance criteria to be used in performance-based seismic design (Hose & Seible, 1999) (FEMA 356, 2000) (ASCE/SEI 41-06, 2007). However, recent occurrence of highly devastating subduction mega earthquakes of long duration (2010, Chile and 2011, Japan) have increased researchers' interest in how earthquake duration and number of cycles affect structural response and collapse assessment. Studies have

[1] Graduate Student Researcher, Department of Civil & Environmental Engineering, Portland State University, USA, rbazaez@pdx.edu.
[2] Associate Professor, Department of Civil & Environmental Engineering, Portland State University, USA, dusicka@pdx.edu.

indicated that ground motion duration and number of cycles have a major role on ductility demands and structural collapse when compared to ground motions of similar peak ground acceleration but less duration, e.g. Dusicka & Knoles (2012), Raghunandan & Liel (2013), Chandramohan et al. (2013). This effect is mostly attributed to the rate of structural strength and stiffness deterioration due to an increase in load reversals imposed for large magnitude and long duration ground motions. Others have revealed that the response of a structure depends significantly not only on the amplitude of the ground motion, but also on its duration (van de Lindt & Goh, 2004) (Chandramohan, et al., 2013). Earthquake ground motion duration has shown to have significant effects on the level of damage sustained by structures during strong earthquakes. This aspect is particularly relevant in subduction zones due to the fact that larger magnitude earthquakes are associated with strong motions of long duration. The main objective of the research summarized in this paper was to develop appropriate loading protocols in order to assess the capacity of reinforced concrete bridge columns subjected to subduction zone earthquakes. Furthermore, the influence of the proposed protocol on a bridge column capacity is briefly examined.

Limited experimental data can be found on columns subjected to long duration protocols that try to simulate subduction zone earthquakes since most of the seismic assessment of bridge columns have been carried out using a standard cyclic loading protocol, as that shown in Figure 1 (Cheung, et al., 1991), (Priestley, et al., 2002), which does not necessarily represent the demands imposed by subduction zone mega earthquakes. Experimental studies have shown that the displacement capacity of structural components is influenced by the loading history applied. A relevant research was carried out by Takemura and Kawashima (1997) to study the influence that different loading histories have on the ductility capacity of reinforced concrete bridge piers. In Takemura's research six nominally identical specimens were tested under different loading protocols resulting in six different responses. Another relevant research was carried out by Kunnath, et al. (1997) to investigate the cumulative seismic damage on circular reinforced concrete bridge columns, which were mostly controlled by flexural behavior. Using the concept of low-cycle fatigue and the cumulative damage model employed in the research carried out by Kunnath, experimental tests were performed at the Washington State University in order to investigate the performance of pre-1975 concrete bridges subjected to subduction earthquakes (McDaniel, et al., 2006). In this research, eight circular lightly confined reinforced concrete columns were tested using different displacement history. The results, as well as those obtained by Kunnath (1997), showed that the failure mode of the columns depends on the displacement history applied to them. A similar study was recently performed at MCEER, University at Buffalo in conjunction with the National Taiwan University of Science and Technology (Ou, et al., 2013). In this case, reinforced concrete bridge columns were tested applying two different loading protocols to investigate the influence of the number of cycles on bridge columns. Test results showed that columns under a long duration protocol behave significantly different in terms of strength and stiffness degradation than those columns under conventional (standard) protocols, showing that in high levels of damage the strength and stiffness degradation of the specimen subjected to long duration earthquakes would increase markedly.

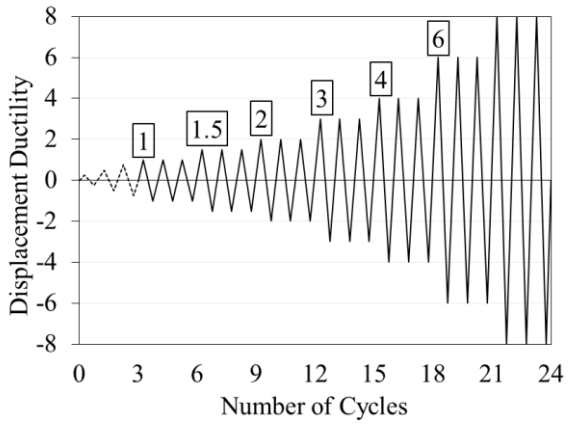

FIGURE 1 STANDARD PROTOCOL.

Cyclic Protocol Development

With the aim of developing representative loading protocols for components of the lateral resisting system of bridges under subduction zone earthquakes, a selection of earthquakes has to be done in order to determine the inelastic demands imposed by subduction earthquakes. The subduction zone earthquake sets used in this study were chosen from the 1985 Valparaiso (COSMOS), 2007 Sumatra (COSMOS), 2010 Maule (U. Chile), and 2011 Tohoku (K-Net) earthquakes with distances to the epicenter greater than 100 km to avoid near-fault pulse characteristics. It can be observed (Table 1) the vast amount of subduction ground motions used in the study, which pretends increase the applicability of the results. Vertical components were not considered due to the complexity to implement this variable in actual tests. A set of crustal earthquakes, on the other hand, was employed to allow demand comparisons. Crustal earthquakes, referred to herein as "Crustal" set, were chosen from the FEMA P695 far-field record (FEMA P695, 2009).

TABLE 1 GROUND MOTION SETS.

Set	M_w[3]	Site Class	PGA Range (g)	Number of Records	Average Bracketed Duration (sec)
Crustal	6.5-7.6	C/D	0.15-0.56	37	15
Valparaiso	7.8[4]	B/D	0.11-0.71	36	39
Sumatra	7.9	-	0.13	2	48
Maule	8.8	B/D	0.09-0.69	31	53
Tohoku1	9.0	B/C/D	0.50-2.01	27	153
Tohoku2	9.0	D/E	0.16-0.81	166	110

In order to predict the damage that a structure undergoes during severe earthquakes, it is important to represent in a realistic way the behavior of structural components during loading reversals. The peak oriented Ibarra-Krawinkler hysteretic model (Ibarra, et al., 2005) as is illustrated in Figure 2, which includes strength

[3] M_w: Moment magnitude
[4] M_s: Surface wave magnitude

capping, residual strength, and strength and stiffness deterioration due to load reversals, was employed. This model was calibrated using test results of bridge columns dominated by flexural behavior (PEER, 2003). This process allowed finding appropriate parameters to closely simulate load-deformation behavior of the components in study. Numerous nonlinear time-history analyses of single degree of freedom systems (SDOF), which were performed in a previous study (Dusicka & Knoles, 2012), were utilized to obtain bridge columns response under the selected subduction zone earthquakes. In that study, the constant ductility inelastic response approach (Ridell & Newmark, 1979) was utilized. Nonlinear analyses were performed to reach determined ductility ratios of 2, 4 and 8 with the aim of being representative of a wide range of structural ductilities in period ranges from 0.2 to 4.0 seconds.

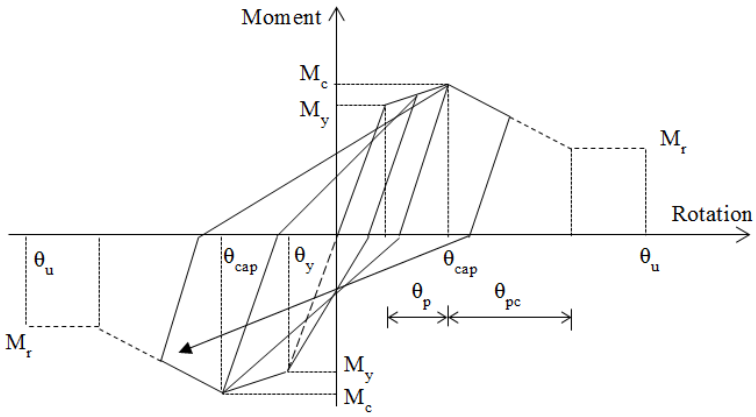

FIGURE 2 STRENGTH AND STIFFNESS DETERIORATION MODEL (OPENSEES, 2011)

Current testing protocol developments and experimental works have been done based on a general cumulative damage concept using the Coffin-Mason model and the Miner's rule of linear damage accumulation as a baseline (Krawinkler, et al., 1983). Another extensively damage index used in reinforced concrete structures it is that formulated by Park and Ang (1985). This damage index considers that damage is caused by structure's maximum deformation and cumulative dissipated energy. However, in order to calculate the damage indices, in a meaningful way, some parameters have to be experimentally obtained and validated, which can lead to undesirable uncertainties and arbitrariness. For that reason, in this study another damage index was employed based on cumulative damage called "Normalized Cumulative Plastic Displacement", which is a metric of structural plastic demand. This index is calculated by adding the ratio of plastic displacement range under an excursion ($\Delta\delta_{pi}$) to the yield displacement (δ_y) as is shown in Eq 1. In this damage index, the number of damaging cycles (N) and the sum of damaging cycle ranges ($\Sigma\Delta\delta_{pi}$) are important parameters in the development of testing protocols. A cycle is considered damaging when its amplitude is greater than the yield displacement.

$$\mathrm{NCPD} = \sum_{i=1}^{N} \frac{\Delta\delta_{pi}}{\delta_y} = \sum_{i=1}^{N} \frac{\delta_i - \delta_y}{\delta_y} \qquad (1)$$

The response shown by a structural component contains excursions that are not symmetric and do not follow a consistent pattern under different ground motions. To rationalize the development of the testing protocol and compare the demands imposed by different sets of ground motion, the time history responses were converted into a series of cycles using the simplified rainflow counting (ASTM E1049-85, 2005). This procedure allows obtaining symmetrical cycles ordered in either decreasing or increasing amplitudes. The rainflow counting procedure was applied to non-linear time history response of structures with periods of 0.2 through 4.0 seconds in order to count the effective number of cycles and their amplitude. Statistical measures become necessary in order to achieve data reduction in a rational way. For that reason, the number of inelastic cycles and NCPD were represented employing the 84th percentile as target value. Statistical analyses of the rainflow counting results show a high dependence of the parameters in the type of earthquake and fundamental period of the bridge, as is illustrated in Figure 3. For that reason, 0.5, 1.0 and 2.0 seconds were selected as a benchmark to be representative of expected bridge fundamental periods. The argument to select different periods is that the use of only one period as a benchmark may lead to overestimate of the amount of inelastic cycles that the structure undergoes and distort the assessment of the behavior through physical testing.

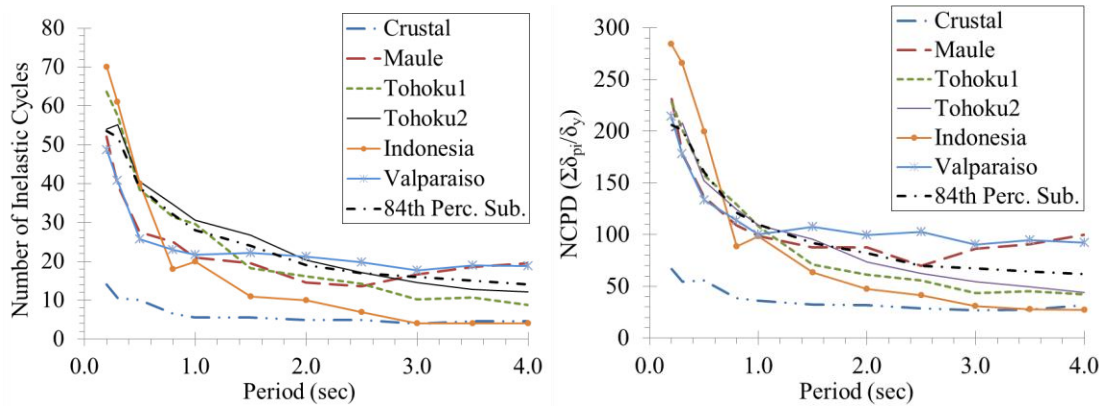

FIGURE 3 INFLUENCE OF PERIOD ON NUMBER OF INELASTIC CYCLES AND NCPD FOR STRUCTURES OF DUCTILITY 8.

For the benchmark periods, results have shown a nearly linear relation in the NCPD for different ductilities as is illustrated in Figure 4. This implies that for structures with other ductilities, the cumulative ductility may be found by linear interpolation of the values presented in Table 2. On the other hand, the number of inelastic cycles does not show a linear relation (Figure 4). Therefore, analyses with other ductilities are necessitated in order to determine a more accurate relationship. Thus, results led to differentiating the testing protocol in terms of ductility and period of the structure. For that reason, in order to closely reflect the subduction zone demands the loading protocols were developed using the target values of the parameters shown in Figure 4 and summarized in Table 2.

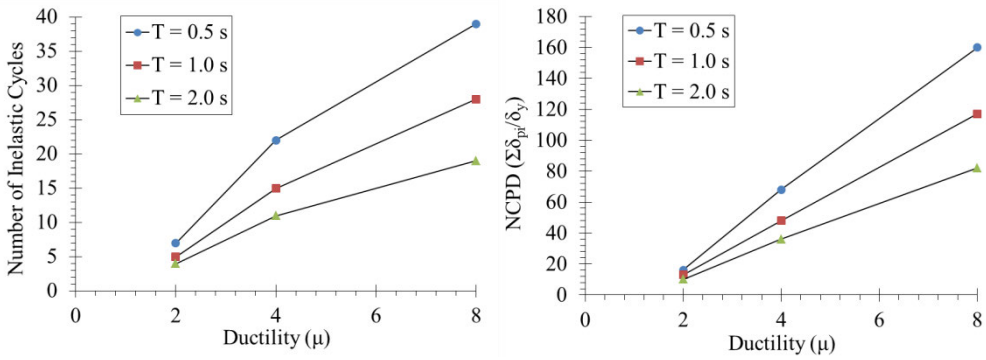

FIGURE 4 NUMBER OF INELASTIC CYCLES AND NCPD FOR DIFFERENT DUCTILITIES.

TABLE 2 TARGET VALUES AND PROPOSED PARAMETERS.

Period T	Max μ	$N_{cycle} > \delta_y$		$\Sigma\Delta\delta_{pi} / \delta_y$	
		Target Value	Proposed	Target Value	Proposed
0.5	2	7	7	16	18
	4	22	22	68	71
	8	39	40	160	177
1.0	2	5	7	13	18
	4	15	15	48	51
	8	28	28	117	119
2.0	2	4	5	10	14
	4	11	11	36	38
	8	19	19	82	88

Proposed Protocols

The proposed loading protocols consider two stages. The first stage consists of three cycles, in each of the following displacements (or loads), $0.25\delta_i$ (V_i), $0.5\delta_i$ (V_i), $0.75\delta_i$ (V_i) and one cycle at $1.0\delta_i$ (V_i) in order to visualize low damage states (e.g. first cracking). Where, δ_i is the theoretical yield displacement and V_i is the theoretical strength at first yield. The second stage of inelastic cycles aims to replicate the demands imposed on concrete bridge columns by subduction zone earthquakes of long duration. The loading histories are illustrated in Figure 5, in which the dotted lines represent the first stage and the solid lines the second stage. It is worth mentioning that the proposed protocols for structures of ductility two ($\mu = 2$) are not presented since they are unlikely to be applicable to typical bridge columns failing in flexure.

Since the proposed protocols are based on increments of ductility it is essential to determine the yield displacement of the specimen. A first estimate of the yield displacement can be found by performing a moment-curvature analysis of the bridge column section based on measured material properties. The moment-curvature analysis also allows the experimentalist to determine the target ductility of the specimen, although it is known that the specimen ductility might decrease during cyclic tests due to the stiffness and strength degradation that the component undergoes under load reversals. In order to determine the ideal yield displacement (δ_y) researchers have employed two approaches. The first approach consists of performing

a monotonic test before cyclic loading tests. The second approach consists of a first stage based on load control. The load control is based on percentages of the theoretical component strength (V_i), usually $0.25V_i$, $0.5V_i$, $0.75V_i$, and V_i. The theoretical strength is determined dividing the first yield moment, which is obtained from a moment-curvature analysis following conventional flexural theory, by the column cantilever length. Then the experimental yield displacement (δ_y) is established by using the ratio of the theoretical force at which the concrete cover reaches a strain of 0.004 to the experimental elastic stiffness (K_e) which is calculated as the ratio of the theoretical first yield force (V_i) to the displacement measured experimentally (δ_y').

Sequence effects have not been fully established in the development of testing protocols (FEMA 356, 2000). In Figure 5 is shown the proposed protocols using the concept of pre-peak excursions cycles. This approach was used since cycles that occur after the maximum displacement will cause less cumulative damage and should be considered separately from pre-peak excursions (Krawinkler, et al., 2000). For that reason, in cases when the specimen does not reach the failure under the applied stepwise loading protocol, the test may continue under lower amplitude cycles (trailing cycles) instead of displacement ductility increments.

Illustrative Numerical Case Study

This study is part of a project which goal is to assess the behavior of pre-1970 bridge columns located in Oregon, USA. The State of Oregon lies near the Cascadia subduction zone, where a mega thrust earthquake of long duration forms a major component of the seismic risk. The case study contemplates the numerical study of a representative pre-1970 bridge column subjected to the standard protocol and the proposed subduction protocol. These columns usually are lightly reinforced and lap-spliced in places where plastic hinge formation is expected. Typical column properties and dimensions are summarized in Table 3 and the cross section is illustrated in Figure 6.

In order to model the inelastic behavior of the column the concentrated plasticity approach was utilized. The plastic hinge was modeled using the hysteretic model developed by Ibarra et al. (2005), as was illustrated in Figure 2, and implemented in the software OpenSees (2011). Model parameters for column hinges, such as moment capacity and rotation capacity, have been obtained from empirical equations based on a vast amount of column tests (Haselton, et al., 2008) (Biskinis & Fardis, 2009).

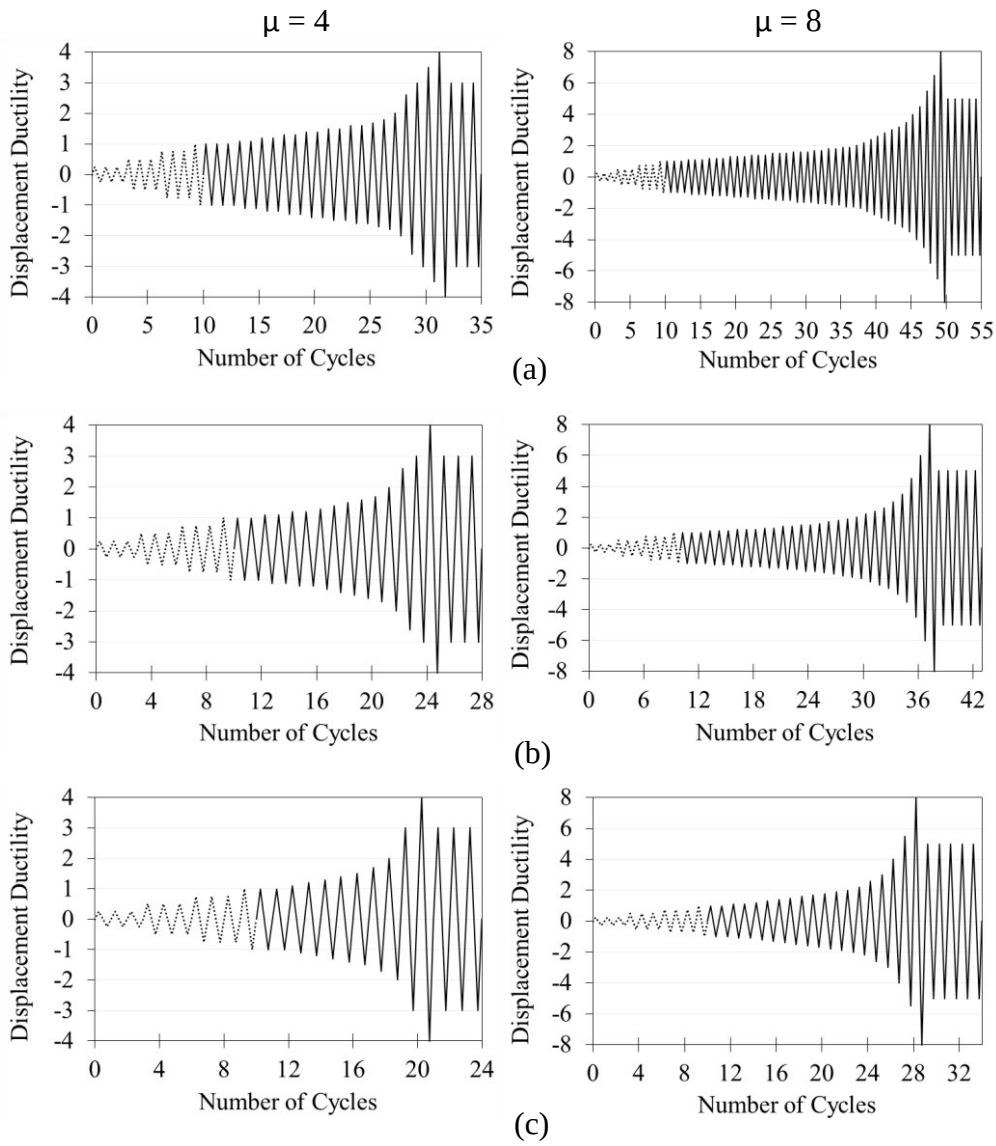

FIGURE 5 PROPOSED LOADING PROTOCOLS FOR DUCTILITIES (μ) = 4 AND 8. (a) T = 0.5 SEC, (b) T = 1.0 SEC, (c) T = 2.0 SEC.

TABLE 3 COLUMN PROPERTIES AND DIMENSIONS.

f'_c (MPa)	f'_{ce} (MPa)	f_y (MPa)	f_{ye} (MPa)	Length[5] (m)	Width (mm)	Depth (mm)	Axial Load (kN)	Axial Load Ratio (%)[6]	ρ_{sh} (%)	ρ_L (%)
22.8	29.6	413.7	468.8	2.82	609.6	609.6	712	6.5	0.094	0.88

[5] Cantilever Length
[6] Axial load ratio = $P/(A_g f'_{ce})$

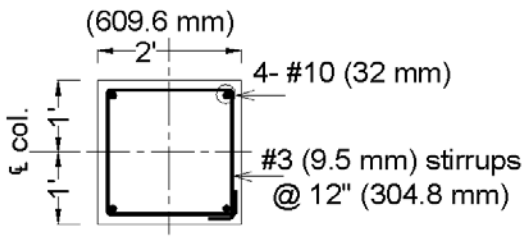

FIGURE 6 CROSS SECTION OF A TYPICAL PRE-1970 RECTANGULAR REINFORCED CONCRETE COLUMN IN OREGON, USA.

The hysteretic energy dissipation capacity plays a fundamental role in the assessment of bridge columns subjected to subduction zone ground motion. Haselton et al. (2008) has proposed equations to calculate this capacity (λ), which according his equation depends on the amount of transverse reinforcement, shear capacity and axial load ratio. Another equation also proposed by Haselton is included in the PEER/ATC 72-1 (2010) report, in which the value of λ only depends on the axial load ratio. The PEER/ATC report stated that for a typical column with seismic detailing, typical values of the parameter λ are on the order of 10 to 20. On the other hand, in the study carry out by Haselton (2008) values from 2 to 5 were employed for highly deteriorated components. This means that a lower λ indicates that the element has a high rate of strength and stiffness deterioration and therefore less capacity to dissipate energy. Since pre-1970 columns were built without seismic detailing the behavior of these columns is expected to be represented by λ values near 2.

The model parameters using equations proposed by Haselton (2008), Biskinis (2009), and moment-curvature analysis are summarized in Table 4. The moment – curvature analysis was based on conventional reinforced concrete flexure theory following AASHTO Specifications (2009). It is worth mentioning that all the analyses utilized the expected material properties, where $f'_{ce} = 1.3f'_c$ and $f_{ye} \approx 1.1f_y$.

TABLE 4 MODEL PARAMETERS.

Reference	My (kN-m)	M_c/M_y	EI_{eff}/EI_c	M_r/M_y	θ_y (rad)	θ_p (rad)	θ_{pc} (rad)	θ_u (rad)	λ
Theory (AASHTO, 2009)	544	1.07	0.29	0.8	0.006	0.043	-	0.049	-
Haselton (2008)	544	1.13	0.20	-	0.009	0.019	0.033	0.062	42
Biskinis (2009)	542	-	0.19	-	0.010	0.022	-	0.032	-
PEER/ATC 72-1 (2010)	544	1.13	0.20	0.0	0.009	0.019	0.033	0.062	24
This study	544	1.13	0.20	0.2	0.009	0.019	0.033	0.062	42 24 2

Some of the shortcomings of the equations proposed by Haselton (2008) and Biskinis & Fardis (2009) is that they do not include the effect of number of cycles on the column rotation capacity. Moreover, Haselton's equations do not account for the effect of lap-spliced rebars in expected plastic hinge locations. Despite this fact, Haselton's and Biskinis's equation lead to similar plastic rotation capacity (θ_p).

Figure 7 shows the results using the model parameters summarized in Table 4. These plots show the effect of the standard protocol and the subduction protocol for structures of ductility 8. Protocols with that target ductility were used because the ductility obtained from moment-curvature analysis was equal to 7. Comparing the results from the two protocols it can be observed that for structures with high values of λ, i.e. low rate of strength and stiffness deterioration, the behavior of the column under both protocols is quite similar in terms of rotation capacity, which is considered as the rotation when a reduction in moment capacity of 20% occurs.

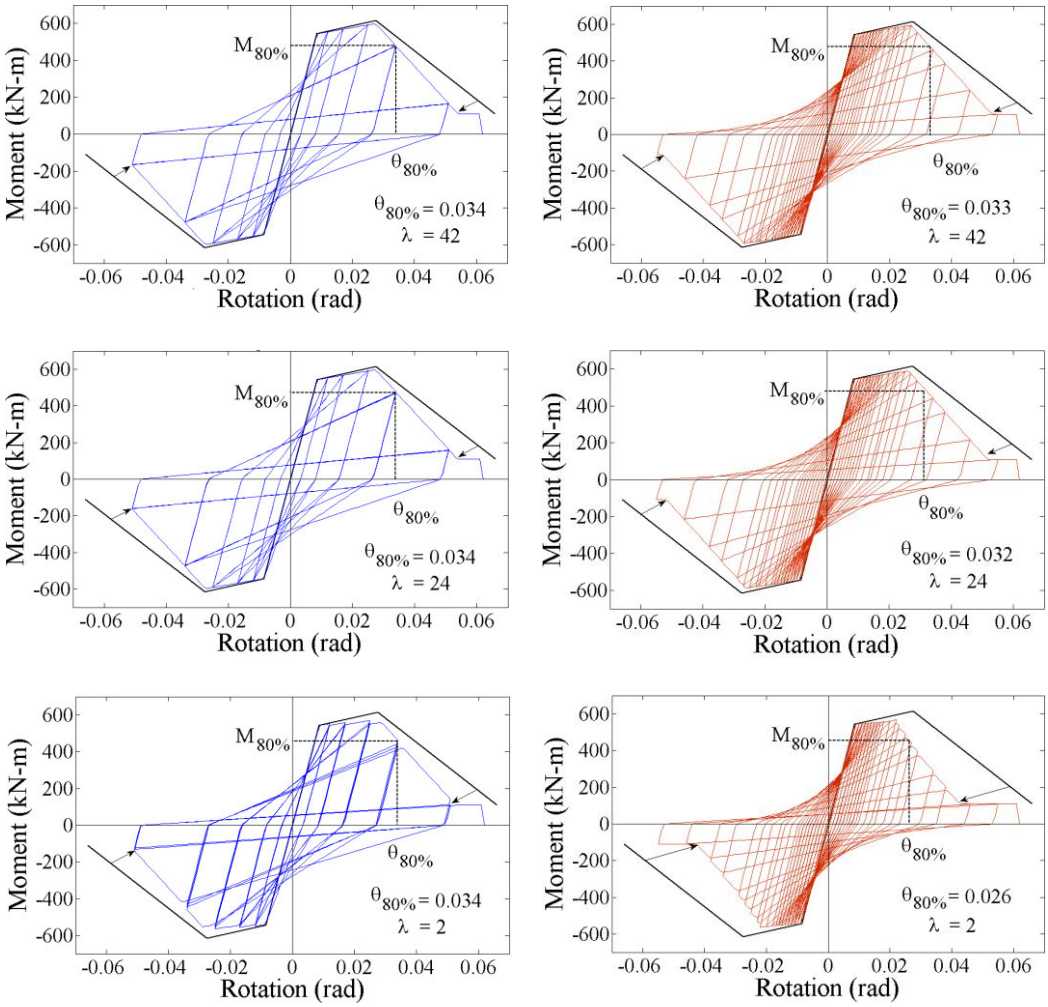

(a) (b)

FIGURE 7 EFFECT OF LOADING PROTOCOL AND MODEL PARAMETERS ON COLUMN RESPONSE. (a) STANDARD PROTOCOL. (b) SUBDUCTION PROTOCOL

On the other hand, if a high rate of deterioration (low λ) is considered the column under the subduction protocol shows less rotation capacity as compared to the column under the standard protocol. This implies that the faster the rate of deterioration, the more significant the expected effect of number of inelastic cycles.

A high rate of deterioration is expected on pre-1970 columns due to the fact that they were built with lap splices in plastic hinge regions and insufficient transverse reinforcement. Therefore, the behavior of these columns would be highly influenced by subduction mega earthquakes. This result is consistent with experimental and numerical studies, e.g. Ibarra & Krawinkler (2005), Borg, et al. (2012), Ou, et al. (2013), Chandramohan, et al. (2013). In those studies were concluded that structural components' capacity and collapse are influenced by the duration of ground motion and the number of inelastic cycles. Thus, the proposed cyclic deformation histories capture more closely the inelastic demands and therefore their application would improve the seismic assessment of bridge columns through testing.

Summary and Conclusions

The simplified rainflow procedure was employed to convert the inelastic response obtained from non-linear time history analyses utilizing recorded strong motion data into symmetric cycles. This procedure also allowed computing required parameters such as number of inelastic cycles and the normalized cumulative plastic displacement metric. Statistical values of those parameters were used in order to develop quasi-static loading protocols. Different loading protocols were proposed for three different column ductilities (2, 4 and 8) and for three different periods of the component (0.5, 1.0 and 2.0 sec). The proposed loading protocols show an increasing number of low amplitude inelastic cycles as compared to the standard protocol, revealing that the standard loading protocol commonly used in experimental testing tends to replicate unrealistic drift demands because numerous large inelastic reversals are imposed in the component.

A representative pre-1970 lightly reinforced and lap-spliced bridge column was studied to observe the effect of the proposed protocol on the behavior of reinforced concrete bridge columns. Despite the fact that the standard protocol contains a higher number of large inelastic excursion, results showed that the use of the subduction protocol can highly influence the response of deteriorating components. Even though, more extensive analytical and experimental studies are needed to reach broader conclusions, the assessment of bridge columns through representative testing load protocols would play a key role in the future establishment of limit states and acceptance criteria to be applied in performance-based seismic design of bridge columns.

Acknowledgments

This paper is based upon research funded by the Oregon Department of Transportation, whose support is gratefully acknowledged. Any opinions, findings, and conclusions or recommendations expressed in this material are those of the authors and do not necessarily reflect the views of the sponsors.

References

AASHTO, 2009. *Guide Specifications for LRFD Seismic Bridge Design,* s.l.: American Association of State Highway and Transportation Officials.

ASCE/SEI 41-06, A. S. o. C. E., 2007. *ASCE/SEI 41-06: Seismic Rehabilitation of Existing Buildings,* Reston, Virginia: American Society of Civil Engineers.

ASTM E1049-85, 2005. *Standard Practices for Cycle Counting in Fatigue Analysis.* West Conshohocken, PA: s.n.

Biskinis, D. & Fardis, M., 2009. *Deformations of Concrete Members at Yielding and Ultimate under Monotonic or Cyclic Loading (Including Repaired and Retrofitted Members),* Patras, Greece: Report No. SEE 2009-0, Department of Civil Engineering, University of Patras.

Borg, R., Rossetto, T. & Varum, H., 2012. *The Effect of the Number of Response Cycles on the Behaviour of Reinforced Concrete Elements Subject to Cyclic Loading.* Lisboa, 15th World Conference on Earthquake Engineering.

Chandramohan, R., Lin, T., Baker, J. & Deierlein, G., 2013. *Influence of ground motion spectral shape and duration on seismic collapse risk.* Tokyo, Japan, 10CUEE CONFERENCE PROCEEDINGS, 10th International Conference on Urban Earthquake Engineering.

Cheung, P., Pauley, T. & Park, R., 1991. *New Zealand tests on full-scale reinforced concrete beam-column-slab sub-assemblages designed for earthquake resistance,* Detroit, MI: ACI Special Publication SP 123-1, American Concrete Institute.

COSMOS, 2012. *Consortium of Organizations for Strong Motion Observation Systems.* [Online] Available at: http://www.cosmos-eq.org/

Dusicka, P. & Knoles, S., 2012. *Subduction Megathrust Earthquake Demands on Ductile Bridge Columns.* Oakland, CA, (7NSC), Seventh National Seismic Conference on Bridges and Highways.

FEMA 356, 2000. *Prestandard and commentary for the seismic rehabilitation of buildings,* Washington, DC: Report No. FEMA 356. Prepared by American Society of Civil Engineers. Prepared for Federal Emergency Management Agency.

FEMA P695, 2009. *Quantification of Building Seismic Performance Factors,* Washington, D.C.: Federal Emergency Managment Agency.

Haselton, C., Liel, A., Taylor, S. & Deierlein, G., 2008. *Beam-Column Element Model Calibrated for Predicting Flexural Response Leading to Global Collapse of RC Frame Buildings,* Berkeley, California: PEER Report 2007/03, Pacific Earthquake Engineering Research Center.

Hose, Y. & Seible, F., 1999. *Performance Evaluation Database for Concrete Bridge Components and Systems under Simulated Seismic Loads,* Berkeley, California: PEER Report 1999/11, Pacific Earthquake Engineering Research Center.

Ibarra, L. & Krawinkler, H., 2005. *Global Collapse of Frame Structures under Seismic Excitations (PEER 2005/06),* Berkeley, CA: Pacific Earthquake Engineering Research Center.

Ibarra, L., Medina, R. & Krawinkler, H., 2005. Hysteretic models that incorporate strenght and stiffness deterioration. *Earthquake Engineering and Structural Dynamics,* Volume 34, pp. 1489-1511.

K-Net, n.d. *National Research Institute for Earth Science and Disaster Prevention. Kyoshin Network Database.* [Online]
Available at: http://www.k-net.bosai.go.jp/

Krawinkler, H. et al., 2000. *Development of a Testing Protocol for Woodframe Structures,* Richmond, CA: CUREE Publication No. W-02.

Krawinkler, H. et al., 1983. *Recommendations for Experimental Studies on the Seismic Behavior of Steel Components and Materials,* s.l.: John A. Blumel Center, Department of Civil Engineering, Stanford University.

Kunnath, S., El-Bahy, A., Taylor, A. & Stone, W., 1997. *Cumulative Seismic Damage of Reinforced Concrete Damage Piers,* Gaithersburg, MD: Building and Fire Research Laboratory, National Institute of Standards and Technology.

Lignos, D. & Krawinkler, H., 2012. *Sidesway collapse of deteriorating structural systems under seismic excitations,* Stanford, CA: Report No. 177, The John A. Blume Earthquake Engineering Center.

McDaniel, C., Cofer, W., D., M. & Rodriguez-Merek, A., 2006. *Performance of pre-1975 Concrete Bridges in Cascadia Subduction-Zone Earthquakes,* Pullman, WA: s.n.

OpenSees, 2011. *Open System for Earthquake Engineering Simulation, Pacific Earthquake Engineering Research Center, University of California, Berkeley.* [Online]
Available at: http://opensees.berkeley.edu

Ou, Y. et al., 2013. Ground Motion Duration Effects on Hysteretic Behavior of Reinforced Concrete Bridge Columns. *Journal of Structural Engineering,* p. Accepted Manuscript.

Park, Y. & Ang, H., 1985. "A Mechanistic Seismic Damage Model for Reinforced Concrete". *Journal of Structural Engineering, ASCE,* 111(4), pp. 722-739.

PEER/ATC-72-1, 2010. *Modeling and acceptance criteria for seismic design and analysis of tall buildings,* Redwood City, California: Prepared by Applied Technology Council. Prepared for Pacific Earthquake Engineering Research Center (PEER).

PEER, 2003. *Structural Performance Database (SPD), Pacific Earthquake Engineering Research Center, University of California, Berkeley.* [Online]
Available at: http://nisee.berkeley.edu/spd/

Priestley, M., Seible, F. & Hines, E., 2002. *Seismic performance of hollow rectangular reinforced concrete piers with highly-confined boundary elements,* La Jolla, California: Department of Structural Engineering, University of California, San Diego. Report No. SSRP-99/15..

Pujol, S., Sozen, M. & Ramirez, J., 2006. Displacement History Effects on Drift Capacity of Reinforced Concrete Columns. *ACI Structural Journal,* 103(2), pp. 253-262.

Raghunandan, M. & Liel, B., 2013. Effect of ground motion duration on earthquake-induced structural collapse. *Structural Safety,* Volume 41, pp. 119-133.

Ridell, R. & Newmark, N., 1979. *Statistical analysis of the response of nonlinear systems subjected to earthquakes,* Urbana: Struct. Res. Series No. 468, University of Illinois.

Takemura, H. & Kawashima, K., 1997. Effect of loading hysteresis on ductility capacity of reinforced concrete bridge piers. *Journal of Structural Engineering,* Volume 43A, pp. 849-858 (in Japanese).

U. Chile, 2010. ,*University of Chile. Earthquakes of Chile.* [Online]
Available at: http://terremotos.ing.uchile.cl/registros/164

van de Lindt, J. & Goh, G., 2004. Effect of earthquake duration on structural reliability. *Engineering Structures,* Volume 26, p. 1585–1597.

PRELIMINARY ANALYSIS ON SEISMIC INPUT LOSS AT A PILE FOUNDATION

Kataoka Shojiro[1], Nagaya Kazuhiro[2] and Kaneko Masahiro[3]

Abstract

Seismic input loss may have significant influence on reducing seismic action, especially in short period range, on structures. Strong motion observation systems including accelerometers on free field and a footing were installed after the 2011 event to clarify characteristics of seismic input loss. A preliminary analysis on the seismic input loss observed at a viaduct is introduced.

Introduction

Strong motions with very high intensity in short period were observed during the 2011 East Japan earthquake (e.g. Kuwabara and Yen, 2011) while little damage to bridge structures was found in the vicinity of the strong motion stations. Progress of seismic retrofit, appropriate revision of design specifications, and difference between predominant period of ground motion and natural period of bridge structures can be pointed out. In addition, seismic input loss might have influenced on reducing seismic action, especially in short period range, on the bridge structures. The seismic input loss is a well-known effect in soil-structure interaction caused by self-cancelling of input waves (e.g. Scanlan, 1976) as shown in Figure 1.

Strong motion observation systems including accelerometers on free-field and on footings were installed at three viaducts after the 2011 event to clarify characteristics of seismic input loss. In this paper, strong motion records obtained during small earthquakes at the Sobanokami viaduct, a steel bridge with pile foundations, are presented as well as a preliminary result of FEM analysis using a model that consists of subsurface ground and simple bridge structure with a pile foundation.

The Sobanokami Viaduct and Observed Records

The location and a photo of the Sobanokami viaduct are shown in Figure 2. It is a part of Sanriku Expressway and located in the city of Ishinomaki, Miyagi prefecture. As shown in Figure 3 and Table 1, the viaduct is 514m long and has 9 spans and deep cast-in-situ pile foundations. It was designed under the Design specifications issued in 1996 (JRA, 1996) and completed in 2003. The seismographs were installed at P8 in 2012 as shown in Figure 4. The foundation of P8 has 9 piles with length of 68m.

Figure 5 shows acceleration waveforms and Fourier spectra of the observed

[1] Senior Researcher, Earthquake Disaster Prevention Division, NILIM
[2] Senior Researcher, Earthquake Disaster Prevention Division, NILIM
[3] Head, Earthquake Disaster Prevention Division, NILIM

motion on the free-field and the P8 footing during the off Miyagi earthquake (M4.7) on Feb. 13, 2013. The peak acceleration observed on the free-field is obviously larger than that on the footing. The Fourier spectra on the free-field have rich short period component, while those on the footing do not. Spectral ratios of the ground motions observed on the footing to those on the free-field are shown in Figure 6. The effect of the seismic input loss can be seen; the ratios are about 1 in the period longer than 0.6s but drop to about 0.5 in the period shorter than 0.4s though there are large fluctuations.

In order to carry out a preliminary FEM analysis for earthquake response of subsurface ground with a pile foundation, the ground motion on engineering bedrock at P8 was estimated by a back analysis using SHAKE (Schnabel et al., 1972) with soil properties shown in Table 2 and Figure 7. Acceleration waveforms and response spectra of the observed ground motion at free-field and the estimated engineering bedrock motion are compared in Figure 8. A little nonlinear response effect can be seen in the response spectra in short period.

A Preliminary FEM Analysis for Seismic Input Loss

An analytical model was made for evaluation of seismic input loss at P8 pile foundation of the Sobanokami viaduct as shown in Figure 9. The structure model consists of bearings (linear spring element), RC piers (linear beam element), footing (rigid), and piles (linear beam element). Soil properties are the same as those used in the back analysis to estimate the engineering bedrock motion.

The FEM analysis was carried out using the engineering bedrock motion (Figure 7) as input motion. Figure 10 shows acceleration waveforms and Fourier spectra of the observed and simulated ground motion on the free-field and the footing. The simulated ground motions show a good agreement with the observed ones. Figure 11 compares Fourier spectra of the ground motions on the free-field and the footing. Both of the observed and simulated ones show the same tendency; the ground motions on the free-field have rich short period component while the others does not. Spectral ratios of the ground motions on the footing to those on the free-field are compared in Figure 12. Though the observed one shows much more fluctuation than the simulated result, the effect of seismic input loss can be clearly seen in the both spectral ratios.

Summary

The effect of seismic input loss has been successfully observed by the new strong motion observation system and simulated by the preliminary FEM analysis. It is important to clarify its dependence on types and dimensions of foundations, soil properties, and ground motion characteristics for further improvement of seismic design of bridges and viaducts.

References

Japan Road Association (1996): Design specifications for highway bridges.

Kuwabara, T. and Yen, W. P. (2011): U.S.-Japan Joint Reconnaissance Report of Bridge Damage due to 2011 Tohoku Earthquake, http://www.pwri.go.jp/eng/ujnr/

tohokueq.htm
Scanlan, R. H. (1976): Seismic wave effects on soil-structure interaction, *Earthquake Engineering & Structural Dynamics*, Vol. 4, pp. 379-388.
Schnabel, P. B., Lysmer, J. and Seed, H. B. (1972): SHAKE – A computer program for earthquake response analysis of horizontally layered sites, Report No. EERC 72-12, University of California, Berkeley.

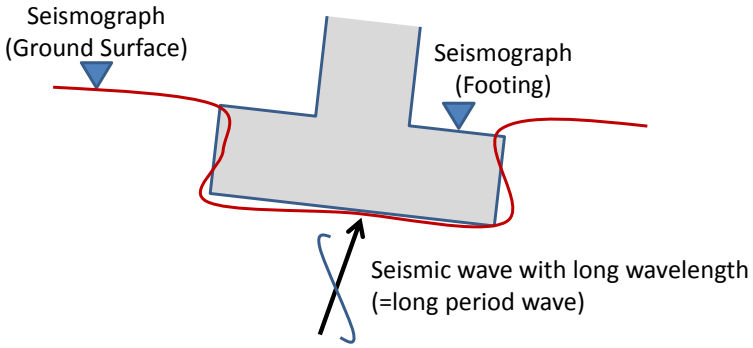

(a) Input motion with long wavelength

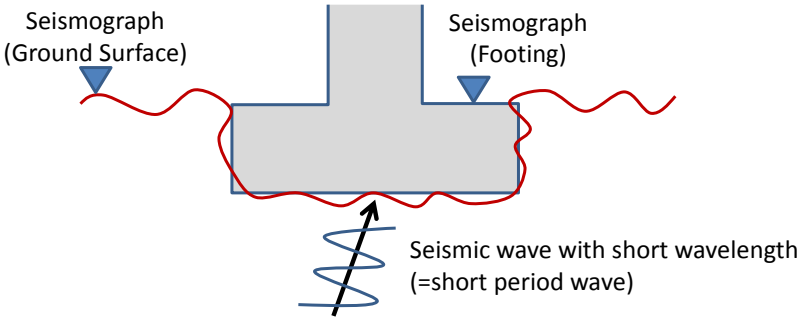

(b) Input motion with short wavelength

Figure 1 Schematic explanation of seismic input loss. A structure footing moves in the same way as ground surface against (a) an input motion with long wavelength but they moves independently against (b) an input motion with short wavelength.

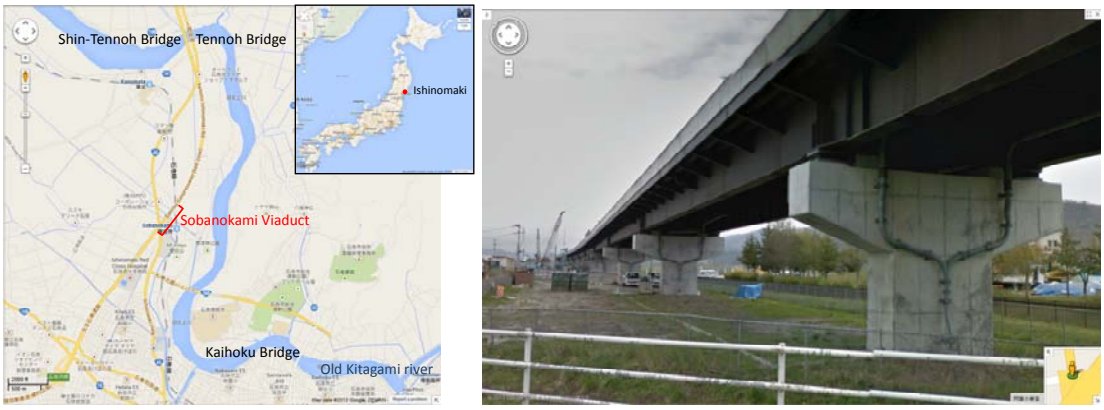

Figure 2 Map showing location of the Sobanokami viaduct and a photo taken from A1 (south) side.

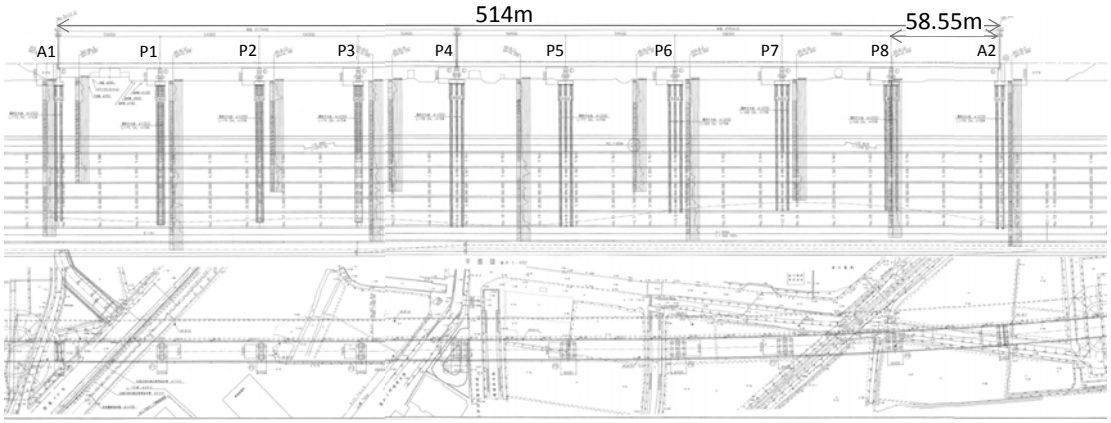

Figure 3 Side and plan views of the Sobanokami viaduct

Table 1 Structural properties

Length/Width	514.0m/11.2m
Span length	55.05+54.0+54.0+53.4m; 58.9+59.5+58.0+59.5+58.55m
Superstructure	4-span & 5-span continuous steel double-I-girders (steel slabs)
Abutment	Inverted T-type, height: 11.9/12.0m (A1/A2)
Pier	T-type RC, height: 7.1/6.9/7.4/6.8/7.3/7.4/7.3/7.3m (P1-8)
Foundation	Cast in-situ pile, ϕ1.2m; length: 68.0-78.0m; number of piles: 5-9
Bearing	Laminated rubber bearings

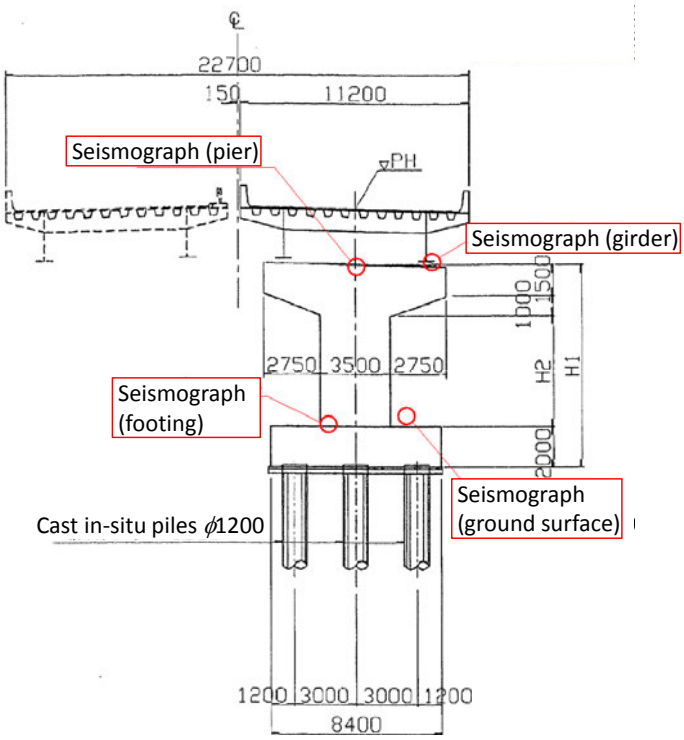

Figure 4 Arrangement of seismographs at P8.

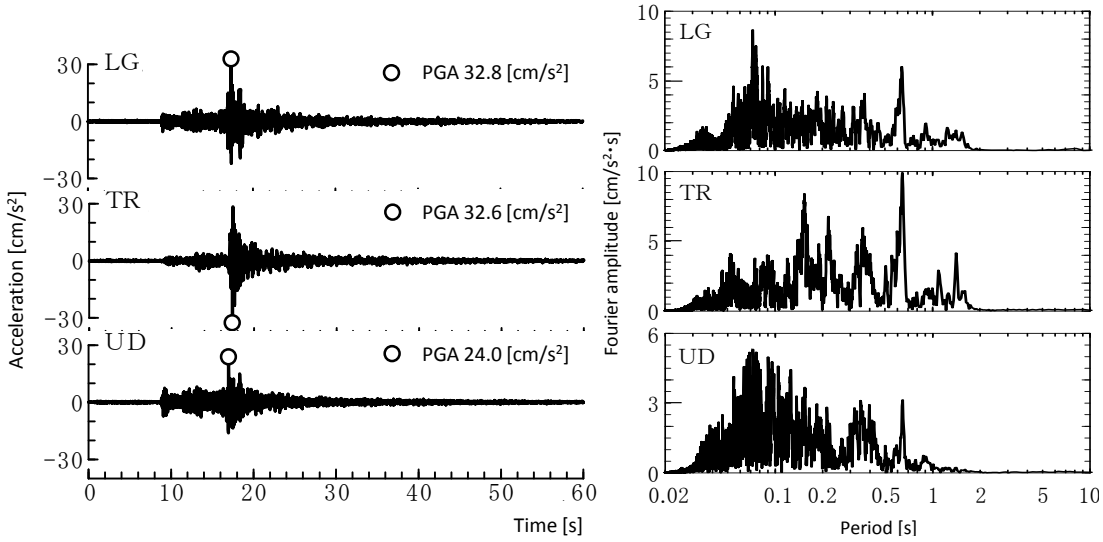

(a) Free-field motion

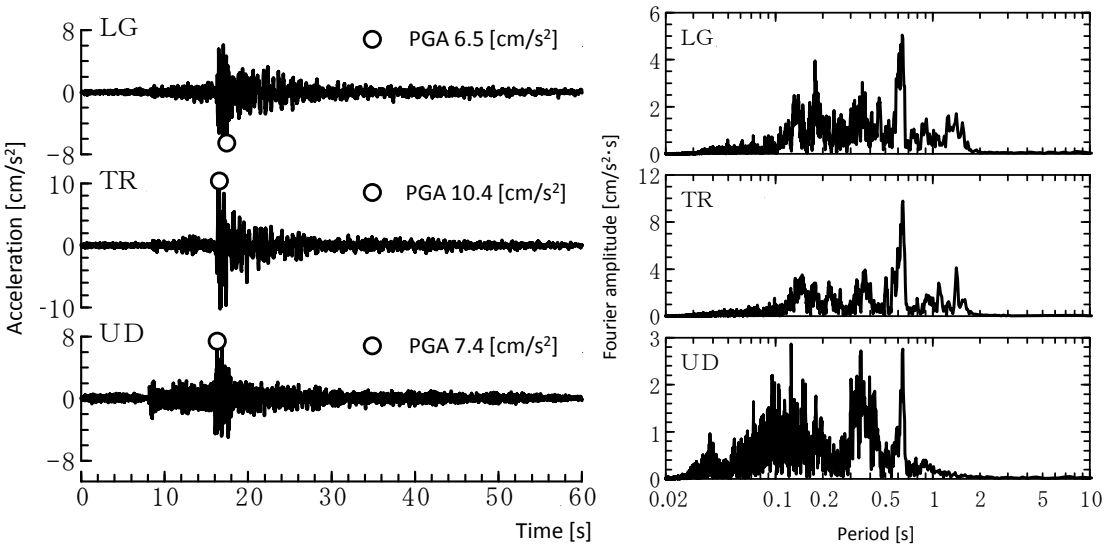

(b) P8 footing

Figure 5 Acceleration waveforms and Fourier spectra of the observed motion on (a) the free-field and (b) the P8 footing during the off Miyagi earthquake (M4.7) on Feb. 13, 2013. LG, TR, and UD denote longitudinal, transverse, and vertical directions, respectively.

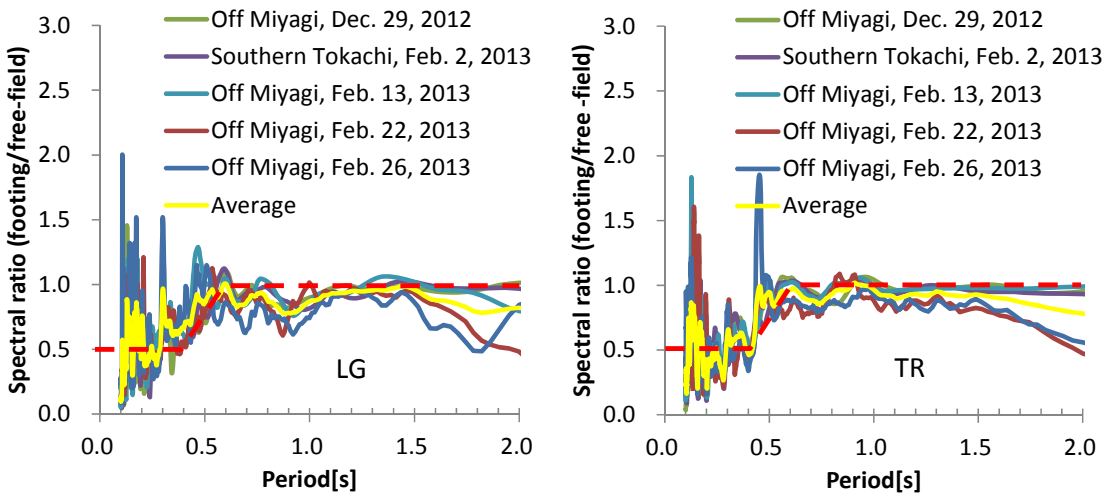

(a) Longitudinal direction (b) Transverse direction

Figure 6 Spectral ratio of the ground motion observed on the footing to that on the free-field during 5 earthquakes. Magnitudes of the earthquakes range from 4.4 to 6.5.

Table 2 Soil properties at P8 of the Sobanokami viaduct. Vs, γ, G_D, ν_D, and E_D denote S-wave velocity, unit weight, dynamic shear coefficient, dynamic Poisson's ratio, and dynamic deformation coefficient, respectively.

No.	Depth [m]	Soil classifi-cation	N-value	Vs [m/s]	γ [kN/m^3]	G_D [kN/m^2]	ν_D	E_D [kN/m^2]	Key depths
1	-	Clay	1	100	15	1.53E+4	0.45	4.44E+4	Ground water level: 0.08m
2	0.08	Clay	1	100	15	1.53 E+4	0.49	4.56E+4	
3	1.70	Sand	3	115	18	2.45 E+4	0.49	7.29E+4	Underside of footing: 2.62m
4	8.63	Clay	2	126	16	2.59 E+4	0.49	7.72E+4	
5	15.83	Clay	3	144	17	3.61 E+4	0.49	1.08E+5	
6	23.33	Sand	5	137	18	3.44 E+4	0.49	1.02E+5	
7	28.13	Clay	6	182	17	5.73 E+4	0.49	1.71E+5	
8	40.33	Clay	11	222	17	8.58 E+4	0.49	2.56E+5	
9	51.93	Sand	17	206	18	7.77 E+4	0.49	2.32E+5	
10	58.73	Clay	12	229	17	9.09 E+4	0.49	2.71E+5	
11	68.83	Clay	26	296	17	1.52E+5	0.49	4.54E+5	Head of piles: 70.44m
12	78.83	Sand	50<	300<	20	1.84E+5	0.49	5.47E+5	

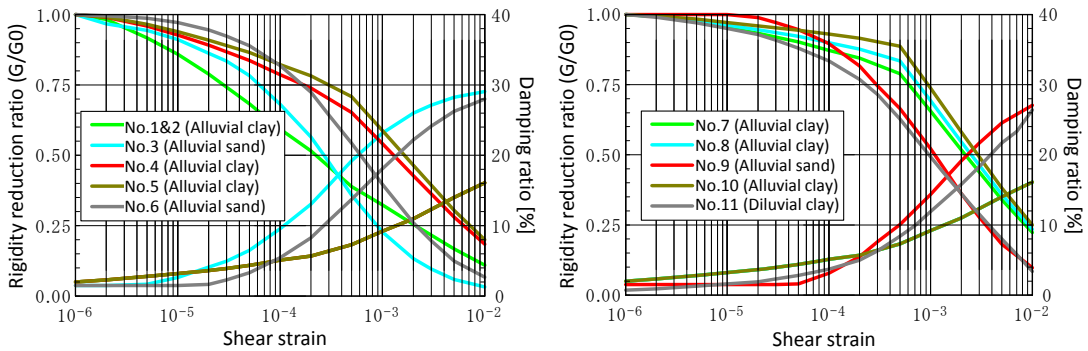

Figure 7 Dynamic properties of the soil layers. The numbers of the layers correspond to those in Table 2.

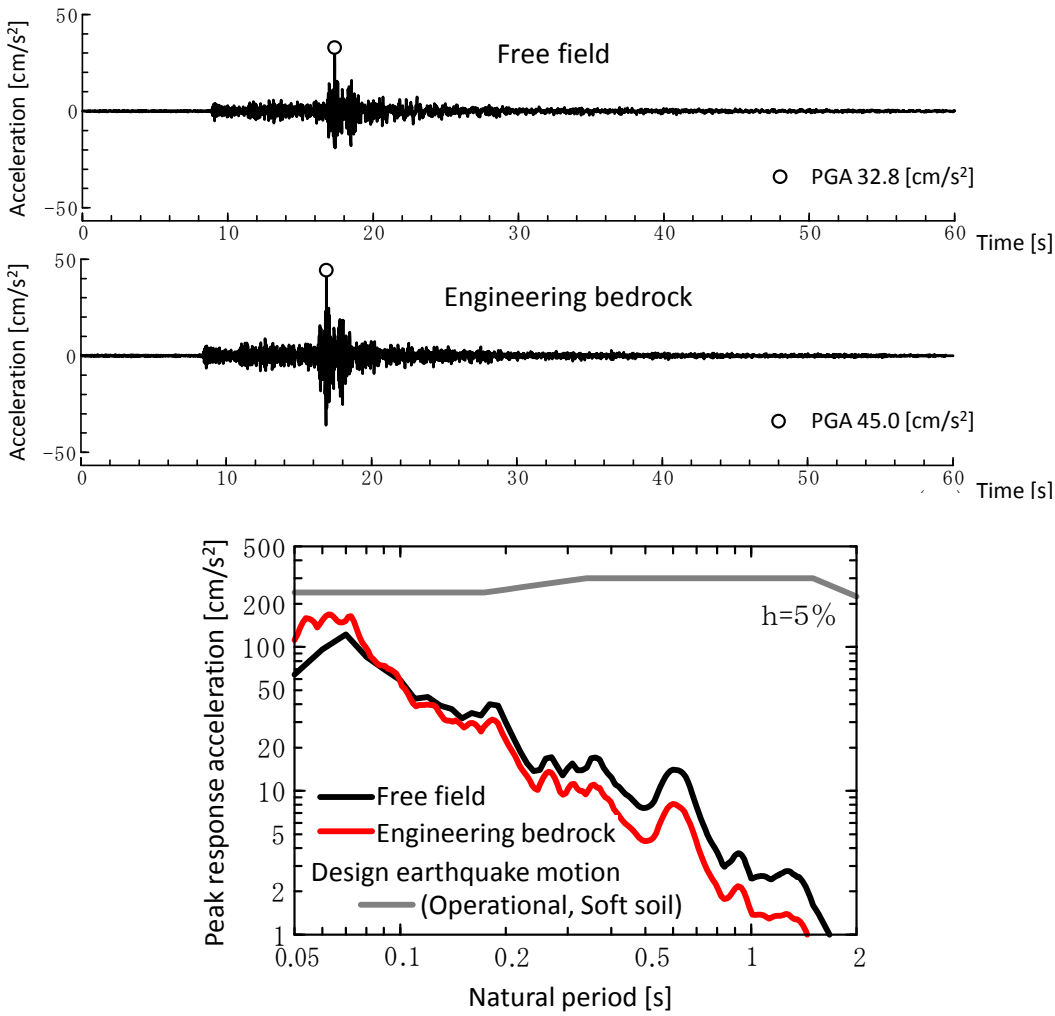

Figure 8 Acceleration waveforms and response spectra of the ground motion in LG direction at free- field and the engineering bedrock.

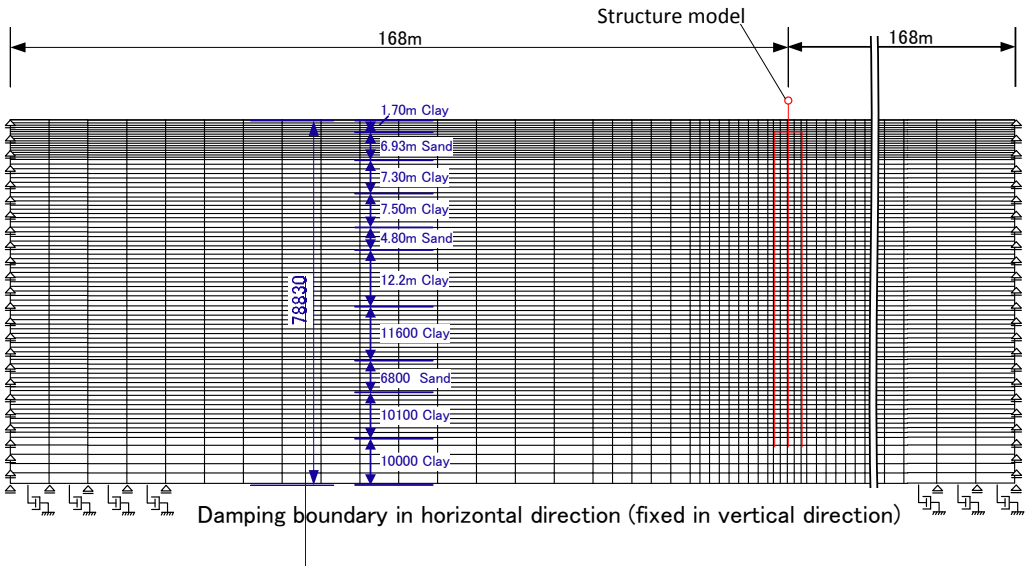

Figure 9 Analytical model for evaluation of seismic input loss at the Sobanokami viaduct. The structure model consists of bearings (linear spring element), RC piers (linear beam element), footing (rigid), and piles (linear beam element). The middle part of right half of the model is omitted.

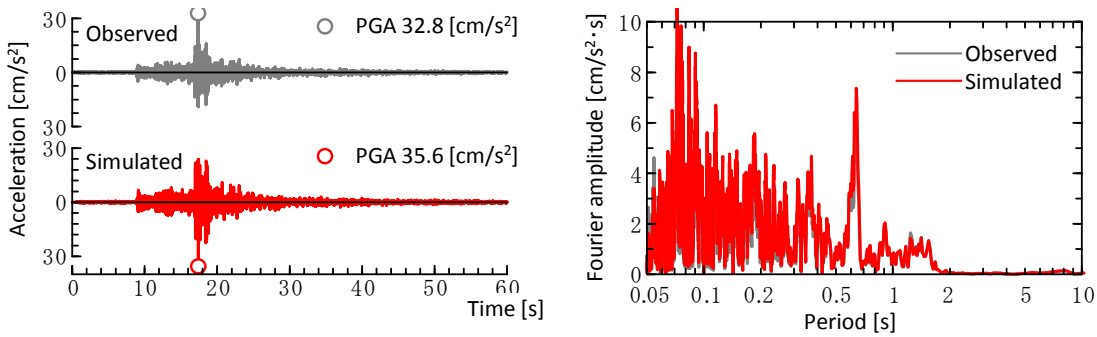

(a) Free-field

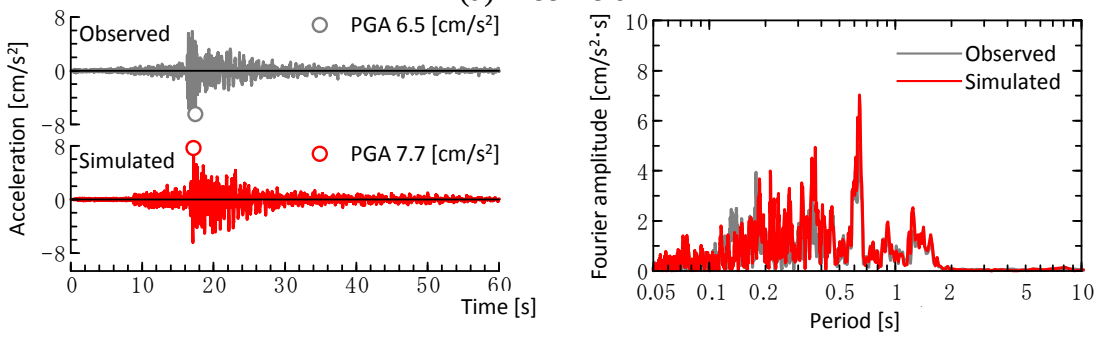

(b) Footing

Figure 10 Acceleration waveforms and Fourier spectra of the observed and simulated ground motion on (a) the free-field and (b) the footing.

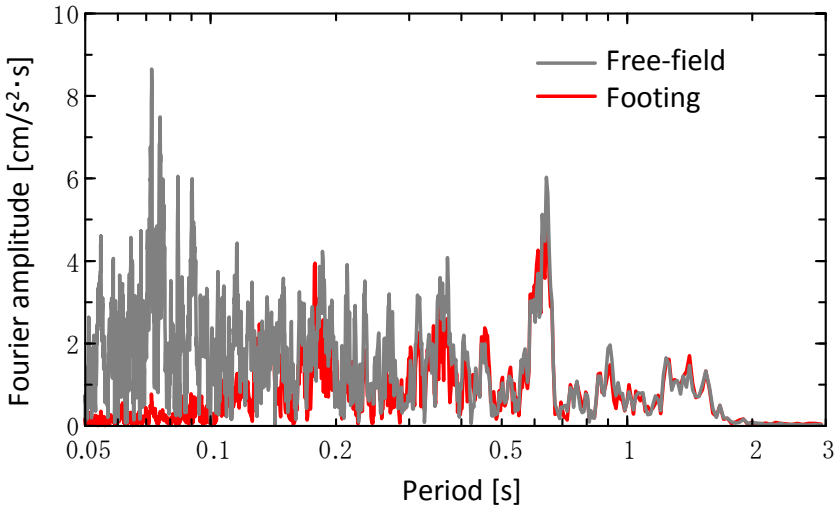

(a) Observed ground motions

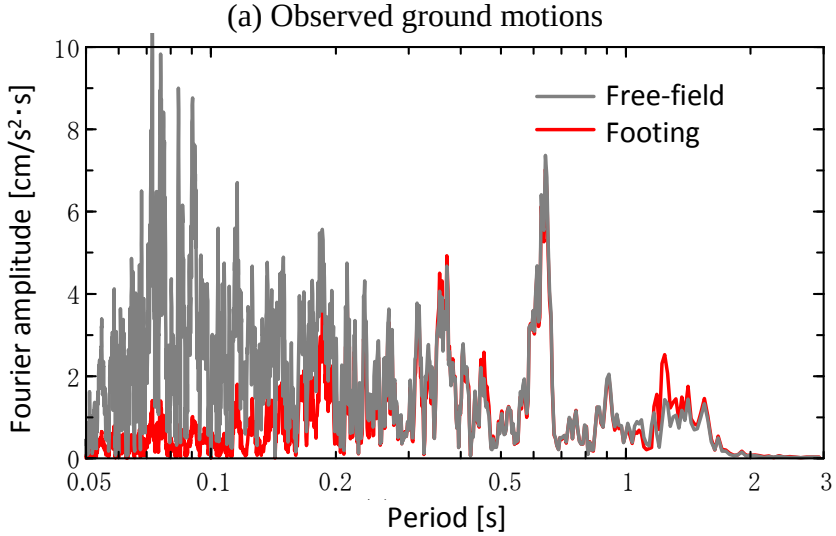

(b) Simulated ground motions

Figure 11 Fourier spectra of the ground motions on the free-field and the footing.

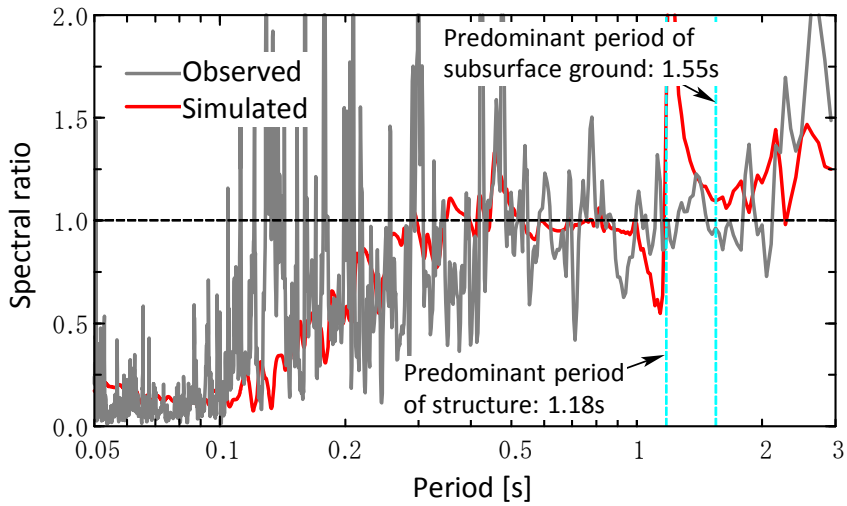

Figure 12 Spectral ratio of the ground motion on the footing to that on the free-field.

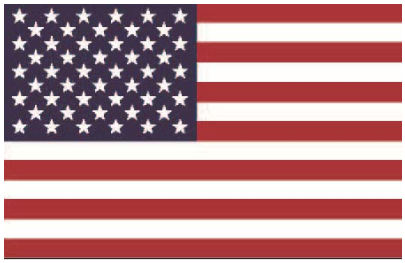

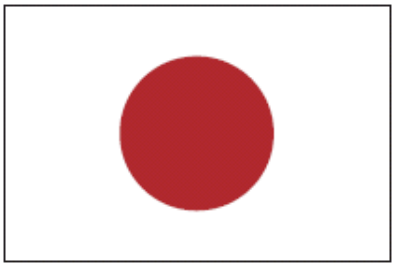

29th US-Japan

Bridge Engineering Workshop

Session 7

Construction and Design 2

PERFORMANCE OF ACCELERATED BRIDGE CONSTRUCTION CONNECTION IN BRIDGES SUBJECTED TO ESTREME EVENTS (NCHRP DOMESTIC SCAN 11-02)

W. Phillip Yen[1]; M. Saiid Saiidi[2]; Michael Keever[3]; Jugesh Kapur[4]; Waseem Dekelbab[5]; Alexander K. Bardow[6]; Joshua J. Sletten[7]; and Daniel H. Tobias[8]

Abstract

This paper summarizes the findings from NCHRP Project 20-68A, Domestic Scan 11-02 on "Best Practices Regarding the Performance of Accelerated Bridge Construction (ABC) Connections in Bridges Subjected to Multi-Hazard and Extreme Events". The objective of this Domestic Scan was to identify connection details that can be used for ABC and which perform well under extreme events, including waves and tidal or storm surge loads, earthquakes, blast, and other large lateral forces. Topics covered include findings on published ABC design guidelines, standard ABC components and connections, research results, field case studies, lessons learned, and Scan Team recommendations.

Introduction

The U.S. Domestic Scan Program is initiated by the National Cooperative Highway Research Program (NCHRP) Project No. 20-68A to collect and disseminate information about innovative transportation-related practices that are used by some agencies and that could be potentially adopted by other transportation agencies to help advance their state-of-the-practice.

[1]Principal Bridge Engineer, Structural Dynamics, Office of Bridge Technology, Federal Highway Administration, 1200 New Jersey Avenue S.E., Washington, DC 20590
[2]Professor, Department of Civil and Environmental Engineering, University of Nevada-Reno, Mail Stop 258, Reno, NV 89557
[3]Chief, Office of Earthquake Engineering, California Department of Transportation, 1801 30th Street, 27 Sacramento, CA 95816
[4]State Bridge Engineer, Bridge & Structures Office, Washington State Department of Transportation, P.O. Box 47340, Olympia, WA 98504
[5]Senior Program Officer, Transportation Research Board, 500 Fifth Street N.W., Washington, DC 20001
[6]Director of Bridge and Structures, Massachusetts Highway Department, 10 Park Plaza, Suite 6430, Boston, MA 02116
[7]Structures Design Manager, Utah Department of Transportation, 4501 South 2700 West, Box 148470, Salt Lake City, UT 84114. 30
[8]Structural Development Engineer, Bureau of Materials and Physical Research, Illinois Department of Transportation, 126 E. Ash Street, Springfield, IL 62704

Accelerated bridge construction (ABC) is one of innovations exercised by a number of states to reduce the duration and overall cost of bridge construction and its impact on the traveling public, improving work-zone safety, quality, and durability, among others [30]. ABC is consistent with the aim of the Federal Highway Administration (FHWA) "Everyday Counts" initiative. To expedite construction, prefabricated bridge elements are essential. However, these elements must be effectively connected to provide structural continuity such that the entire bridge system can effectively resist design loads. Connections of prefabricated elements are particularly critical under extreme event loading such as those acting on bridges subjected to high waves, storm-surges, earthquakes, high winds, blast, and other forces where the lateral loads are substantial.

Domestic Scan 11-02 was aimed at connections that are resistant to this type of loading. The objective of the scan was to identify successful and emerging connections for prefabricated bridge components that are able to resist multi-hazard (MH) loading and extreme events. This paper presents the highlights of the scan activities, its findings, recommendations, and planned implementation.

Scan Objectives and Scope

The overall objective of the scan was to identify connection details that are used in the United States for accelerated bridge construction (ABC) and which perform well under extreme natural and man-made events loading such as those under waves and tidal or storm surges, seismic events, blast, hurricanes, fire, etc.

The project consisted of a "desk scan," scan team meetings, visits to different states, compilation of information, and development of a scan project report. The purpose of the desk scan was to conduct a brief review of the most relevant reports, papers, and web materials; further refine the focus of the scan; and identify the states and agencies to be visited or interacted with to maximize the return from the scan effort. The main part of the desk scan was an extensive survey of nine states with a known history of activities and interest in ABC in which one or more extreme event are relevant. The survey results were analyzed and summarized in a desk scan report, which was discussed at a meeting of the scan team in November 2011. In addition to the discussion of the mission of the scan and the schedule of the visits, a list of amplifying questions was developed at the meeting and the list of states and institutions to be included in the scan was finalized. The scan team travelled to several states for meetings, while others were contacted by conference calls. The states the scan team visited directly, listed in chronological order, were: Massachusetts, Florida, Utah, Washington, and Nevada, with the first two included in the first week of the scan and the latter three in the second week. The state of California participated through several representatives who joined the scan meeting in Nevada. In addition, the states of Texas and South Carolina participated via web conference calls during scan team meetings in Massachusetts and Florida, respectively. The states that provided information for this scan are marked in Fig. 1. The Federal Highway Administration-funded study on MH loading and seismic performance of segmental bridge members at the University of Buffalo was presented and discussed at the meeting of the scan team in Massachusetts via a web conference call.

The scan visits consisted of meetings with officials, engineers, contractors, suppliers, and researchers who had experience with various ABC connections. In addition, select bridge construction sites, completed ABC projects, and research facilities were visited. The findings to be presented in the final report will be based on the face-to-face discussions, presentations, responses to amplifying questions, site visits, and supplementary materials that were provided to the scan team.

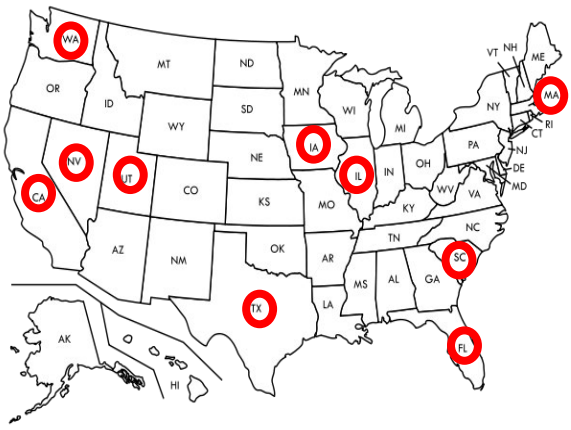

Figure 1. – States providing data on ABC connection practice

General Findings and Observations

ABC connection performance under MH loading is a multi-facetted subject encompassing many inter-related topics, the majority of which are emerging. To help identify and communicate the scan results the findings were grouped into eight topics:

1. Extreme load consideration for bridges and ABC connections
2. ABC connection details
3. ABC connection maintenance
4. Standardization of ABC connection details and processes
5. ABC connection research
6. Innovative ABC connections
7. Monitoring ABC connections and prefabricated bridge elements and systems
8. Other findings

1 - Extreme load consideration for bridges and ABC connections

Multi-hazard loading combinations are considered only to a limited extent even for conventional bridges because of a lack of guidelines and the general belief that the probability of simultaneous occurrence of multiple extreme loads is low. No information on ABC connection design under MH loading could be identified. Even under seismic loading, no specific AASHTO guidelines exist for ABC connection design despite the relative maturity of earthquake engineering of bridges. In fact, one of the key findings from the scan is that restrictions on

splicing longitudinal column reinforcement within the plastic hinge zone in seismic design category (SDC) C or D in the AASHTO Seismic Guide Specifications severely limit the implementation of ABC in high seismic regions of the country. This is consistent with the findings of the scan that there is a correlation between the level of seismicity and the level of implementation of ABC practices. The lack of widely accepted, well developed and proven ABC connection details has prevented extensive application of ABC in high seismic zones.

To address the gap in knowledge and develop MH design guidelines, an FHWA-funded study is in progress at the University at Buffalo, NY, to establish a platform to include MH loading in LRFD for highway bridges (MH-LRFD) [1]. The focus of the study is on bridges in general and is not specific to ABC or ABC connections. The study is primarily of analytical nature because of a lack of extensive field and research data. The current AASHTO LRFD framework is being used for eventual integration of limit states and load factors that will be developed in this study. To help guide the study, a survey of state bridge engineers was conducted [3] and a workshop of state bridge engineers was held. The survey helped establish the current views and practices across different states for MH design. Both multiple simultaneous and cascading events were discussed. Fig. 2 presents a sample of the survey findings for simultaneous action of scour, storm surge. It is evident from the survey that there is considerable variation among the states with respect how extreme load combination is considered depending on the geographical location and extreme load type.

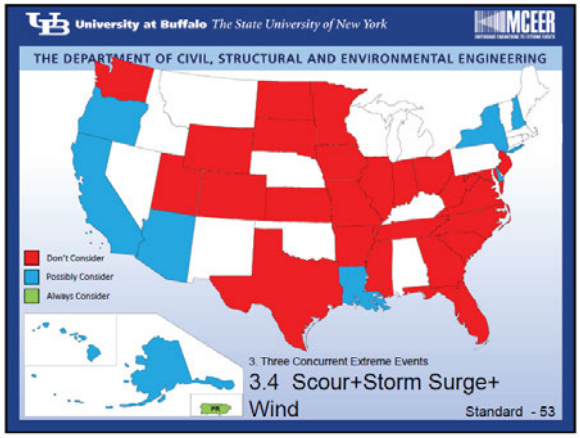

Figure 2. – Survey results for consideration of scour, storm surge, and wind combination

2- ABC Connection Details

Although ABC has been generally applied to a small fraction of the overall bridge population throughout the country, numerous ABC connection types have been used by various states. Some of the connection details from the recently published FHWA manual on ABC are being adopted by several states [2]. Some states allow for unrestrained movement of the

superstructure under lateral loads and design bearing connections for vertical loading alone. Under storm surge, the approach taken by some states is to allow for uplift of the superstructure.

Three types of precast column to pier cap, column to pile cap, and column to pile shaft connections were identified during the scan. In one connection type, the column is embedded into the adjacent member (pile shaft, footing, or cap beam. A second connection type consists of grouted couplers that may be embedded into the column or the adjacent member (Fig. 3). The third connection type uses longitudinal bars extending from a precast column that are inserted into corrugated metal ducts in the adjacent member and the duct is filled with grout.

Some states with a longer history of ABC use have refined connections based on field experience. They have relied on codes other than AASHTO when necessary in design and detailing of some of the ABC connections.

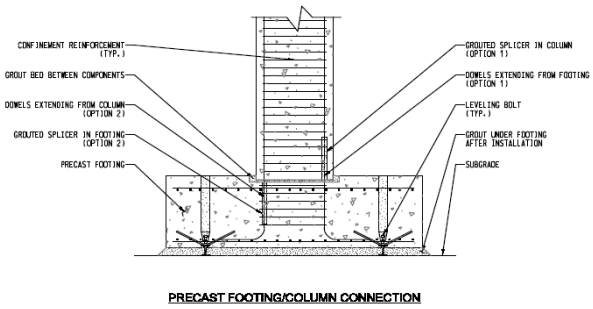

Figure 3. – Precast column to precast footing connection with grouted couplers

3- ABC Connection Maintenance

Due to the relatively short history of ABC application, it is difficult to make a broad statement about maintenance issues or lack thereof in ABC connections. Generally ABC connections are perceived to perform the same as conventional connections over time because they are mostly intended to be emulative. Nonetheless, some states conduct annual inspection of precast elements and joints rather than the normal biennial inspection to monitor. Field observations are documented and lessons learned are used to refine connection designs for future ABC projects. Despite the confidence in emulative ABC details, many precautionary measures are taken to minimize maintenance problems and improve durability. Joint details and construction procedures are evolving based on field experience. This trend is expected to continue.

4- Standardization of ABC Connection Details and Processes

Standardization of ABC applies to design and details in addition to the process by which the ABC alternative is selected for a project.

With expanding popularity of ABC, the need to develop standard connection details is being realized in different states, although philosophies differ among them. While some states believe that preapproved standard ABC connections should be provided, others believe that leaving flexibility in design and detailing could encourage widespread ABC use. There appear to be more states subscribing to the former view. Fig. 4 shows a standard detail adopted in Massachusetts. An example of precast column being placed in cast-in-place footing as part of a Highway For Life project is shown in Fig. 5. Some of the standard details that are being developed do not meet AASHTO requirements. Some states do not allow couplers in plastic hinge regions of columns when the bridge is in SDC C or D because of AASHTO restrictions.

The process by which ABC is selected over conventional construction, although not specific to ABC connections, is important and relevant to the objective of the scan. Decision making tools are evolving at national and state levels and are becoming available. User costs are generally considered and utilized as a means to justify ABC, although in many instances the initial cost is the primary consideration.

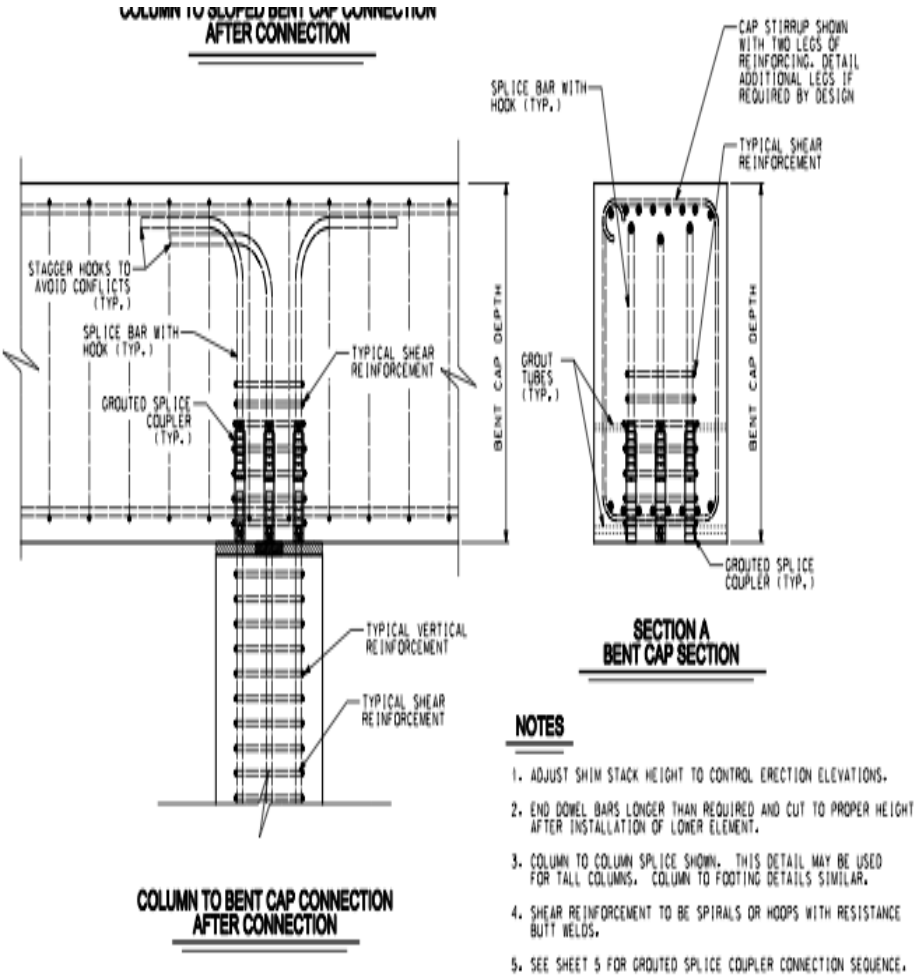

Fig. 4 – Standard cap beam-column connection in Massachusetts

Fig. 5 – Precast column embedded in cast-in-place footing in the State of Washington

5- ABC Connection Research

Research has been conducted on ABC connections with a focus mostly on seismic performance of ABC connections and members. Studies are being carried out on high-early strength concrete with the aim of developing standard mixes that may be used at closure pours joining prefabricated reinforced concrete deck elements.

ABC connections may be placed into two categories - emulative and non-emulative connections. Emulative connection seismic research has focused on providing full continuity at the connection for transfer of critical forces. Precast reinforced concrete columns embedded into footings, piles, or pier caps (Fig. 6) have been studied under cyclic loads with satisfactory results. Using couplers in the plastic hinge zones (Fig. 7) has shown promising results. Also large-diameter bars anchored in corrugated metal ducts or standard couplers of various types for longitudinal bars have been used. Various methods to convert multi-girder pier cap connections into integral pier caps have been also studied (Fig. 8).

The versatility offered by precast members has encouraged research on non-emulative connections response under seismic loads. Post-tensioned segmental columns utilizing different details have been studied under slow cyclic and shake table loading. In some cases, sliding and rocking at joints are allowed to improve energy dissipation. In other studies novel materials such as fiber-reinforced concrete and built-in rubber pads have been used in segmental columns to

improve performance beyond that of conventional columns by minimizing damage. Concrete filled steel and FRP (fiber-reinforced polymer) tubes have been studied by various researchers under slow cyclic and shake table loading. The column models are embedded into footings to provide full moment transfer. Results have demonstrated successful performance of column-footing connections. Other means to improve the seismic performance beyond emulative design has included the use of high-performance concrete, shape memory alloy reinforcement, and steel pipe pins in lieu of conventionally-reinforced pins.

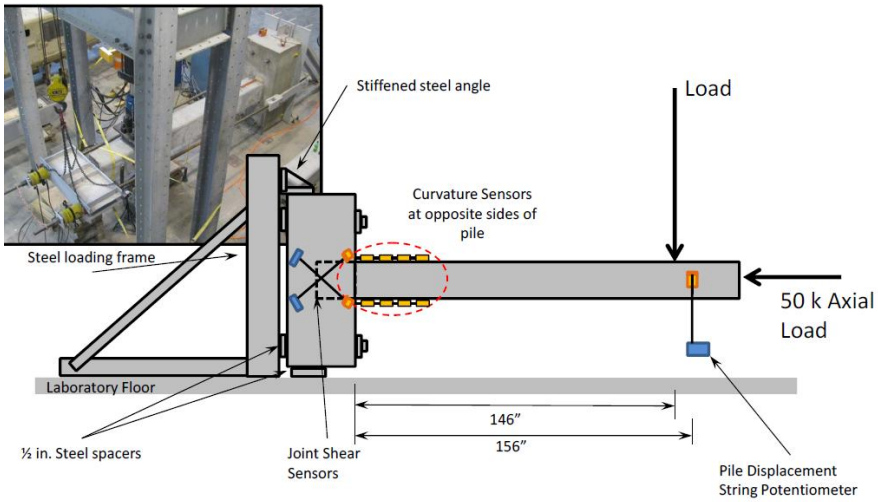

Fig. 6 – Pile cap beam connection model tested at the University of South Carolina

Fig. 7 – Precast column-footing connection model with headed bar couplers tested at the University of Nevada - Reno

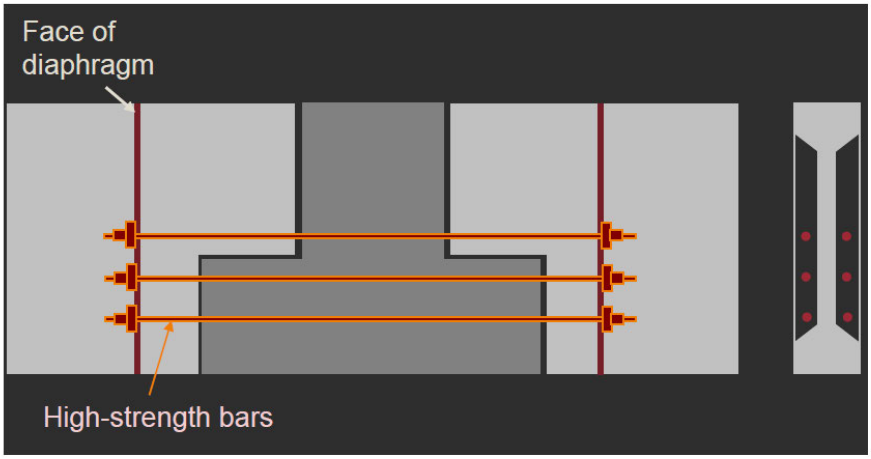

Fig. 8 - Superstructure/cap beam connection with high-strength bars tested by Iowa State University

6- Innovative ABC connections

ABC provides the opportunity to embrace innovation. In addition to research on using high performance concrete, high performance metallic materials, and FRP materials previously described, various forms of innovative precast double-T girders are being considered for bridge superstructure. Folded plate steel girders and concrete-filled FRP tube arches are being implemented in selected bridges. Post-tensioning has been used in bridge girders for decades. Many states are making use of post-tensioning in ABC through post-tensioned bridge decks and abutments. Transverse post-tensioning of girders in cap beam zones are considered as one of the means to convert multi-girder pier cap connections into integral pier caps. Base isolation, although it has been used for conventional bridges, is being considered as a viable alternative to help reduce demand on ABC connections under seismic loads. The FHWA Highways for Life (HFL) Innovative Bridge Research and Deployment (IBRD) programs have served as a mechanism for field implementation of promising innovative concepts that have been developed based on research.

Research on adopting advanced materials in ABC connections has focused on different materials, concepts, and details. Post-tensioned segmental columns with sliding joints have shown promising results for their damping and recentering capability (Fig. 9). Precast concrete-filled fiber-reinforced polymer composite tube columns (Fig. 10) save construction time by reducing the need for formwork, yet they have shown to reduce damage under earthquake loading. Another detail to reduce damage in the plastic hinge of ABC columns is incorporation of rubber pads that are normally used in base isolation, but changing their role form shear deformable elements to flexural members replacing concrete in the plastic hinge (Fig. 11). Recent research has shown superior performance of these pads over conventional plastic hinges.

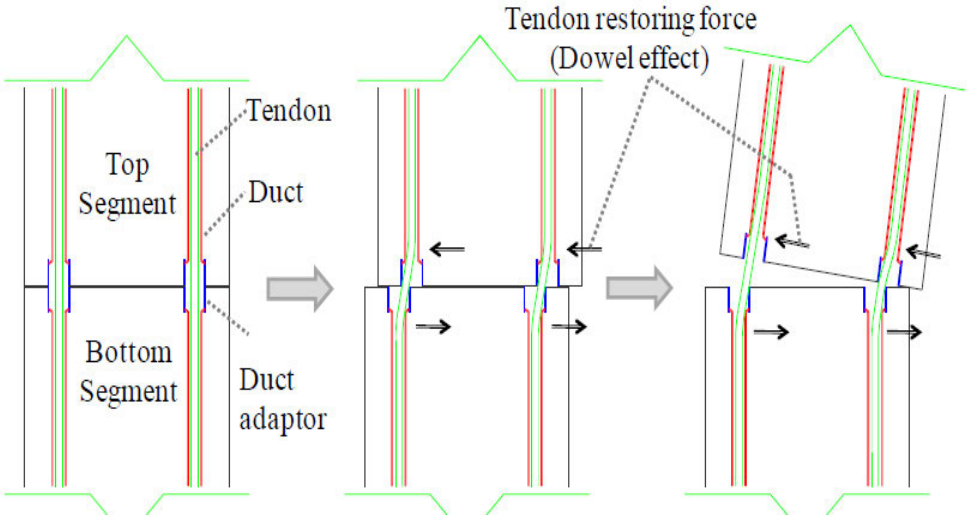

Fig.9 – Segmental column connection with sliding joints tested at the University at Buffalo

Fig. 10 – Precast concrete filled FRP tube column placed in precast footing at the University of Nevada - Reno

Fig.11 – Segmental column model with rubber pad a shake table at the University of Nevada - Reno

7- Monitoring ABC connections and prefabricated bridge elements and systems

Instrumentation and long-term health monitoring of prefabricated bridge components and their connections are conducted by some states on a selected basis only when innovative unconventional elements are utilized in the bridge. The purpose of gathering data on novel bridges, bridge components, and bridge connections is to determine any unexpected behavior and learn about their response. The general view about monitoring is that it may not be necessary, particularly when ABC connections are emulative.

Short-term monitoring of movements is conducted during SPMT moves and placement of precast superstructures to ensure that no overstress occurs in bridge components.

8- Other Findings

Extensive communication among different stakeholders such as designers, contractors, top management, fabricators, industry, and the public appears to have been the key to successful planning and execution of past ABC projects. Early involvement of contractors in the design and planning process has alleviated issues and has encouraged participation of contractors in ABC because of the reduced financial risk and sharing of risk associated with new methods. In some cases remoteness of precast plants relative to the job site might discourage the adoption of ABC.

Although site casting of precast members may be viable, it requires added quality assurance and quality control.

More and more states are becoming aware of the importance of education and training for design and inspection of ABC projects. ABC design tools are also critical and are being developed by different states to become an integral part of their bridge design manuals. Many lessons are being learned about best practices of ABC. Despite the challenges associated with ABC, there is a great deal of enthusiasm and desire to use ABC. The FHWA Highway for Life program and the Innovative Bridge Research and Deployment (IBRD) program provide valuable vehicles to apply and showcase ABC projects.

Team Recommendations

The following recommendations are made based on the scan and discussions during scan team meetings following the visits:

1 Research needs to continue on MH load combination. Studies should provide insight into any considerations that are unique to ABC connections. Once research results are obtained and potential methodologies to incorporate MH in LRFD are developed, an NCHRP project to transfer research into AASHTO guidelines should be undertaken.

2 A national center on ABC under MH loading should be established. The main goals of this center would be to (a) coordinate and integrate ABC research and development of design guidelines for MH loading consideration, (b) ensure that emerging ABC connections are simple and practical, (c) develop a library of standard ABC connections details, (d) provide assessment of different connections, (e) collect, compile, interpret, and develop a data base of field performance of ABC connections, (f) develop performance characteristics of ABC components and connections for performance based design methods, and (g) coordinate with AASHTO to develop bridge design and construction specifications.

3 The FHWA "Everyday Counts" program has set a vision which includes ABC as an important component. Extensive outreach to the bridge contracting community needs to be undertaken to promote ABC. This could be included in the mission of the center discussed under Recommendation 2.

4 The FHWA "Highways for Life" program, and similar programs, should expand its support of demonstration projects utilizing various ABC connections. This would help showcase successful ABC design and support implementation with the goal of promoting ABC in regions of the country where extreme loads are prevalent.

5 Continue to do research on emulative design to help implement AASHTO specifications so that ABC can be fully implemented in regions of high seismicity and other extreme loads.

6 Even though emulative design is the most appropriate initial focus for codifying ABC connections, the use of innovative details, high-performance grouts, concrete, metals, and composite materials should be considered for future development. Innovative methods and materials have the potential to meet or exceed target performance levels of emulative design.

7 Until a sufficiently large data base of field performance of ABC connections is compiled, frequent field investigation and inspection of ABC projects should be conducted, performance data be documented, and lessons learned be identified. This effort may be

undertaken in collaboration with the FHWA Long-Term Bridge Performance monitoring program to utilize the tools and processes that have become available in recent years.

8 Update the AASHTO Seismic Guide Specifications for implementation of ABC in SDC Zones B, C and D.

9 Perform research, field monitoring, and develop design and construction specifications for the use of high early strength concrete and grouts in closure pours for ABC connections.

10 Develop guidelines for shipping with respect to weights and sizes of prefabricated components.

Conclusions

A clear picture of the state of practice on design and construction of ABC connections to resist extreme loads was obtained through Scan 11-02. It was found that design for multi-hazard loading has yet to materialize because of a lack of design procedures and guidelines. Current AASHTO provisions limiting the use of mechanical couplers in column plastic hinges in areas of moderate and high seismicity was noted as an important barrier preventing the earthquake prone states from using ABC. Significant research on emulative and innovative ABC connections has been conducted. It is recommended that a central source to gather and interpret information about construction, detailing, education, design guidelines, and research on ABC be formed and serve as a clearing house to further promote ABC.

Acknowledgements

Funding provided through the NCHRP Project No. 20-68A for Scan 11-02 requested by AASHTO is acknowledged. The NCHRP is supported by annual voluntary contributions from the state DOTs. Additional support for selected scans is provided by the FHWA and other agencies.

DEVELOPMENT AND DESIGN OF NEW STEEL PIPE INTEGRATED PIER WITH SHEAR LINK

Ryohei NAKAMURA[1]*, Hidesada KANAJI[1], and, Takashi KOSAKA[1]

Abstract

We proposed an innovative integrated steel pipe pier using damage control design. The proposed pier is composed of four steel pipes interconnected with shear links along its height. Steel pipes as main members, support vertical load (such as dead load and live load). Shear links as sub members resist horizontal load (such as seismic load). The application of the damage control design can reduce a response of the pier and it can keep steel pipes wholesome during earthquakes. So, not only emergency vehicles but ordinary vehicles can pass immediately after earthquakes. This paper describes a outline of design and construction of highway viaduct supported by new steel pipe integrated pier with shear links applied to Ebie junction which connects the Yodogawa-sagan route to the Kobe route of Hanshin expressway.

Introduction

The proposed pier, steel pipe integrated pier with shear link, is composed of four steel pipes interconnected with shear links along its height (see Figure1). Steel pipes as main members, support vertical load (such as dead load and live load) and shear links as sub-members resist horizontal load (such as seismic load). The stable elastic-plastic behavior of each shear link as hysteretic dampers, which reduce the response of the pier during an earthquake. The application of the damage control design can reduce a response of the pier and it can keep steel pipes wholesome during earthquakes. So, not only emergency vehicles but ordinary vehicles can pass immediately after great earthquakes. And when a restoration is required, a change of shear panels restore the proposed pier. Therefore the seismic life cycle cost can be reduced.

Fig-1 Steel pipe integrated pier

[1] Hanshin Expressway Company Limited, Osaka, Japan

This paper describes an outline of design and construction of highway viaduct supported by new steel pipe integrated pier with shear links where is Ebie junction which connects the Yodogawa-sagan route to the Kobe route of Hanshin expressway (see Pictuire1). The basic seismic performance of the proposed pier was reported in documents 1).

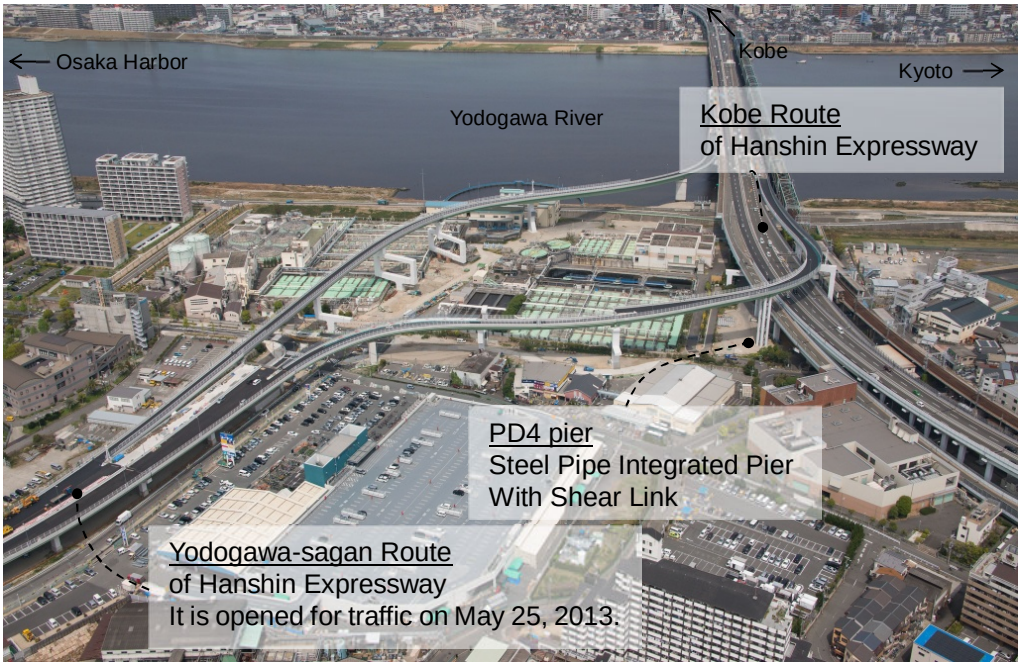

Picture-1 Ebie junction

1. Required performance

A required seismic performance matrix of steel pipe integrated pier is shown in Table 1. The required seismic performance of 4 phases is determined in checking a design of the proposed pier. It has been thought that it is difficult to control damages for great earthquakes in terms of cost performance so far.

Table-1 A required seismic performance matrix of steel pipe integrated pier

Seismic Performance Level / Earthquake	Performance Ⅰ	Performance Ⅱa	Performance Ⅱb	Performance Ⅲ	—
	[Sutructure safty performance]				
	Safty				Failure
	[Usability after earthqueke]				
	No damage	Small damege	Medium damage	Big damage	
Level 1	□ △ ○		Unacceptable		
Level 2		○	△	□	

○—○ Important bridge (Ordinary design condition)

△—△ Important bridge (To keep small damage is illogical subject to special design condition)

□—□ Oirdinary bridge

The application of the damage control design enables the proposed pier to control damage of main member. The proposed pier should be intact for Level 1 earthquake (Seismic performance I). This design method leads major damages into shear panels that connect each steel pipe for level 2 earthquake and keeps steel pipe pier structural elastic-region. Structural elastic-region mean a state that a member makes locally plastic, shows elastic behavior as a structure, keeps sound state and the road can be open to the public after earthquake.

To keep small damage is illogical subject to design condition that a pier such as PD4 pier in Ebie junction resists seismic load in a curved and long span bridge. So this design method allows medium damage, same level as specifications for highway bridges, subject to special design condition (Seismic performance IIb). And this design method allows big damage of the proposed pier on less important structure (Seismic performance III).

2. Member Soundness

Seismic performance of the proposed pier is composed of soundness and damage level of each member. Member soundness matrix for seismic performance of the proposed pier is shown in Table 2. An image of damage level of each member is shown in Figure 2.

Table-2 Member soundness matrix for seismic performance of the proposed pier

Seismic perfomance		Perfomance I	Perfomance II a	Perfomance II b	Perfomance III
Earthquake level		Level1	Level2		
Steel pipe pier	Concrete hollow section	Soundness ①	Soundness ②	Soundness ③	Soundness ④
	Concrete filled section				
Shear link	Shear panel	Soundness ②	Soundness ③	Soundness ③	Soundness ④
	Joint	Soundness ①	Soundness ②	Soundness ②	Soundness ③
	Shear panel-joint	Soundness ①	Soundness ②	Soundness ②	Soundness ③
Joint part	Superstructre-pier	Soundness ①	Soundness ②	Soundness ②	Soundness ③
	Pier-Shear links				
	Pier-Cassion				
Whole structure	Residual displacement	Soundness ①	Soundness ②	Soundness ③	Soundness ④

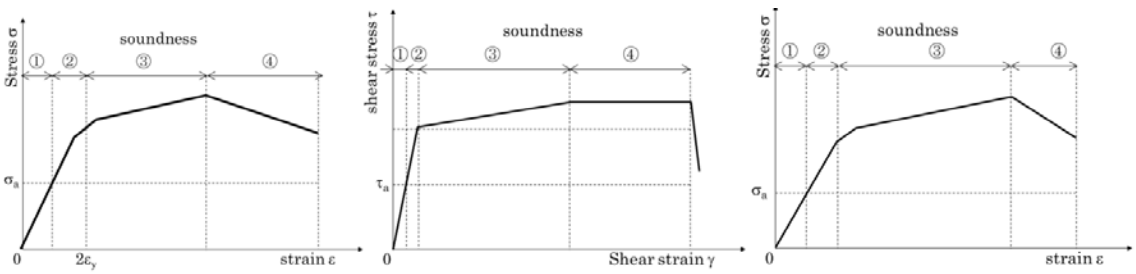

(a) Steel pipe pier (b) Shear panel (c) Joint part

Fig-2 Steel pipe integrated pier

As regards seismic performance Ⅰ, all members except shear panel should satisfy soundness 2 which have a safety factor for yield resistance. And the stress of shear panel is below yield resistance. As regards seismic performance Ⅱa, steel pipe pier should satisfy soundness 2 which is structural elastic-region, shear panel should satisfy soundness 3 which has stable performance, Horizontal member and connection should satisfy soundness 1 which is below allowable stress. As regards seismic performance Ⅱb, steel pipe pier should satisfy soundness 3 which is limiting value for steel pipe pier ruled on specifications for highway bridges. As regards seismic performance Ⅲ, steel pipe pier should satisfy soundness 4 that steel pipes don't collapse, joints between shear panels and steel pipes satisfy soundness 3 which is below load capacity.

3. Analysis Model

The model of the proposed integrated steel pipe pier was created using a fiber model of the beam elements. A biaxial moment and a change of axial load are considered in this analysis. And material nonlinear configuration rules and geometrical nonlinear are considered also. The analysis model of the highway viaduct supported by steel pipe integrated pier is shown in Figure 3, the fiber model is shown in Figure 5 (a) and the fiber cell division of the steel pipe and shear link cross-section is shown in Figure 5 (b)(c)(d). The relationship between shear stress and shear strain is shown in Figure4.

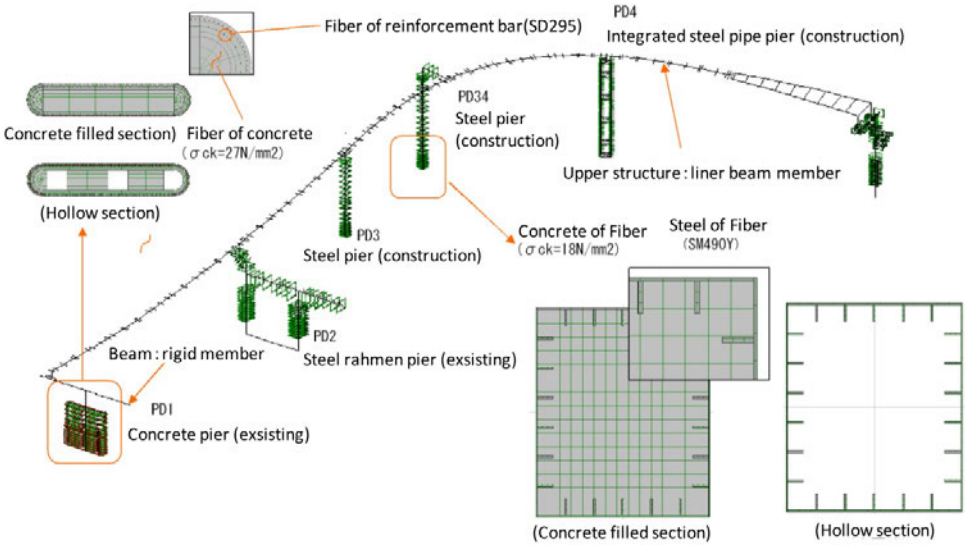

Fig-3 The analysis model for of Highway Viaduct Supported by New Steel Pipe Integrated Pier

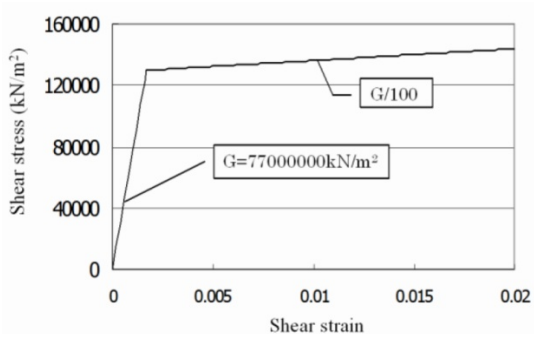

Fig-4 The relationship between shear stress and shear strain

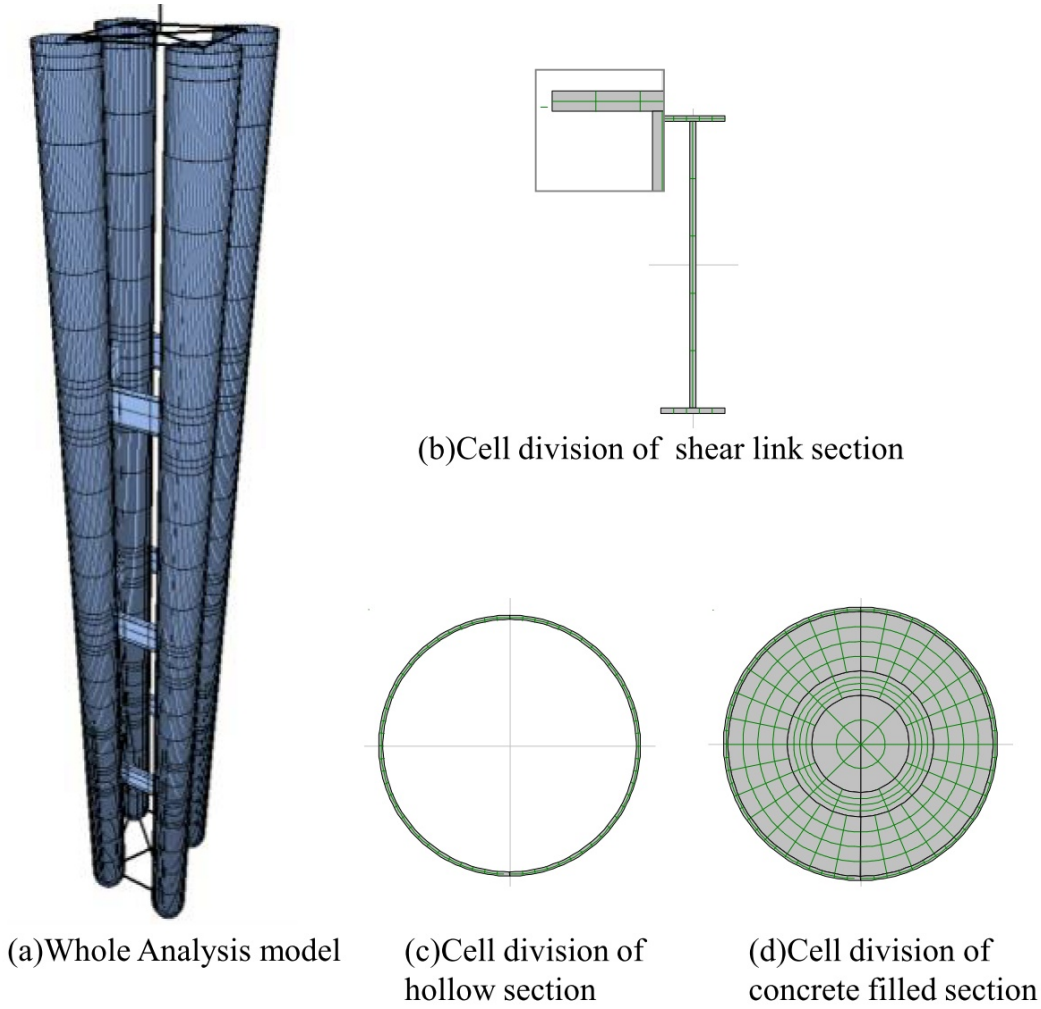

Fig-5 The fiber model of Steel Pipe Integrated Pier

4. Material Configuration rules

With regards to the material configuration rules, those proposed in the documents 2) were used for SM490Y of the steel pipes, beams, horizontal structural member flanges, and the material of the filler concrete. For the dynamic analysis of the strain hardening of the steel materials, the bi-linear model, in which the secondary gradient should be 1% of the primary gradient, was used as the material configuration rule. A representation of the relationship between the shear stress and strain of LY225, used for the web plate of the horizontal structural members, is depicted as a bi-linear model.

5. Pushover Analysis

A pushover analysis was conducted to investigate the deformation performance, load capacity, and plasticization rate. For the load, a dead load was applied in the vertical direction and then a load was gradually increased in the horizontal direction. And a fiber model and shell model for a horizontal member were analyzed to investigate an acting of both models.

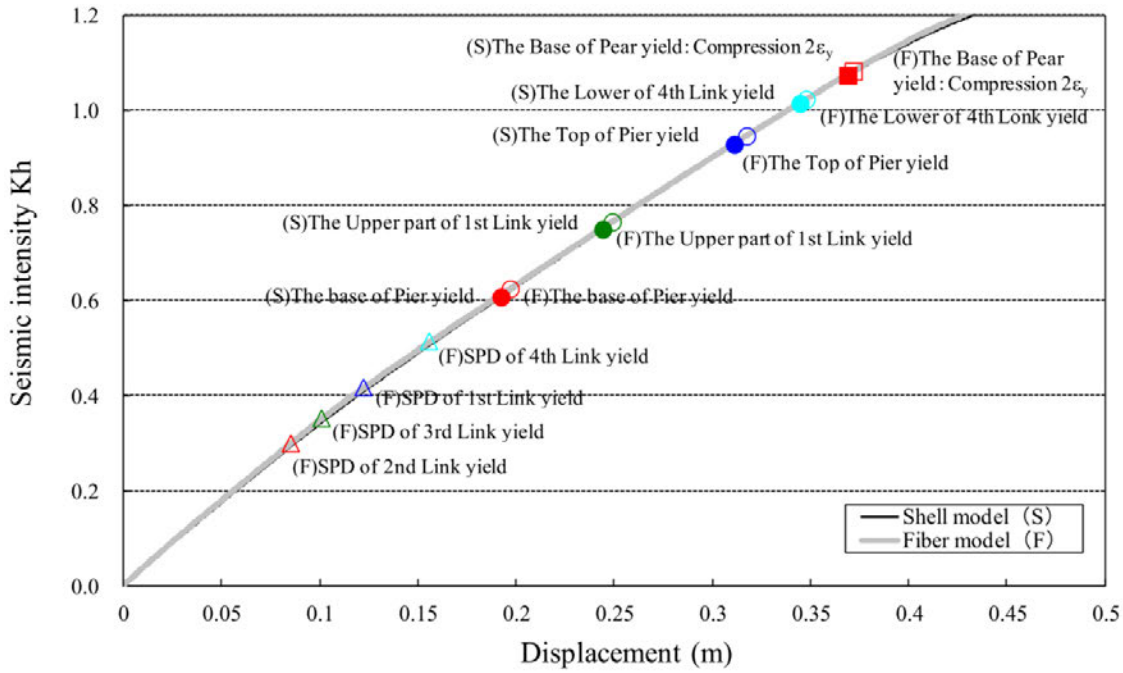

Fig-6 The load-displacement curve resulting from the pushover analysis of the Shell and Fiber models

The load–displacement curve resulting from the pushover analysis of the both models is shown in Figure 6. No significant difference of whole stiffness, a deformation performance, and load capacity of both models was found. The load capacity became larger after a shear panel was yielded. Whole bridge stiffness was controlled by the stiffness of the piers except for PD4 after a shear panel yielded. The plasticization rate (ultimate displacement / yield displacement) of the proposed type was determined to be 2.23. So absorption effects of energy can be expected in this structure.

6. Nonlinear Time History Response Analysis

This analysis was a time history response analysis incorporating geometrically and materially nonlinearity. Six standard seismic waves (Type1:3waves, Type2: 3waves), commonly used for road bridges in Japan, were used. And three scenario seismic waves (Nankai-Tonankai earthquake, Arima-Takatsuki dislocation earthquake, Uemachi dislocation earthquake) were used also. Type III soil, a comparatively poor soil, was employed, while the Newmark-beta method of numerical integration ($\beta = 1/4$) was adopted. The dominant oscillation mode is shown in Table 3. The dominant oscillation mode was in primary mode and secondary mode. In the both modes, PD4 pier was warped as contrasted with other piers.

The time history response displacement of the top of the PD4 pier for standard seismic wave (EW03) is shown in Figure 7. The maximum response displacement of the longitudinal direction was determined to be 0.299m. The maximum response displacement of the transvers direction was determined to be 0.360m. These response displacements were corresponding to allowable residual displacement.

Table-3 The dominant oscillation mode

The primary mode (T=1.06(s), f=0.04(Hz))	The secondary mode (T=0.95(s), f=1.05(Hz))
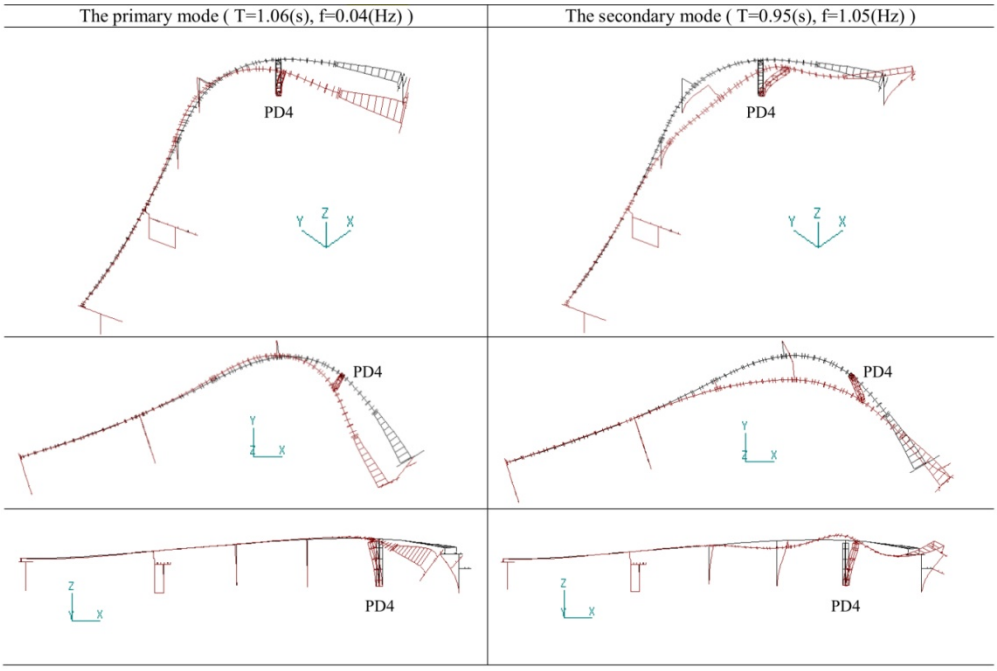	

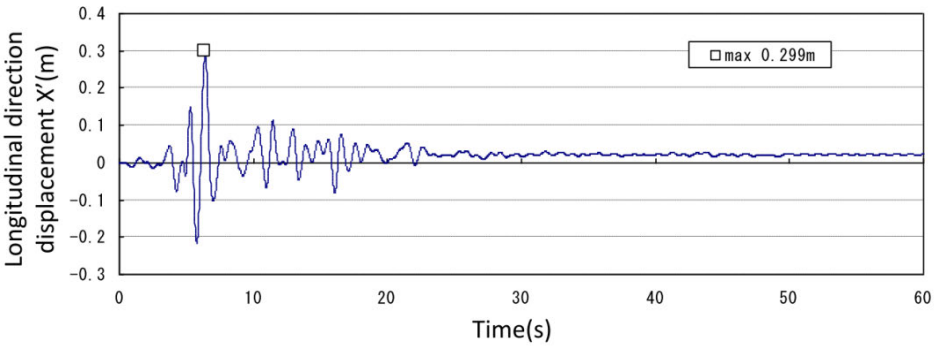

(a) Longitudinal direction

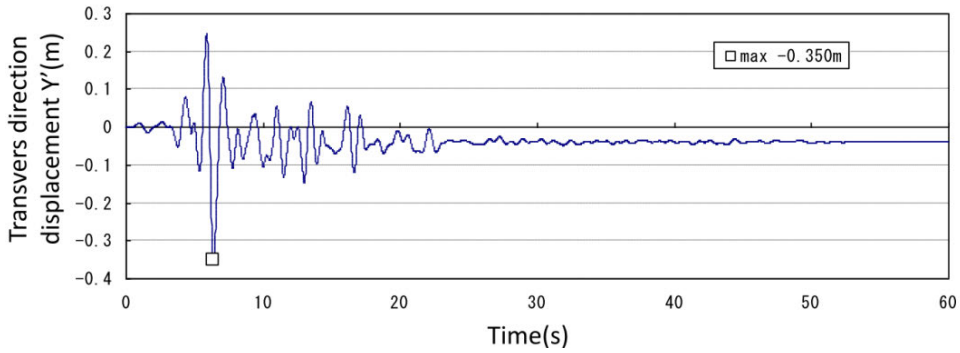

(b) Transvers direction

Fig-7 The time history response displacement of the top of the PD4 pier

In the case of severe seismic direction for PD4 pier, the maximum response strain of steel pipes is shown in Table 4. The maximum response strain of shear panel is shown in Table 5.The average of the maximum response strain of steel pipes on all members

was below $5\varepsilon_y$ correspond to soundness three of seismic performance IIb. Tension strain was determined to be $4.17\varepsilon_y$ in the base of steel pipe, $3.35\varepsilon_y$ in the upper of 1st horizontal member. Compressive strain was determined to be $2.45\varepsilon_y$ in the base of steel pipe, $1.55\varepsilon_y$ in the upper of filled concrete section. The average of maximum shear strain of shear panel was below 8% correspond to soundness three of seismic performance IIb in all shear links. The shear strain of shear panel was determine to be 3.58% as maximum strain in the shear link of 2nd, 3.40% in the shear link of 3rd. It is possible to thin thickness of steel pipe or reduces a number of shear links so that the shear panel was below allowable strain for Level 2 earthquake. But we allow shear panel to yield particularly during for Level 1 earthquake. As regards a number of shear link, energy absorption of 4 links was larger than that of three links as a result of comparison that of three shear links with that of 4 shear links during Level 2 earthquake.

Table-4 The maximum response strain of steel pipes

Part	Concrete	Tension strain $\varepsilon_{max}/\varepsilon_y$				Compressive strain $\varepsilon_{max}/\varepsilon_y$			
		Type2-1	Type2-2	Type2-3	average	Type2-1	Type2-2	Type2-3	average
The top of pier	Hollow	0.96	1.04	0.87	0.96	1.16	1.24	0.78	1.06
The upper part of 4th link	Hollow	0.52	0.56	0.36	0.48	0.58	0.58	0.5	0.55
The lower part of 4th link	Hollow	1.05	1.12	0.89	1.02	1.16	1.2	1.2	1.19
The upper part of 3rd link	Hollow	0.61	0.67	0.72	0.67	0.83	0.92	0.97	0.91
The lower part of 3rd link	Hollow	0.83	0.79	0.83	0.82	1	1.01	1.43	1.15
The upper part of concrete filled section	Hollow	0.76	0.82	0.88	0.82	1.16	1.58	2.51	1.75
The upper part of 2nd link	Concrete Filled	1.04	1.07	1.32	1.14	0.68	0.7	0.76	0.71
The lower part of 2nd link	Concrete Filled	0.82	0.81	0.9	0.84	0.47	0.44	0.5	0.47
The upper part of 1st link	Concrete Filled	3.44	2.99	3.63	3.35	1.55	1.36	1.75	1.55
The lower part of 1st link	Concrete Filled	1.02	1.01	1.26	1.1	0.93	0.9	0.97	0.93
The base of pier	Concrete Filled	4.55	3.78	4.17	4.17	2.79	2.08	2.49	2.45
maximum		4.55	3.78	4.17	4.17	2.79	2.08	2.51	2.45

Table-5 The maximum response shear strain of shear panel (Unit :%)

Shear link position	Allowable Shear Strain	Maximum Shear Strain				Check
		Type2-1	Type2-2	Type2-3	Average	
4th link	8.00	1.53	1.65	1.43	1.54	OK
3rd link	8.00	3.43	3.53	3.23	3.40	OK
2nd link	8.00	3.64	3.67	3.44	3.58	OK
1st link	8.00	1.88	1.85	1.76	1.83	OK

7. Fabrication Accuracy of Steel Pipes

Spiral steel pipes applied to the proposed pier are usually supplied for piles. Therefore the pipe suppliers don't manufacture pipes with high accuracy such as steel piers. The manual for design of the proposed pier[3)] requires that the steel pipe of the proposed pier should meet the accuracy same as general ordinary steel piers. Differences of the fabrication accuracy between the manual and JIS (Japanese Industrial Standards) A 5525 is shown in Table 6. If a manufacture supplied isn't satisfied with the manual, a

fabricator must revise a manufacture to satisfy accuracy of steel pipes. In this construction, a fabricator didn't need to revise a manufacture so that the manufacture supplied was satisfied with the manual. It seems the opportunity to use spiral steel pipes for steel pier increase in the future. So we need to discuss with mill makers about the accuracy of steel pipes.

Table-6 Differences of fabrication accuracy between the manual and JIS A 5525

	The manual of design and construction for Integrated Steel Pipe Pier	JIS A 5525 Japanese Association for Steel Pipe Piles
Circularity of Steel Pipe	Below 0.5% for the internal diamiter	Below 1.0% for the internal diamiter
Dislocation between both plates	±2mm	±4mm
Sampling level of radiographic examination for shop welding joints	1 joint every 1group	1 joint every 10 joints and a fraction

8. Welding Workability

In the junction where a superstructure meets steel pipes, it is worried that an interference of members and a deterioration in the quality of welding workability. So we made sure about interferences of members and the deterioration of welding workability using 3D-CAD. A example of checking interferences of members are shown in Figure 8. Situations of checking the quality of welding workability using full scale model are shown in Picture 2.

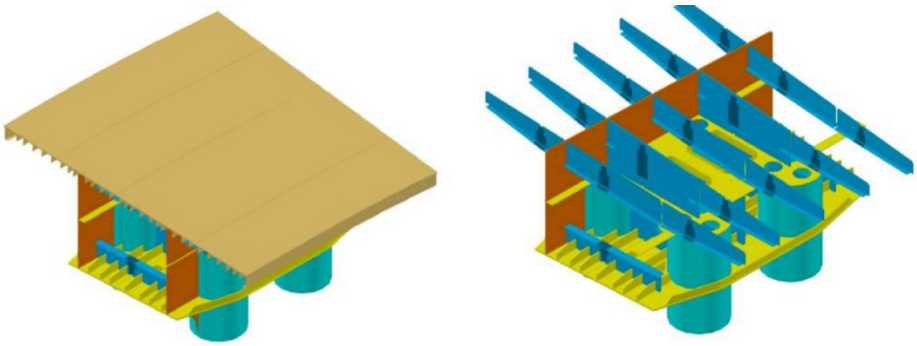

(a) 3D CAD with Deck model (b) 3D CAD without Deck model

Fig-8 3D-CAD example for checking interferences of members

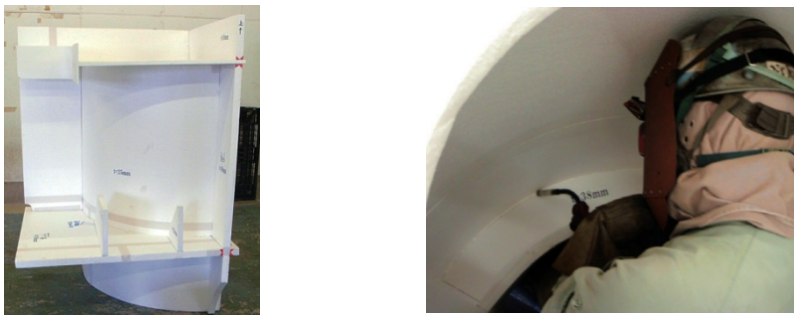

(a) Full scale model (b) Situation for checking the quality of welding workability using full scale model.

Picture-2 Checking the quality of welding workability using full scale model

9. The outline of Construction

The construction flowchart of the proposed pier is shown in Figure 9. The proposed pier under construction is shown in Picture 3 and 4.

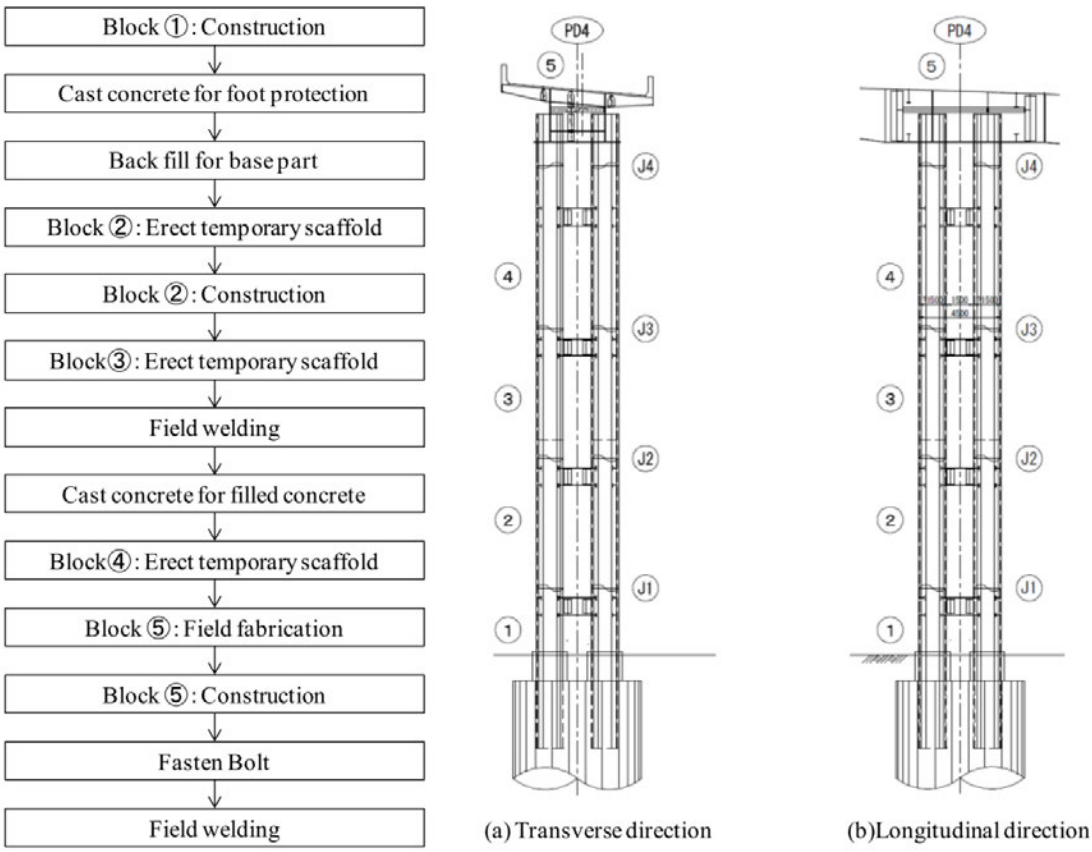

Fig-9 Construction flowchart

Picture-3 A steel pipe under erection

Picture-4 The proposed pier under construction

10. Conclusion

This paper describes the outline of design and construction of highway viaduct supported by new steel pipe integrated pier with shear links where is Ebie junction which connects the Yodogawa-sagan route to the Kobe route of Hanshin expressway (see Picture 5). The following conclusions were made:

(1) We proposed an innovative integrated steel pipe pier using damage control design. This design method leads major damage into shear panels that connect each steel pipe.

(2) The required seismic performance of four phases is determined in checking a design of the proposed pier. It has been thought it is difficult to control damage for great earthquake in terms of cost performance so far. The application of the damage controlled design enables the proposed pier to control damage of main member.

(3) A pushover analysis was conducted to investigate the deformation performance, load capacity, and plasticization rate. The plasticization rate (ultimate displacement / yield displacement) of the proposed type was determined to be 2.23.So absorption effects of energy can be expected in this structure.

(4) As result of time response analysis, the average of the maximum response strain of steel pipes on all members was below $5\varepsilon_y$ correspond to soundness three of seismic performance IIb.

(5) Finally, this paper describes measures against problems on fabrication and the outline of construction of PD4 pier, steel pipe integrated pier.

Picture-5 Steel Pipe Integrated Pier with Shear Link (Ebie junction)

11. References

1) Masatsugu SHINOHARA, Hidesada KANAJI:"Seismic performance of Integrated Steel Pipe Bridge Pier", IABSE Symposium London 2011: Taller, Longer, Lighter, September 2011.
2) Steel Bridge Seismic Resistance Subcommittee of the Performance-based Design Research Committee of the Japanese Society of Steel Construction: Fundamentals and Applications of Seismic Resistant Design for Piers, September 2002.
3) Hanshin Expressway Company Limited: The manual for Design, Fabrication and Construction of the Integrated Steel Pipe Pier, April 2011.
4) Masatsugu SHINOHARA, Hidesada KANAJI, Takashi KOSAKA, Tsutomu IMAI: Design and Construction of Highway Viaduct Supported by New Steel Pipe Integrated Pier with Shear Link, 9th German - Japanese Bridge Symposium, September 2012.

A PRECAST, PRETENSIONED, ROCKING BRIDGE BENT FOR RAPID CONSTRUCTION AND HIGH SEISMIC PERFORMANCE

Marc O. Eberhard[1], John Stanton[2], David Sanders[3], Jeffrey Schaefer[4], Bryan Kennedy[5], Travis Thonstad[6], Olafur Haraldsson[7] and Islam Mantawy[8]

Abstract

A new, rocking, pre-tensioned bridge bent system has been developed that 1) reduces construction time by precasting the beams and columns, 2) minimizes post-earthquake residual displacements by incorporating unbonded, pre-tensioned strands in the columns, and 3) reduces earthquake damage with rocking connections at the ends of the columns. Cyclic tests of subassemblies have demonstrated that the system can deform to drift ratios of around 6% with minimal damage and negligible residual displacements. Planned shaking table tests of a three-bent, two-span bridge at the University of Nevada, Reno will be used to evaluate the dynamic performance of the system.

Introduction

Within the United States, the design of reinforced concrete bridges in seismic regions has changed little since the mid-1970s, when ductile details were first introduced. Nearly all bridge bents (intermediate supports) in seismic regions are constructed of cast-in-place reinforced concrete. Many of these cast-in-place bridges have performed well in the past, but to meet modern design expectations for bridges, new structural systems and construction methods are needed to improve: 1) speed of construction, 2) seismic resilience and 3) durability.

A new concept has been developed that addresses each of these three concerns. This paper describes the concept, constructability and the results of subassembly testing of components of the new system. Two-span, three-bent shaking table tests are planned for 2014 at the University of Nevada, Reno Network for Earthquake Engineering Simulation (NEES) facility.

[1] Professor, University of Washington, Seattle, USA.
[2] Professor, University of Washington, Seattle, USA.
[3] Professor, University of Nevada, Reno, USA
[4] Graduate Student Assistant, University of Washington, Seattle, USA.
[5] Graduate Student Assistant, University of Washington, Seattle, USA.
[6] Graduate Student Assistant, University of Washington, Seattle, USA.
[7] Graduate Student Assistant, University of Washington, Seattle, USA.
[8] Graduate Student Assistant, University of Nevada, Reno, USA.

Concept

The new system, shown schematically in Figure 1, has the following key features.

- The columns and beams are cast off-site and then assembled rapidly once they arrive on-site. Precasting not only accelerates construction, it also tends to improve worker safety and construction quality.

- Construction is further accelerated by using a "wet socket" connection between the column and the spread footing (Haraldsson et al. 2013). In this connection, the precast column is placed in the footing excavation, and the footing concrete is cast in place around it. To facilitate the transfer of forces into the surrounding concrete, the base of the column has a roughened exterior with a saw-tooth detail. No bars cross the interface between the precast column and cast-in-place footing. The column longitudinal bars are not bent out as they are in conventional construction, but instead, they are developed using mechanical anchors within the part of the column that is embedded in the footing. This design facilitates transportation, increases safety (no protruding bars), and improves performance (compared with bent-out bars).

- Post-earthquake residual displacements are reduced by pre-tensioning the precast bridge columns with unbonded tendons, which are designed to return the system to its original plumb position when the ground motion stops.

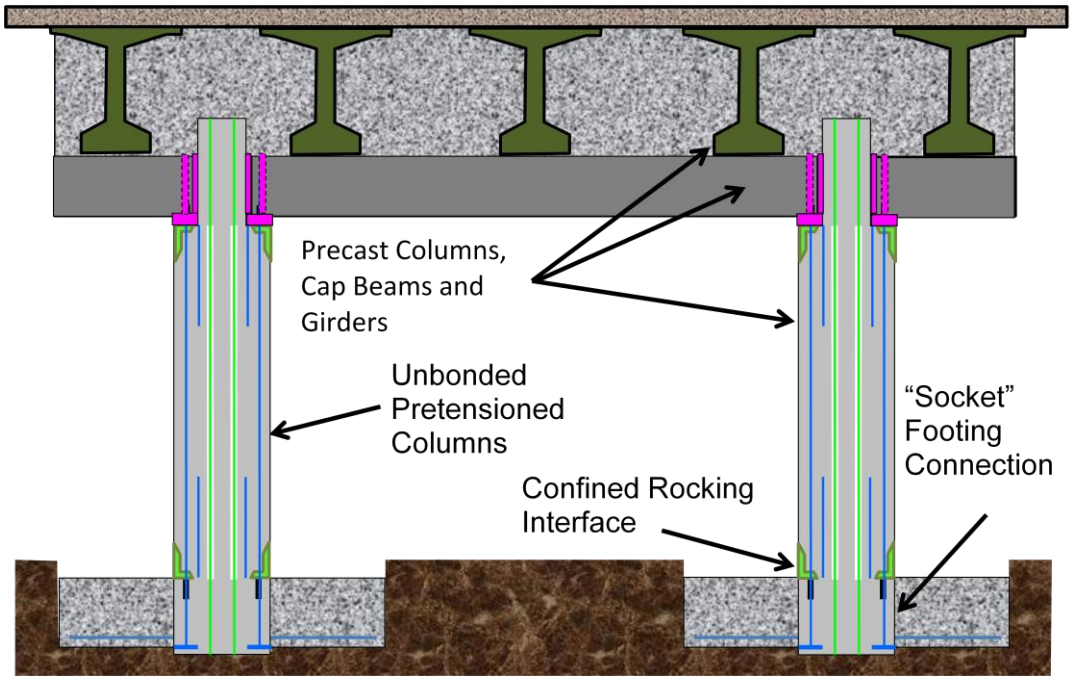

Figure 1. Precast, Pretensioned Rocking Column Bent Concept

- Damage to the system is minimized by incorporating a new rocking detail at the ends of the columns, as shown for the base of the column in Figure 2. The concrete at the interface is confined by a steel jacket (or "shoe"), which consists of circular steel pipe welded to an end plate, upon which the interface rocks. The longitudinal bars are debonded near the interface to distribute the bar elongation over a sufficient length to prevent bar failure at the design deformation. Discontinuous bars are also included in the system to help resist large compressive forces at the rocking interface, and to ensure that deformations are concentrated at this interface rather than above the shoe.

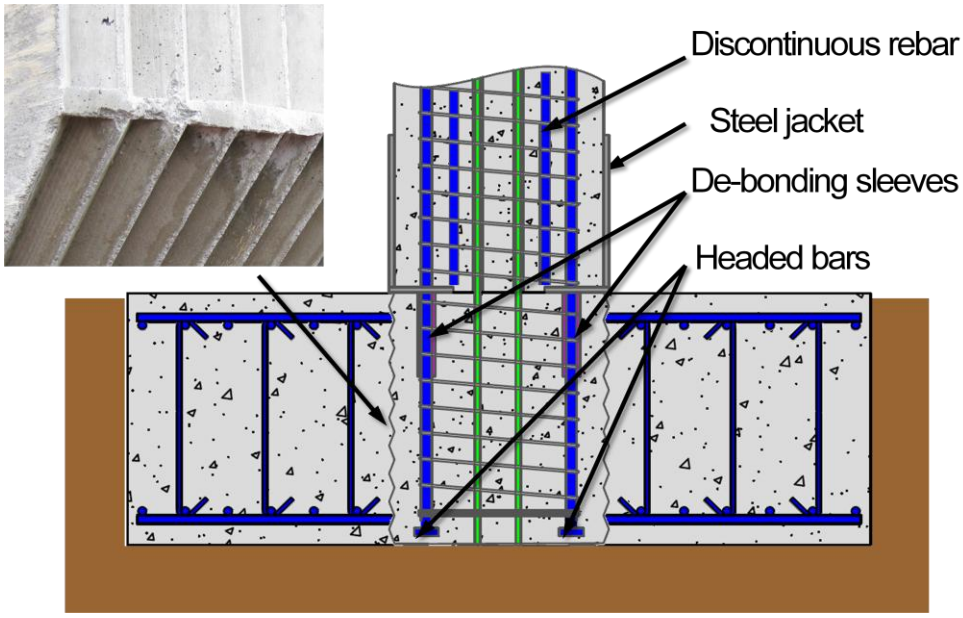

Figure 2. Base Detail for Precast, Pretensioned Rocking Column Bent

Rapid Construction

A non-prestressed version of the precast bent system was deployed in Washington State as part of the construction of a bridge over Interstate-5 (Khaleghi et al. 2012). The bridge had two spans, tall abutments on the ends and a center pier with four columns (Fig. 3).

The precast columns were connected to the cast-in-place spread footings using a wet socket connection (Haraldsson et al. 2013). The tops of the precast columns were connected to the precast cap-beam using a large-bar connection (Pang et al. 2010). The cap-beam was made in two segments because of weight constraints. No major problems were encountered during construction, and alignment was straightforward (Khaleghi et al. 2012). The placement of each cap-beam segment took less than 30 minutes. The precast, pre-tensioned rocking system has similar construction details as the non-prestressed system, so it could be assembled similarly, as illustrated in Figure 4

Figure 3. Construction of Precast Column Bent (without pretensioning)

Test of Sub-Assemblies

The resistance and damage progression of the top and bottom connections were evaluated with quasi-static tests of a column-to-spread-footing connection subassembly (PreT-SF-Rock) and a column-to-cap-beam connection subassembly (PreT-CB-Rock).

The columns were designed to have a strength similar (at 42% scale) to that of a typical reinforced concrete column. For both subassemblies, the octagonal columns had a diameter (flat-to-flat) of 20 in. (508 mm) and a cantilever length of 60 in. (1524 mm), resulting in a cantilever span-to-depth ratio of 3.0. The columns were subjected to a constant axial load while cyclic, lateral displacements were applied to the column. The loading setup is shown in Figure 5.

The cyclic performance of the subassemblies (Figure 6) greatly exceeded that of a comparable conventional reinforced concrete column connection (e.g., Pang et al. 2010).

- For peak drift ratios up to approximately 6%, the columns returned to their undeformed geometry upon unloading.

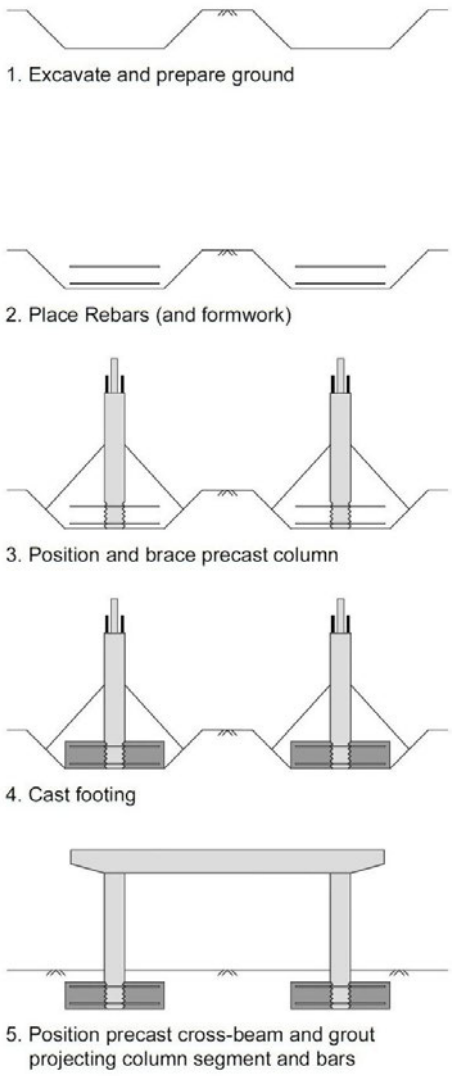

Figure 4. Construction Sequence

- The columns continued to resist nearly 100% of the peak lateral load after having been subjected to two cycles of deformation at a drift ratio of 10.4%.

- No spalling or bar buckling was observed during the tests, and the joint grout in the top connection suffered only cosmetic damage. The longitudinal bars for the column-to-spread-footing specimen fractured after being subjected to a drift ratio of 5.9%. The column-to-cap-beam bars, which had a longer debonded length, fractured after being subjected to a drift ratio of 7.0%.

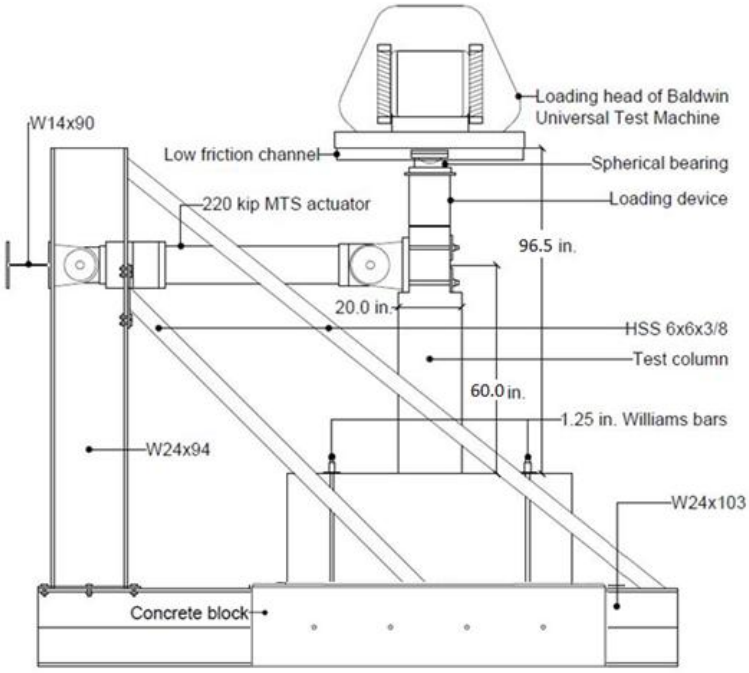

Figure 5. Loading Setup for Subassembly Tests

Planned Shaking Table Tests

The performance of the pretensioned, rocking bridge bent system will be evaluated with a three-bent, two-span shaking table tests at the NEES facility at the University of Nevada, Reno in 2014. The columns of the bents have been designed to perform (at 25% scale) similarly to those tested statically at the University of Washington. Figure 7 shows a schematic drawing of the shaking table specimen.

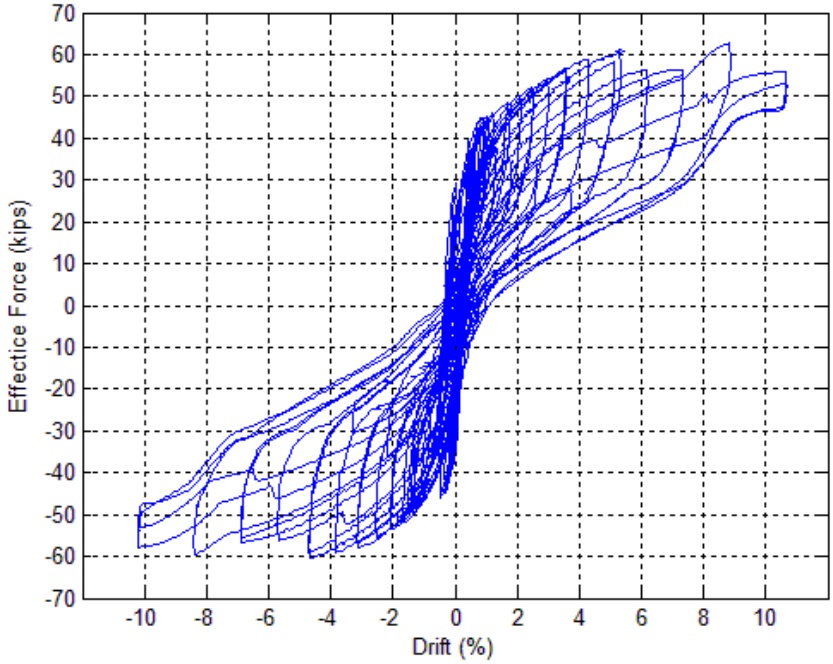

(a) Column Connection to Spread Footing (Pret-SF-Rock)

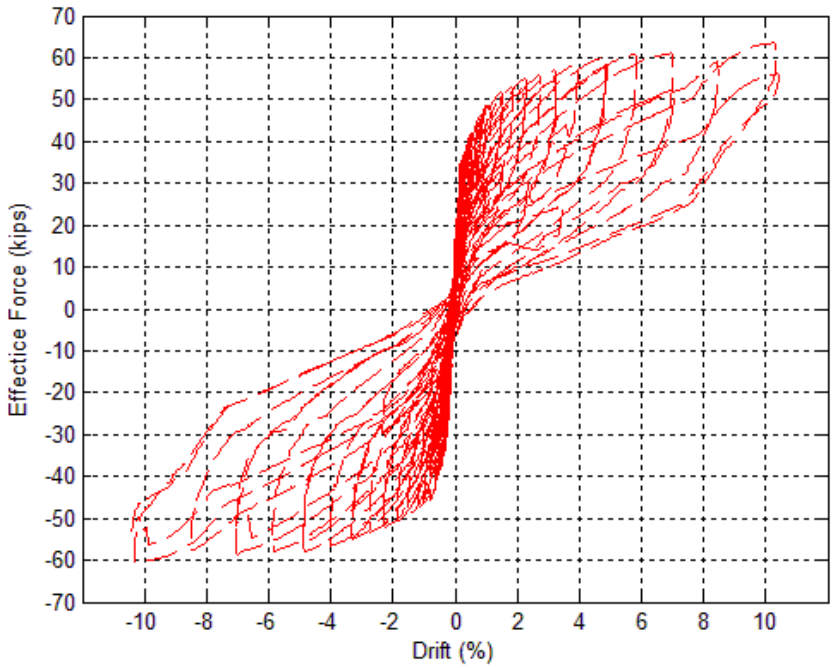

(b) Column Connection to Cap Beam (Pret-CB-Rock)

Figure 6. Measured Effective-Force vs. Drift Ratio Responses of Rocking Connection Sub-Assemblies

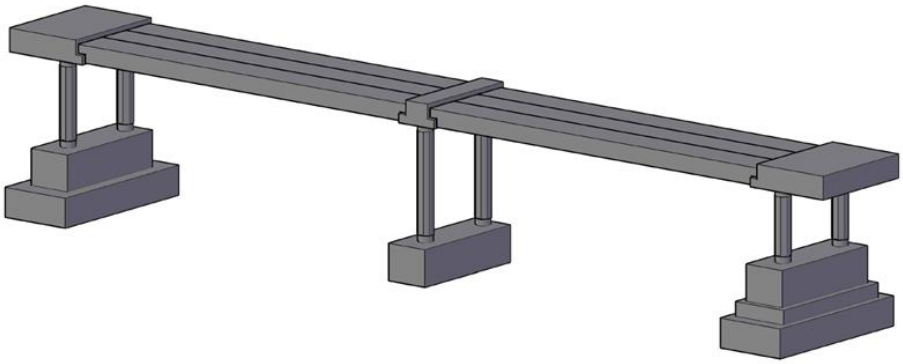

Figure 7. Schematic of Shaking Table Specimen

Conclusions

A new pretensioned, rocking column bridge bent system has been developed to accelerate bridge construction and improve seismic resilience.

- Field experience with a similar, non-prestressed system suggests that the new system could be constructed rapidly.

- Quasi-static tests of a column-to-spread-footing subassembly and a column-to-cap-beam subassembly indicate that the new system would perform better than a conventional reinforced concrete bridge. The lateral strength appears to degrade more slowly, the column re-centers at larger drift ratios, and the column suffers less damage.

- Upcoming shaking table tests of a three bent, two-span bridge will provide an evaluation of the dynamic performance of the system.

Acknowledgments

This research was supported by the Pacific Earthquake Engineering Research (PEER) Center and the National Science Foundation Network for Earthquake Engineering Research Program (Award #1207903). The findings and conclusions contained herein are those of the authors alone.

The quasi-static tests were conducted at the University of Washington with the help of graduate students Lisa Berg, Spencer Livermore, Kevin Martin, Tony Nguyen, Max Stephens and Hung Viet Tran. Further help was provided by undergraduate students Sam Adiputra, Matt Brosman, Nathan Clemens, David Lam, Scott Laws, Kevin Tsuchida, Hin-Kei Wong and Chase Young. The assistance of Professor Donald Janssen and Laboratory Manager Vince Chaijaroen is also gratefully acknowledged.

References

1. Haraldsson, O.S., Janes, T.M., Eberhard, M.O. and Stanton, J.F. (2013). "Seismic Resistance of Socket Connection between Footing and Precast Column." Journal of Bridge Engineering, ASCE, September, pp 910-919. 10.1061/(ASCE)BE.1943-5592.0000413.

2. Khaleghi, B., Schultz, E., Seguirant, S., Marsh, L., Haraldsson, O., Eberhard, M. and Stanton, J. (2012). "Accelerated Bridge Construction in Washington State -- From Research to Practice", PCI Journal, Autumn, pp. 34-49.

3. Pang, J.B.K., Eberhard M.O. and Stanton, J.F. (2010). "Large-Bar Connection for Precast Bridge Bents in Seismic Regions." Journal of Bridge Engineering, ASCE, May-June, pp. 231-239.

An Experimental Study on Seismic Performance of Hybrid Steel piers with Vertical Ribs Made from SBHS700

Kiyoshi Ono[1], Masahide Matsumura[2] and Seiji Okada[3]

Abstract

Some methods for evaluating the seismic performance of steel bridge piers have been already proposed in the previous studies. Steel bridge piers are sometimes required to have seismic performance that ductility is improved with restraining increase in ultimate strength but it is difficult to fulfill such seismic performance by the proposed methods in previous studies. By the way, "Higher yield strength steel plates for bridges" has been standardized in Japanese industrial Standard (JIS). The major feature of higher yield strength steel plates for bridges, SBHS, is high yield strength and high weldability. Among SBHS, SBHS700 has the highest yield strength and the highest tensile strength. There is possibility of fulfilling the seismic performance of steel bridge piers which has been difficult to gain so far by applying SBHS700 to them. Therefore, the purpose of this study is to investigate material properties of SBHS700 and the seismic performance of hybrid steel bridge piers whose vertical ribs are made from SBHS700.

Introduction

The Kobe Earthquake in 1995 caused the huge damage to highway bridges like never seen before in Japan. The seismic design specifications for highway bridges were revised in 1996 (Japan Road Association. 1996) in consideration of the damage and the ductility design method, which had already been adapted to reinforced concrete bridge piers, was also introduced to steel bridge piers. After that, seismic design specifications were revised in 2002 and 2012(Japan Road Association. 2002, 2012) and more detailed seismic design methods for steel bridge piers have been specified in the 2012 seismic design specifications . Steel bridge piers are often constructed under the condition that the area of construction sites is restricted or the soil condition is not good. The seismic performance that ductility is increased with restraining increase in ultimate strength is one of required or desirable performance. However, it is difficult to fulfill such seismic performance by the proposed methods in previous studies.

By the way, "Higher yield strength steel plates for bridges" has been standardized in Japanese industrial Standard, "JIS" (Japanese Standards Association.2008). The major

[1]Associate Professor, Dept. of Civil Engineering, Osaka University
[2] Associate Professor, Dept. of Civil Engineering, Osaka City University
[3] Bridge Design Department, IHI Infrastructure Systems Co., Ltd.

feature of higher yield strength steel plates for bridges, SBHS, is high yield strength and high weldability. Among SBHS, SBHS700 has the highest yield strength and the highest tensile strength. There is possibility of fulfilling the seismic performance of steel bridge piers which has been difficult to gain so far by applying SBHS700 to them. However, information on stress-strain relationship and the mechanical properties like the yield stress, the tensile strength and the elongation of SBHS700 is not sufficient compared with the other rolled steel for welded structure like SM490 and SM570 (Murakoshi et al. 2008). Moreover, little is known about the seismic performance of steel bridge piers made from SBHS700 .

Therefore, this study is intended as an investigation to investigate material properties of SBHS700 and the seismic performance of hybrid steel bridge piers whose vertical ribs are made from SBHS700

Material Properties of SBHS700

(1) Tensile Tests and Mechanical Properties of SBHS700

Table 1 shows the mechanical properties of SBHS700 specified in JIS and those of HT80 specified in Honshu Shikoku Bridge Standards (HBS). HT80 is high strength steel and it was applied to Honshu Shikoku bridges. As shown in Table 1, mechanical properties such as the yield stress and the tensile strength of SBHS700 are almost the same as those of HT80.

Table 2 shows the types of test specimens and the number of test specimens. The tensile tests were conducted with the test specimens made according to specifications in JIS. The test specimens were cut along rolling direction (R-specimen) and perpendicularly to rolling direction (P-specimen). The plate thickness is 9mm and 12mm. The total number of test specimens is 20.

Table 3 shows the average values of test results. Figure 1 shows the nominal stress - nominal strain (σ_N - ε_N) relationship obtained from the tensile tests. Figures 2, 3, 4 and 5 show the fluctuation of yield stress (upper yield stress or proof stress) σ_y, tensile strength σ_u, elongation and yield ratio YR (σ_y/σ_u) , respectively. The blue dotted lines (- - -) in Figures 1 and 2 indicate the minimum yield stress specified in JIS, the green piece of dashed lines (— . —) in Figures 1 and 3 show the range of tensile strength specified in JIS and the red two-dot chain lines (— . . —) in Figure 5 show the minimum elongation specified in JIS. The outline of the mechanical properties of SBHS700 in this study shown in Figures 1～5 is as follows.

(a) The yield stress is much higher than the minimum yield stress in JIS and it is almost the same as the minimum tensile strength in JIS.

(b) The tensile strength is almost the same as the minimum tensile strength in JIS

(c) The yield ratio exists between 92% and 100%. Especially, the mean value of the

yield ratio of test results of R-specimen of 12mm is 99%.

Cyclic Loading Tests of Hybrid Steel Bridge Piers

(1) Test specimens

This study employed two test specimens. One of test specimens is a homogeneous test specimen "HO" and its webs, flanges and vertical ribs are made from SM490. The other is a hybrid test specimen "HY". Webs and flanges of "HY" are made from SM490 and vertical ribs are made from SBHS700. Figure 6 indicates the nominal stress - nominal strain relationship of SBHS700 and SM490 which were used in test specimens. As shown in Figure 6, the yield stress and tensile strength of SBHS700 are much higher than those of SM490.

The outline of the configuration of the test specimens is given in Figure 4. The values of the major parameters of the test specimens are listed in Table 4. In Table 4, N_{yN} is the yield axial force, R_{RN} and R_{FN} are the buckling parameters of the plates between longitudinal stiffeners and overall stiffened plates respectively. $\bar{\lambda}_N$ is the slenderness ratio parameter. The definitions of parameters mentioned above are identical to those stipulated in the 2014 seismic design specifications (Japan Road Association. 2014) and are noted below. As for a hybrid test specimen "HY", yield stress σ_{yN} of webs and flanges are different from that of vertical ribs because web and flanges are made from SM490 and vertical ribs are made from SBHS700. It is impossible to calculate N_{yN}, R_{FN} and $\bar{\lambda}_N$ of a hybrid test specimen "HY" according to the following equations (1), (3) and (4) respectively. Therefore, yield stress of SM490 was substituted into equations (1), (3) and (4) in calculating N_{yN}, R_{FN} and $\bar{\lambda}_N$ of "HY".

$$N_{yN} = \sigma_{yN} \times A \tag{1}$$

$$R_{RN} = \frac{b}{t}\sqrt{\frac{\sigma_{yN}}{E}\frac{12\left(1-\nu^2\right)}{4\pi^2 n^2}} \tag{2}$$

$$R_{FN} = \frac{b}{t}\sqrt{\frac{\sigma_{yN}}{E}\frac{12\left(1-\nu^2\right)}{\pi^2 k_F}} \tag{3}$$

$$\bar{\lambda}_N = \frac{1}{\pi}\sqrt{\frac{\sigma_{yN}}{E}}\frac{2h}{r} \tag{4}$$

where σ_{yN} = nominal yield stress of SM490 specified in JIS (=315N/mm^2); A = sectional area; h = column height (distance from the bottom of the column to the point at which horizontal load is applied); r = radius of gyration of cross section; E = Young's modulus of steel; b = width of flange or web; t = plate thickness of webs and flanges; ν = Poisson's ratio of steel (=0.3); n = number of panels of webs and flanges; k_F = the bucking coefficients.

(2) Loading Conditions

Each test specimen was loaded with hydraulic jacks installed in a stiff frame. In each experiment, the specified compressive axial force shown in Table 7 was first applied to the test specimen using a vertical hydraulic jack. The levels of compressive axial force, N, applied to each test specimen was 15% of yield axial force, N_{yN}, calculated by equation (1) above.

The axial force was kept constant during the cyclic loading experiments. The cyclic loading patterns of horizontal displacement are schematically shown in Figure 8, where δ_{yN} is calculated by the following equation. As for a hybrid test specimen "HY", nominal yield stress of SM490 was substituted into equation (6).

$$P_{yN} = \left(\sigma_{yN} - \frac{N}{A} \right) \frac{Z}{h} \tag{5}$$

$$\delta_{yN} = \frac{P_{yN} h^3}{3EI} \tag{6}$$

where I = moment of inertia and Z = section modulus.

(3) Experimental Results and Comments

Figure 9 shows the horizontal load - horizontal displacement relationship (P-δ relationship). Figure 10 shows enveloped curves gained from P-δ relationship in Figure 9. As shown in Figure 10, maximum horizontal load and the ductility (horizontal displacement at maximum horizontal load) of a hybrid specimen "HY" is larger than those of a homogeneous test specimen "HO". However, increasing rate of the ductility is larger than that of the maximum horizontal load. The test results indicate the possibility that hybrid steel bridge piers whose stiffeners are made from SBHS700 may realize the performance that ductility can be increased with restraining increase in ultimate strength. Figure 11 expresses the progress of the out-of-plane deformation of the flange panel in the compression side at the base section. It is found that out-of-plane deformation of "HY" is smaller than that of "HO" at the same cyclic loop. Judging from Figures 6 and 11, the reason why P-δ relationship that ductility can be increased with restraining increase in ultimate strength can be fulfilled is guessed as follows although the detailed has to be conducted in the future works.

・The yield stress of SBHS700 is much larger than that of SM490 as shown in Figure 6.

・The stress level of vertical ribs made from SBHS700 of a hybrid test specimen remains in elastic range and the vertical ribs have enough stiffness for restraining the large out-of-plane deformation of flange panels although the stress level of flange panels made from SM490 is beyond yielding and reaches plastic range.

・The ductility of a hybrid test specimen is increased compared with a homogenous test specimen which corresponds to a conventional type of steel bridge piers because the progress of out-of-plane deformation of flange panels of a hybrid test specimen are slow as compared with a homogeneous test specimen shown in Figure 11.

Conclusions

In this study, the tensile tests of SBHS700 were conducted. Based on results of tensile tests, the information on mechanical properties and stress-strain relationship of SBHS700 is obtained. Furthermore, cyclic loading experiments were conducted with two types of test specimens. One of test specimens is a homogeneous test specimen whose webs, flanges and vertical ribs are made from SM400. The other is a hybrid test specimen whose webs and flanges are made from SM400 and whose vertical ribs are made from SBSH700. The test results indicate the possibility that hybrid steel bridge piers whose stiffeners are made of SBHS700 may realize the performance that ductility can be increased with restraining increase in ultimate strength.

Acknowledgments

This work was supported by JSPS KAKENHI Grant Number 22560476 and by the Japan Iron and Steel Federation.

References

Honshu-Shikoku Bridge Authority(1978). HBS G 3102.

Japan Road Association (1996). *Specifications for highway bridges, Part V: Seismic Design*.

Japan Road Association (2002). *Specifications for highway bridges, Part V: Seismic Design*.

Japan Road Association (2012). *Specifications for highway bridges, Part V: Seismic Design*.

Japanese Standards Association (2008). Higher yield strength steel plates for bridges, JIS G 3140.

Jun Murakoshi, Naoki Yanadori, Noriyasu Arima, Hideki Shimizu and Daisuke Komori (2008) , “The investigation of the statistical data of the strength of steel materials”, Technical Note of PWRI, No. 4090.

Table 1 Mechanical Properties of SBHS700 and HT 80 Specified in Standard

(a) SBSH700

	Yield stress or Proof stress σ_y (N/mm^2)	Tensile strength σ_u (N/mm^2)	Elongation		
			Plate thickness t (mm)	Test specimen	%
SBHS700	≧700	780～930	6≦ t ≦16	JIS-5	≧16
			16＜ t ≦20	JIS-5	≧24
			20＜ t ≦75	JIS-4	≧16

(b) HT80

	Plate thickness t (mm)	Yield stress or Proof stress σ_y (kg/mm^2)	Tensile strength σ_u (kg/mm^2)	Elongation		
				Plate thickness t (mm)	Test specimen	%
HT80 (HT780)	8≦ t ≦50	≧70	80～95	8≦ t ≦16	JIS-5	≧16
				16＜ t ≦25	JIS-5	≧22
	50＜ t ≦75	≧68	78～93	25＜ t ≦75	JIS-4	≧16

Table 2 Test Specimens of Tensile Tests

	Plate thickness (mm)	Cut direction	Name	Number of test specimens
SBHS700	9	Rolling	R-specimen	5
		Perpendicularly	P-specimen	5
	12	Rolling	R-specimen	5
		Perpendicularly	P-specimen	5

Table 3 Test Results of Tensile Tests

	Plate thickness (mm)	Cut direction	Yield stress σ_y (N/mm^2)	Tensile strength σ_u (N/mm^2)	Yield ratio YR (%)	Elongation (%)
SBHS700	9	Rolling	770	796	96.7	25
		Perpendicularly	784	802	97.8	24
	12	Rolling	772	818	94.4	30
		Perpendicularly	826	835	99.0	28

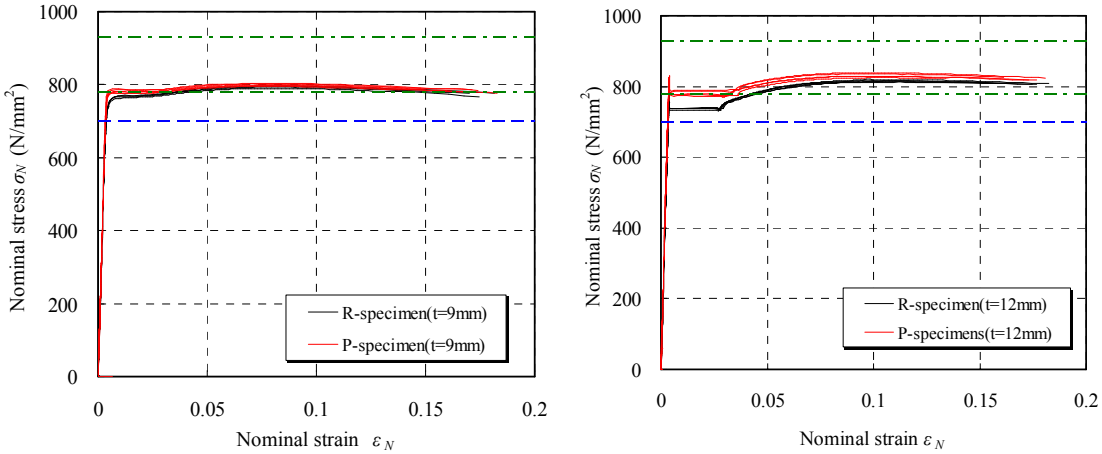

(a) t=9mm (b) t=12mm

Figure 1 Nominal Stress - Nominal Strain Relationship

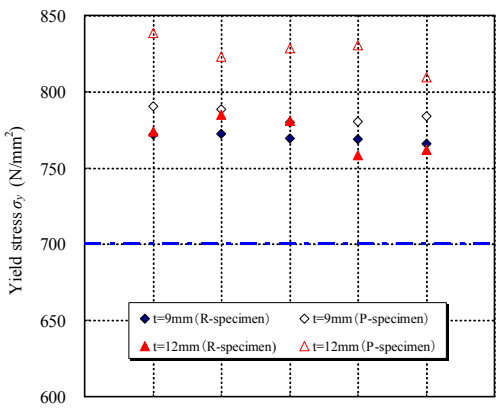

Figure 2 Yield Stress(or proof stress)

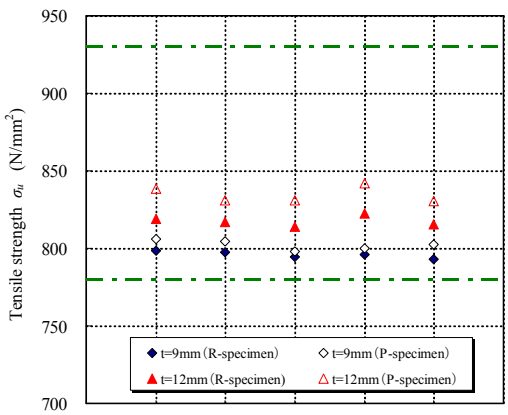

Figure 3 Tensile Strength

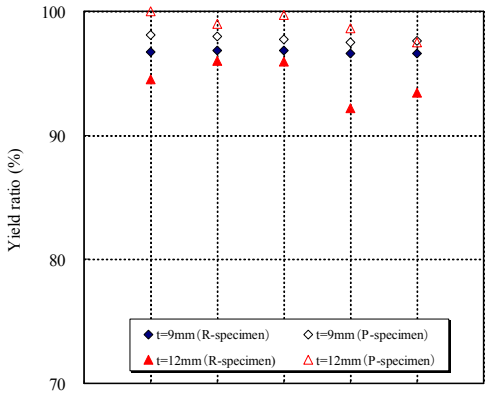

Figure 4 Yield Ratio

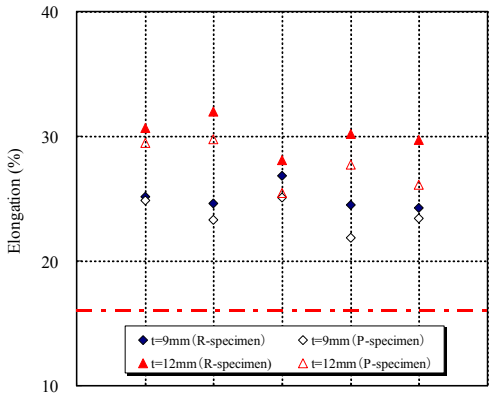

Figure 5 Elongation

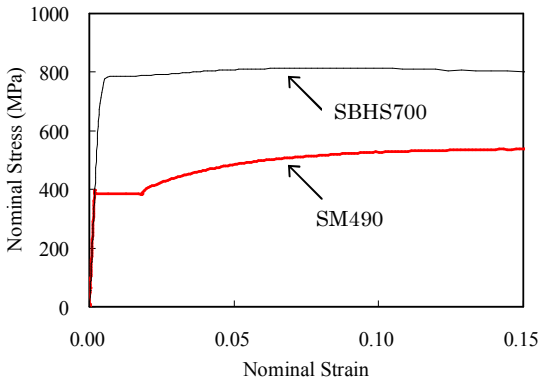

Figure 6 Nominal Stress - Nominal Strain Relationship of SM490 and SBHS700

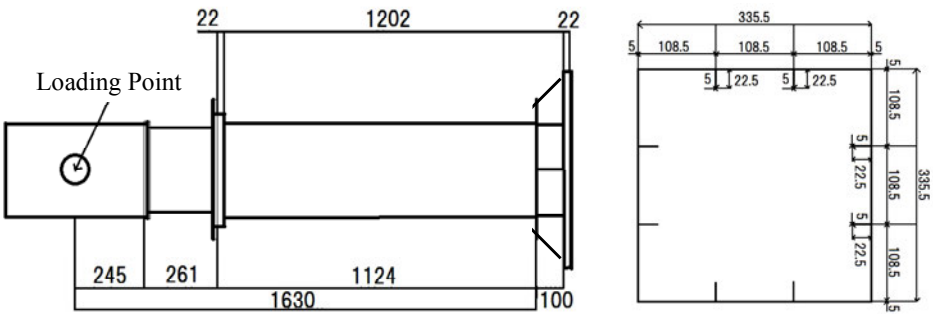

(a) Side View (b) Cross Section

Figure 7 Configuration of Test Specimen

Table 4 Major Parameters of Test Specimens

		HO	HY
N/N_{yN}		0.15	
λ_N		0.32	
R_{RN}		0.49	
R_{FN}		0.44	
Steel grade	Flanges, Webs	SM490	SM490
	Vertical ribs	SM490	SBHS700

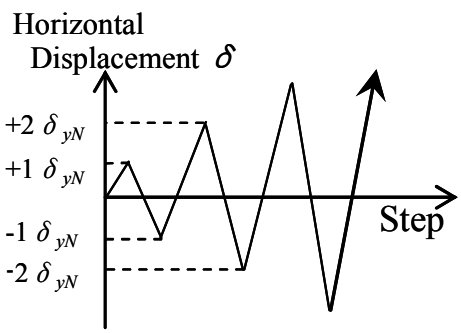

Figure 8 Cyclic Loading Patterns

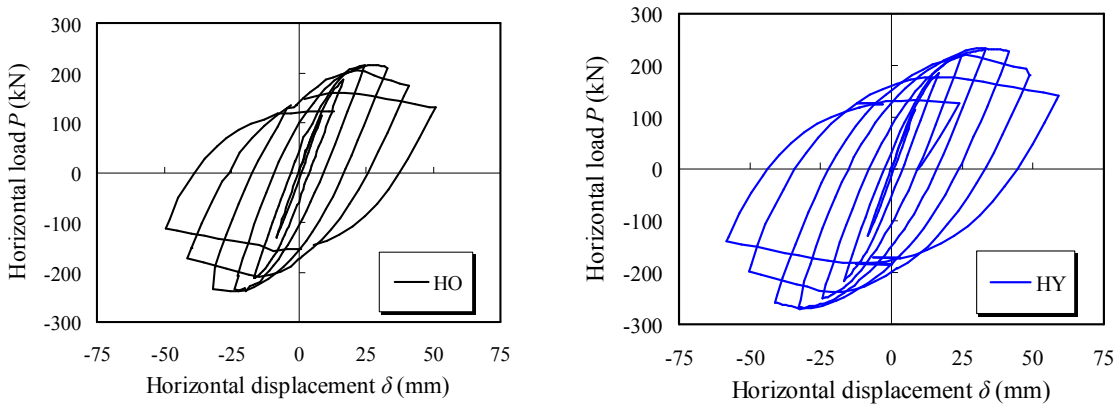

(a) HO (Homogeneous Specimen) (b) HY (Hybrid Specimen)

Figure 9 Horizontal Load - Horizontal Displacement Relationship

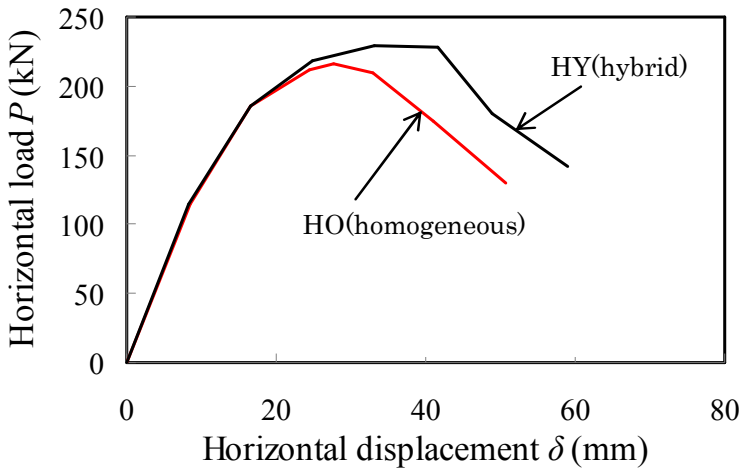

Figure 10 Comparison of Enveloped Curves

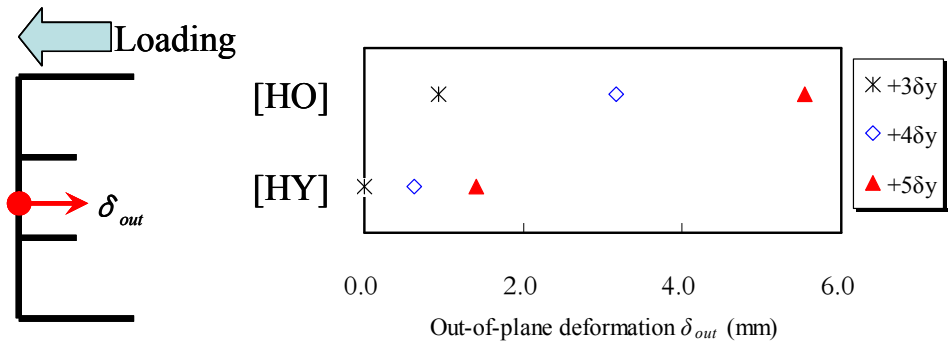

Figure 11 Progress of Out-of-plane Deformation of Flange Panel

A NEW MODEL FOR SUSTAINABLE SOLUTIONS TO BRIDGE INFRASTRUCTURE SUBJECTED TO MULTIPLE THREATS (SSIMT)

Jamie E. Padgett[1]

Abstract

Aging, increased traffic, and natural hazards all threaten bridge performance. These threats result in physical damage, and cascading social, environmental, and economic impacts that impair sustainability. A scientific approach is needed to mitigate risks to bridges posed by multiple threats while balancing broader objectives of sustainability. Therefore this research proposes a new model, "*Sustainable Solutions for Bridge Infrastructure Subjected to Multiple Threats"* (SSIMT), that evaluates the effects of multiple threats on bridge reliability while taking into account sustainability implications. In addition to describing the SSIMT concept, recent developments in multi-threat bridge fragility modeling are summarized, as key input to SSIMT.

Introduction

Bridge infrastructure is susceptible to damage from a large host of threats--aging and deterioration, natural hazards that may become more frequent with climate change, and demands that increase with population growth and urbanization (ASCE 2009; Perry and Mackun 2001; RPA 2005; USDOT 2007b). Though the USDOT and many state departments of transportation (DOTs) have embraced the goal of sustainable transportation infrastructure (Jeon and Amekudzi 2005; National_Research_Council 2009; USDOT 2007a), a scientific approach is needed to mitigate risks to bridges posed by multiple threats while balancing broader objectives of sustainability. While a range of definitions for sustainable engineering exists in the literature (Amekudzi et al. 2009; Daly 1996; Goncz et al. 2007; J. E. Padgett et al. 2009; Pearce and Vanegas 2002; Taylor and Fletcher 2006; USDOE 2003; Vanegas 2003; WCED 1987), in the context of this paper, sustainable built infrastructure (e.g., bridges) effectively serves public needs while limiting adverse environmental, social, and economic impacts. Such impacts might include waste generation, energy expenditure, or emissions associated with bridge construction, maintenance, or post-disaster repair and replacement. Current approaches to bridge engineering and management tend to focus on how a single threat causes failure, and to select design or upgrade strategies using metrics limited to initial cost or deterministic performance. Such existing approaches do not take into account the fundamentals of sustainable design (Adeli 2002; Black et al. 2002; Little 2005; National_Research_Council 2009), the recently recommended principles for infrastructure investment (ASCE 2008), the reality of multiple threat exposure (MCEER 2008; Simpson et al. 2005), or the uncertainty inherent in such an analysis (Biswas 1997; Li and Ellingwood 2006; J. Padgett and DesRoches 2007). Therefore, a new model for bridge infrastructure

[1] Assistant Professor, Department of Civil and Environmental Engineering, Rice University, Houston, TX USA

engineering is proposed in this paper, "*Sustainable Solutions for Bridge Infrastructure Subjected to Multiple Threats*" (SSIMT). This model evaluates the effects of multiple threats on bridge reliability, while taking into account the social, economic, and environmental consequences that are often neglected in designing, maintaining, and rehabilitating these systems.

In the forthcoming section of this paper the proposed SSIMT model is presented, elaborating its conceptual backbone and highlighting the critical input needed to make the model a reality to support bridge engineering and management. The paper then highlights recent advances in multi-threat and multi-hazard bridge fragility modeling. Such models of the conditional probability of damage to bridges subjected to individual hazards (e.g. earthquakes or hurricanes), combined hazards (e.g. earthquakes and scour), or combined threats (e.g. earthquakes and aging/deterioration) offer critical input to the SSIMT framework by uncovering the physical vulnerability that must be modeled in order to effectively quantify sustainable impacts. The paper concludes with an indication of how such reliability models may be integrated into a sustainable assessment and offers insights and suggestions for future research.

The SSIMT Model

Currently, no analysis or upgrade approach exists to mitigate risks posed by multiple threats to bridge infrastructure while balancing broader goals of sustainability. This critical gap is addressed by providing a model for bridge infrastructure enhancement where performance goals are driven by sustainability metrics, such as energy usage, life-cycle cost, and downtime. The proposed model, "Sustainable Solutions for Bridge Infrastructure Subjected to Multiple Threats" (SSIMT), identifies

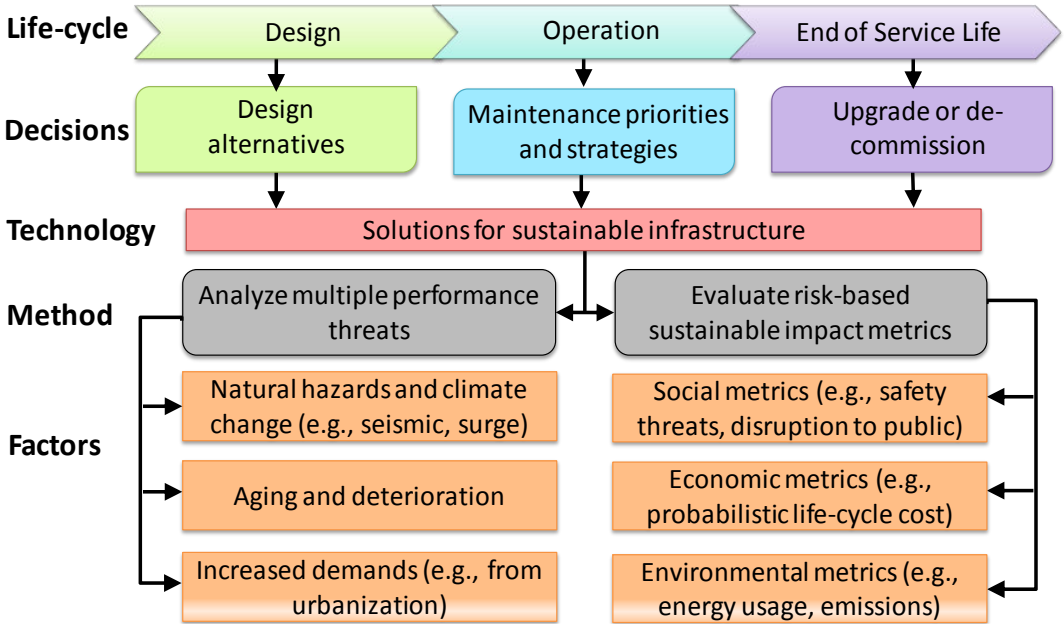

Figure 1. Concept Model for SSIMT, Demonstrating Key Decision Phases Throughout the Infrastructure Life-Cycle that can Benefit From Fusion of Multi-Threat Reliability and Sustainability Models.

methods for design and management using risk-based measures of sustainable performance that consider multiple threats over a bridge's life. Figure 1 illustrates the concept model for SSIMT. Casting multi-threat mitigation decisions within the contextual framework of sustainability provides distinct advantages over traditional approaches. For example, a typical approach for addressing a bridge deficiency to earthquake or hurricane hazards may suggest rebuilding the bridge to current design standards over costly retrofit. However, the increased energy use, waste generation, and disruption to the public may in fact indicate that this solution is misaligned with the objectives of sustainability. The proposed SSIMT model derives solutions where risks from multiple threats are mitigated, while simultaneously promoting system sustainability. Its application results in bridge infrastructure that is safer, due to considering failure probability from multiple threats; is more effective in meeting public needs, by mitigating loss of functionality; and is cost-effective, by accounting for life-cycle cost in the design and management. Detrimental environmental impacts are avoided by selecting strategies based on quantified metrics such as anticipated energy usage or waste generation.

To effectively realize SSIMT, advanced research tools are required that integrate multi-threat vulnerability assessment, life-cycle modeling of sustainability metrics, risk reduction and optimization strategies. This integrated framework can then aid in discerning cost-effective, socially-conscious, and environmentally-friendly solutions to bridge infrastructure deficiencies. Ongoing work in the Padgett Research Group at Rice University (http://www.owlnet.rice.edu/~jp7/) is helping to address input needs for SSIMT, including the following areas of emphasis which align directly with the SSIMT concept model presented in Figure 1:

(1) Probabilistic modeling of the vulnerability of bridges under multiple threats to understand the individual and coupled effects of threats on bridge performance required to assess sustainability.

(2) Life-cycle analysis to relate bridge infrastructure performance to quantifiable objectives for sustainability, including risk-based metrics such as life-cycle cost, energy consumption, waste generation, functionality loss, and safety threats, among others.

(3) Derivation of methods to select bridge retrofit or repair strategies that enhance lifetime sustainability through inverse problem solving or multi-objective optimization to jointly target multiple threats while balancing competing sustainable objectives.

The risk assessment tools for SSIMT are derived through an analytical and simulation based research approach supported by field or test data where viable. Ongoing research is developing multi-threat bridge vulnerability models to uncover the complex coupled effects of hurricane induced storm surge and waves, earthquakes, aging and deterioration, and increased service loads on bridge reliability. The next section of the paper highlights advances in this multi-threat bridge fragility modeling.

In SSIMT, this physical vulnerability is then related to metrics of sustainable performance for specific social, environmental, and economic impacts, ranging from safety to downtime, and from life-cycle cost to energy usage (Figure 1). Although not covered in this paper, examples of this life-cycle modeling of sustainability metrics can be found in Padgett and Tapia (2013) and Padgett (2010). Methods are then formulated to assess and enhance bridge sustainability. Potential tradeoffs and interactions between natural hazard risk mitigation and sustainable engineering are addressed by posing multi-threat upgrade selection in terms of sustainable objectives. While also not the focus of the current paper, early advances in this area include the pursuit of sing and multi-objective optimization frameworks using genetic algorithms to identify sustainable retrofit and repair combinations (Tapia and Padgett 2013).

Advances in Multi-Threat Vulnerability Modeling

As described in the previous section, vulnerability models that characterize the damage potential of bridges when subjected to multiple threats are a key input to the SSIMT framework. The SSIMT approach relies upon fragility models, which offer statements of the conditional probability of failure (or limit state exceedance) given level of threat intensity. In fact, such fragility models offer a building block of many risk assessment frameworks, such as the performance-based earthquake engineering paradigm often reference to support seismic design or upgrade decisions (Moehle et al. 2005). This section describes recent advances in multi-threat fragility modeling of bridges, breaking down the overview into cases that consider: 1) individual threats or natural hazards alone; 2) joint threats; 3) multiple simultaneous natural hazards. Examples of each case are described along with methodological advances relative to the state of the art, sample fragility models or insights from their applications.

Individual Hazards

Traditionally, fragility models for the performance of bridges subjected to natural hazards have been most widespread developed for bridges when subjected to earthquake loads. Although the details may vary on finite element modeling fidelity, level and treatment of uncertainties, and failure modes or bridge components considered in the reliability assessment, seismic fragility models for bridges have been developed by a number of researchers (Mackie 2004; Nielson and DesRoches 2007; Shinozuka et al. 2000). Typically the models condition failure probability on a single ground motion intensity measure (IM) such as the peak ground acceleration, or spectral acceleration, whose selection is guided by such principles as the ability to reduce uncertainty in the predictive model (so called “efficiency”) as well as the ready availability of probabilistic hazard models consistent with the IM (so called “hazard computability”). Recent advances in seismic fragility modeling by the author’s group, collaborators, and others include its application to a number of regional portfolios of structures (e.g., those typical of the state of California, or Central and Eastern Canada); or to the exploration of the influence of alternative design details and site conditions (e.g., the influence of vertical ground motions, seismic versus non-seismic detailing, soil structure interaction and liquefaction effects).

One advance in the seismic fragility modeling of bridges with particular relevance to supporting SSIMT is the recent development of parameterized fragility models for bridges subjected to earthquakes (Ghosh et al. 2013a). In this approach, the failure probability is conditioned not only on the ground motion intensity measure but also a set of structural parameters, x_1 through x_n as shown in Equation 1:

$$P_f = P\left[Demand > Capacity \mid im, x_1, x_2, \ldots, x_n\right] \quad (1)$$

Such parameterize fragility modeling typically takes advantage of the use of surrogate modeling, or metamodels, to enable efficient vulnerability assessment that covers the predictor parameter space. This formulation offers advantages in averting the need to redevelop the fragility model for each bridge within a portfolio of bridges (requiring often computationally expensive finite element simulations); enabling sensitivity studies; supporting the updating of parameters with additional field data; or enabling parameter optimization studies such as those proposed in SSIMT for identifying design or upgrade parameters that support sustainability objectives. As demonstrated in Rokneddin et al. (2013), such parameterized models can also offer advantages of reduced uncertainty (quantified by the dispersion in the fragility curve) relative to the traditional approach of using the IM as the sole predictor of the seismic demand and fragility (Figure 2).

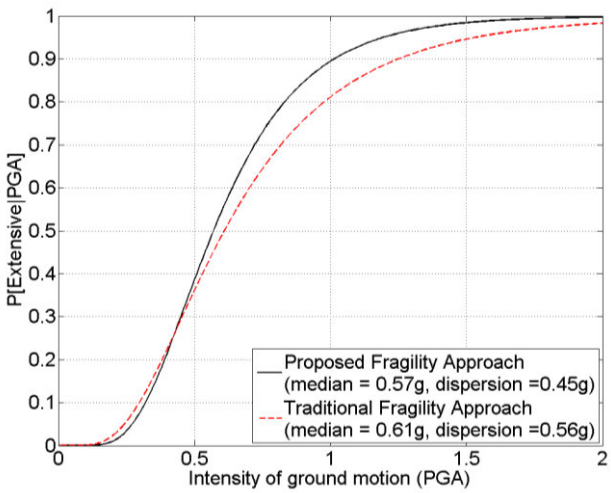

Figure 2. Example Seismic Fragility Curve for a Case Study Multi-Span Simply Supported Concrete Girder Bridge. This Plot Also Shows a Comparison of the Fragility Curve Obtained using the Parameterized Fragility Approach and Traditional Fragility Approach (Rokneddin et al. 2013).

Beyond seismic hazards, recent research has provided the first fragility models for coastal bridges susceptible to hurricane hazards. Past hurricanes, such as Hurricanes Katrina, Ivan, and Ike in the United States have demonstrated the severe consequences of such loads resulting in bridge damage and impairment of transportation network functionality. The predominant failure mode of interest for

these bridges is deck unseating caused by hurricane induced wave and storm surge loading. Figure 3 shows an example of a hurricane fragility curve, developed using a simplified method based upon by Monte Carlo Simulation with static analysis (Ataei and Padgett 2013). The fragility indicates the failure probability for a range of levels of relative surge elevation (Z_c), or surge minus deck elevation, and maximum wave height (H_{max}). The plot reveals a relatively distinct transition zone between failed ad safe regions demarcated by the dashed line in Figure 3, which can be attributed in part to the lack of vertical connectivity between the deck and supports and relatively "brittle" failure mode. More advanced fragility analysis techniques have also been proposed for developing hurricane fragilities to accommodate dynamic analyses or fluid structure interaction, enable additional uncertainty treatment associated with such models, and utilize efficient sampling techniques and surrogate modeling. These fragility models enable for the first time risk assessments of coastal bridge infrastructure under severe storms, which were traditionally limited to inundation analyses, but now can offer predictions of bridge failure potential.

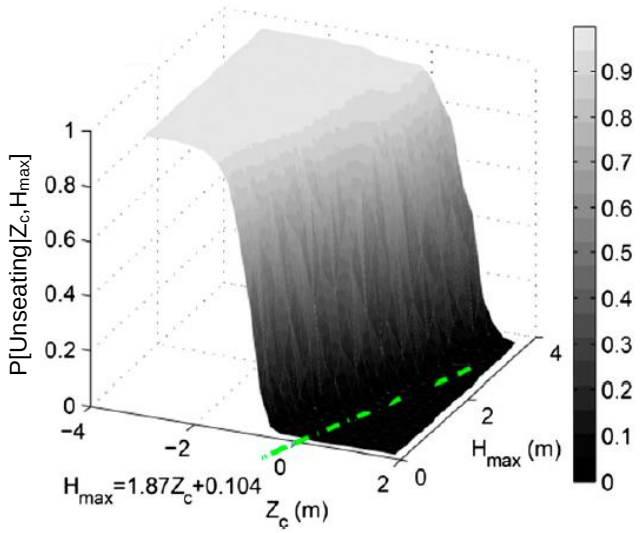

Figure 3. Example Hurricane Fragility Curve For A Case Study Multi-Span Simply Supported Concrete Girder Bridge. This Plot Shows the Failure Probability (y-axis) for Different Levels of Relative Surge Elevation (Z_c) and Maximum Wave Height (H_{max}) (Ataei and Padgett 2013).

Joint Threats

While fragility modeling of bridges has been evolving to consider the vulnerability of bridges against various natural hazards, such as earthquakes and hurricanes, the joint impact of multiple threats has received relatively less attention. In this paper the term "threats" is considered more broadly to encompass not only natural hazards but also other factors that threaten the performance of bridges such as aging and deterioration or service loads. Recent studies have investigated the joint impact of natural hazards (e.g. earthquakes) and simultaneous consideration of aging and deterioration (e.g. from corrosion) or service loads (e.g. truck traffic). The results suggest the importance of considering joint threat occurrence and the influence of these

additional threats on natural hazard fragility. For example, several researchers have investigated the influence of corrosion on the seismic fragility of bridges (Do-Eun et al. 2008; Ghosh and Padgett 2010), albeit with different bridge types and exposure conditions, among other considerations. Ghosh and Padgett (2010) proposed the use of time-dependent fragility curves to reflect the increase in vulnerability throughout the life of a bridge. An illustration is shown in Figure 4 for a case study multi-span continuous steel girder bridge exposed to deicing salts, showing that the median value as well as the dispersion of the lognormally distributed fragility are affected by aging and deterioration. A comparison of different exposure conditions—marine environment, atmospheric condition, deicing salt exposure—revealed that bridges in seismic zones where deicing salts are typical are susceptible to the greatest increase in fragility. Across different bridge types common to the Central and Southeastern United States, multi-span continuous and simply supported bridges are among the most vulnerable types for which aging also has a significant impact on increasing the fragility. This can be attributed in part to the high type steel fixed and rocker bearings as well as the significant demands placed on corroding reinforced concrete columns with limited reinforcement.

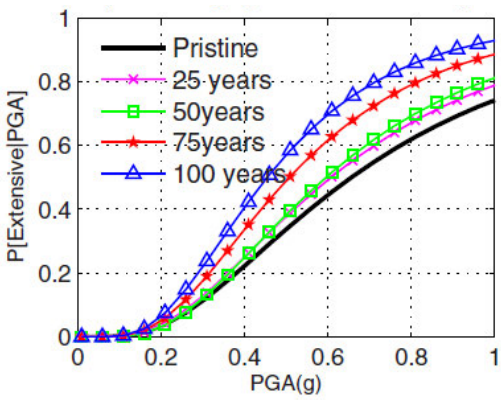

Figure 4. Example Time Dependent Fragility for a Case Study Multi-Span Continuous Steel Girder Bridge, Showing the Joint Consideration of Aging and Seismic Threats (Ghosh and Padgett 2010).

Ghosh et al. (2013b) proposed a framework for joint live load and seismic reliability analysis, to account for the realistic condition that vehicular loads may be present atop a bridge during seismic excitation. Figure 5 shows an illustration of the fragilities derived as statements of bridge failure probability conditioned upon peak ground acceleration as well as truck gross vehicle weight (GVW). This figure suggests that presence of a truck atop a bridge can have an impact on the seismic vulnerability and that this impact is sensitive to the vehicle weight (i.e. almost a linear increase in median value with increase in GVW). The method elaborated in Ghosh et al. further necessitates the integration of a truck gross vehicle weight histogram and truck flow rate and density, to consider the likelihood of truck presence and weight in seismic fragility estimation. The results revealed that for the case study multi-span continuous steel girder bridge (used in Figure 5) and regional weigh in motion data typical of the state of Alabama, that the increased fragility (reduced median PGA) can be small once the probabilities of occurrence of truck presences and GVWs are taken into account.

Never the less, this joint threat may be of interest for priority bridges on key trucking routes, such as access routes to ports.

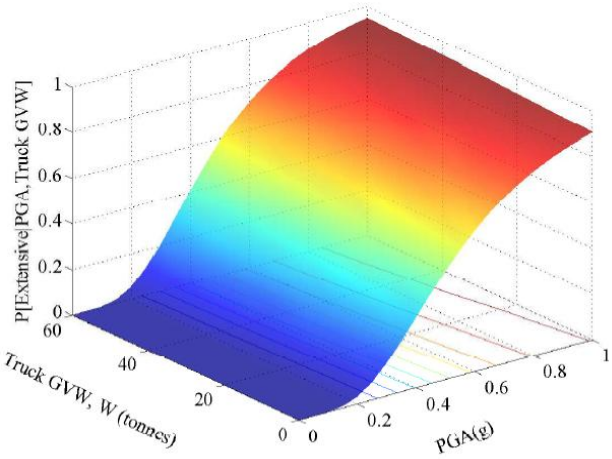

Figure 5. Example Joint Seismic and Live Load Fragility for a Case Study Multi-Span Continuous Steel Girder Bridge. Failure Probability is Conditioned on Earthquake Intensity as PGA and Truck Gross Vehicle Weight (GVW) (Ghosh et al. 2013b).

Multiple Simultaneous Hazards

The last class of fragility models required to enable SSIMT are those that consider the potential simultaneous occurrence of hazards. For many hazards, such as earthquakes and hurricanes presented above, the joint event occurrence potential is negligible. However, there are other cases that have been acknowledged in the literature as simultaneous hazards of practical interest. One such case for bridges is the joint consideration of scour and seismic hazards, which has been recently explored for its impact on seismic fragility as well as implications on load factor derivation (Wang et al. 2013). An example fragility surface is shown in Figure 6 for a case study two-span box girder bridge susceptible to scour and earthquakes. In this figure the failure probability (vertical axis) is a function of the ground motion intensity (IM) (taken here as $S_{a\text{-}05,}$ or the spectral acceleration at 0.5 second) and the scour depth (H). The derivation of this fragility surface is enable by developing multi-hazard probabilistic seismic demand models, in which the bridge response is considered as a function of both IM and H, before comparing with the capacity. The resulting Figure suggests the influence of scour depth on the failure probability of the bridge when an earthquake occurs. In general this case suggests an increase in fragility with H, but there are some cases where the fragility may also decrease slightly due to the elongation of period that accommodates the increase in scour (e.g. an equivalent base isolation effect). The multi-threat fragility models categorized into three subclasses in this paper provide key quantification of the failure probability of bridges for different exposure conditions. Subsequent risk assessment and life-cycle modeling in the SSIMT framework rely upon these fragility estimates to quantify the sustainable impacts of hazard damage and characterize the benefits of design details or upgrades.

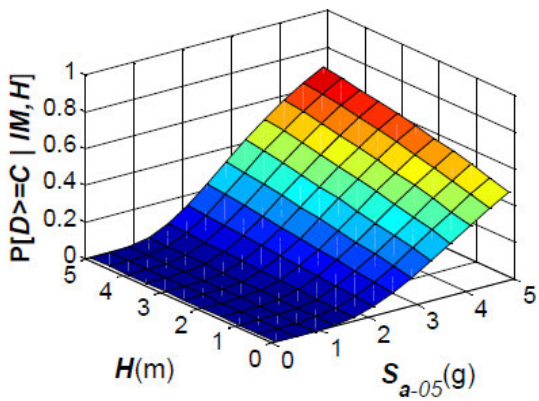

Figure 6. Example Multi-Hazard Scour and Earthquake Fragility Surface for a Case Study Two Span Integral Box Girder Bridge. Failure Probability is Conditioned on Earthquake Intensity Taken as $S_{a\text{-}05}$ and Scour Depth (H) (Wang et al. 2013).

Conclusions

This paper presents "Sustainable Solutions for Bridge Infrastructure Subjected to Multiple Threats" (SSIMT) as a model to identify methods for bridge upgrade and management using risk-based measures of sustainable performance that consider multiple threats over a bridge's life. Overall SSIMT integrates multi-hazard reliability and risk assessment with life-cycle modeling of sustainability metrics, such as cost, energy usage, or fatalities, to support the identification of sustainable designs or retrofits. This approach offers a way to explore the relationship between protection from natural hazards and implications on social, environmental, and economic performance. Prior to quantifying metrics of life-cycle sustainability, SSIMT relies heavily upon the characterization of bridge vulnerability to multiple threats; hence this paper emphasizes recent advances in bridge fragility modeling deemed critical to enable SSIMT. Threats in the SSIMT model include the consideration of natural hazards, aging and deterioration, and potential increases in service loads. The three main categories of multi-threat bridge vulnerability models described in this paper include individual hazards (e.g. hurricane or earthquake fragility); joint threats (e.g. joint aging and seismic fragility); and multiple simultaneous hazards (e.g. scour and earthquake fragility surfaces).

Recent methodological advances in fragility modeling include the use of metamodeling to enable efficient, parameterized bridge fragilities amenable to SSIMT. The models offer flexibility for application across bridge portfolios, for integration of new information collected from the field, and for sensitivity or design parameter optimization to achieve sustainability objectives. Recognizing a key gap in the literature, new probabilistic models of hurricane fragility were developed focusing on the unseating failure mode associated with surge and wave loading. Additional opportunities exist to explore other failure modes, including those associated with hurricane induced scour and debris impact. These fragility models for independent hazards can be used to explore tradeoffs in the risk of damage and subsequent sustainability metrics for bridges in regions prone to earthquakes and hurricanes or typhoons (e.g. the state of South Carolina in the USA, Puerto Rico, Japan). The

examination of joint threats revealed that both aging and deterioration as well as the presence of truck traffic can have an impact on bridge fragility to seismic hazards. However, the relative magnitude of these effects depends heavily on bridge type, exposure condition, and likelihood of the secondary threat. In general the consideration of time-dependent seismic fragility is recommended for life-cycle analysis of the sustainability of bridges to account for the impacts of aging on seismic performance; however, the joint consideration of truck and earthquake loads may not have a significant impact on the fragility unless the bridge is located on a heavily traveled route. It is acknowledged that further studies with a wide array of bridge types are required to confidently generalize these findings. Additionally, the joint impact of earthquakes, aging, and traffic has yet to be explored in the literature. However, the methods presented in this paper and its associated references can offer viable approaches to consider these joint threats. Finally, while the simultaneous occurrence of natural hazards may be impractical for some cases, others like the joint occurrence of scour and earthquake have received increasing attention in the literature. The derivation of multi-hazard demand models and fragility surfaces, such as that presented in this paper for scour and earthquake, offer a basis to conduct multi-hazard risk and life-cycle assessments in the SSIMT model. Future opportunities exist to extend this multi-hazard framework to other hazards, including triggered hazards such as fire following earthquake or tsunami. By integrating these multi-threat fragility models in a life-cycle framework, the impact of hazard exposure on bridge sustainability can be better understood and the potential synergies and tradeoffs in hazard protection and sustainable design revealed.

Acknowledgments

This research is supported by the National Science Foundation (NSF) through Grant No. CMMI-1055301. Any opinions, findings, and conclusions or recommendations expressed in this material are those of the authors and do not necessarily reflect the views of the National Science Foundation. In addition the input of multiple students and collaborators cited in the references and contributing to the case study illustrations of multi-threat fragility modeling is gratefully acknowledged.

References

Adeli, Hojjat (2002), 'Sustainable Infrastructure Systems and Environmentally-Conscious Design---A View for the Next Decade', *Journal of Computing in Civil Engineering*, 16 (4), 231-33.

Amekudzi, Adjo A., Khisty, C. Jotin, and Khayesi, Meleckidzedeck (2009), 'Using the sustainability footprint model to assess development impacts of transportation systems', *Transportation Research Part A*, 43, 339–48.

ASCE (2008), 'Principles for Infrastructure Stimulus Investment', (Washington, D.C.: American Society of Civil Engineers).

--- (2009), 'Report Card for America's Infrastructure', (Reston, VA: American Society of Civil Engineers).

Ataei, Navid and Padgett, J. E. (2013), 'Probabilistic Modeling of Bridge Vulnerability

Subjected to Hurricane Loads: A case study with Houston infrastructure', *Journal of Bridge Engineering*, 18 (4), 275-86.
Biswas, Tapan (1997), *Decision-making under uncertainty* (New York, N.Y.: St. Martin's Press).
Black, J. A., Paez, A., and Suthanaya, P. A. (2002), 'Sustainable Urban Transportation: Performance Indicators and Some Analytical Approaches', *Journal of Urban Planning and Development*, 128 (4), 184-209.
Daly, Herman (1996), *Beyond Growth: The economics of sustainable development* (Boston: Beacon Press).
Do-Eun, Choe, et al. (2008), 'Probabilistic capacity models and seismic fragility estimates for RC columns subject to corrosion', *Reliability Engineering and System Safety*, 93 (3), 383-93.
Ghosh, J. and Padgett, J. E. (2010), 'Aging Considerations in the Development of Time-Dependent Seismic Fragility Curves ', *Journal of Structural Engineering*, 136 (12), 1497-511.
Ghosh, J., Padgett, J. E., and Dueñas-Osorio, L. (2013a), 'Surrogate Modeling and Failure Surface Visualization for Efficient Seismic Vulnerability Assessment of Highway Bridges', *Probabilistic Engineering Mechanics*, DOI:10.1016/j.probengmech.2013.09.003.
Ghosh, J., Caprani, C., and Padgett, J. E. (2013b), 'Influence of Traffic Loading on the Seismic Reliability Assessment of Highway Bridge Structures', *ASCE Journal of Bridge Engineering*, DOI:10.1061/(ASCE)BE.1943-5592.0000535.
Goncz, Elzbieta, et al. (2007), 'Increasing the rate of sustainable change: a call for a redefinition of the concept and the model for its implementation', *Journal of Cleaner Production*, 15 (6), 525-37.
Jeon, Christy Mihyeon and Amekudzi, Adjo (2005), 'Addressing sustainability in transportation systems: Definitions, indicators, and metrics', *Journal of Infrastructure Systems*, 11 (1), 31-50.
Li, Yue and Ellingwood, Bruce R. (2006), 'Hurricane damage to residential construction in the US: Importance of uncertainty modeling in risk assessment', *Engineering Structures*, 28 (7), 1009-18.
Little, R. G. (2005), 'Tending the infrastructure commons: ensuring the sustainability of our vital public systems', *Structure and Infrastructure Engineering*, 1 (4), 263-70.
Mackie, Kevin (2004), 'Fragility Based Seismic Decision Making for Highway Overpass Bridges', (University of California, Berkeley).
MCEER (2008), 'Design of Highway Bridges Against Extreme Hazard Events: Issues, Principles and Approaches', in George C. Lee, M. Tong, and W. Phillip Yen (eds.), *MCEER Special Report Series on Multiple Hazard Bridge Design* (MCEER and FHWA), 110.
Moehle, J., et al. (2005), 'An application of PEER performance-based earthquake engineering methodology', *Research digest*.
National_Research_Council (2009), 'Sustainable Critical Infrastructure Systems—A Framework for Meeting 21st Century Imperatives', (Washington, D.C.: Toward Sustainable Critical Infrastructure Systems: Framing the Challenges Workshop Committee; National Research Council).

Nielson, Bryant and DesRoches, R. (2007), 'Seismic Fragility Curves for Typical Highway Bridge Classes in the Central and Southeastern United States', *Earthquake Spectra*, 23 (3), 615-33.

Padgett, J. and DesRoches, R. (2007), 'Sensitivity of Seismic Response and Fragility to Parameter Uncertainty', *Journal of Structural Engineering*, 133 (12), 1710-18.

Padgett, J. E. (2010), 'Sustainability as a Guide for Selecting and Prioritizing Seismic Retrofit', *2010 Concrete Bridge Conference* (Phoenix, AZ).

Padgett, J. E. and Tapia, C. (2013), 'Sustainability of Natural Hazard Risk Mitigation: A Life-Cycle Analysis of Environmental Indicators for Bridge Infrastructure', *ASCE Journal of Infrastructure Systems*, DOI:10.1061/(ASCE)IS.1943-555X.0000138.

Padgett, J. E., Dennemann, K., and Ghosh, Jayadipta (2009), 'System Sustainability: A Criterion for Seismic Retrofit Selection ', *Transportation Research Board Annual Meeting* (Washington, DC).

Pearce, A. R. and Vanegas, Jorge A. (2002), 'Defining sustainability for build environmental systems', *International Journal of Environmental Technology and Management*, 2 (1), 94-113.

Perry, Mark J. and Mackun, Paul J. (2001), 'Population Change and Distribution, 1990-2000', *Census Brief 2000* (US Census Bureau).

Rokneddin, K., et al. (2013), 'Seismic Reliability Assessment of Aging Highway Bridge Networks with Field Instrumentation Data and Correlated Failures. II: Applications', *Earthquake Spectra*, doi: 10.1193/040612EQS160M.

RPA (2005), 'America 2005: A Prospectus', (New York, NY: Regional Plan Association's National Committee for America 2050).

Shinozuka, Masanobu, et al. (2000), 'Statistical analysis of fragility curves', *Journal of Engineering Mechanics*, 126 (12), 1224.

Simpson, David M., et al. (2005), 'Framing a new approach to critical infrastructure modelling and extreme events', *International Journal of Critical Infrastructures*, 1 (2-3), 125-43.

Tapia, C. and Padgett, J.E. (2013), ' Life-Cycle Optimization of Structural Retrofit and Repair Based On Sustainability Criteria', *11th International Conference on Structural Safety & Reliability (ICOSSAR)* (Columbia University, New York, NY).

Taylor, Andre C. and Fletcher, T. D. (2006), '"Triple-bottom-line" assessment of urban stormwater projects', *Water Science and Technology*, 54 (6-7), 459-66.

USDOE 'Ten steps to sustainability', *Energy Efficiency and Renewable Energy Network* <www.sustainable.doe.gov/management/tensteps.shtml>, accessed May 2008.

USDOT 'U.S. Department of Transportation Mission and History', <http://www.dot.gov/mission.htm>, accessed March 2008.

--- (2007b), 'Impacts of Climate Change and Variability on Transportation Systems and Infrastructure: Gulf Coast Study, Phase I', in J. R. Potter, Virginia R. Burkett, and Michael J. Savonis (eds.), (Draft edn.: U.S. Department of Transportation).

Vanegas, Jorge A. (2003), 'Road Map and Principles for Built Environment Sustainability', *Environmental Science and Technology*, 37 (23), 5363-72.

Wang, Z., Padgett, J.E, and Dueñas-Osorio, L. (2013), 'Risk-consistent calibration of

load factors for the design of reinforced concrete bridges under the combined effects of earthquake and scour hazards', *Engineering Structures*, In Review.
WCED (1987), *Our common journey* (World Commission on Environment and Development Oxford, England: Oxford Univ. Press).

A DESIGN, CONSTRUCTION OF THE SOCKET ANCHORING SYSTEM BETWEEN STEEL PIER AND THE FOUNDATION IN MORIGUCHI JCT

Hiroyuki Nagareta & Nobuya Okazaki [1]
Muneyuki Yamana, Takashi Kosaka & Tsutomu Nakai [1]

Abstract

Moriguchi JCT which is under construction is the ramp connecting Hanshin Expressway Moriguchi Route with Kinki Expressway. Because the foundation of the ramp bridges are strictly limited in space due to the underground installation, the socket anchoring system was adopted instead of the conventional anchor frame system. This system is one of the methods to anchor the steel pier into the foundation and consists of steel pier with PBL and socket steel pipe. Main reinforcements of the foundation are arranged and in-situ concrete is filled between the steel pier and socket steel pipe and inside the steel pier.

This paper summarize a construction of the socket anchoring system adapted to the highway bridge for the first time. Although socket anchoring system is adopted by some railroad structures and few road structures.

Introduction

Moriguchi JCT connects Hanshin Expressway Moriguchi Route with Kinki Expressway (Figure-1). Moriguchi JCT will disperse the traffic concentrated in the center of Osaka city, prepare alternative route at the time of the accident or disaster, and mitigate congestion at local street by connecting Hanshin Expressway Moriguchi Route and Kinki Expressway.

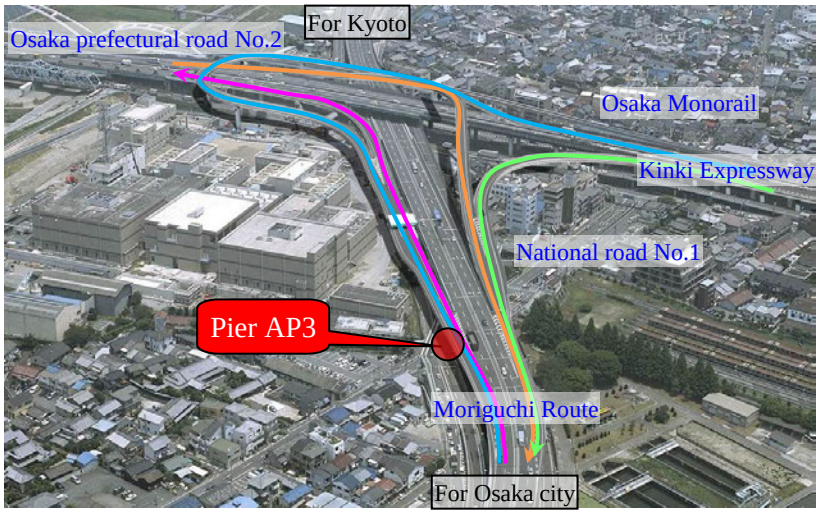

Figure-1 Moriguchi JCT construction site

[1] Hanhin Expressway Company Limited, Osaka, Japan

Moriguchi JCT is surrounded by Hanshin Expressway Moriguchi Route (about 40,000 cars/day) , Kinki Expressway (about 90,000 cars/day) , Osaka prefectural road No.2, National road No.1 (about 100,000 cars/day), and Osaka Monorail. These structures make construction space very narrow. Moreover, by widening the existing RC piers and RC slabs, construction of Moriguchi JCT is very difficult.

This paper reports the socket anchoring system adopted in order to widen the existing piers and slab in the narrow construction space.

1. Structure summary

The outline of the socket anchoring system is shown Figure-2. This system is one of the methods to anchor the steel pier into the foundation and consists of steel pier with PBL and socket steel pipe. Main reinforcements of the foundation are arranged and in-situ concrete is filled between the steel pier and socket steel pipe and inside of steel pier. The socket anchoring system can expectedly reduce the cost and construction period by omitting anchor frame which is used for traditional anchor system.

Figure-3 shows the general drawing of pier AP3 using socket anchoring system. As shown in the section of the superstructure in Figure-3, we adopt rigid connection of new and existing concrete slab, and remove longitudinal joint from the viewpoint of easy maintenance, running comfortability. Therefore new pier foundation has to be placed in the same section of the existing pier foundation, and also connected rigidly with it.

However, if we place in the same section of the existing pier foundation, the AP3 pier is interfered underground installation, waterway and road, and AP3 pier foundation is limited in its structural size (Figure-4).

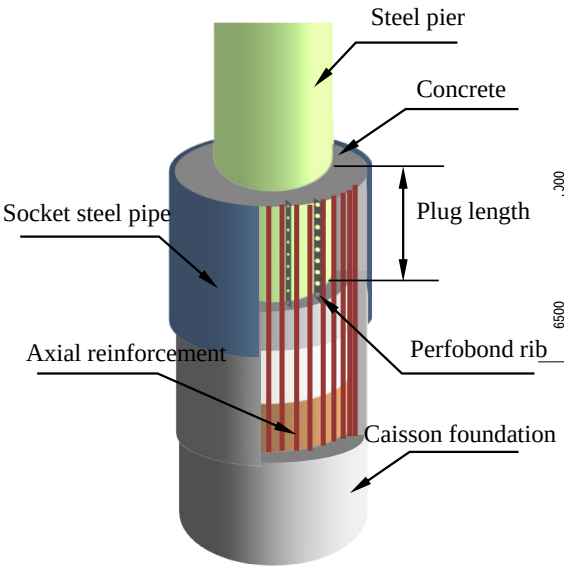

Figure-2 Structural drawing of socket anchoring system

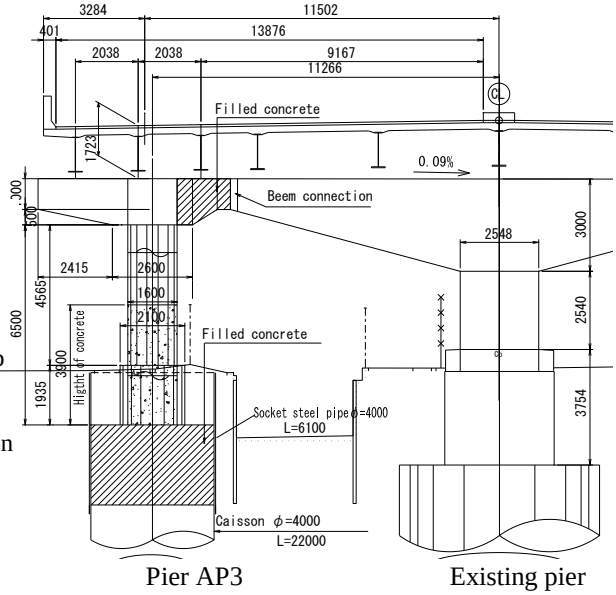

Figure-3 General drawing of pier AP3

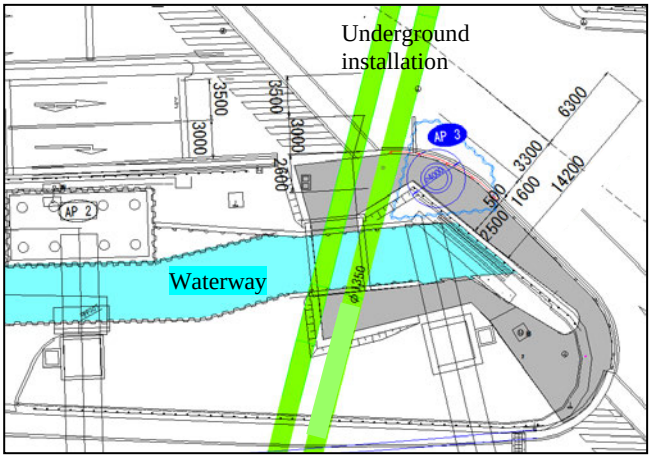

Figure-4　Ground plan around pier AP3

Table-1 compares three types of the foundation and shows that socket anchoring system is the most economical and able to mitigate the influence to the crossing road of the AP3 pier.

	①Genneral way 【RC pier + caisson foundation】	②Genneral way 【Two piles method】	③Adopted method 【Socket anchoring system】
Outline figure	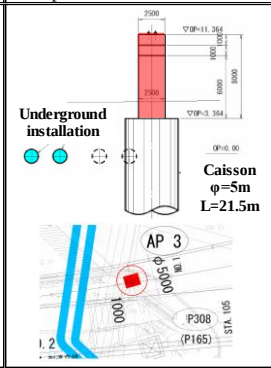	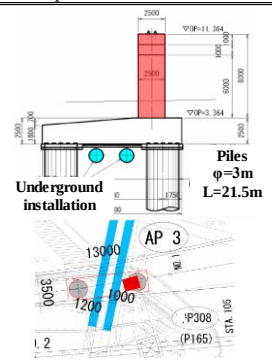	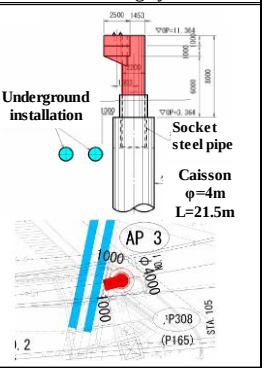
Pier	RC pier	RC pier	Steel pier
Foundation	Caisson foundation (φ=5m)	Cast-in-situ concrete piles (φ=3m×2)	Caisson foundation (φ=4m)
Underground installation	Transfer	Not transfer	Not transfer
Traffic impact	Large	Very large	Small
Construction period	About 12 months	About 4.1months	About 7.5 months
Cost (compared with ③)	2.3	1.5	1.0

Table-1　AP3 pier foundation form comparison

Finally, socket anchoring system was chosen, however, there are not so many practical structures, just some for railroad and a few for road bridges, and Kosaka viaduct[1)] of the Ministry of Land, Infrastructure Transport and Tourism Shikoku Regional Development Bureau is the only for the large-scale load bridge. Thus Moriguchi is the first adoption for the expressway.

2. Design summary

Figure-5 shows the design flow of the socket anchoring system. "Design Standards for

Railway Structures and Commentary[2)]" and the Kosaka viaduct design documents were referred for the design policy this time.

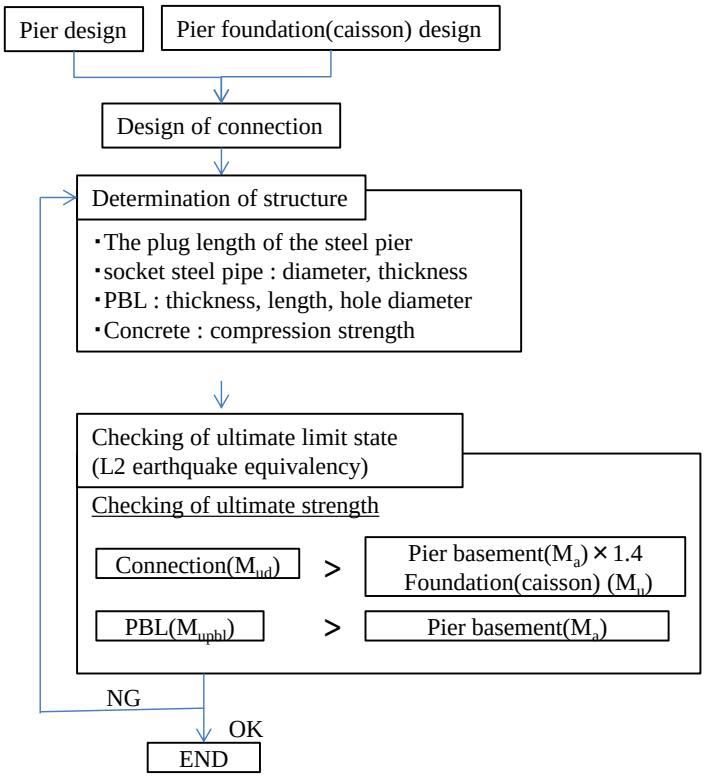

Ma：Bending moment of pier base when a steel member reached the allowable strain ($\varepsilon_a = 5\varepsilon_y$), Mu：Bending moment when the caisson reached ultimate strength

Figure-5 Design flow of socket anchoring system

In this design policy, the collapse of the pier correspond the ultimate state of the steel pier basement due to the plasticizing and following conditions need to be provided for appropriate collapse.

Steel pier < Foundation (open caisson) < Socket anchoring system

And the bending strength of socket anchoring system has to be more than 1.4 times of the bending strength of steel pier basement and also more than ultimate bending strength of foundation (open caisson).

Here, the design bending strength of socket anchoring system is to be given using the formula of “Design Standards for Railway Structures and Commentary”. Figure-6 shows the load model of the socket anchoring system. In this calculating formula, It is supposed that couple of forces of bearing pressure between the steel pier and socket steel pipe and couple of forces of frictional forces between steel pier and filling concrete resists the bending moment and shear force to act on steel pier. The bending strength（M_{ud}）of the connection can be obtained in the next formula by solving a balance moment shown in Figure-6.

$$M_{ud} = T \cdot \left(\frac{2\sqrt{2}}{\pi} \right) \cdot d - \frac{L \cdot P^2}{3(2P-Q)} + (P-Q) \cdot \frac{L(5P-2Q)}{3(2P-Q)} \qquad (1)$$

Here,

M_{ud} : The bending strength of socket connection, T : The maximum resultant frictional force to act on a steel pier, P : The maximum resultant bearing pressure to act on a steel pier, Q : The shear force of socket connection, d : Outer diameter of steel pier, L : The plug length to a socket steel pipe of the steel pier

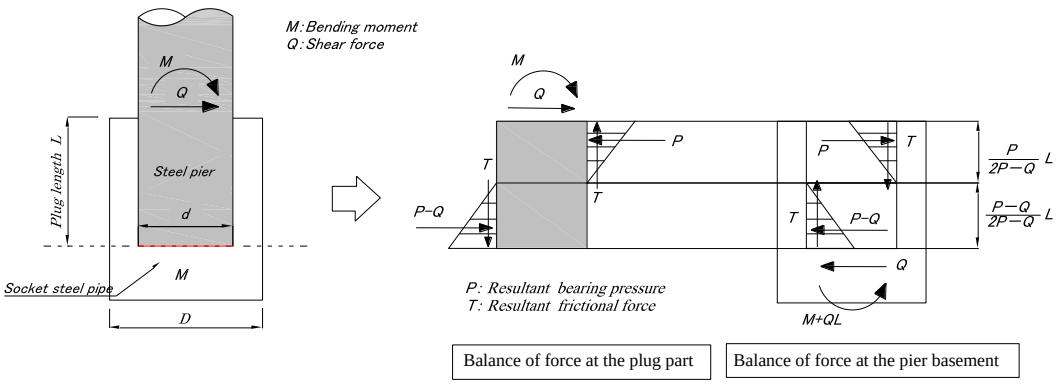

Figure-6 Load model of the socket anchoring system

Inside of the socket steel pipe, shear connector (D13 reinforcement) was provided for the strength improvement which was shown in the past experiment[3), 4)] . In addition, six PBLs (perfobond ribs) were adopted and welded on the outside of the steel pier for the safer structure. Figure-7 shows the load model of shear connector by PBL, and its strength was evaluated by following equation.

$$M_{pbl} = \sum_{i=1}^{n} m \cdot P_{upbl} \cdot h_r \cdot \cos\theta_{ri} \qquad (2)$$

Here,

M_{pbl} : Bending strength of PBL, P_{upbl} : Shear strength per one hole of PBL, θ_r : Angle of PBL arrangement, m : The hole number per one plate, h_r : Distance from the steel pier section center to hole center

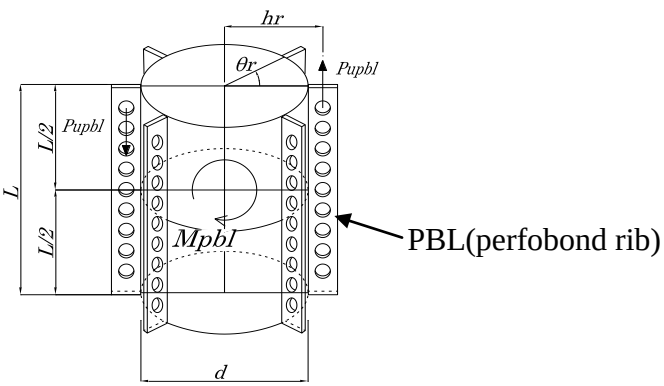

Figure-7 Load model of shear connector by PBL

The plug length of the steel pier into the caisson and the outer diameter of socket steel pipe were determined as follow.

- The plug length of the steel pier: L (plug length) ≧ 1.5d (outer diameter of steel pier) in accordance with “Design Standards for Railway Structures and Commentary”
- The outer diameter of socket steel pipe = Outer diameter of the caisson. The socket steel pipe thickness was determined concerning the ultimate strength and extra 1mm was added in consideration of corrosion.

Figure-8 shows the detail of socket anchoring system of AP3. Socket steel pipe is D=4,000mm in outer diameter, and steel pier is d=1,600mm in outer diameter, thus the ratio of them is D/d =2.5, which is in the range of D/d=1.47～3 indicated in the past experiments[3), 4)].

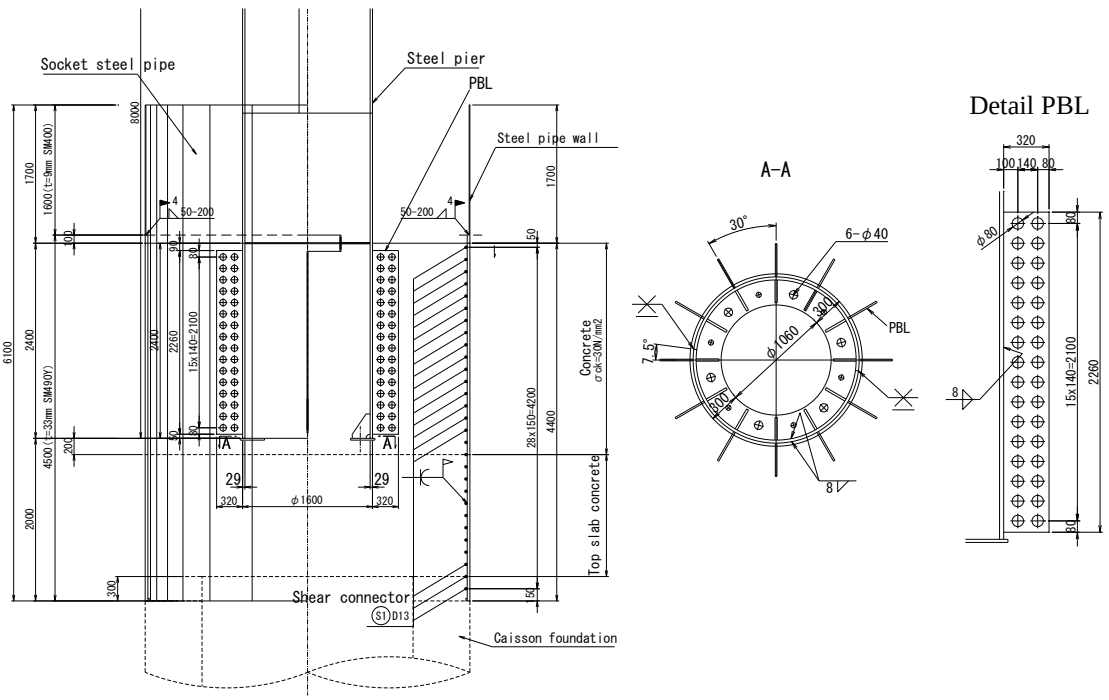

Figure-8 Detail of socket anchoring system

3. Construction summary

Figure-9 and Photo-1～6 show construction steps of socket anchoring system.

【STEP1】First, the steel sheet piles for the protection of adjacent structures was constructed, four lots of open caisson were penetrated into the ground by oil jacks. Then, quarterly divided socket steel pipe in which displacement preventing reinforcement is welded in the factory were erected by the rough terrain crane on the top slab of the open caisson. After welding anti-distortion materials, each parts of the socket steel pipe were welded to each other in the construction site. Then the socket steel pipe and open caisson was penetrated to a predetermined position.

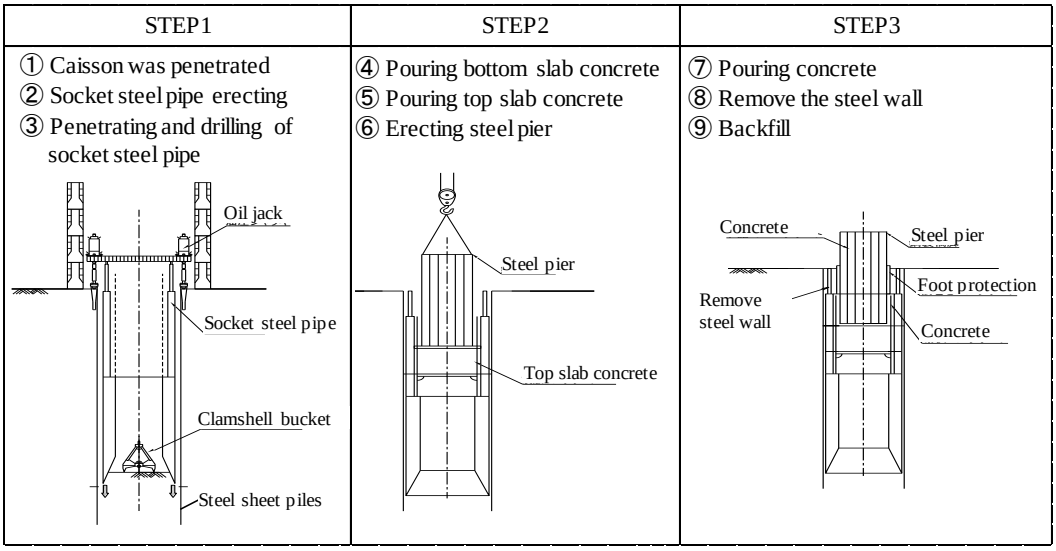

Figure-9 Construction step

Photo-1 Erecting socket steel pipe

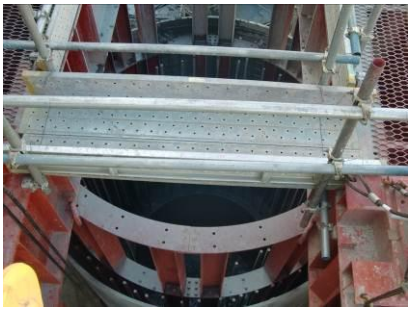

Photo-2 Penetrating socket steel pipe

【STEP2】Top slab of the caisson was constructed and then the steel pier was erected onto the top slab. During erection of the pier, the highway Moriguchi Route was closed.

Photo-3 Erecting steel pier

Photo-4 Inside the socket steel pipe

【STEP3】 Concrete was pouring in the gap between the steel piers and socket steel pipe first, which integrated the both members, and then inside the steel pier. Finally, the steel pier's foot protection was constructed around it in the extent of underground level. The temporary steel pipe which was upper part (t=9mm part) of the socket steel pipe, was removed and the ground was backfilled around the pier.

Photo-5 Pouring concrete

Photo-6 Finished construction

Conclusions

Because the foundation of Moriguchi junction pier AP3 was strictly limited in space due to the underground installation and also surrounding general road, the socket anchoring system was adopted for rigid connection of steel pier and caisson foundation instead of the conventional anchor frame system.

This structure which consists of socket steel pipe, PBL, steel pier and concrete is much compact and smaller than anchor frame, and thus it can make the foundation smaller and more economical. Because there is not any erection works of anchor frame in the caisson's top slab with crowded reinforcement arrangement, construction of the socket anchoring system is much simpler and faster in terms of site works.

As of now the socket anchoring system can be adopted when the ratio of outer diameter of the socket steel pipe to the one of the steel pier is in the range of value indicated in the past experiments. However, this will be still effective and beneficial structure in the future especially in the case of limited space and conditions.

References

1) Construction subcommittee in Technical committee of Japan Bridge Association corporation :Construction method of rapid three-dimensional at the intersection －Quick bridge construction method in construction of KOSAKA viaduct－, 2008 bridge technology presentation,2008

2) Railway Technical Research Institute ：Design Standards for Railway Structures and Commentary (Steel-Concrete Hybrid Structures),2012-2

3) Shin-ichiro NOZAWA , Masanori KINOSHITA, Daisuke TSUKISHIMA and Tadayoshi ISHIBASHI：Ultimate Strength of Sleeve Joint between Concrete-Filled Circular Steel Pipes with Shear Connector, Proceedings of JSCE 634, 71-89, 1999-11-20

4)Yutaka Takashima ,Takeshi Kanbara ,Yasutaka Sasaki ,Shoji Oda and Nobuo Yoshikawa：Estimation Method of Ultimate Strength of the Socket Connection with Perfobond Strip between Steel Pier and Foundation, Journal of Structural Engineering of JSCE Vol.54A, 798-806, 2008-3

Seismic Performance of Precast Concrete Bents used for Accelerated Bridge Construction

Bijan Khaleghi[1]

Abstract

Ductility of precast prestressed girder bridges can be achieved by proper detailing of pier diaphragm through extended strands, column bars, and joint reinforcement. Extended strands at intermediate crossbeams are used to connect the ends of girders with diaphragms and resist loads from creep effects, shrinkage effects, and seismic positive moments. This paper describes the development and implementation of a precast concrete bridge bent system suitable for accelerated bridge construction in high seismic zones. At the base of the bent, the column is connected to a spread footing using a socket connection, while at the top the column is joined to the cap beam using bars grouted in ducts. In both cases the connection was verified by testing before the system was implemented. This paper describes the development, experimental validation, and implementation of a precast concrete bridge bent system that is intended to meet those challenges. A precast concrete bridge bent system is presented that is conceptually simple, can be constructed rapidly, and offers excellent seismic performance.

Introduction

Seismic design of precast concrete bridges begins with a global analysis of the response of the structure to earthquake loadings and a detailed evaluation of connections between precast girders and connections between the superstructure and the supporting substructure. Ductile behavior is desirable under earthquake loadings for both the longitudinal and transverse directions of the bridge. Further, the substructure must be made to either protect the superstructure from force effects due to ground motions through fusing or plastic hinging, or to transmit the inertial forces that act upon the bridge to the ground through a continuous load path.

Connections in precast concrete substructures are typically made at the beam-column and column-foundation interfaces to facilitate fabrication and transportation. However, for structures in seismic regions, those interfaces represent locations of high moments and shears and large inelastic cyclic strain reversals. Devising connections that can accommodate inelastic cyclic deformations and are readily constructible is the primary challenge for ABC in seismic regions.

Performance Criteria For Prestressed Girder Ordinary Bridges

Designing for life safety means that significant damage can result. Significant damage includes permanent offsets and damage between approach structures and the bridge superstructure, and between spans at expansion joints, permanent changes in bridge span lengths, and permanent the basis of their stiffness distribution factors. This moment

[1] State Bridge Design Engineer, Washington State Department of Transportation, Bridge and Structures Office

displacements at the top of bridge columns. Damage also consists of severe concrete cracking, reinforcement yielding and buckling, major spalling of concrete and severe cracking of the bridge deck slab. These conditions may require closure of the bridge to repair the damages. Partial or complete replacement of columns may be required in some cases. For sites with lateral flow due to liquefaction, piles and shafts may suffer significant inelastic deformation, and consequently, partial or complete replacement of the columns, piles and shafts may be necessary. If replacement of columns or other components is to be avoided, a design strategy that produces minimal or moderate damage, such as seismic isolation or a control and reparability design concept, should be used. Figure 1 shows the connection concept is commonly used by WSDOT for bridges in moderate and high seismic zones.

Girders and deck slab are continuous at piers with girders framed into the pier diaphragm. Such structures are thought to exhibit behavior as a continuous superstructure with a fixed moment resistant connection to the substructure.

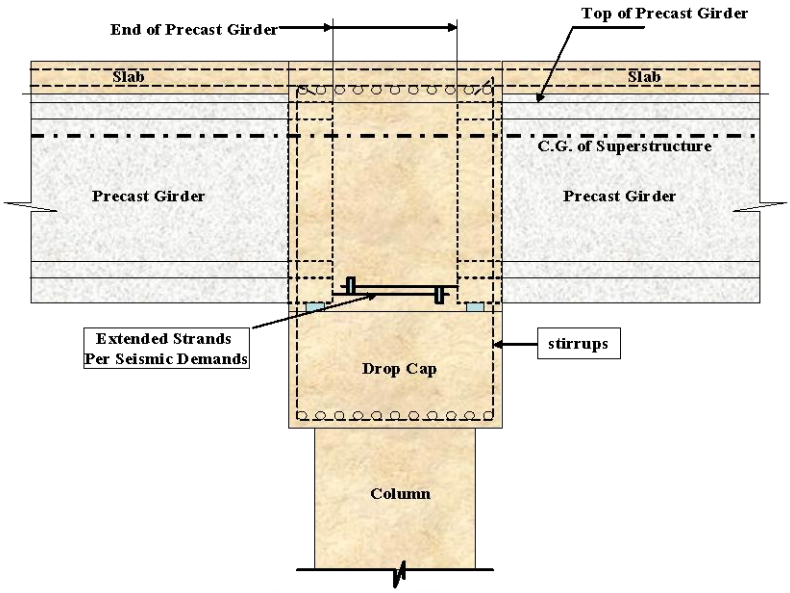

Figure 1: Pier with Girders Framed into the Pier Diaphragm

Plastic hinges form before any other failure due to overstress or instability in either the overall structure, or in the foundation, or both. Plastic hinges are permitted only at locations in columns where they can be readily inspected and repaired. Superstructure and substructure components and their connections to columns that are not designed to yield are rather designed to resist overstrength moments and shears of ductile columns. The plastic moment capacity for reinforced concrete columns is determined using a moment curvature section analysis, taking into account the expected yield strength of the materials, the confined concrete properties, and the strain-hardening effects of the longitudinal reinforcement.

Capacity-protected members such as bent caps, joints at top and bottom of column, and integral superstructure elements that are adjacent to the plastic hinge locations are designed to remain essentially elastic when the plastic hinge reaches its overstrength moment capacity. The superstructure is designed as a capacity protected member. Any moment demand caused by dead load or secondary prestress effects in case of continuous tendons over piers is distributed to the entire width of the superstructure. The column overstrength moment, in addition to the moment induced due to the eccentricity between the plastic hinge location and the center of gravity of the superstructure, is distributed to the spans framing into the bent on

demand is considered within the effective width of the superstructure.

Positive Moment Connection At Pier Diaphragms

The procedure used to calculate the required number of extended strands is described in this section. Calculations assume the development of the tensile strength of the strands at ultimate loads. Strands used for this purpose must be developed within the short distance between the two girder ends.2

The design moment at the center of gravity of the superstructure, Mpo CG is calculated using the following equation:

$$M_{po}^{CG} = M_{po}^{top} + \frac{\left(M_{po}^{top} + M_{po}^{Base}\right)}{L_c} h \qquad (1)$$

Where:

M_{po}^{top} = plastic overstrength moment at top of column, ft-kips

M_{po}^{Base} = plastic overstrength moment at base of column, ft-kips

h = distance from top of column to c.g. of superstructure, ft

Lc = column clear height used to determine overstrength shear associated with the overstrength moments, ft

This moment is resisted by the bent cap through torsion. The torsional capacity of the bent cat shall be investigated. The torsion in the bent cap is distributed into the superstructure based on the relative flexibility of the superstructure and the bent cap. Hence, the superstructure does not resist column overstrength moments uniformly across its width. To account for this, an effective width approximation is used, where the maximum resistance per unit of superstructure width of the actual structure is distributed over an equivalent effective width to provide an equivalent resistance[3]. The equivalent width concept is illustrated in Figure 2.

For concrete bridges, with the exception of box girders and solid superstructures, this effective width can be calculated as follows:

$$Beff = D_c + D_s \qquad (2)$$

Where:

D_c diameter of column

D_s depth of superstructure including cap beam

Total number of extended straight strands, Nps, needed to develop the required moment capacity at the end of girder is based on the yield strength of the strands:

$$N_{ps} = 12\left[M_{sei} \cdot K - M_{SIDL}\right] \cdot \frac{1}{0.9\phi A_{ps} f_{py} d} \qquad (3)$$

where:

A_{ps} area of each extended strand, in.2

f_{py} yield strength of prestressing steel, ksi

d distance from top of slab to c.g. of extended strands, in.

MSIDL moment due to SIDL (traffic barrier, sidewalk, etc.) per girder

K span moment distribution factor

ϕ strength reduction factor for flexure

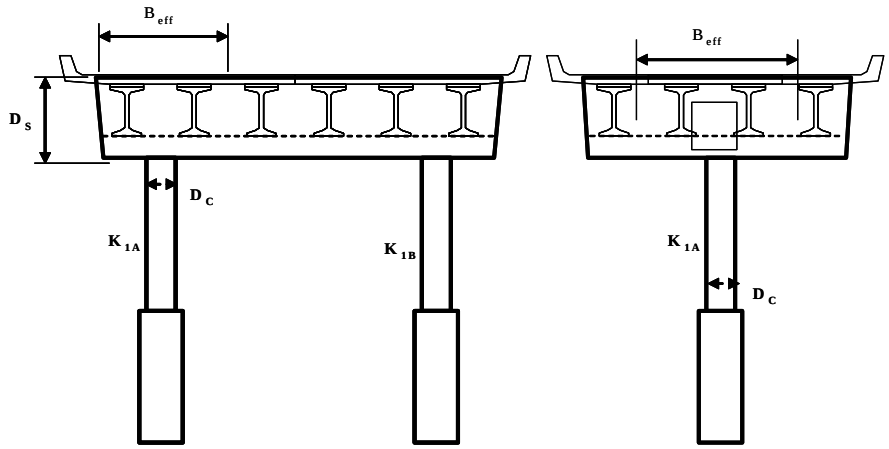

Figure 2: Effective Superstructure Width for Extended Strand Design

Continuity Of Extended Strands

Continuity of extended strands is essential for all prestressed girder bridges with fixed diaphragms at piers. Strand continuity may be achieved by directly overlapping extended strands as shown in Figure 3a, by use of strand ties as shown in Figure 3b in case of curved superstructures with corded precast girders, by the use of the crossbeam ties as shown in Figure 4 along with strand ties, or by a combination of all three methods.

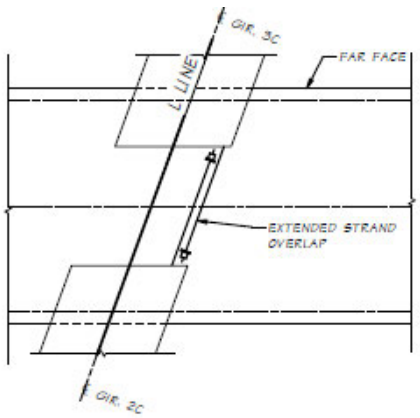

EXTENDED STRAND OVERLAP

3a: Overlapping Extended Strand

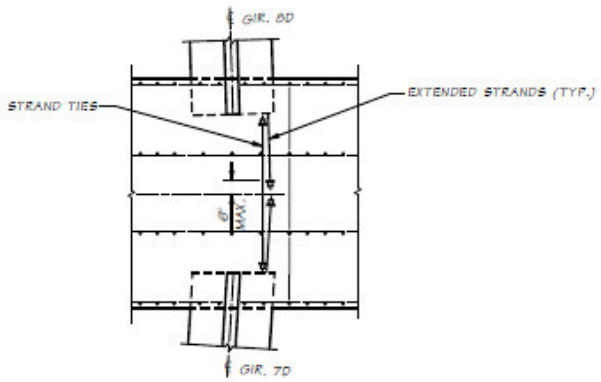

STRAND TIE DETAIL

3b: Strand Ties

Figure 3: Overlapping Extended Strand and Strand Ties

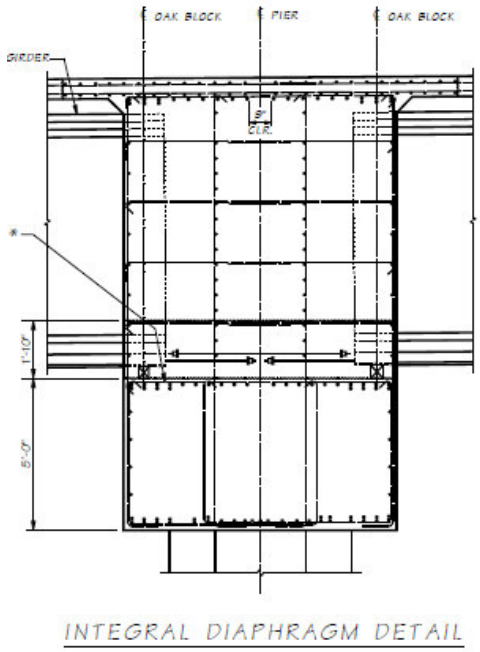

Figure 4: Lower Crossbeam Ties

Strand ties are used at piers with a girder angle point due to horizontal curvature where extended strands are not parallel and would cross during girder placement. The area of transverse ties considered effective for strand ties development in lower crossbeam should not exceed:

$$A_s = \frac{1}{2}\frac{A_{ps} f_{py} n_s}{f_{ye}} \qquad (4)$$

Where:

A_{ps}	Area of strand ties, in2
n_s	Number of extended strands that are spliced with strand and crossbeam ties
f_{py}	Yield strength of extended strands, ksi
f_{ye}	Expected yield strength of reinforcement, ksi

The above equation is driven from the strut and tie model considering the 3-dimensional effect and conservative engineering judgment. Two-thirds of As is placed directly below the girder and the remaining part of As is placed outside the bottom flange width. The size of strand ties is the same as the extended strands, and is placed at the same level and proximity of the extended strands.

Joint Performance For SDCs C And D

Moment-resisting connections for prestressed girder bridges in SDCs C and D are designed to transmit the maximum forces produced when the column has reached its overstrength capacity. A "rational" design is required for joint reinforcement when principal tension stress levels become excessive. The amounts of reinforcement required are based on a strut and tie mechanism similar to that shown in Figure 5 for a hammerhead pier crossbeam[4].

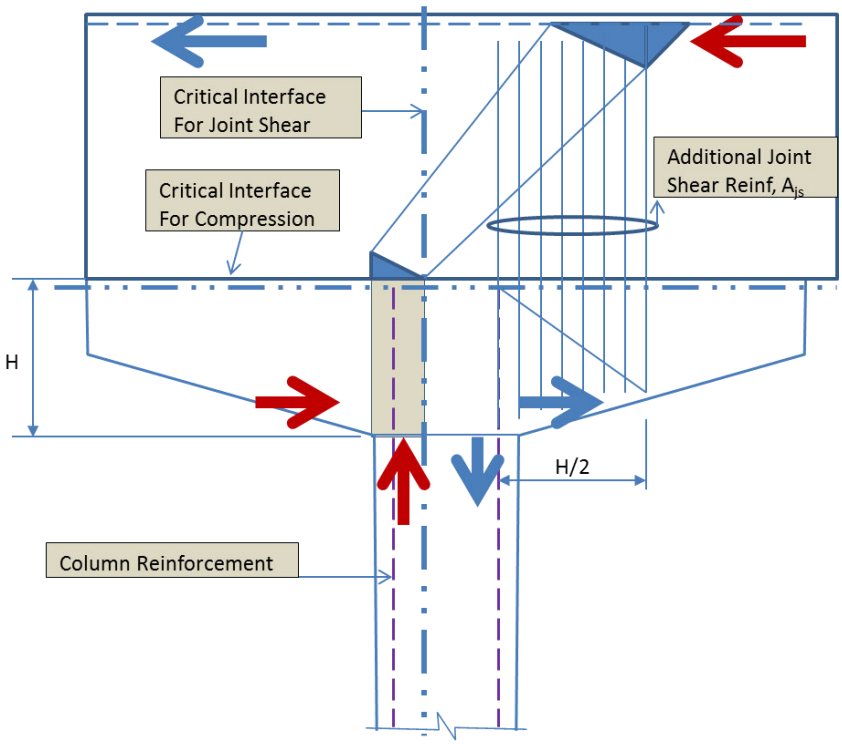

Figure 5: Strut and Tie Model of Intermediate Diaphragm

For precast prestressed girder bridges in SDCs C and D with fixed diaphragms at piers, all column longitudinal reinforcement should be extended into the cast-in-place concrete diaphragm on top of the crossbeam. For bridges in SDC B with fixed diaphragms at piers, column longitudinal reinforcement can be terminated at top of lower crossbeam. Column longitudinal reinforcement can be terminated at top of lower crossbeam in all SDCs if analysis shows that plastic hinging will not occur at the top of column under the design earthquake.

In case of interference, column longitudinal reinforcement obstructing the extended strands should be terminated at the top of the lower crossbeam, and should be replaced with the equivalent full height stirrups extending from the lower to upper crossbeam within the effective zone. The effective zone is defined as the width Dc+Ds1 for columns without headed bars and Dc+2 Ds1 for columns with headed bars, where Dc is the column width or diameter, and Ds1 is the depth of lower crossbeam. Headed bars are only used if the depth of the lower crossbeam is less than 1.25 times the tension development length of column longitudinal reinforcement.

ASTM A706 Grade 80 reinforcing steel may be used for capacity-protected members such as footings, bent caps, oversized shafts, joints, and integral superstructure elements that are adjacent to the plastic hinge locations if the expected nominal moment capacity is determined by strength design based on the expected concrete compressive strength with a maximum usable strain of 0.003, and a reinforcing steel yield strength of 80 ksi with a maximum usable strain of 0.090 for #10 bars and smaller, and 0.060 for #11 bars and larger. The resistance factors for seismic related calculations are taken as 0.90 for shear and 1.0 for bending. ASTM A706 Grade 80 reinforcing steel should not be used for transverse reinforcement in members resisting torsion. The applicability of AASHTO SGS is limited to grade 60 ksi reinforcing steel. Since the suitability of ASTM A706 Grade 80 ksi reinforcing bars for ductility and

confinement has not been tested, the applicability should be limited only to non-ductile elements.

Design Specifications And Guidelines

There are two methods for seismic design of bridges: force-based design by the American Association of State Highway and Transportation Officials' AASHTO LRFD Bridge Design Specifications1 and displacement-based design by the AASHTO Guide Specification for LRFD Seismic Bridge Design.

WSDOT's seismic design is based on the AASHTO guide specification modified by the WSDOT Bridge Design Manual. Displacement-based design is intended to achieve a no-collapse condition for bridges using one level of seismic safety evaluation. The fundamental design principle is capacity protection, where selected elements are identified for plastic hinging while others are protected against potential damage by providing them with sufficient strength to resist the forces consistent with the plastic hinge strengths.

Displacement-based analysis is an inelastic static analysis using the expected material properties of the modeled members. This methodology, commonly referred to as pushover analysis, is used to determine the reliable displacement capacity of a structure as it reaches its limit of structural stability[4].

The procedure outlined in the following steps is for displacement-based analysis and is applicable to bridges made of precast concrete components. The underlying assumption is that the displacement demand obtained from linear-elastic response spectrum analysis can be used to estimate the displacement demand even if there is considerable nonlinear plastic hinging.

1. Develop an analytical model with appropriate foundation stiffness and yielding member stiffness based on moment-curvature relationships. For capacity-protected members, including the precast concrete girder-to-diaphragm connection, consider the properties of the cracked section.
2. Perform linear elastic response spectrum analysis of the bridge based on design acceleration spectra given in national or local specifications.
3. Determine the lateral and longitudinal displacement demands at each pier, including appropriate directional combinations.
4. Perform pushover analysis of each pier in the local transverse longitudinal directions. For this purpose, the plastic hinging behavior for each column must be included, and this will generally be based on the moment-curvature relationships used in step 1. Use foundation stiffness that are consistent with those used in the displacement demand model.
5. Compare the total displacement capacity of the pier, based on concrete and steel strain limits, with the displacement demand. Also compare the displacement ductility demand with the permissible capacity. If either the displacement or ductility capacity is insufficient, revise accordingly.
6. Capacity protect the superstructure and foundation for the overstrength forces (typically, 20% higher than the plastic capacity of the columns) to make sure that plastic hinges occur within the column. Capacity protect the column in shear for these same overstrength forces.

Implementation – From Research To Practice

Figure 6 shows the configuration of the bridge bent system that was developed. It consists of

a cast-in-place concrete spread footing, a precast concrete column, and a precast concrete first-stage cap beam. The second-stage cap beam is cast in place, just as it would be in a fully cast-in-place concrete system[5].

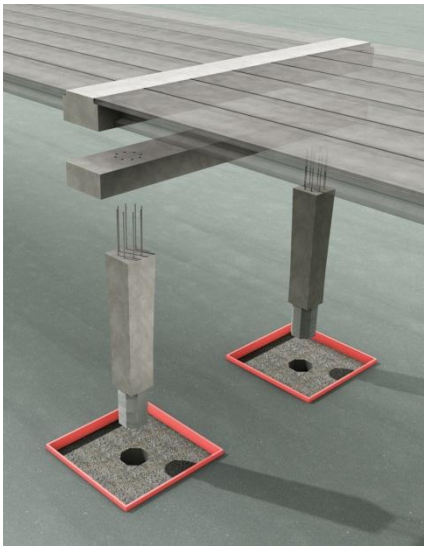

Figure 6. Precast concrete bent system configuration.

Figure 7. Previous use of precast concrete cap beam that used in Washington State.

The socket concept was used previously in Washington in a modified form. In that case, the contract called for cast-in-place concrete columns, but the contractor elected to precast them on-site and use a socket connection to save time. The footing was 6 ft (1.8 m) thick, the columns were 4 ft (1.2 m) square, and the connection between them was made by roughening the column surface locally and adding horizontal form-saver bars. Those bars screwed into threaded couplers embedded in the face of the column within the depth of the footing to provide shear friction across the interface and were inserted after the column had been placed.

The column-to-cap beam connection was made with vertical bars projecting from the column that were grouted into ducts in the cap beam. Again, this concept has been used previously, but primarily in regions of low seismicity where the number of bars needed for the connection was small and the loading was not cyclic. The concept was also used once in the high seismic zone in western Washington. The bridge site is in a congested urban area with high visibility from the traveling public and high scrutiny from associated municipalities. To open the bridge as quickly as possible, the contractor proposed precasting the cap beams for

the intermediate piers instead of casting them in place as shown on the contract plans. This change saved the owner and the contractor several weeks. The columns were reinforced with the same fourteen no. 14 (43M) column bars as on the original plans. They were grouted into 4 in. (100 mm) galvanized steel ducts that were placed in the precast concrete cap beam using a template. The cap beams weighed approximately 200 kip (890 kN) each and were precast on the ground adjacent to the columns.

The material characteristics in the tests included ASTM A70610 Grade 60 (410 MPa) deformed reinforcing bars, corrugated galvanized pipes, and cementitious grout with compressive strength of 8.0 ksi (56 MPa). The corrugated pipes are available in diameters from 6 in. (150 mm) to 12 ft (3.7 m). The pipes have thicker walls, deeper corrugations, and potentially better bond and confinement properties than those of standard posttensioning ducts.

Figure 8 summarizes the results of the pullout tests. It shows the bar stress at failure plotted against the ratio of embedment length to bar diameter le/dbto permit comparison among different bar sizes. In the nomenclature for the tests, 18N06 means a no. 18 (57M) bar with no fiber in the grout embedded 6 bar diameters. The letter F signifies fibers in the grout, N signifies no fibers, and S indicates a failure near the surface, which was controlled by a tension failure cone in the concrete surrounding the duct, rather than a shear failure in the grout.

The fibers were polypropylene with a dosage of 3 lb/yd3 (1.8 kg/m3). They were used in some pull- out specimens, but they adversely affected the grout strength and therefore the anchorage performance, so they were not used in the final connection. A non- linear numerical model was calibrated against the test results, and the model's results are also shown. Finally, separate lines show the nominal yield and ultimate stresses of the bars.

Three outcomes can be seen from the tests. First, the bar stress at failure is essentially proportional to le/db. This implies that the bond stress is constant along the bar and the same in all specimens and that failure was by plastic shear failure in the grout. Visual observations supported that finding. Second, the bar can be anchored to reach yield and fracture if the embedment lengths are 6db and 10db, respectively.

Once the anchorage properties under monotonic tension loading had been established, column-to-cap beam connection tests were conducted under cyclic lateral loading. Figure 10 shows a typical test. The specimens were tested upside down so that the cap beam could be bolted to the base of the test rig. The specimens were 42% scale, so the 20 in. (500 mm) test column represented a 48 in. (1200 mm) prototype. The goal was to investigate the behavior of complete grouted bar connections under cyclic lateral load[6].

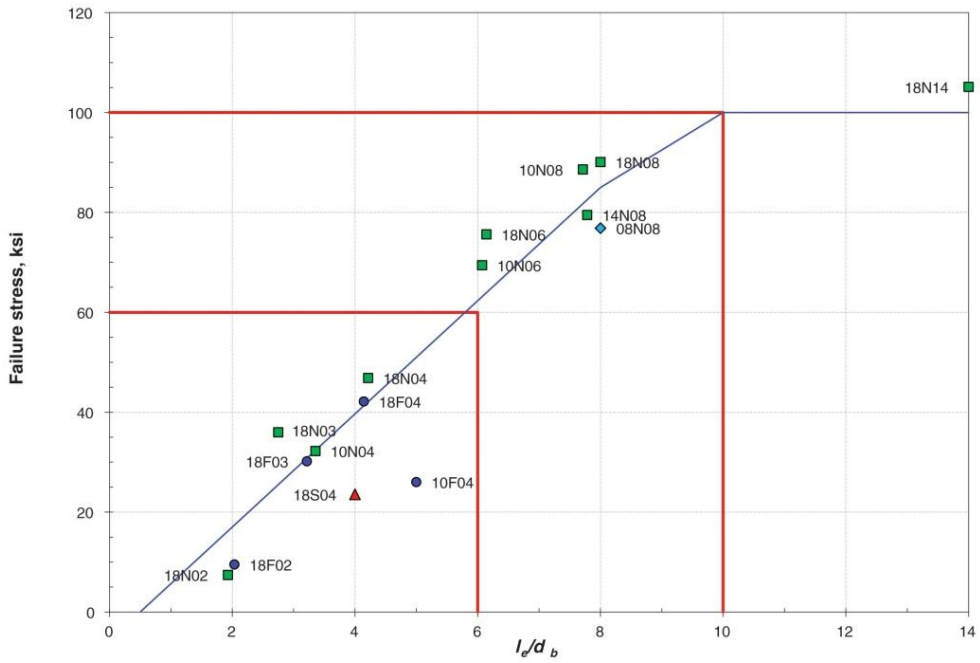

Figure 8. Grouted bar-duct pullout test results. Note: db = bar diameter; le = embedment length. 1 ksi = 6.895 MPa.

The cyclic tests were performed on three variations of the large bar precast concrete system, as well as a typical cast-in-place concrete connection for comparison. All three variations of the proposed system performed satisfactorily to a drift ratio of 5.5%, after which longitudinal bar buckling and fracture occurred. This value is approximately three times the demand expected in a major earthquake and is comparable to the value achieved with a cast-in- place concrete system. In all cases the failure occurred in the plastic hinge region of the column. This finding suggests that the large-bar, large-duct precast concrete system has sufficient strength and ductility capacity for all foreseeable seismic demands and system performance is similar to that of cast-in-place concrete construction.

Figure 9. Construction and testing of precast concrete column-to-footing connection.

Site implementations- From Research to Practice

Figures 10 through 12 show the details of this project. The bridge features include the

following:

- unique socket connection of precast concrete column to footing
- precast concrete columns fabricated in segments and joined by bars grouted in ducts
- precast concrete cap beam made in two segments that were joined by a cast-in-place concrete closure
- precast concrete superstructure with cast-in-place concrete closure at intermediate pier

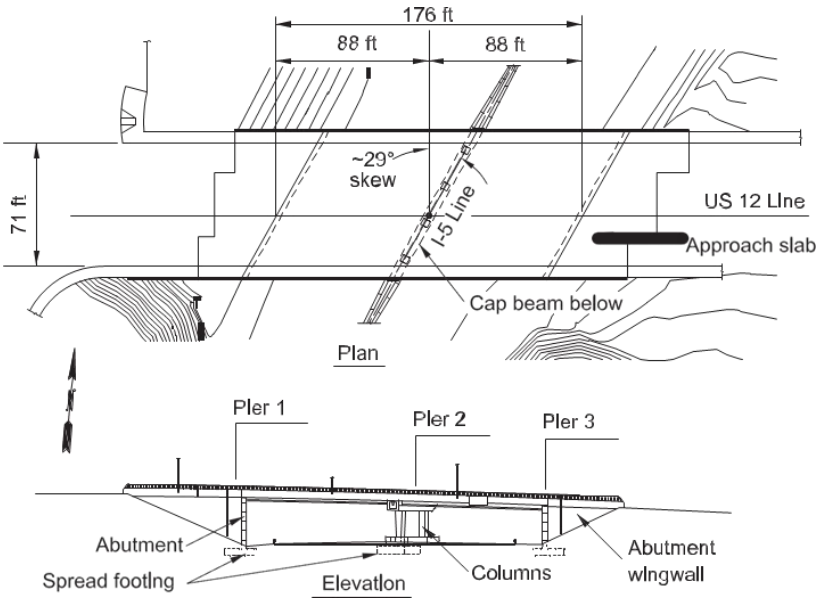

Figure 10. Bridge layout for demonstration project.

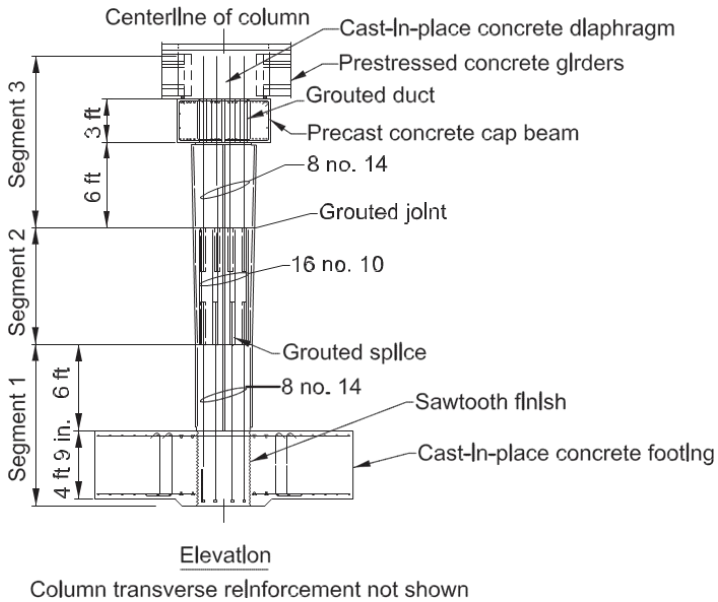

Figure 11. Demonstration bridge column details for elevation.

The construction sequence for placement of the precast concrete superstructure at the intermediate pier is as follows:

- Place precast concrete girders on oak blocks.
- Install girder bracing as necessary.
- Complete welded ties between girders.

- Join flange shear keys and grout intermediate diaphragms.
- Place slab reinforcement and cast concrete.
- Cast pier diaphragm concrete 10 days after slab casting. Each deck bulb tee was fitted with precast concrete transverse end walls to serve as side forms for the cast-in-place concrete pier diaphragm.

Figure 12. Placement of precast concrete cap beam.

Conclusion

The precast concrete bridge bent system presented that conceptually simple, can be constructed rapidly, and offers excellent seismic performance. Precast concrete bridge systems are an economical and effective means for rapid bridge construction. Precasting eliminates traffic disruptions during bridge construction while maintaining quality and long-term performance. The following conclusions are drawn:

1. The system described here addresses the demands of both seismic performance and constructability. It provides an example of a successful transfer of research to practice but was possible only through the close cooperation between team members representing research, design, fabrication, and construction.
2. The column-to-cap beam connection is made with a small number of large bars grouted into ducts in the cap beam. Their small number and the correspondingly large ducts sizes that are possible lead to a connection that can be assembled easily on-site.
3. The development length of a reinforcing bar grouted into a corrugated steel pipe is much shorter than implied by current code equations for a bar embedded directly in concrete.
4. The socket connection between the cast-in- place spread footing and the precast concrete column provides excellent performance under combined constant vertical and cyclic lateral loading and is quick and easy to construct.
5. Column longitudinal reinforcement can be terminated at the top of the lower crossbeam in all SDCs if analysis shows that plastic hinging will not occur at the top of the column under the design earthquake.

References

1. AASHTO Guide Specifications for LRFD Seismic Bridge Design, 2nd Edition,

2011.

2. Bridge Design Manual, Publication No. M23-50, Washington State Department of Transportation, Bridge and Structures Office, Olympia, Washington, 2010.
3. Khaleghi, B. 2010. “Washington State Department of Transportation Plan for Accelerated Bridge Construction.” Transportation Research Record: Journal of the Transportation Research Board (2200): 3–11.
4. Marsh, M. L., M. Wernli, B. E. Garrett, J. F. Stanton, M. O. Eberhard, and M. D. Weinert. 2011. “System Performance of Accelerated Bridge Construction (ABC) Connections in Moderate-to-High Seismic Regions.” NCHRP (National Cooperative Highway Research Program) Synthesis of Highway Practice report 698. Washington, DC: NCHRP.
5. WSDOT Highways for LIFE (HfL) Project. “US 12 over I-5, Grand Mound to Maytown Interchange Phase 2 Bridge 12/118 Replacement.” WSDOT Olympic Region.
6. Stanton, J. F., M. O. Eberhard, M. L. Marsh, B. Khaleghi, O. S. Haraldsson, T. M. Janes, H. Viet Tran, and P. Davis. 2012. “Bent on Safety: New Design Toughens ABC During Seismic Events.” Roads and Bridges 50 (1): 36–41.

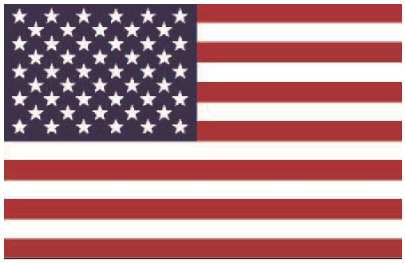

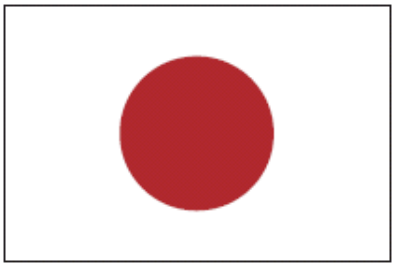

29th US-Japan

Bridge Engineering Workshop

Appendix 1:

Japan Participants

Hidekazu Hayashi
Researcher
Road Research Department Bridge Division
Nippon Expressway Research Institute Company Limited
1-4-1, Tadao, Machida-shi, Tokyo, 194-8508, Japan
Phone: +81-42-791-1625
Fax: +81-42-791-2380
E-mail: h.hayashi.ac@ri-nexco.co.jp

Yusuke Honjo
Professor
Department of Civil Engineering, Gifu-University
1-1 Yanagito, Gifu-shi, Japan 501-1193
Phone: +81-58-293-2435
Fax: +81-58-293-2398,
E-mail: honjo@gifu-u.ac.jp

Hidetaka Homma
Senior Researcher
Bridge and Structural Technology Research Group
Center for Advanced Engineering Structural Assessment and Research
Public Works Research Institute (PWRI)
1-6, Minamihara, Tsukuba, Ibaraki, 305-8516, Japan
Phone: +81-29-879-6773
Fax: +81-29-879-6739
E-mail: honma@pwri.go.jp

Jun-ichi Hoshikuma
Chief Researcher
Bridge and Structural Technology Research Group
Center for Advanced Engineering Structural Assessment and Research
Public Works Research Institute (PWRI)
1-6, Minamihara, Tsukuba, Ibaraki, 305-8516, Japan
Phone: +81-29-879-6793
Fax: +81-29-879-6739
E-mail: hosikuma@pwri.go.jp

Masahiro Ishida
Chief Researcher
Bridge and Structural Technology Research Group
Center for Advanced Engineering Structural Assessment and Research
Public Works Research Institute (PWRI)
1-6, Minamihara, Tsukuba, Ibaraki, 305-8516, Japan
Phone: +81-29-879-6793
Fax: +81-29-879-6739
E-mail: ishida@pwri.go.jp

Yuichi Ishikawa
Assistant Manager
Road Engineering Department, Kanazawa Branch
Central Nippon Highway Engineering Nagoya Co. Ltd.
3-7-1 Ekinishi-Honmachi, Kanazawa
ISHIKAWA, 920-0025, JAPAN
Ph: +81-76-264-7872
FAX: +81- 76-264-7878
Email: y.ishikawa.a@c-nexco-hen.jp

Shojiro Kataoka
Senior Researcher
Earthquake Disaster Prevention Division
National Institute for Land and Infrastructure Management (NILIM)
Ministry of Land, Infrastructure, Transport and Tourism (MLIT)
1 Asahi, Tsukuba 305-0804, Japan
Phone: +81-29-864-7682
Fax: +81-29-864-0598
Email: kataoka-s92rc@nilim.go.jp

Yoshitomi Kimura
Chief Researcher
Bridge and Structural Technology Research Group
Center for Advanced Engineering Structural Assessment and Research
Public Works Research Institute (PWRI)
1-6, Minamihara, Tsukuba, Ibaraki, 305-8516, Japan
Phone: +81-29-879-6793
Fax: +81-29-879-6739
E-mail: y-kimura@pwri.go.jp

Kenji Kosa
Professor of Civil Engineering
Kyushu Institute of Technology
Department of Civil Engineering
Kyushu Institute of Technology
Sensui 1-1, Tobata, Kitakyushu, 804-8550 JAPAN
Phone & Fax: +81-93-884-3123
E-mail: kosa@civil.kyutech.ac.jp

Tsuyoshi Kosugi
Third Management Division,
Structural Management Department,
Shutoko Engineering Co., LTD.
2-6-4, Kanagawa, Kanagawa-ku,
Yokohama, Kanagawa Prefecture
Phone: +81-45-461-6159
Fax: +81-461-6472
Email: kosugi@shutoko-eng.jp

Takaaki Kusakabe
Research Coordinator for Earthquake Disaster Prevention
Research Center for Disaster Management
National Institute for Land and Infrastructure Management (NILIM)
Asahi 1, Tsukuba-shi, Ibaraki-ken 305-0804 Japan
Phone: +81-29-864-4963
Fax: +81-29-864-0903
E-mail kusakabe-t88d8@nilim.go.jp

Masato Matsumoto
Executive Vice President, NEXCO-West USA, Inc.
1015, 18th Street, N.W., Suite 504
Washington, D.C., 20036
Phone: 202- 223-7040
Fax: 202- 296-5373
Email: m.matsumoto@w-nexco-usa.com

Hiroshi Matsuura
Director of Bridge and Structural Engineering Research Group,
Center for Advanced Engineering Structural Assessment and Research
Public Works Research Institute (PWRI)
1-6 Minamihara, Tsukuba-shi, Ibaraki-ken 305-8516 Japan
Phone: +81-29-879- 6726
Fax: +81-29-879-6739
E-mail h-matsuura @pwri.go.jp

Jun Murakoshi
Chief Researcher,
Bridge and Structural Technology Research Group
Center for Advanced Engineering Structural Assessment and Research
Public Works Research Institute (PWRI)
1-6, Minamihara, Tsukuba, Ibaraki, 305-8516, Japan
Phone: +81-29-879-6773
Fax: +81-29-879-6739
E-mail:murakosi@pwri.go.jp

Hiroyuki Nagareta
Chief
Moriguchi Junction Construction Supervision office,
Osaka Construction Department,
Hanshin Expressway Company Limited, Osaka, Japan
2-82-22, Yagumohigashimachi, Moriguchi-shi,
Osaka, 570-0021, Japan
Ph: +81-6-4301-3600
FAX: +81-6-6901-3618
Email: hiroyuki-nagareta@hanshin-exp.co.jp

Ryohei Nakamura
Engineer
Design Estimation and Appraisal Group,
Construction Management Headquarters,
Hanshin Expressway Company Limited, Osaka, Japan
1-3-15, Awaza, Nishi-ku, Osaka, 550-0011, Japan
Ph: +81-6-6535-9544
FAX: +81-6-6535-0733
Email: ryohei-nakamura@hanshin-exp.co.jp

Hisashi Nakao
Research Specialist
Bridge and Structural Technology Research Group
Center for Advanced Engineering Structural Assessment and Research
Public Works Research Institute (PWRI)
1-6, Minamihara, Tsukuba, Ibaraki, 305-8516, Japan
Phone: +81-29-879-6773
Fax: +81-29-879-6739
E-mail: nakao55@pwri.go.jp

Toshiaki Nanazawa
Chief Researcher
Bridge and Structural Technology Research Group
Center for Advanced Engineering Structural Assessment and Research
Public Works Research Institute (PWRI)
1-6, Minamihara, Tsukuba, Ibaraki, 305-8516, Japan
Phone: +81-29-879-6773
Fax: +81-29-879-6739
Email: nanazawa@pwri.go.jp

Hideaki Nishida
Senior Researcher
Bridge and Structural Technology Research Group
Center for Advanced Engineering Structural Assessment and Research
Public Works Research Institute (PWRI)
1-6, Minamihara, Tsukuba, Ibaraki, 305-8516, Japan
Phone: +81-29-879-6773
Fax: +81-29-879-6739
Email: nisida@pwri.go.jp

Kiyoshi Ono
Associate Professor of Civil Engineering
Osaka University, Department of Civil Engineering
Graduate school of Engineering
Osaka University
2-1 Yamadaoka, Suita City, Osaka 565-0871, Japan
Phone: +81-6-6879-7598
Fax: +81-6-6871-7601
E-mail: k-ono@civil.eng.osaka-u.ac.jp

Masatsugu Shinohara
Senior Researcher
Bridge and Structural Technology Research Group
Center for Advanced Engineering Structural Assessment and Research
Public Works Research Institute (PWRI)
1-6, Minamihara, Tsukuba, Ibaraki, 305-8516, Japan
Phone: +81-29-879-6773
Fax: +81-29-879-6739
E-mail: shinohara@pwri.go.jp

Masahiro Shirato
Senior Researcher,
Bridge and Structures Division, Road Department
National Institute for Land and Infrastructure Management
Ministry of Land, Infrastructure, Transport and Tourism (MLIT)
1 Asahi, Tsukuba, Ibaraki, 305-0804 JAPAN
Phone: +81-29-864-4919
Fax: +81-29-864-0178
Email: shirato-m92ta@nilim.go.jp

Takashi Tamakoshi
Head,
Bridge and Structures Division, Road Department
National Institute for Land and Infrastructure Management
Ministry of Land, Infrastructure, Transport and Tourism (MLIT)
1 Asahi, Tsukuba, Ibaraki, 305-0804 JAPAN
Phone: +81-29-864-4919
Fax: +81-29-864-0178
Email: tamakoshi-t92gd@nilim.go.jp

Tomonobu Tokuchi
Deputy Design Manager
Nhat Tan Project Dept.
Overseas Project Div.
IHI Infrastructure systems Co., Ltd
3 Ohama Nishi-machi, Sakai-ku, Sakai-city,Osaka 590-0977 Japan.
Ph: +81-(72) 223-0915
FAX: +81-(72) 223-0972
Email: Tomonobu_Tokuchi@iis.ihi.co.jp

Shigeki Unjoh
Research Coordinator for Earthquake Engineering
Center for Advanced Engineering Structural Assessment and Research
Public Works Research Institute (PWRI)
Minamihara 1-6, Tsukuba-shi, Ibaraki-ken 305-8516 Japan
Phone: +81- 879-6721
E-mail unjoh@pwri.go.jp

Eiki Yamaguchi
Professor of Civil Engineering
Dept. of Civil Engineering
Kyushu Institute of Technology
Kitakyushu, 804-8550, Japan
Phone: +81-93-884-3110
Fax: +81-93-884-3100
E-mail: yamaguch@civil.kyutech.ac.jp

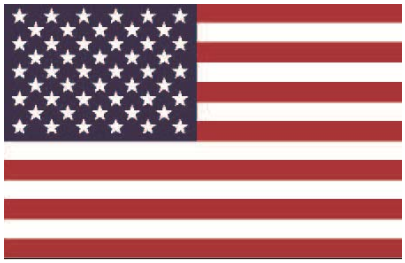

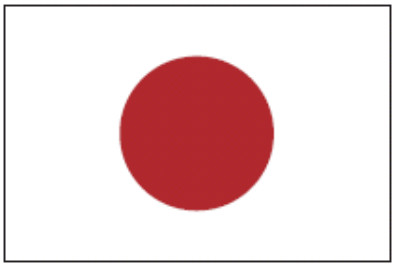

29th US-Japan

Bridge Engineering Workshop

Appendix 2:

US Participants

Tony M. Allen
State Geotechnical Engineer
Washington State Dept. of Transportation
State Materials Laboratory
P.O. Box 47365, Olympia, WA 98504-7365
Phone: (360) 709-5450,
E-mail: allent@wsdot.wa.gov

Raimondo Betti
Professor of Civil Engineering and Engineering Mechanics
Columbia University, New York
Dept. of Civil Engr. and Engr. Mech./640
Columbia University, New York, NY 10027
Phone: (212) 854-6388
Fax: (212) 854-6267
Email: rb68@columbia.edu

Ian G. Buckle
Foundation Professor, and
Director, Center for Civil Engineering Earthquake Research
University of Nevada, Reno
Dept. of Civil and Environmental Engineering, MS 258
Reno, NV 89557-0152
Phone: 775-784-1519
Fax: 775-784-4213
Email: igbuckle@unr.edu

Xiaohua "Hannah" Cheng
Principal Engineer, Bureau of Structural Engineering
New Jersey Department of Transportation
1035 Parkway Ave., Trenton, NJ 08625, USA
Phone: (609) 530-2464
FAX: (609) 530-2704
Email: Xiaohua.Cheng@dot.state.nj.us

Peter Dusicka
Associate Professor of Civil and Environmental Engineering
Portland State University
Department of Civil and Environmental Engineering
Portland State University PO BOX 751, Portland, OR 97207
Phone: (503) 725-9558
FAX: (503) 725-5950
Email: dusicka@pdx.edu

Christopher C. Higgins
Professor of Civil and Construction Engineering
Oregon State University, Corvallis, OR
Visiting Professor
Tokyo Institute of Technology

School of Civil and Construction Engineering
101 Kearney Hall
Oregon State University; Corvallis, OR 97331
Phone: (541) 737-8869
Fax: (541) 737-3052
Email: chris.higgins@oregonstate.edu

Bruce Johnson
State Bridge Engineer
Oregon DOT Bridge Section
ODOT Bridge Section
4040 Fairview Industrial Dr. SE, Salem, Oregon 97302
Phone: 503-986-3344
Email: Bruce.V.Johnson@odot.state.or.us

Bijan Khaleghi
State Bridge Design Engineer
Washington State Department of Transportation
7345 Linderson Ave SW
Tumwater WA 98501
Phone: (360) 705-7181
Fax: (360) 705-6812
Email: khalegb@wsdot.wa.gov

Ali Maher
Professor and Director
Center for Advanced Infrastructure and Transportation
Civil and Environmental Engineering
Rutgers University
Center for Advanced Infrastructure and Transportation
Rutgers University
100 Brett Road
Piscataway, NJ 08854
Phone: (848) 445-2951
Fax: (732) 445-3325
Email: mmaher@rci.rutgers.edu

Jamie Ellen Padgett
Assistant Professor of Civil and Environmental Engineering
Rice University
6100 Main Street, MS-318
Rice University
Houston, TX 77056
Phone: (713) 348-2325
Fax: (713) 348-5268
Email: jamie.padgett@rice.edu

Mark L. Reno
Principal Engineer
Quincy Engineering, Inc.
3247 Ramos Circle
Sacramento, CA 95827-2501
Phone: (916) 368-9181
Fax: (916) 368-1308
Email: markr@quincyeng.com

David Sanders
Professor
Department of Civil and Environmental Engineering
University of Nevada, Reno
1664 N. Virginia St/MS 258
Reno, NV 89557-0258
Phone: 775-784-4288
Fax: 775-784-1390
Email: sanders@unr.edu

Mark Yashinsky
Senior Bridge Engineer at the California Department of Transportation (Caltrans)
Caltrans Office of Earthquake Engineering MS9
1801 30th Street, Sacramento, CA 95816
Phone: (916) 227-8719
Fax: (916) 227-8898
Email: mark.yashinsky@dot.ca.gov

W. Phillip Yen
Principal Bridge Engineer - Structural Dynamics
Office of Bridge Technology, FHWA
1200 New Jersey Avenue, SE, HIBT-1/E73-421
Washington, DC 20590
Phone: 202-366-5604

Fax: 202-366-3077
Email: Wen-huei.yen@dot.gov